

University of Wollongong

Research Online

---

University of Wollongong Thesis Collection  
2017+

University of Wollongong Thesis Collections

---

2017

## Development and Application of Porphyrin-Maquette Complexes: Towards Artificial Photosynthesis

Christopher James Hobbs  
*University of Wollongong*

Follow this and additional works at: <https://ro.uow.edu.au/theses1>

**University of Wollongong**

**Copyright Warning**

You may print or download ONE copy of this document for the purpose of your own research or study. The University does not authorise you to copy, communicate or otherwise make available electronically to any other person any copyright material contained on this site.

You are reminded of the following: This work is copyright. Apart from any use permitted under the Copyright Act 1968, no part of this work may be reproduced by any process, nor may any other exclusive right be exercised, without the permission of the author. Copyright owners are entitled to take legal action against persons who infringe their copyright. A reproduction of material that is protected by copyright may be a copyright infringement. A court may impose penalties and award damages in relation to offences and infringements relating to copyright material.

Higher penalties may apply, and higher damages may be awarded, for offences and infringements involving the conversion of material into digital or electronic form.

Unless otherwise indicated, the views expressed in this thesis are those of the author and do not necessarily represent the views of the University of Wollongong.

---

### Recommended Citation

Hobbs, Christopher James, Development and Application of Porphyrin-Maquette Complexes: Towards Artificial Photosynthesis, Doctor of Philosophy thesis, School of Chemistry, University of Wollongong, 2017. <https://ro.uow.edu.au/theses1/227>

Research Online is the open access institutional repository for the University of Wollongong. For further information contact the UOW Library: [research-pubs@uow.edu.au](mailto:research-pubs@uow.edu.au)

AGREEMENT FOR DEPOSIT OF HDR THESIS IN DIGITAL REPOSITORY - KEY DETAILS

UOW is committed to making HDR theses publicly available but restricted access is possible for reasons nominated under 10, below. If you wish for access to your thesis to be restricted, your Principal Supervisor must approve and sign this form. If access to the thesis is unrestricted then no supervisor signature is necessary.

1.	Student Name	Christopher J. Hobbs	
2.	Student No	3279601	3. Email address ch147@uowmail.edu.au
4.	School	Chemistry	
5.	Faculty	SMAH	
6.	Supervisor	Prof. David Officer	
7.	Title of thesis	Development and Application of Porphyrin-Maquette Complexes: Towards Artificial Photosynthesis	
8.	Keywords	List up to 6 keywords Maquette, porphyrin, artificial photosynthesis, de novo designed, protein immobilization, TIO2	
9.	*Field of Research (FOR) codes (optional) See explanation over page	List up to 4 FOR codes (4 or 6 digit codes only) 030304	
10.	Restricted Access If a restriction is required, please consult your supervisor prior to completing this section	<p>Is a restriction required for this thesis, or part thereof?            Yes <input type="checkbox"/> No <input checked="" type="checkbox"/></p> <p>If Yes:            a) Nominate restriction period: 6 <input type="checkbox"/> 12 <input type="checkbox"/> 18 <input type="checkbox"/> 24 <input type="checkbox"/> months            b) Provide details of the reason for the restriction:            Publishing <input type="checkbox"/> Third party copyright <input type="checkbox"/>            Commercial/ in confidence <input type="checkbox"/> Other (please specify) <input type="checkbox"/></p> <p><b>NOTE:</b> If you require sections of your thesis to be restricted, you must supply 2 copies - the original copy for library records and the restricted copy, which will be made publicly available during the restricted period.</p>	
11.	Release of thesis automatically at the end of the expiry period (if applicable)	<p>Yes <input type="checkbox"/> No <input type="checkbox"/></p> <p>(To ensure your thesis is deposited and accessible via the UOW digital repository at the expiry of the restriction period, tick Yes)  <b>NOTE:</b> If you tick No, the Library will contact your supervisor at the end of the expiry period to request release of the thesis</p>	
12.	Third party copyright material that has been used without consent (if applicable)	<p>If the thesis contains material whose copyright belongs to a third party and has been used without consent:            a) Would gaining consent to include the third party copyright material in the electronic copy of the thesis be onerous or expensive?            Yes <input type="checkbox"/> No <input type="checkbox"/>            b) Would removal of the copyright material compromise the thesis?            Yes <input type="checkbox"/> No <input type="checkbox"/></p>	

\*Field of Research (FoR) code classifications are used in the measurement and analysis of research and experimental development (R&D) undertaken in Australia, according to the field of research. In this respect, it is the methodology used in the R&D that is being considered. UOW uses FoR codes to classify research outputs, and has been used to report research data to the Commonwealth Government.

The FoR has three hierarchical levels, namely Divisions (at the broadest subject or discipline level), Groups and Fields (at finer levels). Students submitting their HDR thesis have the option to classify their research using the Group level (4 digit code) or Field level (6 digit code). All Divisions, Groups and Fields are assigned unique codes.

## TERMS & CONDITIONS

### 1. Definitions

#### 1.1. In this Agreement:

"Digital Repository" means Research Online or any other open access electronic repository operated by UOW or its agents;

"UOW" means the University of Wollongong;

"Work" means the thesis you are depositing including any abstract, object, text, image and related data;

"You" means the Candidate identified in Item 1 of the Key Details;

"Third party copyright" means any material where the copyright is owned by another person

### 2. Your warranties

#### 2.1. You warrant that:

(a) all or part of the Work is your original work;

(b) the Work does not violate or infringe any copyright, trademark, patent or other rights of any person;

(c) if you have used another person's copyright work or intellectual property rights:

(i) you have obtained permission from that person for the use of this material as contemplated by this agreement; or

(ii) you have confirmed in item 12 of the Key Details reasons you have not obtained permission to use or to grant to UOW the licence contemplated by this agreement;

(d) if the Work has been commissioned, sponsored or supported in any way, you have fulfilled all obligations required by such contract or agreement;

(e) the Work may be deposited in the Digital Repository without breaching the intellectual property rights of any third party provided UOW complies with any restrictions identified in items 10 and 12 of the Key Details.

### 3. UOW rights

#### 3.1. You grant UOW a perpetual, non-exclusive, worldwide, royalty-free, sub-licensable licence to:

(a) deposit the Work in the Digital Repository;

(b) distribute copies of the Work (including the abstract) in electronic format;

(c) electronically store and copy the Work; and

(d) convert the Work to any format necessary for the preservation of the Work or the deposit on the Digital Repository.

#### 3.2. UOW:

(a) may remove the Work from the Digital Repository for professional or administrative reasons at its sole discretion;

(b) is not under any obligation to take legal action on your behalf in the event breaches of your intellectual property rights stem from the deposit of the work in the Digital Repository;

(c) is not under any obligation to reproduce, transmit, broadcast or display the work in any particular format; and

(d) is not liable for any loss or damage to the Work whilst stored in the Digital Repository.

#### 3.3. If you have used another person's copyright work without consent as identified under item 12 of the Key Details UOW may:

- (a) remove this material from the Work and deposit in the Digital Repository;
- (b) deposit only the metadata of the Work in the Digital Repository; or
- (c) elect not to deposit the Work in the Digital Repository.

I declare my digital thesis is the final version approved by the University for the award of the degree.

  
30-04-2018

Student (candidate) signature

Date of student (candidate) signature

If restricted access is nominated, your Principal Supervisor must sign

Signature of Principal Supervisor

Date of supervisor signature

**Development and Application of Porphyrin-Maquette  
Complexes:  
Towards Artificial Photosynthesis**

---



A thesis submitted in (partial) fulfilment of the requirements for the award of the degree of

**Doctor of Philosophy**

**in Chemistry**

at

**The University of Wollongong**

**Australia**

**Christopher James Hobbs**

**Supervisors**

Professor David L. Officer

Doctor Klaudia Wagner

Doctor Pawel Wagner

March 2017

---

*Thesis Declaration*

---

This is a declaration that this thesis, submitted by Christopher J. Hobbs, is wholly my own work unless otherwise referenced or acknowledged, submitted in partial fulfilment of the requirements of the award of Doctor of Philosophy, in the School of Chemistry at the University of Wollongong. This document has not been submitted for qualifications at any other academic institution.



Christopher James Hobbs

March 2017

## Acknowledgements

This thesis is ultimately the culmination of many (and quite frankly, far too many) years of study. It has not only made me struggle in every facet of the word, but also gained new appreciation for exploring the what's, why's, and how's of the world. These can be summated as curiosity, with everyone born with unprecedented curiosity about the natural world, immortalised by Einstein with (paraphrasing) 'I have no special talent, I am only passionately curious' conveying how much can be accomplished if one were to follow their curiosity- just look at Einstein's accomplishments. As such, I implore you, whoever is reading this thesis, to have curiosity whilst exploring this work.

Ultimately, I would have not been able to produce this thesis without the explicit impacts that many people have had on my studies- to which I will try to acknowledge and ask forgiveness from anyone missed.

First and foremost, my parents Wayne R. Hobbs and Helen A. Hobbs, needing no other explanation for their incomparable impact on this work other than the fact that I would not have been able to accomplish nor even attempt to undertake this monumental task along with the many experiences made available during the whole of my studies.

My supervisors Professor David Officer along with Dr Klaudia Wagner and Dr Pawel Wagner, consistently surprising me with and making available their wealth of knowledge in the many aspects of scientific research. Your guidance, recommendations, and general mentoring were invaluable for the completion of this thesis, and will not be easily forgotten.

My go-to chemists, Nicholas Roach and Rhys Mitchell, allowing me to constantly pester with questions regarding what is possible with regards to synthesising random compounds. But maybe a greater contribution was their friendship and simultaneous struggles during the PhD process- it seemed easier to be suffering together rather than alone.

I am forever appreciative of Professor Leslie Dutton and Professor Keith Gordon of the University of Pennsylvania and the University of Otago, respectively, for allowing visits to their laboratories and constant collaborative efforts throughout my thesis. Furthermore, Dr. Bohdana Discher for allowing me to graciously stay at here place during my visits to Pennsylvania. This had an impact on my life to almost a degree to which this thesis has.

Finally, two major players in the photovoltaics lab of IPRI, Dr Andrew Nattestad and Joseph Giorgio for their guidance with using previously unknown and obscure equipment. Without their help, half of the available equipment would likely still be a mystery to me.

## Abstract

This study looks at developing an artificial reaction centre with photogenerated electron transfer. Naturally occurring photosynthetic reaction centres utilise proteins to house photoactive material, which is coupled with redox enzymes for catalytic reactions to produce chemical fuels. Photosynthetic systems provide inspiration for designing new means to produce renewable energy, whereby sunlight can produce fuels in the form of chemical energy. Artificially designed proteins with synthetically produced porphyrins can potentially be employed to mimic the natural photosynthetic reaction centre for light-induced charge separation. This charge separation is fundamental for conversion of light energy to other forms of energy.

*De novo* designed proteins (maquettes) have been specially synthesised to simplify the complexity of natural proteins, whilst retaining specific functionality. Maquettes can incorporate a range of cofactors, including photo-active materials such as porphyrins, with the non-covalent binding akin to the proteins of reaction centres in nature. Porphyrin synthesis is relatively cheap and simple, allowing for tailoring of the material for specific functions. Furthermore, porphyrins incorporate a metal centre, which is exploited for binding into maquettes via ligation to histidine residues. Therefore, the key objective of this thesis was to develop and study porphyrin-maquette complexes in order to create an artificial reaction centre model for light induced charge separation.

The effect of the hydrophobic/hydrophilic functionality of cofactors (such as porphyrins) for optimal binding within maquettes is largely unknown. Within this study, UV-vis. and resonance Raman spectroscopy was used to explore a variety of porphyrins of increasing hydrophilicity for potential incorporation within maquettes. Both cationic and anionic porphyrin substituent aryl groups were explored for increasing the porphyrin hydrophilicity, and the impact of these charged groups on maquette binding assessed. Free-base and zinc metallated porphyrins were exploited for the analysis of hydrophobic partitioning forces that drive maquette incorporation and ligation. Furthermore, the hydrophobic substituent was altered from a phenyl to a butyl group, for exploration of the impact that hydrophobic substituent(s) has on the porphyrin partitioning into maquettes. It was shown that the more hydrophobic porphyrins aggregated rapidly within aqueous solution, which impeded incorporation into maquettes. The most hydrophilic porphyrins were stable in



aqueous solution, but did not bind to the maquettes. However, the charges associated with the porphyrin can interact with the opposing charges on the outer surface of the maquette, resulting in some non-specific interactions. Amphiphilic porphyrins bound within maquettes via hydrophobic partitioning (and histidinal ligation for zinc porphyrins) producing stable porphyrin-maquette complexes, with those that were most stable in aqueous solution binding to the maquette fastest due to no competing aggregative effects.

With the degree of porphyrin amphiphilicity to drive maquette binding determined, larger more complex dyad porphyrins were assessed for maquette binding. The anionic charges associated with the hydrophilicity of the dyad were once again observed to interact with opposing charges of the maquette, resulting in non-specific interactions. However, zinc dyads were shown to ligate to maquettes via hydrophobic partitioning and histidinal ligation of the hydrophobic porphyrin in the dyad.

Following the development of stable porphyrin-maquette complexes, their immobilization onto TiO<sub>2</sub> was investigated. The purification of maquette complexes containing 2 porphyrin moieties in a ligated state was achieved, corresponding to both the available binding sites within the maquette being filled. Subsequent immobilization of purified porphyrin-maquette complexes was analysed. Both electrostatic and covalent attachment of porphyrin-maquette complexes was explored and achieved using two maquettes specially designed by collaborators at the University of Pennsylvania. It was shown that the charges associated with the more positively charged maquette facilitated electrostatic interaction and binding to the TiO<sub>2</sub> substrate. Furthermore, covalent attachment of the second maquette with a cysteine linker to a modified TiO<sub>2</sub> surface with post-introduction of porphyrins into the maquette can be achieved. The use of maquettes inhibits porphyrin aggregation from aqueous solution on the TiO<sub>2</sub> substrate.

Electrochemical analyses of various porphyrins were explored, with the effects of substituent groups on the electronic energies determined. Electronic energies of Zinc tetraphenylporphyrin was shown to be altered through additions of carboxylic-functional groups to the *para*-position of the phenyl groups, whereby subsequent additions resulted in a decrease in HOMO energy levels with increases in LUMO energy levels. Conversely, addition of ammonium salt substituents decreased the LUMO energy level of the porphyrin, significantly decreasing its band-gap. Replacement of the butyl groups of a porphyrin moiety

with phenylcarboxylates was also explored, and led to a drastic decrease in the HOMO energy levels, with a slight decrease in the LUMO energy levels. The butyl substituents were shown to have a greater impact on the electronic state of the porphyrin compared to phenyl groups, predominantly due to the non-conjugation of the phenyl group with the porphyrin core.

Variouly treated TiO<sub>2</sub> surfaces with porphyrin or maquette-porphyrin complexes were incorporated into DSSCs, with their photovoltaic responses measured and electron transfer processes probed of at specific interfaces. Devices using maquette-porphyrin complexes electrostatically bound to TiO<sub>2</sub> resulted in a reduced photocurrent response compared to those with porphyrin covalently attached directly to TiO<sub>2</sub> (up to 2-fold lower). However, the reduction in photocurrent can easily be explained as the quantity of the photoactive material (porphyrin) present was up to 6-times lower than in devices using maquette-porphyrin complexes. This was not surprising due to the physical dimensions of the protein taking up physical space on the surface, which reduces the over-all quantity able to bind. Nonetheless, utilising porphyrin-maquette complexes increased the  $V_{oc}$  and FF, with increases in the electron lifetime (>1 ms) by >2-fold. This was attributed to maquettes inhibiting unwanted electron recombination processes whilst electron injection into the CB of TiO<sub>2</sub> was not significantly affected. Devices utilising covalently attached porphyrin-maquette complexes to a modified TiO<sub>2</sub> surface further increased the electron lifetime to 5.74 ms.

To explore the potential of site-specific binding of two different porphyrin moieties into a single maquette structure, the differential binding of zinc and gallium porphyrins was explored. The preferential binding of a gallium porphyrin to a bis-His binding site was shown, with subsequent binding of a zinc porphyrin to a single histidine binding site allowing for site-specific incorporations. The resulting complex was successfully immobilised onto an electrode and developed into a DSSC for photovoltaic responses. The differential binding broadens the absorbance cross-section of the nano-structured complex. The successful differential binding of porphyrins into maquettes and employment within DSSCs opens up opportunities to develop custom designed porphyrins and larger porphyrin arrays for developing artificial reaction centres that could be employed in future light-harvesting devices.

## Table of Contents

Declaration Page	i
Acknowledgments	ii
Abstract	iii
Table of Contents	vi
List of Figures	x
List of Tables	xviii
List of Abbreviations	xix
<b>I- General Introduction</b>	<b>1</b>
1- General Introduction	2
2- Photosynthesis	3
2.1- Light harvesting	3
2.2- The photosynthetic reaction centre	4
2.3- The Oxygen Evolving Complex	5
3- Porphyrins	6
3.1- Porphyrins in nature	6
3.2- From nature to the laboratory	7
4- Maquettes	10
4.1- Structure	10
4.2- Function	11
4.3- Artificial reaction centre	12
5- Protein Immobilization on Conductive Surfaces	15
5.1- Conductive surfaces	15
5.2- Protein immobilization	16
6- Dye Sensitized Solar Cells (DSSCs)	17
6.1- Typical DSSC construct	17
6.2- DSSC characterisation	18
7- Research Aims	19
8- References	22
<b>II- General Experimental</b>	<b>32</b>
1- Materials and Reagents	33
2- Methods	34
2.1- Buffer solutions	34
2.2- Maquette-porphyrin binding in solution	34
2.2.1- Solution UV-Visible and fluorescence spectroscopy equipment	34
2.2.2- Porphyrins in DMSO and CHES buffer	34
2.2.3- Maquette-porphyrin measurements over time	35
2.2.4- Dyads	35
2.2.5- Maquette-porphyrin titrations	35

2.2.6-	Maquette-porphyrin emission/excitation	36
2.2.7-	Maquette-porphyrin isolation and purification	36
2.3-	TiO <sub>2</sub> electrodes preparation	37
2.4-	Immobilization onto TiO <sub>2</sub> electrodes	38
2.4.1-	Porphyrin sensitization from THF	38
2.4.2-	Porphyrin and maquette-porphyrin ensemble immobilization from aqueous buffer	38
2.4.3-	TiO <sub>2</sub> modification and binding	39
2.5-	Electrochemical analysis	40
2.6-	Dye sensitized solar cell (DSSC) based devices	41
2.7-	Device measurements and characterisations	42
2.7.1-	Photovoltage and photocurrent testing	42
2.7.2-	Incident photon-to-current conversion efficiency (IPCE) measurements	43
2.7.3-	Electrochemical impedance spectroscopy (EIS) measurements	43
2.8-	Gallium-based porphyrins	44
2.9-	Resonance Raman spectroscopy	44
3-	References	46

### **III- Maquette-Porphyrin Binding in Solution** 47

1-	Introduction	48
2-	Results	52
2.1-	Absorbance profiles of porphyrins in DMSO	52
2.1.1-	Absorbance of Zn-based tetraphenylporphyrin carboxylic acids	52
2.1.2-	Absorbance of free-base tetraphenylporphyrin carboxylic acids	54
2.1.3-	Absorbance of Zn-based tetraphenylporphyrin ammonium salts	55
2.1.4-	Absorbance of Zn-based butylporphyrin carboxylic acids	56
2.2-	Emission spectra of porphyrins in DMSO	58
2.2.1-	Emission of Zn-based tetraphenylporphyrin carboxylic acids	58
2.2.2-	Emission of free-base tetraphenylporphyrin carboxylic acids	59
2.2.3-	Emission of Zn-based tetraphenylporphyrin ammonium salts	60
2.2.4-	Emission of Zn-based butylporphyrin carboxylic acids	61
2.3-	Absorbance profiles of maquettes in aqueous buffer	63
2.4-	Time resolved binding of maquettes and porphyrin in buffer	64
2.4.1-	Binding of Zn-based tetraphenylporphyrin carboxylates	64
2.4.2-	Binding of free-base tetraphenylporphyrin carboxylates	72
2.4.3-	Binding of Zn-based tetraphenylporphyrin ammonium salts	79
2.4.4-	Binding of Zn-based butylporphyrin carboxylates	85
2.5-	Binding titration of maquettes with porphyrins	90
2.5.1-	Titration of maquettes with P1a	90
2.5.2-	Titration of maquettes with P1b	92
2.5.3-	Titration of maquettes with P1c	94
2.5.4-	Titration of maquettes with P1d	96
2.6-	Maquette-porphyrin emission and excitation spectra in aqueous buffer	98
2.6.1-	P1d in aqueous buffer and with maquettes	98
2.6.2-	P2d in aqueous buffer and with maquettes	99
2.6.3-	P3d in aqueous buffer and with maquettes	100
2.6.4-	P4d in aqueous buffer and with maquettes	101
2.7-	Resonance Raman in aqueous buffer	102
2.7.1-	BT-maquette and zinc based carboxylic substituted porphyrins	102
2.7.2-	GL-maquette and zinc based carboxylic substituted porphyrins	104

---

3- Discussion	106
3.1- Porphyrins in DMSO	106
3.2- Maquette and porphyrin binding in aqueous buffer	106
3.3- Maquette-porphyrin titrations	108
3.4- Maquette-porphyrin emissions and resonance Raman	111
4- Conclusions	113
5- References	116
<b>IV- Dyad Porphyrins and Maquettes in Solution</b>	<b>122</b>
1- Introduction	123
2- Results	126
2.1- Conjugated dyads in DMSO	126
2.2- Conjugated dyads binding to maquettes	128
2.3- Non-conjugated dyad in DMSO	135
2.4- Non-conjugated dyad binding with maquette	136
3- Discussion	138
4- Conclusions	142
5- References	143
<b>V- Immobilization onto TiO<sub>2</sub> Electrodes</b>	<b>144</b>
1- Introduction	145
2- Results	150
2.1- Maquette-porphyrin ensembles extinction coefficient	150
2.2- Purification of maquette-porphyrin ensembles	153
2.2.1- Size-exclusion chromatography	153
2.2.2- Protein centrifugal filtration	154
2.3- Binding directly to TiO <sub>2</sub>	156
2.3.1- Sensitization of porphyrin via THF	156
2.3.2- Immobilization of porphyrin from aqueous buffer	157
2.3.3- Immobilization of ensembles from aqueous buffer	161
2.4- TiO <sub>2</sub> modification for covalent attachment of maquette	166
2.4.1- 3-Phosphonopropionic acid modification for NHS-EDC reaction	166
2.4.2- 2-Aminoethylphosphonic acid modification for cysteine-maleimide reaction	170
2.5- Resonance Raman of treated TiO <sub>2</sub> electrodes	174
3- Discussion	176
3.1- Binding of P1d directly to TiO <sub>2</sub>	176
3.2- Binding of maquette-P1d ensembles	176
3.3- Binding of maquette-P3d ensembles	179
3.3- Structural integrity of the maquette on TiO <sub>2</sub>	180
4- Conclusions	181
5- References	184
<b>VI- Electrochemical Analysis</b>	<b>189</b>
1- Introduction	190
2- Results	192
2.1- Porphyrins in solution	192
2.1.1- Ferrocene as an internal reference	192

---

2.1.2-	ZnTPP	193
2.1.3-	Carboxylate substituted tetraphenylporphyrins (P1a-P1e)	195
2.1.4-	Zn butyl-substituted phenylporphyrin carboxylates (P4a-P4d)	200
2.1.5-	Zn-tetraphenyl tri-ammonium salt porphyrin (P3d)	205
2.2-	Electrochemistry of porphyrins on TiO <sub>2</sub>	206
3-	Discussion	208
4-	Conclusions	211
5-	References	212
<b>VII- Solar Cell Devices</b>		<b>214</b>
1-	Introduction	215
2-	Results	221
2.1-	P1d on non-treated TiO <sub>2</sub>	221
2.1.1-	Devices using sensitized P1d	221
2.1.2-	Devices using P1d bound from aqueous buffer	221
2.1.3-	Devices using maquette-P1d ensembles	226
2.1.4-	Charge retention	229
2.1.5-	Quantification of P1d on TiO <sub>2</sub>	230
2.2-	Devices using maquette-P3d ensembles	232
2.3-	P1d with functionalised TiO <sub>2</sub>	235
2.3.1-	Devices using covalently attached <i>cysGL</i> -P1d ensembles	235
2.3.2-	Devices using covalently attached maquette with post introduction of P1d	237
2.4-	Attempt to determine porphyrin-maquette injection kinetics and overall yield	239
3-	Discussion	240
4-	Conclusions	246
5-	References	247
<b>VIII- Gallium Based Porphyrin-Maquette Ensembles</b>		<b>251</b>
1-	Introduction	252
2-	Results	254
2.1-	PGa in solvents and ligation to maquette <sub>2</sub>	254
2.2-	PGa titration with maquette	255
2.3-	Electrochemical analysis of PGa	257
2.4-	PGa in DSSC based devices	258
2.5-	PGa and P1d differential binding into maquettes	261
3-	Discussion	266
4-	Conclusions	272
5-	References	273
<b>IX- Future Prospects</b>		<b>275</b>
	References	280

## List of Figures

Figure #	Title	Page #
<b>Chapter I- General Introduction</b>		
Figure I-1	Photon energy transfer in chlorophyll molecules.....	4
Figure I-2	S-state hypothesis for water oxidation in photosynthesis.....	5
Figure I-3	Schematic of a porphyrin core.....	6
Figure I-4	Heme porphyrin.....	6
Figure I-5	Structure of chlorophyll-a molecule.....	7
Figure I-6	Tetraphenylporphyrin (TPP) absorbance and emission spectra.....	8
Figure I-7	A representation of a four $\alpha$ -helix maquette structure.....	10
Figure I-8	Maquettes are capable of binding a range of cofactors.....	12
Figure I-9	Schematic representation of an artificial photosynthetic system for water splitting.....	14
Figure I-10	DSSC construct with electron flow diagram.....	17
Figure I-11	Binding of maquette-porphyrin complexes to a conductive surface.....	20
<b>Chapter II- General Experimental</b>		
Figure II-1	Ramping profile for sintering screen-printed TiO <sub>2</sub> .....	38
Figure II-2	Schematic representation of three electrode cell for solution based electrochemistry.....	41
Figure II-3	Schematic representation of a three electrode cell for film based electrochemistry.....	41
Figure II-4	Schematic representation of a DSSC construct.....	42
Figure II-5	A typical current-voltage ( <i>IV</i> ) curve from a device.....	43
<b>Chapter III- Maquette-Porphyrin Binding in Solution</b>		
Figure III-1	Maquette structure and sequence.....	49
Figure III-2	Porphyrin models based on a tetraphenylporphyrin of increasing hydrophilicity for binding to maquettes.....	50

---

Figure III-3	Porphyrin models based on a porphyrin of increasing hydrophilicity for binding to maquettes.....	51
Figure III-4	Absorbance spectra of carboxylic substituted zinc based tetraphenylporphyrin in DMSO.....	53
Figure III-5	Absorbance spectra of carboxylic substituted free-base tetraphenylporphyrins in DMSO.....	54
Figure III-6	Absorbance spectra of trimethylammonium substituted zinc based tetraphenylporphyrins in DMSO.....	55
Figure III-7	Absorbance spectra of carboxylic substituted zinc based butylporphyrins in DMSO.....	56
Figure III-8	Emission spectra of carboxylic substituted zinc tetraphenylporphyrins in DMSO.....	58
Figure III-9	Emission spectra of carboxylic substituted free-base tetraphenylporphyrins in DMSO.....	59
Figure III-10	Emission spectra of trimethylammonium substituted zinc tetraphenylporphyrins in DMSO.....	60
Figure III-11	Emission spectra of phenyl-carboxyl substituted porphyrins in DMSO.....	61
Figure III-12	UV-vis. absorption spectra of maquettes in aqueous buffer.....	63
Figure III-13	UV-vis. absorption spectra characterisation of P1a in aqueous buffer with maquette.....	67
Figure III-14	UV-vis. absorption spectra characterisation of P1b in aqueous buffer with maquette.....	68
Figure III-15	UV-vis. absorption spectra characterisation of P1c in aqueous buffer with maquette.....	69
Figure III-16	UV-vis. absorption spectra characterisation of P1d in aqueous buffer with maquette.....	70
Figure III-17	UV-vis. absorption spectra characterisation of P1e in aqueous buffer with maquette.....	71
Figure III-18	UV-vis. absorption spectra characterisation of P2a in aqueous buffer with maquette.....	74
Figure III-19	UV-vis. absorption spectra characterisation of P2b in aqueous buffer with maquette.....	75
Figure III-20	UV-vis. absorption spectra characterisation of P2c in aqueous buffer with maquette.....	76



---

Figure III-21	UV-vis. absorption spectra characterisation of P2d in aqueous buffer with maquette.....	77
Figure III-22	UV-vis. absorption spectra characterisation of P2e in aqueous buffer with maquette.....	78
Figure III-23	UV-vis. absorption spectra characterisation of P3a in aqueous buffer with maquette.....	80
Figure III-24	UV-vis. absorption spectra characterisation of P3b in aqueous buffer with maquette.....	81
Figure III-25	UV-vis. absorption spectra characterisation of P3c in aqueous buffer with maquette.....	82
Figure III-26	UV-vis. absorption spectra characterisation of P3d in aqueous buffer with maquette.....	83
Figure III-27	UV-vis. absorption spectra characterisation of P3e in aqueous buffer with maquette.....	84
Figure III-28	UV-vis. absorption spectra characterisation of P4a in aqueous buffer with maquette.....	86
Figure III-29	UV-vis. absorption spectra characterisation of P4b in aqueous buffer with maquette.....	87
Figure III-30	UV-vis. absorption spectra characterisation of P4c in aqueous buffer with maquette.....	88
Figure III-31	UV-vis. absorption spectra characterisation of P4d in aqueous buffer with maquette.....	89
Figure III-32	Titration of BT-maquette with P1a.....	91
Figure III-33	Titration of GL-maquette with P1a.....	91
Figure III-34	Titration of BT-maquette with P1b.....	93
Figure III-35	Titration of GL-maquette with P1b.....	93
Figure III-36	Titration of BT-maquettes with P1c.....	95
Figure III-37	Titration of GL-maquettes with P1c.....	95
Figure III-38	Titration of BT-maquette with P1d.....	97
Figure III-39	Titration of GL-maquette with P1d.....	97
Figure III-40	Emission and excitation spectra of P1d.....	98
Figure III-41	Emission and excitation spectra of P2d.....	100

---

Figure III-42	Emission and excitation spectra of P3d.....	101
Figure III-43	Emission and excitation spectra of P4d.....	102
Figure III-44	Resonance Raman spectra from solutions of BT-maquette and zinc based carboxylic substituted porphyrins in aqueous buffer.....	103
Figure III-45	Resonance Raman spectra from solutions of GL-maquette and zinc based carboxylic substituted porphyrin in aqueous buffer.....	105
Figure III-46	SVD analysis of titrating P1a-d with the BT-maquette.....	111
Figure III-47	Hydrophilicity/hydrophobicity dependencies of zinc based porphyrins for ligation to maquettes.....	114
Figure III-48	Electrostatic interactions facilitating ligation to maquettes.....	115
 <b>Chapter IV- Dyad Porphyrins and Maquettes in Solution</b>		
Figure IV-1	The structure of dyads D1-D6, designed for amphiphilicity.....	123
Figure IV-2	Proposed dyad binding into maquettes.....	124
Figure IV-3	Absorbance of non-conjugated and conjugated zinc oligomers.....	125
Figure IV-4	UV-vis. absorption data for conjugated dyads with different metal insertions.....	127
Figure IV-5	UV-vis. absorption spectral characterisation of D1 in aqueous buffer with maquette.....	129
Figure IV-6	UV-vis. absorption spectral characterisation of D2 in aqueous buffer with maquette.....	130
Figure IV-7	UV-vis. absorption spectral characterisation of D3 in aqueous buffer with maquette.....	132
Figure IV-8	UV-vis. absorption spectral characterisation of D4 in aqueous buffer with maquette.....	133
Figure IV-9	UV-vis. absorption spectral characterisation of D5 in aqueous buffer with maquette.....	134
Figure IV-10	UV-vis. absorption of non-conjugated dyad D6 in DMSO.....	135
Figure IV-11	UV-vis. absorption spectral characterisation of D6 in aqueous buffer with maquette.....	137

### Chapter V- Immobilization onto TiO<sub>2</sub> Electrodes

Figure V-1	Porphyrins used for binding to TiO <sub>2</sub> .....	146
Figure V-2	Sensitization modes to TiO <sub>2</sub> via carboxylic groups.....	147
Figure V-3	Binding modes of phosphonic acid to TiO <sub>2</sub> .....	147
Figure V-4	EDC-NHS reaction schematic.....	148
Figure V-5	Cysteine-maleimide reaction schematic.....	149
Figure V-6	A <i>new</i> GL-maquette (' <i>cysGL</i> -maquette') sequence design.....	149
Figure V-7	Determination of Molar Extinction of P1d ligated with GL-maquette in aqueous buffer.....	151
Figure V-8	Determination of Molar Extinction of P1d ligated with BT-maquette in aqueous buffer.....	152
Figure V-9	Size-exclusion chromatography elution profiles.....	154
Figure V-10	Centrifugal filtration purification of maquette-P1d ensembles.....	155
Figure V-11	Absorbance of sensitized P1d to TiO <sub>2</sub> .....	156
Figure V-12	Absorbance of (attempted) sensitized P3d to TiO <sub>2</sub> .....	157
Figure V-13	Absorbance of TiO <sub>2</sub> treated with P1d from aqueous buffer.....	158
Figure V-14	Absorbance of TiO <sub>2</sub> treated with P3d from aqueous buffer.....	159
Figure V-15	Absorbance of TiO <sub>2</sub> treated with P1d from aqueous buffer over time.....	160
Figure V-16	Absorbance of TiO <sub>2</sub> treated with maquette-P1d ensembles.....	162
Figure V-17	Absorbance of TiO <sub>2</sub> treated with GL-maquette and P1d ensembles from aqueous buffer over time.....	163
Figure V-18	Absorbance of TiO <sub>2</sub> treated with increasing concentrations of GL-maquette and P1d.....	164
Figure V-19	Absorbance of TiO <sub>2</sub> treated with GL-maquette and P3d.....	165
Figure V-20	Absorbance of modified TiO <sub>2</sub> covalently attached GL-P1d ensembles via NHS-EDC.....	167
Figure V-21	Absorbance of modified TiO <sub>2</sub> reacted with NHS-EDC and exposed to P1d.....	169
Figure V-22	Absorbance of modified TiO <sub>2</sub> with covalently attached <i>cysGL</i> -P1d ensembles via cysteine-maleimide.....	171
Figure V-23	Absorbance of treated TiO <sub>2</sub> , reacted with maleimide and exposed to P1d.....	172

---

Figure V-24	Absorbance of modified TiO <sub>2</sub> , reacted with maleimide and exposed to P3d.....	173
Figure V-25	Resonance Raman of TiO <sub>2</sub> with GL-maquette and P1d.....	175
Figure V-26	Interactions of P1d/P3d or GL-P1d/P3d ensembles with TiO <sub>2</sub> .....	182
Figure V-27	TiO <sub>2</sub> modification for covalent linking of maquette with porphyrin or ensemble binding.....	183

### **Chapter VI- Electrochemical Analysis**

Figure VI-1	An example of cyclic voltammetry of a metallic porphyrin.....	190
Figure VI-2	CV and SWV of ferrocene for calibration of electrochemical analysis.....	193
Figure VI-3	Electrochemical analysis of ZnTPP.....	194
Figure VI-4	Electrochemical analysis of P1a.....	195
Figure VI-5	Electrochemical analysis of P1b.....	196
Figure VI-6	Electrochemical analysis of P1c.....	197
Figure VI-7	Electrochemical analysis of P1d.....	198
Figure VI-8	Electrochemical analysis of P1e.....	199
Figure VI-9	Electrochemical analysis of P4a.....	201
Figure VI-10	Electrochemical analysis of P4b.....	202
Figure VI-11	Electrochemical analysis of P4c.....	203
Figure VI-12	Electrochemical analysis of P4d.....	204
Figure VI-13	Electrochemical analysis of P3d.....	205
Figure VI-14	Square-wave voltammetry of P1d on TiO <sub>2</sub> .....	207
Figure VI-15	HOMO-LUMO energies of measured porphyrins in solution.....	209

### **Chapter VII- Solar Cell Devices**

Figure VII-1	A typical current-voltage ( <i>IV</i> ) curve from a DSSC.....	216
Figure VII-2	Example of impedance measurements from a TiO <sub>2</sub> based porphyrin DSSC.....	217
Figure VII-3	Driving forces associated with DSSCs using P1d or P3d.....	218
Figure VII-4	Circuit model used for analysing resistances and capacitances.....	219

Figure VII-5	Device measurements utilizing sensitized P1d from THF and E1.....	222
Figure VII-6	Device measurements utilizing sensitized P1d from THF and E2.....	223
Figure VII-7	Device measurements utilizing P1d bound from aqueous buffer and E1.....	224
Figure VII-8	Device measurements utilizing P1d bound from aqueous buffer and E2.....	225
Figure VII-9	Device measurements utilizing maquette-P1d ensembles electrostatically bound from aqueous buffer and E1.....	227
Figure VII-10	Device measurements utilizing maquette-P1d ensembles electrostatically bound from aqueous buffer and E2.....	228
Figure VII-11	Device open circuit voltage decay using electrolyte E2 or electrolyte E1.....	229
Figure VII-12	Standard curve determination of P1d in 2 M HCl/THF.....	231
Figure VII-13	Device measurements utilizing maquette-P3d ensembles from aqueous buffer.....	233
Figure VII-14	Device measurements utilizing maquette-P3d ensembles from MES buffer.....	234
Figure VII-15	Device measurements utilizing maquette-P1d ensembles covalently linked from MES buffer.....	236
Figure VII-16	Device measurements utilizing P1d exposed to modified TiO <sub>2</sub> with and without covalently linked cysGL-maquette.....	238
Figure VII-17;	Photoinduced electron transfer processes.....	246

### **Chapter VIII- Gallium Based Porphyrin-Maquette Ensembles**

Figure VIII-1	Modified GL-maquette sequences for bis-His ligation.....	252
Figure VIII-2	Gallium porphyrin (PGa) structure.....	253
Figure VIII-3	UV-vis. absorption spectral characterisation of PGa in DMSO, aqueous buffer, and with 4- <i>his</i> GL-maquette.....	254
Figure VIII-4	Titration of PGa with 4- <i>his</i> GL-maquette.....	256
Figure VIII-5	Electrochemistry of PGa in solution.....	257
Figure VIII-6	Driving forces associated with DSSCs using P1d or PGa.....	258
Figure VIII-7	Device measurements utilizing sensitized PGa or PGa-maquette ensembles with E1.....	260
Figure VIII-8	Differential binding of P1d and PGa into a maquette.....	263

---

Figure VIII-9	Device measurements utilizing covalently attached P1d-PGa and 3- <i>his</i> GL- maquette ensembles.....	265
Figure VIII-10	Binding preferences of P1d and PGa into a maquette.....	269

### **Chapter IX- Future Prospects**

Figure IX-1	Potential future design of porphyrin arrays for light harvesting and maquette binding.....	278
Figure IX-2	Schematics for potential future application of maquettes with porphyrin arrays for catalytic reactions.....	279

## List of Tables

Figure #	Title	Page #
<b>Chapter I- General Introduction</b>		
Table I-1	Semiconductor properties.....	15
<b>Chapter II- General Experimental</b>		
<b>Chapter III- Maquette-Porphyrin Binding in Solution</b>		
Table III-1	Absorbance spectral data in DMSO.....	57
Table III-2	Emission spectral data in DMSO.....	62
Table III-3	Peak positions of P1a-e with and without maquette presence.....	72
Table III-4	Peak positions of P2a-e with and without maquette presence.....	79
Table III-5	Peak positions of P3a-e with and without maquette presence.....	85
Table III-6	Peak positions of P4a-d with and without maquette presence.....	89
<b>Chapter IV- Dyad Porphyrins and Maquettes in Solution</b>		
<b>Chapter V- Immobilization onto TiO<sub>2</sub> Electrodes</b>		
<b>Chapter VI- Electrochemical Analysis</b>		
Table VI-1	Determination of HOMO-LUMO energy levels of ZnTPP.....	194
Table VI-2	Determination of HOMO-LUMO energy levels of P1a-P1e.....	200
Table VI-3	Determination of HOMO-LUMO energy levels of P4a-P4d.....	204
Table VI-4	Determination of HOMO-LUMO energy levels of P3d.....	206
<b>Chapter VII- Solar Cell Devices</b>		
Table VII-1	Quantification of P1d within devices .....	231
Table VII-2	Photovoltaic data of devices using non-functionalised TiO <sub>2</sub> .....	242
Table VII-3	Photovoltaic data of devices using functionalised TiO <sub>2</sub> .....	245
<b>Chapter VIII- Gallium Based Porphyrin-Maquette Ensembles</b>		
Table VIII-1	Comparisons of photovoltaic data of devices using gallium and maquettes .....	270
<b>Chapter IX- Future Prospects</b>		

---

## List of Abbreviations

$\epsilon$	Extinction Coefficient
$\tau$	Electron lifetime
3- <i>his</i>	Three-Histidine
4- <i>his</i>	Four-Histidine
ACN	Acetonitrile
AFM	Atomic Force Microscopy
bis-His	Bis-Histidine
BMII	1-Butyl-3-Methylimidazolium Iodide
C	Capacitance
CB	Conduction Band
CHES	N-Cyclohexyl-2-Aminoethansulfonic Acid
Chl	Chlorophyll
CV	Cyclic Voltammetry
DCM	Dichloromethane
DFT	Density Functional Theory
DMSO	Dimethyl Sulfoxide
DSSC(s)	Dye Sensitised Solar Cell(s)
E1 or 2	Electrolyte 1 or 2
EDC	N-(3-dimethylaminopropyl)-N'-Ethylcarbodiimide Hydrochloride
EIS	Electrochemical Impedance Spectroscopy
ET	Electron Transfer
FF	Fill Factor
FTO	Fluorine-Doped Tin Oxide
H <sub>2</sub> TPP	Tetraphenylporphyrin



---

HCl	Hydrochloric Acid
His	Histidine
HOMO	Highest Occupied Molecular Orbital
$I_0$	Incident Photons
$I_2$	Iodine
$I_{MP}$	Maximum Power Current
IPCE	Incident Photon-To-Current Efficiency
$I_{SC}$	Short Circuit Current
ITO	Indium Tin Oxide
$J_{SC}$	Short Circuit Current Density
KCl	Potassium Chloride
$K_D$	Dissociation Constant
KI	Potassium Iodide
KOH	Potassium Hydroxide
LDAO	N,N-Dimethyldodecylamine N-Oxide
LHC(s)	Light Harvesting Complex(es)
LiI	Lithium Iodide
LUMO	Lowest Unoccupied Molecular Orbital
MES	2-(N-morpholino)ethanesulfonic Acid
MWCO	Molecular Weight Cut-Off
$\eta$	Over-all Efficiency (of DSSC)
NHE	Normalised Hydrogen Electrode
NHS	N-Hydroxysuccinimide
OEC	Oxygen Evolving Complex
Ox	Oxidation
$PQ_{A/B}$	Plastoquinone A/B

---

PQH <sub>2</sub>	Plastoquinol
<i>R</i>	Resistance
R <sub>O</sub>	Ohmic Resistance
RC(s)	Reaction Centre(s)
Red	Reduction
RT	Room Temperature
SAM(s)	Self Assembled Monolayer(s)
SnO <sub>2</sub>	Tin Oxide
SWV	Square Wave Voltammetry
TBAI	Tetrabutylammonium Iodide
TBAP	Tetrabutylammonium Perchlorate
THF	Tetrahydrofuran
TiO <sub>2</sub>	Titanium Dioxide
UV-vis.	Ultraviolet-Visible
V <sub>MP</sub>	Maximum Power Voltage
VN	Valeronitrile
V <sub>OC</sub>	Open Circuit Voltage
ZnO	Zinc Oxide
ZnTPP	Zinc Tetraphenylporphyrin

# **Chapter I**

## **General Introduction**

## 1- General Introduction

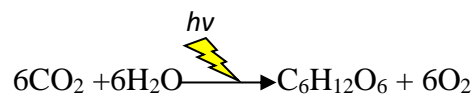
The need for sustainable and renewable energy source is becoming widely recognized. Approximately 80% of the energy used comes from burning fossil fuels, fuels which take millions of years to generate [1]. In 2010, the estimated energy consumption on Earth was 16.3 terawatts (TW) of energy per year and, based on the predicted increase in energy consumption from both population and gross domestic product, is expected to rise to 30 TW by 2050 [2, 3]. This is a significant problem as the reservoirs of fossil fuels are diminishing at alarming rates. Oil reserves are expected to last for another 40 years, natural gas for 60 years and coal for approximately 200 years [1]. With the world becoming more and more dependent on energy, the need for a sustainable and efficient renewable energy resource is ever increasing.

A potential solution to providing a renewable energy source can be found in nature, specifically plants. Plants, for billions of years, have been using the energy obtained from the sun with the by-product being oxygen. To look for new sources of energy, perhaps we should be looking at the ways nature has exploited energy capture, as nature has had billions of years to adapt and evolve effective and efficient means of harvesting 'renewable' energy. Plants use an antenna system to expose themselves to a large area of solar energy, and use this solar energy to drive reactions that ultimately split water into hydrogen and oxygen. The oxygen is released as a waste product, with the hydrogen coupled with carbon dioxide to produce carbohydrates in the form of sugars. The sugars are essentially the stored energy captured from the sun, which the plant uses for metabolic purposes. If we look at the processes employed by plants to harness solar energy, we could potentially design a similar system which harnesses solar energy to produce a desirable product, such as electricity or a chemical fuel. Harvesting of solar energy is of great potential as the amount of solar energy striking the earth is approximately 120,000 TW [4, 5]. Therefore, harnessing solar energy could generate the large amounts of energy needed to sustain the predicted energy growth and demand well into the future.

## 2- Photosynthesis

### 2.1 - Light harvesting

The capture of solar energy and its conversion to chemical energy is a fundamental process, which is the ultimate source of nearly all biological energy. The solar energy captured by photosynthetic organisms is the quantum energy of visible light, known as a photon ( $h\nu$ ). In plants, and various other organisms such as algae and cyanobacteria, photons are harvested, and the obtained energy is used to split water into oxygen and ‘hydrogen’. The process of splitting water into ‘hydrogen’ allows for carbon fixation to store the harvested photon energy in the form of carbohydrates [6]. The overall simplified chemical reaction in photosynthesis is;



The above ‘simplified’ equation indicates that carbon dioxide, water and photons are needed by photosynthetic organisms, with the by-products of the reaction being the oxygen and the carbohydrate in the form of a sugar. The oxygen evolved is released as a ‘waste product’, with the carbohydrate stored, representing the stored form of the harvested photons.

In plants, photons are collected through an antenna system known as Light-Harvesting Complexes (LHCs), present in the chloroplasts of leaves [7]. The LHC is a highly ordered array of chlorophyll (Chl) molecules in photosynthetic bacteria [8], however is much less ordered in the leaves of plants [9, 10]. Nonetheless, the LHC in photosynthetic organism shuttle photons to a desired ‘centre’, known as the Reaction Centre’ (RC), to harness solar energy. The RC is where energy conversion to electrochemical potential takes place, also known as charge separation. In the LHCs, a photon raises the chlorophyll molecule to an excited state ( $\text{Chl}^*$ ), which can then pass its increased energy state (exciton) to a nearby Chl molecule via a process known as resonance energy transfer (Figure I-1). Carotenoids are employed as an ‘accessory’ pigment, allowing the LHCs to absorb a wider range of photons from the electromagnetic spectrum.

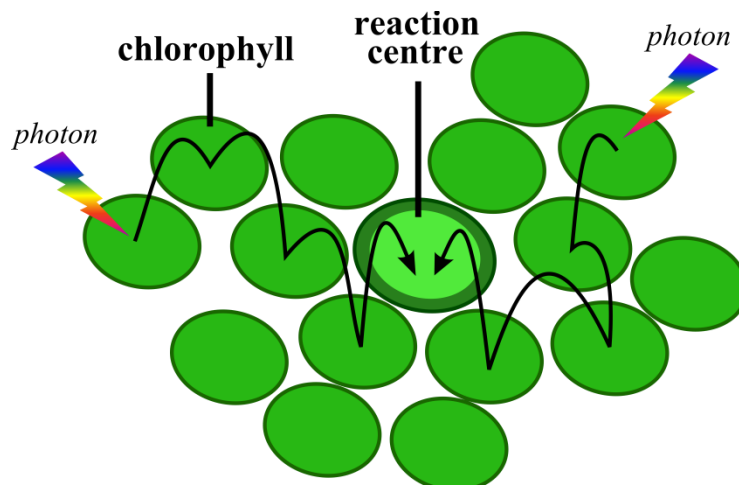


**Figure I-1: Photon energy transfer in chlorophyll molecules.** Resonance energy transfer within light-harvesting arrays transfers energy captured from photons to a reaction centre, where energy conversion to electrochemical potential takes place.

## 2.2 – The photosynthetic reaction centre

The resonance energy transfer through the LHC antenna will eventually reach a reaction centre (RC). The RC is a complex of Chl molecules, proteins, and co-factors that use the ‘funnelled’ energy from the LHCs to drive electron transfer reactions that ultimately result in the production of chemical energy. A dimer of Chl molecules resides at the reaction centre, often referred to as P680 (pigment 680), referencing the visible light absorption maximum of the Chl pigment. When this dimer of Chl absorbs the resonance energy from the LHC, the resulting electron is transferred to a nearby pheophytin molecule. This excited pheophytin molecule passes the electron to a tightly-bound plastoquinone (PQ<sub>A</sub>), which results in the electron being passed to a second loosely bound plastoquinone (PQ<sub>B</sub>). PQ<sub>B</sub> is then combined with two protons to form plastoquinol (PQH<sub>2</sub>), with this molecule capable of diffusing away from the RC [10].

As an electron is transferred from P680 to the pheophytin molecule, a positive charge is left on P680, to form P680<sup>+</sup>. The P680<sup>+</sup> is a powerful oxidising agent, sufficiently strong enough via the use of a water oxidising catalyst to pull electrons from water (redox potential of +0.82 V), and split water into its components.

### 2.3 – The Oxygen Evolving Complex

The formation of  $O_2$  through water splitting is theorised to require a near simultaneous loss of four electrons from two molecules of water. However, this cannot be completed by P680, capable of generating one oxidizing equivalent at a single time. The ‘S-state’ hypothesis is the generally accepted theory on how the photosystem accumulates four oxidizing equivalents needed to oxidize water. Close to the RC is a cluster of five metal ions, consisting of four manganese (Mn) ions and one calcium ion (Ca). These ions are stabilized by a number of proteins that together form the Oxygen Evolving Complex (OEC). The OEC accumulates four oxidizing equivalents by transferring four electrons, one at a time, to the nearby  $P680^+$ . The transfer of each electron to the  $P680^+$  is through an intermediate electron carrier, a tyrosine residue ( $Tyr_z$ ). Following absorption of photons by the LHC, the  $P680^+$  becomes re-oxidised back to P680. In this process, four oxidising equivalents are driven by the successive absorption of four photons in the LHC. Once this has occurred, the system catalyses the removal of four electrons from two  $H_2O$  molecules (Figure I-2).

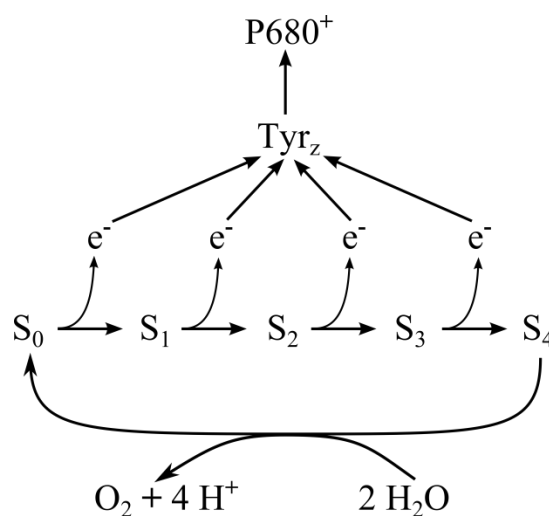


**Figure I-2: S-state hypothesis for water oxidation in photosynthesis.** The S-state hypothesis of the manganese-calcium cluster whereby the cluster can accumulate 4 oxidising equivalents ( $S_4$ ), which can then catalyse the removal of four  $e^-$  from two water molecules. The electrons from the splitting of water are passed from the cluster to a  $Tyr_z$  intermediate electron carrier, which then passes the electron to  $P680^+$

With Chl employed in nature as a light-absorber, an increasing number of artificially created light-absorbers are continually being developed, based on a similar core structure as Chl, which is a reduced porphyrin [11-16]. The predominant aim for developing porphyrins is to tune the functionality of the molecule for a desired outcome, often light-absorbing properties.

### 3- Porphyrins

#### 3.1 – Porphyrins in nature

Porphyrins are a group of organic compounds that are employed in a vast number of ways within nature. The general core structure of a porphyrin is a heterocyclic macrocycle, being fully conjugated and aromatic, containing 22  $\pi$ -electrons (Figure I-3).

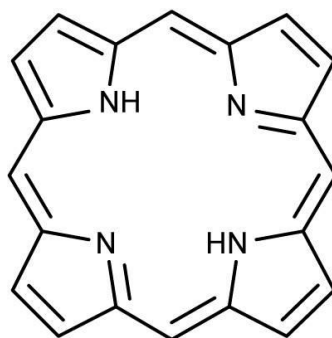


**Figure I-3: Schematic of a porphyrin core.** The core structure of a porphyrin containing 22  $\pi$ -electrons.

Porphyrin compounds are repeatedly found within nature across a range of species, containing a vast array of functions. Haemoglobin is a molecule employed within organisms to bind and circulate oxygen within the blood. The haemoglobin molecule consists of four globular protein subunits, known as a heme group. Each heme group contains a porphyrin molecule, with an iron (Fe) ion at the centre of the porphyrin, to which oxygen can reversibly bind (Figure I-4).

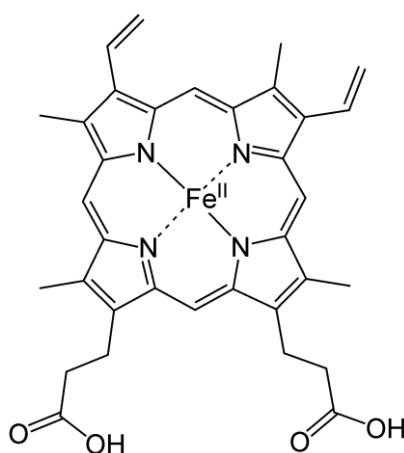


**Figure I-4: Heme porphyrin.** The structure of a heme porphyrin found within haemoglobin and paramount for the transport of oxygen within blood.



Porphyrins are not only employed in the chemistry of life for mammals, but are also vital for the survival of plants. Chlorophyll molecules are structurally related to porphyrins, being incorporated into plants to function as efficient photon harvesters, fundamentally vital for the process of photosynthesis. Chlorophyll molecules are the pigments found within chloroplasts of plants and algae, capable of absorbing light due to the porphyrin-based structure (Figure I-5).

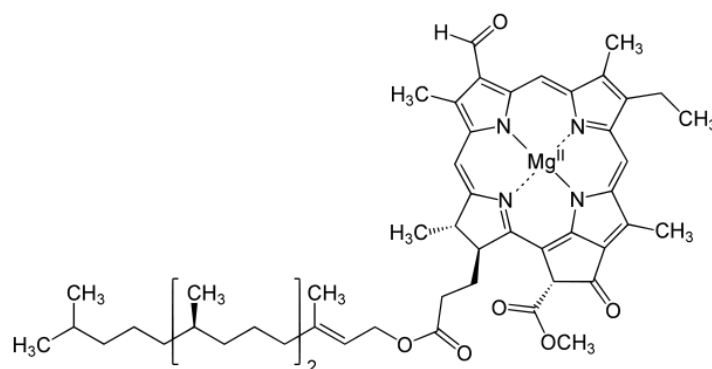


**Figure I-5: Structure of chlorophyll-a molecule.** Chlorophyll-a structure, which contains a magnesium ion at the centre of the core. The structure of the molecule is closely linked to its desired function, being the collection of photon energy.

### 3.2 – From nature to the laboratory

Porphyrins have gained increasing attention in the past few decades due to their ease of synthesis, high extinction coefficients, and high stabilities, which are applicable in a large range of areas including use in light harvesting, catalysis, and biomedical applications [11-16]. Metalloporphyrins have gained particular attention, with their application in dye sensitised solar cells (DSSCs), with the electronic structure tuneable through additions of substituents to the  $\beta$ -pyrrolic or *meso*-positions of the porphyrin core. The structure of the porphyrin is highly correlated to the absorption spectrum, with the structure affecting the distribution and densities of the  $\pi$ -electron system [17-19]. Zinc tetraphenylporphyrin (ZnTPP, Figure I-6) is a common metalloporphyrin, which is often used as a core porphyrin with substituents added, and whose absorbance and emission in organic solvents are well characterised. As shown in Figure I-6, the absorbance of ZnTPP displays a sharp Soret peak at 423 nm (with  $\epsilon = 574,000 \text{ M}^{-1} \text{ cm}^{-1}$ ), with two Q-bands present, when dissolved in toluene [20]. Absorbances of metalloporphyrins

display these common distinct features arising from orbital energies of the conjugated  $\pi$ -electron system. The four orbital model is the most commonly accepted depiction for the unique absorption spectrum displayed by porphyrins [21]. The emission spectrum of ZnTPP in toluene shows two pronounced peaks when excited at 550 nm (Figure I-6), arising from the electron rich conjugated core [22]. The absorbance and emission of monomeric porphyrins dissolved in solution show these common features, with aggregation often distorting the spectra [23, 24]. A free-base tetraphenylporphyrin ( $H_2TPP$ ) displays a sharp Soret peak at 419 nm (with  $\epsilon = 410,000 \text{ cm}^{-1} \text{ M}^{-1}$ ), with four Q-bands present (Figure I-6) [20]. The free-base porphyrins display four Q-bands due to the symmetry of the molecule being broken [25]. Similar to ZnTPP, the emission spectrum of  $H_2TPP$  displays two distinct peaks. It is noted that the molar extinction coefficient of the Soret peak is reduced and slightly blue-shifted when zinc is not complexed in the porphyrin. In contrast, the complexation of zinc reduces the intensity of the emissions. In general, the chemistry of different metalloporphyrins is controlled by the complexed metal in conjunction with the kind of peripherally and/or axially fixed substituents, with these factors influencing the electronic density distribution within the core of the macrocycle [26].

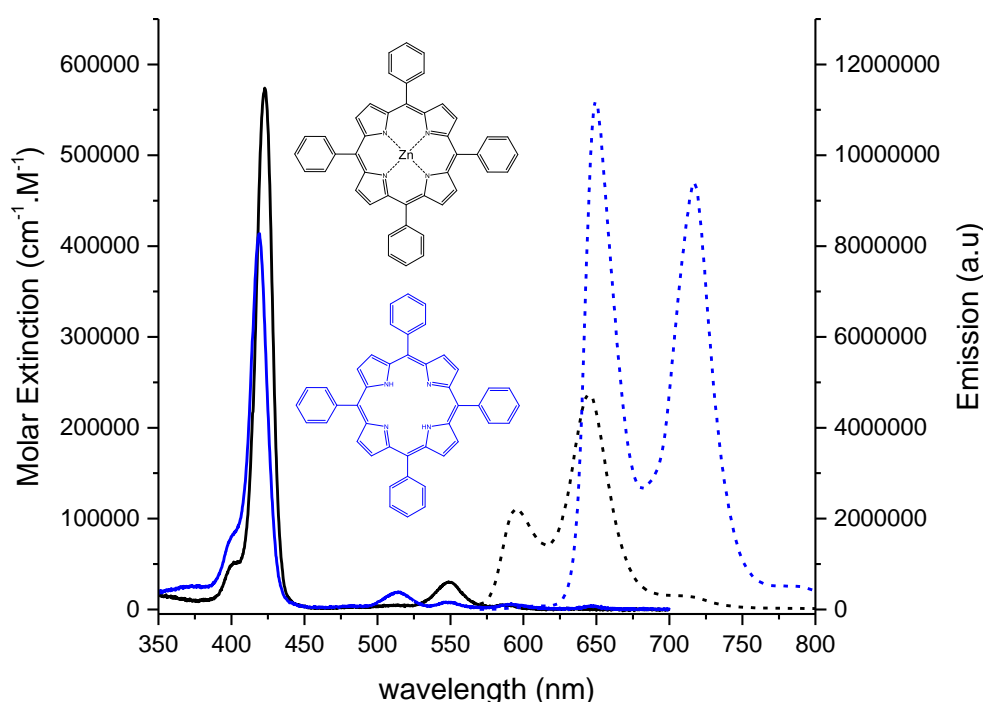


**Figure I-6; Tetrathenylporphyrin (TPP) absorbance and emission spectra.** The spectra of zinc tetraphenylporphyrin (ZnTPP, black) and free-base tetraphenylporphyrin ( $H_2TPP$ , blue) dissolved in toluene. The absorbances (solid lines) and emissions (dotted lines; excited at 550 nm for ZnTPP and 514 nm for  $H_2TPP$ ) are depicted. Figure adapted from [20, 22].

The ability to change the structure of a porphyrin molecule, including the substituents, inherently changes the photophysical properties of the molecule. This has led to the design of numerous porphyrin photonic assemblies, designed to harvest photons in a similar manner to that within chloroplasts of plants [27-29]. In more recent times, the linking of porphyrins together to create an ‘array’, so that peripheral porphyrins absorb the energy from a photon, capable of passing the energy to a nearby porphyrin has been investigated, with the process mimicking that of the LHC in nature [30-32]. The porphyrin array is constructed to direct the excited energy state towards a specified molecule, so that the absorbed energy can be turned into chemical energy, capable of being exploited for potential renewable energy sources. Various structural motifs of porphyrins have been linked together that are capable of absorbing light energy and rapidly transferring the excitation to ‘sinks’ such as a fullerene compound [33-36]. The push for research has evolved from porphyrin arrays and energy transfers, to mimicking the reaction centre found in plants. The formation of an artificial reaction centre would create a site where the light harvesting array (porphyrins) would direct the absorbed excitation energy from the photons to a single target molecule. This molecule would either reduce an electron acceptor, or conversely oxidise an electron donor. In this instance, the excitation energy would then be transformed into ‘usable’ chemical energy, capable of creating charge separated states for use in various chemical reactions via catalysts.

The incorporation of synthetic porphyrins within systems for light harvesting provides a unique opportunity to tune the light-absorbing properties of the system. To attain a light-harvesting complex resembling that found in nature, the light-absorbing porphyrins need to be ‘housed’ in proteins for efficient charge separation and electron transfer. One such protein is a man-made peptide known as a maquette, capable of housing porphyrins in a specific mode.

## 4- Maquettes

### 4.1 – Structure

The age of designing and altering proteins at single amino-acid scales, and translating such alterations to a defined and functionally relevant tertiary structure is beginning to present itself [37, 38]. Defined as a simplified functional protein scaffold, maquettes were produced through the need to reproduce a simplistic version of the large and complex proteins observed in nature [37]. Many proteins found within nature have a complex design arising from Darwin's principle of multiple utility, with the maquette reducing the number of interdependencies often observed in nature through simplification of the amino acid sequence and tertiary structure [39, 40]. The maquette, being a *de novo* designed protein, is not only intended to simplify the sequence and structure of a protein, but also to simplify cofactor incorporation, with proteins in nature often being utilised as multi-cofactor complexes.

The maquette structure is often a four  $\alpha$ -helix bundle (although can range from 2 to 6), with each helix typically 30-40 amino acids in length, and can contain two central histidines for ligation to cofactors [40, 41] (Figure I-7). The centre of the four  $\alpha$ -helices predominantly consists of hydrophobic residues, with the exposed outer areas consisting predominantly of hydrophilic residues. This design helps not only the folding of the protein into a native conformation, but helps the maquettes stability and functionality. There has been much success with incorporating metallic porphyrins into the maquette bundle via histidine axial coordination [42-44].

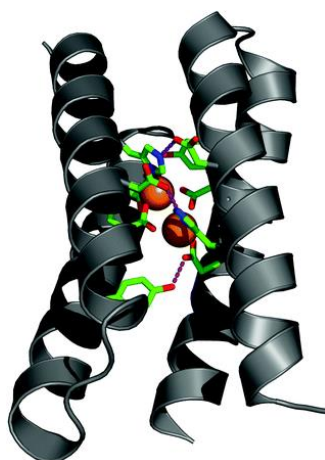


**Figure I-7: A representation of a four  $\alpha$ -helix maquette structure.** A typical maquette structure is shown with a cofactor bound within the centre of the bundle through histidine axial coordination. Figure from [37].

The maquettes have been shown to bind various cofactors with adaptability, with the hydrophobic interior often containing explicitly placed histidine residues for ligation to cofactors [45, 46]. Various maquettes have been shown to bind a range of cofactors including flavins, iron-sulfur clusters, chlorophylls, chlorins, various forms of heme, and porphyrins [47-51]. The hydrophobic core of the maquette facilitates folding, assembly, and stability of the peptide in conjunction with assisting partitioning of amphiphilic cofactors for ligation to the histidine residues within maquettes [41, 52, 53] (Figure I-7). Incorporation of various cofactors into maquettes is likened to biological proteins and their integration of cofactors for specialised functions. For example, the placement of heme derivatives into maquettes is similar to haemoglobin, with respect to functionality of O<sub>2</sub> and CO affinities [54]. Furthermore, binding of chlorophyll derivatives into maquettes has been shown to induce light-driven electron transfer, a process having close similarities to photosynthetic proteins [49, 55, 56]. To date, optimal conditions for incorporation of zinc porphyrins with maquettes is not well established. It has been shown that zinc binds strongly to a maquette via axial ligation to a histidine residue [50, 57]. Within this thesis, the role of hydrophilicity/hydrophobicity associated with porphyrins is explored in context of stabilities in aqueous solution and for binding to maquettes

## 4.2 –Function

The maquette bundle has been shown to bind not only a range of porphyrins, but a number of cofactors such as iron-sulfur clusters, flavins, chlorophylls and various forms of heme [47, 53, 58, 59], as shown in Figure I-8. Maquettes are particularly useful as a scaffold to house complexes, which drive electron transfer (ET) reactions. This is due to the rate of long range ET in redox proteins, such as those found in photosynthetic reaction centres, which is often orders of magnitude faster than for the corresponding reaction in aqueous solution [60, 61]. The rate-accelerating effect observed when proteins are used is based on the protein environment reducing the reorganization upon ET, while maintaining electron coupling from the donor to the acceptor [62].

Cofactor incorporation within proteins forms the basis of the majority of natural protein catalysts in based on ET processes. With maquettes shown to bind various metallic cofactors, the ET processes within cofactor-maquette ensembles for potential use in catalytic reactions is slowly becoming the main focus of maquette research [63]. Maquettes containing a zinc cofactor (zinc protoporphyrin IX) have been shown to electrostatically bind to the oxide

surfaces titanium dioxide ( $\text{TiO}_2$ ) and tin oxide ( $\text{SnO}_2$ ), with light-activated electron injection from the singlet excited state of the porphyrin into the conduction band of the surface [64]. Maquettes have also been utilized on a modified gold surface, with electrostatically bound maquettes containing heme derivatives displaying fully reversible electrochemistry, with reversible CO binding to the reduced heme [65]. Furthermore, covalent attachment of maquettes containing iron protoporphyrin IX to a modified gold surface has been demonstrated, with the substrate-bound maquette in conjunction with a naturally occurring protein based catalyst, used for the electrocatalyzed reduction of  $\text{NO}_3^-$  [66]. Furthermore, these substrate-substrate bound maquettes (with protoporphyrin IX) have been shown to mediate electron transfer to the naturally occurring redox protein cytochrome c [66]. Further understanding and demonstration of the ET processes within maquette-cofactor ensembles would provide grounds for development of more complex systems for potential use in catalysis and generation of usable fuels.

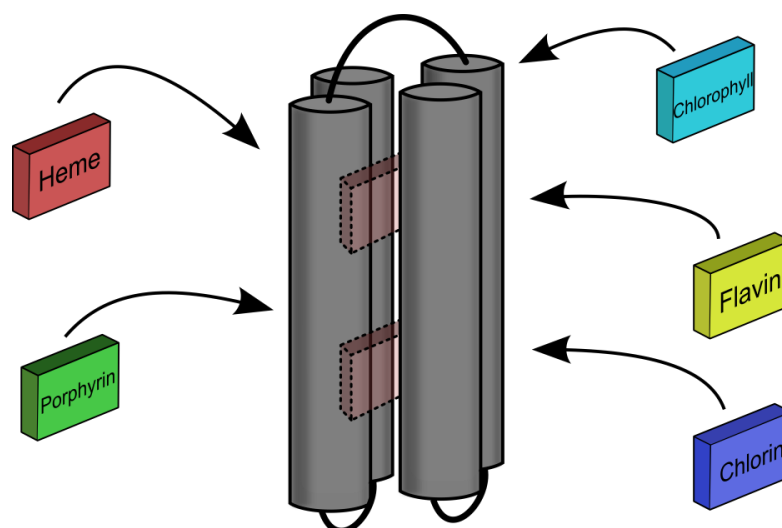


**Figure I-8: Maquettes are capable of binding a range of cofactors.** A schematic representation of a maquette, which can bind a range of cofactors including iron-sulfur clusters, flavins, chlorophylls, chlorins, and various forms of heme.

### 4.3 –Artificial reaction centre

In a photosynthetic reaction centre, excitation energy obtained from a light harvesting antenna drives electron transfer to an electron acceptor. This electron transfer generates a charge-separated state, preserving the absorbed photon energy as electrochemical energy, with this process of converting light to energy being the basis of photosynthesis. Reaction centres (RCs) found in photosystems create charge separated states physically separate from oxidizing

equivalents through the use of the membranes in chloroplasts. Artificial RCs will need to essentially produce charge separated states, as do natural RCs, however, artificial RCs need to be designed so that the charge separated states live long enough so that their oxidising and reducing effects can be utilised by catalysts.

Much of the current research into artificial RCs focuses on the incorporation of an electron accepting unit which is capable of holding long-lived photoinduced charge separation for coupling to catalysts. The introduction of a fullerene acceptor moiety to light-harvesting compounds is ascribed to significantly advancing the prospects of artificial RCs, with high stability and long-lived charge retention [67-70]. Although fullerene moieties display a long-lived charge separated state with small recombination processes [71], they substantially differ from natural systems, with the non-covalent interactions between photo- and redox-active components arranged within a protein. The synthesis of scaffolds capable of non-covalent organisation of cofactors with linked electron donor-acceptor systems would hence be a promising construct that mimics closely the natural photosynthetic systems, as opposed to the covalent linking used with fullerene moieties [72]. Furthermore, the formation of fullerene moieties linked with light-harvesting arrays is synthetically demanding, with the formation of self-organising non-covalent systems for redox activities being comparatively less challenging.

To circumvent the challenge of synthesising complex charge separating moieties, naturally occurring photosynthetic RCs have been bound to substrates for photovoltaic responses. For example, PSII has been bound to transparent conductive substrates and subsequent photocurrent and O<sub>2</sub>/H<sub>2</sub> generation demonstrated [73, 74]. However, the photocurrent responses from the PSII treated substrates were small (up to 22  $\mu\text{A cm}^{-2}$ ), attributed to the ‘bulkiness’ of the natural protein minimising the amount of PSII able to bind to the surface. Artificial RCs developed from man-made proteins would be similar to naturally occurring RCs and considerably easier to construct on a large scale and bind to the conductive surface. Maquettes are a promising candidate to be employed as an artificial RC, with the incorporation of specially designed cofactors undergoing photoinduced ET to produce charge-separated states. Furthermore, artificial RCs should suppress undesirable electron recombination processes, as observed with proteins found in natural systems, with the maquette expected to protect against this recombination.

The maquette can potentially be utilised as a scaffold to house porphyrins, or porphyrin arrays, with the array designed to harvest solar energy and direct the excited energy into the maquette in a similar way that the LHC directs excited energy to the RC (P680) in natural photosystems. Furthermore, maquettes can bind to conductive surfaces, such as gold, through electrostatic interactions, allowing for electron transfer through the maquette to the conductive surface [75]. The photochemistry of the system could hence potentially generate electricity, or possibly be coupled with enzymes or catalysts to produce molecular fuels, such as hydrogen (Figure I-9). For the artificial RC to be efficient, recombination of the resulting charge separated state through migration of an electron back to the oxidised complex needs to be significantly lower than the rate of electron transfer to a desired catalyst or electrode [76]. Furthermore, an artificial photosynthetic RC needs to have an abundance of the electron donor substrate [2]. The binding of maquette-cofactor ensembles to conductive surfaces would allow for the development of a device, such as a dye sensitized solar cell (DSSC) [77]. Development of such devices allows for the various electron transfer processes to be analysed in context for potential application as an artificial RC, with photoinduced charge transfer processes mimicking that of the photosynthetic pathways.

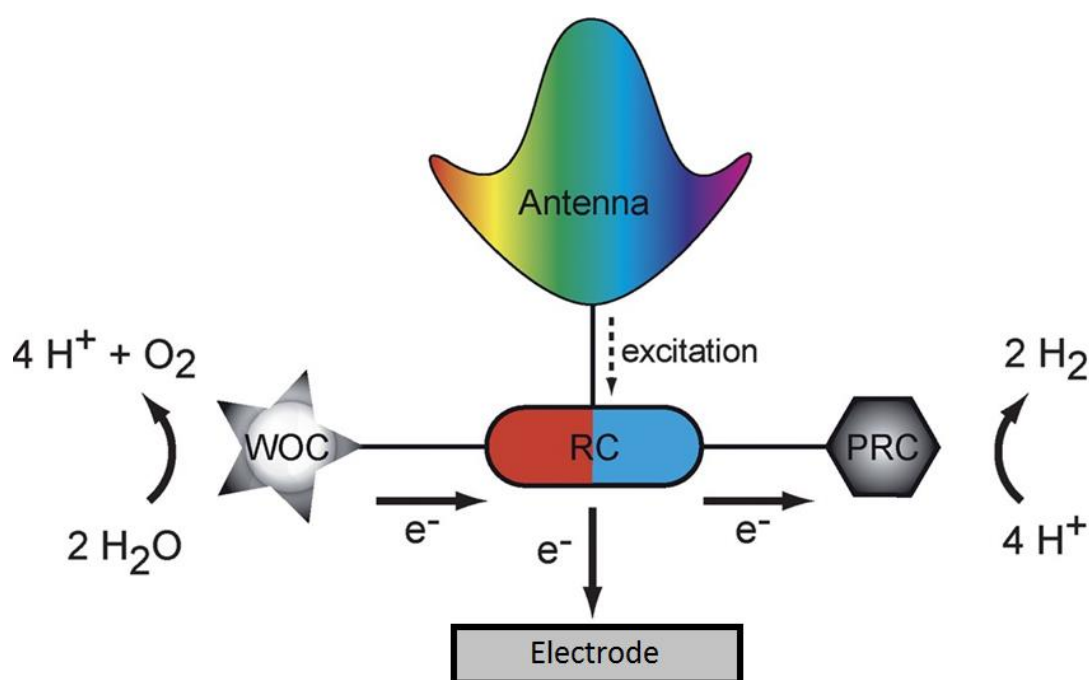


**Figure I-9: Schematic representation of an artificial photosynthetic system for water splitting.** A light harvesting 'antenna' generates a charge separated state by photoinduced electron transfer. Electrons from the RC can be used to reduce hydrogen ions to hydrogen gas at a proton reduction catalyst (PRC) or be injected into an electrode. The oxidised RC is regenerated by electrons from a water oxidation catalyst (WOC), converting water into oxygen and hydrogen ions (Figure adapted from [76]).



## 5- Protein Immobilization on Conductive Surfaces

### 5.1 – Conductive surfaces

Fabricated nanotechnology based conductive surfaces are increasingly utilised in a variety of research areas. Much of the research presently focuses on zinc oxide (ZnO), tin oxide (SnO<sub>2</sub>), or indium tin oxide (ITO) glass. These surfaces are all conductive, easy to fabricate, and semi-transparent, making them good surfaces for a range of research areas (Table I-1).

**Table I-1: Semiconductor properties.** Comparisons of zinc oxide (ZnO), tin oxide (SnO<sub>2</sub>), and indium tin oxide (ITO) glass parameters. Optical band gap ( $E_g$ ), density on the surface ( $\text{g cm}^{-3}$ ), lattice structure, crystal structure and lattice parameters  $a$  and  $c$  (nm) [78, 79].

Parameter	ZnO	SnO <sub>2</sub>	ITO
$E_g$ (eV)	3.4	3.6	3.6
Density ( $\text{g cm}^{-3}$ )	5.67	6.99	7.12
Lattice Structure	Hexagonal	Tetragonal	Cubic
Parameters $a, c$ (nm)	0.325, 0.5207	0.474, 0.319	1.012

Transparent conductive surfaces provide a large conductive surface area, which is often exploited for use in solar cell research and fabrication. Dye-sensitised solar cells which have been developed for the past two decades, exploit conductive surfaces through the use of semiconductor layers sensitised with inorganic and/or organic dye molecules such as porphyrins [80]. Conductive surfaces have significant potential for exploitation as a novel substrate for protein immobilization. Protein adsorption can be readily achieved on a range of conductive surfaces, driven mainly by electrostatic interactions between surface charges and the proteins, with high binding stability and minimal to no denaturation detectable [81-83]. This process is of value, as it allows the function of the immobilized protein on the surface to be incorporated optically, electrochemically and spectro-electrochemically without additions of electron mediators or promoters. This can be used in a range of sensing strategies which use proteins to detect trace amounts of compounds, based on the molecular interactions of the immobilised proteins.

## 5.2 – Protein immobilization

There is currently immense interest in the use of protein immobilization on conductive surfaces for the development of optical bioanalytical devices, along with various other forms of biosensing devices [83-85]. Biosensors are becoming more potent for the screening of a wide variety of compounds in many different fields. These devices exploit the intimate connections between a biorecognition element, such as a protein, and the analyte of interest, relaying to a transducer element that converts the connection into a measurable signal. This process is gaining growing interest and momentum due to its high selectivity and sensitivity, low costs, ease of use and the quick speed of the test [85]. The immobilization of biomolecules on electrodes is the key in the development of electrochemical biosensors. The most common strategy used for increasing sensitivity of a biosensor is achieved through the selectivity of the protein to a target analyte.

Immobilization of a protein onto a surface may lead to partial or complete loss of protein activity, due to orientation of binding or denaturation. In order to maintain protein activity, the orientation is often needed to be pre-determined. The physiochemical and chemical properties of both the surface and the protein affect the immobilization of the protein. Since the functionality of the protein needs to be preserved, the surface is often treated to optimize protein immobilization [86]. Oxide conductive surfaces can be treated with cationic polypeptides (such as poly-lysine) or an aminosilane to enhance protein immobilization based on favourable electrostatic interactions [87]. The treatment of the surfaces does not affect the electrochemistry nor the electron transfers associated with the immobilised proteins [85].

The binding of maquettes to various surfaces, such as gold, SnO, and TiO<sub>2</sub> has been reported, often via the interactions to the treated surface [64-66, 75]. In a similar fashion, maquettes containing specially designed cofactors (porphyrins) could be bound to a TiO<sub>2</sub> substrate, with the resulting surface analysed for photovoltaic responses, with the treatment of the surfaces not expected to affect the electron transfer processes [85]. The development of a TiO<sub>2</sub> surface with bound maquettes into a device, such as a DSSC, would allow for the various ET transfer processes to be probed and analysed.

## 6- Dye Sensitized Solar Cells (DSSCs)

### 6.1 – Typical DSSC construct

A typical DSSC consists of two electrodes, a photo-active anode and cathode. The anode is often a transparent conducting glass electrode covered with a monocrystalline semiconductor such as  $\text{TiO}_2$ ,  $\text{ZnO}$ , or  $\text{SnO}_2$ , to which a photosensitizing dye is attached [88]. The oxide surface is mesoporous, giving a high surface area for binding and hence more potential to harness incident photons. The photoanode is immersed in an electrolyte containing a redox mediator to transport positive charges to the counter electrode (cathode). Efficient charge separation is achieved through photoinduced electron injection from the photoexcited state of the bound dye into the conduction band of the semiconductor (Figure I-10). The resulting dye cations are subsequently regenerated through reduction by the redox mediator, with the redox mediator regenerated at the counter electrode. The solar power to electricity conversion efficiencies within DSSCs depends on a balance of the kinetics for injection, regeneration, and recombination reactions [89]. A typical DSSC construct is shown in Figure I-10, with the electron flow and relative energy levels shown.

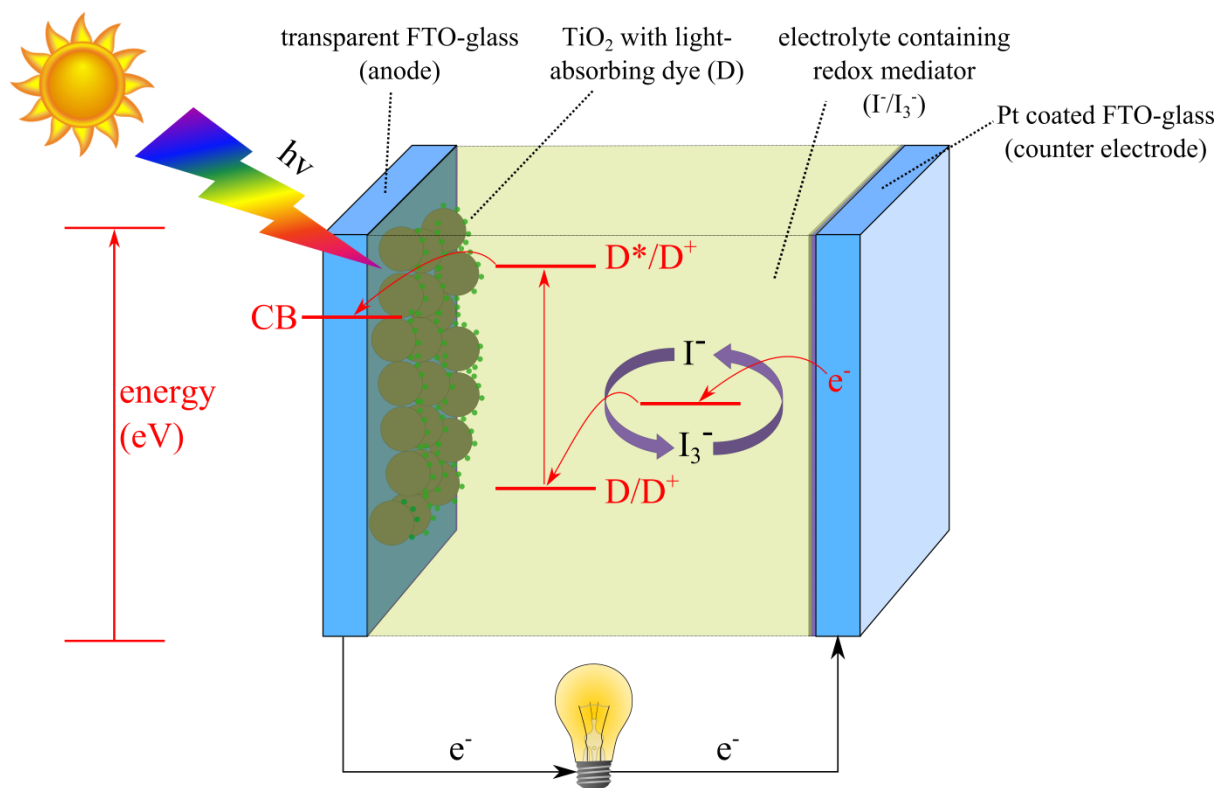


**Figure I-10; DSSC construct with electron flow diagram.** The DSSC construct is of two FTO-coated glass electrodes, one photoactive anode typically made with a transparent semiconductor such as  $\text{TiO}_2$ . The counter electrode is typically coated with platinum for increased conduction, with a redox mediator (such as  $\text{I}^-/\text{I}_3^-$ ) regenerating dye cations for photo-induced electron injection into the conduction band (CB) of  $\text{TiO}_2$ .

Charge generation and recombination pathways in DSSCs are exclusively interfacial reactions. Furthermore, photoexcitation of dyes in DSSCs does not generate charge separation directly, but rather requires an additional charge separation step through electron injection into the semiconductor CB from the excited dye. The effective charge separation is therefore reliant on a kinetic balance between the desired electron injection into the CB, the dye cation regeneration, and the undesirable recombination reactions. The current generation in DSSCs is dependent upon three processes, being the absorption of light by the bound dye, injection of electrons into the CB of the semiconductor from the photoexcited state, and charge transport through the CB of the semiconductor film. The voltage generated from DSSCs is given by the difference in the Fermi energy of electrons between the two electrodes. Under open circuit conditions under illumination, the concentration of electrons in the semiconductor increases to a steady state value, determined by the balance of electron injection and recombination. The photovoltage, which corresponds to the increase in the electron Fermi level, is therefore determined by the ratio of the free electron concentration in the semiconductor under illumination and in the dark.

## 6.2 –DSSC characterisation

The solar-to-electricity power conversion efficiency of DSSCs,  $\eta$ , is determined from the intensity of incident photons ( $P_{in}$ ), the short circuit current density ( $J_{sc}$ ), the open circuit voltage ( $V_{oc}$ ), and the fill factor (FF) of the device (the ratio between maximum power of the device and theoretical maximum at  $J_{sc}$  and  $V_{oc}$ ). The efficiency of DSSCs is thus determined by the following equation;

**Equation 1**

$$\eta (\%) = (J_{sc} V_{oc} FF) / P_{in}$$

DSSC constructs for light harvesting are increasingly gaining attention due to low-costs of materials and easy construction. As such, characterisation of the various ET processes within the device are commonly probed, with electrochemical impedance spectroscopy (EIS) and incident photon to current efficiency (IPCE) in conjunction with  $JV$  measurements giving insights into device performance [88]. The resulting IPCE spectra can be used to infer the wavelengths at which the device is absorbing photons and converting to electricity. Furthermore, EIS can give valuable information regarding the electron transfer processes occurring at specific interfaces within the DSSC [90, 91].

## 7- Research Aims

The binding via axial ligation from histidine groups within the maquette to the metal centre of porphyrins (Mg, Fe) has been well characterised, whereas Zn porphyrins are not as commonly represented in the literature [92]. Furthermore, the binding of maquettes and porphyrins produces shifts in the UV-vis. spectra peak positions compared to unbound porphyrin. This allows for characterisation of the binding of a porphyrin to a maquette. Much of the literature depicts the amphiphilic nature of the cofactor being a significant contributing factor for possible ligation within the maquette, however, no systematic study to date has been undertaken to analyse the role of hydrophobic partitioning. **The first aim of this thesis study** was the exploration of the binding of zinc and free-base porphyrins into maquette structures in the context of their hydrophobicity/hydrophilicity.

The systematic analysis of the effects of hydrophobic partitioning for ligation of porphyrins into a maquette was undertaken through the use of specially designed zinc porphyrins, incrementally increasing their hydrophilicity. Furthermore, a set of free-base porphyrins being analogous to the zinc porphyrin set were designed. This allowed for direct comparisons between hydrophobic partitioning and potential for ligation. The hydrophobic portion of the porphyrin was also investigated for potential influences for partitioning.

With determination of the influences of hydrophobic partitioning and ligation for porphyrin binding with maquettes, larger porphyrin arrays could be used for potential ligation within maquettes. Therefore, **the second aim of this study** was to explore the potential of binding a two porphyrin array (dyad) to a maquette. This required amphiphilic porphyrin dyads that were comprised of one hydrophilic porphyrin and one hydrophobic porphyrin. In order to explore the control of porphyrin binding to the maquette, variously metallated and conjugated dyads were studied.

Many naturally occurring proteins such as cytochromes and haemoglobins, containing porphyrins, have been bound to conductive surfaces [93-95]. This immobilization provides electron transfer to the conductive surface. In a similar manner, the maquette-porphyrin complex could be bound to a conductive surface, with photoinduced electron injected into the substrate. As the binding of proteins to surfaces is often through hydrophobic and electrostatic interactions, both the maquette and the surface can be designed and altered to support idealistic binding. **The third aim** was to bind stable maquette-porphyrin complexes onto a conductive or

semi-conductive surface, and use the porphyrin to absorb light and induce transport of electrons into the surface, resulting in a charge separated state (Figure I-11). This conversion of light energy to a charge separated state closely resembles the processes involved in reaction centres within natural photosystems (discussed previously). The binding of maquette-porphyrin complexes onto conductive surfaces needed to be characterised and analysed in the context of the impact maquettes would have on light-harvesting and electron injection. It was expected that the maquette (essentially a small protein) would not negatively affect electron transfer, but rather promote charge separation in a similar manner as proteins within photosystems.

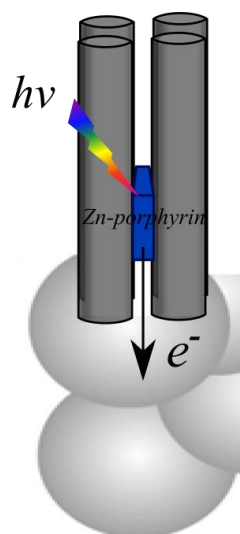


**Figure I-11: Binding of maquette-porphyrin complexes to a conductive surface.** The immobilization of complexes to conductive surfaces allows for absorbance of light via the porphyrin molecules, with the resulting photoexcited porphyrin to transfer electrons into the conductive surface.

With identification of zinc porphyrin structures that form optimally bound and stable maquette complexes, the subsequent electrostatic or covalent immobilization of the porphyrin-maquette complexes onto semiconductive titanium dioxide ( $\text{TiO}_2$ ) was investigated. Following determination of the optimal functionalised  $\text{TiO}_2$  surface, the ability of this structure to be used as the photoanode in a DSSC construct was explored. The DSSCs were characterised for photovoltaic responses, with further analysis from IPCE and EIS. This analysis allowed for interpretation of how the maquette influenced charge separation. The photovoltaic characterisation of the porphyrin-maquette solar cell provided insights into the ability of the ensembles to act as artificial RCs.

**The fourth aim of this study** was to explore the possibility of differential binding of porphyrins into maquettes. As gallium porphyrins would bind to maquettes via bis-his ligation and zinc porphyrins binding via single histidinal ligation, the binding of the porphyrins were

explored for site specificity self organisation within a maquette. The differential binding of two porphyrins within a single maquette would potentially increase the cross section absorbance of the solar spectrum compared to using a single porphyrin. With the differential binding into maquettes achieved, the resulting nano-structured complex was developed into a DSSC and analysed in an identical manner as was undertaken with the aforementioned complexes. The successful differential binding and light-harvesting capabilities would allow for future developments into more complex systems utilising maquettes as artificial RCs, becoming more and more closely aligned to the natural RCs.

## 8- References; General Introduction

1. Li B, Wang L, Kang B, Wang P, Qiu Y: **Review of recent progress in solid-state dye-sensitized solar cells.** *Solar Energy Materials and Solar Cells* 2006, **90**(5):549-573.
2. Hingorani K, Hillier W: **Perspectives for photobiology in molecular solar fuels.** *Australian Journal of Chemistry* 2012, **65**(6):643-651.
3. Kamat PV: **Meeting the clean energy demand: nanostructure architectures for solar energy conversion.** *The Journal of Physical Chemistry C* 2007, **111**(7):2834-2860.
4. Grätzel M: **Photoelectrochemical cells.** *Nature* 2001, **414**(6861):338-344.
5. Abbott D: **Keeping the energy debate clean: how do we supply the world's energy needs?** *Proceedings of the IEEE* 2010, **98**(1):42-66.
6. Bennett J: **Regulation of photosynthesis by reversible phosphorylation of the light-harvesting chlorophyll a/b protein.** *Biochemical Journal* 1983, **212**(1):1.
7. Ogawa T, Obata F, Shibata K: **Two pigment proteins in spinach chloroplasts.** *Biochimica et Biophysica Acta (BBA)-Biophysics including Photosynthesis* 1966, **112**(2):223-234.
8. McDermott G, Prince S, Freer A, Hawthornthwaite-Lawless A, Papiz M, Cogdell R, Isaacs N: **Crystal structure of an integral membrane light-harvesting complex from photosynthetic bacteria.** *Nature* 1995, **374**(6522):517-521.
9. Damjanović A, Vaswani HM, Fromme P, Fleming GR: **Chlorophyll Excitations in Photosystem I of Synechococcus elongatus.** *The Journal of Physical Chemistry B* 2002, **106**(39):10251-10262.
10. Mirkovic T, Ostroumov EE, Anna JM, van Grondelle R, Govindjee, Scholes GD: **Light Absorption and Energy Transfer in the Antenna Complexes of Photosynthetic Organisms.** *Chemical Reviews* 2017, **117**(2):249-293.
11. Griffith MJ, Mozer AJ: **Porphyrin based dye sensitized solar cells:** INTECH Open Access Publisher; 2011.



12. O'Regan B, Graetzel M: **A low-cost, high-efficiency solar cell based on dye-sensitized colloidal TiO<sub>2</sub> films.** *Nature* 1991, **353**:737-740.
13. Kennedy JC, Pottier RH: **New trends in photobiology.** *Journal of Photochemistry and Photobiology B: Biology* 1992, **14**(4):275-292.
14. Papkovsky DB, O'Riordan TC: **Emerging Applications of Phosphorescent Metalloporphyrins.** *Journal of Fluorescence* 2005, **15**(4):569-584.
15. Yella A, Lee H-W, Tsao HN, Yi C, Chandiran AK, Nazeeruddin MK, Diao EW-G, Yeh C-Y, Zakeeruddin SM, Grätzel M: **Porphyrin-Sensitized Solar Cells with Cobalt (II/III)-Based Redox Electrolyte Exceed 12 Percent Efficiency.** *Science* 2011, **334**(6056):629-634.
16. Huang H, Song W, Rieffel J, Lovell JF: **Emerging Applications of Porphyrins in Photomedicine.** *Frontiers in Physics* 2015, **3**.
17. Caughey W, Eberspaecher H, Fuchsman W, McCoy S, Alben J: **PI-INTERACTIONS IN METALLOPORPHYRINS AND HEMEPROTEINS.** *Annals of the New York Academy of Sciences* 1969, **153**(3):722-737.
18. Hunter CA, Sanders JK: **The nature of. pi.-. pi. interactions.** *Journal of the American Chemical Society* 1990, **112**(14):5525-5534.
19. Weinkauff JR, Cooper SW, Schweiger A, Wamser CC: **Substituent and solvent effects on the hyperporphyrin spectra of diprotonated tetraphenylporphyrins.** *The Journal of Physical Chemistry A* 2003, **107**(18):3486-3496.
20. Barnett GH, Hudson MF, Smith KM: **Concerning meso-tetraphenylporphyrin purification.** *Journal of the Chemical Society, Perkin Transactions 1* 1975(14):1401-1403.
21. Gouterman M, Wagnière GH, Snyder LC: **Spectra of porphyrins.** *Journal of Molecular Spectroscopy* 1963, **11**(1):108-127.
22. Harriman A: **Luminescence of porphyrins and metalloporphyrins. Part 1.-Zinc(II), nickel(II) and manganese(II) porphyrins.** *Journal of the Chemical Society, Faraday Transactions 1: Physical Chemistry in Condensed Phases* 1980, **76**(0):1978-1985.

23. Pasternack RF, Francesconi L, Raff D, Spiro E: **Aggregation of nickel(II), copper(II), and zinc(II) derivatives of water-soluble porphyrins.** *Inorganic Chemistry* 1973, **12**(11):2606-2611.
24. Gandini SCM, Yushmanov VE, Tabak M: **Interaction of Fe(III)- and Zn(II)-tetra(4-sulfonatophenyl) porphyrins with ionic and nonionic surfactants: aggregation and binding.** *Journal of Inorganic Biochemistry* 2001, **85**(4):263-277.
25. Hashimoto T, Choe Y-K, Nakano H, Hirao K: **Theoretical study of the Q and B bands of free-base, magnesium, and zinc porphyrins, and their derivatives.** *The Journal of Physical Chemistry A* 1999, **103**(12):1894-1904.
26. Słota R, Broda MA, Dyrda G, Ejsmont K, Mele G: **Structural and Molecular Characterization of meso-Substituted Zinc Porphyrins: A DFT Supported Study.** *Molecules* 2011, **16**(12):9957.
27. Gust D, Moore TA, Moore AL: **Molecular mimicry of photosynthetic energy and electron transfer.** *Accounts of Chemical Research* 1993, **26**(4):198-205.
28. Kay A, Graetzel M: **Artificial photosynthesis. 1. Photosensitization of titania solar cells with chlorophyll derivatives and related natural porphyrins.** *The Journal of Physical Chemistry* 1993, **97**(23):6272-6277.
29. Campbell WM, Jolley KW, Wagner P, Wagner K, Walsh PJ, Gordon KC, Schmidt-Mende L, Nazeeruddin MK, Wang Q, Grätzel M: **Highly efficient porphyrin sensitizers for dye-sensitized solar cells.** *The Journal of Physical Chemistry C* 2007, **111**(32):11760-11762.
30. Burrell AK, Officer DL, Plieger PG, Reid DC: **Synthetic routes to multiporphyrin arrays.** *Chemical reviews* 2001, **101**(9):2751-2796.
31. Mozer AJ, Griffith MJ, Tsekouras G, Wagner P, Wallace GG, Mori S, Sunahara K, Miyashita M, Earles JC, Gordon KC: **Zn-Zn porphyrin dimer-sensitized solar cells: toward 3-D light harvesting.** *Journal of the American Chemical Society* 2009, **131**(43):15621-15623.

32. Nakamura Y, Aratani N, Osuka A: **Cyclic porphyrin arrays as artificial photosynthetic antenna: synthesis and excitation energy transfer.** *Chemical Society Reviews* 2007, **36**(6):831-845.
33. Moore TA, Moore AL, Gust D: **The design and synthesis of artificial photosynthetic antennas, reaction centres and membranes.** *Philosophical Transactions of the Royal Society of London B: Biological Sciences* 2002, **357**(1426):1481-1498.
34. Seth J, Palaniappan V, Wagner RW, Johnson TE, Lindsey JS, Bocian DF: **Soluble synthetic multiporphyrin arrays. 3. Static spectroscopic and electrochemical probes of electronic communication.** *Journal of the American Chemical Society* 1996, **118**(45):11194-11207.
35. Wagner RW, Johnson TE, Lindsey JS: **Soluble synthetic multiporphyrin arrays. 1. Modular design and synthesis.** *Journal of the American Chemical Society* 1996, **118**(45):11166-11180.
36. Wasielewski MR: **Photoinduced electron transfer in supramolecular systems for artificial photosynthesis.** *Chemical Reviews* 1992, **92**(3):435-461.
37. Koder RL, Dutton PL: **Intelligent design: the de novo engineering of proteins with specified functions.** *Dalton Transactions* 2006(25):3045-3051.
38. Lichtenstein BR, Farid TA, Kodali G, Solomon LA, Anderson JR, Sheehan MM, Ennist NM, Fry BA, Chobot SE, Bialas C: **Engineering oxidoreductases: maquette proteins designed from scratch.** *Biochemical Society Transactions* 2012, **40**(3):561-566.
39. Moser CC, Page CC, Dutton PL: **Darwin at the molecular scale: selection and variance in electron tunnelling proteins including cytochrome c oxidase.** *Philosophical Transactions of the Royal Society B: Biological Sciences* 2006, **361**(1472):1295-1305.
40. Dutton PL, Moser CC: **Engineering enzymes.** *Faraday discussions* 2011, **148**:443-448.
41. Gibney BR, Rabanal F, Skalicky JJ, Wand AJ, Dutton PL: **Design of a unique protein scaffold for maquettes.** *Journal of the American Chemical Society* 1997, **119**(9):2323-2324.

42. Sharp RE, Diers JR, Bocian DF, Dutton PL: **Differential binding of iron (III) and zinc (II) protoporphyrin IX to synthetic four-helix bundles.** *Journal of the American Chemical Society* 1998, **120**(28):7103-7104.
43. Shifman JM, Gibney BR, Sharp RE, Dutton PL: **Heme redox potential control in de novo designed four- $\alpha$ -helix bundle proteins.** *Biochemistry* 2000, **39**(48):14813-14821.
44. Razeghifard MR, Wydrzynski T: **Binding of Zn-chlorin to a synthetic four-helix bundle peptide through histidine ligation.** *Biochemistry* 2003, **42**(4):1024-1030.
45. Robertson DE, Farid RS, Moser CC, Urbauer JL, Mulholland SE, Pidikiti R, Lear JD, Wand AJ, DeGrado WF, Dutton PL: **Design and synthesis of multi-haem proteins.** *Nature* 1994, **368**(6470):425-432.
46. Bryson JW, Betz SF, Lu HS, Suich DJ, Zhou HX, O'Neil KT, DeGrado WF: **Protein Design: A Hierarchic Approach.** *Science* 1995, **270**(5238):935-941.
47. Sharp RE, Moser CC, Rabanal F, Dutton PL: **Design, synthesis, and characterization of a photoactivatable flavocytochrome molecular maquette.** *Proceedings of the National Academy of Sciences* 1998, **95**(18):10465-10470.
48. Mulholland SE, Gibney BR, Rabanal F, Dutton PL: **Determination of Nonligand Amino Acids Critical to [4Fe-4S] $_{2+}$  Assembly in Ferredoxin Maquettes.** *Biochemistry* 1999, **38**(32):10442-10448.
49. Eggink LL, Hooper JK: **Chlorophyll Binding to Peptide Maquettes Containing a Retention Motif.** *Journal of Biological Chemistry* 2000, **275**(13):9087-9090.
50. Razeghifard MR, Wydrzynski T: **Binding of Zn-Chlorin to a Synthetic Four-Helix Bundle Peptide through Histidine Ligation.** *Biochemistry* 2003, **42**(4):1024-1030.
51. Huang SS, Koder RL, Lewis M, Wand AJ, Dutton PL: **The HP-1 maquette: From an apoprotein structure to a structured hemoprotein designed to promote redox-coupled proton exchange.** *Proceedings of the National Academy of Sciences of the United States of America* 2004, **101**(15):5536-5541.

52. Lichtenstein Bruce R, Farid Tammer A, Kodali G, Solomon Lee A, Anderson JLR, Sheehan Molly M, Ennist Nathan M, Fry Bryan A, Chobot Sarah E, Bialas C *et al*: **Engineering oxidoreductases: maquette proteins designed from scratch.** *Biochemical Society Transactions* 2012, **40**(3):561-566.
53. Solomon LA, Kodali G, Moser CC, Dutton PL: **Engineering the Assembly of Heme Cofactors in Man-Made Proteins.** *Journal of the American Chemical Society* 2014, **136**(8):3192-3199.
54. Koder RL, Anderson JLR, Solomon LA, Reddy KS, Moser CC, Dutton PL: **Design and engineering of an O<sub>2</sub> transport protein.** *Nature* 2009, **458**(7236):305-309.
55. Noy D, Discher BM, Rubtsov IV, Hochstrasser RM, Dutton PL: **Design of Amphiphilic Protein Maquettes: Enhancing Maquette Functionality through Binding of Extremely Hydrophobic Cofactors to Lipophilic Domains.** *Biochemistry* 2005, **44**(37):12344-12354.
56. Chen M, Eggink LL, Hooper JK, Larkum AWD: **Influence of Structure on Binding of Chlorophylls to Peptide Ligands.** *Journal of the American Chemical Society* 2005, **127**(7):2052-2053.
57. Sharp RE, Diers JR, Bocian DF, Dutton PL: **Differential binding of iron(III) and zinc(II) protoporphyrin IX to synthetic four-helix bundles.** *Journal of the American Chemical Society* 1998, **120**(28):7103-7104.
58. Kennedy ML, Gibney BR: **Proton coupling to [4Fe-4S] 2<sup>+/+</sup> and [4Fe-4Se] 2<sup>+/+</sup> oxidation and reduction in a designed protein.** *Journal of the American Chemical Society* 2002, **124**(24):6826-6827.
59. Gibney BR, Isogai Y, Rabanal F, Reddy KS, Grosset AM, Moser CC, Dutton PL: **Self-assembly of heme A and heme B in a designed four-helix bundle: implications for a cytochrome c oxidase maquette.** *Biochemistry* 2000, **39**(36):11041-11049.
60. Gray HB, Winkler JR: **Electron flow through proteins.** *Chemical physics letters* 2009, **483**(1):1-9.
61. Moser CC, Keske JM, Warncke K, Farid RS, Dutton PL: **Nature of biological electron transfer.** *Nature* 1992, **355**(6363):796-802.

62. Tipmanee V, Oberhofer H, Park M, Kim KS, Blumberger J: **Prediction of reorganization free energies for biological electron transfer: a comparative study of Ru-modified cytochromes and a 4-helix bundle protein.** *Journal of the American Chemical Society* 2010, **132**(47):17032-17040.
63. Peacock AFA: **Recent advances in designed coiled coils and helical bundles with inorganic prosthetic groups — from structural to functional applications.** *Current Opinion in Chemical Biology* 2016, **31**:160-165.
64. Topoglidis E, Discher BM, Moser CC, Dutton PL, Durrant JR: **Functionalizing Nanocrystalline Metal Oxide Electrodes With Robust Synthetic Redox Proteins.** *ChemBioChem* 2003, **4**(12):1332-1339.
65. Chen X, Discher BM, Pilloud DL, Gibney BR, Moser CC, Dutton PL: **De Novo Design of a Cytochrome b Maquette for Electron Transfer and Coupled Reactions on Electrodes.** *The Journal of Physical Chemistry B* 2002, **106**(3):617-624.
66. Willner I, Heleg-Shabtai V, Katz E, Rau HK, Haehnel W: **Integration of a Reconstituted de Novo Synthesized Hemoprotein and Native Metalloproteins with Electrode Supports for Bioelectronic and Bioelectrocatalytic Applications.** *Journal of the American Chemical Society* 1999, **121**(27):6455-6468.
67. Liddell PA, Kuciauskas D, Sumida JP, Nash B, Nguyen D, Moore AL, Moore TA, Gust D: **Photoinduced Charge Separation and Charge Recombination to a Triplet State in a Carotene–Porphyrin–Fullerene Triad.** *Journal of the American Chemical Society* 1997, **119**(6):1400-1405.
68. Liddell PA, Sumida JP, Macpherson AN, Noss L, Seely GR, Clark KN, Moore AL, Moore TA, Gust D: **PREPARATION AND PHOTOPHYSICAL STUDIES OF PORPHYRIN-C60 DYADS.** *Photochemistry and Photobiology* 1994, **60**(6):537-541.
69. Imahori H, Hagiwara K, Aoki M, Akiyama T, Taniguchi S, Okada T, Shirakawa M, Sakata Y: **Linkage and Solvent Dependence of Photoinduced Electron Transfer in Zincporphyrin-C60 Dyads.** *Journal of the American Chemical Society* 1996, **118**(47):11771-11782.

70. Kuciauskas D, Liddell PA, Lin S, Stone SG, Moore AL, Moore TA, Gust D: **Photoinduced Electron Transfer in Carotenoporphyrin–Fullerene Triads: Temperature and Solvent Effects.** *The Journal of Physical Chemistry B* 2000, **104**(18):4307-4321.
71. Llansola-Portoles MJ, Gust D, Moore TA, Moore AL: **Artificial photosynthetic antennas and reaction centers.** *Comptes Rendus Chimie* 2017, **20**(3):296-313.
72. El-Khouly ME, El-Mohsnawy E, Fukuzumi S: **Solar energy conversion: From natural to artificial photosynthesis.** *Journal of Photochemistry and Photobiology C: Photochemistry Reviews* 2017, **31**:36-83.
73. Kato M, Cardona T, Rutherford AW, Reisner E: **Photoelectrochemical water oxidation with photosystem II integrated in a mesoporous indium-tin oxide electrode.** *J Am Chem Soc* 2012, **134**(20):8332-8335.
74. Kato M, Cardona T, Rutherford AW, Reisner E: **Covalent Immobilization of Oriented Photosystem II on a Nanostructured Electrode for Solar Water Oxidation.** *Journal of the American Chemical Society* 2013, **135**(29):10610-10613.
75. Davis J, Wrathmell C, Zhao J, Fletcher J: **The tunnelling conductance of molecularly ordered metalloprotein arrays.** *Journal of Molecular Recognition* 2004, **17**(3):167-173.
76. Gust D, Moore TA, Moore AL: **Realizing artificial photosynthesis.** *Faraday discussions* 2012, **155**:9-26.
77. O'Regan B, Gratzel M: **A low-cost, high-efficiency solar cell based on dye-sensitized colloidal TiO<sub>2</sub> films.** *Nature* 1991, **353**(6346):737-740.
78. Hartnagel H, Dawar A, Jain A, Jagadish C: **Semiconducting transparent thin films:** Institute of Physics Bristol; 1995.
79. Armstrong NR, Veneman PA, Ratcliff E, Placencia D, Brumbach M: **Oxide contacts in organic photovoltaics: Characterization and control of near-surface composition in indium– tin oxide (ITO) electrodes.** *Accounts of chemical research* 2009, **42**(11):1748-1757.

80. Nazeeruddin MK, Zakeeruddin S, Humphry-Baker R, Jirousek M, Liska P, Vlachopoulos N, Shklover V, Fischer C-H, Grätzel M: **Acid-base equilibria of (2, 2'-bipyridyl-4, 4'-dicarboxylic acid) ruthenium (II) complexes and the effect of protonation on charge-transfer sensitization of nanocrystalline titania.** *Inorganic Chemistry* 1999, **38**(26):6298-6305.
81. Topoglidis E, Lutz T, Willis RL, Barnett CJ, Cass AE, Durrant JR: **Protein adsorption on nanoporous TiO<sub>2</sub> films: a novel approach to studying photoinduced protein/electrode transfer reactions.** *Faraday discussions* 2000, **116**:35-46.
82. Topoglidis E, Campbell CJ, Cass AE, Durrant JR: **Factors that affect protein adsorption on nanostructured titania films. A novel spectroelectrochemical application to sensing.** *Langmuir* 2001, **17**(25):7899-7906.
83. Topoglidis E, Cass AE, Gilardi G, Sadeghi S, Beaumont N, Durrant JR: **Protein adsorption on nanocrystalline TiO<sub>2</sub> films: an immobilization strategy for bioanalytical devices.** *Analytical chemistry* 1998, **70**(23):5111-5113.
84. Dunn B, Miller J, Dave B, Valentine J, Zink J: **Strategies for encapsulating biomolecules in sol-gel matrices.** *Acta Materialia* 1998, **46**(3):737-741.
85. Campàs M, Prieto-Simón B, Marty J-L: **A review of the use of genetically engineered enzymes in electrochemical biosensors.** In: *Seminars in cell & developmental biology: 2009.* Elsevier: 3-9.
86. Rusmini F, Zhong Z, Feijen J: **Protein immobilization strategies for protein biochips.** *Biomacromolecules* 2007, **8**(6):1775-1789.
87. Topoglidis E, Palomares E, Astuti Y, Green A, Campbell CJ, Durrant JR: **Immobilization and electrochemistry of negatively charged proteins on modified nanocrystalline metal oxide electrodes.** *Electroanalysis* 2005, **17**(12):1035-1041.
88. Hagfeldt A, Boschloo G, Sun L, Kloo L, Pettersson H: **Dye-Sensitized Solar Cells.** *Chemical Reviews* 2010, **110**(11):6595-6663.
89. Haque SA, Palomares E, Cho BM, Green ANM, Hirata N, Klug DR, Durrant JR: **Charge Separation versus Recombination in Dye-Sensitized Nanocrystalline Solar**



- Cells: the Minimization of Kinetic Redundancy.** *Journal of the American Chemical Society* 2005, **127**(10):3456-3462.
90. Bisquert J, Fabregat-Santiago F, Mora-Seró I, Garcia-Belmonte G, Giménez S: **Electron Lifetime in Dye-Sensitized Solar Cells: Theory and Interpretation of Measurements.** *The Journal of Physical Chemistry C* 2009, **113**(40):17278-17290.
91. Hoshikawa, T., Yamanda, M., Kikuchi, R., Eguchi, K.: **Impedance analysis of internal resistance affecting the photoelectrochemical performance of dye-sensitized solar cells.** 2005, **152**(2).
92. Farid TA, Kodali G, Solomon LA, Lichtenstein BR, Sheehan MM, Fry BA, Bialas C, Ennist NM, Siedlecki JA, Zhao Z *et al*: **Elementary tetrahelical protein design for diverse oxidoreductase functions.** *Nature Chemical Biology* 2013, **9**(12):826-833.
93. Topoglidis E, Astuti Y, Duriaux F, Grätzel M, Durrant JR: **Direct electrochemistry and nitric oxide interaction of heme proteins adsorbed on nanocrystalline tin oxide electrodes.** *Langmuir* 2003, **19**(17):6894-6900.
94. Ruger P, Ambrosius D, Schmidt B, Sluka P, Guder H-J, Kopetzki E: **Electrochemical sensor containing an enzyme linked to binding molecules bound to a noble metal surface.** In.: Google Patents; 1998.
95. Fragoso A, Caballero J, Almirall E, Villalonga R, Cao R: **Immobilization of adamantane-modified cytochrome c at electrode surfaces through supramolecular interactions.** *Langmuir* 2002, **18**(13):5051-5054.

# **Chapter II**

## **General Experimental**

## 1- Materials and Reagents; General Experimental

All porphyrins were synthesised in house at the Intelligent Polymer Research Institute (IPRI, University of Wollongong) by Nick Roach, Rhys Mitchell, and/or Dr. Pawel Wagner. Maquette sequences were re-designed, expressed, cleaved, and characterised at the University of Pennsylvania (UPENN) by members of Prof. Leslie Dutton's research group. Maquettes were obtained in freeze-dried forms, with subsequent re-suspension in appropriate buffer, followed by centrifugation at 12,000 rpm for 15 min to precipitate any denatured peptides. The concentration of the resulting supernatant was determined via absorbance at 280 nm, corresponding to the absorbance maximum of tryptophan (W) residues. With the extinction coefficient of W known in conjunction with the number of W in the maquette sequence (Chapter III), the concentration of maquette in solution was calculated. Maquettes were all prepared at concentrations  $<100 \mu\text{M}$  so as to reduce concentration-based aggregative tendencies of proteins at high concentrations, with maquette solutions subsequently stored at in the fridge at  $4^\circ\text{C}$ .

The reagents N-cyclohexyl-2-aminoethanesulfonic acid (CHES; Sigma-Aldrich), 2-(N-morpholino)ethanesulfonic acid (MES; Sigma-Aldrich), potassium chloride (KCl; Sigma-Aldrich), potassium hydroxide (KOH; Sigma-Aldrich), tetrabutylammonium perchlorate (TBAP; Sigma-Aldrich), tetrabutylammonium iodide (TBAI; Sigma-Aldrich), 2-aminoethylphosphonic acid (Sigma-Aldrich), 3-phosphonopropionic acid (Sigma-Aldrich), N-hydroxysuccinimide (NHS; Sigma-Aldrich), N-(3-dimethylaminopropyl)-N'-ethylcarbodiimide hydrochloride (EDC; Sigma-Aldrich), 3-(maleimido)propionic acid N-hydroxysuccinimide ester (Sigma-Aldrich), 4-tertbutylpyridine (Sigma-Aldrich), 1-butyl-3-methylimidazolium iodide (BMII; Sigma-Aldrich), 1,2-dimethyl-3-propylimidazolium (Sigma-Aldrich), lithium iodide (LiI; Sigma-Aldrich), potassium iodide (KI; Sigma-Aldrich), and iodine ( $\text{I}_2$ ; Merck) were all purchased reagent grade and used without further treatment.

Solvents dimethyl sulfoxide (DMSO; Sigma-Aldrich), hydrochloric acid (HCl; Sigma-Aldrich), anhydrous valeronitrile (VN; Sigma-Aldrich), anhydrous acetonitrile (ACN; Sigma-Aldrich), anhydrous dichloromethane (DCM; Sigma-Aldrich), and anhydrous tetrahydrofuran (THF; Sigma-Aldrich) were all purchased and used without further purification.

Fluorine-doped tin oxide (FTO) coated glass ( $R_s \leq 8$  ohms/square) (Hartford TEC8) was used for conductive substrates. Several  $\text{TiO}_2$  pastes were employed depending on thicknesses required, with a transparent (DSL 18 NR-T  $\text{TiO}_2$  paste, Dyesol) and a reflective (WER2-0  $\text{TiO}_2$  paste, Dyesol) titanium dioxide ( $\text{TiO}_2$ ) layer screen printed onto the FTO coated glass.

## 2- Methods; General Experimental

### 2.1- Buffer solutions

'Aqueous buffer' was prepared using CHES (150 mM), and KCl (200 mM), in milli-Q water, adjusted to pH 8.5 with KOH, and stored at 4 °C ('aqueous buffer' also referred to as 'CHES buffer'). 'MES buffer' was prepared using MES (150 mM), KCL (200 mM) in milli-Q water, adjusted to pH 6.8 using KOH, and stored at 4 °C.

### 2.2- Maquette-porphyrin binding in solution

#### 2.2.1- Solution UV-Visible and fluorescence spectroscopy equipment

UV-vis. spectra of all porphyrin compounds were obtained between 250 and 800 nm, recorded using a Shimadzu UV 1601 spectrophotometer connected to a PC running UV-vis. Probe software. Solution based measurements were undertaken using a 1 cm path length quartz cuvette. All absorbance data was referenced to a control sample before measurements, with the absorbance at 800 nm normalised.

Emission and excitation were measured on a Spec Fluorolog 3-22 spectrofluorometer connected to a PC running Jobin Yvon DataMax software. Excitation and emission slits were kept identical for all measurements, with samples measured in a 1 cm path length cuvette, excited using a xenon lamp. Samples were excited at appropriate (stated) wavelengths, with resulting emissions detected at an angle of 90° with respect to the excitation beam.

#### 2.2.2- Porphyrins in DMSO and CHES buffer

All porphyrins used were weighed using a 5-digit milligram balance ( $\pm 0.001$  mg; Sartorius) and prepared in DMSO solution to a concentration of 200  $\mu\text{M}$ . The stock solutions were used to measure extinction coefficients in a 1 mL quartz cuvette with DMSO or CHES buffer, whereby the final concentration was 1  $\mu\text{M}$ . This results in a 0.5 % of the stock DMSO

being present in the CHES, not expected to significantly influence measurements. UV-Vis. absorbance and excitation/emission spectra of resulting solutions were obtained as described above.

### **2.2.3- Maquette-porphyrin measurements over time**

For porphyrins in aqueous buffer, 2  $\mu\text{M}$  porphyrin was prepared in CHES buffer from 200  $\mu\text{M}$  stock solutions in a 1 mL quartz cuvette. The solution was mixed for 10 sec via pipette before measuring the absorbance every 5 mins (including 0 min) for 2 h. To observe porphyrins mixed with BT- or GL-maquette, 5  $\mu\text{M}$  maquette and 2  $\mu\text{M}$  porphyrin was prepared in a 1 mL quartz cuvette, with the solution mixed for 10 sec via pipette action before measuring the absorbance every 5 mins (including 0 min) for 2 h.

### **2.2.4- Dyads**

The dyads were weighed using a 5-digit milligram balance ( $\pm 0.001$  mg; Sartorius) and prepared in a DMSO solution to a concentration of 200  $\mu\text{M}$ . The stock solutions were used to measure extinction coefficients in a 1 mL quartz cuvette with DMSO, whereby the final concentration was 1  $\mu\text{M}$ .

For dyads in aqueous buffer, 3  $\mu\text{M}$  porphyrin was prepared in CHES buffer from 200  $\mu\text{M}$  stock solutions in a 1 mL quartz cuvette. The solution was mixed for 10 sec via pipette before measuring the absorbance every 30 mins (including 0 min) for 18 h. To observe porphyrins mixed with BT- or GL-maquette, 5  $\mu\text{M}$  maquette and 3  $\mu\text{M}$  porphyrin was prepared in a 1 mL quartz cuvette, with the solution mixed for 10 sec via pipette action before measuring the absorbance every 30 mins (including 0 min) for 18 h.

The surfactant N,N-dimethyldodecylamine N-oxide (LDAO; Sigma-Aldrich) was employed at a concentration of 2 mM, being pre-mixed with the aqueous buffer before application with dyads and maquettes.

### **2.2.5- Maquette-porphyrin titrations**

Binding titrations of porphyrin to maquette were undertaken by adding aliquots of 1  $\mu\text{l}$  from a stock porphyrin solution (200  $\mu\text{M}$  porphyrin in DMSO) to 2 ml of 0.5  $\mu\text{M}$  maquette solution in aqueous buffer, increasing porphyrin concentration by 0.1  $\mu\text{M}$  per aliquot.

Absorbance spectra were measured following mixing via pipette action after each additional aliquot for 1 min. By plotting the change in absorbance at the maximum of the bound porphyrin vs the concentration of porphyrin added, the calculated extinction coefficient, dissociation constant ( $K_D$ ), and stoichiometric relationship of a modelled fit (using OriginPro 8 Software) was obtained using the equation [1] below;

**Equation 2 [1]**      
$$Fit = Ltot * efree + (ebound - efree) * \frac{(Kd + Ptot + Ltot - ((Kd + Ptot + Ltot)^2 - 4 * Ptot * Ltot)^{0.5})}{2}$$

Where; Ltot = concentration of porphyrin\*, efree = extinction coefficient of free porphyrin#, ebound = extinction coefficient of bound porphyrin#, Ptot = concentration of maquette+, Kd = Dissociation constant#

\*denotes data parameter obtained

#denotes parameter free for data fitting

+denotes fixed parameter

### 2.2.6- Maquette-porphyrin emission/excitation

For porphyrins in aqueous buffer, 0.1  $\mu$ M porphyrin was prepared in CHES buffer from 200  $\mu$ M stock porphyrin solutions in a 1 mL quartz cuvette. The solution was mixed for 10 sec via pipette before measuring emission with the appropriate excitation wavelength (corresponding to the absorbance at the Soret peak maxima) further described in Chapter III. The excitation spectrum was measured using the same solution, with the detector set at the maximum emission peak wavelength (as described in Chapter III). Maquette-porphyrin solutions were prepared with 0.1  $\mu$ M maquette and 0.1  $\mu$ M porphyrin in CHES buffer in a 1 mL quartz cuvette, with the solution mixed for 10 sec via pipette action before measuring emission and excitation spectra (as described above).

### 2.2.7- Maquette-porphyrin isolation and purification

Size exclusion chromatography was undertaken using a PD-10 Desalting Column (GE Healthcare Life Sciences), containing 8.3 mL of Sephadex G-25 resin. Columns were rinsed with CHES buffer (10 mL) prior to use. 2.5 mL of 20  $\mu$ M maquette with 60  $\mu$ M porphyrin in CHES buffer (pre-mixed for 5 min) was added to the column, with 3.5 mL of CHES buffer used for elution.

Protein centrifugal filtration was undertaken using 3 kDa molecular weight cut-off (MWCO) Amicon Ultra-4 centrifugal filters (Sigma-Aldrich). Filters were spun at 12,000 rpm for 15 min with CHES buffer prior to use. 2 mL of 20  $\mu$ M maquette with 60  $\mu$ M porphyrin in CHES buffer was used as starting material, which was spun in the filter tube at 12,000 rpm for 20 min per cycle. Before the start of the following cycle, CHES buffer was added to the filter so that the total volume was  $\sim$ 2 mL.

### **2.3– TiO<sub>2</sub> electrodes preparation**

FTO-glass was sonicated in milli-Q water with detergent for 15 min, followed by sonication with acetone for 15 min, with a final sonication in ethanol for 15 min and with drying via a N<sub>2</sub> gas-stream directly prior to use. TiO<sub>2</sub> was screen-printed onto the cleaned glass substrate using a 90T screen with 4 x 4 mm areas, with transparent TiO<sub>2</sub> used as supplied to produce films with thicknesses of 2.5  $\mu$ m. Thinner films (600 nm) were produced by mixing transparent paste with terpineol (Sigma-Aldrich) in a ratio of 1:2 (w/w %), respectively. If employed, additional layers of TiO<sub>2</sub> were screen printed directly on top of previously printed films, whereby after each layer the films were left to rest for 10 min, followed by heating to 110°C for 15 min, and cooling to room temperature (RT) for 5 min prior to the addition of further layers. On completion of additional layers, substrates were sintered using a ramped temperature profile, containing a series of increasing temperatures and hold times (Figure II-1). Film thicknesses were determined by AFM profilometry (Dektak 150, Veeco). 2.5  $\mu$ m films were comprised of a single layered transparent paste, with 8.5  $\mu$ m films developed with two layers of transparent and a third layer of reflective paste.

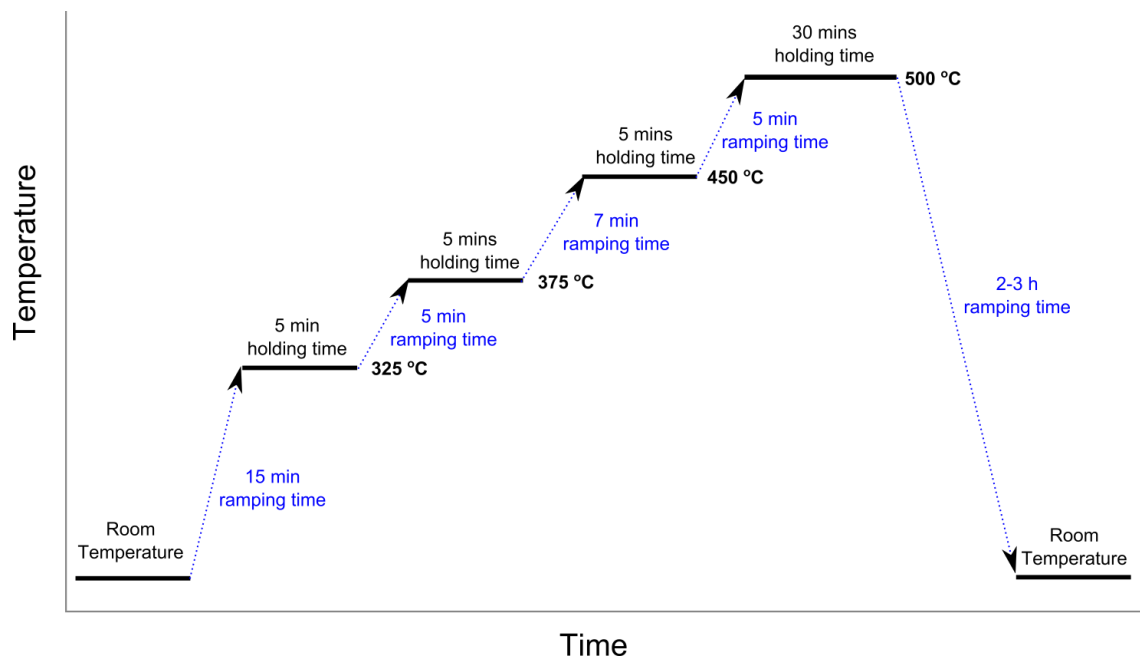


**Figure II-1; Ramping profile for sintering screen-printed TiO<sub>2</sub>.** The ramped temperature profile used for sintering TiO<sub>2</sub> on FTO substrate post printing, with temperature holding and ramping times shown.

## 2.4- Immobilization onto TiO<sub>2</sub> electrodes

Substrates were cut to appropriate sizes and reheated to 500 °C, ramping time 20 min, holding for 30 min, followed by cooling to 110 °C for 60 min prior to any use. This process removes any absorbed water, or other possible organic contaminants. If maquette was used directly onto the cleaned TiO<sub>2</sub>, the substrate was cooled for a further 20 min to 40 °C.

### 2.4.1- Porphyrin sensitization from THF

For sensitizing porphyrins onto TiO<sub>2</sub>, cleaned substrates were submerged into freshly prepared 200 μM of the appropriate porphyrin in anhydrous THF. Solutions containing substrates were left for 3 h at RT, kept in the dark. Following solution exposure, substrates were removed and rinsed by dipping substrates into ACN with subsequent immediate drying via a N<sub>2</sub> gas stream.

### 2.4.2- Porphyrin and maquette-porphyrin ensemble immobilization from aqueous buffer

For binding porphyrins directly to TiO<sub>2</sub> from aqueous buffer, cleaned substrates were submerged into 80 μM of the appropriate porphyrin in aqueous buffer. Porphyrin in aqueous buffer was prepared through the use of a stock solution, prepared in DMSO at a concentration of 2 mM, so that the amount of DMSO was ≤ 5 %. Similarly, when maquette-porphyrin



ensembles were used with submersion of substrates, 42  $\mu\text{M}$  GL-maquette was prepared with 80  $\mu\text{M}$  porphyrin in aqueous buffer. Solutions containing substrates were sealed via parafilm, covered in foil, and left in the fridge ( $4^{\circ}\text{C}$ ) for the times specified. Following exposure, substrates were removed and rinsed by dipping into aqueous buffer with subsequent drying via a  $\text{N}_2$  gas stream.

If drop-casting of solutions onto  $\text{TiO}_2$  was employed, the solutions were prepared to concentrations specified. Following mixing via vortexing, 100  $\mu\text{l}$  of the solution was pipetted onto the cleaned substrate. If ‘purified solutions’ were used (typically with a maquette to porphyrin ratio of 1:1.95), centrifugal filtration was used for the ensembles, with the solution after 5-cycles obtained and diluted to an appropriate concentration, which was subsequently drop-cast (100  $\mu\text{l}$ ) onto the substrate. Substrates were placed in a petri-dish, sealed with parafilm, covered in foil, and left in the fridge ( $4^{\circ}\text{C}$ ) for the times specified. Following immobilization, substrates were removed and rinsed by dipping into aqueous buffer with subsequent drying via a  $\text{N}_2$  gas stream.

#### **2.4.3- $\text{TiO}_2$ modification and binding**

Modification of  $\text{TiO}_2$  with self assembled monolayers (SAMs) utilizing the well characterised phosphonic acid groups was undertaken on cleaned  $\text{TiO}_2$ . Electrodes were submerged in either 2 mM 2-aminoethylphosphonic acid in milli-Q water or 2 mM 3-phosphonopropionic acid in ethanol for 24 h at RT. Following this, samples were rinsed in either milli-Q water (for 2-aminoethylphosphonic acid) or ethanol (for 3-phosphonopropionic acid) for 24 h at RT, followed by heating to  $120^{\circ}\text{C}$  for 24 h, with a final rinse before further use.

For covalent attachment via EDC/NHS reaction, 50  $\mu\text{l}$  of pre-mixed 42  $\mu\text{M}$  GL-maquette and 80  $\mu\text{M}$  porphyrin in MES buffer was drop-casted onto the surface of  $\text{TiO}_2$  modified with 3-phosphonopropionic acid. The electrode was sealed in a petri dish with parafilm, covered in foil and left in the fridge ( $4^{\circ}\text{C}$ ) for 24 h. Following this, 50  $\mu\text{l}$  of EDC (36 mM) and NHS (17mM) in MES buffer was drop-casted onto the sample, left at RT for a further 24 h, sealed in a Petri dish and covered with foil. Electrodes were then rinsed by dipping into aqueous buffer and drying via a  $\text{N}_2$  gas stream.

For covalent attachment via 3-(maleimido)propionic acid N-hydroxysuccinimide ester, the  $\text{TiO}_2$  substrate was modified with 2-aminoethylphosphonic acid. Before attachment, 1.0 mM

3-(maleimido)propionic acid N-hydroxysuccinimide ester was dissolved in DMSO and drop-casted (100  $\mu$ l) onto the modified surface for 3 h at RT. Following this, the surface was rinsed with milli-Q water and dried with a  $N_2$  gas-stream before further use. Either the maquette by itself (at 40  $\mu$ M) or the pre-formed ensembles (42  $\mu$ M maquette with 80  $\mu$ M porphyrin) were prepared in MES buffer. The maquette solution was drop-casted (50  $\mu$ l) and left on the surface, sealed in a petri dish with parafilm, covered in foil and left in the fridge (4°C) for 24 h. For comparisons, if no maquette was present, the surface was still exposed to MES buffer under the same conditions. The electrodes were then rinsed in aqueous buffer before being submerged into 100  $\mu$ M porphyrin in aqueous buffer for 24 h. For ensembles, 100  $\mu$ l was drop-casted onto the surface, sealed in a petri dish with parafilm, covered in foil and left in the fridge (4°C) for 48 h. Following attachment, electrodes were rinsed in aqueous buffer and dried via a  $N_2$  gas-stream.

### 2.5- Electrochemical analysis

Electrochemical characterisation was performed using an eDAQ potentiostat to deliver a voltage and an eDAQ e-corder 201 to interface the potentiostat with a PC with EChem software. Cyclic voltammetry (CV) and square wave voltammetry (SW) were performed using a three electrode cell comprised of a platinum disc working electrode (8 mm<sup>2</sup> active area), a platinum mesh auxiliary electrode, and an Ag/Ag<sup>+</sup> reference electrode constructed by submerging a silver wire into an 0.01 M AgNO<sub>3</sub> solution in ACN containing 0.1 M TBAP as a supporting electrolyte. CV and SW measurements were performed in 0.8 mM porphyrin solutions in DMF with 0.1 M TBAP, scanned at a rate of 50 mV s<sup>-1</sup> for CV and 20 mV s<sup>-1</sup> for SW. 1 mM ferrocene solution in DMF with 0.1 M TBAP was used as an internal reference for calibrating potentials to a normalised hydrogen electrode (NHE). Solutions were purged with argon for 20 min before measurements within an argon environment. Pre and post measuring, electrodes were cleaned, with the working electrode rinsed with THF, sonicated in acetone for 10 min, and polished using a slurry created from 0.2  $\mu$ m silica powder. The auxiliary electrode was cleaned via heating with a Bunsen burner, with the reference electrode rinsed in ACN for 10 min. The apparatus and configuration used for electrochemical acquisition is shown schematically in Figure II-2. If electrochemical analysis was performed on TiO<sub>2</sub> films directly, the working platinum electrode was replaced with the film (Figure II-3). The area of TiO<sub>2</sub> used was 0.16 cm<sup>2</sup>, with the solvent used being 0.1 M TBAP in ACN.

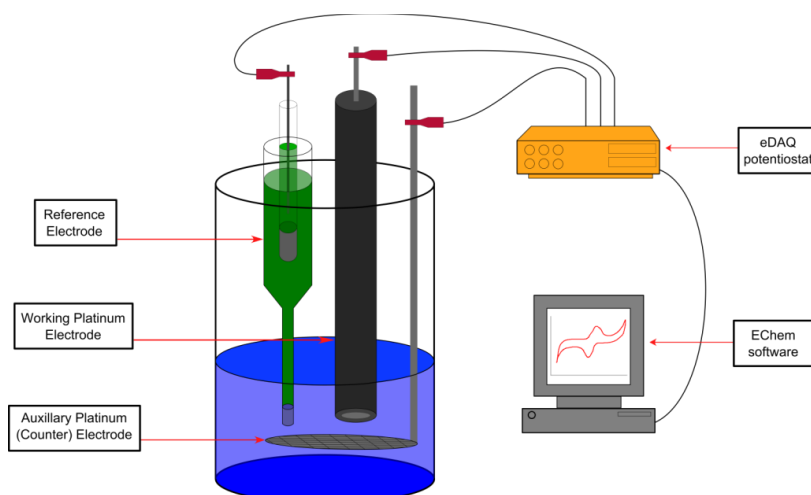


**Figure II-2; Schematic representation of three electrode cell for solution based electrochemistry.** Set up of a three electrode system for acquisition of electrochemical data using a platinum working electrode, platinum auxiliary electrode, and  $\text{Ag}/\text{Ag}^+$  reference electrode, used with a potentiostat and EChem software.

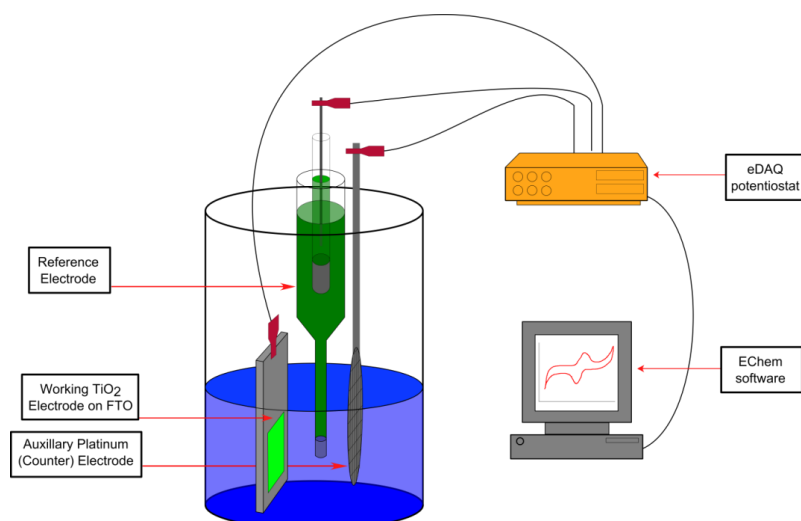


**Figure II-3; Schematic representation of three electrode cell for film based electrochemistry.** Set up of a three electrode system for acquisition of electrochemical data using a  $\text{TiO}_2$  working electrode, platinum auxiliary electrode, and  $\text{Ag}/\text{Ag}^+$  reference electrode, used with a potentiostat and EChem software.

## 2.6- Dye sensitized solar cell (DSSC) based devices

Counter electrodes were prepared by cutting appropriately sized FTO-glass (eg. 8x8 mm), followed by drilling a hole into the corner of the electrode. Following this, electrodes were sonicated in milli-Q water containing detergent for 15 min, followed by sonication with acetone for 15 min, a final sonication in ethanol for 15 min and drying via a  $\text{N}_2$  gas-stream directly prior to drop-casting 100  $\mu\text{l}$  of 10 mM  $\text{H}_2\text{PtCl}_6$  (Sigma-Aldrich) in ethanol onto the FTO-coated side. Electrodes were then heated to 500  $^\circ\text{C}$ , ramping time 20 min, holding for 30 min, followed by cooling to RT.

Directly following TiO<sub>2</sub> treatments, devices were prepared by sealing the counter electrode and FTO anode together around the TiO<sub>2</sub> using a 25 μm hot-melt polymer gasket (meltronix, Solaronic). The appropriate electrolyte (outlined below) was introduced to the sealed volume between electrodes by dropping 20 μl on top of the hole in the counter electrode, covering with a cover-slip, and applying vacuum before slowly releasing pressure. The hole was then sealed with aluminium foil and hot-melt polymer. An illustration of a typical completed device is shown in Figure II-4. Both electrodes had wires attached using a USS-9200 ultrasonic soldering system (MBR Electronics) in order to provide good electrical contacts for characterisation.

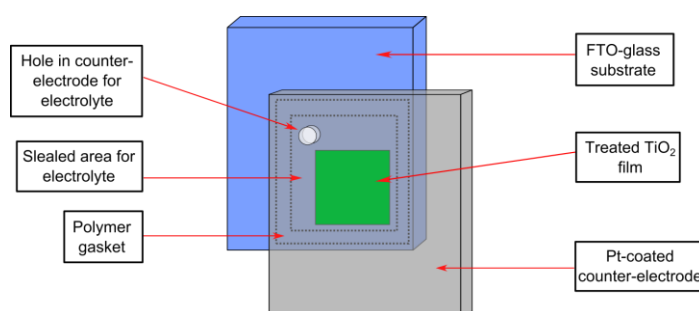


**Figure II-4; Schematic representation of a DSSC construct.** Conventional dye sensitized solar cell (DSSC) construct, illustrating the components and manufacture set-up of devices fabricated.

Electrolyte compositions employed within this study included;

**Electrolyte 1 (E1):** Prepared with 85:15 vol% acetonitrile/valeronitrile and 0.03 M iodine (I<sub>2</sub>), 0.6 M BMII, and 0.5 M 4-tbp.

**Electrolyte 1 (E2):** Prepared with 85:15 vol% acetonitrile/valeronitrile and 0.03 M iodine (I<sub>2</sub>), 0.6 M BMII, 0.1 M LiI, and 0.5 M 4-tbp.

## 2.7- Device measurements and characterisations

The absorbance of films were recorded using a 4 mm<sup>2</sup> ‘window’, positioned within the centre of the 16 mm<sup>2</sup> TiO<sub>2</sub> so as to ensure consistency between film measurements. The TiO<sub>2</sub> film was positioned perpendicular to the incident beam, with films referenced against a cleaned sample of the same thickness of TiO<sub>2</sub> film being measured. The absorbance measurements for all samples were normalised at 800 nm (baseline).

### 2.7.1- Photovoltage and photocurrent testing

Current and voltage (*IV*) responses to light exposure were recorded using a feedback controlled solar simulator which illuminates devices with a 100 mW cm<sup>-2</sup> simulated air mass (AM) 1.5 light source (Oriel) (1 sun illumination), calibrated using a certified silicon diode. *IV*

curves were recorded using a Keithley 2400 source measurement unit to measure the output current and linearly sweep the applied voltage to devices, from -0.05 to 0.85 V at a scan rate of  $25 \text{ mV s}^{-1}$ . The  $I_{sc}$  (short circuit current, when  $V=0$ ),  $V_{oc}$  (open circuit voltage, when  $I=0$ ), maximum current point ( $I_{mp}$ ), maximum voltage point ( $V_{mp}$ ) were determined from  $IV$  curves, allowing for subsequent calculation of fill factor (FF). Each of the measured points is illustrated in the idealized  $IV$  curve in Figure II-5. Solar-to-electrical energy efficiencies were then determined from the  $I_{sc}$ ,  $V_{oc}$ , FF, and the applied light intensity.

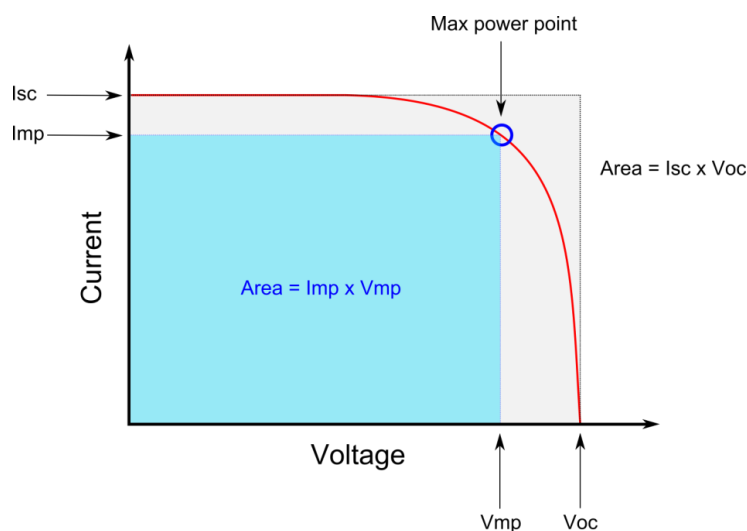


**Figure II-5; A typical current-voltage ( $IV$ ) curve from a device.** The short-circuit current ( $I_{sc}$ ) is equal to that when voltage is 0, and correspondingly the open-circuit voltage ( $V_{oc}$ ) is equal to that when the current is 0. The maximum power current ( $I_{mp}$ ) and maximum power voltage ( $V_{mp}$ ) is the current and voltage (respectively) obtained from the device at maximum power output.

### 2.7.2- Incident photon-to-current conversion efficiency (IPCE) measurements

Incident photon-to-current conversion efficiencies (IPCE) were measured using a QEX10 instrument (PV-Measurements), which was calibrated using a certified silicon diode before each measurement. Devices were recorded every 1 nm for 0.3 seconds, for wavelengths of 300 to 800 nm with a 5 millisecond delay between wavelength measurements.

### 2.7.3- Electrochemical impedance spectroscopy (EIS) measurements

Electrochemical impedance spectroscopy (EIS) was undertaken using a Potentiostat Reference 600 (Gamry Instruments). Measurements were recorded with a  $100 \text{ mW cm}^{-2}$  simulated air mass (AM) 1.5 light source (Oriel), under  $V_{oc}$  conditions from  $1 \times 10^6$  to 0.1 Hz with AC perturbations of 10 mV RMS.

## 2.8- Gallium-based porphyrins

As was undertaken with previous porphyrins, the gallium-based porphyrin (PGa) was weighed using a 5-digit milligram balance ( $\pm 0.001$  mg; Sartorius) and prepared in a DMSO solution to a concentration of 200  $\mu\text{M}$ . The stock solutions were used to measure extinction coefficients in a 1 mL quartz cuvette with DMSO or CHES buffer, whereby the final concentration was 1  $\mu\text{M}$ . This results in a 0.5 % of the stock DMSO being present in the CHES, expected to not significantly influence measurements.

For porphyrins in aqueous buffer, 2  $\mu\text{M}$  porphyrin was prepared in CHES buffer from 200  $\mu\text{M}$  stock solutions in a 1 mL quartz cuvette. The solution was mixed for 10 sec via pipette before measuring the absorbance every 5 mins (including 0 min) for 30 min. To observe porphyrins mixed with 4-*his* GL-maquette, 5  $\mu\text{M}$  maquette and 2  $\mu\text{M}$  porphyrin were prepared in a 1 mL quartz cuvette, with the solution mixed for 10 sec via pipette action before measuring the absorbance every 5 mins (including 0 min) for 30 min.

The binding titration of porphyrin to maquette was undertaken by adding aliquots of 1  $\mu\text{l}$  from a stock porphyrin solution (200  $\mu\text{M}$  porphyrin in DMSO) to 2 ml of 0.3  $\mu\text{M}$  maquette solution in aqueous buffer, increasing porphyrin concentration by 0.1  $\mu\text{M}$  per aliquot. Absorbance spectra were measured after mixing each additional aliquot for 20 sec via pipette action. By plotting the change in absorbance at the maximum of bound porphyrin vs the concentration of porphyrin added, the calculated extinction coefficient, dissociation constant ( $K_D$ ), and stoichiometric relationship of a modelled fit were obtained using Equation 2 (shown above).

Electrochemical analysis of PGa was undertaken as described previously for solution based porphyrin, except that the solvent used was THF as opposed to DMF.

Immobilization onto  $\text{TiO}_2$ , device preparation, and all measurements utilizing PGa or complexation with maquettes were undertaken as described previously with P1d (Section 2.4).

## 2.9- Resonance Raman spectroscopy

All resonance Raman spectroscopy was carried out by either Holly van der Salm or Jonathan E. Barnsley under supervision of Prof. Keith C. Gordon of the University of Otago, New Zealand (collaborators). Solution-based measurements were prepared at the University of Otago (by me), whereby solid-state measurements were prepared at the University of Wollongong and sent to the University of Otago. Before solid state measurements, the UV-vis.

absorbance profile of each sample was measured to determine that the sample had not been disrupted. All UV-vis. data measured at the University of Otago was identical to when the solid-state samples were measured at the University of Wollongong, indicating that the samples were not disrupted and stable.

Solution-based resonance Raman spectra were collected using a setup which has been previously described [2]. In short, it is composed of an excitation beam and collection lens in a 135° backscattering arrangement. Scattered photons were focused on the entrance slit of an Acton SpectraPro500i spectrograph with a 1200 grooves/mm grating, which disperses the radiation in a horizontal plane on a Princeton Instruments Spec10 liquid-nitrogen-cooled CCD detector. A solid-state CrystaLaser was used for 448.0 nm excitation wavelength and a notch filter (Kaiser Optical, Inc.) matched to this wavelength was used to remove the laser excitation line. Samples were all measured in CHES buffer, with 20  $\mu\text{M}$  of BT- or GL-maquette used to determine maquette signals. Porphyrin concentration in CHES buffer alone was 20  $\mu\text{M}$ , with concentrations of 20, 40, or 80  $\mu\text{M}$  with 20  $\mu\text{M}$  of either BT- or GL-maquette to produce intended ratios. Porphyrin samples were diluted from a stock solution of 1 mM in DMSO.

Solid-state measurements were collected using an identical setup as described above, however, two wavelengths measurements were undertaken (406.7, produced by an Innova I-302 krypton ion laser (Coherent Inc.), and 448.0 nm), with the dry film ( $\text{TiO}_2$  sample) secured in air. Samples were prepared using 2.5  $\mu\text{m}$   $\text{TiO}_2$  on FTO with an area of 4x4 mm, as described previously. Four different samples were prepared, included a negative control of  $\text{TiO}_2$  with no further treatment post sintering. A second control sample was also prepared, by drop-casting 100  $\mu\text{l}$  of 50  $\mu\text{M}$  GL-maquette in CHES buffer onto the  $\text{TiO}_2$  film. The porphyrin (P1d) was covalently bound via submerging the  $\text{TiO}_2$  film into 200  $\mu\text{M}$  anhydrous THF solution for 3 h, followed by rinsing in ACN and drying via  $\text{N}_2$  gas stream. The porphyrin salt was bound via drop-casting 100  $\mu\text{l}$  of 50  $\mu\text{M}$  P1d in CHES buffer onto the  $\text{TiO}_2$  film. Electrostatic immobilization of ensemble was prepared by mixing 50  $\mu\text{M}$  with 50  $\mu\text{M}$  GL-maquette in CHES buffer, with drop-casting 100  $\mu\text{l}$  onto the  $\text{TiO}_2$  film. Drop-casted samples were all sealed in a petri dish, and left in the dark at 4 °C for four days, followed by rinsing in CHES buffer and drying via  $\text{N}_2$  gas stream.

### 3- References; General Experimental

1. Farid TA, Kodali G, Solomon LA, Lichtenstein BR, Sheehan MM, Fry BA, Bialas C, Ennist NM, Siedlecki JA, Zhao Z *et al*: **Elementary tetrahelical protein design for diverse oxidoreductase functions**. *Nature Chemical Biology* 2013, **9**(12):826-833.
2. Horvath R, Gordon KC: **Understanding excited-state structure in metal polypyridyl complexes using resonance Raman excitation profiles, time-resolved resonance Raman spectroscopy and density functional theory**. *Coordination Chemistry Reviews* 2010, **254**(21–22):2505-2518.



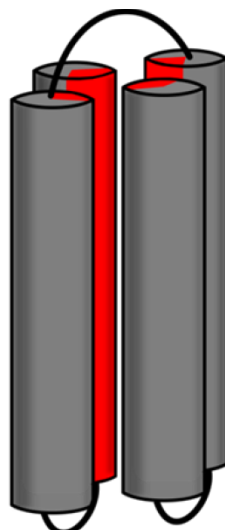
## **Chapter III**

# **Maquette-Porphyrin Binding in Solution**

## 1- Introduction; Maquette-Porphyrin Binding in Solution

Binding of metal-substituted cofactors to maquettes via axial ligation to the histidine residue of the maquette is well characterised, with the spectral changes associated with the cofactor often indicative of ligation within the maquette [1-5]. The metallic centre of porphyrins offers a unique opportunity to ligate within maquettes, as there is only the one metal present on the porphyrin. In addition, the porphyrins are easily altered via substituents for specific functionality. Furthermore, zinc-based porphyrins have a high absorbance coefficient along with a sharp Soret peak (compared to iron-based porphyrins), making it a useful tool for the analysis of interactions. This chapter looks at the effects of altering the substituents of zinc-based porphyrins to increase hydrophilicity (decreasing hydrophobicity) and the impacts the substituents and hydrophilicity have on ligation to maquettes. Furthermore, free-base porphyrins, which cannot ligate to histidine residues, are explored with substituent alterations for increasing hydrophilicity. This allows for the effects of hydrophilicity associated with the porphyrin to be explored in the context of hydrophobic partitioning within the maquette, which is assumed to be a significant force attributed to facilitating ligation of cofactors.

Two maquette sequences were chosen for this study, being a BT-maquette and a GL-maquette, named after the designers of each maquette sequence (Figure III-1). The number of amino acids, type of protein structure, along with the hydrophobic interior of the maquette remained unchanged between the maquettes. The difference between the two maquettes arises from the polar amino acids on the exterior of the hydrophilic surface of the maquettes, whereby the charges of the associated residues results in the GL-maquette having two helices, which are over-all slightly positive, with the BT-maquette having all four helices overall slightly negative (Figure III-1).

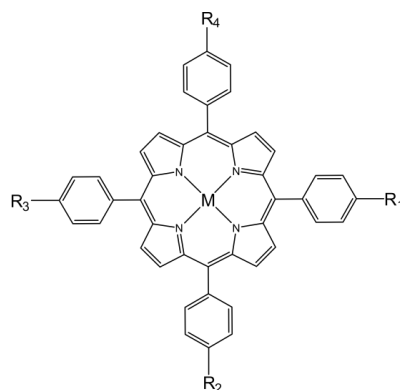


### Polar / Non-Polar

Helix Number	Overall Charge	BT-Maquette Sequence	Loop-Region
I	-4	<b>G</b> E I W K Q <b>H</b> E D A L Q K F E E A L N Q F E D L K Q L	G G S G S G S G G
II	-4	E I W K Q A E D A L Q K F E E A L N Q F E D L K Q L	G G S G S G S G G
III	-4	E I W K Q A E D A L Q K F E E A L N Q F E D L K Q L	G G S G S G S G G
IV	-4	E I W K Q <b>H</b> E D A L Q K F E E A L N Q F E D L K Q L	
Helix Number	Overall Charge	GL-Maquette Sequence	Loop-Region
I	-4	<b>G</b> E I W K Q <b>H</b> E D A L Q K F E E A L N Q F E D L K Q L	G G S G S G S G G
II	+2	E I K Q R A E D A L R K F E E A L K R F E D K K Q K	G G S G S G S G G
III	-4	E I W K Q A E D A L Q K F E E A L N Q F E D L K Q L	G G S G S G S G G
IV	+2	E I K Q R <b>H</b> E D A L R K F E E A L K R F E D K K Q K	

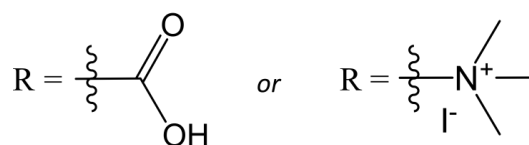
**Figure III-1; Maquette structure and sequence.** A schematic of a four  $\alpha$ -helix maquette bundle is shown, with the hydrophobic core in red. Sequences of two maquette sequences are shown, highlighting the polar (black) and non-polar (red) residues, with the histidine residue (bold) highlighted, located specifically for metal ligation to cofactors.

Porphyrins were designed to contain a zinc centre for potential ligation to histidine residues within the maquette, in conjunction with variations of carboxylic or trimethylammonium groups, used to explore impacts of increasing hydrophilicity for maquette interactions (Figure III-2). Furthermore, free-base versions were designed to explore the interaction between the porphyrin and maquette, whereby interactions being primarily driven by hydrophobic partitioning of the porphyrin with the interior of the maquette (P2a-P2e, Figure III-2). To analyse the potential electrostatic solvent and protein interactions facilitating ligation between zinc-based porphyrins and maquettes, zinc-TPP porphyrins with various trimethylammonium functional groups were used (P3a-P3e). This allowed for a direct comparison of the effects of opposing charges associated with the carboxylate and ammonium groups on the zinc porphyrins, in the context of facilitating maquette interaction.



Where;

M = Zinc (Zn), or free-base (H<sub>2</sub>)

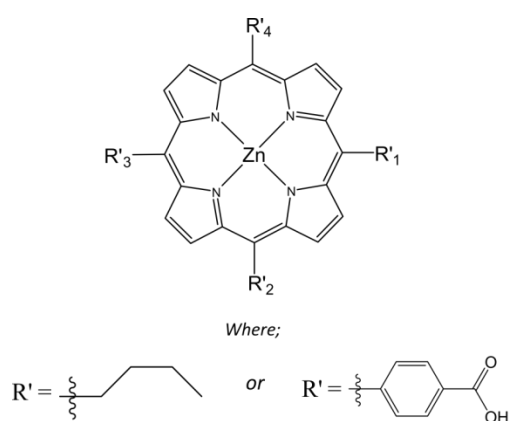


Porphyrin Name	R1	R2	R3	R4	M
P1a	COOH	H	H	H	Zn
P1b	COOH	COOH	H	H	Zn
P1c	COOH	H	COOH	H	Zn
P1d	COOH	COOH	COOH	H	Zn
P1e	COOH	COOH	COOH	COOH	Zn
P2a	COOH	H	H	H	H <sub>2</sub>
P2b	COOH	COOH	H	H	H <sub>2</sub>
P2c	COOH	H	COOH	H	H <sub>2</sub>
P2d	COOH	COOH	COOH	H	H <sub>2</sub>
P2e	COOH	COOH	COOH	COOH	H <sub>2</sub>
P3a	NMe <sub>3</sub> I	H	H	H	Zn
P3b	NMe <sub>3</sub> I	NMe <sub>3</sub> I	H	H	Zn
P3c	NMe <sub>3</sub> I	H	NMe <sub>3</sub> I	H	Zn
P3d	NMe <sub>3</sub> I	NMe <sub>3</sub> I	NMe <sub>3</sub> I	H	Zn
P3e	NMe <sub>3</sub> I	NMe <sub>3</sub> I	NMe <sub>3</sub> I	NMe <sub>3</sub> I	Zn

**Figure III-2; Porphyrin models based on a tetraphenylporphyrin of increasing hydrophilicity for binding to maquettes.** The core structure used is a tetraphenylporphyrin, with additions of carboxylic or trimethylammonium functional groups for analysis of increasing hydrophilicity, in conjunction with using zinc and free-base porphyrins for potential ligations to histidine.

Exploring porphyrin interactions with maquettes was analysed through hydrophobicity/hydrophilicity via controlling substituent groups. To further analyse potential bindings into maquettes, the hydrophobic substituents on the porphyrin core were varied (Figure III-3). A butyl group was used, compared to a phenyl, with the hydrophilic group

remaining the same (Figure III-4; P4a-P4d). This porphyrins series was designed to explore if the hydrophobic substituents played a role in the hydrophobic partitioning of the porphyrin into the maquette. All porphyrins used within this chapter were synthesised in house by Nicholas Roach [6].



Porphyrin Name	R' <sub>1</sub>	R' <sub>2</sub>	R' <sub>3</sub>	R' <sub>4</sub>
P4a	Ar-COOH	<i>n</i> -Bu	<i>n</i> -Bu	<i>n</i> -Bu
P4b	Ar -COOH	Ar -COOH	<i>n</i> -Bu	<i>n</i> -Bu
P4c	Ar -COOH	<i>n</i> -Bu	Ar -COOH	<i>n</i> -Bu
P4d	Ar -COOH	Ar -COOH	Ar -COOH	<i>n</i> -Bu

**Figure III-3; Porphyrin models based on a porphyrin of increasing hydrophilicity for binding to maquettes.** The core structure used is a zinc porphyrin, with additions of aromatic carboxylic functional groups for increasing hydrophilicity, with butyl groups for hydrophobicity.

## 2- Results; Maquette-Porphyrin Binding in Solution

To ascertain the absorbance profile of porphyrins, it is imperative that the porphyrin is solubilized and monomeric. Furthermore, porphyrins are known to be highly sensitive to their environment, whether in regards to planarity, solvation, or aggregation [7-10]. Therefore, a solvent capable of solvating the porphyrins presented here was used, being dimethyl sulfoxide (DMSO). DMSO is expected to solubilize all porphyrins, with no dissociation of the carboxylic substituents of P1a-P1e, P2a-P2e, and P4a-P4d, as the pKa of benzoic acid is 11.1 in DMSO [11]. With the absorbance profile of each porphyrin in DMSO known, potential aggregation affects in other solvents, such as aqueous solutions can be analysed. Soret peak positions and corresponding extinction coefficients (to the nearest  $100 \text{ M}^{-1} \text{ cm}^{-1}$ ) from porphyrins presented here in DMSO are tabulated in Table III-1.

### 2.1- Absorbance profiles of porphyrins in DMSO

#### 2.1.1- Absorbance of Zn-based tetraphenylporphyrin carboxylic acids

In order to explore the absorbance changes resulting from carboxylic group substitution of a zinc tetraphenylporphyrin, the absorbance spectra of the monomeric (non-aggregated) porphyrin were measured DMSO (Figure III-4) and the results tabulated in Table III-1 below. All porphyrins were observed to have a distinctly sharp and symmetrical Soret peak along with two Q-bands, with a typical shoulder on the lower wavelength side of the Soret peak. These characteristics are indicative of solubilised monomeric porphyrin species [12]. The general trend for addition of carboxylic functionality groups to a zinc tetraphenylporphyrin results in a slight red-shift of the absorbance profile (Table III-1). The mono-carboxylic porphyrin (P1a) has a Soret peak which becomes red-shifted by 2 nm when three carboxylic functional groups are added (forming P1e). Similarly, the Q-bands are red-shifted by 1 nm for P1a compared to P1e. This result is expected, as modifications of aromatic substituents are known to have minimal impact on spectral characteristics due to negligible influence on the conjugated core of the porphyrin [13, 14].

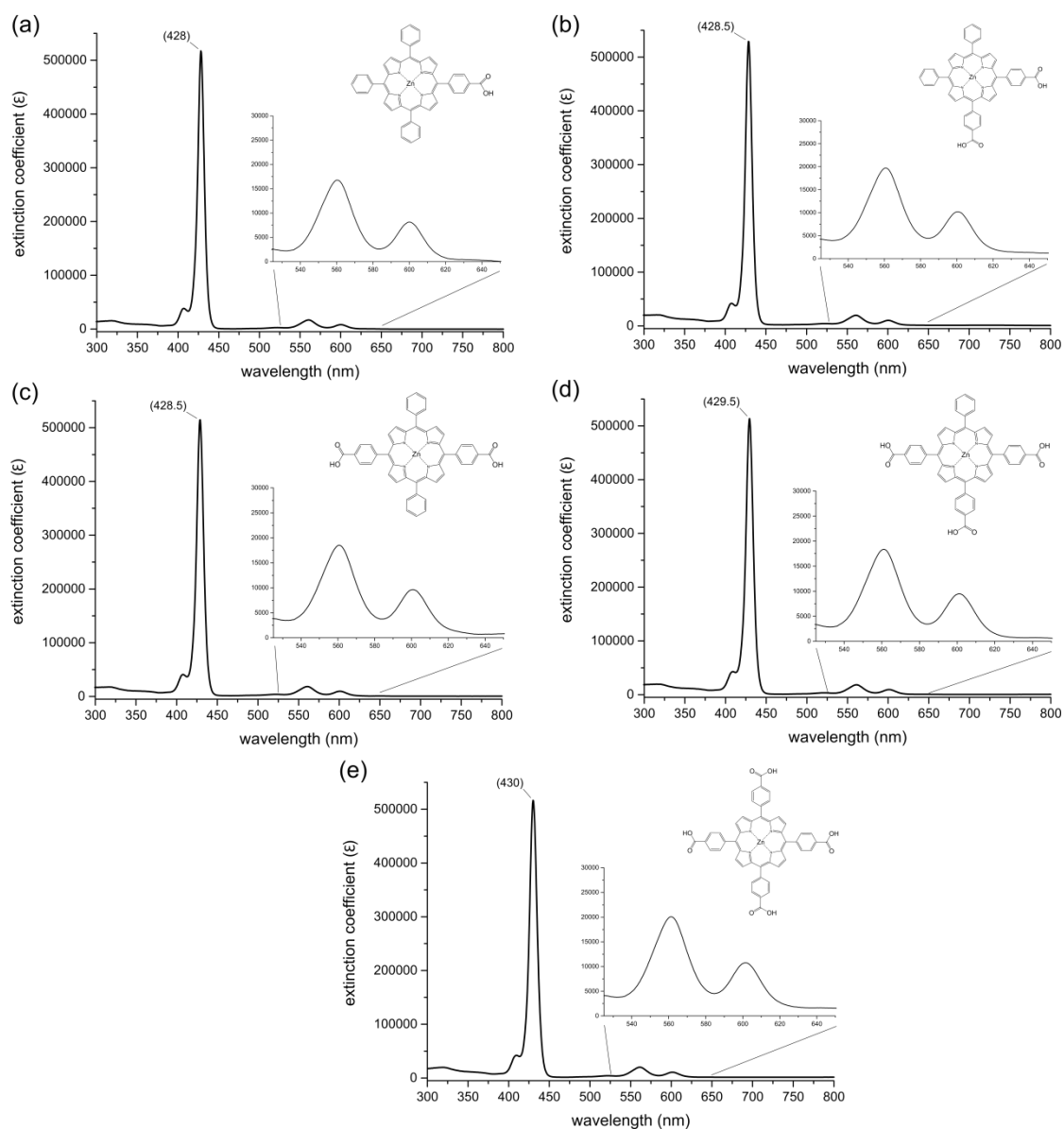


**Figure III-4; Absorbance spectra of carboxylic substituted zinc based tetraphenylporphyrin in DMSO. (a) P1a. (b) P1b. (c) P1c. (d) P1d. (e) P1e.**

### 2.1.2- Absorbance of free-base tetraphenylporphyrin carboxylic acids

In order to explore the absorbance changes resulting from carboxylic acid substitution of a free-base tetraphenylporphyrin, the absorbance spectra of the porphyrins were measured in DMSO (Figure III-5), with peak positions tabulated (Table III-1). The trend is identical to that observed for P1a-P1e, whereby additions of carboxylic acids results in a slight red-shift of the absorbance profile. The Soret peak red-shifts by 2 nm for when a mono-carboxylic porphyrin (P2a) has three carboxylic acids added (forming P2e). The Q-band at the highest wavelength (646 nm) did not change with additions of carboxylic acids, whereas the remaining three Q-bands red-shifted by 1-2 nm (Table III-1). As stated previous, the modification of the aromatic substituents is expected to not induce significant spectral changes.

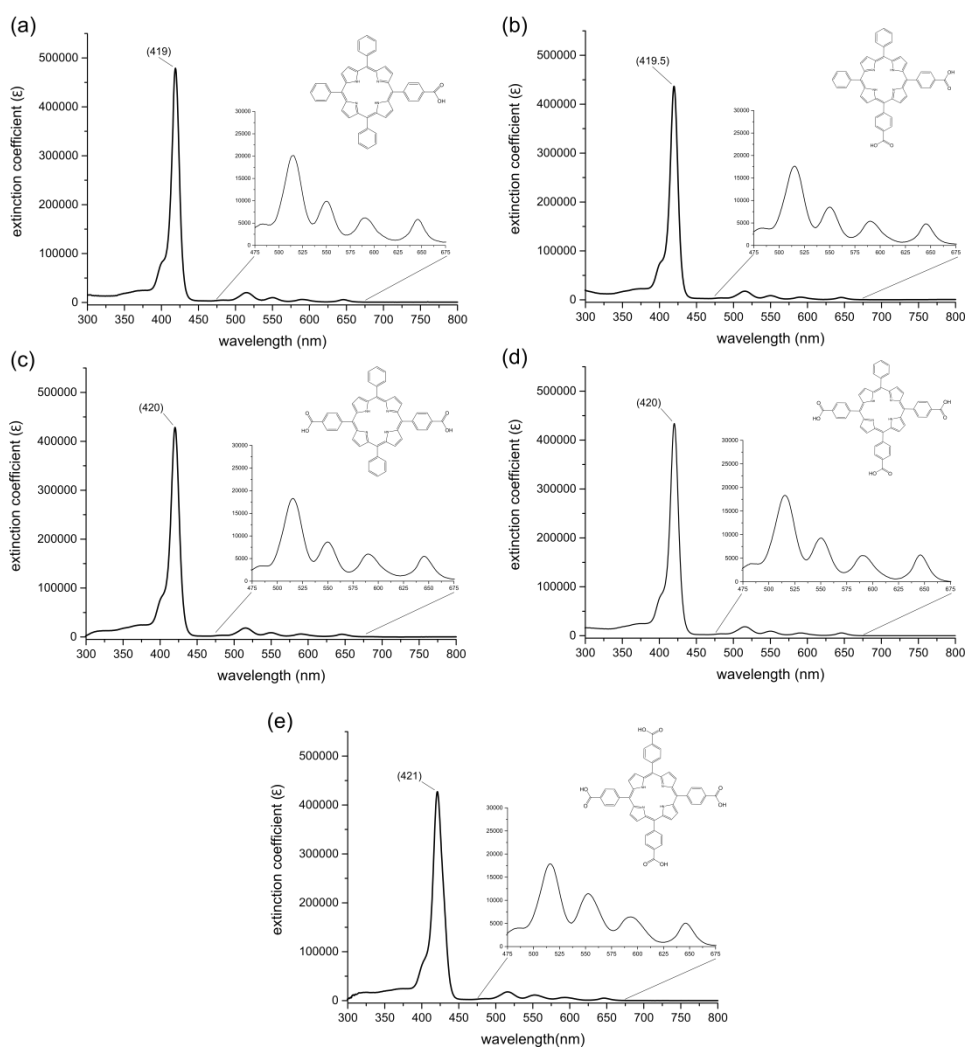


**Figure III-5; Absorbance spectra of carboxylic substituted free-base tetraphenylporphyrins in DMSO. (a) P2a. (b) P2b. (c) P2c. (d) P2d. (e) P2e.**



### 2.1.3- Absorbance of Zn-based tetraphenylporphyrin ammonium salts

Further exploration of absorbance changes through hydrophobicity/hydrophilicity functionality group, zinc tetraphenylporphyrin with substituted trimethylammonium functional groups were prepared in DMSO. As previously observed, all porphyrins displayed absorbance profiles which are indicative of monomeric and solubilised entities (Figure III-6) and resulting peak positions tabulated (Table III-1). The general trend observed with additions of trimethylammonium groups is that the absorbance profile slightly red-shifts (Table III-1). Direct comparison of the mono-trimethylammonium porphyrin (P3a) to the tetra-trimethylammonium porphyrin (P3e) shows that the Soret and Q-bands red-shift by 1 and 0.5 nm, respectively. As stated previously, modifications of aromatic substituents are expected to not induce significant spectral changes.

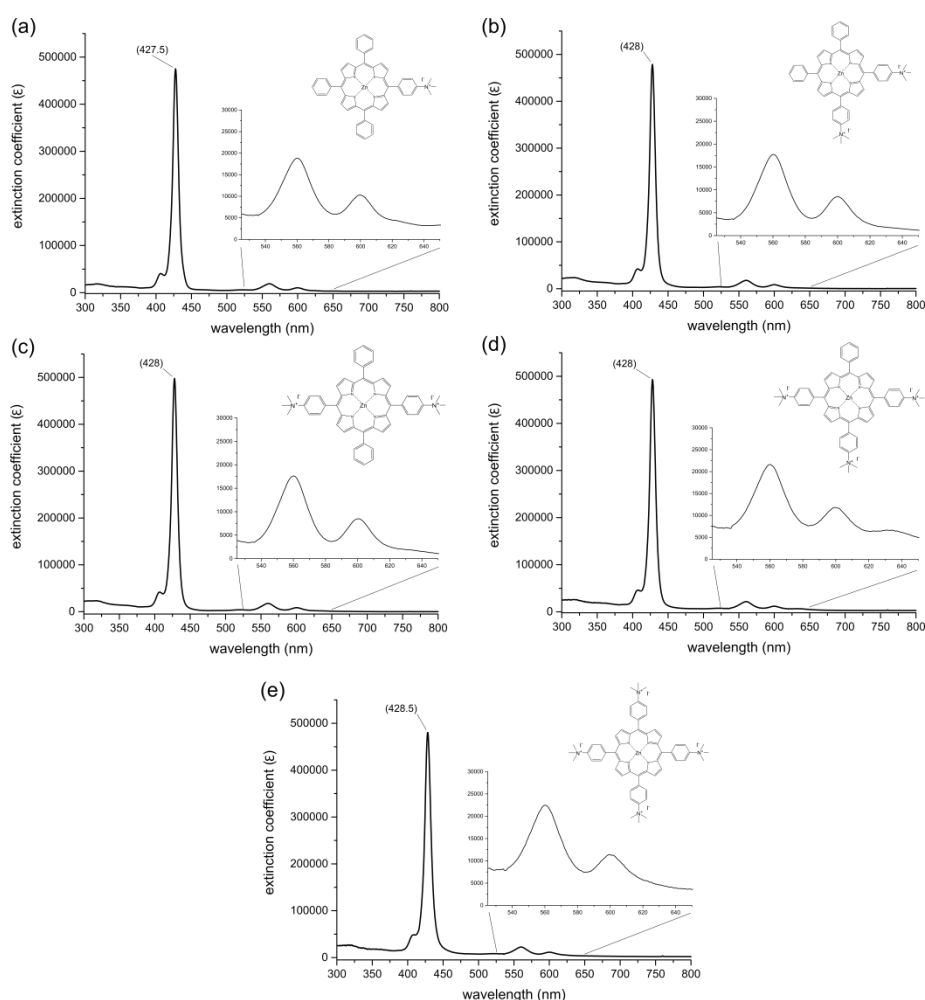


**Figure III-6; Absorbance spectra of trimethylammonium substituted zinc based tetraphenylporphyrins in DMSO. (a) P3a. (b) P3b. (c) P3c. (d) P3d. (e) P3e.**

### 2.1.4- Absorbance of Zn-based butylporphyrin carboxylic acids

To determine the absorbance changes of zinc-based porphyrins as a result of substituting a butyl group with an aromatic carboxylic acid, the butylporphyrin absorbance spectra were measured in DMSO (Figure III-7), with peak positions tabulated (Table III-1). All porphyrins were determined to be solubilised and monomeric in DMSO. The general trend observed was that replacing a butyl group with an aromatic carboxylic acid slightly red-shifts the Soret peak, with the Q-bands slightly blue-shifting (Table III-1). Comparison of P4a to P4d, it is apparent that the Soret peak has red-shifted by 1 nm, while contrastingly, the Q-bands had blue-shifted by 2-3 nm. As was stated previously, modifications of aromatic substituents are expected to not induce significant spectral changes.

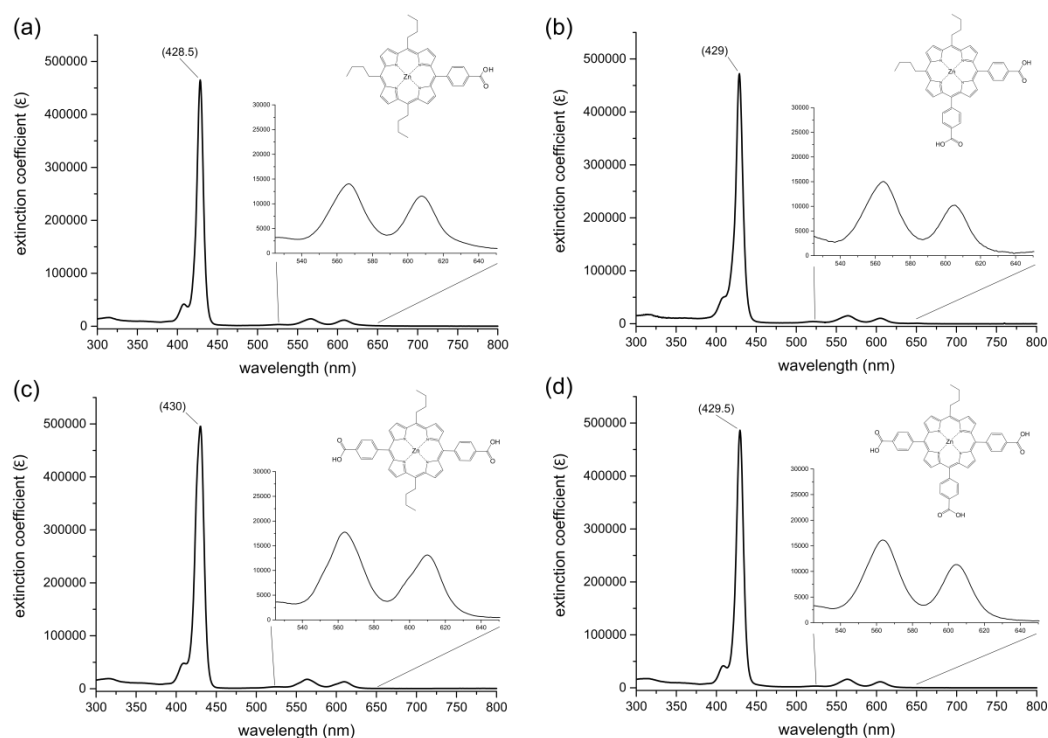


**Figure III-7; Absorbance spectra of carboxylic substituted zinc based butylporphyrins in DMSO. (a) P4a. (b) P4b. (c) P4c. (d) P4d.**

**Table III-1; Absorbance spectral data in DMSO.** Absorbance peaks obtained from porphyrins measured in DMSO.

<b>Porphyrin</b>	<b>Soret peak (nm / M<sup>-1</sup> cm<sup>-1</sup>)</b>		<b>Q-band positions (nm)</b>
P1a	428	517,400	561, 601
P1b	428.5	529,100	561, 601
P1c	428.5	514,200	561, 601
P1d	429.5	514,600	562, 601
P1e	430	516,500	562, 602
P2a	419	479,100	515, 551, 590, 646
P2b	419.5	436,800	515, 550, 590, 646
P2c	420	428,500	515, 550, 590, 646
P2d	420	433,900	516, 551, 591, 646
P2e	421	427,300	516, 552, 593, 646
P3a	427.5	475,200	560, 600
P3b	428	478,800	560.5, 600.5
P3c	428	498,000	560.5, 600.5
P3d	428	493,100	560.5, 600.5
P3e	428.5	480,400	560.5, 600.5
P4a	428.5	465,200	566, 608
P4b	429	495,400	564, 605
P4c	430	495,400	565, 608
P4d	429.5	486,400	564, 605

## 2.2- Emission spectra of porphyrins in DMSO

### 2.2.1- Emission of Zn-based tetraphenylporphyrin carboxylic acids

In order to explore the emission changes resulting from carboxylic group substitution of a zinc tetraphenylporphyrin, the emission spectra of the monomeric (non-aggregated) porphyrin were measured DMSO (Figure III-8) and Tabulated in Table III-2. All porphyrin were excited at the maximum absorbance of the Soret peak of the porphyrin in DMSO, resulting in two emission peaks being observed (Section 2.1). The general trend observed is that when a carboxylic group is added to a zinc tetraphenylporphyrin, the two emission peaks are slightly red-shifted (Table III-2). The mono-carboxylic porphyrin (P1a) has two emission peaks which red-shift by 2-3 nm when three carboxylic functional groups are added (forming P1e). The minimal difference observed for emissions from aromatic modifications are in agreement with the absorbance characteristics.

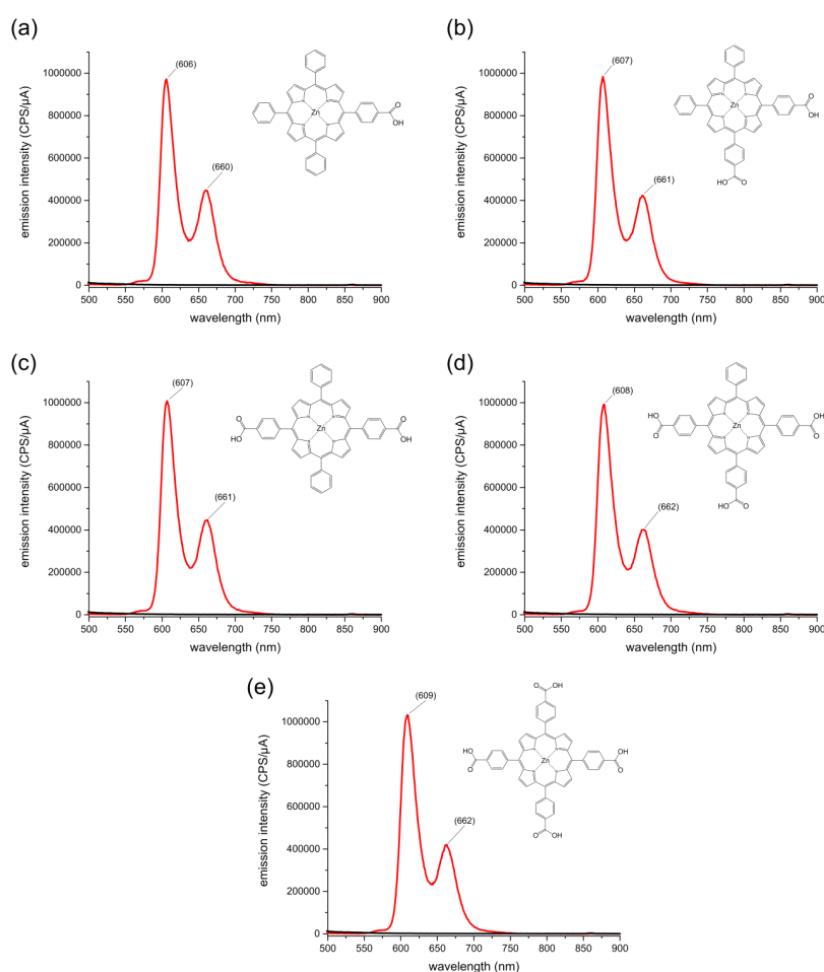


**Figure III-8; Emission spectra of carboxylic substituted zinc tetraphenylporphyrins in DMSO.** (a) P1a, excited at 428 nm. (b) P1b, excited at 428.5 nm. (c) P1c, excited at 428.5 nm. (d) P1d, excited at 429.5 nm. (e) P1e, excited at 430nm.

### 2.2.2- Emission of free-base tetraphenylporphyrin carboxylic acids

Emission spectral changes resulting from the carboxylic acid substitution of porphyrins was further analysed through the use of free base tetraphenylporphyrins. Emission of each porphyrin was measured in DMSO, with the excitation wavelength matching that of the Soret peak maximum (from Section 2.1). All porphyrins displayed two distinct emission peaks (Figure III-9) with the peak position tabulated (Table III-2). The emission profile red-shifts by 4 nm for when a mono-carboxylic porphyrin (P2a) has three carboxylic acids added to forming P2e (Table III-2). This trend is similar to that observed with the zinc-based equivalent porphyrins, shown previous.

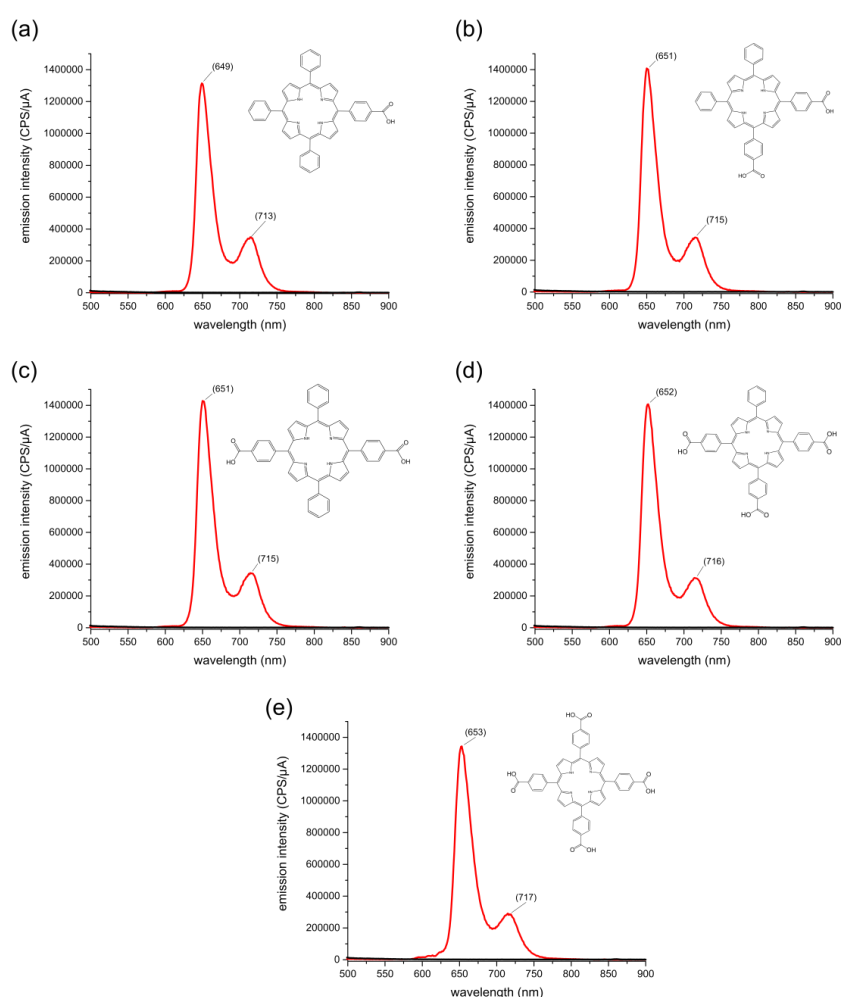


**Figure III-9; Emission spectra of carboxylic substituted free-base tetraphenylporphyrins in DMSO.** (a) P2a, excited at 419 nm. (b) P2b, excited at 419.5 nm. (c) P2c, excited at 420 nm. (d) P2d, excited at 420 nm. (e) P2e, excited at 421 nm.

### 2.2.3- Emission of Zn-based tetraphenylporphyrin ammonium salts

Emission changes resulting from substituting zinc tetraphenylporphyrin with trimethylammonium groups were determined in DMSO (Figure III-10) and tabulated (Table III-2). Each porphyrin was measured with excitation corresponding to the maximum absorbance (Soret peak) in DMSO, with two distinct emission peaks apparent. No discernible trend is observed from the emission profiles with additions of trimethylammonium groups (Table III-2). This is in correlation with the absorbance spectra, with minimal influence of aromatic modification on spectral characteristics.

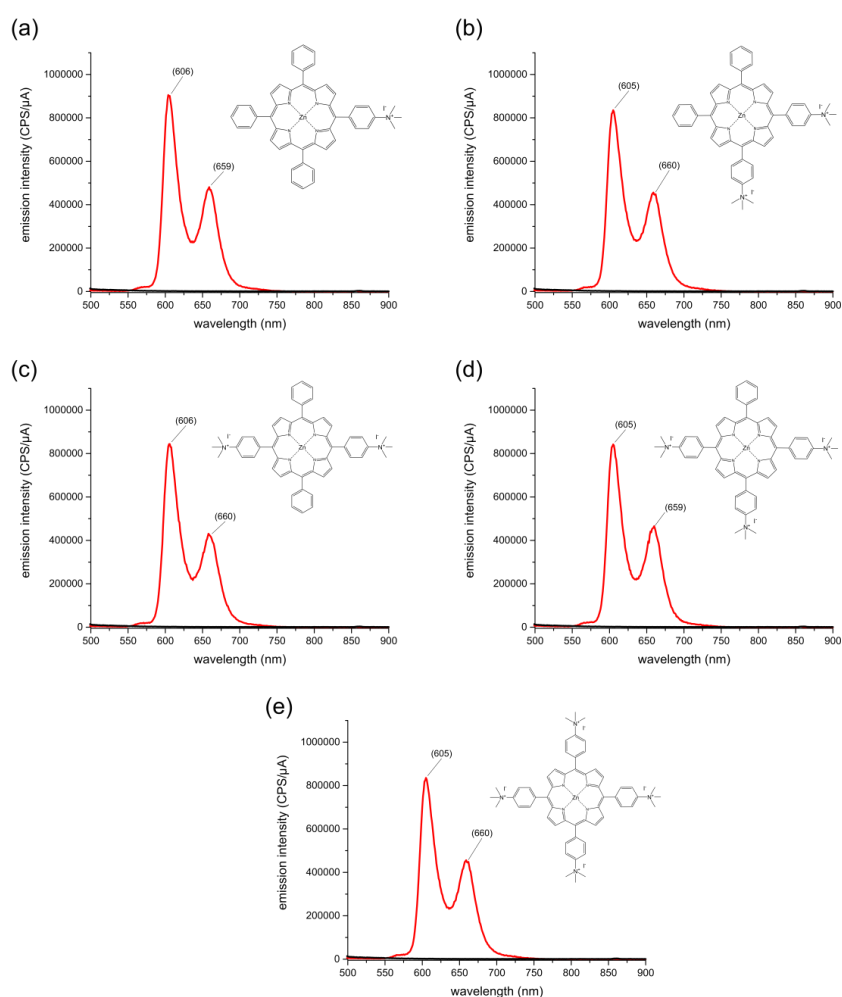


**Figure III-10; Emission spectra of trimethylammonium substituted zinc tetraphenylporphyrins in DMSO.** (a) P3a, excited at 427.5 nm. (b) P3b, excited at 428 nm. (c) P3c, excited at 428 nm. (d) P3d, excited at 428 nm. (e) P3e, excited at 428.5 nm.

### 2.2.4- Emission of Zn-based butylporphyrin carboxylic acids

Determination of emission changes through altering hydrophobicity/hydrophilicity via substituting of functional groups was explored. The emission profiles of zinc based porphyrins resulting from substituting a butyl group with an aromatic carboxylic acid were measured in DMSO (Figure III-11) and tabulated (Table III-2). The emission profiles all exhibit two distinct peaks, with the peaks blue-shifting by 2-4 nm when two butyl-groups are substituted with two aromatic carboxylic acid groups (P4a compared to P4d, Table III-2).

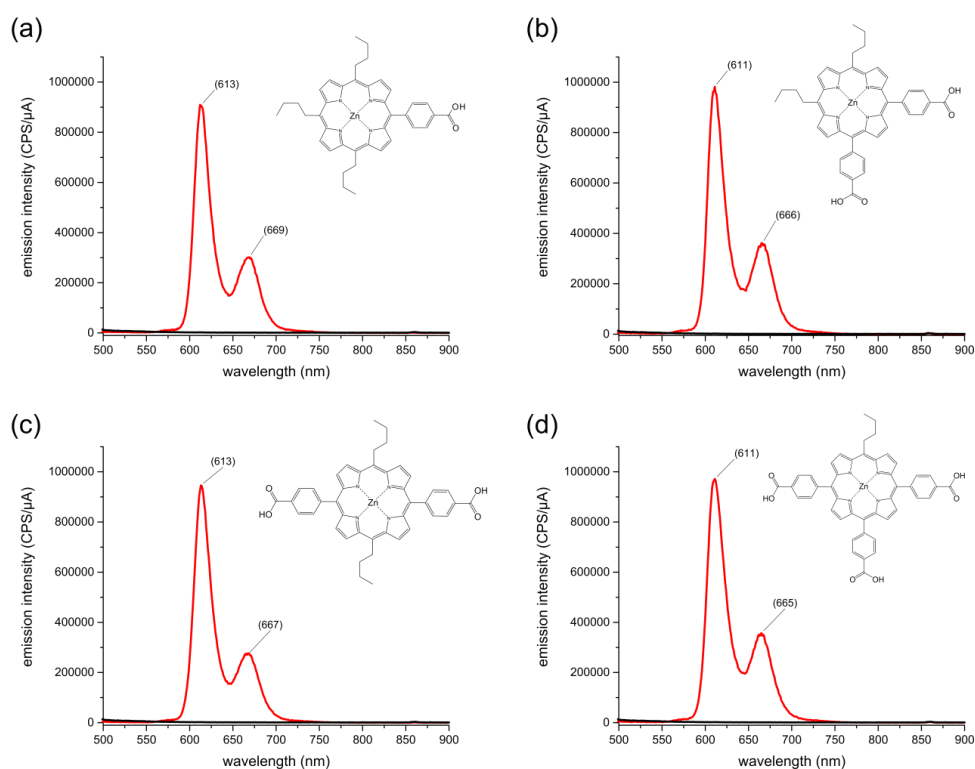


**Figure III-11; Emission spectra of phenyl-carboxyl substituted porphyrins in DMSO.** (a) P4a, excited at 428.5 nm. (b) P4b porphyrin, excited at 429 nm. (c) P4c, excited at 430 nm. (d) P4d, excited at 429.5 nm.

**Table III-2; Emission spectral data in DMSO.** Emission peaks obtained from porphyrins measured in DMSO, excited at maximum absorbance peak position.

<b>Porphyrin</b>	<b>Emission peaks (nm)</b>	<b>Excitation (nm)</b>
P1a	606, 660	428
P1b	607, 661	428.5
P1c	607, 661	428.5
P1d	608, 662	429.5
P1e	609, 662	430
P2a	649, 713	419
P2b	651, 715	419.5
P2c	651, 715	420
P2d	652, 716	420
P2e	653, 717	421
P3a	606, 659	427.5
P3b	605, 660	428
P3c	606, 660	428
P3d	605, 659	428
P3e	605, 660	428.5
P4a	613, 669	428.5
P4b	611, 666	429
P4c	613, 667	430
P4d	611, 665	429.5



### 2.3- Absorbance profiles of maquettes in aqueous buffer

The UV-vis. spectrum of the maquette was determined in order to identify its contribution to the absorbance profile when maquettes are present with porphyrin in solution. Figure III-12 shows the absorbance profiles for the BT- and GL-maquettes used. Both maquettes have negligible absorbance above 400 nm, with no discernible peaks above 320 nm. BT-maquette has a peak maximum at 280 nm, of greater intensity than that of the GL-maquette. This originates from the (intentionally placed) tryptophan residues, which have an absorbance maximum at 280 nm. The GL-maquette has 2 tryptophan residues, resulting in an extinction coefficient of  $11,200 \text{ M}^{-1} \text{ cm}^{-1}$  at 280 nm, whereas the BT-maquette contains 4 tryptophan residues with an extinction coefficient of  $22,400 \text{ M}^{-1} \text{ cm}^{-1}$  at 280 nm, which is the sole reason for the difference in absorbance measured below 300 nm.

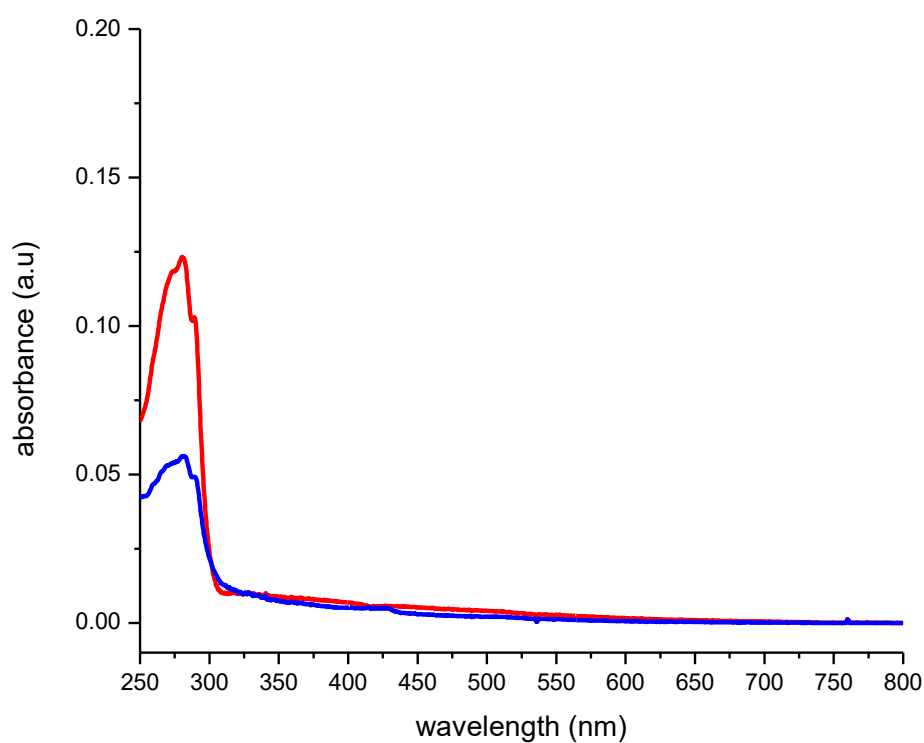


**Figure III-12; UV-vis. absorption spectra of maquettes in aqueous buffer.** 5  $\mu\text{M}$  BT-maquette (red) and 5  $\mu\text{M}$  GL-maquette (blue) absorption profiles.

## 2.4- Time resolved binding of maquettes and porphyrin in buffer

Many of the porphyrins presented here were not expected to be soluble in aqueous solutions, therefore, each porphyrin was prepared in DMSO before introduction into aqueous solution. The concentration of DMSO within the aqueous solution was always <5 % (v/v), with DMSO needed to introduce carboxylic acid porphyrins to the aqueous solution in monomeric states. Once introduced to the pH 8.5 buffered solution, carboxylic acid substituents will dissociate into carboxylates since the pKa of benzoic acid being 4.2 in aqueous solution [15, 16]. Although the pKa of benzoic acid is 11.1 in DMSO (*vide supra*), the small amount of DMSO within the buffer is not expected to substantially affect the dissociation of the porphyrins.

To determine the stability of each porphyrin in the aqueous environment, absorbance profiles were measured every 5 min. Hydrophobic porphyrins are expected to aggregate in the aqueous solution, with two distinct aggregates of porphyrins known, J- and H-aggregates [17, 18]. H-aggregates can result in a red-shifting of the spectra with a sharp Soret peak, whereby J-aggregates often lead to a blue-shifting with a broadened Soret peak, relative to the monomer in solution [18]. The stabilities and aggregative tendencies of the porphyrin salts in the aqueous solution are then compared to solutions with maquette present. Porphyrin ligation to maquettes will result in spectral changes, often a distinct red-shifting [1-5]. Maquettes were present in excess, so that the limiting factor for binding interactions would be primarily due to porphyrin hydrophobicity/hydrophilicity.

### 2.4.1- Binding of Zn-based tetraphenylporphyrin carboxylates

Zinc tetraphenylporphyrins with substituted carboxylates (P1a-P1e) were used to explore the impact of increasing hydrophilicity. As shown in Figure III-13a, P1a is expected to be largely hydrophobic, containing a single carboxyl group. Indeed, the absorbance profile obtained does not resemble that of a monomeric zinc porphyrin, with two distinct peaks around 400 nm observed (Figure III-13b). The peak at 386 nm likely arises from the aggregation of the porphyrin in aqueous solution, however this does not appear to have been previously reported. Nonetheless, peaks at ~400 nm are known to arise via porphyrin immobilization on surfaces from aqueous solutions [19, 20]. In contrast, an absorbance profile resembling that of monomeric P1a becomes apparent over time when in aqueous buffer with either BT- (Figure III-13c) or GL-maquette (Figure III-13d) present. This indicates that the monomeric form of

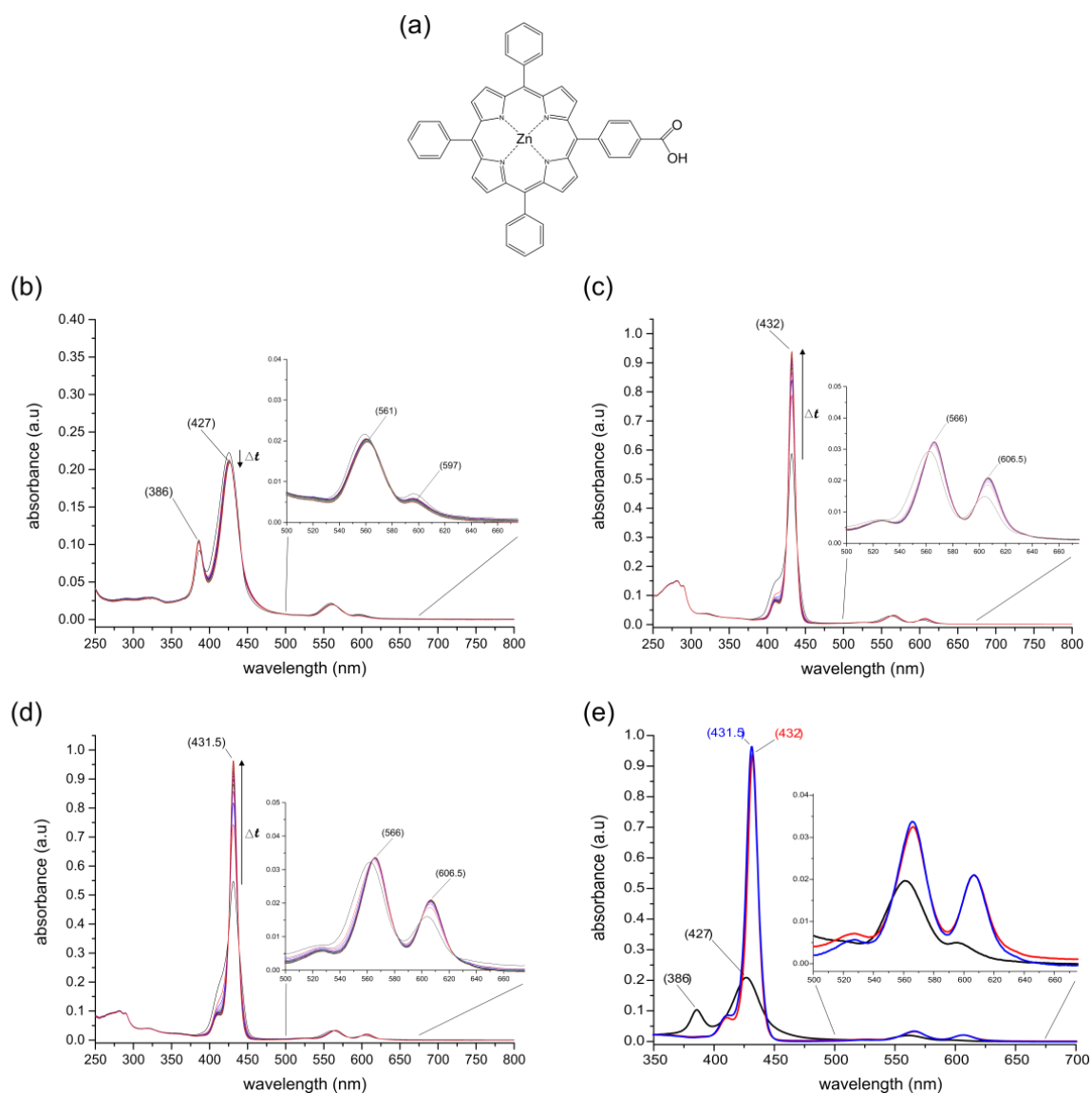
P1a is binding to the maquette and becoming stabilized in a monomeric form through ligation. The peak intensities for P1a in solution without maquette is significantly reduced compared to when with either maquette. This is due to alteration of the electronic state of P1a via exciton coupling of the aggregated porphyrin, which results in decreased intensity of peaks and broadening [21]. The increase in the absorbance spectra when P1a is with either maquette is due to the aggregated state of P1a being in equilibrium with the monomeric state, capable of being controlled by the ionic strength [22]. Therefore, with the assumption that the equilibrium is in favour of an aggregated state, ligation of P1a to the maquette in a monomeric state would occur slowly (>90 min). The ligation of P1a to either maquette results in a red-shifting of peak positions, indicative of axial ligation of the zinc (Table III-3).

Increasing hydrophilicity via the addition of a second carboxyl group to form P1b is expected to increase stability of the porphyrin in aqueous solutions. P1b in aqueous buffer shows an absorbance profile with a Soret peak which is broadened due aggregation (Figure III-14b). In conjunction with aforementioned effects of aggregation on porphyrin spectral properties, the spectrum of P1b is continually decreasing over time, indicating P1b is precipitating out of the solvent. In contrast, and as was evident with P1a, an absorbance profile resembling a monomeric state of P1b is apparent when either BT- (Figure III-14c) or GL-maquette (Figure III-14d) is present in conjunction with a 1-12 nm red-shifting of peaks (Table III-3). This indicates that P1b has ligated to the maquette, which once again stabilizes the monomeric porphyrin state. These observations are identical for when P1c is with either BT- (Figure III-15c) or GL-maquette (Figure III-15d), however, P1c absorbance peaks in solution does not display a broadening (Figure III-15b). Both P1b and P1c are shown to ligate to either BT- or GL- maquette quickly (<1 min).

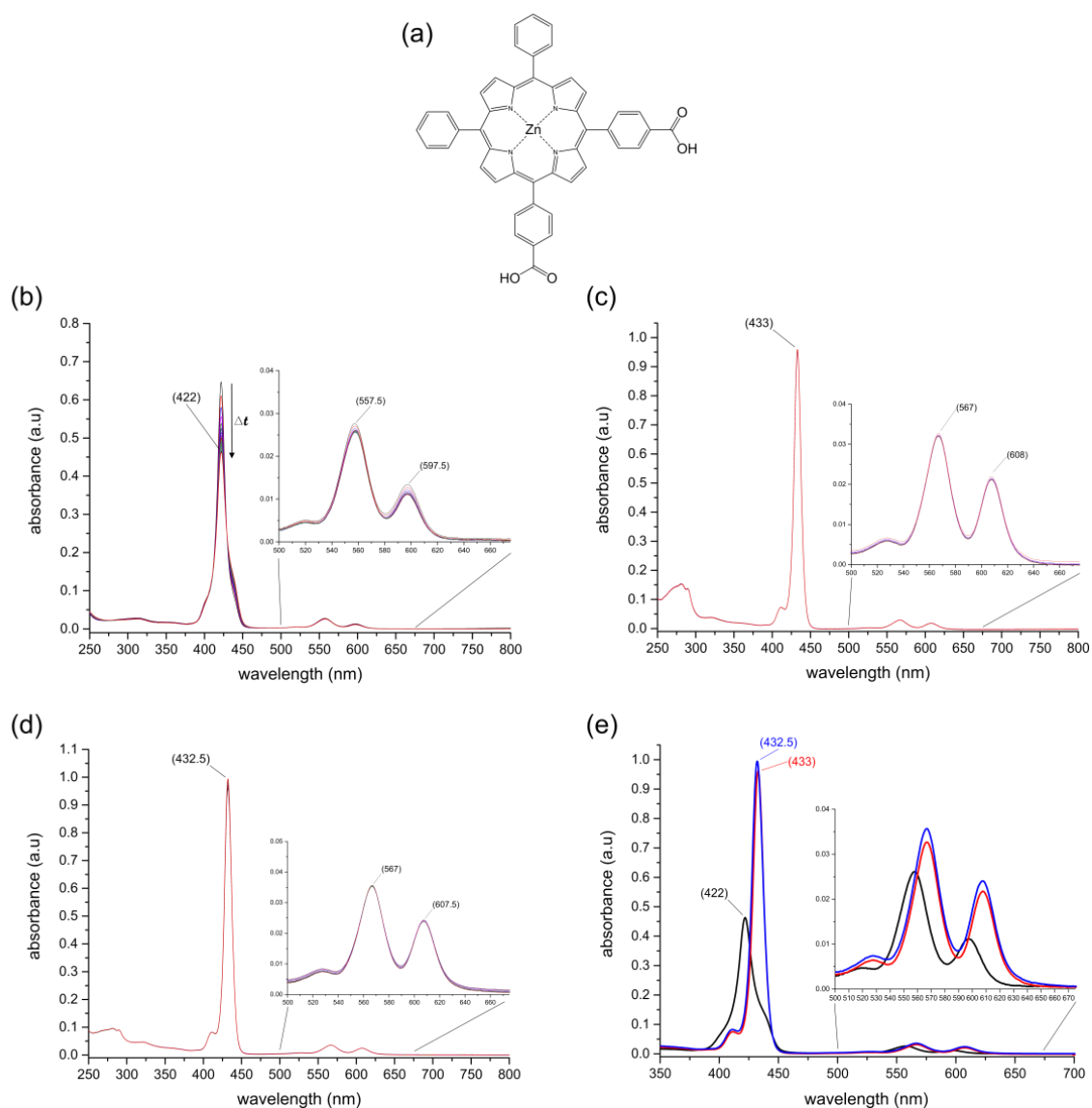
Further increase in hydrophilicity via additions of carboxyl groups to form P1d produces a stable absorbance spectrum in aqueous buffer (Figure III-16b). Furthermore, the absorbance profile is highly similar to that of when P1d is DMSO, indicating a solubilized monomeric state. When either BT- (Figure III-16c) or GL-maquette (Figure III-16d) is present with P1d, distinct red-shifts in the peak positions are again observed (Table III-3). This indicates that P1d ligates to either maquette, with the produced ensemble being stable in solution. As was observed with P1b and P1c, P1d ligates to either BT- or GL-maquette quickly (<1 min). The formation of a highly hydrophilic porphyrin through an addition of a carboxyl group to form P1e displays a stable absorbance spectrum in aqueous buffer (Figure III-17b). In contrast to previous

porphyrins, when P1e is present with BT-maquette (Figure III-17c), no significant change in the absorbance spectrum is observed when compared to when P1e is in solution. In contrast, when P1e is present with GL-maquette (Figure III-17d), a red-shift in the Soret peak and Q-bands is observed, indicating ligation (Table III-3).

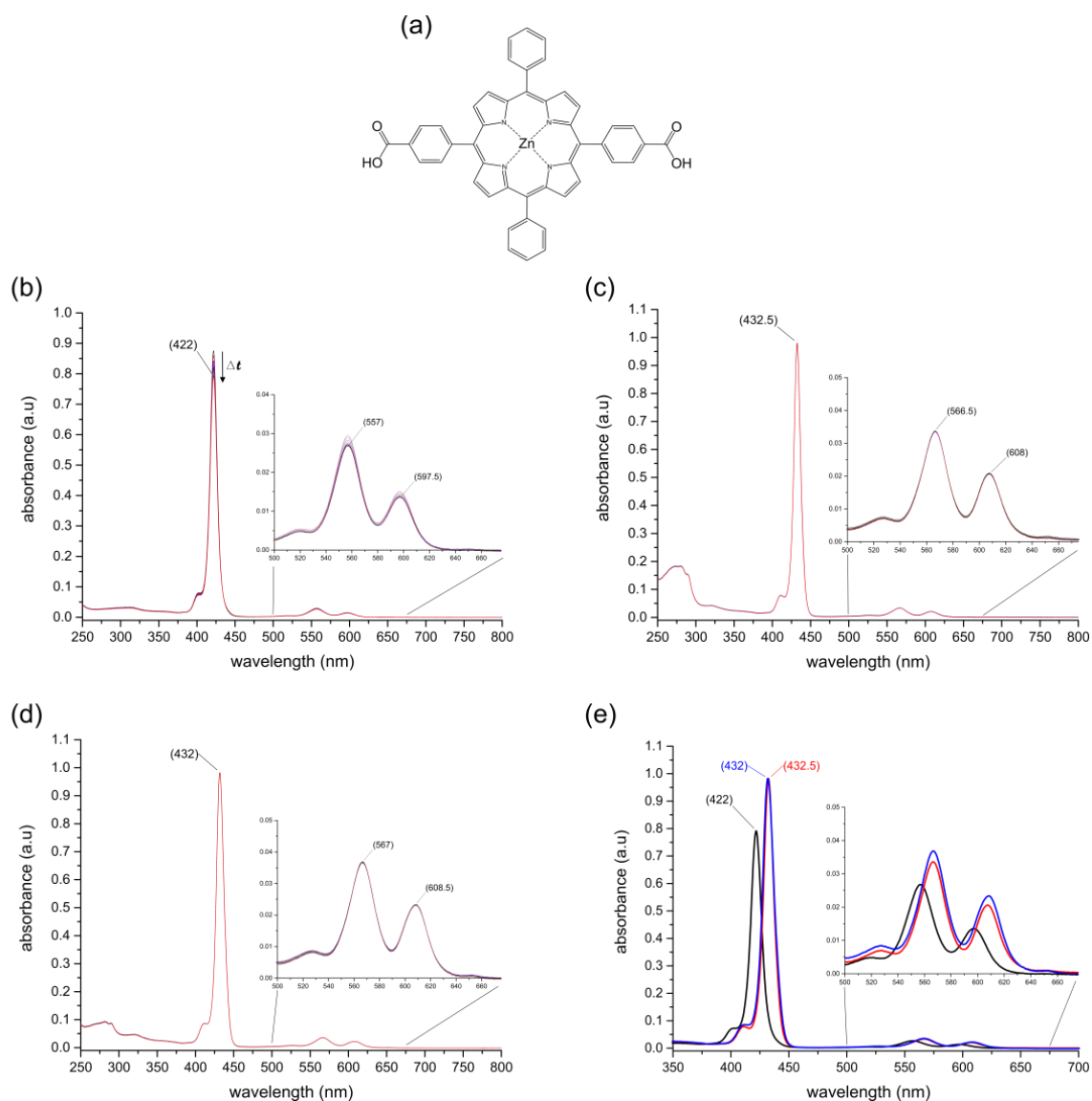
In general, additions of carboxyl groups to Zn-based tetraphenylporphyrin can stabilise the porphyrin in aqueous buffer. P1a is shown to be in a highly aggregated state in aqueous buffer, compared to P1d and P1e existing in stable monomeric states within aqueous buffer. However, regardless of hydrophobicity, all porphyrins (P1a-e) were shown to ligate to GL-maquette, evident by a 10-12 nm red-shift in the Soret and Q-bands when compared to being free in solution (Table III-3). In contrast, all porphyrins except for P1e were also shown to ligate to the BT-maquette, shown through the red-shifting of the absorbance spectra. When P1e was present with BT-maquette, it is apparent that P1e does not interact, but rather, stays in a 'free' monomeric state in solution.



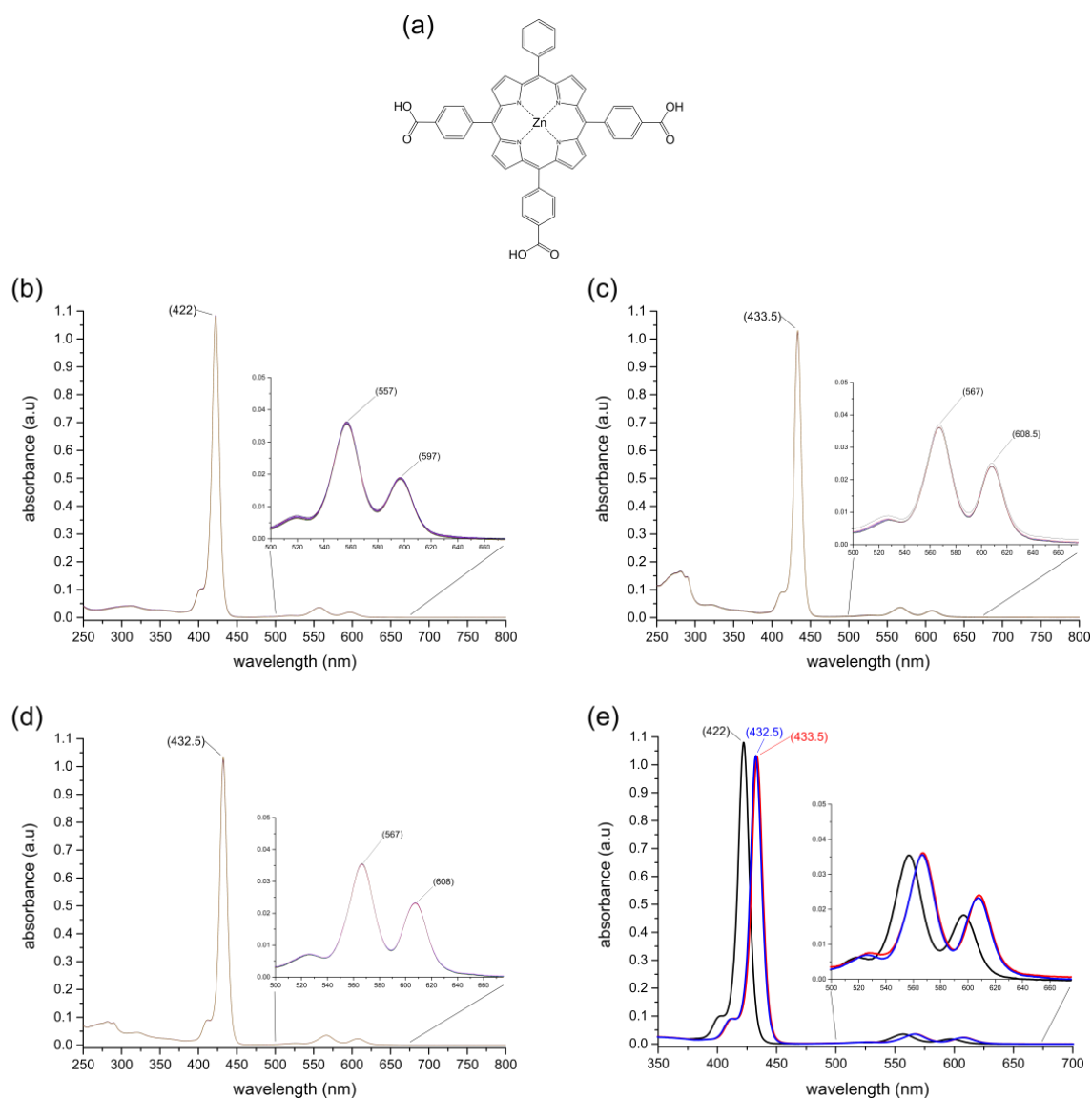
**Figure III-13; UV-vis. absorption spectra characterisation of P1a in aqueous buffer with maquette.** (a) Structure of P1a. (b) P1a in aqueous buffer; measured every 5 min for 2 h. (c) P1a and BT-maquette in aqueous buffer; measured every 5 min for 2 h. (d) P1a and GL-maquette in aqueous buffer; measured every 5 min for 2 h. (e) Absorption of P1a in aqueous buffer after 2 h (black), with BT-maquette (red), and with GL-maquette (blue).



**Figure III-14; UV-vis. absorption spectra characterisation of P1b in aqueous buffer with maquette.** (a) Structure of P1b. (b) P1b in aqueous buffer; measured every 5 min for 2 h. (c) P1b and BT-maquette in aqueous buffer; measured every 5 min for 2 h. (d) P1b and GL-maquette in aqueous buffer; measured every 5 min for 2 h. (e) Absorption of P1b in aqueous buffer after 2 h (black), with BT-maquette (red), and with GL-maquette (blue).



**Figure III-15; UV-vis. absorption spectra characterisation of P1c in aqueous buffer with maquette.** (a) Structure of P1c. (b) P1c in aqueous buffer; measured every 5 min for 2 h. (c) P1c and BT-maquette in aqueous buffer; measured every 5 min for 2 h. (d) P1c and GL-maquette in aqueous buffer; measured every 5 min for 2 h. (e) Absorption of P1c in aqueous buffer after 2 h (black), with BT-maquette (red), and with GL-maquette (blue).





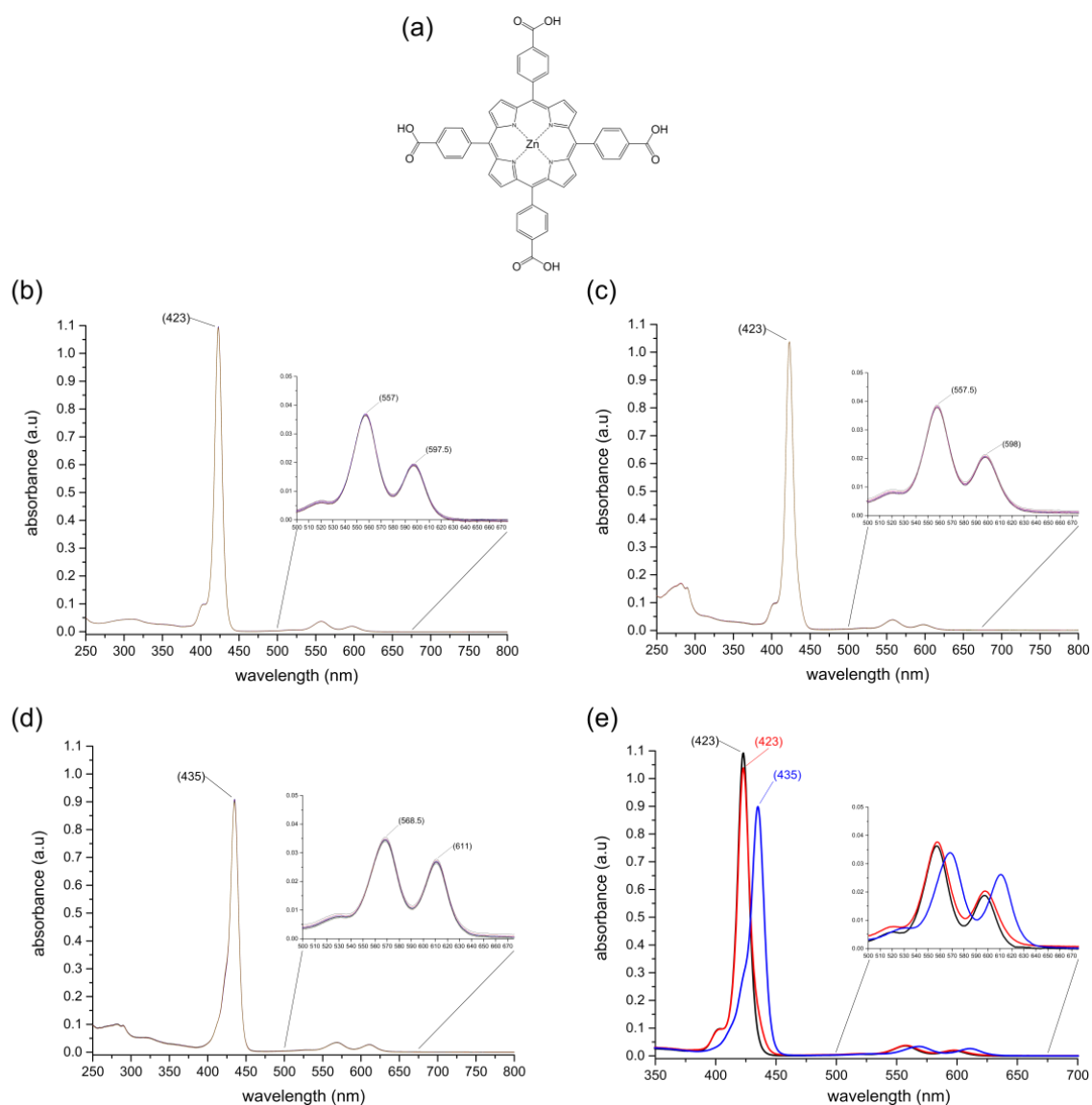


**Figure III-17; UV-vis. absorption spectra characterisation of P1e in aqueous buffer with maquette.** (a) Structure of P1e. (b) P1e in aqueous buffer; measured every 5 min for 2 h. (c) P1e and BT-maquette in aqueous buffer; measured every 5 min for 2 h. (d) P1e and GL-maquette in aqueous buffer; measured every 5 min for 2 h. (e) Absorption of P1e in aqueous buffer after 2 h (black), with BT-maquette (red), and with GL-maquette (blue).

**Table III-3; Peak positions of P1a-e with and without maquette presence.** The peak positions of P1a-e after 2 h in aqueous buffer compared with either BT- or GL-maquette being present in solution.

Porphyrin	Soret peak (nm)			Q-bands (nm)		
	No maquette	BT-maquette	GL-maquette	No maquette	BT-maquette	GL-maquette
P1a	386 / 427	432	431.5	561, 597	566, 606.5	566, 606.5
P1b	422	433	432.5	557.5, 597.5	567, 608	567, 607.5
P1c	422	432.5	432	567, 597.5	566.5, 608	567, 608.5
P1d	422	433.5	432.5	557, 597	567, 608.5	567, 608
P1e	423	423	435	557, 597.5	557.5, 508	568.5, 611

#### 2.4.2- Binding of free-base tetraphenylporphyrin carboxylates

Free-base tetraphenylporphyrins with substituted carboxylates (P2a-P2e) were used to further explore the impact of increasing hydrophilicity in context of interactions with maquettes. As shown in Figure III-18a, P2a is expected to be largely hydrophobic, containing a single carboxyl group. When P2a is in the buffer (Figure III-18b), with BT- (Figure III-18c) or GL-maquette (Figure III-18d), it is apparent that the Soret peak is largely broadened, resulting from the aggregation tendencies of hydrophobic porphyrins as mentioned previous. However, it is observed that absorbance peaks for P2a without maquette continues to decrease in intensity over time, with red-shifting in the Soret peak region over time. This indicates that the porphyrin is continuing to aggregate, likely precipitating out of solution. In contrast, the spectral peaks are more stable over time when P2a is with either maquette. This is likely due to porphyrins aggregating and interacting with lysine residues via electrostatic interaction.

As was shown previously for P1b-P1d with maquettes, the free-base versions P2b-P2d all display signs of interaction with maquettes. The absorbance of P2b (Figure III-19a) in aqueous buffer displays a Soret peak which continually decreases in intensity over time (Figure III-19b). As was determined with the Zn-based equivalent (P1b), this is attributed to aggregation. In contrast, when P2b is in aqueous solution with either BT- (Figure III-19c) or GL-maquette (Figure III-19d), the Soret peak is red-shifted by 7-8 nm (Table III-4), with the absorbance peaks being more intense and sharp, attributed to the porphyrin being in monomeric state, as was determined previously. However, these spectra decrease slightly in intensity over time, which demonstrates that the porphyrin is not stable in the ‘bound’ state with maquette.

Similar to P2b, when P2c (Figure III-20a) is in aqueous buffer, the absorbance spectrum is observed to have Soret peak which is broadened and diminishes in intensity over time, indicative of aggregation (Figure III-20b). In contrast, when either BT- (Figure III-20c) or GL-maquette (Figure III-20d) is present, two distinct peaks are apparent within the Soret peak region, tabulated in Table III-4. The 438-440 nm is apparent when maquette is not present, which diminishes over time in all cases. In contrast, the peak at 422-423 nm is only observed when either maquette is present, increasing in intensity over time. This peak is attributed to P1c binding to the maquette slowly, with the peak at 438-440 nm attributed to the porphyrin being in the highly ordered H-aggregates, as was discussed previously. Therefore, it would appear that the maquette can interact with monomeric porphyrin entities and stop them aggregating, similar to micellar action, whereby micelles can result in spectral shift of monomeric states [23].

The more hydrophilic P2d (Figure III-21a) has an absorbance profile in aqueous buffer which is not stable over time, indicating aggregating (Figure III-21b). This can be compared to the Zn-based equivalent (P1d), whereby the porphyrin is highly stable and soluble in the buffer. The difference in solubility is due to free-base porphyrins inherently being more hydrophobic than metal-based equivalents [24]. When either BT- (Figure III-21c) or GL-maquette (Figure III-21d) is present, a red-shifting of the Soret peak by 7-8 nm is apparent, indicating interaction (Table III-4). The spectrum is observed to be stable when GL-maquette is present, which demonstrates that P2d binds to GL-maquette in a more stable form compared to when bound to BT-maquette. The most hydrophilic porphyrin, P2e (Figure III-22a), is observed to have an absorbance spectrum in aqueous buffer which is highly stable (Figure III-22b). This spectrum is identical for when BT-maquette is present (Figure III-22c), however red-shifting of the Soret peak is apparent when GL-maquette is present (Figure III-22d). This indicates that P2e does not interact with the BT-maquette but can bind to the GL-maquette, highlighted by the peak positions in Table III-4.

In general, addition of carboxyl groups to free-base tetraphenylporphyrin improves the stability of the porphyrin in aqueous buffer, with the most hydrophilic P2e being highly stable in aqueous solution. Porphyrins (P2b-d) were all shown to bind to both the BT- and GL-maquettes, evident by a 7-8 nm red-shift in the Soret peak (Table III-4). However, as P2c formed H-aggregates which induced a distinct red-shifting of the Soret-peak, its binding to maquettes was observed here to be blue-shifted, although incomplete binding for both

maquettes. Despite this, it can be assumed that P2b-d all bind to maquettes in similar monomeric modes, with Soret peaks shifted to 421-422 nm when with maquette. P2e was shown to interact with GL-maquette, however, when present with BT-maquette it is apparent that P1e does not interact, but rather, stays in a monomeric state in solution. The trend for P2e is identical to that of the Zn-based equivalent (P1e), indicating that the ligation of the metal is not the sole driving force for interactions.

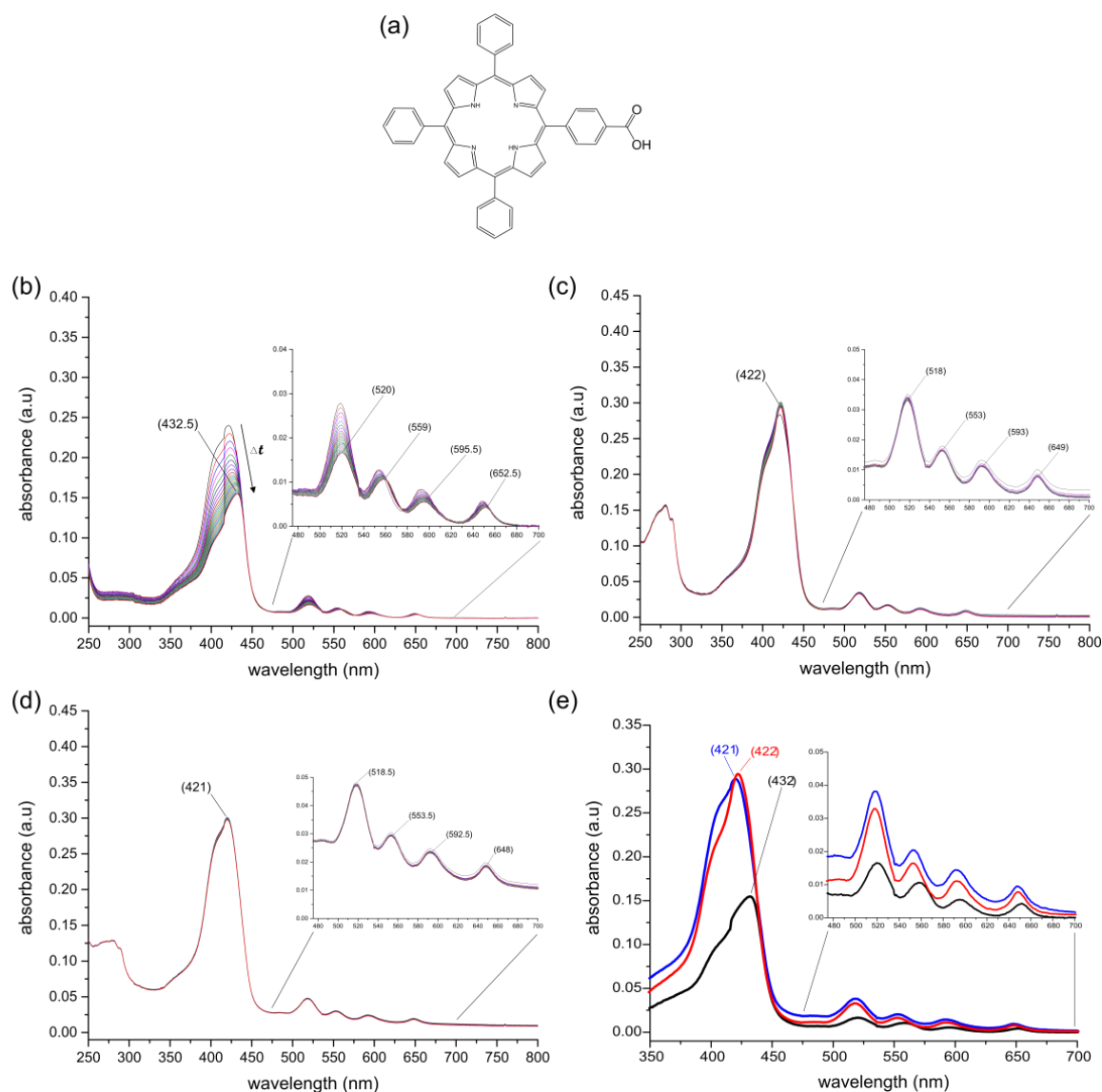


**Figure III-18; UV-vis. absorption spectra characterisation of P2a in aqueous buffer with maquette.** (a) Structure of P2a. (b) P2a in aqueous buffer; measured every 5 min for 2 h. (c) P2a and BT-maquette in aqueous buffer; measured every 5 min for 2 h. (d) P2a and GL-maquette in aqueous buffer; measured every 5 min for 2 h. (e) Absorption of P2a in aqueous buffer after 2 h (black), with BT-maquette (red), and with GL-maquette (blue).

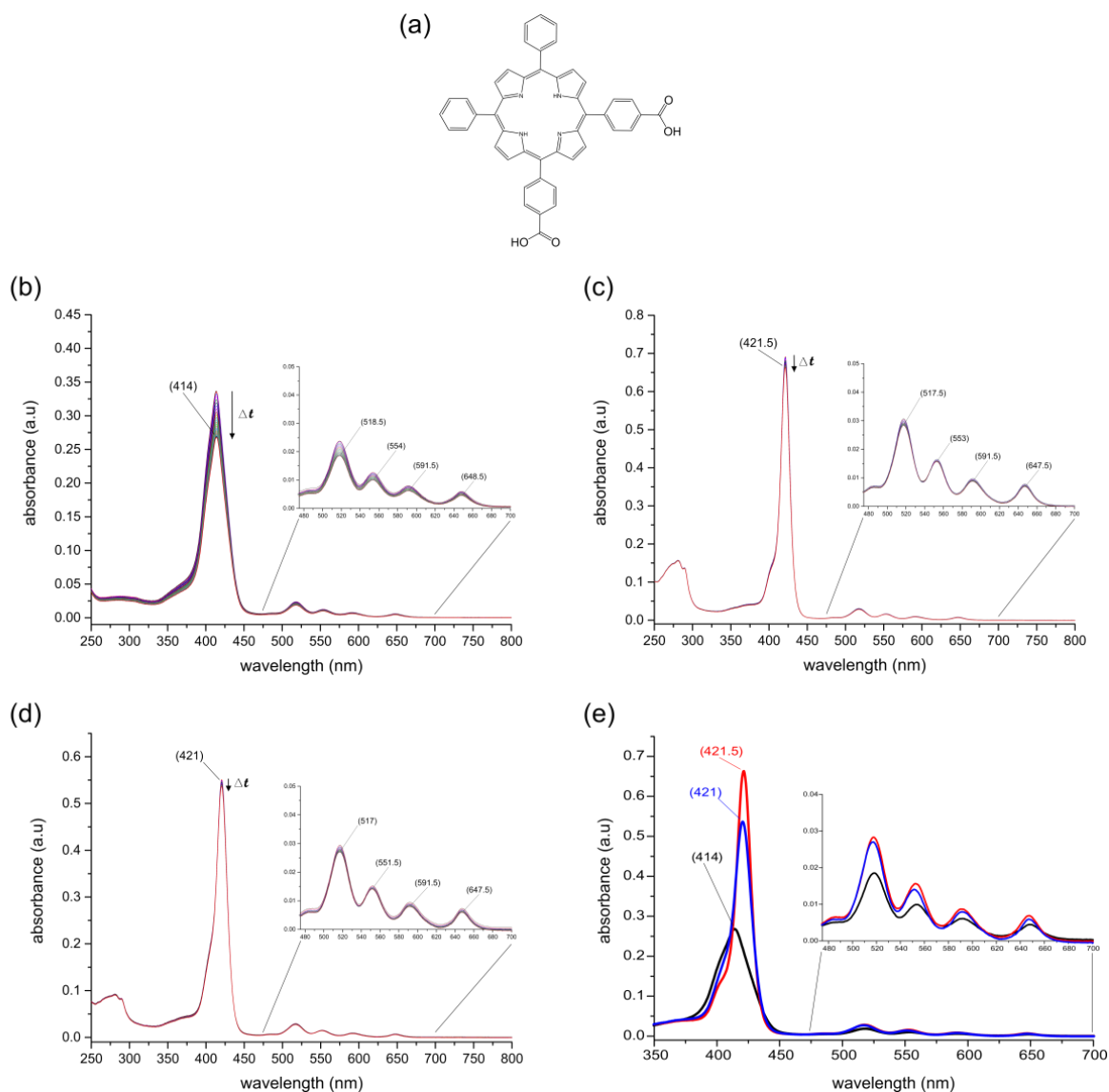


**Figure III-19; UV-vis. absorption spectra characterisation of P2b in aqueous buffer with maquette.** (a) Structure of P2b. (b) P2b in aqueous buffer; measured every 5 min for 2 h. (c) P2b and BT-maquette in aqueous buffer; measured every 5 min for 2 h. (d) P2b and GL-maquette in aqueous buffer; measured every 5 min for 2 h. (e) Absorption of P2b in aqueous buffer after 2 h (black), with BT-maquette (red), and with GL-maquette (blue).

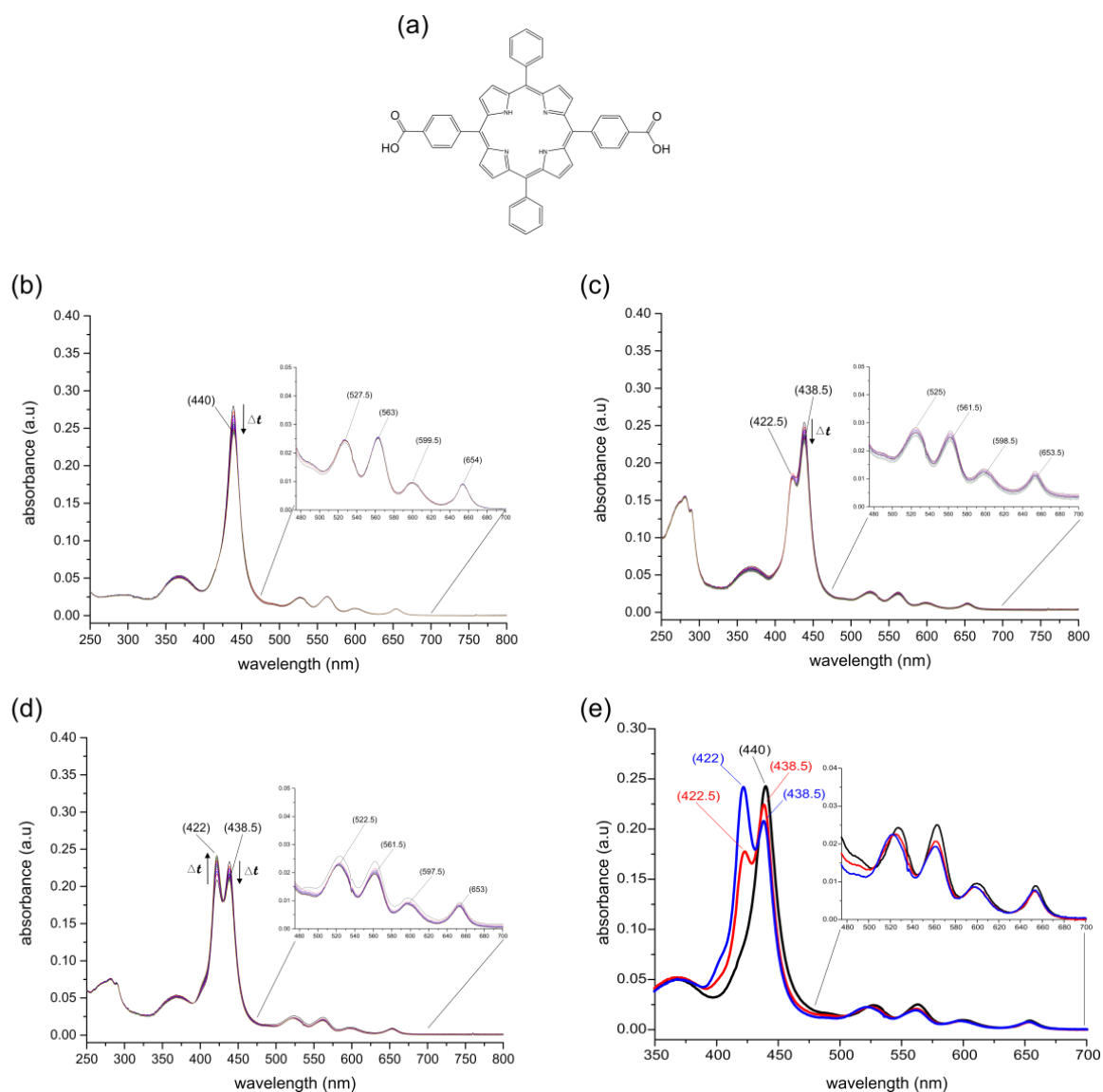


**Figure III-20; UV-vis. absorption spectra characterisation of P2c in aqueous buffer with maquette.** (a) Structure of P2c. (b) P2c in aqueous buffer; measured every 5 min for 2 h. (c) P2c and BT-maquette in aqueous buffer; measured every 5 min for 2 h. (d) P2c and GL-maquette in aqueous buffer; measured every 5 min for 2 h. (e) Absorption of P2c in aqueous buffer after 2 h (black), with BT-maquette (red), and with GL-maquette (blue).

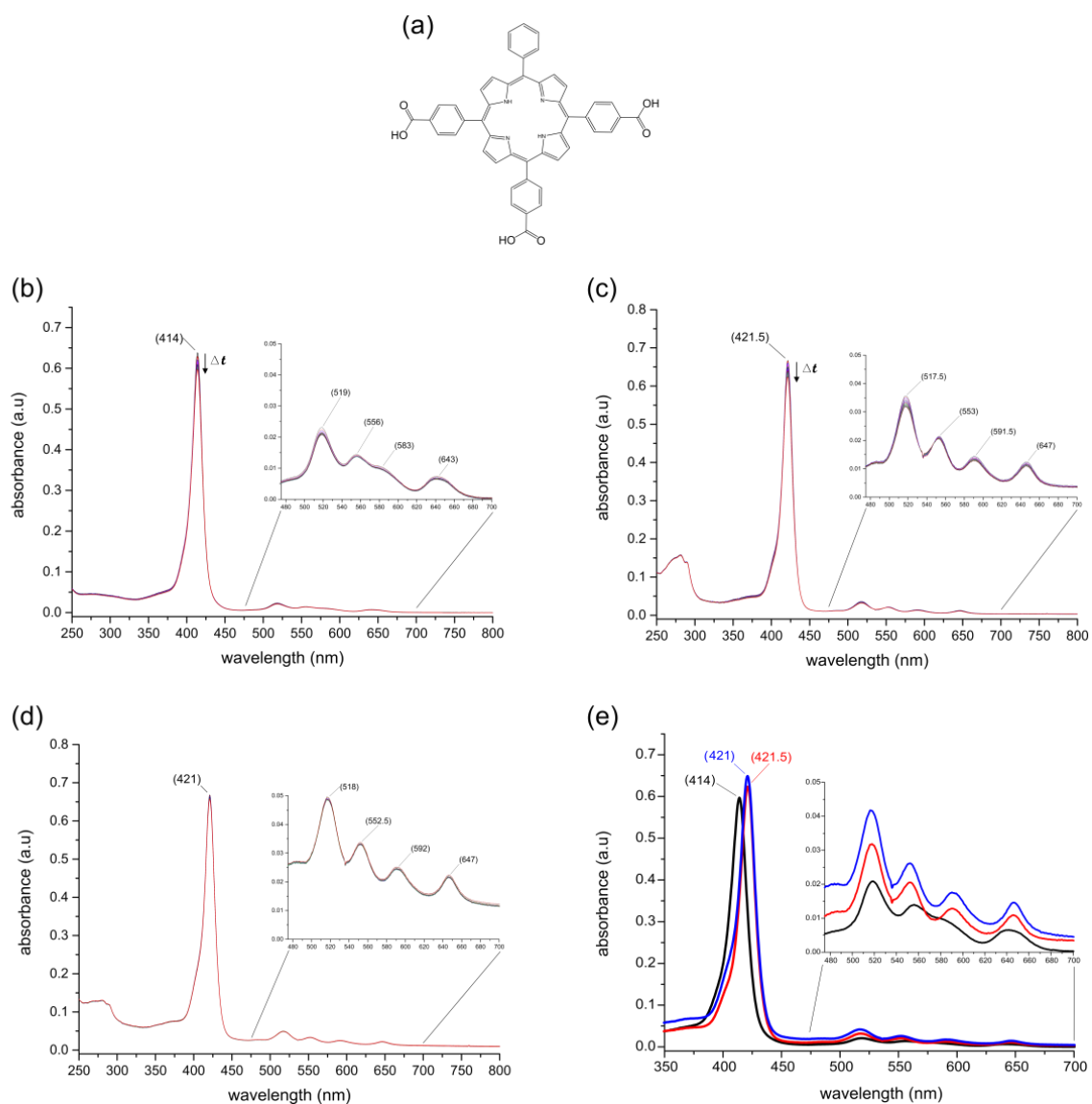


**Figure III-21; UV-vis. absorption spectra characterisation of P2d in aqueous buffer with maquette.** (a) Structure of P2d. (b) P2d in aqueous buffer; measured every 5 min for 2 h. (c) P2d and BT-maquette in aqueous buffer; measured every 5 min for 2 h. (d) P2d and GL-maquette in aqueous buffer; measured every 5 min for 2 h. (e) Absorption of P2d in aqueous buffer after 2 h (black), with BT-maquette (red), and with GL-maquette (blue).

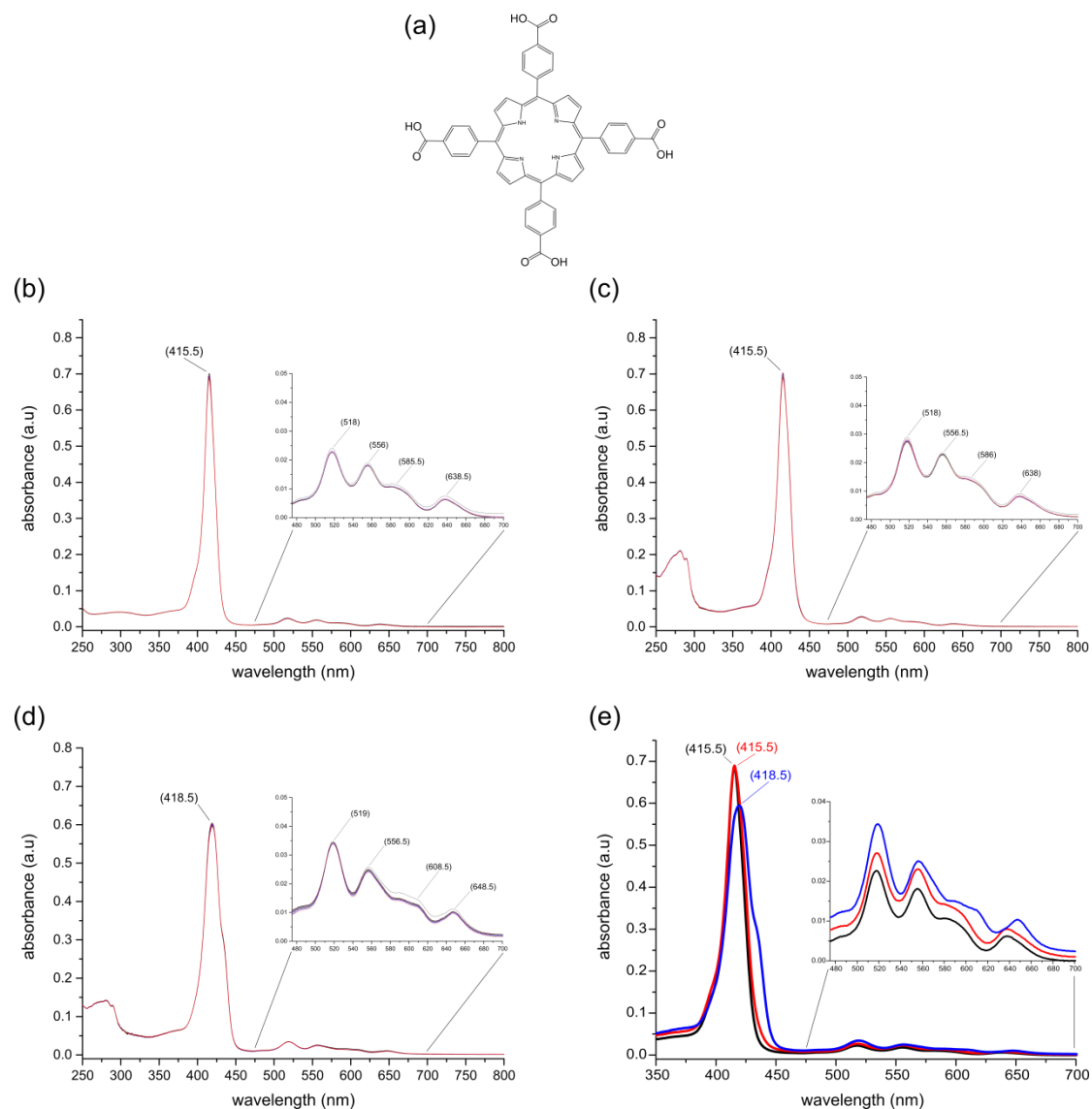


**Figure III-22; UV-vis. absorption spectra characterisation of P2e in aqueous buffer with maquette.** (a) Structure of P2e. (b) P2e in aqueous buffer; measured every 5 min for 2 h. (c) P2e and BT-maquette in aqueous buffer; measured every 5 min for 2 h. (d) P2e and GL-maquette in aqueous buffer; measured every 5 min for 2 h. (e) Absorption of P2e in aqueous buffer after 2 h (black), with BT-maquette (red), and with GL-maquette (blue).



**Table III-4; Peak positions of P2a-e with and without maquette presence.** The peak positions of P2a-e after 2 h in aqueous buffer compared with either BT- or GL-maquette being present in solution.

Porphyrin	Soret peak (nm)			Q-bands (nm)		
	No maquette	BT-maquette	GL-maquette	No maquette	BT-maquette	GL-maquette
P2a	432.5	422	421	520, 559, 595.5, 652.5	518, 553, 593, 649	518.5, 553.5, 592.5, 648
P2b	414	421.5	421	518.5, 554, 591.5, 648.5	517.5, 553, 591.5, 647.5	517, 551.5, 591.5, 647.5
P2c	440	422.5, 438.5	422, 438.5	527.5, 563, 599.5, 654	525, 561.5, 598.5, 653.5	522.5, 561.5, 597.5, 653
P2d	414	421.5	421	519, 556, 583, 643	517.5, 553, 591.5, 647	518, 552.5, 592, 647
P2e	415.5	415.5	418.5	518, 556, 585.5, 638.5	518, 556.5, 586, 638	519, 556.5, 608.5, 648.5

#### 2.4.3- Binding of Zn-based tetraphenylporphyrin ammonium salts

Exploring electrostatic influences in context of porphyrin binding with maquettes, trimethylammonium substituted tetraphenylporphyrins were used in comparison of carboxyl substitution (P1a-e). P3a (Figure III-23), P3b (Figure III-24), and P3c (Figure III-25) all show identical trends to that of P1a-c whereby the porphyrin aggregates in aqueous buffer, resulting in a broadened Soret peak which diminishes over time (as was discussed previously). As was observed for P1a, when either BT- or GL-maquette is with P3a, ligation of either maquette in a monomeric state occurs slowly (>90 min). Similarly, ligation of P3b or P3c to either maquette is apparent by a red-shifting of peak positions, indicative of axial ligation of the zinc (Table III-5). The ligation of P3b or c to either maquette occurs quicker than P3a (<10 min compared to >90 min, respectively). In contrast to P1d and e, P3d and e both display absorbance spectrum with a Soret peak which diminishes over time (Figure III-26 and 27, respectively). This is indicative of both porphyrin forming aggregates and precipitating out of solution. When P3d is with either BT- or GL-maquette, an 11-12 nm red-shift of the Soret peak is apparent (Table III-5). In contrast, when P3e is with BT-maquette, two peaks in the Soret region are apparent, at 422.5 and 432 nm. This is likely due to P3e existing in two distinct states when BT-maquette is present in solution. The peak at 422.5 nm corresponds to P3e being ‘free’ in the solvent,

whereby 432 nm arises from P3e being ligated the BT-maquette (Figure III-27c). This is compared to when P3e is present in aqueous solvent with the GL-maquette (Figure III-27d), whereby one single Soret peak is observed, however, a shoulder is apparent at approximately 432 nm. As was with the BT-maquette, this indicates that P3e is (mostly) in the solvent with a small amount ligated to the maquette. As all concentrations remained constant, it can be assumed that the forces attributing to P3e ligating to the BT-maquette is stronger than that for ligation to GL-maquette, resulting in a higher amount binding to BT- maquette compared to the GL-maquette.

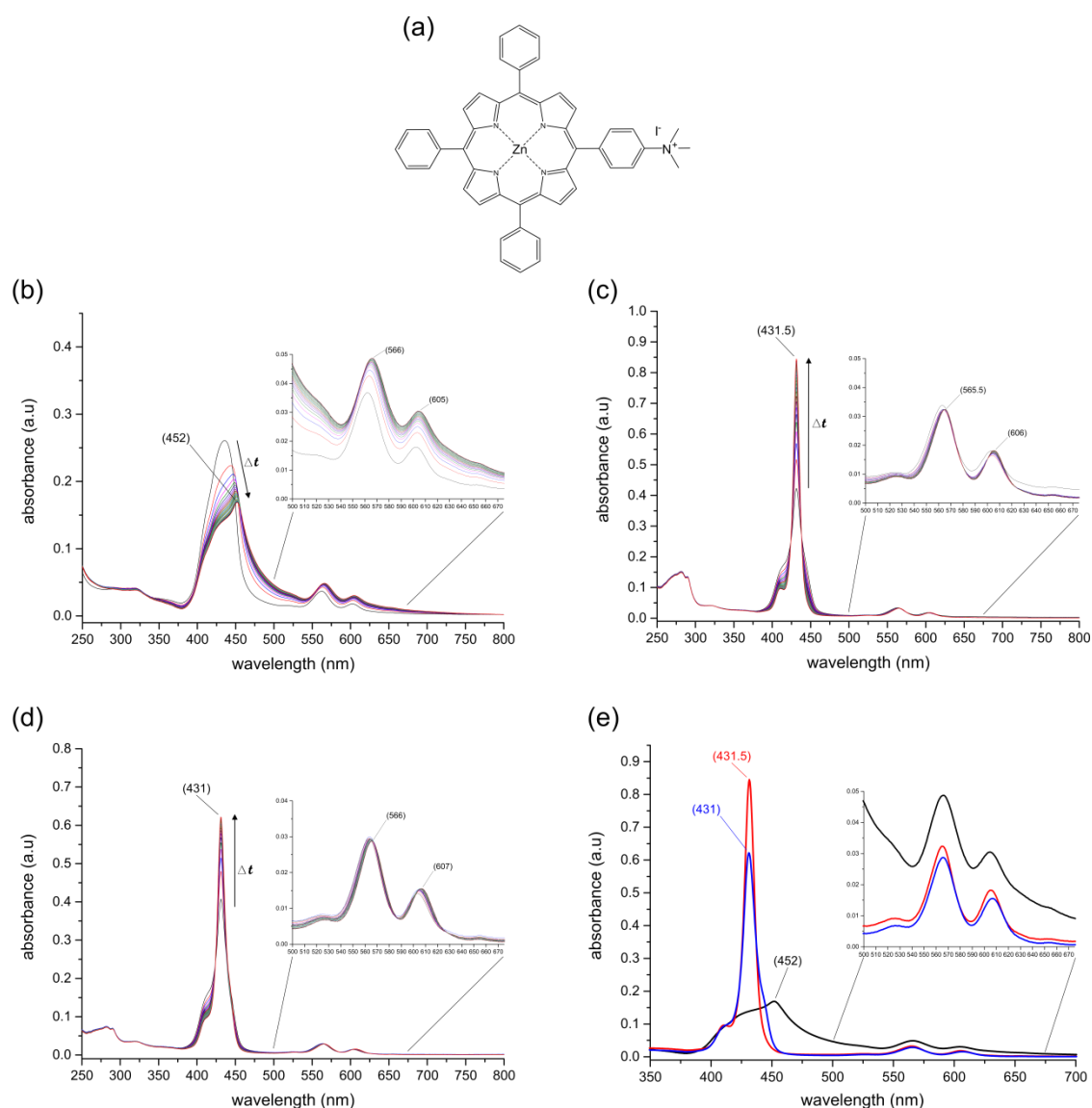


**Figure III-23; UV-vis. absorption spectra characterisation of P3a in aqueous buffer with maquette.** (a) Structure of P3a. (b) P3a in aqueous buffer; measured every 5 min for 2 h. (c) P3a and BT-maquette in aqueous buffer; measured every 5 min for 2 h. (d) P3a and GL-maquette in aqueous buffer; measured every 5 min for 2 h. (e) Absorption of P3a in aqueous buffer after 2 h (black), with BT-maquette (red), and with GL-maquette (blue)

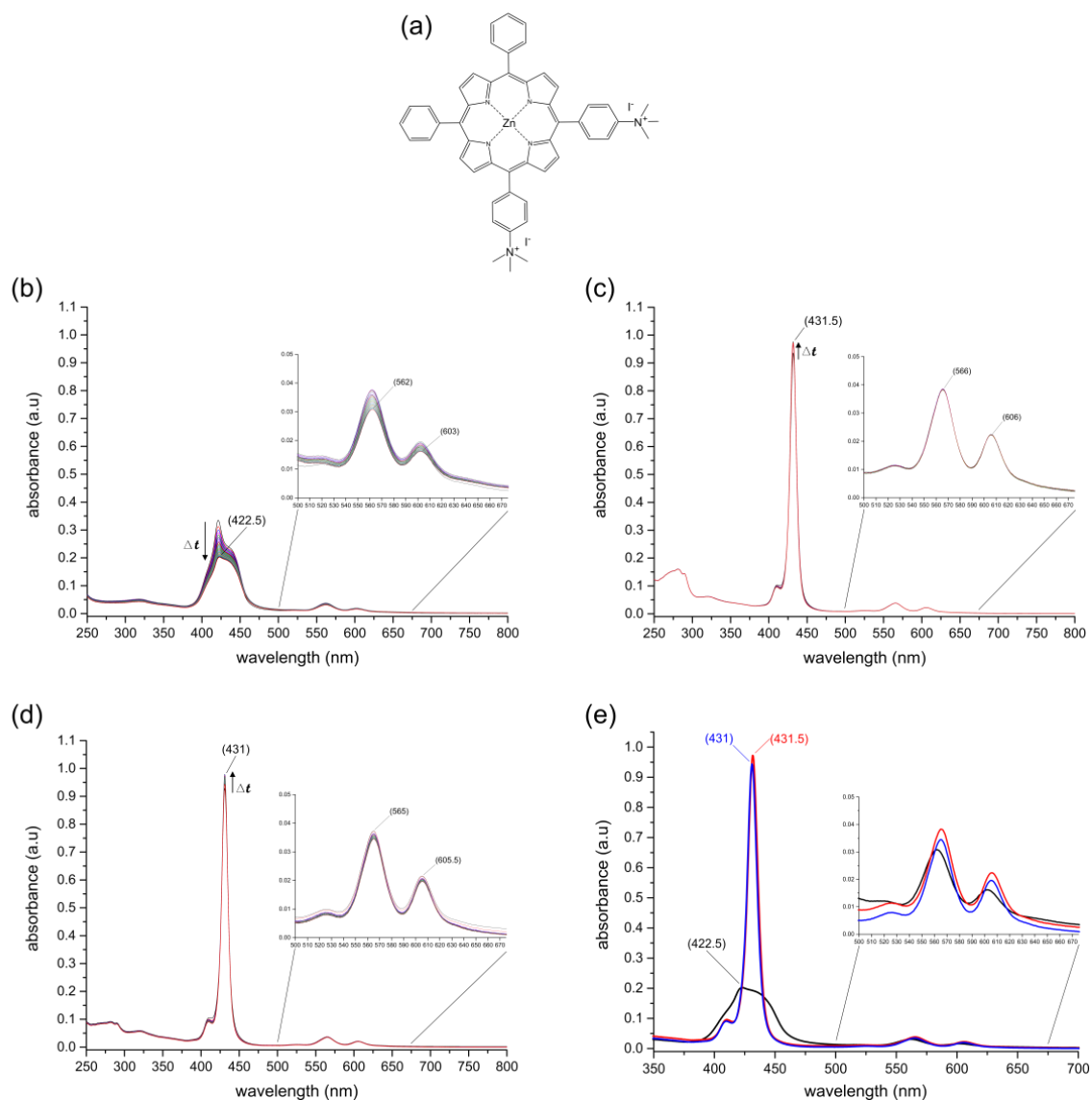


**Figure III-24; UV-vis. absorption spectra characterisation of P3b in aqueous buffer with maquette.** (a) Structure of P3b. (b) P3b in aqueous buffer; measured every 5 min for 2 h. (c) P3b and BT-maquette in aqueous buffer; measured every 5 min for 2 h. (d) P3b and GL-maquette in aqueous buffer; measured every 5 min for 2 h. (e) Absorption of P3b in aqueous buffer after 2 h (black), with BT-maquette (red), and with GL-maquette (blue).

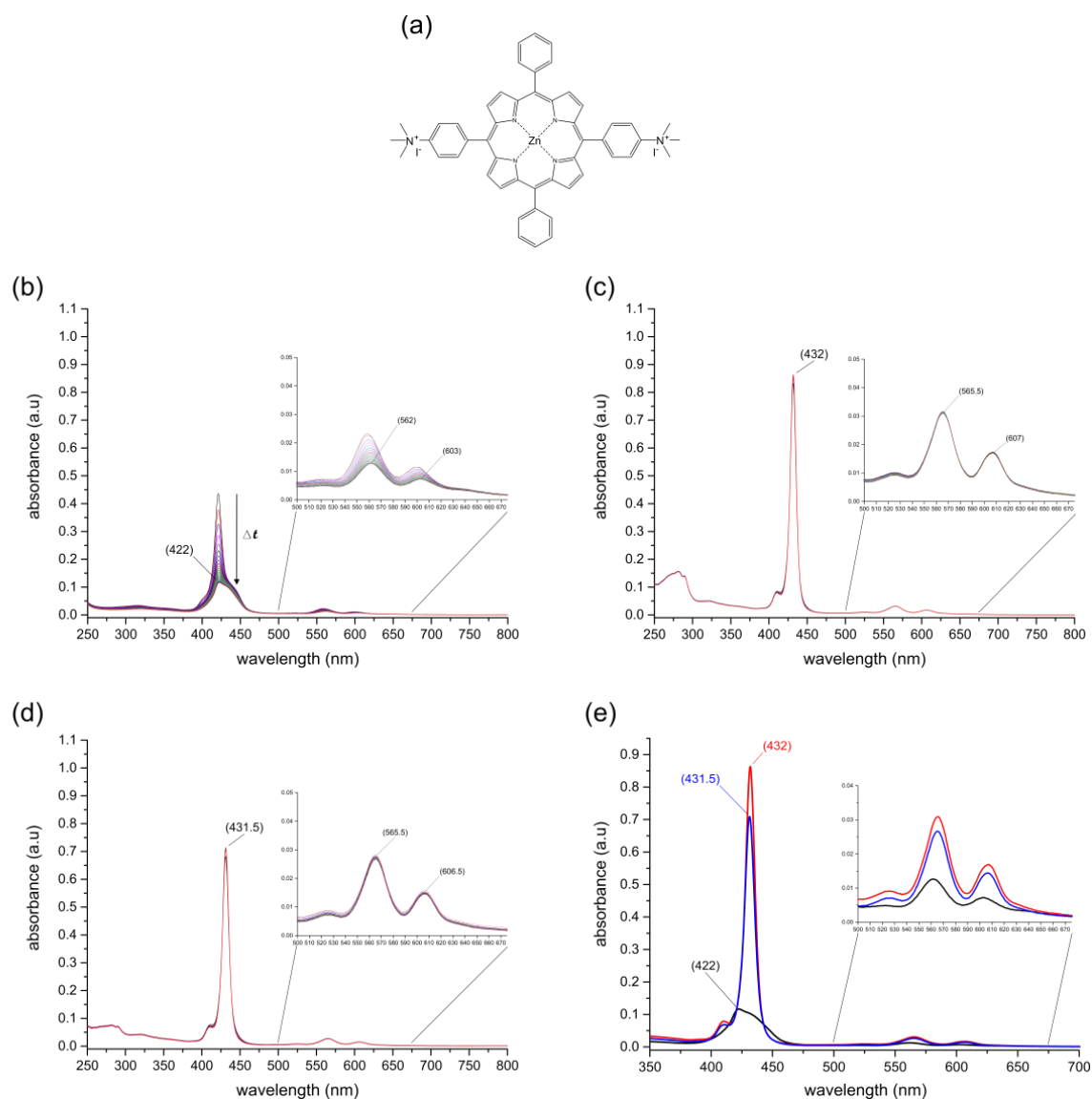


**Figure III-25; UV-vis. absorption spectra characterisation of P3c in aqueous buffer with maquette.** (a) Structure of P3c. (b) P3c in aqueous buffer; measured every 5 min for 2 h. (c) P3c and BT-maquette in aqueous buffer; measured every 5 min for 2 h. (d) P3c and GL-maquette in aqueous buffer; measured every 5 min for 2 h. (e) Absorption of P3c in aqueous buffer after 2 h (black), with BT-maquette (red), and with GL-maquette (blue).

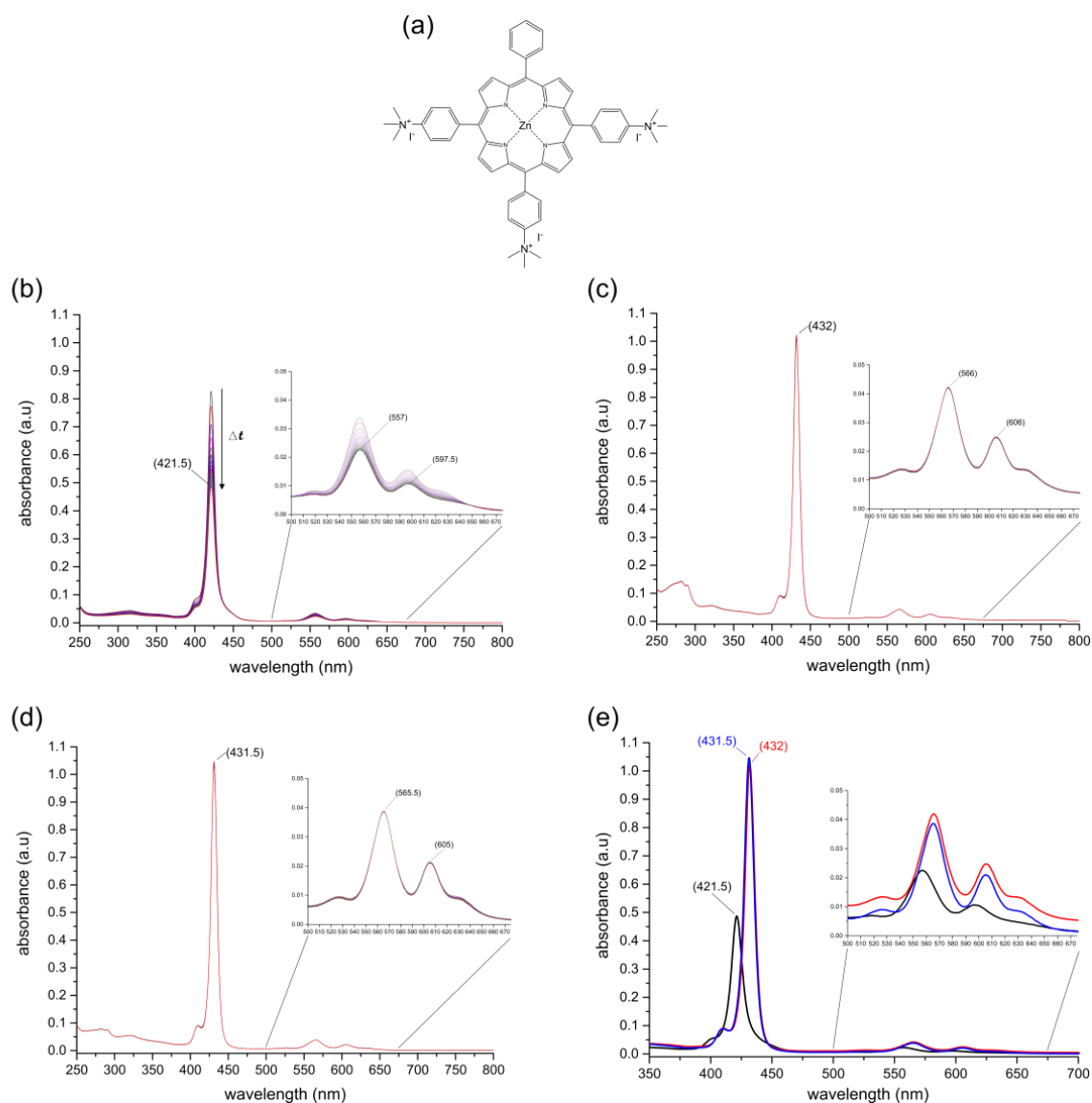


**Figure III-26; UV-vis. absorption spectra characterisation of P3d in aqueous buffer with maquette.** (a) Structure of P3d. (b) P3d in aqueous buffer; measured every 5 min for 2 h. (c) P3d and BT-maquette in aqueous buffer; measured every 5 min for 2 h. (d) P3d and GL-maquette in aqueous buffer; measured every 5 min for 2 h. (e) Absorption of P3d in aqueous buffer after 2 h (black), with BT-maquette (red), and with GL-maquette (blue).

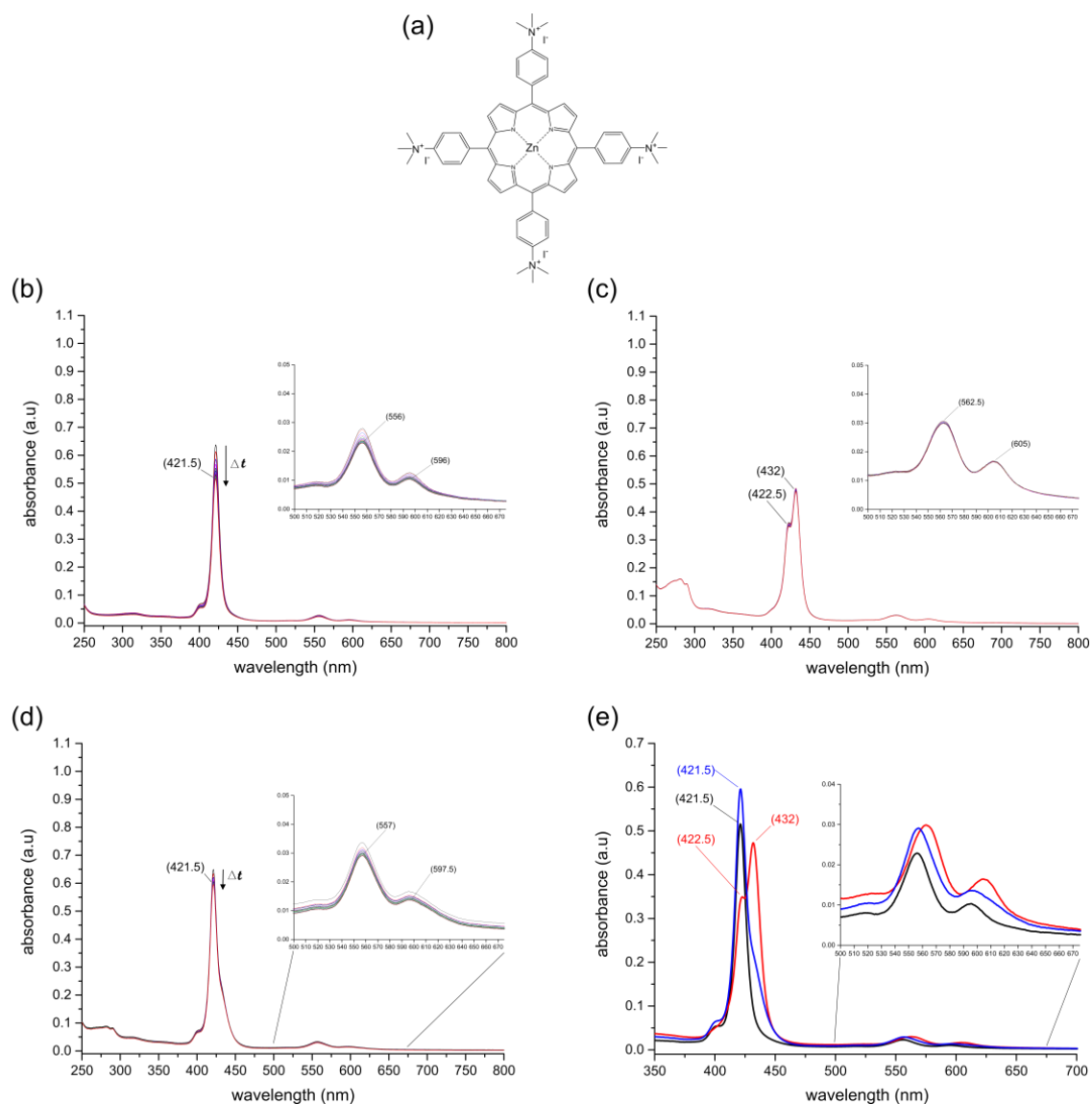


**Figure III-27; UV-vis. absorption spectra characterisation of P3e in aqueous buffer with maquette.** (a) Structure of P3e. (b) P3e in aqueous buffer; measured every 5 min for 2 h. (c) P3e and BT-maquette in aqueous buffer; measured every 5 min for 2 h. (d) P3e and GL-maquette in aqueous buffer; measured every 5 min for 2 h. (e) Absorption of P3e in aqueous buffer after 2 h (black), with BT-maquette (red), and with GL-maquette (blue).

**Table III-5; Peak positions of P3a-e with and without maquette presence.** The peak positions of P3a-e after 2 h in aqueous buffer compared with either BT- or GL-maquette being present in solution.

Porphyrin	Soret peak (nm)			Q-bands (nm)		
	No maquette	BT-maquette	GL-maquette	No maquette	BT-maquette	GL-maquette
P3a	452	431.5	431	566, 605	565.5, 606	566, 607
P3b	422.5	431.5	431	562, 603	566, 606	565, 605.5
P3c	422	432	431.5	562, 603	565.5, 607	565.5, 606.5
P3d	421.5	432	431.5	557, 597.5	566, 606	565.5, 605
P3e	421.5	432, 422.5	421.5	556, 596	562.5, 605	557, 597.5

#### 2.4.4- Binding of Zn-based butylporphyrin carboxylates

Further analysis of hydrophobicity/hydrophilicity of zinc based porphyrins for stability in aqueous solution and binding to maquettes was explored in context of the hydrophobic substituent. Butyl groups were used as the hydrophobic substituent, as opposed to the phenyl groups used previously. When P4a (Figure III-28a) is in aqueous buffer (Figure III-28b), the absorbance spectrum has a broad peak in the Soret region which decreases over time. As discussed previously, this is due to P4a aggregating and precipitating within the aqueous solution. This is compared to when P4a is with either BT- (Figure III-28c) or GL-maquette (Figure III-28d). Two peaks are apparent with either maquette, with the peak at 433/432 nm increasing over time in conjunction with the peak at 405 nm decreasing (tabulated in Table III-6). The peak at 405 nm is attributed to P4a being in the buffer, whereby the peak at 433/432 nm is the ligation of the monomeric porphyrin to either BT- or GL-maquettes respectively. This trend is identical to P1a and P3a, attributed to the slow ligation of porphyrin within the maquette being hindered due to the high aggregative tendencies of the porphyrin. Increasing hydrophilicity, P4b (Figure III-29a) is shown to aggregate and precipitate out of solution (Figure III-29b). In contrast, when either maquette is present, an 11-12 nm shift is observed in the Soret peak, which increases in intensity over time (Figure III-29c or d), once again, ligation being limited by the aggregative tendencies of the porphyrin in solution.

P4c (Figure III-30a) in aqueous buffer has a single Soret peak (Figure III-30b), which diminished over time, indicating that the porphyrin is not stable in the solvent, therefore aggregating and precipitating. When P4c is with either maquette (Figure III-30c or d) however, an 11-12 nm shift in the Soret peak is apparent (Table III-6). The peak increases slightly over time when with GL-maquette, compare to when with BT-maquette which does not change. This

indicates that P4c ligates with the BT-maquette more quickly than compared to GL-maquette, becoming stable in a monomeric ligated state with either maquette. Similarly, P4d (Figure III-31a) is shown to not be stable in the aqueous solution (Figure III-31b). However, with either the BT- (Figure III-31c) or GL-maquette (Figure III-31d), P4d ligates quickly (<1 min), evident by a red-shift of 11-12 nm of the Soret peak (Table III-6). In general, all the butylporphyrins were shown to not be stable in aqueous solution, however, all ligate to either BT- or GL-maquette and become stabilised in the solvent.

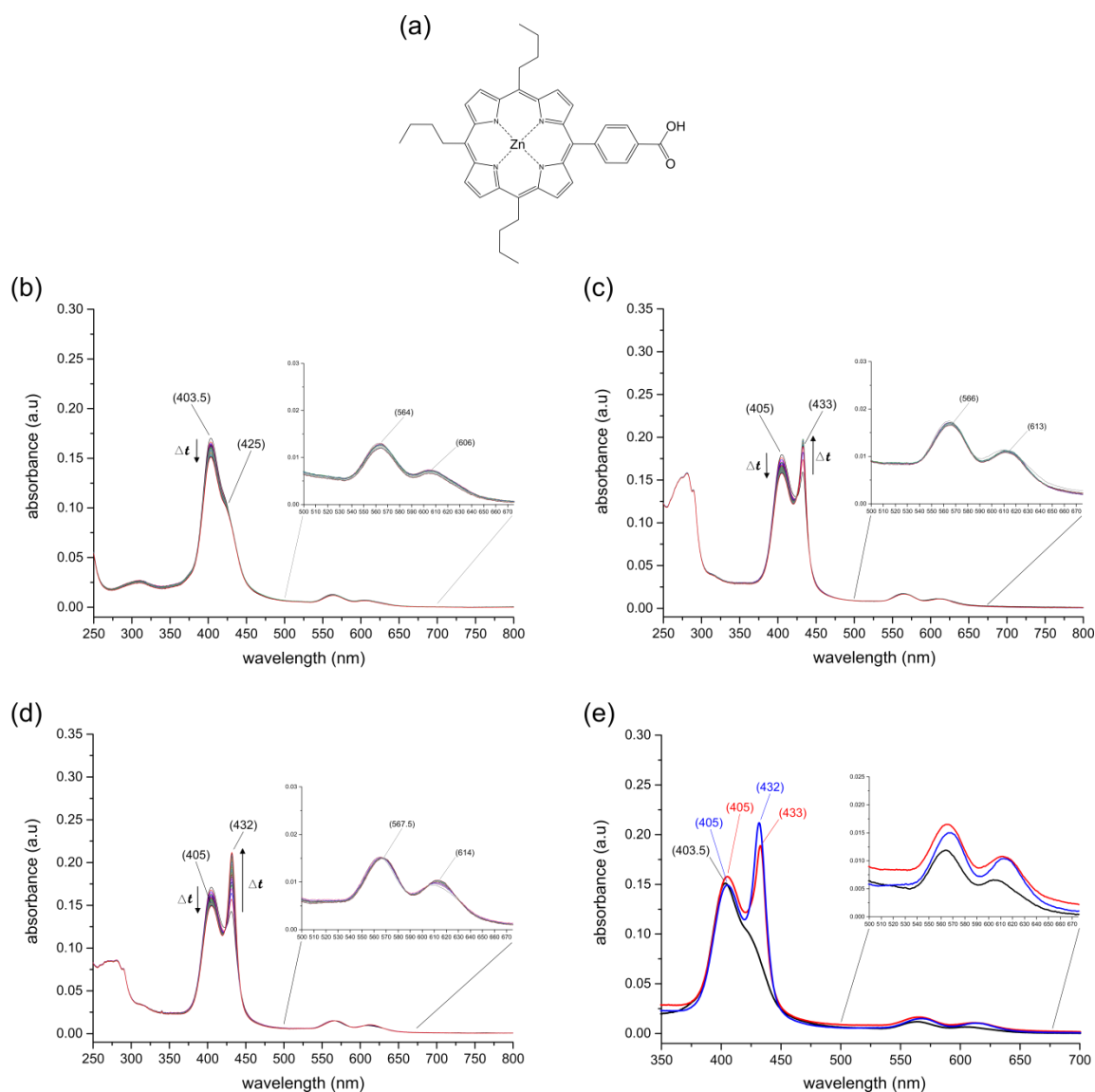


**Figure III-28; UV-vis. absorption spectra characterisation of P4a in aqueous buffer with maquette.** (a) Structure of P4a. (b) P4a in aqueous buffer; measured every 5 min for 2 h. (c) P4a and BT-maquette in aqueous buffer; measured every 5 min for 2 h. (d) P4a and GL-maquette in aqueous buffer; measured every 5 min for 2 h. (e) Absorption of P4a in aqueous buffer after 2 h (black), with BT-maquette (red), and with GL-maquette (blue).



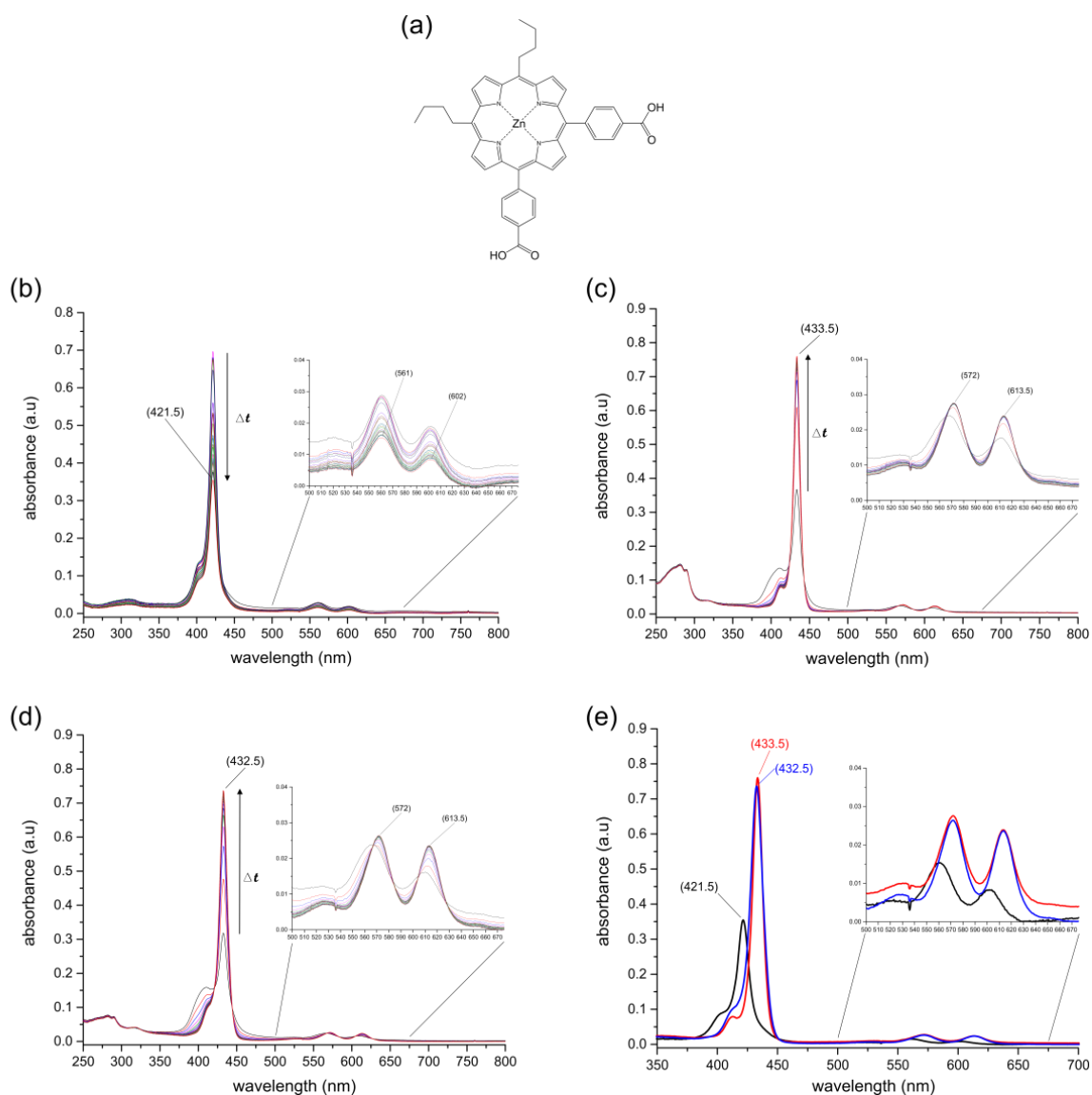


**Figure III-29; UV-vis. absorption spectra characterisation of P4b in aqueous buffer with maquette.** (a) Structure of P4b. (b) P4b in aqueous buffer; measured every 5 min for 2 h. (c) P4b and BT-maquette in aqueous buffer; measured every 5 min for 2 h. (d) P4b and GL-maquette in aqueous buffer; measured every 5 min for 2 h. (e) Absorption of P4b in aqueous buffer after 2 h (black), with BT-maquette (red), and with GL-maquette (blue).

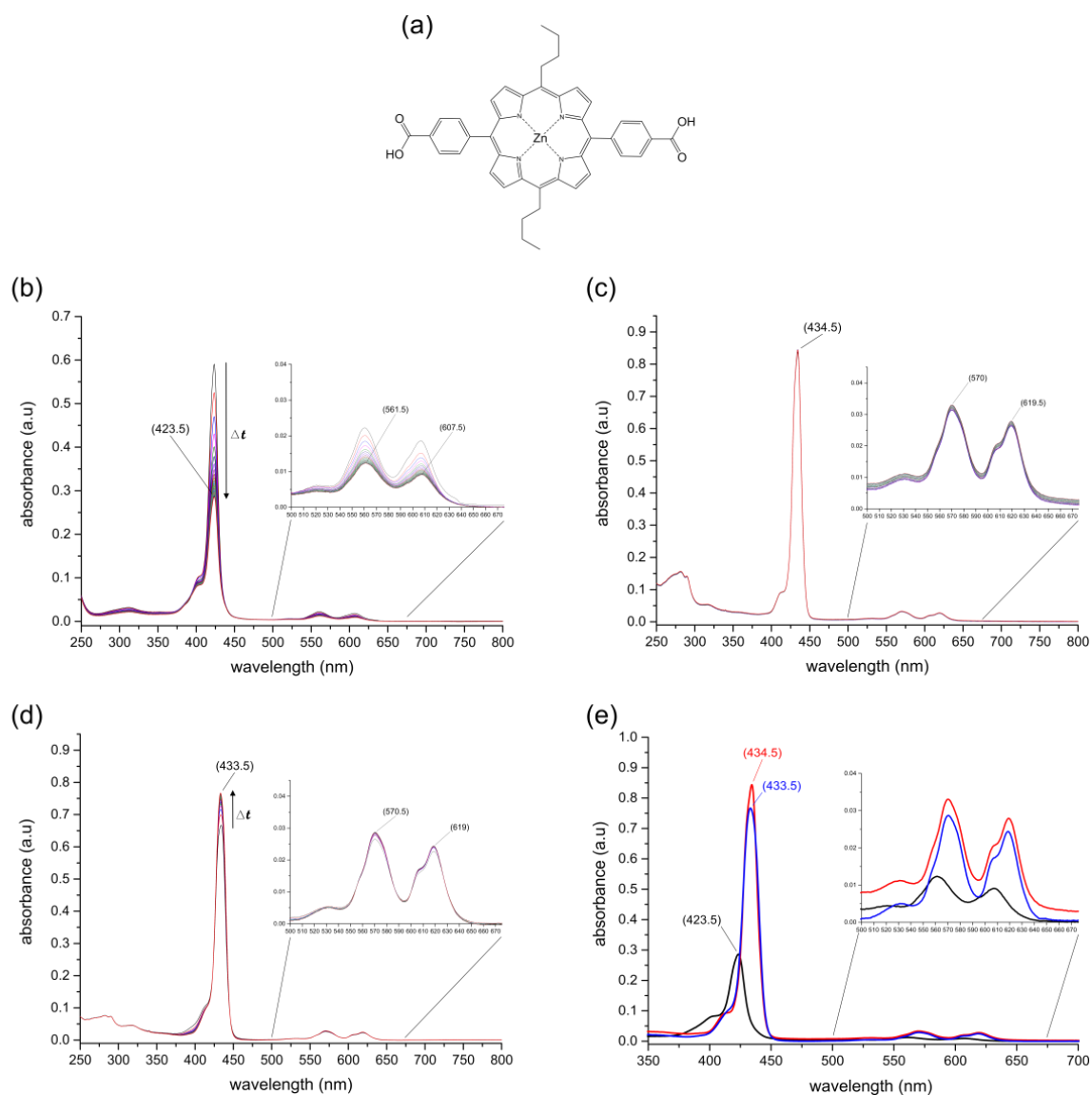


**Figure III-30; UV-vis. absorption spectra characterisation of P4c in aqueous buffer with maquette.** (a) Structure of P4c. (b) P4c in aqueous buffer; measured every 5 min for 2 h. (c) P4c and BT-maquette in aqueous buffer; measured every 5 min for 2 h. (d) P4c and GL-maquette in aqueous buffer; measured every 5 min for 2 h. (e) Absorption of P4c in aqueous buffer after 2 h (black), with BT-maquette (red), and with GL-maquette (blue).

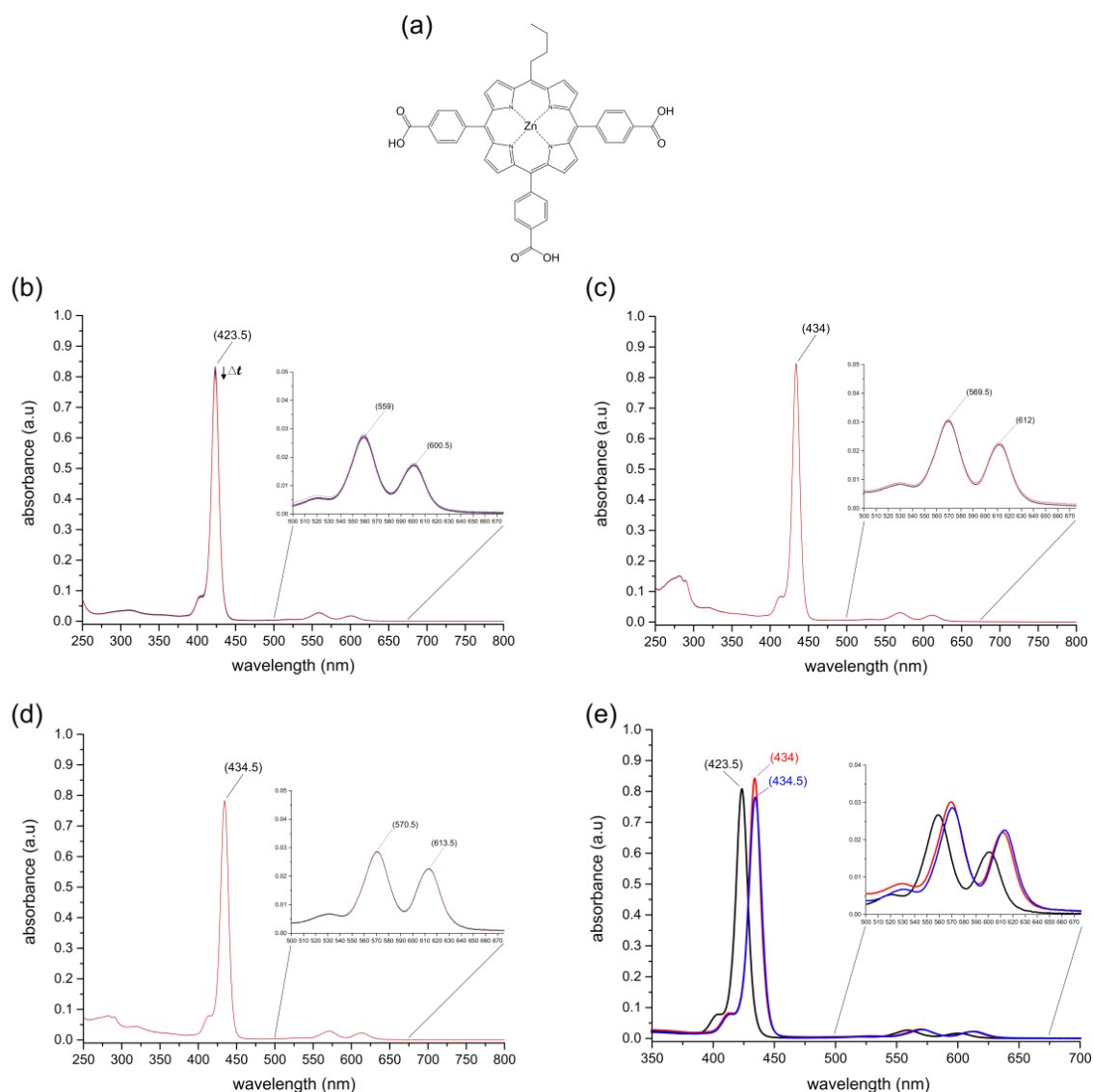


**Figure III-31; UV-vis. absorption spectra characterisation of P4d in aqueous buffer with maquette.** (a) Structure of P4d. (b) P4d in aqueous buffer; measured every 5 min for 2 h. (c) P4d and BT-maquette in aqueous buffer; measured every 5 min for 2 h. (d) P4d and GL-maquette in aqueous buffer; measured every 5 min for 2 h. (e) Absorption of P4d in aqueous buffer after 2 h (black), with BT-maquette (red), and with GL-maquette (blue).

**Table III-6; Peak positions of P4a-d with and without maquette presence.** The peak positions of P4a-d after 2 h in aqueous buffer compared with either BT- or GL-maquette being present in solution.

Porphyrin	Soret peak (nm)			Q-bands (nm)		
	No maquette	BT-maquette	GL-maquette	No maquette	BT-maquette	GL-maquette
P3a	403.5, 525	405, 433	405, 432	564, 606	566, 613	567.5, 614
P3b	421.5	433.5	432.5	561, 602	572, 613.5	572, 613.5
P3c	423.5	434.5	433.5	561.5, 607.5	570, 619.5	570.5, 619
P3d	423.5	434	434.5	559, 600.5	569.5, 612	570.5, 613.5

## 2.5- Binding titration of maquettes with porphyrins

Binding titrations are a useful analytical method for the determination of binding cofactors to maquettes, with the analysis of dissociation constants ( $K_D$ ), stoichiometric relationships, and extinction coefficients obtained [25-28]. Binding titrations here were performed by adding aliquots of porphyrin to a solution containing maquette, incrementally increasing the concentration of porphyrin present with maquette. Aliquots were added at 0.1  $\mu\text{M}$  per aliquot to a 0.5  $\mu\text{M}$  maquette solution in aqueous buffer, with the binding followed by UV-Vis. spectroscopy. The Soret peak position for the first aliquots corresponds to porphyrin ligation with maquette, with this peak position plotted against the concentration of porphyrin present. Modelling this plot in accordance with Equation 2 (Chapter II) allows for analysis of  $K_D$ , stoichiometry, and extinction coefficients. P1a-P1d were chosen for titrations with maquettes due to the porphyrin series being shown to be the most stable in aqueous buffer in conjunction with ligation to maquettes occurring (previous results).

### 2.5.1- Titration of maquettes with P1a

Figure III-32 shows the binding titration of P1a to the BT-maquette in aqueous buffer, with the inset showing the change in absorbance at the maximum peak (of bound state) with additions of P1a. As shown, the bound P1a absorbance has a maximum at 432 nm, which continues to increase with all subsequent increments. When P1a increments are plotted against the rise at 432 nm (Figure III-32, inset), there is a distinctive bend in the obtained curve, relating to P1a being in a bound state before the bend, and un-bound after. With the starting concentration of maquette and of the increments of P1a known, the equivalents of P1a compared to maquette are known, indicating that 2 equivalents of P1a bind to 1 equivalent of maquette, with subsequent P1a being in an unbound state. The titration spectra does not contain a distinct peak for unbound P1a, as the porphyrin aggregates quickly in the solvent, with a broadened peak in the Soret region, as shown previously. Analysis of the fit (Equation 2, Chapter II) gave an extinction coefficient of bound P1a of  $353,432 (\pm 3,587) \text{ M}^{-1} \text{ cm}^{-1}$  at 432 nm, and the dissociation constant ( $K_D$ ) of  $17 (\pm 3.7) \text{ nM}$ .

Similarly, when P1a is titrated with the GL-maquette, a single peak at 431.5 nm is apparent for all additions of porphyrin (Figure III-33). This is due to the excess 'unbound' P1a existing in an aggregated state, as mentioned previously. Analysis of the titration displays that approximately 2 equivalents of porphyrin binds to 1 equivalent maquette, with subsequent P1a being in an unbound state. Analysis of the fit (Equation 2) gave an extinction coefficient of

bound P1a of  $264,400 (\pm 1,544) \text{ M}^{-1} \text{ cm}^{-1}$  at 431.5 nm, and the dissociation constant ( $K_D$ ) of  $10 (\pm 3.3) \text{ nM}$ .

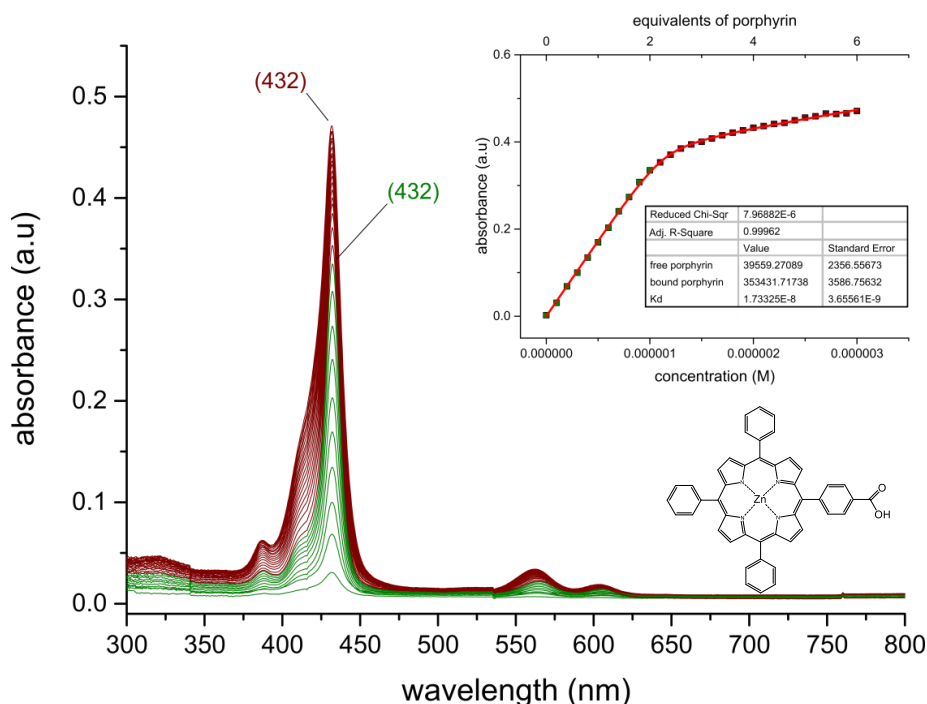


**Figure III-32; Titration of BT-maquette with P1a.**  $0.5 \mu\text{M}$  BT-maquette with increments of  $0.1 \mu\text{M}$  P1a in aqueous buffer. Inset shows the increase in absorbance of bound 'P1a' at Soret peak maxima against concentration of P1a, and resulting equivalents of porphyrin compared to maquette, along with calculated data from this plot using Equation 2 (Chapter II).

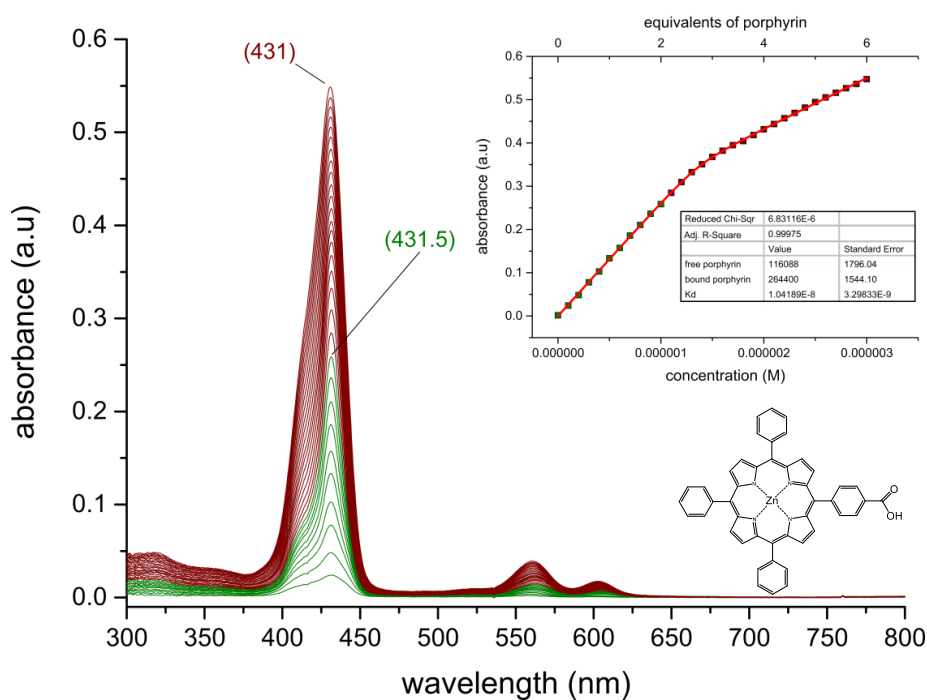


**Figure III-33; Titration of GL-maquette with P1a.**  $0.5 \mu\text{M}$  GL-maquette with increments of  $0.1 \mu\text{M}$  P1a in aqueous buffer. Inset shows the increase in absorbance of bound 'P1a' at Soret peak maxima against concentration of P1a, and resulting equivalents of porphyrin compared to maquette, along with calculated data from this plot using Equation 2 (Chapter II).

### 2.5.2- Titration of maquettes with P1b

P1b was titrated with maquettes to further analyse ligation. Figure III-34 shows the binding titration of P1b to the BT-maquette in aqueous buffer, with the inset showing the change in absorbance at the maximum peak (of bound state). As shown, the bound P1b absorbance has a maximum at 433 nm, which continues to increase with all subsequent increments. However, a distinctive peak at 423 nm becomes apparent during the titration. When P1b increments are plotted against the rise at 433 nm (Figure III-34, inset), there is a distinctive bend in the obtained curve, relating to P1b being in a bound state before the bend, and un-bound after. The unbound state of P1b is the reason for the observed peak occurring at 423 nm, becoming apparent after the stoichiometric limit of P1b and maquette is reached. With the starting concentration of maquette and of the increments of P1b known, the equivalents of P1b compared to maquette are known indicating that 2 equivalents of P1b binds to 1 equivalent maquette, with subsequent P1b being in an unbound state. Analysis of the fit (Equation 2) calculated the extinction coefficient of bound P1b of  $412,544 (\pm 5,119) \text{ M}^{-1} \text{ cm}^{-1}$  at 433 nm, and the dissociation constant ( $K_D$ ) of  $26 (\pm 5.1) \text{ nM}$ .

Figure III-35 shows the binding titration of P1b to the GL-maquette in aqueous buffer. Dissimilar to P1b with the BT-maquette, bound P1b with GL-maquette has a maximum peak at 432.5 nm, which continues to increase with all subsequent increments but shifts towards 429 nm during the titration. When P1b increments are plotted against the rise at 432.5 nm (Figure III-35, inset), there is a distinctive bend in the obtained curve. The unbound state of P1b is the reason for the observed shifting towards 429 nm, becoming apparent after the stoichiometric limit of P1b and maquette is reached. The bend is shown to occur at 2 equivalents of porphyrin, indicating that 2 equivalents of P1b bind to 1 equivalent maquette, with subsequent P1b being in an unbound state. Analysis of the fit (Equation 2) calculated the extinction coefficient of bound P1b of  $409,058 (\pm 3,186) \text{ M}^{-1} \text{ cm}^{-1}$  at 432.5 nm, and the dissociation constant ( $K_D$ ) of  $15 (\pm 2.6) \text{ nM}$ .

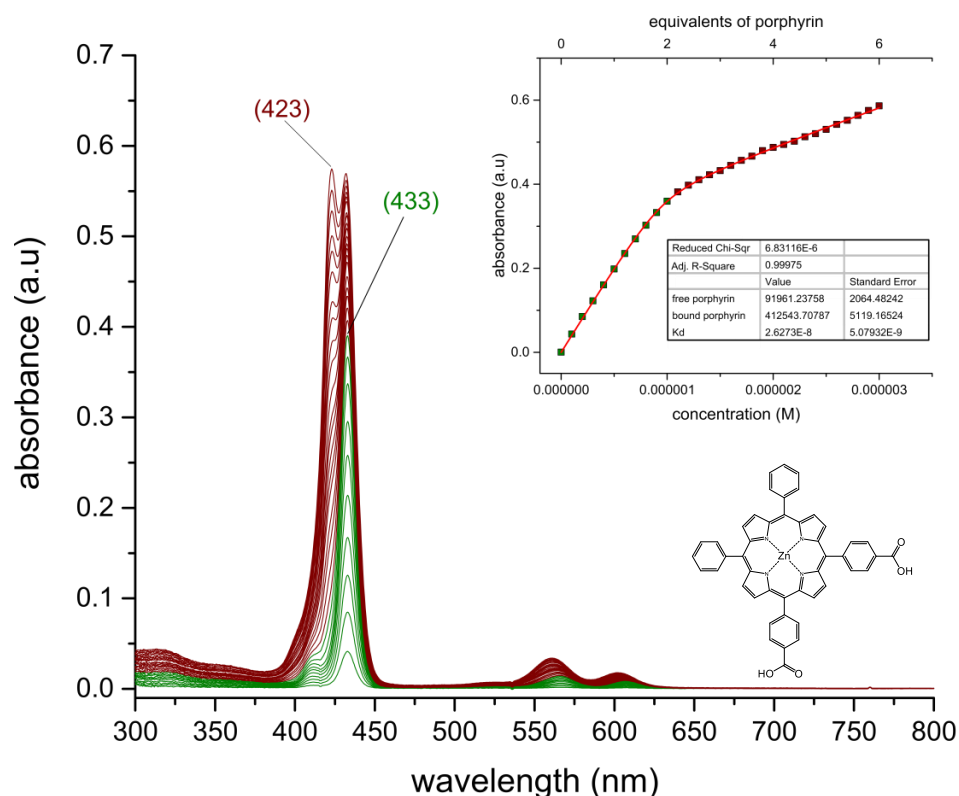


**Figure III-34; Titration of BT-maquette with P1b.** 0.5  $\mu\text{M}$  BT-maquette with increments of 0.1  $\mu\text{M}$  P1b in aqueous buffer. Inset shows the increase in absorbance of bound 'P1b' at Soret peak maxima against concentration of P1b, and resulting equivalents of porphyrin compared to maquette, along with calculated data from this plot using Equation 2 (Chapter II).

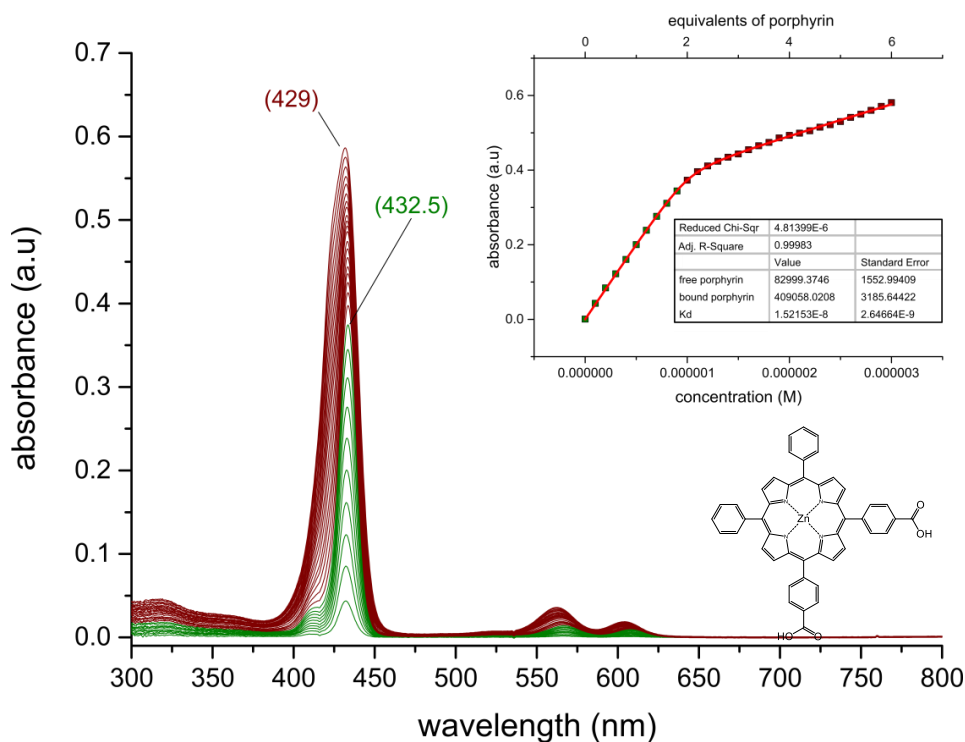


**Figure III-35; Titration of GL-maquette with P1b.** 0.5  $\mu\text{M}$  GL-maquette with increments of 0.1  $\mu\text{M}$  P1b in aqueous buffer. Inset shows the increase in absorbance of bound 'P1b' at Soret peak maxima against concentration of P1b, and resulting equivalents of porphyrin compared to maquette, along with calculated data from this plot using Equation 2 (Chapter II).

### 2.5.3- Titration of maquettes with P1c

Further analysis of P1c ligation to maquettes was completed via titrations. Figure III-36 shows the binding titration of P1c to the BT-maquette in aqueous buffer, with the inset the change in absorbance at the maximum peak (of bound state) with additions of P1c. As shown, the bound P1c has a maximum peak at 432.5 nm, which continues to increase with all subsequent increments. However, a distinctive peak at 422 nm becomes apparent during the titration, eventually becoming the dominant peak. When P1c increments are plotted against the rise at 432.5 nm (Figure III-36, inset), there is a distinctive bend in the obtained curve, relating to P1c being in a bound state before the bend, and un-bound after. The unbound state of P1c is the observed peak occurring at 422 nm, becoming apparent after the stoichiometric limit of P1c and maquette is reached. With the starting concentration of maquette and of the increments of P1c known, the number of equivalents of P1c compared to maquette is known. The bend is shown to occur at 2 equivalents of porphyrin, indicating that 2 equivalents of P1c bind to 1 equivalent maquette, with subsequent P1c being in an unbound state. Analysis of the fit (Equation 2) calculated the extinction coefficient of bound P1c of  $470,950 (\pm 15,008) \text{ M}^{-1} \text{ cm}^{-1}$  at 432.5 nm, and the dissociation constant ( $K_D$ ) of  $30 (\pm 10) \text{ nM}$ .

P1c titration with GL-maquette in aqueous buffer is near identical to that of the titration results with BT-maquette. As shown, the bound P1c has a maximum peak at 432 nm, with a distinctive peak at 423 nm becoming apparent during the titration, eventually becoming the dominant peak. When P1c increments are plotted against the rise at 432 nm (Figure III-37, inset), there is a distinctive bend in the curve at the stoichiometric limit. The bend occurs at 2 equivalents of porphyrin, with subsequent P1c being in an unbound state. Analysis of the fit (Equation 2) provided an extinction coefficient of bound P1c of  $386,876 (\pm 10,345) \text{ M}^{-1} \text{ cm}^{-1}$  at 432 nm, and the dissociation constant ( $K_D$ ) of  $36 (\pm 8.2) \text{ nM}$ .



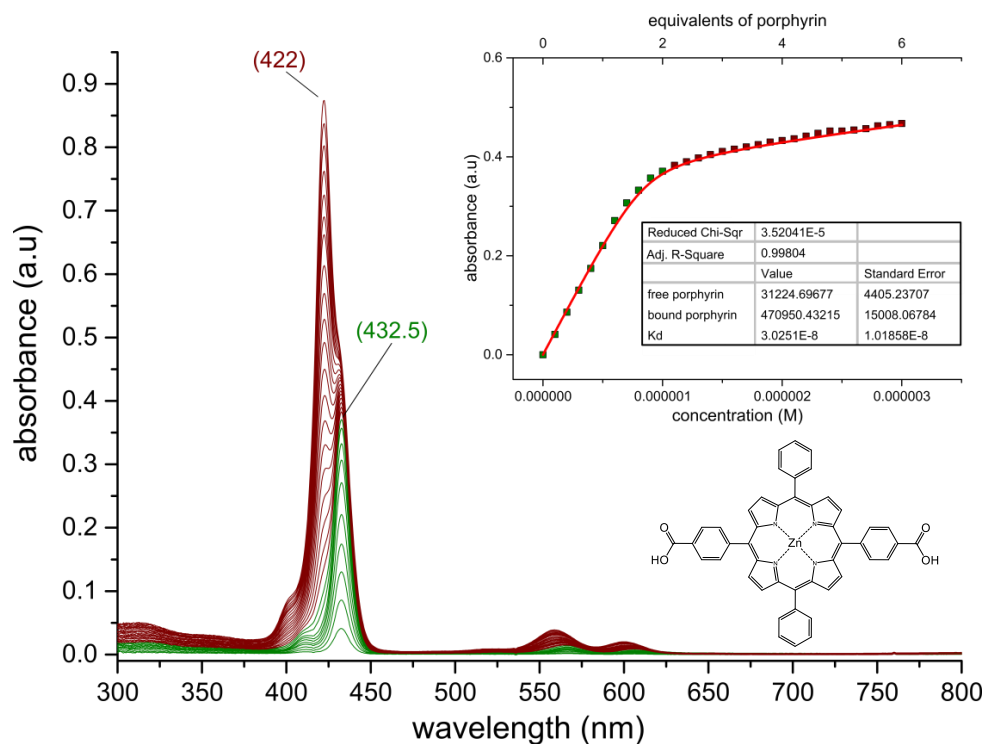


**Figure III-36; Titration of BT-maquettes with P1c.** 0.5  $\mu\text{M}$  BT-maquette with increments of 0.1  $\mu\text{M}$  P1c in aqueous buffer. Inset shows the increase in absorbance of bound 'P1c' at Soret peak maxima against concentration of P1c, and resulting equivalents of porphyrin compared to maquette, along with calculated data from this plot using Equation 2 (Chapter II).

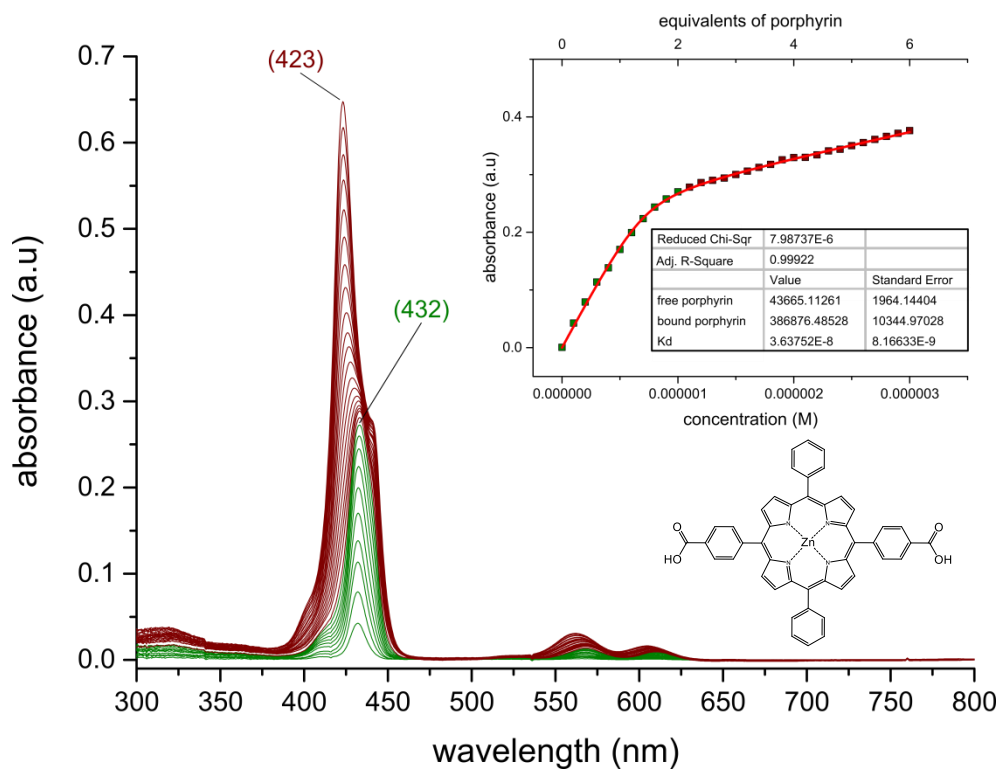


**Figure III-37; Titration of GL-maquettes with P1c.** 0.5  $\mu\text{M}$  GL-maquette with increments of 0.1  $\mu\text{M}$  P1c in aqueous buffer. Inset shows the increase in absorbance of bound 'P1c' at Soret peak maxima against concentration of P1c, and resulting equivalents of porphyrin compared to maquette, along with calculated data from this plot using Equation 2 (Chapter II).

#### 2.5.4- Titration of maquettes with P1d

Analysis of P1d binding to maquettes was further explored via titrations. Figure III-38 shows the binding titration of P1d to the BT-maquette in aqueous buffer, with the inset giving the change in absorbance at the maximum peak (of bound state) with additions of P1d. As shown, the bound P1d has a maximum peak at 433.5 nm, which continues to increase with all subsequent increments. However, a distinctive peak at 422.5 nm becomes apparent during the titration, eventually becoming the dominant peak. When P1d increments are plotted against the rise at 433.5 nm (Figure III-38, inset), there is a distinctive bend in the obtained curve, relating to P1d being in a bound state before the bend, and unbound after. The unbound state of P1d is the observed peak occurring at 422.5 nm, becoming apparent after the stoichiometric limit of P1d and maquette is reached. With the starting concentration of maquette and of the increments of P1d known, the number of equivalents of P1d compared to maquette is known. The bend is shown to occur at 2 equivalents of porphyrin, indicating that 2 equivalents of P1d binds to 1 equivalent maquette, with subsequent P1d being in an unbound state. Analysis of the fit (Equation 2) calculated the extinction coefficient of bound P1d of  $493,932 (\pm 3,915) \text{ M}^{-1} \text{ cm}^{-1}$  at 433.5 nm, and the dissociation constant ( $K_D$ ) of  $21 (\pm 2.0) \text{ nM}$ .

The results for P1d with the GL-maquette are shown in Figure III-39, which is near identical to that of the results obtained with BT-maquette. Analysis of the fit (Equation 2) calculated the extinction coefficient of bound P1d of  $540,993 (\pm 5,913) \text{ M}^{-1} \text{ cm}^{-1}$  at 433 nm, and the dissociation constant ( $K_D$ ) of  $25 (\pm 3.0) \text{ nM}$ .

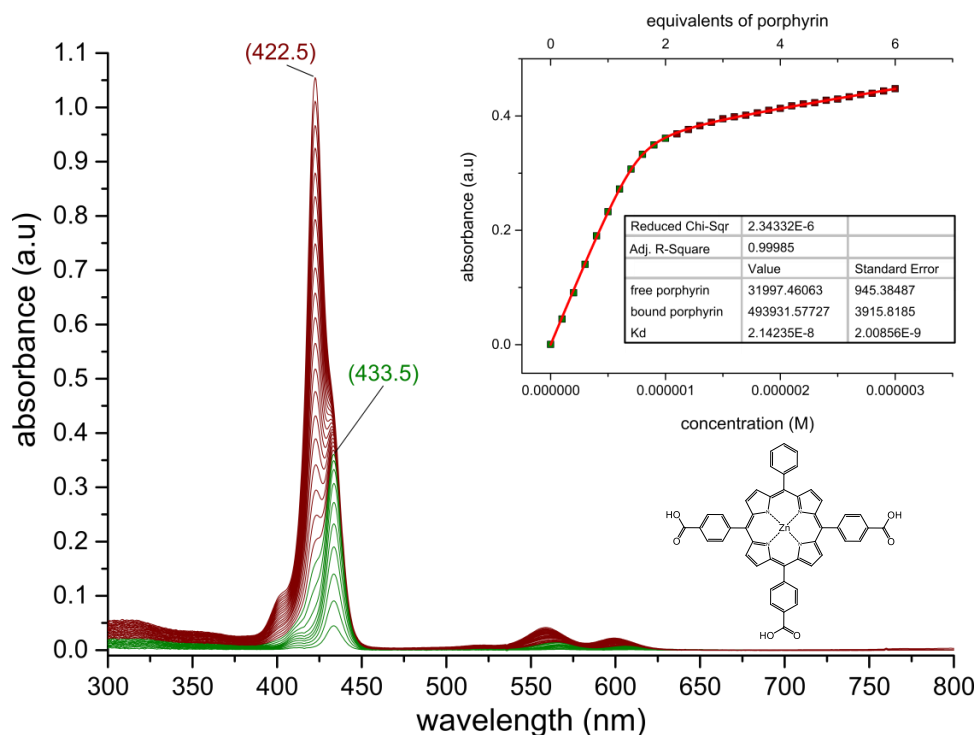


**Figure III-38; Titration of BT-maquette with P1d.** 0.5  $\mu\text{M}$  BT-maquette with increments of 0.1  $\mu\text{M}$  P1d in aqueous buffer. Inset shows the increase in absorbance of bound 'P1d' at Soret peak maxima against concentration of P1d, and resulting equivalents of porphyrin compared to maquette.

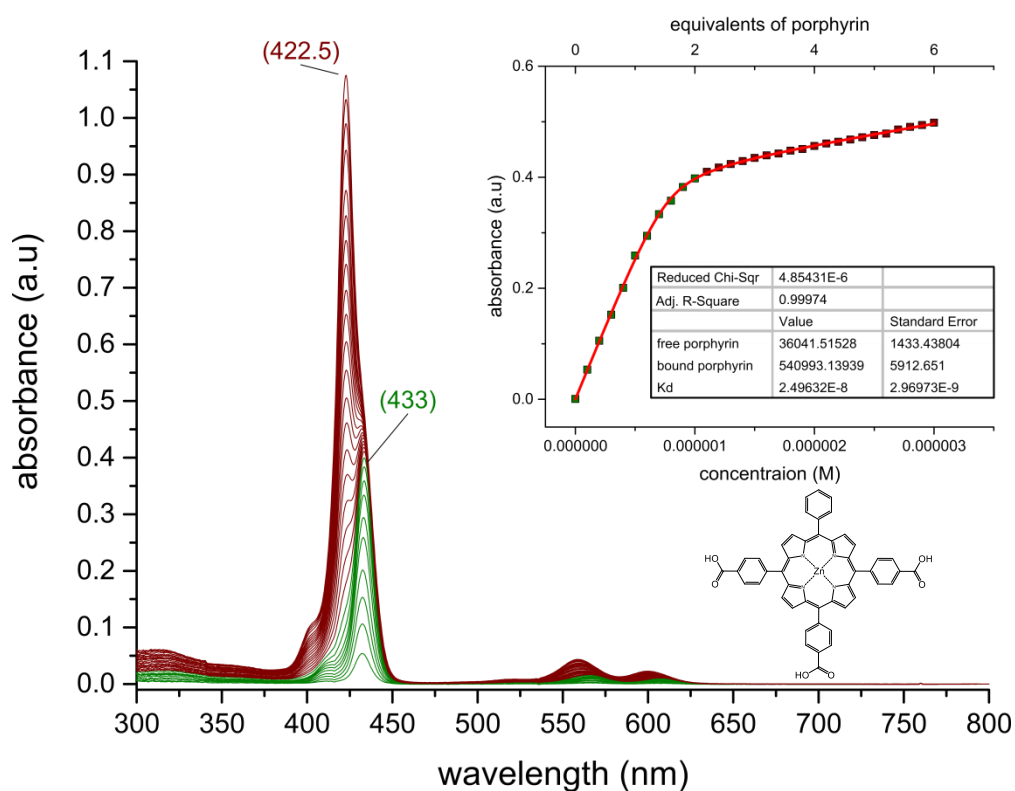


**Figure III-39; Titration of GL-maquette with P1d.** 0.5  $\mu\text{M}$  GL-maquette with increments of 0.1  $\mu\text{M}$  P1d in aqueous buffer. Inset shows the increase in absorbance of bound 'P1d' at Soret peak maxima against concentration of P1d, and resulting equivalents of porphyrin compared to maquette.

## 2.6- Maquette-porphyrin emission and excitation spectra in aqueous buffer

As there is observed to be significant shifts in absorbance spectra when porphyrin entities are interacting with maquettes (Chapter III, Section 2.4), potential shifts in the emission spectra were investigated. As the tri-substituted porphyrins (P1d, P2d, P3d, P4d) were observed to be the most stable in aqueous buffer in conjunction with ligating to maquettes quickly, these porphyrins were chosen to observe changes in emission and excitation spectra. For the following excitation spectra, the red-bar indicates where the detector was interfered by scattering/refraction from the incident beam (excitation wavelength).

### 2.6.1- P1d in aqueous buffer and with maquettes

P1d in aqueous buffer was analysed via emission spectroscopy, excited at its Soret peak maxima (422 nm), with the obtained emission and excitation spectra shown in Figure III-40. Two emission peaks are apparent when P1d is in aqueous buffer, which become red-shifted 10-12 nm when with either BT- or GL-maquette (excited at Soret peak maximums). To determine which entities are contributing to the emission spectrum, an excitation spectrum can be obtained by measuring the peak emission wavelength. When P1d is in aqueous buffer, the excitation spectrum resembles that of the P1d absorbance spectrum. This excitation spectrum is red-shifted by 11 nm when either BT- or GL-maquette is present, as was observed with the absorbance spectra. These results indicate that the shifts in emissions spectra originate from the red-shifted absorbance spectra of P1d due to the porphyrin being in a ligated state.

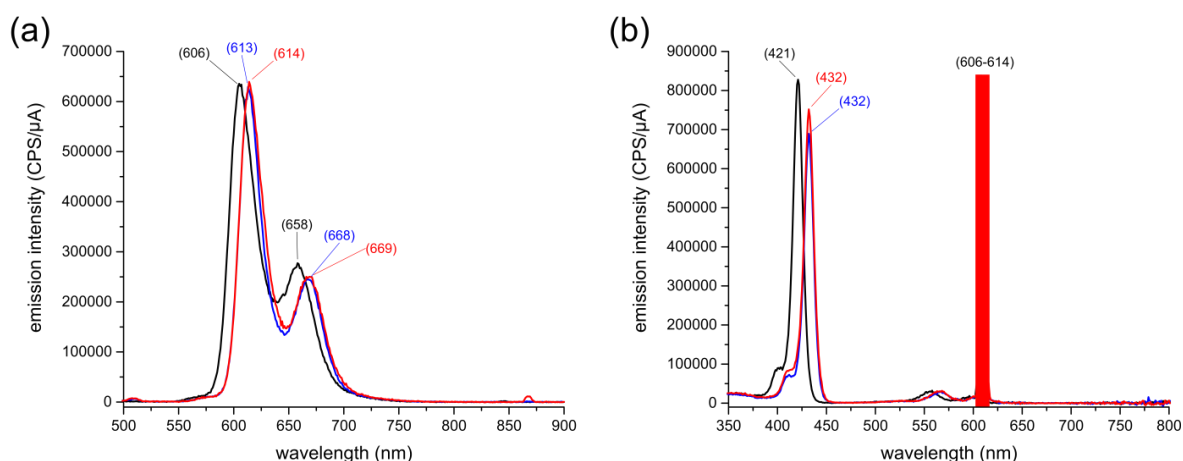


**Figure III-40; Emission and excitation spectra of P1d.** (a) Emission of P1d in aqueous buffer (black), P1d with BT-maquette (red), and P1d with GL-maquette (blue); all emission data result from excitation at Soret peak maximum absorbances. (b) Excitation of P1d in aqueous buffer (black), P1d with BT-maquette (red), and P1d with GL-maquette (blue); excitation spectra measured by recording emission at the peak intensities shown.

### 2.6.2- P2d in aqueous buffer and with maquettes

P2d was prepared in aqueous buffer, with the emission spectra measured when excited at its Soret peak maxima (414 nm), and the obtained spectra shown in Figure III-41. Two peaks are apparent, compared to when either maquette is present in aqueous buffer with P2d. When P2d is with GL-maquette, a distinct red-shift of 10-13 nm of the peaks is observed. It is apparent that the second peak is more pronounced when P2d is with GL-maquette. When BT-maquette is in aqueous buffer with P2d, two peaks are observed, shown to be red-shifted by 4-5 nm when compared to P1d in solution. This shift is not as pronounced as when GL-maquette is present, along with the second emission peak not being as prominent. To determine which entities are contributing to the emission spectrum, an excitation spectrum of P2d under each condition was obtained. A peak excitation is shown to occur at 414 nm when P2d is in aqueous buffer, indicative that the monomeric porphyrin is contributing to the emission spectrum obtained. This is compared to GL-maquette and P2d in aqueous buffer having an excitation peak at 421 nm, identical to the absorbance profile shown previously (Figure III-22e). Conversely, when BT-maquette is present with P2d in aqueous buffer, the excitation spectrum shows a peak at 416 nm. This excitation spectrum is slightly blue-shifted compared to the absorbance profile shown previously (Figure III-22e). The resulting solution from the measured BT-maquette with P2d had an absorbance spectrum which matched that of the excitation spectra (data not shown). This indicates that P2d interacts with the GL-maquette more strongly, staying in a bound state when dilute. Comparatively, the P2d interaction with BT-maquette must be weaker in nature, with the P2d emission and excitation spectra displaying spectra lying between the bound and unbound states of P2d.

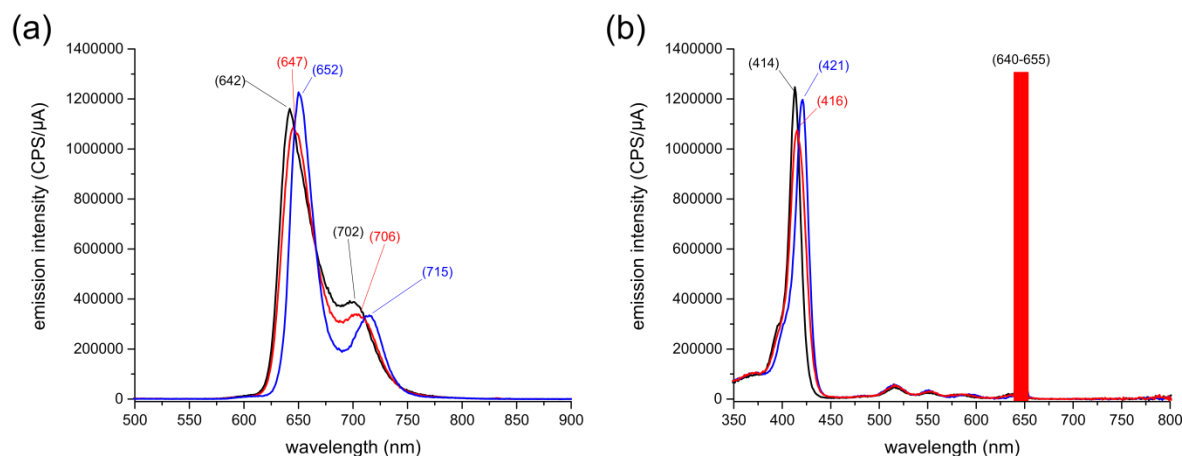


**Figure III-41; Emission and excitation spectra of P2d.** (a) Emission of P2d in aqueous buffer (black), P2d with BT-maquette (red), and P2d with GL-maquette (blue); all emission result from excitation at Soret peak maximum absorbances. (b) Excitation of P2d in aqueous buffer (black), P2d with BT-maquette (red), and P2d with GL-maquette (blue); excitation spectra measured by recording emission at the peak intensities shown.

### 2.6.3- P3d in aqueous buffer with maquettes

The emission spectra of P3d in aqueous buffer, when excited at its Soret peak maxima (421 nm), are shown in Figure III-42. Two peaks are apparent when either maquette is present, which are red-shifted by 8-9 nm. To determine which entities are contributing to the emission spectrum, an excitation spectrum was obtained. When P3d is free in aqueous buffer, the excitation spectrum shows a distinctively sharp and symmetrical Soret peak resembling that of the absorbance profile, indicating that the monomeric porphyrin is contributing to the emission spectrum obtained. This is compared to when BT- or GL-maquettes are present in the solution with P3d that show excitation spectra which are 10-11 nm red-shifted. This is identical to the shifts observed in the absorbance profiles, indicating that the shifts in the emissions spectra directly correspond with the shifts in the absorbance when P3d is ligated to maquette. The intensity for P3d is observed to be diminished compared to when maquette is present, which is accounted for by P3d being shown previously to precipitate out of the solution over time, whilst being stable with the maquettes.

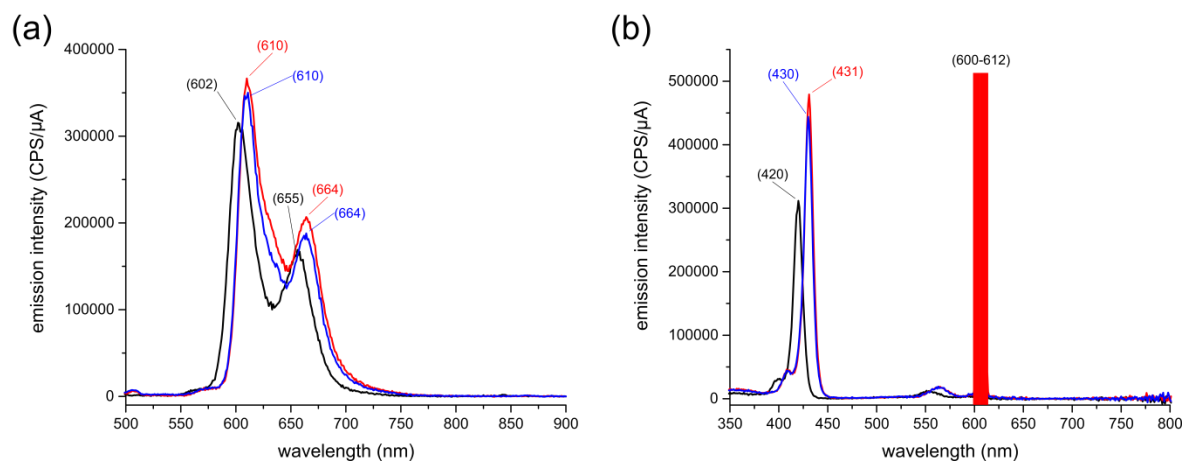


**Figure III-42; Emission and excitation spectra of P3d.** (a) Emission of P3d in aqueous buffer (black), P3d with BT-maquette (red), and P3d with GL-maquette (blue); all emission data result from excitation at Soret peak maximum absorbances. (b) Excitation of P3d in aqueous buffer (black), P3d with BT-maquette (red), and P3d with GL-maquette (blue); excitation spectra measured by recording emission at the peak intensities shown.

#### 2.6.4- P4d in aqueous buffer and with maquettes

The emission spectra of P4d in aqueous buffer, when excited at its Soret peak maxima (423 nm), are shown in Figure III-43. Two peaks are apparent which, when either maquette is present, become red-shifted by 10-12 nm. To determine which entities are contributing to the emission spectrum, an excitation spectrum is obtained. When P4d is free in aqueous buffer, the excitation spectrum shows a distinctively sharp and symmetrical Soret peak resembling that of the absorbance profile, indicating that the monomeric porphyrin is contributing to the emission spectrum obtained. When the BT- or GL-maquette are present in the solution with P3d, the excitation spectra are 11-12 nm red-shifted. This is identical to the shifts observed in the absorbance profiles, indicating that the shifts in the emissions spectra correspond with the shifts in the absorbance for when P3d is ligated to maquette.

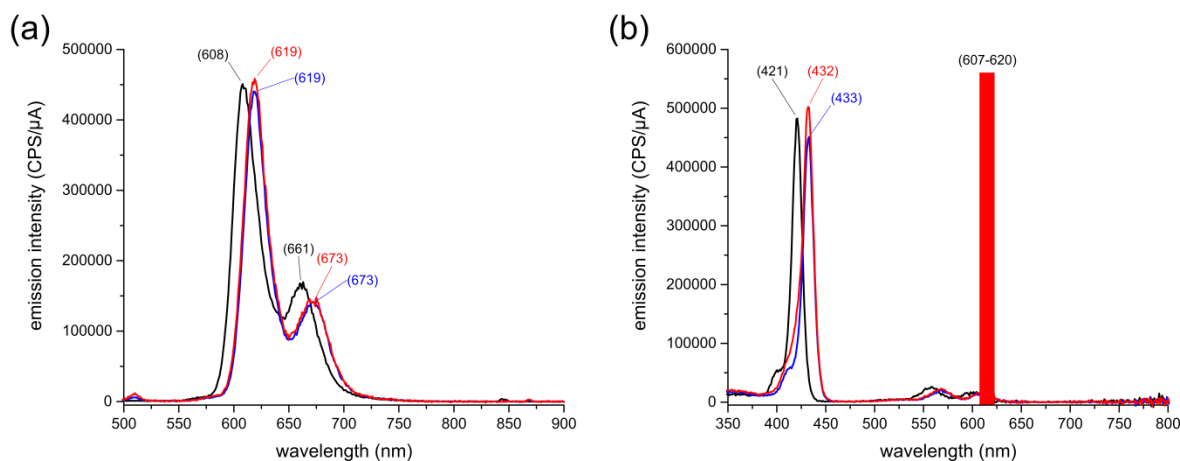


**Figure III-43; Emission and excitation spectra of P4d.** (a) Emission of P4d in aqueous buffer (black), P4d with BT-maquette (red), and P4d with GL-maquette (blue); all emission data result from excitation at Soret peak maximum absorbances. (b) Excitation of P4d in aqueous buffer (black), P4d with BT-maquette (red), and P4d with GL-maquette (blue); excitation spectra measured by recording emission at the peak intensities shown.

## 2.7- Resonance Raman in aqueous buffer

Resonance Raman spectroscopy was carried out by Holly van der Salm and Jonathan E. Barnsley under supervision of Prof. Keith C. Gordon of the University of Otago, New Zealand (collaborators). Resonance Raman spectroscopy was used to analyse the ‘core size’ marker bands of the porphyrins in solution and with maquettes, known to be sensitive to changes in environment and presence of auxiliary moieties [7-10, 29].

### 2.7.1- BT-maquette and zinc based carboxylic substituted porphyrins

Solutions of BT-maquette with porphyrins P1a-d were analysed for Raman shifts (Figure III-44). The resonance Raman results show spectroscopic changes for a number of bands with the presence of the maquette. The band near  $1000\text{ cm}^{-1}$  shows intensity changes of the  $995\text{ cm}^{-1}$  shoulder (P1a) and blue shifts (P1a, P1c, and P1d) when the maquette is present with the porphyrins. These same behaviours are also exhibited by the two bands at  $\sim 1350\text{ cm}^{-1}$  (for all porphyrins). The band at  $1354\text{ cm}^{-1}$  for P1b free aqueous buffer shows a significant shoulder at  $1342\text{ cm}^{-1}$  becoming apparent when the maquette is present in stoichiometric amount (Figure III-44b). This shoulder diminishes significantly when the porphyrin is in excess (ie. when P1b is in both an interacted state and free in solution). This is identical for P1c, where



the band at  $1356\text{ cm}^{-1}$  contains a significant shoulder at  $1342\text{ cm}^{-1}$  with maquette interactions. (Figure III-44c). The intensity of the band at  $1420\text{ cm}^{-1}$  is observed to consistently decrease with all porphyrins with the presence of maquette. Low frequency ( $150\text{--}250\text{ cm}^{-1}$ ) resonance Raman data shows discernible differences between porphyrins with and without maquette, with the change in core size marker bands indicating ligation with the maquette.

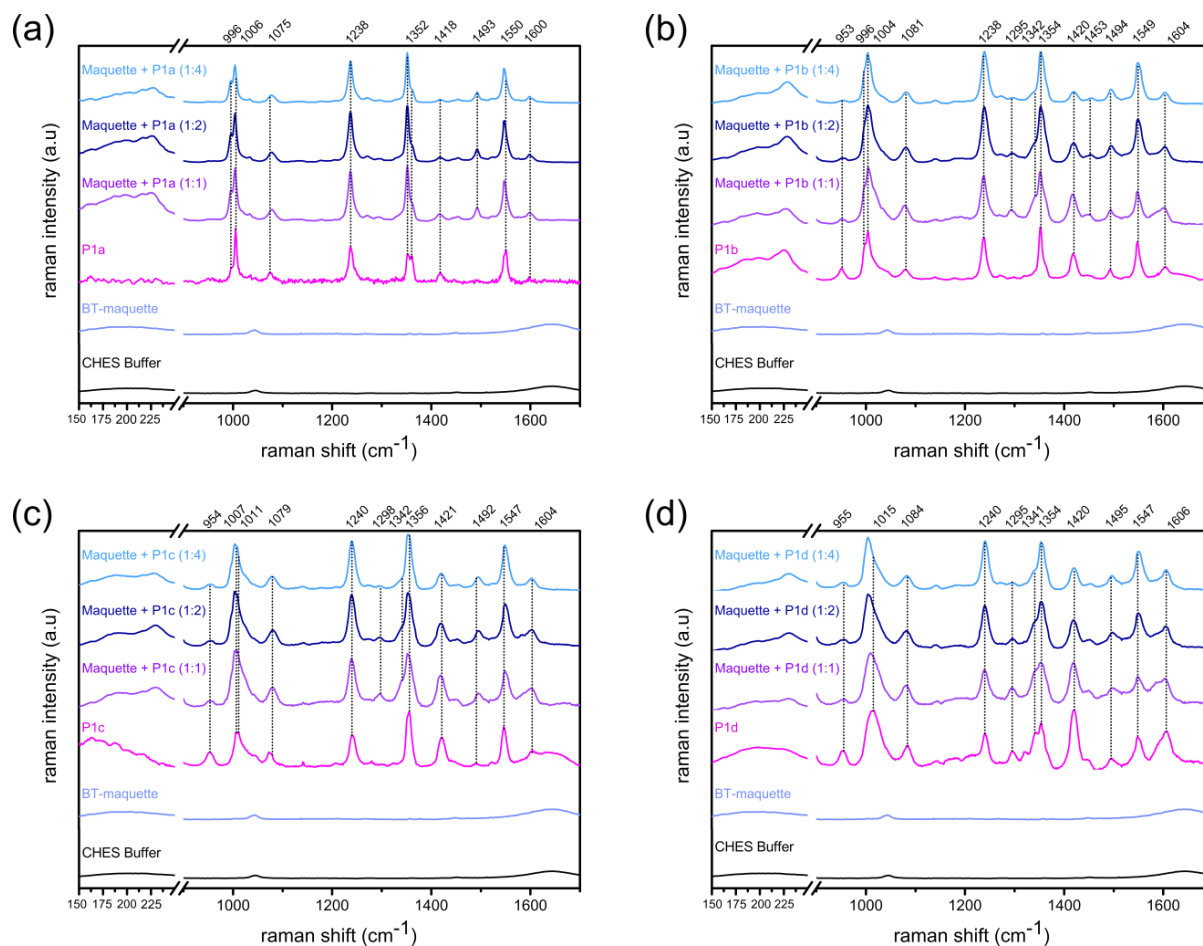


**Figure III-44; Resonance Raman spectra from solutions of BT-maquette and zinc based carboxylic substituted porphyrins in aqueous buffer.** (a) Spectra of BT-maquette with P1a in ratios of 1:4, 1:2, 1:1, P1a in aqueous buffer, maquette in aqueous buffer, and buffer. (b) Spectra of BT-maquette with P1b in ratios of 1:4, 1:2, 1:1, P1b in aqueous buffer, maquette in aqueous buffer, and buffer. (c) Spectra of BT-maquette with P1c in ratios of 1:4, 1:2, 1:1, P1c in aqueous buffer, maquette in aqueous buffer, and buffer. (d) Spectra of BT-maquette with P1d in ratios of 1:4, 1:2, 1:1, P1d in aqueous buffer, maquette in aqueous buffer, and buffer.

### 2.7.2- GL-maquette and zinc based carboxylic substituted porphyrins

Solutions of the GL-maquette with porphyrins P1b-d were analysed for Raman shifts (Figure III-45), and the results show spectroscopic changes for a number of bands with the presence of the maquette. Spectroscopic changes for core size marker bands with the presence of maquette are indicative of ligation. The relative intensities for bands within the 890-1610  $\text{cm}^{-1}$  range increase when compared to the bands at  $\sim 678$  and  $\sim 714$   $\text{cm}^{-1}$  for all porphyrins measured when the maquette is within stoichiometric ratio limits (specifically 1:2, porphyrin:maquette). Relative band intensities for bands between 1339-1353  $\text{cm}^{-1}$  also change, with increases by over 20% for P1d with the maquette (Figure III-45c). Similarly, a distinct shoulder at  $\sim 1340$   $\text{cm}^{-1}$  becomes apparent when P1b or P1c is with the maquette below stoichiometric amounts (Figure III-45a and b). At the lower energy region, there is a small blue shift of the 1003  $\text{cm}^{-1}$  band to 1006  $\text{cm}^{-1}$  with all porphyrins with the maquette presence. Resonance Raman data shown serves as supporting evidence that structural changes have occurred through the immediate porphyrin environments changing, which is a result of binding into the maquette. As was shown previously, low frequency (150-250  $\text{cm}^{-1}$ ) resonance Raman data shows discernible differences between porphyrins with and without maquette.

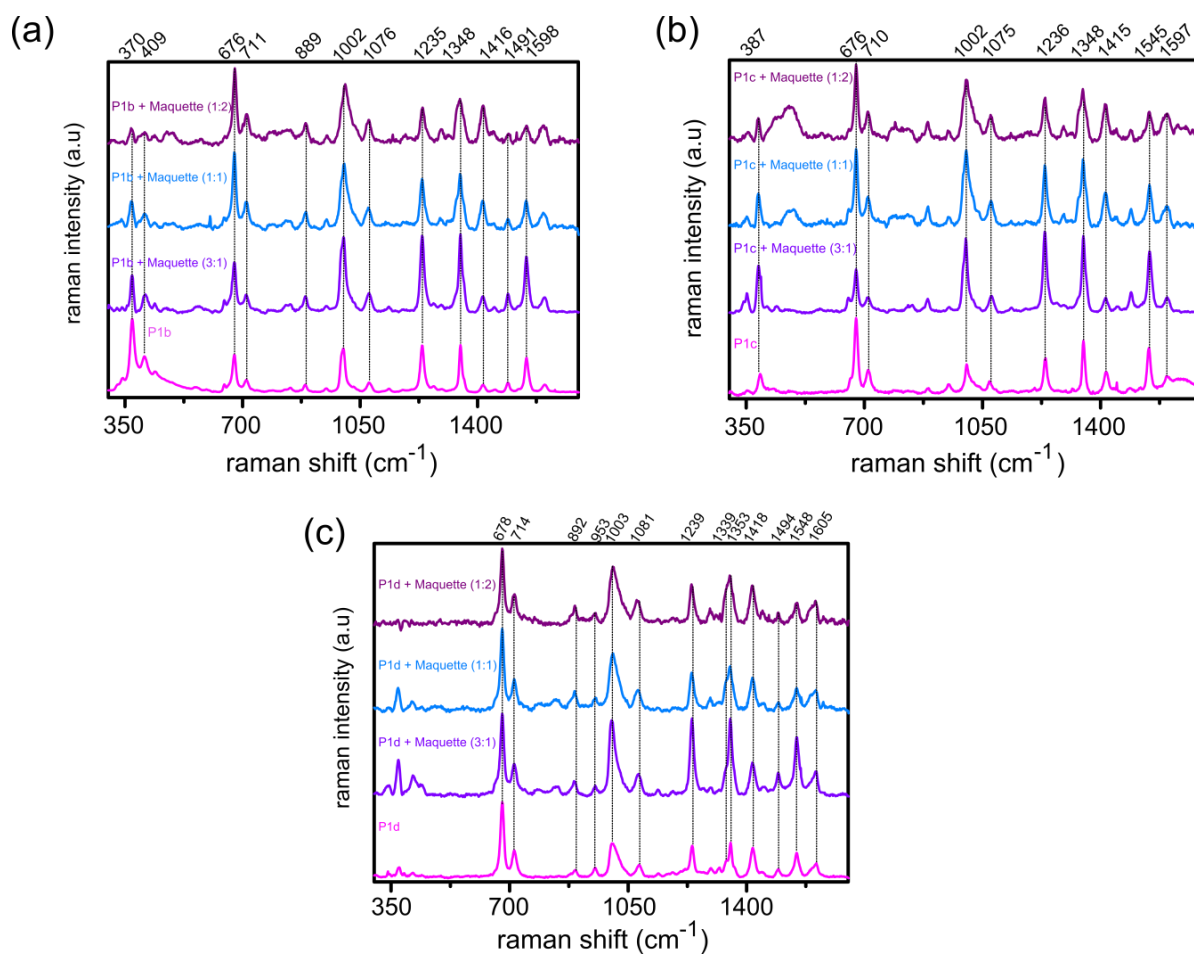


**Figure III-45; Resonance Raman spectra from solutions of GL-maquette and zinc based carboxylic substituted porphyrin in aqueous buffer.** (a) Spectra of P1b with GL-maquette in ratios of 1:2, 1:1, 3:1 in aqueous buffer, and P1b without maquette in buffer. (b) Spectra of P1c with GL-maquette in ratios of 1:2, 1:1, 3:1 in aqueous buffer, and P1c without maquette in buffer. (c) Spectra of P1d with GL-maquette in ratios of 1:2, 1:1, 3:1 in aqueous buffer, and P1d without maquette in buffer.

### 3- Discussion; Maquette-Porphyrin Binding in Solution

#### 3.1- Porphyrins in DMSO

Zinc tetraphenylporphyrin is known to have a high extinction coefficient in organic solvent ( $>550,000 \text{ M}^{-1} \text{ cm}^{-1}$ ), displaying a single Soret peak, with a shoulder on the lower wavelengths and two Q-bands [30, 31]. This is identical to that of all zinc porphyrins measured in DMSO within this study (P1a-e, P3a-e, P4a-d). This is in agreement with the view that all the porphyrins are in a monomeric state (ie. not aggregated) in DMSO, apparent by the shape and intensity of the Soret peak and Q-bands. Similarly, H<sub>2</sub>TPP shows a single Soret peak with shoulder at the lower wavelengths, with four Q-bands present. This is identical to the free-base porphyrins measured in DMSO within this study (P2a-e), whereby the porphyrins are all observed to be monomeric in the solution. Similarly, the shape of the emissions peaks from each porphyrin in DMSO supports the view that each porphyrin is a monomeric entity in solution. It is therefore most appropriate to refer to the spectral profiles of the individual porphyrin species in DMSO when comparing the spectra from aqueous solvents, in respect to aggregation and spectral changes. To the best of my knowledge, no porphyrins presented here have been previously reported in regards to absorbance in DMSO.

Slight shifts in the absorbance and emission spectra were observed for all porphyrins within DMSO with additions of substituents. For all porphyrin substituent additions the shifts were  $\leq 2$  nm between the mono- and tetra-substituted analogues. This is relatively insignificant, indicating that these substituents do not significantly alter the electronic state of the porphyrin.

#### 3.2- Maquette and porphyrin binding in aqueous buffer

The trend observed regarding hydrophilicity of porphyrins in the aqueous solvent is that the addition of carboxylic groups increases hydrophilicity, with additions of trimethylammonium groups not producing a hydrophilic porphyrin. This is exemplified through the tetra substituted zinc carboxylic and trimethylammonium porphyrins (P1e and P3e, respectively). P1e shows a highly stable spectrum in aqueous buffer (Figure III-17b) where as P3e does not have a stable spectrum over time (Figure III-27b). Furthermore, P1d is observed to be highly stable when in aqueous buffer. It is shown that P1d, P1e, and P2e are the only porphyrins presented here to show high stability in the aqueous buffer, suggesting that they are

the most hydrophilic porphyrins presented here, with all other porphyrins measured becoming aggregated in the aqueous buffer.

Two distinct types of porphyrin aggregation are known when dissolved in aqueous solvents, the highly ordered J- and H-aggregates [17, 18]. It is known that J-aggregates result in red-shifting of the spectra with a sharp peak, whereas H-aggregates lead to a blue-shifting, often with a broadened peak, relative to the monomer in solution [18]. It can be expected that P1d and P1e are monomeric in aqueous solution with a Soret peak at 422 and 423 nm, respectively, showing no signs of aggregation and high solution stability. As P1a-P1e are all shown to have Soret peaks that shift by up to 2 nm (from spectra in DMSO), it can be assumed that P1a-P1c would have a Soret peak at 421-423 nm in the aqueous solvent, if they were monomeric. Shifts and broadening in the spectrum would explicitly be produced from aggregation. P1a shows two peaks, which can be accounted for by two forms of aggregation (J- and H-aggregates). The peak at 386 nm is significantly blue-shifted, implying the presence of H-aggregates, with the peak at 427 nm being red-shifted (relative to the expected peak of a monomer), implying the presence of J-aggregates. In contrast, P1b shows a peak at 422 nm with a shoulder evident at red-shifted wavelengths, diminishing over time. This indicates that some of the porphyrin species is present in J-aggregates, and that the porphyrin is precipitating out of the solution and thus not contributing to the absorbance measured, resulting in the observed decrease in absorbance. This is similar for P1c whereby the porphyrin exists in J-aggregates, which precipitate out of solution, resulting in the decrease in absorbance over time.

Despite many of the carboxyl substituted tetraphenylporphyrins aggregating in aqueous buffer, all (apart from the tetra-carboxyl, P1e) ligate with both maquettes and become stabilised in the aqueous solution. The Soret peaks for ligated carboxyl substituted tetraphenylporphyrins are 432-434 nm, red-shifted by 11-12 nm due to the axial ligation and environment of the porphyrin within the maquette [30].

Free-base versions (P2a-P2e) of the zinc porphyrins P1a-P1e show similar trends in aggregation, however, it is apparent that the zinc helps stabilise the porphyrin in aqueous buffer. This is apparent with P2d not being as stable as P1d in the aqueous buffer. P2a is observed to have a broadened peak that drifts significantly towards the red, which implies that the porphyrin is forming J-aggregates. P2b is shown to have a broadened peak at 414 nm, with aggregation apparent, the absorbance is significantly reduced over time due to precipitation of the porphyrin

out of solution. Conversely, P2c has a sharp peak at 440 nm, which is significantly red-shifted, indicating the presence of J-aggregates, which once again precipitate out of solution. Amphiphilic free-base porphyrins P2b-d all displayed signs of maquette interactions via hydrophobic partitioning, apparent by red-shifting of the absorbance spectra. Unlike the zinc based porphyrins, any observable shifts of the porphyrin spectra come solely from the immediate environment effects [6-9]. Interaction between the free-base porphyrins and maquettes result in a more stable spectrum compared to when free in solution. However, the spectra still diminish slightly over time, likely due to the interactions between porphyrin and maquette being weak resulting in the porphyrin ‘coming out’ of the maquette and aggregating in solution.

All zinc based tetraphenylporphyrin ammonium salts measured here were not stable in aqueous buffer, aggregating and precipitating out of the solvent. This is evident through the spectra diminishing over time, whereby the porphyrin coming out of solution and therefore not contributing to the absorbance. However, all (apart from the tetra-ammonium salt, P3e) ligate with both maquettes and become stabilised in the aqueous buffer. The Soret peaks for ligated trimethylammonium substituted tetraphenylporphyrins are 431-432 nm, red-shifted by 10-11 nm due to the axial ligation and environment of the porphyrin with the maquette.

This trend is similar for all butylporphyrins measured, whereby all porphyrins aggregated and precipitated out of solution, with all shown to ligate within both maquettes producing red-shifts of the Soret peak of 10-12 nm. This distinct red-shifting is due to the axial ligation and environment of the porphyrin within the maquette [30].

### **3.3- Maquette–porphyrin titrations**

Titration between the porphyrins P1a-P1d and BT- or GL-maquettes were done to determine the stoichiometric relationships and binding strengths (dissociation constants) between porphyrin and maquette. The titrations of P1a with BT- and GL-maquettes show near identical behaviours, whereby the first addition produced a Soret peak maximum at 432 and 431.5 nm, respectively (Figure III-32/33). Furthermore, the absorbance profile resembles that of a monomeric porphyrin entity, indicating that the porphyrin has bound to the maquette without aggregation. The peaks of the spectra (in both cases) are shown to continually grow,

and not shift. Spectral differences become apparent when plotting the rate of increase at the maxima to the porphyrin concentration present. The distinct bend in the plot indicates the difference in spectral species being present, namely, the bound and unbound porphyrins. This occurs at an expected 2:1 ratio (porphyrin:maquette). This is due to both maquettes containing two histidine residues, which are specifically placed to ligate to the metallic centre of cofactors, in this instance, the zinc centre of P1a. The unbound spectral species does not induce significant changes to the spectra upon additions as P1a is known to aggregate quickly with a highly diminished spectrum (previous results). The calculated extinction coefficient at the Soret peak position from the titration of ligated P1a with both maquettes was distinctly lower compared to when P1a is solubilised in DMSO. This likely arises due to the small amounts of P1a remaining in an aggregated state which is known to diminish the peak intensities [18]. This is evidence by the fact that Soret peak of P1a is not symmetrical when interacting with either maquette (Figure III-32/III-33), indicative of some of P1a being aggregated.

Similar to the titration results with P1a, titrations of P1b with BT- and GL-maquettes display absorbance spectra which indicate that the porphyrin is bound to the maquette in a monomeric state, apparent by the shape of the absorbance profile and the red-shift of the peak maxima (Figure III-34/35). Plotting of this bound state maxima to the concentration of porphyrin, a distinct bend in the fit is apparent, pertaining to the stoichiometric relationship, occurring at an expected 2:1 ratio (porphyrin:maquette). This is expected due to the presence of the two histidine residues capable of ligating to the zinc centre of the porphyrin. The titration of P2b with the BT-maquette shows that when P2b is present in the solvent at concentrations higher than the stoichiometric ratio, a second peak becomes apparent at 423 nm, attributed to the unbound porphyrin in solvent. This is in contrast to the titration of P2b with GL-maquette, where a small blue-shift towards 429 nm occurs. This indicates that although the specific binding which results in an absorbance at 432.5 nm is expected, the excess porphyrin species is not free and unbound within the solvent, suggesting that the porphyrin has unspecific interactions with GL-maquette.

Titration results from P1c and BT- or GL-maquette display near identical results to that observed for titrations with P1b and maquettes (Figure III-36/37). A single bound species of P1c is observed at the beginning of titrations with both BT- and GL-maquettes, occurring at 432.5 and 432 nm respectively. The plotting of this bound state maxima to the concentration of porphyrin, a distinct bend in the fit is apparent, pertaining to the stoichiometric relationship,

occurring at an expected 2:1 ratio (porphyrin:maquette). This is expected due to the presence of the two histidine residues capable of ligating to the zinc centre of the porphyrin. When excess P1c is added in excess of this stoichiometric limit, a second peak becomes apparent at 422-423 nm in the titrations with both maquettes. This peak arises from the unbound P1c being free in the solution, with minimal overlap between bound and unbound spectra allowing for the two species to be easily identified.

Results from the titration of P1d and BT- or GL-maquette show the most distinct difference between bound and unbound states of the porphyrin (Figure III-38/39). As is observed for all porphyrins measured, P1d shows a significantly red-shifted spectrum of the bound state compared to an unbound state, occurring at 433.5 and 433 nm when interacting with BT- or GL-maquette, respectively. As the titrations continue, a second distinct peak becomes prominent, occurring at 422.5 nm in each result. This peak is attributed to the excess P1d being free in the solvent, in an unbound state. When plotting the bound state maxima to the concentration of P1d present, a distinct bend in the plot is observed, pertaining to the stoichiometric relationship between P1d and the maquettes. This occurs at a ratio of 2:1, P1d:maquette, for both BT- and GL-maquettes. This indicates that two monomeric P1d entities are able to bind to a maquette, which is expected due to the two histidine residues being present for ligation to the zinc centre of the porphyrin.

Results from titrating porphyrins P1a-P1d with the BT-maquette were further analysed using a custom singular value decomposition (SVD) algorithm by Prof. Chris Moser (University of Pennsylvania, USA). The SVD analysis has recently been published [32], with the  $K_D$  values displaying stronger binding constants than those presented previously, as shown in Figure III-46. SVD analysis of the titration allows for the two species (bound porphyrin and unbound porphyrin) to be analysed independently. Analysis results in the bound porphyrin to be examined independently, with the additions of unbound porphyrin into the titration solution not affecting the bound porphyrin spectra (Figure III-46, insets). This method resulted in the  $K_D$  being half of that which was presented previously for P1b-d with BT-maquette. As P1a aggregates quickly in an unbound state, the  $K_D$  was evaluated to be strongest using SVD analysis, being 0.14 ( $\pm 2$  nM) compared to 17 ( $\pm 3.7$ ) nM presented previously.



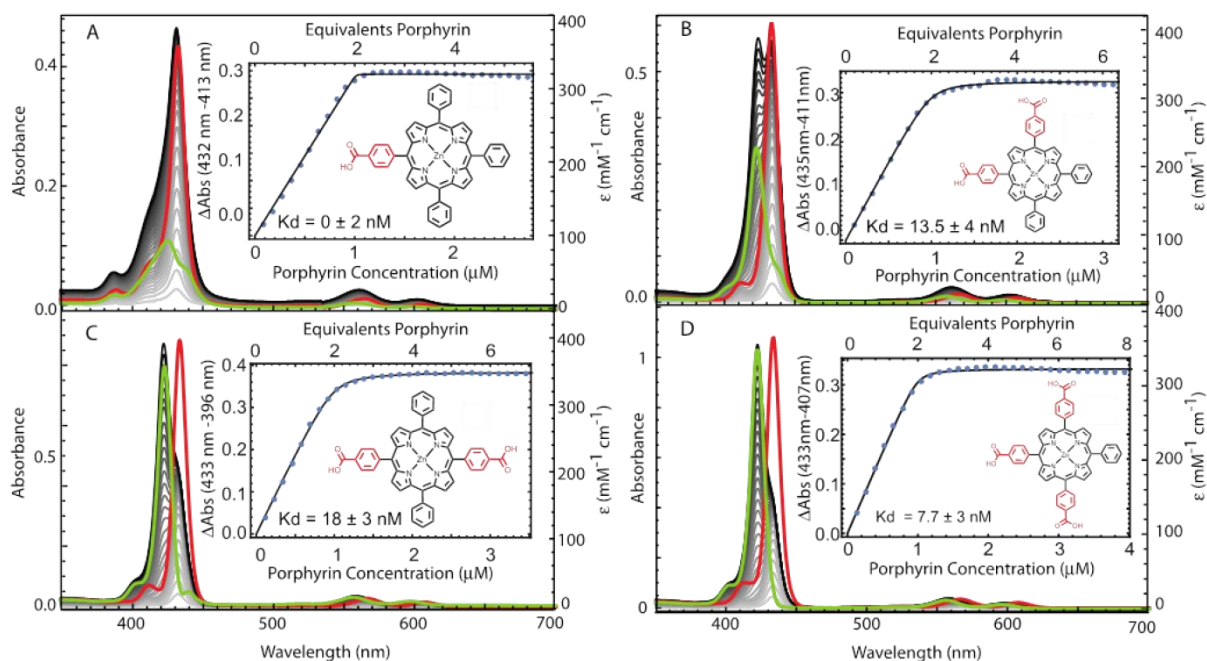


**Figure III-46; SVD analysis of titrating P1a-d with the BT-maquette.** Custom SVD algorithm (Prof. Chris Moser) was used to analyse titration results presented previous, which result in stronger binding constants. Absorbance spectra in red correspond to bound porphyrin, with the absorbance spectra in green corresponding to unbound porphyrin. Figure from [32].

### 3.4- Maquette–porphyrin emissions and resonance Raman

Emission shifts were measured when maquette was present in excess of the stoichiometric relationship of porphyrin binding. This ensures that the porphyrins would all be in a bound state to the maquette. Furthermore, the amphiphilic versions, being the tri-substituted porphyrins were chosen to observe potential shifts in emissions due to their stabilities in the aqueous solvent in conjunction with the ability to bind to the maquettes. As was evident with the absorbance spectra, the emissions spectra shows a distinct red-shift when the zinc-porphyrins are with either maquette compared to when they are unbound in solution (P1d, P3d, and P4d). This red-shift is shown to be 10-12 nm, which is shifted identically to the observed shifts in absorbance when bound with maquette compared to unbound porphyrin. The excitation spectra verify that the spectral species producing the emission is indeed coming from either the unbound porphyrin, or the bound porphyrin with maquette. The excitation spectra show the distinct profile of a monomeric porphyrin, with a 10-12 nm red-shift when bound to either BT- or GL-maquette (for P1d, P3d, and P4d). Differences in the emission are apparent when the

free base porphyrin (P2d) emission and excitation is obtained. The emission and excitation spectra of the unbound P2d are as expected, as is when P2d is with GL-maquette, producing a red-shift of both the emission and excitation spectra due to interactions. However, it is apparent that when P2d is with BT-maquette, both the emission and excitation spectra lie between the unbound P2d and bound P2d as seen with GL-maquette. This can be explained with the absorbance results previously showing that P2d is more stable with GL-maquette than it is with BT-maquette, indicating that the binding is weaker with the latter. As the concentrations is lower in the emission and excitation measurements compared to the absorbance (although ratios remain unchanged), results indicate that the interactions between P2d and BT-maquette are also concentration dependent, with the forces involved being too weak to induce interaction when concentrations of P2d are low.

Resonance Raman spectroscopy was used to further analyse the interactions between maquettes and zinc porphyrins. Porphyrin vibrational modes are known to show considerable sensitivity to the environment, whether in regards to planarity, metal oxidation state/spin or the presence of an axillary moiety [7-10, 29]. Resonance Raman results show distinct spectroscopic changes for a number of bands when zinc porphyrins were in the presence of either maquette compared to free in solution. These spectral changes are a result of the immediate environment of the porphyrin changing, through binding to the maquettes, likely through the ligation of the central zinc to the histidine residue of the maquette. The bands obtained from resonance Raman spectroscopy is correspondent to the vibrational energy levels of specific bonds within the molecule. These vibrational energy levels ( $\nu$ ) are able to be assigned, with vibrational modes and the corresponding bonds of zinc porphyrins well reported [14, 33-37]. The presence of either BT- or GL-maquette with porphyrins presented here distinctly changed the vibrational energies occurring at  $\sim 1350$  and  $1005\text{ cm}^{-1}$  (Figure III-44/45), which are directly correspondent to changes in the environment close to the porphyrin core [10].

Feitelson & Spiro have shown that low frequency ( $150\text{-}250\text{ cm}^{-1}$ ) resonance Raman data is strong evidence for the Zn-histidine stretch [38], however, within obtained data in the low frequency regions, determination of the highly informative Zn-histidine mode is unlikely due to the bands not being able to be resolved from the background (Figure III-43).

#### 4- Conclusions; Maquette-Porphyrin Binding in Solution

The results give evidence for the factors and forces contributing to cofactor binding to maquettes. Maquettes are intentionally designed to induce hydrophobic partitioning of cofactors, with histidine residues specifically located to ligate to metals of cofactors. Ligation to histidine residues within maquettes by a central iron of a porphyrin occurs with a dissociation constant in the nanomolar range, indicative of strong binding between cofactor and maquette [39]. Furthermore, the zinc present within zinc chlorins have similarly been demonstrated to bind with maquettes via axial ligation to the histidine residues [4, 40]. The results presented here indicate a zinc porphyrin readily ligates to the histidine residues within the two maquettes presented here. This is evident through the resonance Raman and binding titrations, showing a porphyrin to maquette ratio of 2:1, indicating that each histidine present can ligate one zinc porphyrin.

The literature for maquette-porphyrin hydrophobic partitioning has focused on implementing maquettes void of histidine, often substituted with alanine [3]. This allows for the situation whereby the cofactor containing a metal (often iron or zinc) can be analysed for interaction with maquettes without potential for axial ligation [41]. Shifts in absorbance of cofactors to histidine-free maquettes are attributed to hydrophobic interactions. Conversely, we can remove potential axial ligation through removal of the metal from cofactors, whilst keeping the maquette unchanged. Free-base porphyrins P2b-d were all shown to bind to both maquettes presented here, evident by the shift in the absorbance profiles in conjunction with the stability of a monomeric entity in bound state. This indicates strongly that the maquettes are capable of associating amphiphilic cofactors via hydrophobic partitioning. This trend is further observed for all amphiphilic zinc porphyrins (Figure III-46). The mostly hydrophobic zinc porphyrins (P1a, P3a, and P4a) were all shown to slowly ligate in a monomeric state, stabilising the porphyrin through this interaction. The free-base version (P2a) however, did not show any signs of hydrophobic partitioning in a monomeric state, whereby P2b-d displayed hydrophobic partitioning. This gives evidence that hydrophobic partitioning facilitates incorporation of cofactors to maquettes, but the specific metallic ligation to histidine residues is needed for increasing binding strengths to overcome aggregation tendencies. However, if the zinc porphyrin is too hydrophilic (as shown by the tetra-substituted porphyrins), the porphyrin will remain in the aqueous buffer as opposed to ligating within the maquette. Furthermore, charges associated with the porphyrin and on the surface of the maquette are shown to influence ligation.

This is particularly apparent with the P1e and P2e, with the more positive maquette (GL-maquette) associating with both porphyrins, whereas the BT-maquette shows no interaction (Figure III-47). Further to this, reversing the charges of the substituent facilitates interaction with the BT-maquette, with minimal interaction with GL-maquette. This is likely due to the GL-maquette having two helices over-all negative, which can facilitate interaction in a similar mode to the BT-maquette.

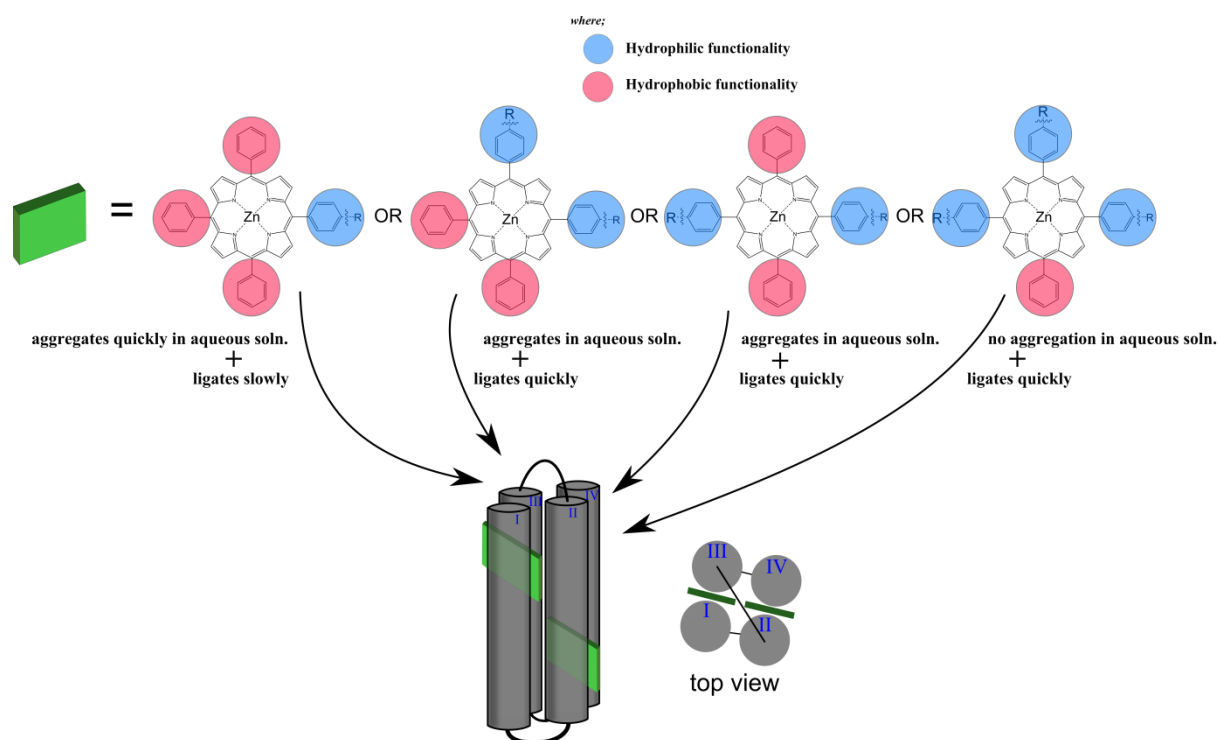


**Figure III-47; Hydrophilicity/hydrophobicity dependencies of zinc based porphyrins for ligation to maquettes.** The tendency for hydrophobic porphyrins to aggregate in aqueous solution results in slow ligation into maquettes, whereby more hydrophilic porphyrins leads to stability in aqueous solvents allowing for quickened interactions.

The results presented here give empirical evidence for the factors that contribute to porphyrins interacting and binding into maquettes. The amphiphilic nature of the cofactor, in this case a porphyrin, is essential, whereby a porphyrin too hydrophilic reduces potential partitioning into the hydrophobic core of the maquette. In contrast, a porphyrin too hydrophobic will invariably aggregate quickly in an aqueous solution, which significantly inhibits binding to maquettes. Further, the maquette is to be likened to a micelle, whereby the binding of a hydrophobic porphyrin (or cofactor) can indeed keep the porphyrin monomeric and stabilised in an aqueous solution. The ligation of zinc porphyrins to maquettes can be directed by the ligation to histidine residues located within the maquette, with the binding significantly altering

the electronic state of the porphyrin, resulting in red-shifting of the absorbance and emissions spectra, typically by 10-12 nm. Therefore, the ligation of zinc porphyrins to maquettes can be evaluated via this shift in the Soret and Q-bands.

Helix Number	Overall Charge	BT-Maquette Sequence				Loop-Region	
I	-4	G	EIWKQHE	DALQKFE	EALNQFE	DLKQL	GGSGSGSGG
II	-4		EIWKQAE	DALQKFE	EALNQFE	DLKQL	GGSGSGSGG
III	-4		EIWKQAE	DALQKFE	EALNQFE	DLKQL	GGSGSGSGG
IV	-4		EIWKQHE	DALQKFE	EALNQFE	DLKQL	
Helix Number	Overall Charge	GL-Maquette Sequence				Loop-Region	
I	-4	G	EIWKQHE	DALQKFE	EALNQFE	DLKQL	GGSGSGSGG
II	+2		EIKQRAE	DALRKFE	EALKRFE	DKKQK	GGSGSGSGG
III	-4		EIWKQAE	DALQKFE	EALNQFE	DLKQL	GGSGSGSGG
IV	+2		EIKQRHE	DALRKFE	EALKRFE	DKKQK	

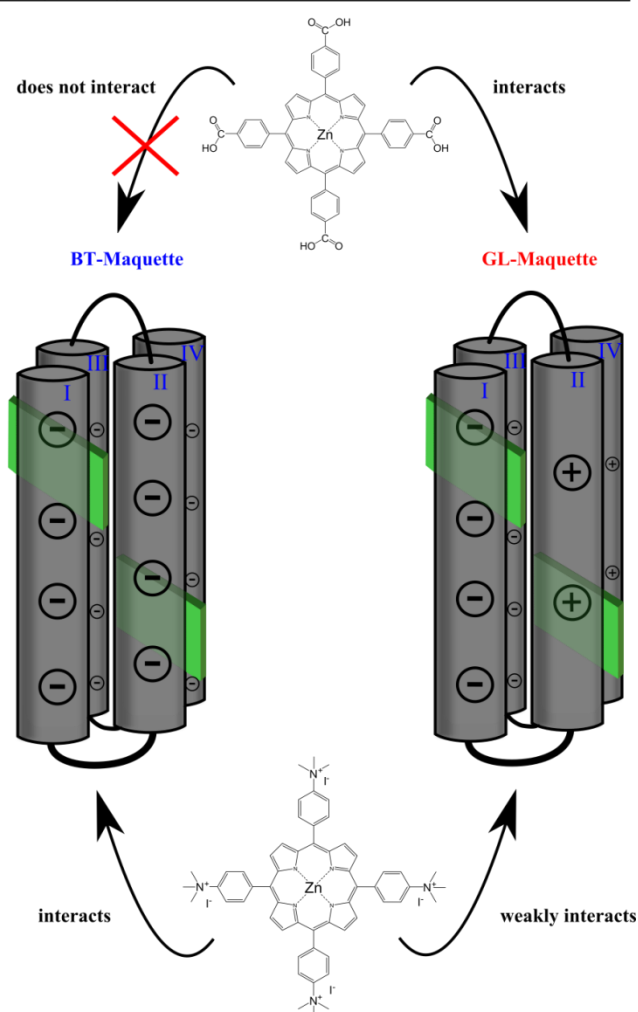


**Figure III-48; Electrostatic interactions facilitating ligation to maquettes.** BT- and GL-maquettes, which contain differing surface charges, either facilitates the hydrophilic zinc porphyrin to ligate, or weakly interacts, depending on the opposing charges associated with the cofactor.

## 5- References; Maquette-Porphyrin Binding in Solution

1. Shifman JM, Moser CC, Kalsbeck WA, Bocian DF, Dutton PL: **Functionalized de Novo Designed Proteins: Mechanism of Proton Coupling to Oxidation/Reduction in Heme Protein Maquettes.** *Biochemistry* 1998, **37**(47):16815-16827.
2. Sharp RE, Moser CC, Rabanal F, Dutton PL: **Design, synthesis, and characterization of a photoactivatable flavocytochrome molecular maquette.** *Proceedings of the National Academy of Sciences* 1998, **95**(18):10465-10470.
3. Gibney BR, Dutton PL: **Histidine placement in de novo–designed heme proteins.** *PRS* 1999, **8**(09):1888-1898.
4. Razeghifard MR, Wydrzynski T: **Binding of Zn–Chlorin to a Synthetic Four-Helix Bundle Peptide through Histidine Ligation.** *Biochemistry* 2003, **42**(4):1024-1030.
5. Huang SS, Koder RL, Lewis M, Wand AJ, Dutton PL: **The HP-1 maquette: From an apoprotein structure to a structured hemoprotein designed to promote redox-coupled proton exchange.** *Proceedings of the National Academy of Sciences of the United States of America* 2004, **101**(15):5536-5541.
6. Roach N: **Synthesis of Amphiphilic Porphyrins and Porphyrin Arrays.** *PhD Thesis.* University of Wollongong; 2016.
7. Spiro TG, Stong JD, Stein P: **Porphyrin core expansion and doming in heme proteins. New evidence from resonance Raman spectra of six-coordinate high-spin iron(III) hemes.** *Journal of the American Chemical Society* 1979, **101**(10):2648-2655.
8. Spiro TG, Streckas TC: **Resonance Raman spectra of heme proteins. Effects of oxidation and spin state.** *Journal of the American Chemical Society* 1974, **96**(2):338-345.
9. Shelnut JA, Alston K, Ho JY, Yu NT, Yamamoto T, Rifkind JM: **Four- and five-coordinate species in nickel-reconstituted hemoglobin and myoglobin: Raman**

- identification of the nickel-histidine stretching mode.** *Biochemistry* 1986, **25**(3):620-627.
10. Shelnutt JA, Medforth CJ, Berber MD, Barkigia KM, Smith KM: **Relationships between structural parameters and Raman frequencies for some planar and nonplanar nickel(II) porphyrins.** *Journal of the American Chemical Society* 1991, **113**(11):4077-4087.
  11. Olmstead WN, Bordwell FG: **Ion-pair association constants in dimethyl sulfoxide.** *The Journal of Organic Chemistry* 1980, **45**(16):3299-3305.
  12. Sander JKM, Bampos N, Clyde-Watson Z, Darling SL, Hawley JC, Kim H-JM, Chi Ching , Webb SJ: **Axial Coordination Chemistry of Metalloporphyrins.** In: *The Porphyrin Handbook*. Edited by Kadish KM, Van Caemelbecke E, Royal G, vol. 3. San Diego: Academic Press; 2000.
  13. Campbell WM, Jolley KW, Wagner P, Wagner K, Walsh PJ, Gordon KC, Schmidt-Mende L, Nazeeruddin MK, Wang Q, Grätzel M *et al*: **Highly Efficient Porphyrin Sensitizers for Dye-Sensitized Solar Cells.** *The Journal of Physical Chemistry C* 2007, **111**(32):11760-11762.
  14. Wang Q, Campbell WM, Bonfantani EE, Jolley KW, Officer DL, Walsh PJ, Gordon K, Humphry-Baker R, Nazeeruddin MK, Grätzel M: **Efficient light harvesting by using green Zn-porphyrin-sensitized nanocrystalline TiO<sub>2</sub> films.** *The Journal of Physical Chemistry B* 2005, **109**(32):15397-15409.
  15. Bacarella AL, Grunwald E, Marshall HP, Purlee EL: **The potentiometric measurement of acid dissociation constants and pH in the system methanol-water, pK<sub>a</sub> values for carboxylic acids and anilinium ions.** *The Journal of Organic Chemistry* 1955, **20**(6):747-762.
  16. Avdeef A, Comer JEA, Thomson SJ: **pH-Metric log P. 3. Glass electrode calibration in methanol-water, applied to pK<sub>a</sub> determination of water-insoluble substances.** *Analytical Chemistry* 1993, **65**(1):42-49.

17. Kano K, Fukuda K, Wakami H, Nishiyabu R, Pasternack RF: **Factors Influencing Self-Aggregation Tendencies of Cationic Porphyrins in Aqueous Solution.** *Journal of the American Chemical Society* 2000, **122**(31):7494-7502.
18. Maiti NC, Mazumdar S, Periasamy N: **J- and H-Aggregates of Porphyrin–Surfactant Complexes: Time-Resolved Fluorescence and Other Spectroscopic Studies.** *The Journal of Physical Chemistry B* 1998, **102**(9):1528-1538.
19. Azumi R, Matsumoto M, Kawabata Y, Kuroda S, Sugi M, King LG, Crossley MJ: **Orientation change of porphyrin in Langmuir-Blodgett films caused by a trigger molecule.** *The Journal of Physical Chemistry* 1993, **97**(49):12862-12869.
20. Schick GA, Schreiman IC, Wagner RW, Lindsey JS, Bocian DF: **Spectroscopic characterization of porphyrin monolayer assemblies.** *Journal of the American Chemical Society* 1989, **111**(4):1344-1350.
21. Shibata Y, Tateishi S, Nakabayashi S, Itoh S, Tamiaki H: **Intensity Borrowing via Excitonic Couplings among Soret and Qy Transitions of Bacteriochlorophylls in the Pigment Aggregates of Chlorosomes, the Light-Harvesting Antennae of Green Sulfur Bacteria.** *Biochemistry* 2010, **49**(35):7504-7515.
22. Kano H, Kobayashi T: **Time-resolved fluorescence and absorption spectroscopies of porphyrin J-aggregates.** *Journal of Chemical Physics* 2002, **116**(1):184-195.
23. Kadish KM, Maiya BG, Araullo-McAdams C: **Spectroscopic characterization of meso-tetrakis(1-methylpyridinium-4-yl)porphyrins, [(TMpyP)H<sub>2</sub>]<sup>4+</sup> and [(TMpyP)M]<sup>4+</sup>, in aqueous micellar media, where M = VO<sub>2</sub><sup>+</sup>, Cu(II), and Zn(II).** *The Journal of Physical Chemistry* 1991, **95**(1):427-431.
24. Kadish KM, Maiya G, Araullo C, Guillard R: **Micellar effects on the aggregation of tetraanionic porphyrins. Spectroscopic characterization of free-base meso-tetrakis (4-sulfonatophenyl) porphyrin,(TPPS) H<sub>2</sub>, and (TPPS) M (M= zinc (II), copper (II), and vanadyl) in aqueous micellar media.** *Inorganic Chemistry* 1989, **28**(14):2725-2731.



25. Sharp RE, Diers JR, Bocian DF, Dutton PL: **Differential binding of iron (III) and zinc (II) protoporphyrin IX to synthetic four-helix bundles.** *Journal of the American Chemical Society* 1998, **120**(28):7103-7104.
26. Anderson JLR, Armstrong CT, Kodali G, Lichtenstein BR, Watkins DW, Mancini JA, Boyle AL, Farid TA, Crump MP, Moser CC *et al*: **Constructing a man-made c-type cytochrome maquette in vivo: electron transfer, oxygen transport and conversion to a photoactive light harvesting maquette().** *Chemical science (Royal Society of Chemistry : 2010)* 2014, **5**(2):507-514.
27. Grosset AM, Gibney BR, Rabanal F, Moser CC, Dutton PL: **Proof of Principle in a De novo Designed Protein Maquette: An Allosterically Regulated, Charge-Activated Conformational Switch in a Tetra- $\alpha$ -Helix Bundle.** *Biochemistry* 2001, **40**(18):5474-5487.
28. Hecht MH, Vogel KM, Spiro TG, Rojas NRL, Kamtekar S, Simons CT, McLean JE, Farid RS: **De novo heme proteins from designed combinatorial libraries.** *Protein Science* 1997, **6**(12):2512-2524.
29. Zhang Y-H, Zhao W, Jiang P, Zhang L-J, Zhang T, Wang J: **Structural parameters and vibrational spectra of a series of zinc meso-phenylporphyrins: A DFT and experimental study.** *Spectrochimica Acta Part A: Molecular and Biomolecular Spectroscopy* 2010, **75**(2):880-890.
30. Nappa M, Valentine JS: **The influence of axial ligands on metalloporphyrin visible absorption spectra. Complexes of tetraphenylporphinatozinc.** *Journal of the American Chemical Society* 1978, **100**(16):5075-5080.
31. Barnett GH, Hudson MF, Smith KM: **Concerning meso-tetraphenylporphyrin purification.** *Journal of the Chemical Society, Perkin Transactions 1* 1975(14):1401-1403.
32. Kodali G, Mancini JA, Solomon LA, Episova TV, Roach N, Hobbs CJ, Wagner P, Mass OA, Aravindu K, Barnsley JE *et al*: **Design and engineering of water-soluble light-harvesting protein maquettes.** *Chemical Science* 2016.

33. Atamian M, Donohoe RJ, Lindsey JS, Bocian DF: **Resonance Raman spectra and normal-coordinate analysis of reduced porphyrins. 1. Zinc (II) tetraphenylporphyrin anion.** *The Journal of Physical Chemistry* 1989, **93**(6):2236-2243.
34. Walsh PJ, Gordon KC, Officer DL, Campbell WM: **A DFT study of the optical properties of substituted Zn(II)TPP complexes.** *Journal of Molecular Structure: THEOCHEM* 2006, **759**(1-3):17-24.
35. Parthasarathi N, Hansen C, Yamaguchi S, Spiro T: **Metalloporphyrin core size resonance Raman marker bands revisited: implications for the interpretation of hemoglobin photoproduct Raman frequencies.** *Journal of the American Chemical Society* 1987, **109**(13):3865-3871.
36. Walters VA, De Paula JC, Babcock GT, Leroi GE: **Resonance Raman spectrum of the lowest triplet state of zinc (II) tetraphenylporphyrin.** *Journal of the American Chemical Society* 1989, **111**(21):8300-8302.
37. Walsh PJ, Gordon KC, Wagner P, Officer DL: **Resonance Raman Studies of  $\beta$ -Substituted Porphyrin Systems with Unusual Electronic Absorption Properties.** *ChemPhysChem* 2006, **7**(11):2358-2365.
38. Feitelson J, Spiro TG: **Bonding in zinc proto- and mesoporphyrin substituted myoglobin and model compounds studied by resonance Raman spectroscopy.** *Inorganic Chemistry* 1986, **25**(6):861-865.
39. Choma CT, Lear JD, Nelson MJ, Dutton PL, Robertson DE, DeGrado WF: **Design of a heme-binding four-helix bundle.** *Journal of the American Chemical Society* 1994, **116**(3):856-865.
40. Mennenga A, Gartner W, Lubitz W, Gerner H: **Effects of noncovalently bound quinones on the ground and triplet states of zinc chlorins in solution and bound to de novo synthesized peptides.** *Physical Chemistry Chemical Physics* 2006, **8**(46):5444-5453.

41. Farid TA, Kodali G, Solomon LA, Lichtenstein BR, Sheehan MM, Fry BA, Bialas C, Ennist NM, Siedlecki JA, Zhao Z *et al*: **Elementary tetrahelical protein design for diverse oxidoreductase functions**. *Nature Chemical Biology* 2013, **9**(12):826-833.

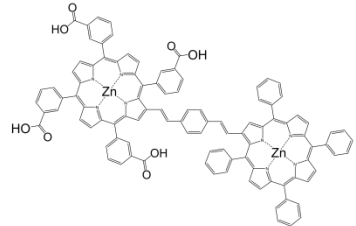
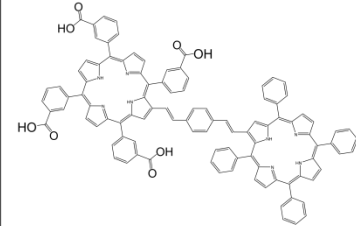
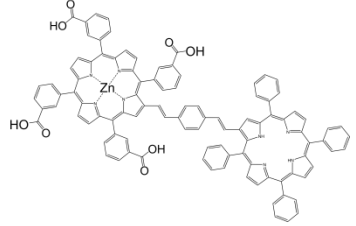
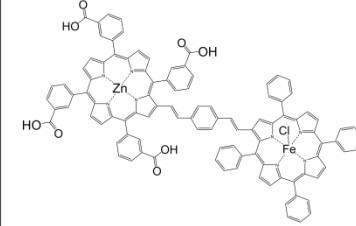
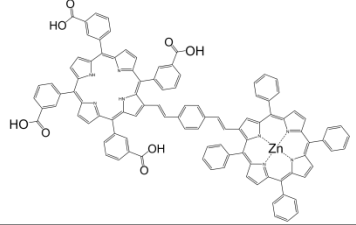
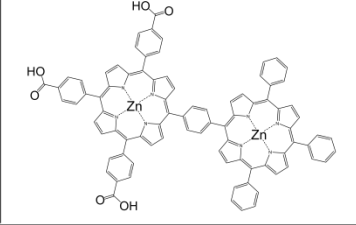
# **Chapter IV**

## **Dyad Porphyrins and Maquettes in Solution**

## 1- Introduction; Dyad Porphyrins and Maquettes in Solution

With maquettes shown previously to incorporate porphyrins based on a combination of ligation and hydrophobic partitioning (Chapter III), dyads were designed (in house) to contain a hydrophobic and a hydrophilic portion (Figure VII-3) [1, 2] for maquette binding. Dyads can potentially be used to increase light-harvesting capabilities through capturing a broader section of incident sunlight wavelengths (with the dyad typically having a broadened absorbance spectrum compared to monomeric porphyrin), with each porphyrin in an ‘array’ able to contribute to electron flow in a device [3].

The dyads used within this study are outlined in Figure IV-1, with free-base designs used to determine hydrophobic partitioning effects. The dyads (D1-6) would be expected to partition through hydrophobic forces, as was shown previously for the monomeric porphyrins (P1a, P3a, P4a), with the hydrophilic portion of the dyad being expected to remain outside of the maquette, as illustrated in Figure IV-2.

Porphyrin	Structure	Porphyrin	Structure
D1		D4	
D2		D5	
D3		D6	

**Figure IV-1; The structure of dyads D1-D6, designed for amphiphilicity.** The design of dyads was chosen to contain hydrophobic and hydrophilic portions for potential interaction with maquettes.

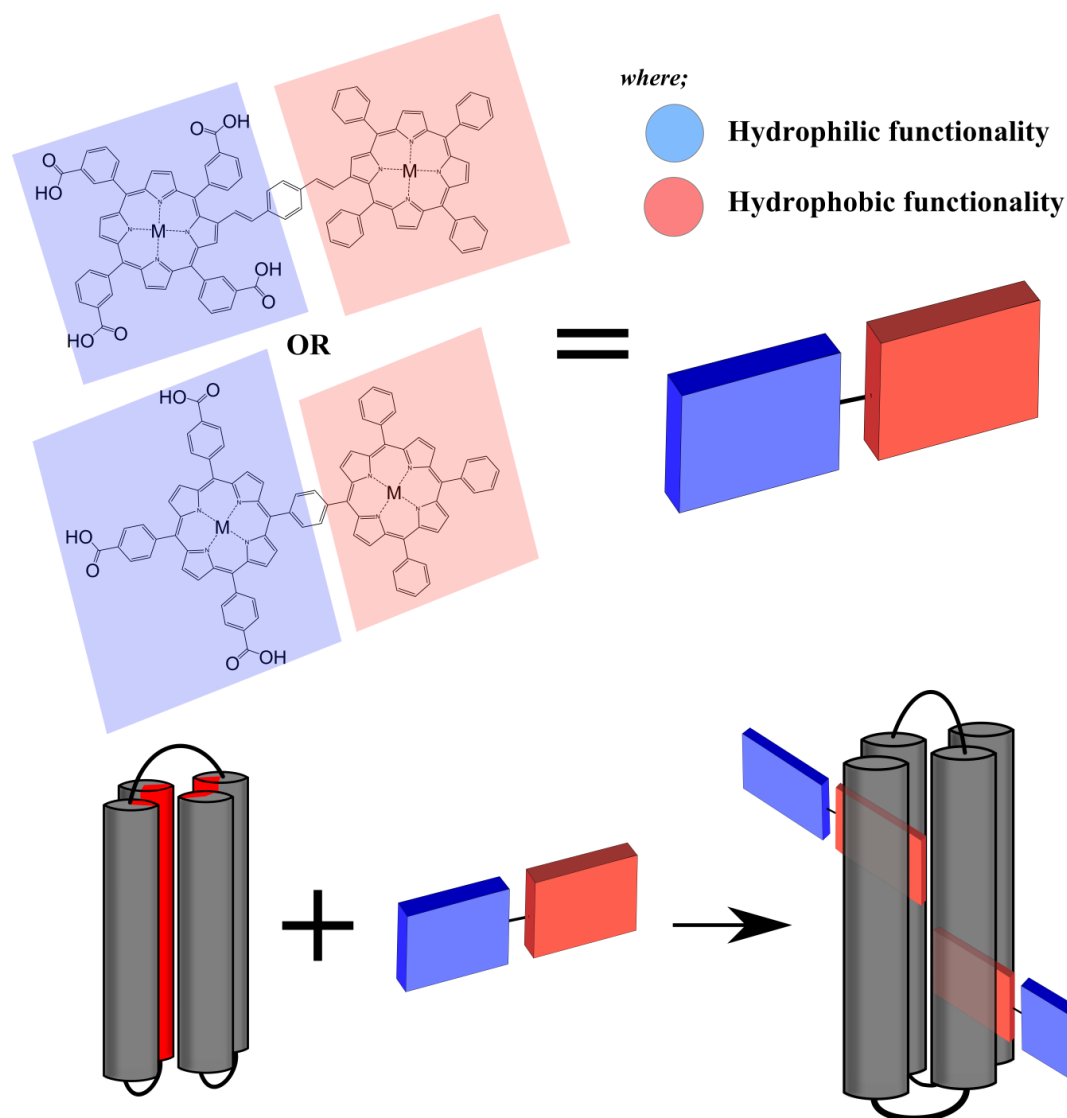


**Figure IV-2; Proposed dyad binding into maquettes.** The design of dyads was chosen to exploit potential ligation and hydrophobic partitioning into the hydrophobic core of maquettes.

The two dyad designs shown in Figure VI-1 display either conjugated dyads (D1-5) or a non-conjugated form (D6). This conjugation (or non-conjugation) would be expected to result in distinct differences in absorbance profiles. The conjugation of dyads (such as that for D1-5) would result in a broadening of the Soret peak and distortion of the Q-bands (Figure IV-3) [4]. In comparison, non-conjugated dyads result in a splitting of the Soret peak, which only increases in intensity (and Q-band intensity) with additional ‘monomers’ (Figure IV-3) [4]. The Soret splitting is due to Frankel excitons, with no electronic interaction between the adjacent chromophores, unlike that for the conjugated dyads [4].

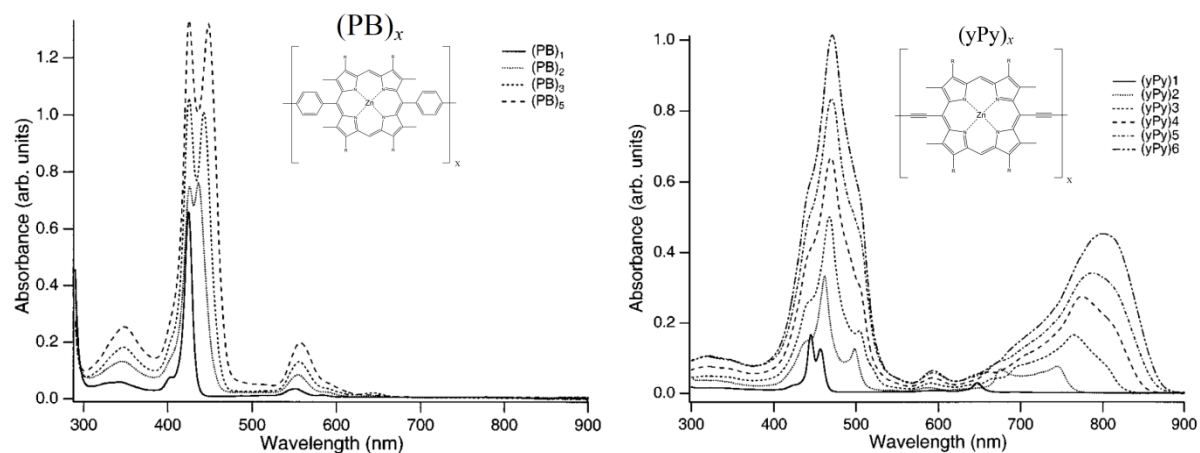


**Figure IV-3; Absorbance of non-conjugated and conjugated zinc oligomers.** The change in absorbance profiles due to additions of chromophore entities in non-conjugated (left) or conjugated (right) oligomers. Reproduced from [4].

Within this chapter the dyads were explored in context of ligation within maquettes, with the potential for dyads to increase the absorbance incident wavelengths compared to monomeric porphyrins. As was evident with monomeric porphyrins from Chapter III, absorbance changes would indicate dyad-maquette interactions, with the free-base versions further giving evidence for hydrophobic interactions. No interaction between dyads and maquettes has been previously reported.

## 2- Results; Dyad Porphyrins and Maquettes in Solution

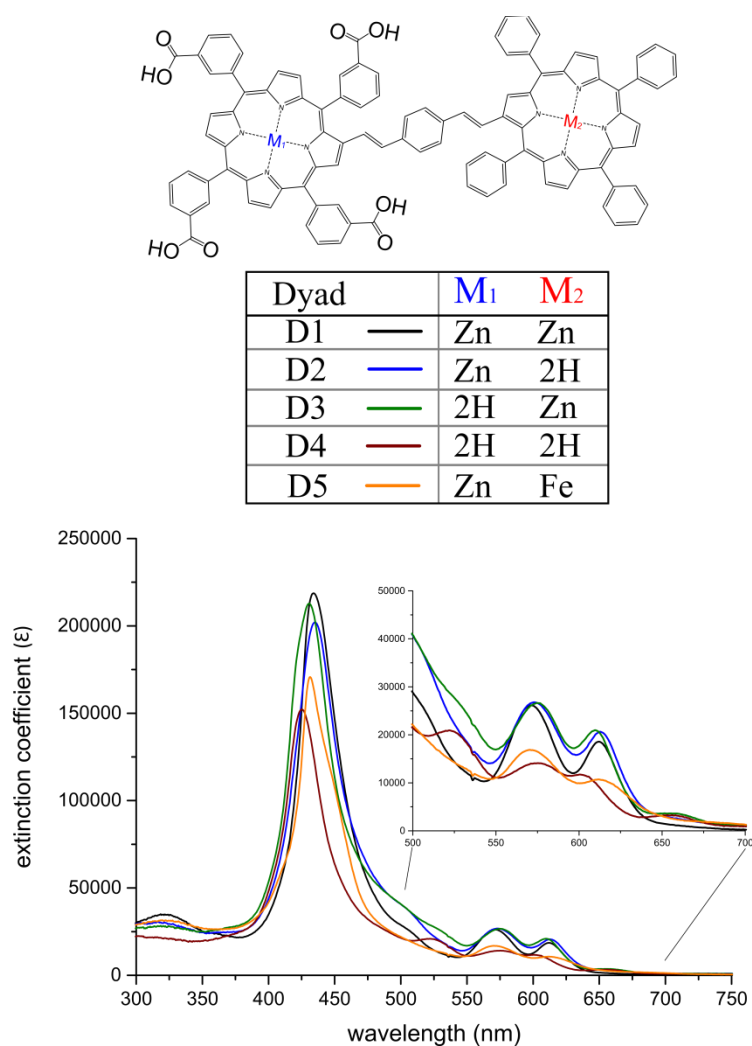
### 2.1- Conjugated dyads in DMSO

Dyads are promising materials for incorporation into light-harvesting applications, such as DSSCs, as they often absorb an increased spectrum of light compared to monomeric porphyrins. Therefore, this increase in absorbance could potentially be translated to more available light being turned into usable energy, with the enhancement of solar-to-electrical energy efficiencies by dyads and arrays theoretically demonstrated [5]. Furthermore, the application of dyads in DSSC constructs has been experimentally demonstrated, with each porphyrin present in the dyad contributing to current generation [3]. The use of dyads and larger porphyrin arrays could potentially be employed with maquettes, with the maquette ligating to the metallic centre of one of the porphyrin moieties. Dyads 1-5 (D1-D5), as shown in Figure IV-4, are covalently linked, with the absorbance profile expected to be broadened [4].

As evident with the monomeric porphyrins presented in previously Chapter III, dyads presented here are expected to be in a non-aggregated state in DMSO. The absorbance profiles of the conjugated dyads (D1-D5) were therefore measured in DMSO (Figure IV-4). As was expected with a conjugated dyad, all dyads produced an absorbance profile with Soret peak broadening compared to monomeric zinc and free-base porphyrins [4].

Interestingly, an iron porphyrin typically displays a highly broadened Soret peak compared to a zinc porphyrin [6]. However, the incorporation of iron into one of the porphyrin centres in the dyads presented (D5) does not significantly broaden the Soret peak compared to dyads consisting of zinc or free-base entities (Figure IV-4). Despite this, it is apparent that the Soret peak is not highly symmetrical like the dyads D1-D4, with D5 displaying a distinct broad shoulder at ~450 nm.





Porphyrin	Soret peak (nm)	Q-bands (nm)
<b>D1</b>	434	571, 612
<b>D2</b>	435.5	574, 613
<b>D3</b>	430	575.5, 610
<b>D4</b>	425	524, 576, 603, 658
<b>D5</b>	431.5	571, 613

**Figure IV-4; UV-vis. absorption data for conjugated dyads with different metal insertions.** The structure of the conjugated dyad used for various metal insertions (top), with the resulting absorbance profiles of each dyad in DMSO shown (middle). The tabulated Soret peak and Q-band positions of each dyad is shown (bottom).

## 2.2- Conjugated dyads binding to maquettes

Conjugated dyads were explored in the context of their ligation into maquettes. The more hydrophilic porphyrin in the dyad construct contains tetra-carboxylic substituent groups, previously shown to not interact with the BT-maquette (Chapter III). Therefore, it is expected that any interaction with the BT-maquette would occur through ligation to the hydrophobic porphyrin of the dyad.

Investigation into dyad binding with maquettes was undertaken in an identical manner as was done previously with the monomeric porphyrin (Chapter III). The absorbance of dyads was first analysed in aqueous buffer, with the absorbance measured every 30 min for 18 h. In direct comparison, the dyad was analysed in aqueous buffer with an excess of either BT- or GL-maquette present, with the absorbance measured every 30 min for 18 h. Therefore, the stabilities in aqueous buffer, along with any aggregative tendencies or potential interactions with either of maquette can be assessed.

As shown in Figure IV-5a, D1 contains two zinc porphyrins, with potential ligations with either BT- or GL-maquette explored. Figure IV-5b indicates that D1 aggregates and precipitates out of an aqueous buffer, as was shown previously with the hydrophobic monomeric porphyrins in Chapter III, evident by the absorbance profile diminishing in intensity over time. When the dyad is in aqueous buffer with either BT- (Figure IV-5c) or GL-maquette (Figure IV-5d), the absorbance increases in intensity slightly over time, with red-shifts in the Soret peak and Q-band positions when compared to D1 in aqueous buffer (Figure IV-5e). As was shown previously for monomeric porphyrins, this red-shifting is indicative of ligation to the maquette. The GL-maquette induced a larger red-shift in the Soret peak position than the BT-maquette, however, displays a more 'rounded' peak. As the GL-maquette was shown to interact with a tetra-carboxyl porphyrin (Chapter III), it is likely that the more hydrophilic porphyrin within D1 could interact with the GL-maquette. In contrast, the BT-maquette would only be expected to interact with the more hydrophobic porphyrin in D1, predominantly through hydrophobic partitioning and subsequent ligation.

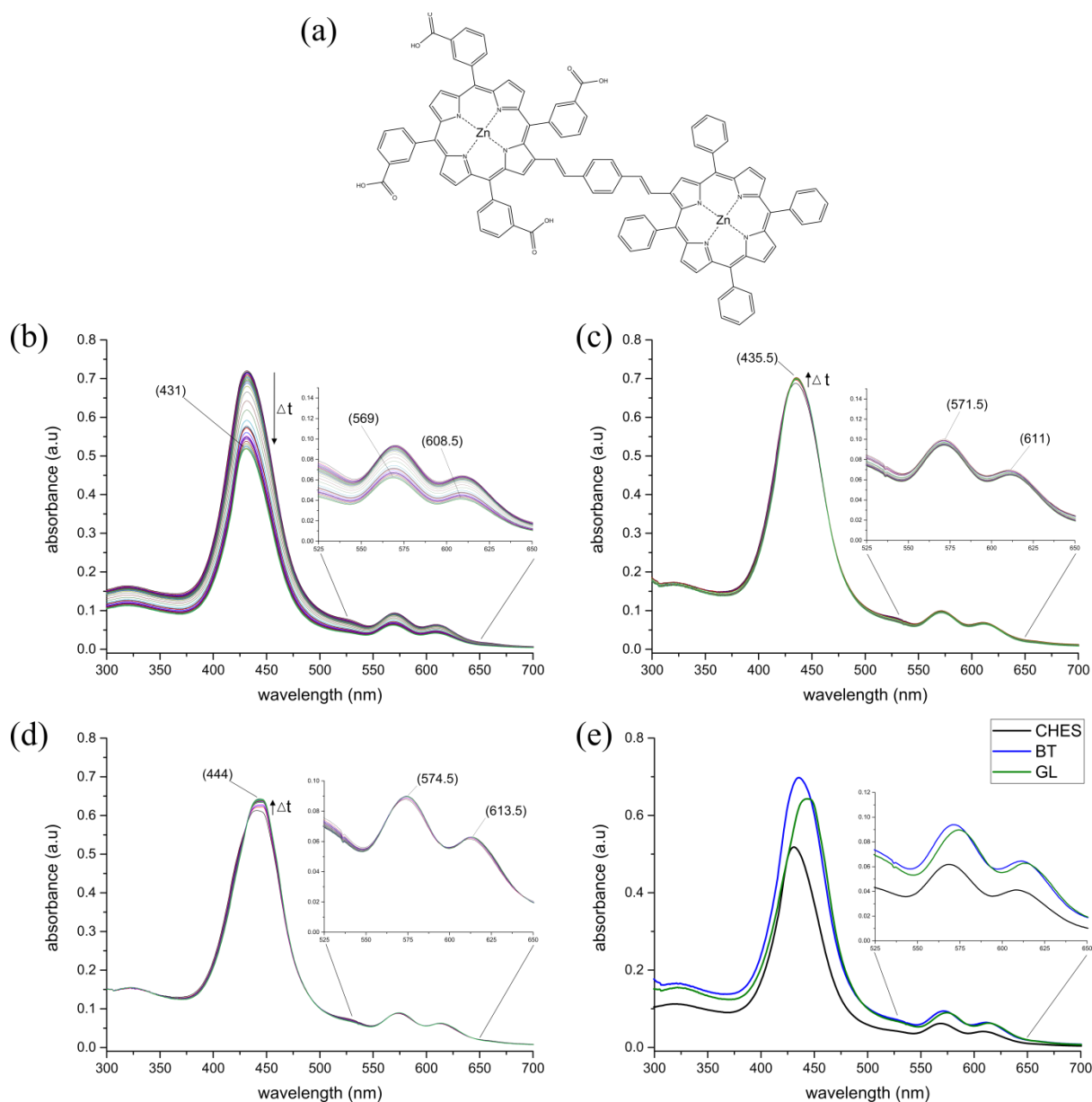


**Figure IV-5; UV-vis. absorption spectral characterisation of D1 in aqueous buffer with maquette.** (a) Structure of D1. (b) D1 in aqueous buffer; measured every 30 min for 18 h. (c) D1 and BT-maquette in aqueous buffer; measured every 30 min for 18 h. (d) D1 and GL-maquette in aqueous buffer; measured every 30 min for 18 h. (e) Absorption of D1 in aqueous buffer after 18 h (black), with BT-maquette (blue), and with GL-maquette (green).

To further gain insight into potential ligations and modes of binding of dyads with maquettes, free-base versions of the conjugated dyad construct were explored. As shown in Figure IV-6a, D1 contains a hydrophilic zinc porphyrin connected to a hydrophobic free-base porphyrin, with potential interactions with either BT- or GL-maquette explored. It is expected that the hydrophobic porphyrin would interact weakly with the maquettes through hydrophobic partitioning, with this interaction shown to induce red-shifts in the monomeric free-base porphyrins (Chapter III). As was shown with D1, Figure IV-6b indicates that D2 aggregates

and precipitates out of an aqueous buffer. When the dyad is in aqueous buffer with either BT- (Figure IV-6c) or GL-maquette (Figure IV-6d), the absorbance spectra shown to be stable over time, with slight red-shifts in the Soret peak and Q-band positions when compared to D2 in aqueous buffer (Figure IV-6e). As was the case with D1, the GL-maquette induces a larger red-shifting in the Soret peak, likely due to the capability of the more hydrophilic porphyrin to interact with the maquette. However, it can be assumed that BT-maquette only interacts with the more hydrophobic porphyrin via hydrophobic partitioning, inducing a red-shift of 4-5 nm and hindering aggregation.

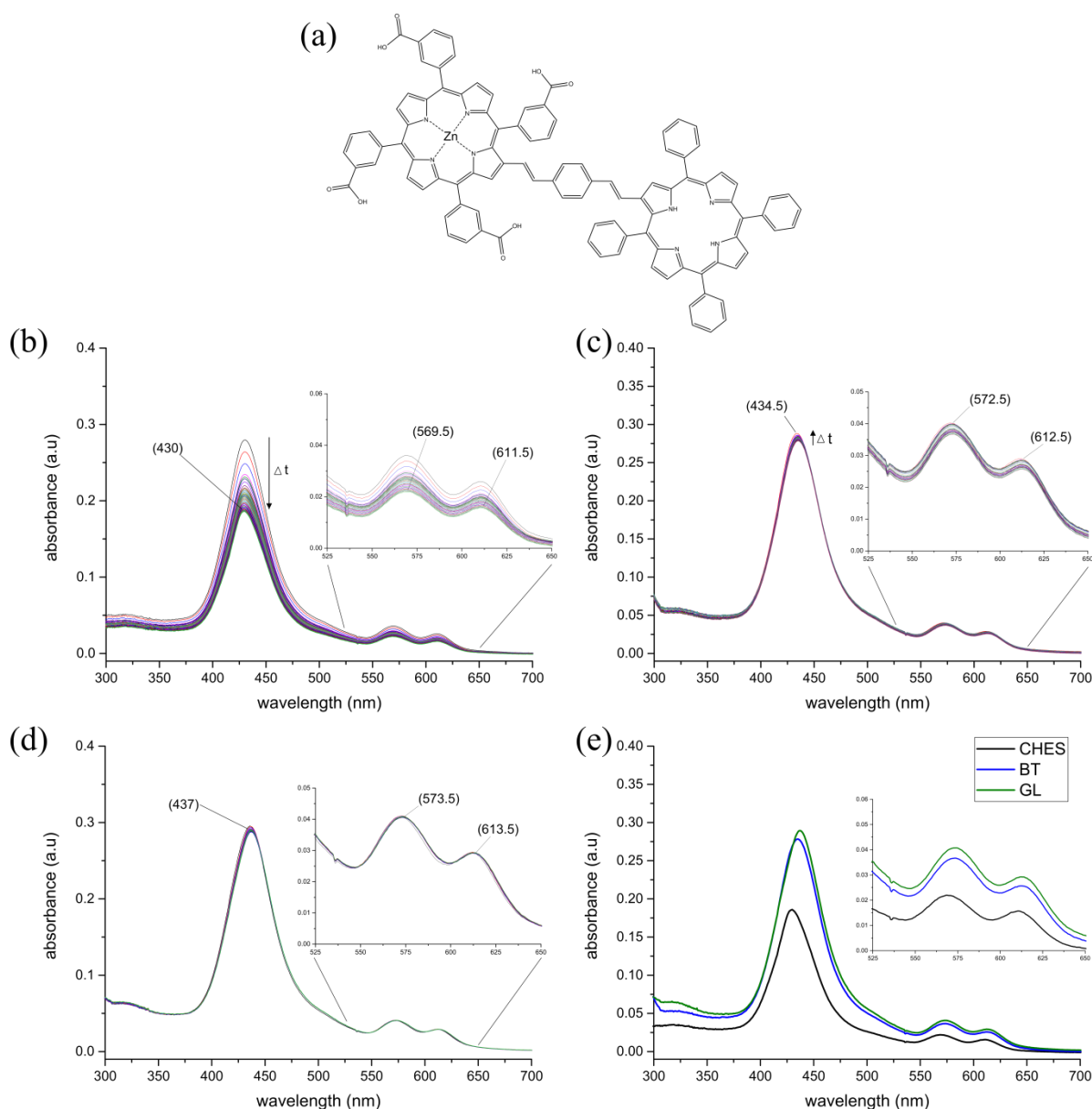


**Figure IV-6; UV-vis. absorption spectral characterisation of D2 in aqueous buffer with maquette.** (a) Structure of D2. (b) D2 in aqueous buffer; measured every 30 min for 18 h. (c) D2 and BT-maquette in aqueous buffer; measured every 30 min for 18 h. (d) D2 and GL-maquette in aqueous buffer; measured every 30 min for 18 h. (e) Absorption of D2 in aqueous buffer after 18 h (black), with BT-maquette (blue), and with GL-maquette (green).

In contrast to D2, D3 contains a hydrophilic free-base porphyrin connected to a hydrophobic zinc porphyrin (Figure IV-7a), with potential interactions with either BT- or GL-maquette explored. It is expected that the hydrophobic porphyrin would interact strongly with the maquettes through hydrophobic partitioning and zinc-ligation, whereby the free-base hydrophilic porphyrin would interact weakly (if not negligibly). As was shown with D2, Figure IV-7b indicates that D3 aggregates and precipitates out of the aqueous buffer. When the dyad is in aqueous buffer with either BT- (Figure IV-7c) or GL-maquette (Figure IV-7d), the absorbance spectra is shown to be more stable over time, with 8-9 nm red-shifts in the Soret peak positions when compared to D3 in aqueous buffer (Figure IV-7e). This stabilization and red-shifting is attributed to the hydrophobic zinc porphyrin of D3 ligating and partitioning with the maquettes. Furthermore, as it was shown previously that a free-base tetra-carboxylic porphyrin does not interact with the BT-maquette, it is highly likely that the zinc porphyrin of D3 is the only portion of the dyad interacting with the BT-maquette. In addition, with the absorbance profiles of D3 with BT-maquette being identical to that of D3 with GL-maquette, the hydrophobic partitioning and ligation of the zinc porphyrin in D3 to both maquettes can be assumed.

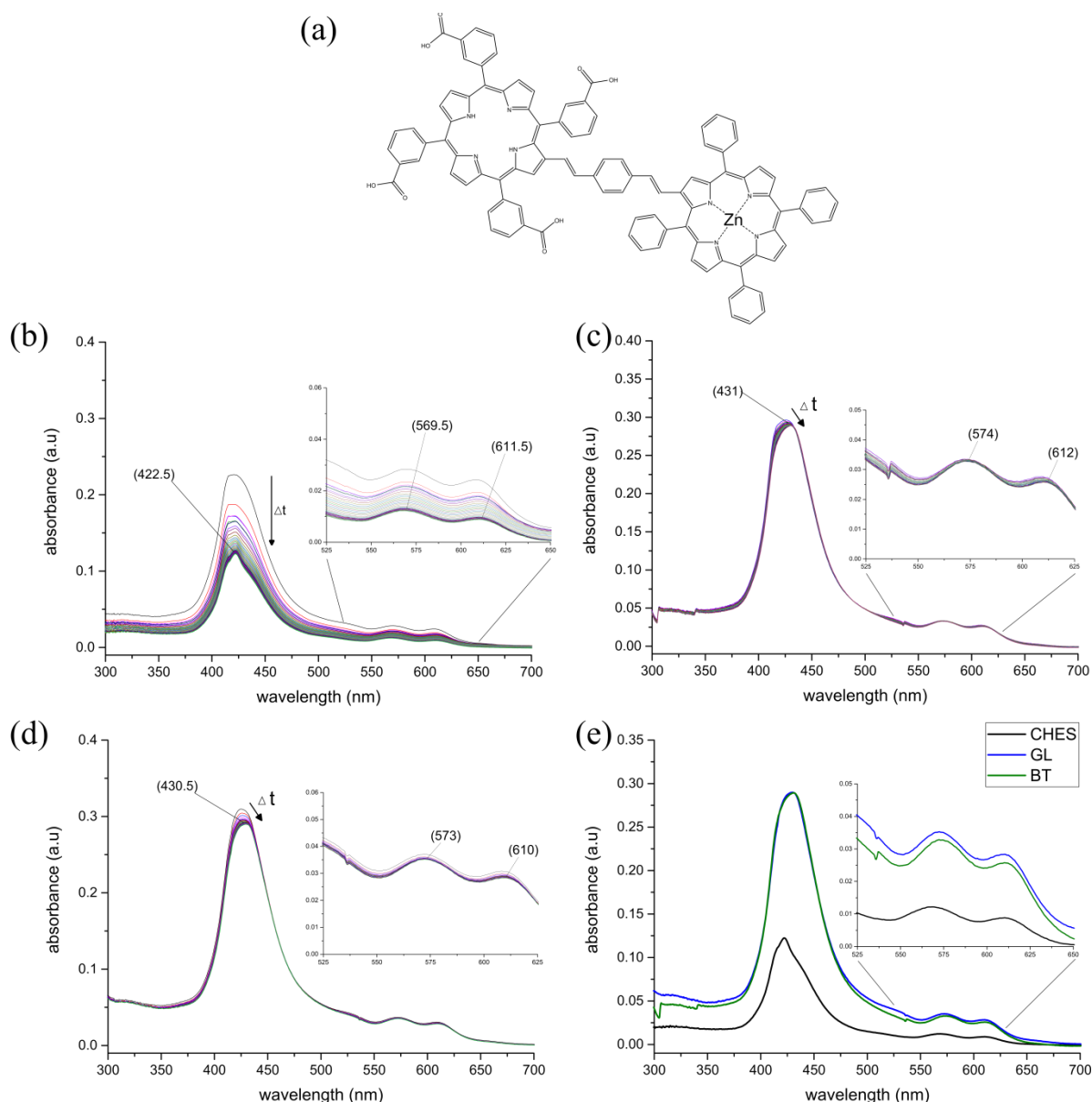


**Figure IV-7; UV-vis. absorption spectral characterisation of D3 in aqueous buffer with maquette.** (a) Structure of D3. (b) D3 in aqueous buffer; measured every 30 min for 18 h. (c) D3 and BT-maquette in aqueous buffer; measured every 30 min for 18 h. (d) D3 and GL-maquette in aqueous buffer; measured every 30 min for 18 h. (e) Absorption of D3 in aqueous buffer after 18 h (black), with BT-maquette (blue), and with GL-maquette (green).

To further explore the interactions of free-base entities of a conjugated dyad with maquettes, D4 was employed, containing a hydrophilic free-base porphyrin connected to a hydrophobic free-base porphyrin (Figure IV-8a). Any potential interactions with either BT- or GL-maquette were explored, with the hydrophilic porphyrin not expected to interact with the maquettes, but rather, the hydrophobic porphyrin potentially interacting via hydrophobic partitioning. As was shown for D1-3, D4 aggregates and precipitates in the aqueous buffer

(Figure IV-8b). When the D4 is in aqueous buffer with either BT- (Figure IV-8c) or GL- maquette (Figure IV-8d), the absorbance spectra is shown to be more stable over time, with no distinct shifts compared to D4 in aqueous buffer (Figure IV-8e). This stabilization is attributed to the hydrophobic partitioning of D4 into the maquette. Potential shifts in the absorbance spectra are notably absent, assumed to be due to the conjugated form of the dyad, whereby the hydrophobic partitioning of the hydrophobic part of the dyad does not significantly influence the electronic structure of the dyad and so does not influence the absorbance profile.

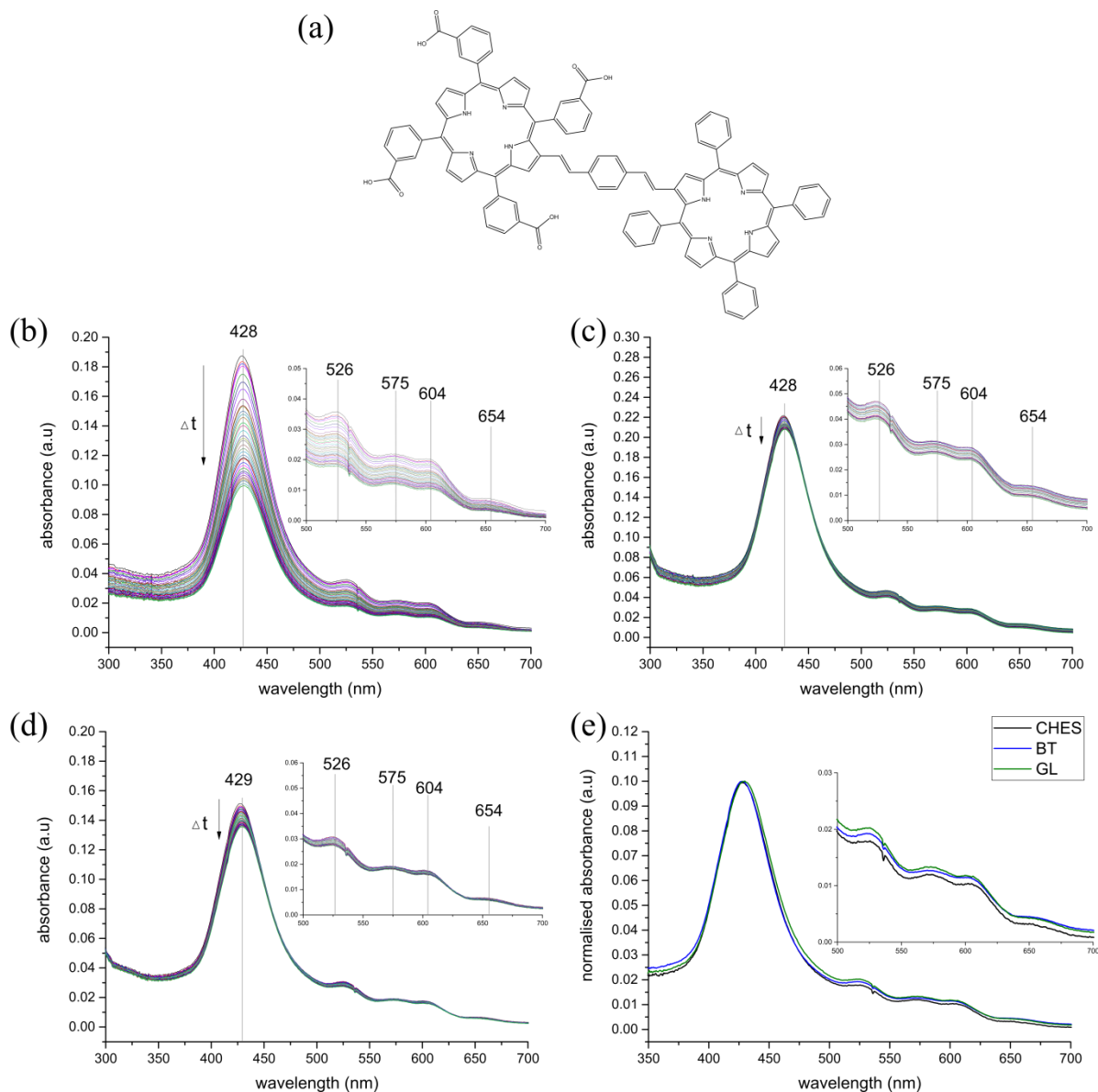


**Figure IV-8; UV-vis. absorption spectral characterisation of D4 in aqueous buffer with maquette.** (a) Structure of D4. (b) D4 in aqueous buffer; measured every 30 min for 18 h. (c) D4 and BT-maquette in aqueous buffer; measured every 30 min for 18 h. (d) D4 and GL-maquette in aqueous buffer; measured every 30 min for 18 h. (e) Normalised absorption of D4 in aqueous buffer after 18 h (black), with BT-maquette (blue), and with GL-maquette (green).

A bis-histidine (bis-His) ligation to metals such as iron is more thermodynamically favourable than a single histidinal ligation [6]. Therefore, employing a four-histidine (*4-his*) GL-maquette (sequence shown in Chapter IX) with an iron-based dyad, such as that shown in Figure IV-9a, it would be expected that the iron would ligate strongly. Once again, as shown with D1-4, D5 is seen to aggregate and precipitate within the aqueous buffer (Figure IV-9b). However, when *4-his* GL-maquette is present within aqueous buffer with D5, the dyad displays a highly stable absorbance spectrum over time (Figure IV-9c). Furthermore, distinct red-shifts in the Soret and Q-band peaks indicate that D5 has interacted with the maquette (Figure IV-9d). However, although the absorbance spectrum is stable when D5 interacts with the maquette, a distinct shoulder (at 424 nm) is apparent, which is not observed when D5 is in DMSO (Figure IV-4). This shoulder could be due to some of the Zn porphyrin and the Fe porphyrin no longer being fully conjugated due to disruption of the conjugation via maquette interactions.

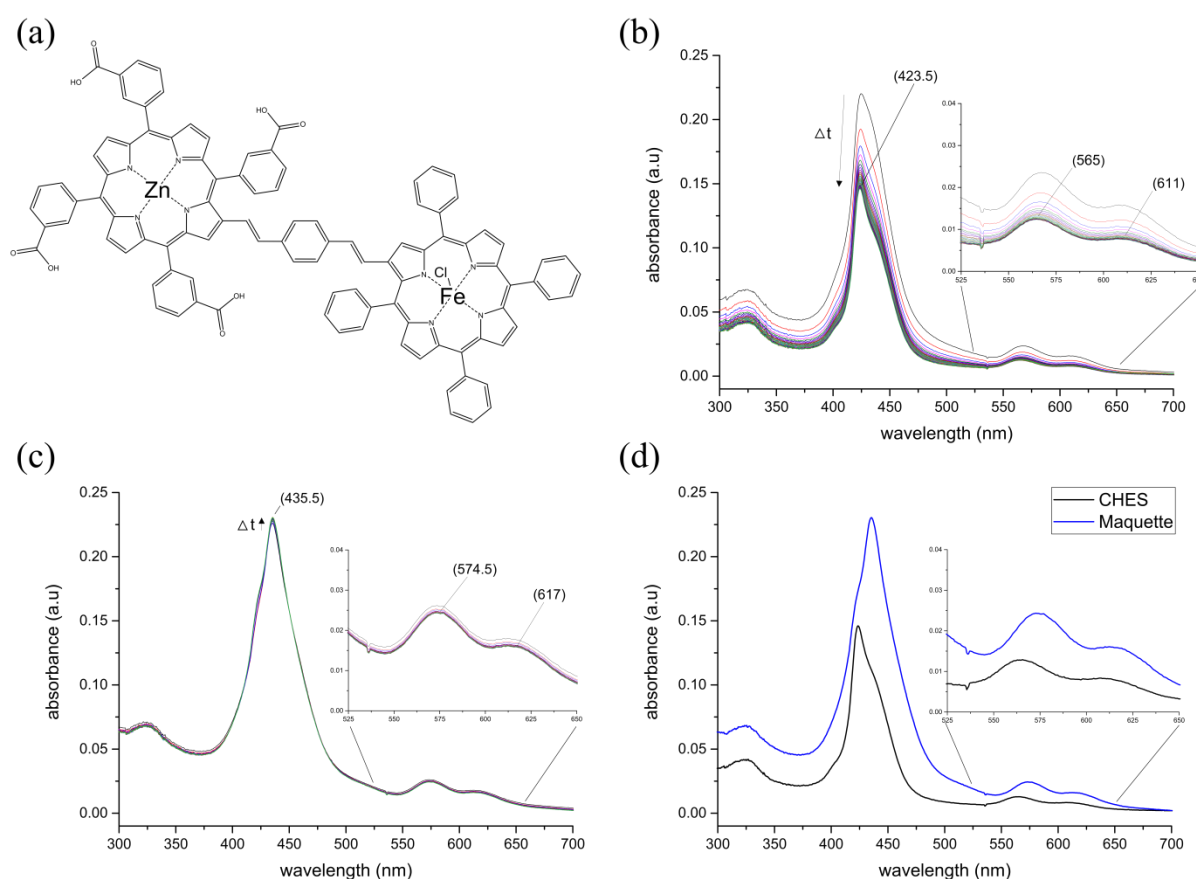


**Figure IV-9; UV-vis. absorption spectral characterisation of D5 in aqueous buffer with maquette.** (a) Structure of D5. (b) D5 in aqueous buffer; measured every 30 min for 18 h. (c) D5 and *4-his* GL-maquette in aqueous buffer; measured every 30 min for 18 h. (d) Absorption of D5 in aqueous buffer after 18 h (black), and D5 with *4-his* GL-maquette in aqueous buffer after 18 h (blue).



### 2.3- Non-conjugated dyad in DMSO

In contrast to the conjugated dyads D1-D5, the absorbance profile of non-conjugated dyads show a distinctly sharp and split Soret peak [4]. The dyad D6 (shown below) is an example of a non-conjugated dyad, with the absorbance profile expected to display a splitting in the Soret peak when fully solubilised (non-aggregated state), which is in direct contrast to the broadening effect of conjugated dyads and polymers [4]. The dyad is soluble in DMSO, with the absorbance spectrum measured in DMSO in order to compare to the spectrum in aqueous based solvents later. As was expected, the dyad D6 was shown to contain a split Soret peak, with two distinct Q-bands (Figure IV-10).

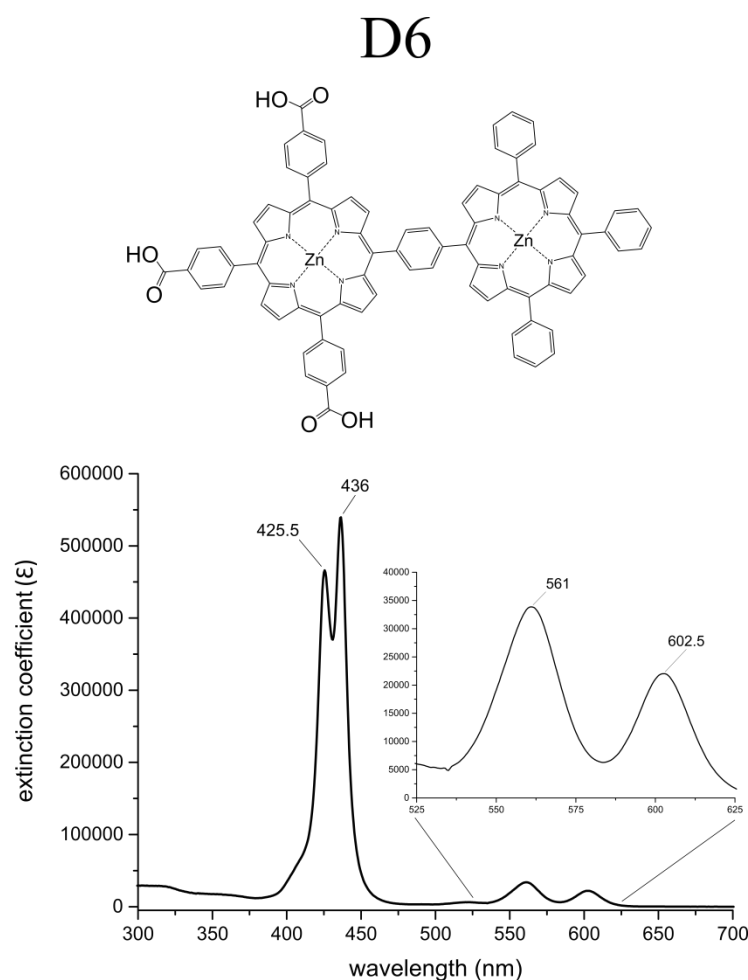


**Figure IV-10; UV-vis. absorbance of a non-conjugated dyad D6 in DMSO.** The structure of the non-conjugated dyad D6 is shown (top), with the resulting absorbance in DMSO (bottom).

#### 2.4- Non-conjugated dyad binding with maquette

As for the conjugated dyads (D1-D5), the non-conjugated dyad (D6) was expected to interact with maquettes by hydrophobic partitioning and ligation to the histidine via the hydrophilic zinc porphyrin of the dyad (Figure IV-11a). Firstly, the solubility and stability in aqueous buffer was assessed by measuring the absorbance spectrum every 30 min for 18 h (Figure IV-11b). In comparison, the absorbance spectrum was assessed in aqueous buffer with an excess of GL-maquette present in aqueous buffer, once again measured every 30 min for 18 h (Figure IV-11c).

As was observed for all of the non-conjugated dyads shown previously, D6 was shown to aggregate and precipitate in aqueous buffer over time (Figure IV-11b). Furthermore, this aggregation results in a broadening of the Soret peak, with the splitting observed in DMSO no longer apparent. In contrast, when D6 was in aqueous buffer with GL-maquette present, two distinct peaks in the Soret region became apparent over time (Figure IV-11c). These two peaks continually increased over time, and did not reach full equilibrium (Figure IV-11d) after 18 h. The formation of the split peak is attributed to the dyad becoming ligated into the maquette in a non-aggregated state, with the absorbance profile resembling that of D6 in DMSO.

To further probe the ligation of D6 into maquette, a surfactant, N,N-dimethyldodecylamine N-oxide (LDAO) was employed. It was anticipated that the surfactant would better solubilise the dyad in the aqueous phase, allowing a split Soret band to be observed and therefore a clearer band shift if the dyad was binding into the maquette. When LDAO was used in the aqueous buffer, an identical spectrum to the D6 DMSO spectrum (Figure IV-10) was obtained with only slight shifts (2-3.5 nm) in the band positions (Figure IV-11f; blue spectrum), indicating that the surfactant had prevented aggregation. Subsequent addition of the GL-maquette showed the same distinct split Soret peaks that were stable over 18 h (Figure IV-11e), but red-shifted a further 4 nm; the Q-band positions were also significantly red-shifted compared to the maquette-free spectrum (Figure IV-11f). These shifted peak positions (and absorbance profile) are identical to when D6 was in aqueous buffer in the presence of maquette after 18 h (Figure IV-11f). This gives evidence that D6 has ligated within the maquette, with the presence of LDAO preventing aggregation in aqueous solution whilst still facilitating ligation with the maquette.

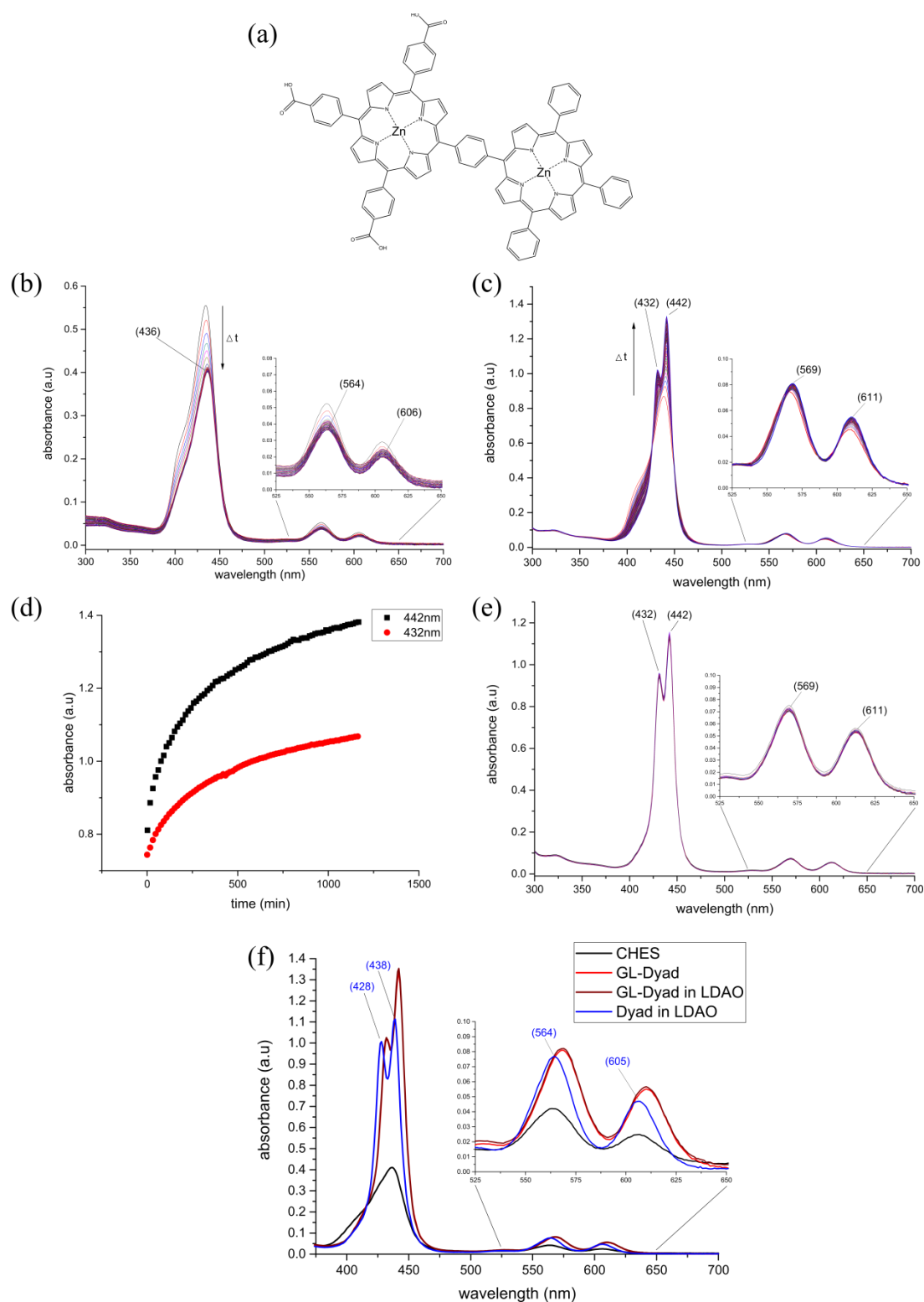


**Figure IV-11; UV-vis. absorption spectral characterisation of D6 in aqueous buffer with maquette.** (a) Structure of D6. (b) D6 in aqueous buffer; measured every 30 min for 18 h. (c) D6 and GL-maquette in aqueous buffer; measured every 30 min for 18 h. (d) Absorbance changes at 432 and 442 nm over time. (e) D6 and GL-maquette in aqueous buffer containing 2 mM LDAO; measured every 30 min for 18 h. (f) Absorption of D6 in aqueous buffer after 18 h (black), D6 with GL-maquette in aqueous buffer after 18 h (red), D6 with GL-maquette in aqueous buffer with 2 mM LDAO after 18 h (maroon), and D6 in aqueous buffer with 2 mM LDAO (blue).

### 3- Discussion; Dyad Porphyrins and Maquettes in Solution

The successful ligation of metallated hydrophobic porphyrins into maquettes as described in Chapter III held promise that larger porphyrin arrays containing a metallated hydrophobic porphyrin could also be bound into maquette, creating more efficient light harvesting complexes. A series of porphyrin dyads containing various metallated porphyrins in the dyads (Figure IV-1) were synthesised in our laboratories and characterised by UV-vis. absorbance spectroscopy. Each dyad (D1-D6) was characterised in DMSO, being highly solubilised, with the resulting absorbance profile allowing for direct comparisons to dyads in aqueous solutions.

The conjugated dyads (D1-D5) all produced an absorbance profile with a broadened Soret peak compared to monomeric zinc and free-base porphyrins [4]. This broadening of the Soret region makes it relatively difficult to observe shifts arising from ligation of hydrophobic partitioning compared to porphyrins with sharp Soret peaks. Therefore, a non-conjugated dyad (D6) was designed, containing two distinctly sharp peaks in the Soret region, which would allow for spectral changes in the absorbance arising from ligation into maquettes to be more readily observed. The conjugated dyads presented all display broadened Soret peaks, which inherently makes small shifts in peak positions more difficult to assess compared to the sharp peaks of the monomeric counterparts. However, this broadening may make them more suitable for many applications for light harvesting.

The solubilities of all dyads presented here (D1-D6) were shown to decrease in aqueous buffer over time, with the absorbance significantly diminishing in intensity. This trend is identical to the hydrophobic porphyrin monomers presented in Chapter III, and is attributed to the porphyrin (or this case the dyad) aggregating in the aqueous solution. Furthermore, the splitting of the Soret peak for the non-conjugated dyad D6 was no longer apparent in the aqueous buffer (including at 0 min). This gives further evidence that D1-D6 were all aggregating in the aqueous buffer.

In contrast to dyad aggregation in aqueous buffer, all dyads presented here (D1-D6) were stabilised in the aqueous solution when maquette was present. This alone gives evidence that all dyads are interacting with the maquette. To help differentiate between hydrophobic partitioning and metallic ligation between dyad and maquette, binding of various free-base (2H) dyads (D2-D4) was explored.

The binding of dyads into maquettes was shown to be facilitated by hydrophobic partitioning in conjunction with ligation. As was shown by D4, containing two free-base centres, the absorbance spectrum shows no significant shifts in band positions when in aqueous buffer compared to when either BT- or GL-maquette is present (Figure IV-8); although becomes significantly more stable in the aqueous environment when maquette is present, likely due to hydrophobic partitioning and possible electrostatic interactions. As a tetra-carboxylic porphyrin (albeit para-substituted) was previously shown to not interact with the more negatively charged BT-maquette (Chapter III), the stability of D4 would likely arise from a hydrophobic partitioning effect.

Further evidence for hydrophobic partitioning and ligation into maquettes comes from D3, which contains a zinc in the hydrophobic porphyrin of the dyad. The observed red-shift in peak positions in aqueous buffer when either BT- or GL-maquette was present is likely due to the zinc centre of the hydrophobic porphyrin ligating within the maquette (Figure IV-7), with hydrophobic partitioning and ligation preventing aggregation of D4 in aqueous solution. In direct contrast, when D1 (containing two zinc centres) was exposed to the BT-maquette, the absorbance spectrum is significantly altered compared to when D1 was with the GL-maquette in aqueous buffer (Figure IV-5), indicating that D1 was present in different states in the two solutions. This is due to the tetra-carboxylic acid porphyrins being known (shown previously in Chapter III) to interact with the GL-maquette, and subsequently facilitate ligation into the maquette. Therefore, when D1 is with GL-maquette in aqueous solution, either the zinc centres from the hydrophilic or from the hydrophobic porphyrin of D1 could potentially ligate, which would result in the different states of D1 being observed, and subsequently broaden the Soret peak due to the presence of multiple electronic states.

The absorbance spectrum of the dyad D2 (which contains a zinc in the hydrophilic porphyrin and free-base in hydrophobic porphyrin of the dyad) in aqueous buffer is largely unstable, diminishing significantly over time. This is attributed to the dyad aggregating in the aqueous solvent, as discussed previously. When either BT- or GL-maquette is present with D2 in the aqueous solution however, the absorbance spectrum (of D2) becomes stabilised, with a red-shift in the peak positions (Figure IV-6). This is indicative of interactions between D2 and either maquette in solution. Furthermore, the trends observed were similar to the binding of D1 to BT- or GL-maquettes, with the dyad D2 having a slightly increased red-shifted absorbance spectrum when the GL-maquette is present compared to the BT-maquette. However, as

discussed above, the hydrophilic tetra-carboxylic porphyrin component of the dyad does not typically interact with the BT-maquette. Therefore, the slight red-shifting observed in the D2 absorbance spectrum with the BT-maquette is likely due to the free-base hydrophobic porphyrin of the dyad becoming partitioned into the centre of the maquette (hydrophobic partitioning), which stabilises the dyad in the aqueous solvent. In contrast, the GL-maquette can coordinate with a zinc tetra-carboxylic acid porphyrin (shown in Chapter III when comparing zinc ligation to hydrophilic partitioning of free-base porphyrin moieties). It is therefore possible that the zinc centre of the hydrophilic porphyrin of the dyad could have become ligated to the maquette, resulting in a larger red-shifted spectrum. However, as the spectra of D2 with the BT- or GL-maquettes are similar, it may be that D2 also bound to the GL-maquette in a similar manner to the way D2 bound with the BT-maquette; that is, hydrophobic partitioning of the free-base porphyrin. Given that the Soret band shifts do not allow the different binding modes to be distinguished, it is not clear here whether there is a dual binding mode for D2 with the GL-maquette.

The dyad D5 was designed to exploit the preference of bis-His ligation of iron centres in porphyrin. D5 contained an iron core in the hydrophobic porphyrin, with zinc in the hydrophilic porphyrin of the dyad. It was expected that using a maquette with two bis-His binding sites (*4-his* GL-maquette), D5 would preferentially bind into the maquette through bis-His ligation with the iron of the hydrophobic porphyrin. However, although a large shift in band positions was evident when maquette was present in the aqueous buffer (Figure IV-9), a clear shoulder was present in the Soret peak region. This shoulder could arise due to a number of reasons. It is possible that the hydrophobic partitioning and ligation forces are not strong enough to overcome the aggregated state of D5 in aqueous buffer to bind all dyad present. This may reflect the ability of the carboxylate functionality to act as a ligand to the iron atom leading to dyad oligomers in solution that may be more difficult to break down than the aggregated dyad. Conversely, the conjugation between the Zn porphyrin and the Fe porphyrin of the dyad may have become disrupted through interactions with the maquette, with the apparent peak being unbound Zn porphyrin within the aqueous buffer. However, these potential causes were not determined as this was an explorative experiment. The cause of this observation should be analysed in the future for potential applications in differentially binding Fe-Zn dyads within maquettes.

The use of the non-conjugated dyad, D6, allows for easier analysis of spectral shifts due to the sharp peaks in the Soret region (Figure IV-10). As there is a significant difference in absorbance profiles for D6 was in aqueous buffer compared to when the GL-maquette was present, the ligation of D6 with GL-maquette is strongly inferred (Figure IV-11). Furthermore, the Soret peak splitting, which became evident with the presence of maquette (after a period of time), is attributed to the dyad being in a non-aggregated state through ligation and hydrophobic partitioning within the maquette. Further evidence for this was obtained with the use of the surfactant LDAO. As shown (Figure IV-11f), the surfactant solubilised D6 in the aqueous solvent. When the GL-maquette was present with LDAO, D6 was observed to be stable over time, with a split Soret peak. However, the peak positions red-shifted compared to when the maquette was absent. Furthermore, the peak position for the LDAO/D6/maquette mixture is identical to D6 and maquette in aqueous buffer (after 18 h). This red-shifting in the peak positions in conjunction with the stabilisation of D6 with the presence of maquette indicates D6 ligates within the maquette, likely driven by hydrophobic partitioning, however, is very slow. The presence of LDAO in the aqueous solution not only stabilises the dyad, but readily facilitates ligation with the maquette, reaching an equilibrium state in minutes, compared to >18 h when LDAO is not used.

#### 4- Conclusions; Dyad Porphyrins and Maquettes in Solution

Work presented here shows that it is possible to bind dyads to appropriate maquettes, which may increase the light harvesting potential of the porphyrin-maquette ensembles. The binding of two types of dyad, conjugated and non-conjugated, were studied. Conjugated dyads inherently contain broadened absorption peaks, which essentially makes their shifts in the absorbance spectrum induced by ligation within maquettes more difficult to analyse, compared to their monomeric counterparts. Nonetheless, when a more anionic maquette such as the BT-maquette was used for the ligation of an amphiphilic dyad, the hydrophobic component of the dyad was preferentially partitioned into the maquette whether the zinc was present or not, affording a more stable aqueous porphyrin-maquette construct; if zinc was present in the hydrophobic dyad porphyrin there was a clear increase in stability presumably as a result of tighter binding of the zinc to the maquette histidine.

In contrast, non-conjugated dyads contain sharp absorbance (split Soret) peaks. Due to this sharpness, potential shifts in peak positions induced by ligation with maquettes would become more readily apparent compared to conjugated dyads. The non-conjugated dyad (D6) was evidently not stable in aqueous solvent, with the signature split Soret peak not observed, instead the spectrum contained a broadened absorbance that diminished over time due to the propensity of the hydrophobic portion of the dyad to induce aggregation. However, a split Soret peak was evident when the non-conjugated dyad was in aqueous solution with maquette, evidence that the dyad being was in a non-aggregated state. Furthermore, the use of a surfactant which inhibited aggregation of the dyad produced an absorbance with a split Soret peak that became red-shifted when maquette was present. The red-shifting of the absorbance spectrum in conjunction with the split Soret peak was evidence that the non-conjugated dyad was ligating with the maquette and that construct was stable in an aqueous environment.

The successful incorporation of dyads into maquettes opens up the possibility of creating devices with enhanced light harvesting. The use of a dyad for enhanced light harvesting has been previously demonstrated for dye sensitized solar cells [3]. The formation of these porphyrin dyad-maquette ensembles represents a significant step towards the formation of an effective artificial photosynthetic centre.



## 5- References; Dyad Porphyrins and Maquettes in Solution

1. Mitchell R: **Synthesis of Water Soluble Porphyrins and their Applications.** *PhD Thesis.* University of Wollongong; 2016.
2. Roach N: **Synthesis of Amphiphilic Porphyrins and Porphyrin Arrays.** *PhD Thesis.* University of Wollongong; 2016.
3. Mozer AJ, Griffith MJ, Tsekouras G, Wagner P, Wallace GG, Mori S, Sunahara K, Miyashita M, Earles JC, Gordon KC: **Zn–Zn porphyrin dimer-sensitized solar cells: toward 3-D light harvesting.** *Journal of the American Chemical Society* 2009, **131**(43):15621-15623.
4. Piet JJ, Taylor PN, Wegewijs BR, Anderson HL, Osuka A, Warman JM: **Photoexcitations of Covalently Bridged Zinc Porphyrin Oligomers: Frenkel versus Wannier–Mott Type Excitons.** *The Journal of Physical Chemistry B* 2001, **105**(1):97-104.
5. Hasselman GM, Watson DF, Stromberg JR, Bocian DF, Holten D, Lindsey JS, Meyer GJ: **Theoretical solar-to-electrical energy-conversion efficiencies of perylene-porphyrin light-harvesting arrays.** *The Journal of Physical Chemistry B* 2006, **110**(50):25430-25440.
6. Sharp RE, Diers JR, Bocian DF, Dutton PL: **Differential binding of iron (III) and zinc (II) protoporphyrin IX to synthetic four-helix bundles.** *Journal of the American Chemical Society* 1998, **120**(28):7103-7104.

# **Chapter V**

## **Immobilization onto TiO<sub>2</sub> Electrodes**

## 1- Introduction; Immobilization onto TiO<sub>2</sub> Electrodes

Porphyrins have gained increasing attention in the past few decades due to their ease of synthesis, high extinction coefficients, and high stabilities which are applicable in a large range of areas including use in light harvesting, catalysis, and biomedical applications [1-6]. The binding of porphyrin entities to a surface, in particular an oxide surface, has generated great interest, with an oxide surface useful as a transparent semiconductor. With monomeric porphyrins well characterised for the sensitization of oxide surfaces through the carboxylic functional groups from organic solvents, attention has shifted towards other modes of binding and incorporations. Lysine residues of proteins are known to bind to oxide rich surfaces such as TiO<sub>2</sub>, with lysine-based peptides adsorbing onto TiO<sub>2</sub> (at pH 7.4) from the negative and positive charges of TiO<sub>2</sub> and the peptide, respectively [7-10]. The incorporation of porphyrins with dendrimers (often comprised of poly-lysine) has shown promise for biomedical applications, with immobilization to oxide surfaces showing promise for applications in a range of areas such as low level detections [11-13]. Furthermore, surface charges associated with Photosystem II have been exploited for both electrostatic and covalent linking to TiO<sub>2</sub>, with photo-induced injection of electrons into the semiconductor [14, 15].

The incorporation of porphyrins into artificial protein maquettes provides the possibility to associate porphyrins with oxide rich surfaces via maquette interactions. The maquette is designed to have a hydrophilic surface and hydrophobic core, to help with correct folding, structural integrity, and hydrophobic partitioning of cofactors. As a TiO<sub>2</sub> surface is expected to be negatively charged in an aqueous buffer (at pH>6) [16-18], the surface of the maquette was designed to contain a number of lysine residues which would potentially interact with a TiO<sub>2</sub> surface. The GL-maquette was specifically designed to contain two helices, which contain a larger number of lysine residues than the BT-maquette equivalent, facilitating a stronger interaction with TiO<sub>2</sub>. With the modification of oxide surfaces well characterised, along with the subsequent covalent linking of peptides through specific residues to the surface [19], maquettes with porphyrins ligated can potentially be covalently bound to TiO<sub>2</sub>. The binding of similar maquette structures to TiO<sub>2</sub> has been achieved, with electrostatic interactions between maquette and TiO<sub>2</sub> occurring in an aqueous buffer with high binding stability and no detectable protein denaturation [20, 21]. Furthermore, the incorporation of positively charged residues on the maquette surface has been shown to promote interactions with the TiO<sub>2</sub> surface [22, 23].

Two porphyrins were chosen for incorporation with maquettes and binding onto  $\text{TiO}_2$ . P1d and P3d, as shown in Figure V-1, were chosen due to their quick ligation with maquette (<1 min, Chapter III). Furthermore, P1d has been shown to be highly stable in aqueous buffer, allowing for direct comparison to when P1d is ligated with maquettes. In contrast to P1d containing negatively charged substituents, whereby the carboxylic acid will dissociate to carboxylates (pKa of benzoic acid being 4.2 in aqueous solution [24, 25], P3d contains positively charged substituents. Although these positive charges would incur an electrostatic interaction with a negatively charged  $\text{TiO}_2$  surface, the trimethyl groups would be expected to reduce potential interactions.

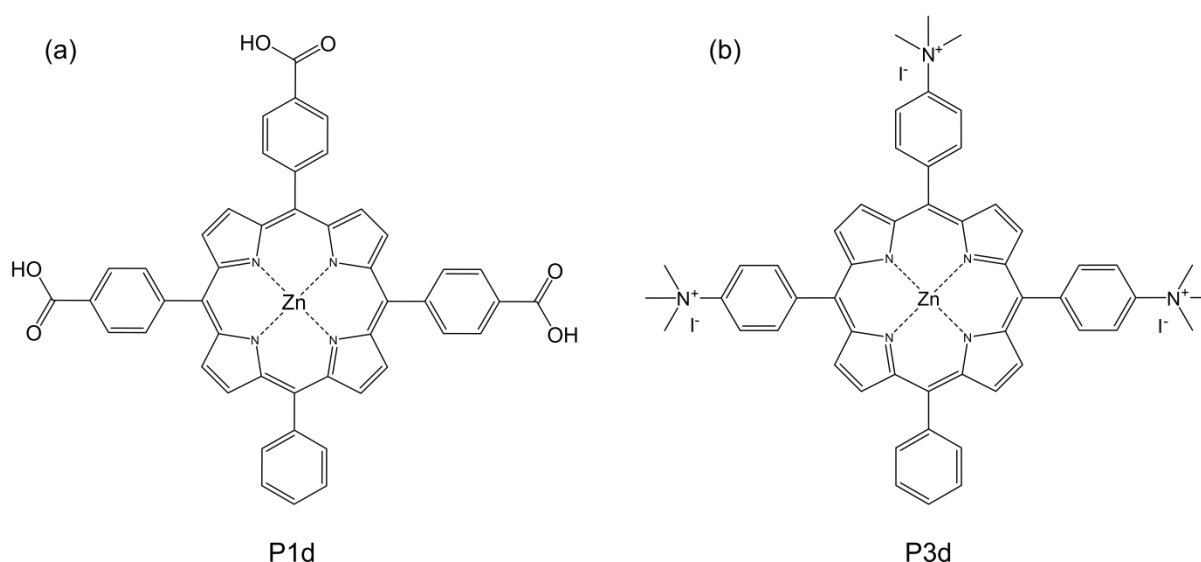


**Figure V-1; Porphyrins used for binding to  $\text{TiO}_2$ .** The two porphyrins used for binding to maquettes and  $\text{TiO}_2$  interactions. (a) P1d. (b) P3d.

Binding between maquette and  $\text{TiO}_2$  from aqueous solutions occurs via electrostatic interactions, with the potential for the charged substituents of porphyrins to similarly interact with the surface. In contrast, porphyrins are typically covalently attached to  $\text{TiO}_2$  from organic solvents, such as THF [26, 27]. Carboxyl groups are well characterised for sensitization to  $\text{TiO}_2$  surfaces, whereby carboxylic or sulfonic acid ‘anchoring’ groups are specifically added to porphyrins and dyes for binding to oxide rich surfaces [26, 27]. Therefore, P1d would be expected to interact and covalently attach to  $\text{TiO}_2$  from organic solvents, with P3d expected to display no interaction with the surface. The carboxylate anchoring group is known to show three distinct modes of binding, being a bidentate chelating, bidentate bridging, or an ester

linking (Figure V-2) [28]. It has been shown that porphyrins with carboxylate anchoring groups will predominantly sensitize from organic solvents to  $\text{TiO}_2$  through a combination of bidentate chelating and bidentate bridging.

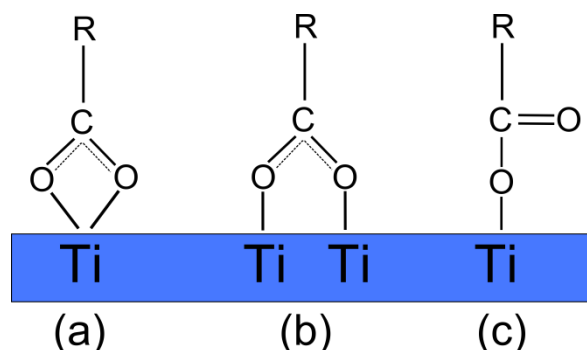


**Figure V-2; Sensitization modes to  $\text{TiO}_2$  via carboxylic groups.** The predominant binding modes of the carboxylic functional group to  $\text{TiO}_2$ . (a) bidentate chelating, (b) bidentate bridging, (c) ester linking. Porphyrins are known to predominantly bind through modes (a) and (b), as opposed to (c) [28].

Oxide rich surfaces can be modified through linkers, often utilising the interaction between phosphonic acid and the surface. Phosphonic acid is known to interact with  $\text{TiO}_2$  through a variety of modes (Figure V-3). The possible binding modes are monodentate, bridging bidentate, bridging tridentate, and chelating bidentate, with the binding to  $\text{TiO}_2$  shown to be predominantly via the bridging modes, as opposed to chelating modes [29].

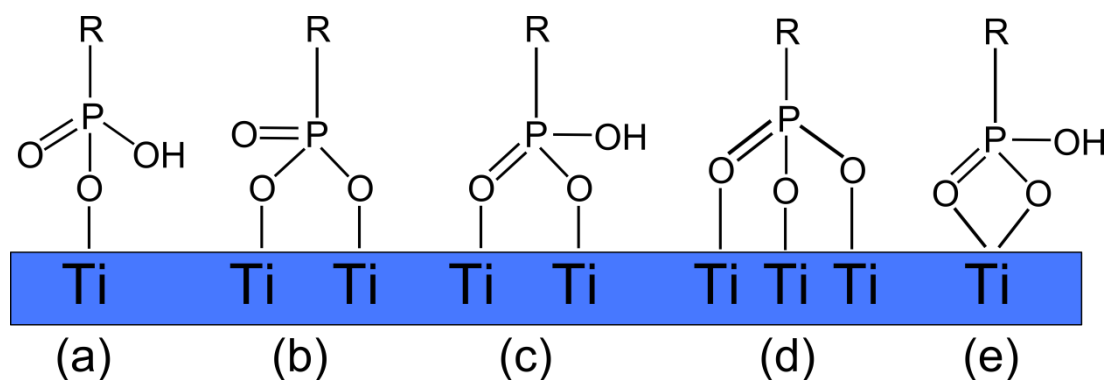


**Figure V-3; Binding modes of phosphonic acid to  $\text{TiO}_2$ .** The predominant binding modes of the phosphonic functional group to  $\text{TiO}_2$ . (a) monodentate, (b,c) bridging bidentate, (d) bridging tridentate, (e) Chelating bidentate. It is known that binding of phosphonic groups is predominantly via bridging (b,c,d), as opposed to a chelating mode (e) [29].

The modified  $\text{TiO}_2$  surface through the use of phosphonic acid (Figure V-3) can then be exploited for covalent linking of amino acid residues to the surface. Through the use of the well-known conjugative reactants 1-ethyl-3-(3-dimethylaminopropyl) carbodiimide hydrochloride (EDC) and N-hydroxysulfosuccinimide (NHS), linking between a carboxylic

group and a primary amine of residues can be achieved for covalently linking proteins to surfaces such as  $\text{TiO}_2$  [30], as displayed in the schematic Figure V-4. Therefore, if a phosphonic group was used for attachment to  $\text{TiO}_2$ , which contains a carboxylic group at the opposite end of a chain (such as 3-phosphonopropionic acid), then the EDC-NHS reactants can conjugate the modified  $\text{TiO}_2$  surface to primary amines of a maquette, such as with lysine residues. However, the linking between carboxylic groups and primary amines can induce cross-linking between maquettes, in which carboxylic groups from aspartic and glutamic acid residues can link to the primary amine group of lysine residues.

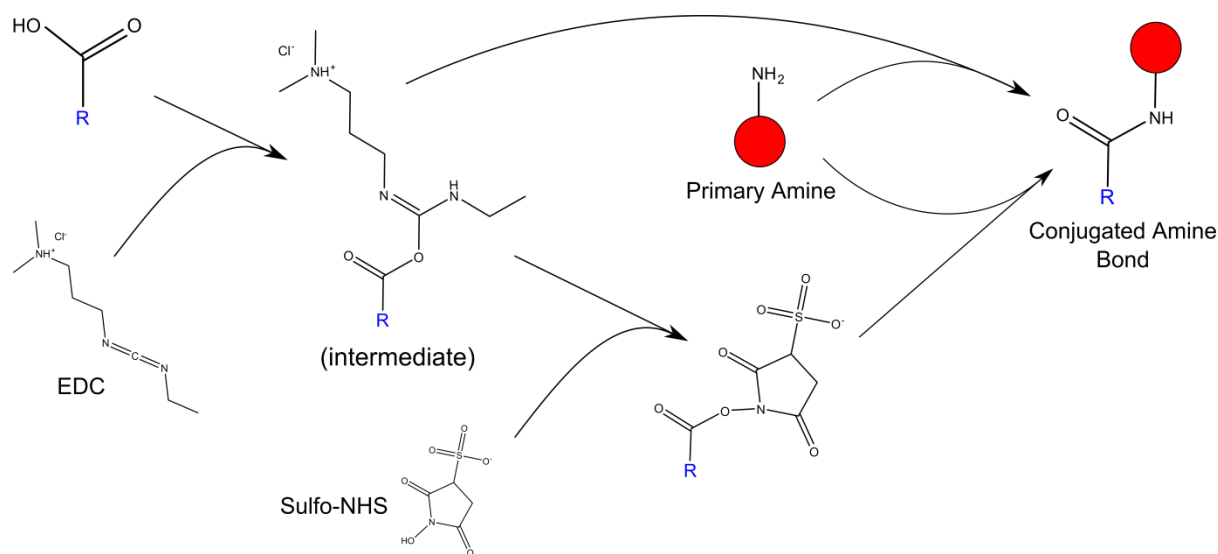


**Figure V-4; EDC-NHS reaction schematic.** The EDC-NHS reaction schematic, displaying how a carboxylic group is used for covalent binding to primary amines.

With the EDC-NHS reaction for conjugative linking between a  $\text{TiO}_2$  surface and a protein (such as maquette) being predominantly through the primary amine groups, the specific orientation of a bound protein cannot be determined for certain. Therefore, a second, site-specific conjugative method can be employed. The sulfhydryl-maleimide conjugation exploits a sulfhydryl group found on only one amino acid, being the cysteine residue (Figure V-5). Therefore, if a protein or maquette structure incorporates a single cysteine residue, the orientation of a protein on the surface via formation of a conjugative link between can be known [31, 32].

N-succinimidyl 3-maleimidopropionate ester

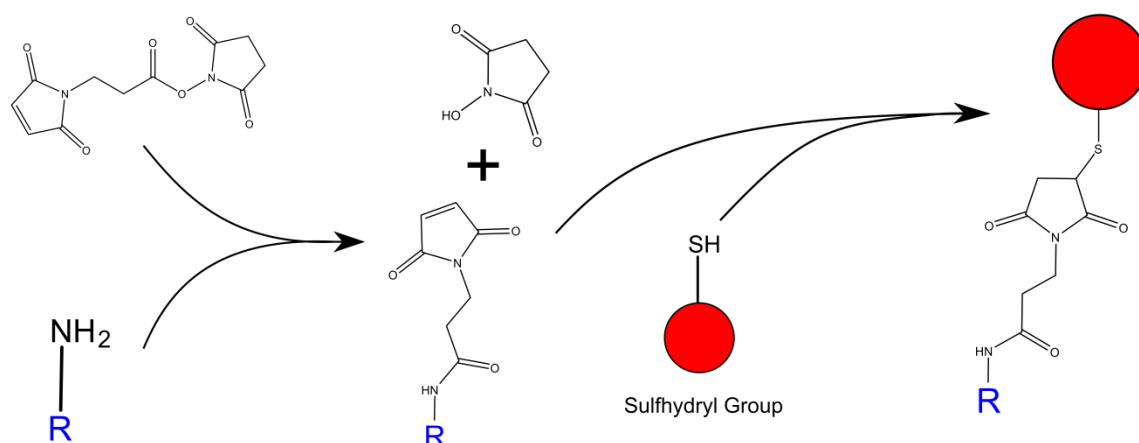
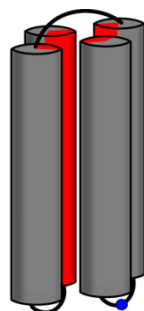


**Figure V-5; Cysteine-maleimide reaction schematic.** The maleimide reaction with sulfhydryl groups schematic, displaying how an amine group is used for covalent binding to sulfhydryl groups (often on cysteine residues).

As the original BT- and GL-maquette sequence do not contain cysteine residues, the cysteine-maleimide conjugation to TiO<sub>2</sub> would not be possible. Therefore, the GL-maquette was re-sequenced to introduce a single cysteine in the loop region, which can be exploited for conjugation to TiO<sub>2</sub> (Figure V-6). Subsequently, the maquette (designated *cysGL*-maquette or *cysGL*) would conjugate to TiO<sub>2</sub> from a single point, in contrast to EDC-NHS based conjugation. The GL-maquette was chosen to be modified with a cysteine residue as it allows for direct comparisons with methods involving electrostatic binding and conjugation via EDC-NHS reactions to surfaces.



Polar / Non-Polar

Helix Number	Overall Charge	New GL-Maquette Sequence	Loop-Region
I	-4	G E I W K Q H E D A L Q K F E E A L N Q F E D L K Q L G G C G	G G C G
II	+2	E I K Q R A E D A L R K F E E A L K R F E D K K Q K G G S G	G G S G
III	-4	E I W K Q A E D A L Q K F E E A L N Q F E D L K Q L G G S G	G G S G
IV	+2	E I K Q R H E D A L R K F E E A L K R F E D K K Q K	

**Figure V-6; A new GL-maquette ('cysGL-maquette') sequence design.** The GL-maquette was redesigned to incorporate a cysteine residue within the loop region of the maquette (highlighted in blue), exploited for cysteine-maleimide linking reactions. Furthermore, the sequence of the loop region was shortened, with the primary sequence remaining unchanged to previous GL-maquette sequence.

## 2- Results; Immobilization onto TiO<sub>2</sub> Electrodes

The binding of maquettes to the surface of TiO<sub>2</sub> is needed to first be established before electron transfer processes can be analysed. As interactions between carboxylic acids and TiO<sub>2</sub> is known to occur, maquette-porphyrin ensembles needs to be analysed in contrast to direct porphyrin interactions with TiO<sub>2</sub>. This is due to the possibility that the functional substituents of the porphyrin may be interacting with the surface, as opposed to the intended maquette-TiO<sub>2</sub> interaction for when maquette-porphyrin ensembles are immobilized on TiO<sub>2</sub>.

### 2.1- Maquette-porphyrin ensemble extinction coefficient

Binding of maquettes containing ligated porphyrins (ensembles) to TiO<sub>2</sub> occurs from an aqueous solution. To analyse ensemble interactions with the surface, the solution must contain no (or minimal) non-ligated porphyrin and no maquettes which do not contain porphyrin. As such, the purification of ensembles from a solution containing maquette with excess porphyrin is needed. Therefore, the concentration of maquette and also ligated porphyrin needs to be determined from a solution as to ascertain the stoichiometry. The problem that needs to be overcome is that porphyrin have slight absorbance <300 nm which interferes with the determination of maquette concentration via absorbance at 280 nm. The concentration of ligated porphyrin can be determined with a standard curve, whereby if maquette is in excess, all porphyrin would be expected to ligate. The increase in the 'ligated' Soret peak plotted against the porphyrin concentration gives a gradient correspondent to the extinction coefficient of ligated porphyrin at that particular wavelength. This increase in absorbance at the Soret peak and also be plotted against the increase of absorbance at 280 nm, with the resulting gradient being the relative ratio between the two wavelengths for ligated porphyrin. Therefore, assuming a pure sample, the absorbance at the ligated Soret peak for a porphyrin can be used to ascertain the concentration of porphyrin (using extinction coefficient at this wavelength), and using the relative ratio's, the 'expected' absorbance at 280 nm. Any increase in the measured absorbance at 280 nm compared to the 'expected' absorbance results from the maquette, which can be used to determine the concentration, as shown by Equation 3.

Figure V-7a shows the absorbance profile of increasing ligated P1d concentration to GL-maquette, with the inset displaying the corresponding standard curve to determine extinction coefficient at the absorbance maximum (433 nm). The extinction coefficient is shown to be 505,900 ( $\pm 11,900$ ) M<sup>-1</sup> cm<sup>-1</sup> at the Soret peak. Further to this, the relative rise of the ligated P1d Soret peak is plotted against the rise at 280 nm, with a gradient obtained (Figure



V-7b). This gradient ( $28.1 \pm 0.5$ ) represents the relative increase in absorbance at the ligated Soret peak compared to the increase at 280 nm. Therefore, with the extinction coefficient known for ligated P1d to GL-maquette, concentrations of both ligated P1d and GL-maquette can be calculated from a solution containing purely ligated P1d to GL-maquette according to Equation 3.

### Equation 3

$$[\text{maquette}] = (A_p - (S_p/R)) / \epsilon_M$$

Where;  $A_p$  = absorbance at 280 nm,  $S_p$  = absorbance at Soret peak of ligated porphyrin,  $R$  = ratio of ligated Soret peak to maquette absorbance,  $\epsilon_M$  = extinction coefficient of the maquette at 280 nm.

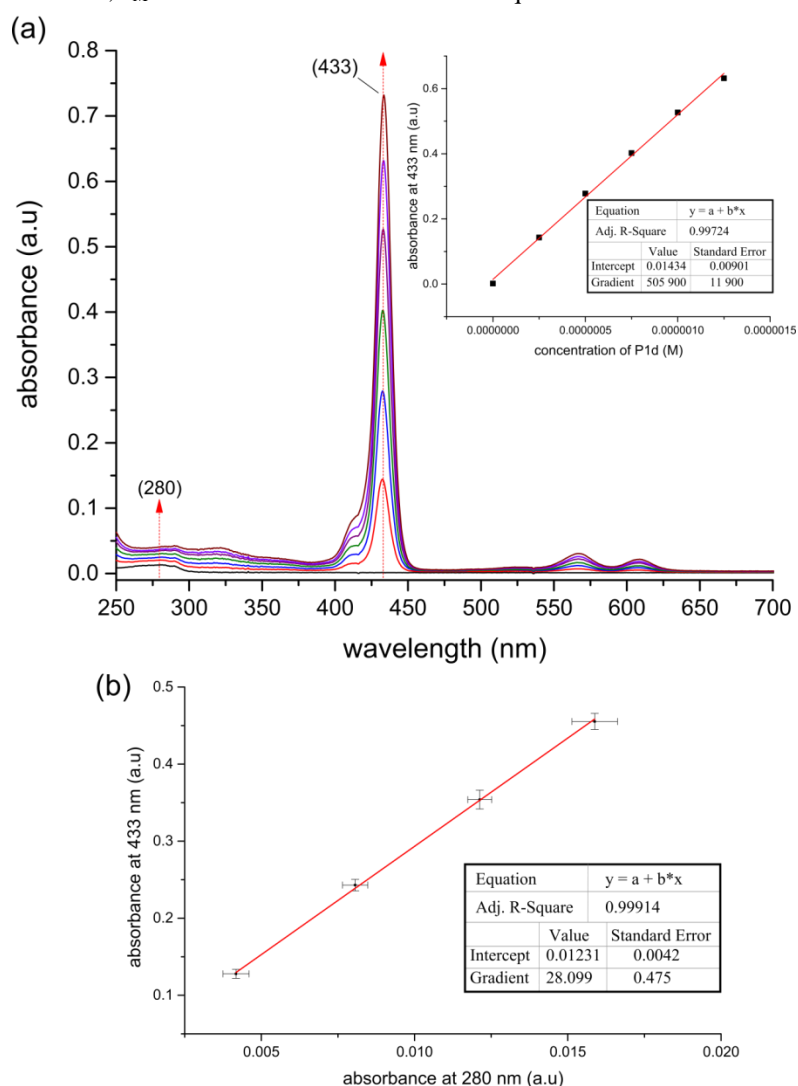


**Figure V-7; Determination of Molar Extinction of P1d ligated with GL-maquette in aqueous buffer.** (a) 0.25  $\mu\text{M}$  increments of P1d were added to 1  $\mu\text{M}$  of GL-maquette, so that the increase in absorbance at the Soret peak maxima for ligated P1d (433 nm), analogous to the extinction coefficient, could be determined, corresponding to an extinction coefficient of  $505,900 (\pm 11,900) \text{ M}^{-1} \text{ cm}^{-1}$  at 433 nm (inset). (b) The relative increase in the Soret peak of porphyrin compared to increase at 280 nm, being maximum peak for maquette, to obtain a relationship of relative increases at extinction coefficient maxima.

As was with the GL-maquette and P1d, the extinction coefficient of ligated P1d to BT-maquette was determined via the use of a standard curve. The increasing concentration of ligated P1d was plotted against the absorbance maximum of the ligate P1d Soret peak (433.5 nm), as shown in Figure V-8a. The inset displays the corresponding standard curve that can be used to determine extinction coefficient at the ligated Soret peak, which is  $477,800 (\pm 10,100) \text{ M}^{-1} \text{ cm}^{-1}$ . Further to this, the relative rise of the ligated P1d Soret peak plotted against the rise at 280 nm (corresponding to the maquette absorbance maxima) results in a gradient being obtained (Figure V-8b). This gradient ( $27.8 \pm 1.8$ ) represents the relative increase in absorbance at the ligated Soret peak compared to increase at 280 nm. Therefore, with the extinction coefficient known for ligated P1d to GL-maquette, concentrations of both ligated P1d and BT-maquette can be calculated according to Equation 3.

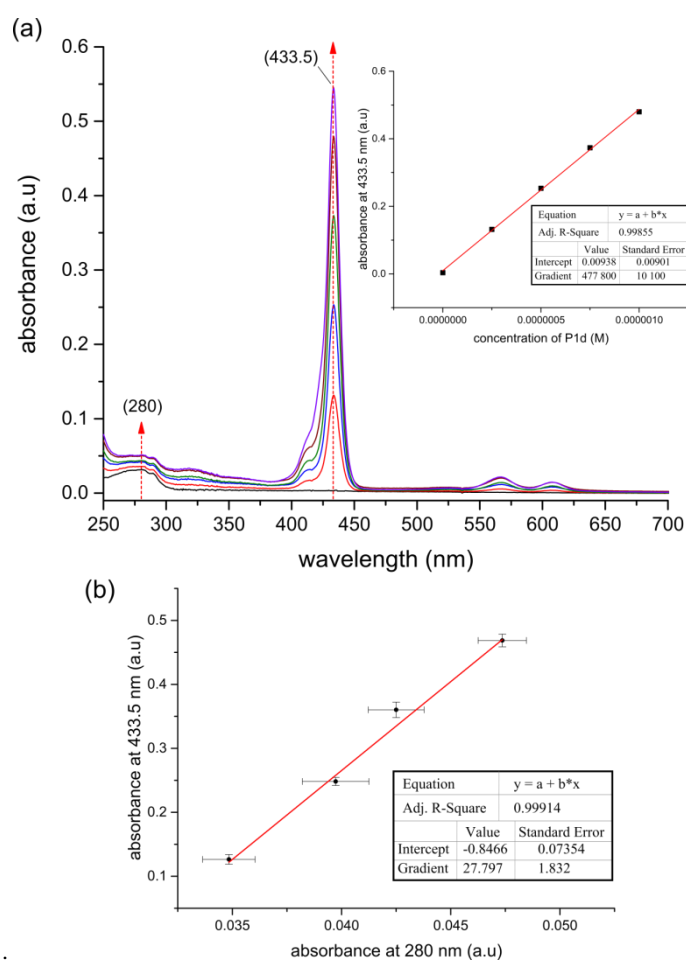


**Figure V-8; Determination of Molar Extinction of P1d ligated with BT-maquette in aqueous buffer.** (a) 0.25  $\mu\text{M}$  increments of P1d were added to 1  $\mu\text{M}$  of BT-maquette, so that the increase in absorbance at the Soret peak maxima for ligated P1d (433 nm), analogous to the extinction coefficient, could be determined, corresponding to an extinction coefficient of  $477,800 (\pm 10,100) \text{ M}^{-1} \text{ cm}^{-1}$  at 433 nm (inset). (b) The relative increase in the Soret peak of porphyrin compared to increase at 280 nm, being maximum peak for maquette, to obtain a relationship of relative increases at extinction coefficient maxima.

## 2.2- Purification of maquette-porphyrin ensembles

### 2.2.1- Size-exclusion chromatography

Size-exclusion chromatography is a useful tool for separating two entities in solution based on size. As ligated porphyrin to maquette results in a molecule that is significantly larger than a monomeric solubilised porphyrin, size-exclusion chromatography can be used to separate excess porphyrin and obtain a solution of pure porphyrin-maquette ensemble. Figure V-9 shows the absorbance profiles from the resulting elution's using P1d with either BT-maquette or GL-maquette. Monomeric and solubilised P1d in the aqueous buffer is displayed, highlighting the distinct shifts observed for ligated P1d and validate purification via size-exclusion chromatography. Indeed, when P1d is ligated to BT- or GL-maquette, the elution is of pure porphyrin-maquette ensembles, displaying no evidence of 'free' porphyrin in solution.

Using the extinction coefficients of ligated P1d to the specific maquettes in conjunction with Equation 3, the ratio of maquette to P1d can be determined. With respect to the ligated P1d and BT-maquette elution, the concentration of maquette is determined to be  $0.63 (\pm 0.04) \mu\text{M}$ , with P1d being  $0.30 (\pm 0.01) \mu\text{M}$ . Similarly, the ligated P1d to GL-maquette elution displays a maquette concentration of  $0.77 (\pm 0.01) \mu\text{M}$ , with P1d being  $0.28 (\pm 0.01) \mu\text{M}$ . This indicates that for the P1d-BT-maquette ensembles, the ratio of maquette to porphyrin is 1:0.48, with P1d to GL-maquette displaying a ratio of 1:0.36 (maquette:porphyrin). This is significantly lower than the stoichiometric relationship of 1:2 (maquette:porphyrin), indicating that the size-exclusion processing is not adequate for obtaining a pure solution of porphyrin-maquette ensembles. It is likely that the zinc centre of the porphyrin has a strong affinity to the column, which results in P1d being removed from the maquettes. This is apparent as the porphyrin molecules are unable to be washed from the column, indicating tight binding.

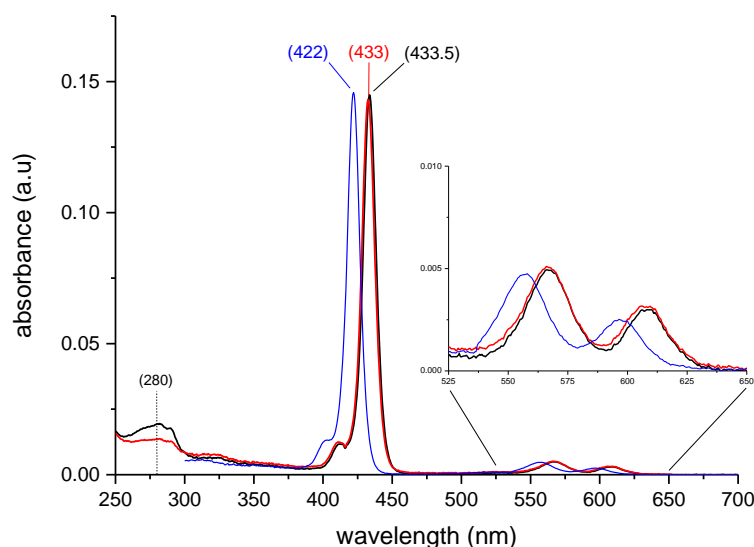


**Figure V-9; Size-exclusion chromatography elution profiles.** Elution absorbance of BT-maquette with excess P1d in aqueous buffer (black). Elution absorbance of GL-maquette with excess P1d in aqueous buffer (red). P1d absorbance in aqueous buffer (blue).

### 2.2.2- Protein centrifugal filtration

The principles behind centrifugal filtration are similar to that of size-exclusion chromatography, in which a solution can be separated via the differences in molecular weights. The filtrate passes through a membrane, with the larger molecules collected (and concentrated). Figure V-10a shows the absorbance profiles after two centrifugal run cycles of the filtrate and the concentrated collected solutions which did not pass through the membrane from a mixed solution of excess P1d and GL-maquette. As shown, the filtrate resembles that of monomeric P1d in the aqueous buffer, with two distinct peaks for the collected sample. These two peaks correspond to that of a ligated P1d (at 433 nm) and free monomeric P1 (422 nm), indicating that the purification process via centrifugal filtration needed further cycles. Figure V-10b displays the absorbance profiles of centrifugal filtration separation after 5-cycles. The profiles display single peaks at 433.5 and 433 nm when P1d is with BT- and GL-maquette, respectively. This indicates that the porphyrin present is in its ligated state, with the profile signifying that it is monomeric with negligible P1d free in solution.

As was done for the size-exclusion chromatography elutions, the ratio of maquette to porphyrin can be calculated based on Equation 3. With respect to the ligated P1d to BT-

maquette, the concentration of maquette is determined to be  $1.42 (\pm 0.09) \mu\text{M}$ , with P1d being  $2.04 (\pm 0.05) \mu\text{M}$ . Ligated P1d to GL-maquette displays a maquette concentration of  $1.00 (\pm 0.02) \mu\text{M}$ , with P1d being  $1.96 (\pm 0.05) \mu\text{M}$ . This indicates that for the P1d-BT-maquette ensembles, the ratio of maquette to porphyrin is 1:1.44, with P1d to GL-maquette displaying a ratio of 1:1.96 (maquette:porphyrin). This is significantly closer to the stoichiometric relationship of 1:2 (maquette:porphyrin) than observed for size-exclusion chromatography, indicating that centrifugal filtration is a better technique to obtain purified porphyrin-maquette ensembles. This difference between the two methods is due to the high affinity of the zinc porphyrin to the column, pulling the porphyrin out of the maquette. In contrast, the centrifugal filtration uses centripetal forces, which would not be a significant force to remove porphyrins from a bound state.

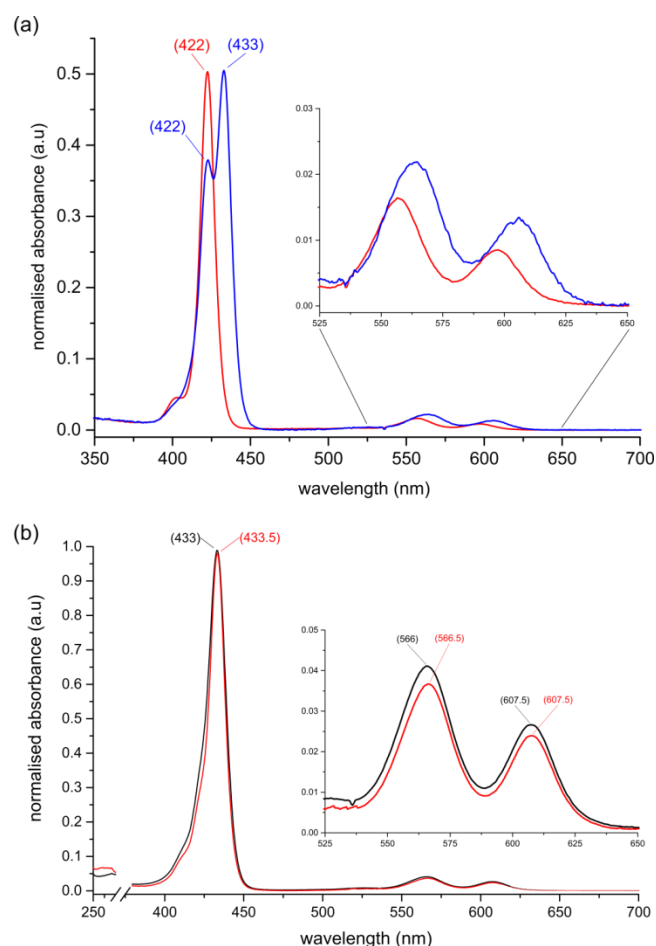


**Figure V-10; Centrifugal filtration purification of maquette-P1d ensembles.** (a) The centrifugal purification was run for 2 cycles, with the absorbance of the collected filtrate (red) and the collected solution (blue). (b) The centrifugal purification was run for 5 cycles, with the absorbance spectra of the GL-maquette with P1d solution (black) and BT-maquette with P1d solution (red) shown.

## 2.3- Binding directly to TiO<sub>2</sub>

The TiO<sub>2</sub> used for all subsequent experiments were prepared on FTO-coated glass substrate, consisting of a transparent 18NR-T TiO<sub>2</sub> paste (average nanoparticle size of 20 nm), sintered to produce a film. The thickness of the films was controlled as to regulate quantity of material binding, and hence the resulting colour of the films to be measurable within UV-Vis. equipment.

### 2.3.1- Sensitization of porphyrins via THF

The porphyrin P1d is expected to sensitize TiO<sub>2</sub> via the carboxylic functional groups. Films of 600 nm and 2.5  $\mu\text{m}$  were submerged into 200  $\mu\text{M}$  of P1d in THF for 3 h, with the resulting films rinsed and dried before measurements. Figure V-11 displays the UV-Vis. absorbance profiles from TiO<sub>2</sub> sensitized with P1d. The 2.5  $\mu\text{m}$  film allows for the determination of Q-band positions, but this results in Soret peak absorbance being in excess of the measurable range (Figure V-11a). Therefore, 600 nm films were used to determine the profile of sensitized P1d on TiO<sub>2</sub> within the Soret region (Figure V-11b). The Soret peak maximum is observed to be at 426 nm, with two distinct Q-bands shown at 558 and 600 nm.

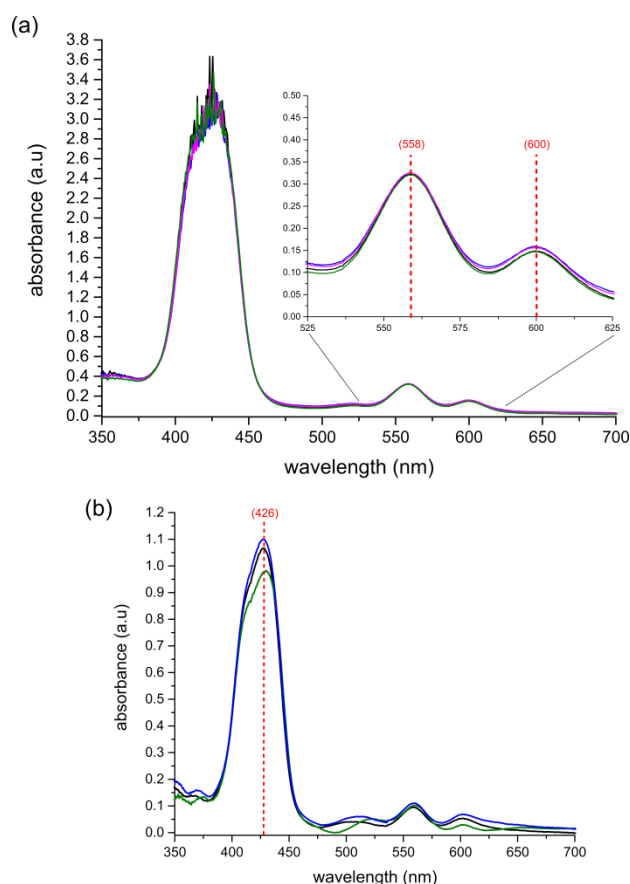


**Figure V-11; Absorbance of sensitized P1d to TiO<sub>2</sub>.** (a) 2.5  $\mu\text{m}$  TiO<sub>2</sub> sensitized with P1d from THF showing four repeats. (b) 600 nm TiO<sub>2</sub> sensitized with P1d from THF, showing three repeats.

Unlike the aromatic carboxylic groups of porphyrins, ammonium salt functional groups are not expected to sensitize  $\text{TiO}_2$ ; P3d is therefore not likely to lead to significant colouration of the  $\text{TiO}_2$ . In the same manner as  $\text{TiO}_2$  was sensitized with the carboxylic porphyrin P1d (previous results),  $\text{TiO}_2$  films 2.5  $\mu\text{m}$  were submerged in 200  $\mu\text{M}$  of P3d in THF for 3 h. As expected, minimal colour (and hence UV-Vis. absorbance) is observed when  $\text{TiO}_2$  was exposed to P3d in THF (Figure V-12). The absorbance (and slight colour) observed is likely due to the difficulty of rinsing the porphyrin out of the  $\text{TiO}_2$  nanopores following sensitization.

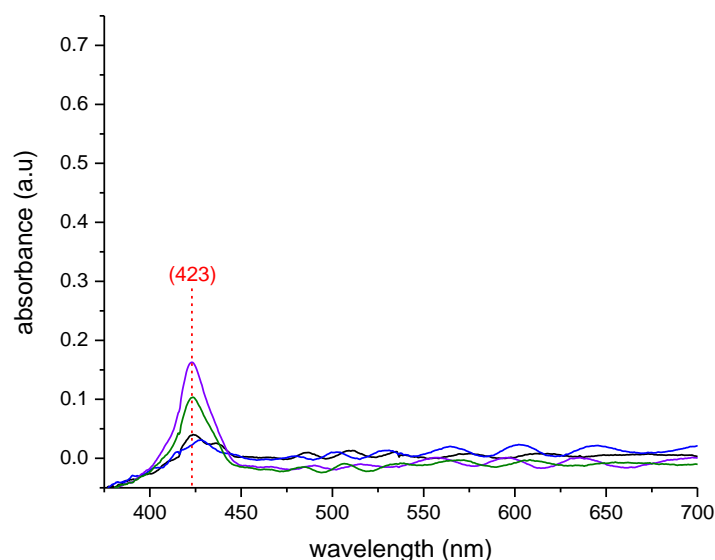


**Figure V-12; Absorbance of (attempted) sensitized P3d to  $\text{TiO}_2$ .** 2.5 $\mu\text{m}$   $\text{TiO}_2$  exposed to P3d in THF, showing four repeats.

### 2.3.2- Immobilization of porphyrin from aqueous buffer

As with sensitization of P1d to  $\text{TiO}_2$ ,  $\text{TiO}_2$  is shown to interact with P1d from aqueous buffer, likely to dissociate from carboxylic acid and exist as the tri carboxylate salt (pKa of benzoic acid being 4.2 in aqueous solution) [24, 25].  $\text{TiO}_2$  films of 600 nm and 2.5  $\mu\text{m}$  were submerged into 80  $\mu\text{M}$  of P1d in aqueous buffer for 3 d, followed by rinsing and drying before measurements. Figure V-13a displays 2.5  $\mu\text{m}$   $\text{TiO}_2$  which has been exposed to P1d in aqueous buffer, showing two distinct Q-bands at 560 and 601 nm. However, the Soret peak region is in excess of the measurable range, therefore a 600 nm  $\text{TiO}_2$  film was used to observe the Soret region (Figure V-13b). The resulting absorbance displays two distinct peaks in the Soret peak

region, occurring at 405 and 425 nm. This indicates that the porphyrin exists on the surface in two states.

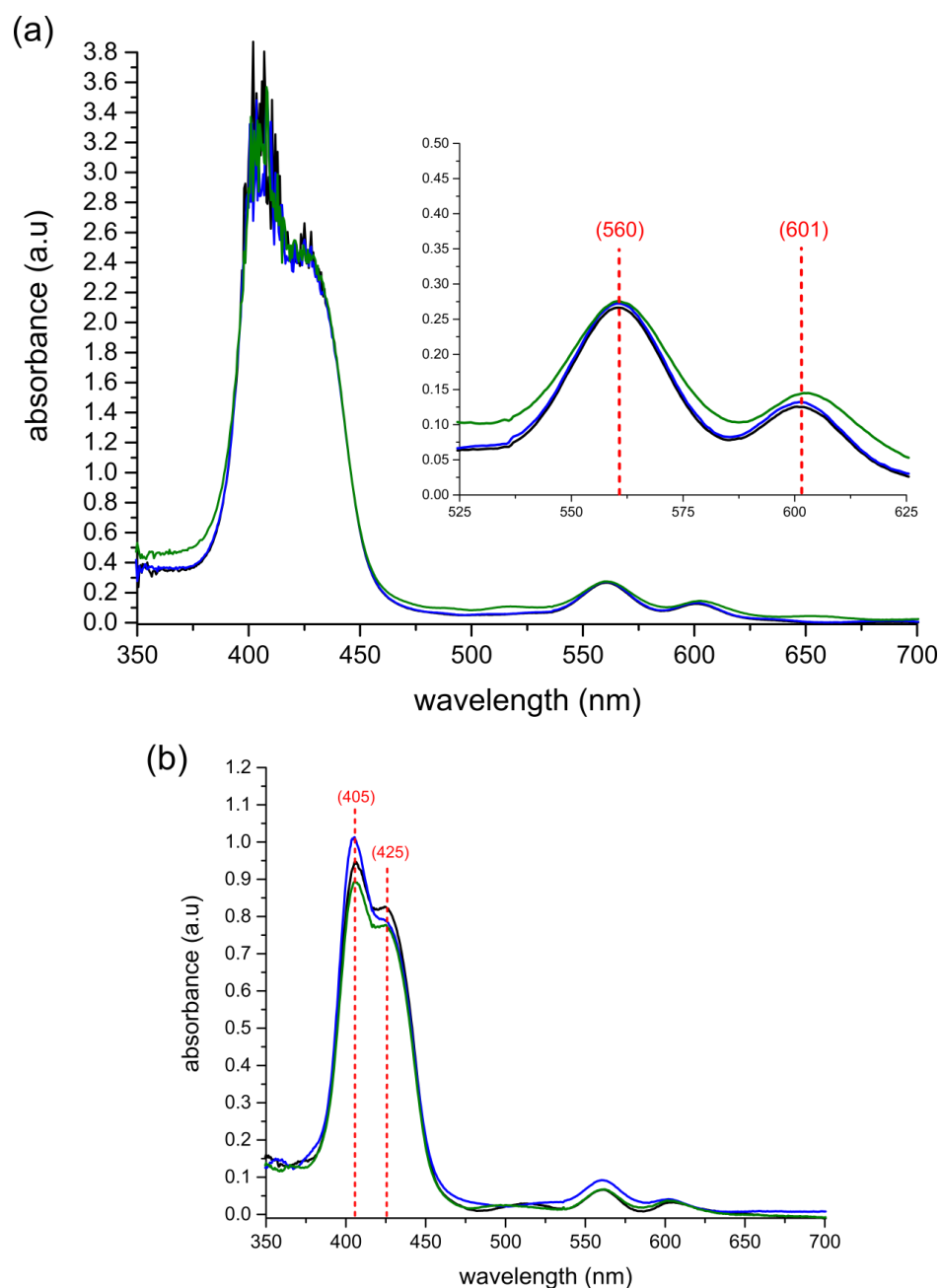


**Figure V-13; Absorbance of TiO<sub>2</sub> treated with P1d from aqueous buffer.** (a) 2.5 μm TiO<sub>2</sub> exposed to P1d from aqueous buffer, showing three repeats. (b) 600 nm TiO<sub>2</sub> exposed to P1d from aqueous buffer, showing three repeats.

As was undertaken with the carboxyl porphyrin P1d, TiO<sub>2</sub> was submerged in the ammonium salt porphyrin P3d from aqueous buffer. TiO<sub>2</sub> with a thickness of 2.5 μm was submerged in 80 μM P3d in aqueous buffer for 3 d, followed by rinsing and drying before measurements. As was observed when TiO<sub>2</sub> was treated with P3d from THF, TiO<sub>2</sub> is shown to



have negligible interaction with P3d from aqueous buffer (Figure V-14). The small peak observed at 426 nm is likely due to the difficulty of rinsing the porphyrin out of the TiO<sub>2</sub> nanopores following exposure.

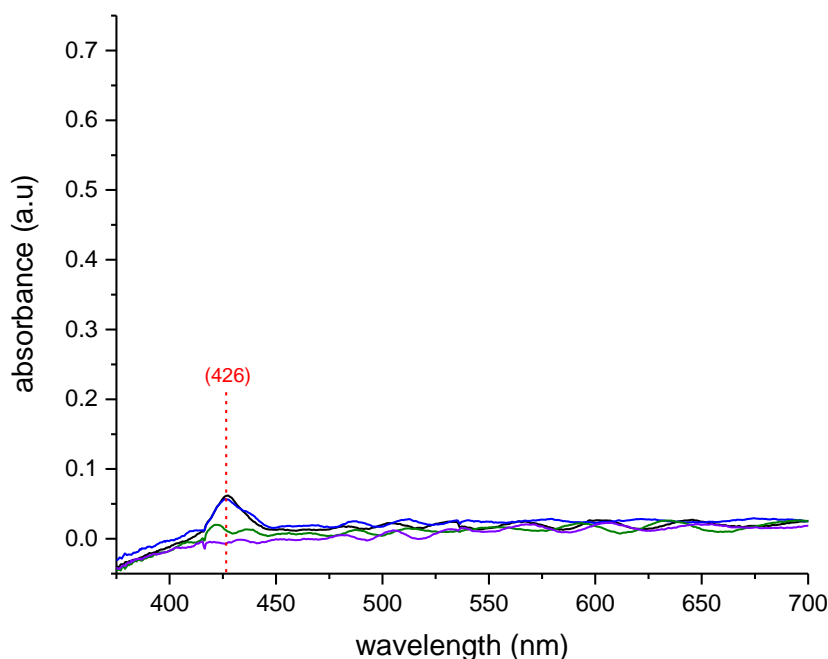


**Figure V-14; Absorbance of TiO<sub>2</sub> treated with P3d from aqueous buffer.** 2.5 $\mu$ m TiO<sub>2</sub> exposed to P3d in aqueous buffer, showing four repeats.

As P1d was observed to bind to TiO<sub>2</sub> from aqueous buffer in two distinct modes, resulting in two peaks in the absorbance profile (Figure V-13), a time-based analysis of TiO<sub>2</sub> in an aqueous buffer with P1d was carried out. Films of 600 nm were used to explore the absorbance in the Soret peak region, with 12.5  $\mu$ m films used for Q-band analysis (Figure V-15a, and inset, respectively). The thinner films (600 nm) consistently produced interference absorbance at higher wavelengths. This is notable in Figure V-15, with small absorbance peaks occurring at  $>450$  nm, with the need for thicker films further exemplified to identify porphyrin Q-band positions.

As previously observed, the Soret peak region displays two distinct peaks at 406 and 425 nm which significantly increase and/or decrease over time. This trend is also observed within the Q-bands, with the change in absorbance at 560 nm for the 12.5  $\mu$ m film shown in Figure V-15b. This shows the absorbance significantly increasing from 0-24 h, before

decreasing and becoming relatively stable between 72 and 140 h. This trend is the same as observed for the Soret peak changes on the 600 nm film. The results indicate that two states of bound P1d are possible on the TiO<sub>2</sub>, which takes >70h to become equilibrated.

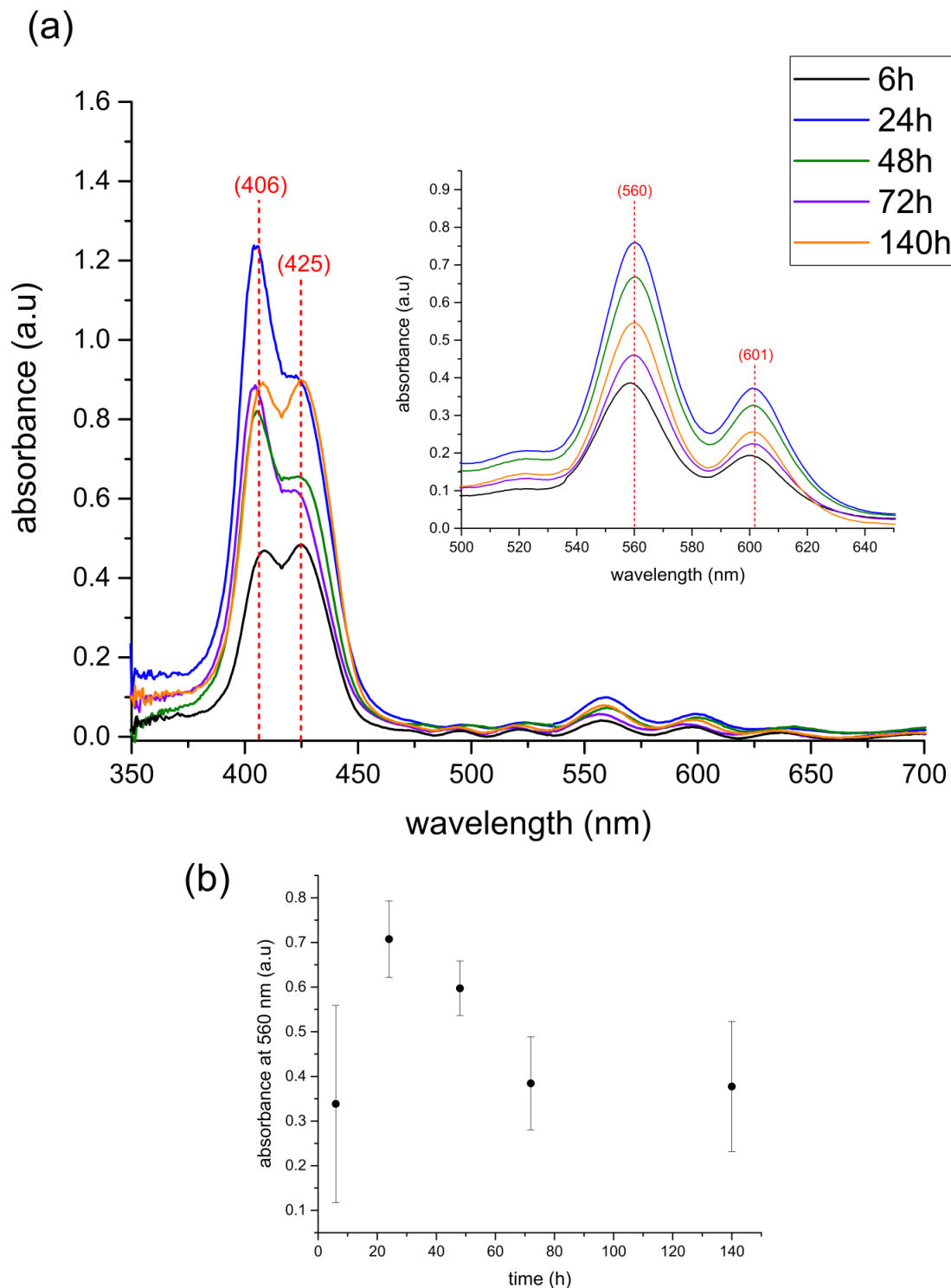


**Figure V-15; Absorbance of TiO<sub>2</sub> treated with P1d from aqueous buffer over time.** (a) 600 nm TiO<sub>2</sub> exposed to 80  $\mu$ M P1d from aqueous buffer, with inset showing Q-band region from 12.5  $\mu$ m TiO<sub>2</sub>. (b) Absorbance changes over time occurring at 560 nm (Q-band) from 12.5  $\mu$ m TiO<sub>2</sub> exposed to 80  $\mu$ M P1d in aqueous buffer. Averages shown with standard deviations, where n=4.

### 2.3.3- Immobilization of ensembles from aqueous buffer

For comparisons with results for when TiO<sub>2</sub> was exposed to P1d from aqueous buffer (previous result), TiO<sub>2</sub> was exposed to aqueous buffer with P1d ligated to maquette. As there were differences in stoichiometric relationships obtained when BT-maquette was isolated with P1d compared to when GL-maquette was isolated with P1d (shown previously), non-treated solutions of either BT- or GL-maquette mixed with P1d were used. The maquette concentration used was 46 μM, mixed with 80 μM P1d for 10 mins before use. Therefore, the stoichiometric relationship is ~1:1.75 for maquette:porphyrin, with near all porphyrin expected to be in a ligated state (with the stoichiometric limit being 1:2, as shown in previous Chapters). With the concentrations of BT- and GL-maquette with P1d being identical, the resulting absorbances on TiO<sub>2</sub> can be compared directly. 100 μl of either BT-P1d or GL-P1d ensembles were drop-casted onto 2.5 μm TiO<sub>2</sub> films, left for 3 d in a sealed petri-dish at 4 °C in the dark. The resulting films were rinsed in aqueous buffer and dried via N<sub>2</sub> gas stream before measurements.

When P1d is ligated with BT-maquette and immobilised on TiO<sub>2</sub> (Figure V-16a), the resulting absorbance is lower than compared to when P1d is ligated with GL-maquette and immobilised (Figure V-16b). As the conditions were identical, this indicates that the GL-maquette interacts with TiO<sub>2</sub> more strongly than the BT-maquette, being attributed to the increased number of lysine residues on the surface of the GL-maquette likely facilitating a stronger interaction with the surface. The absorbances obtained for either BT- or GL-P1d ensembles immobilised onto TiO<sub>2</sub> displays a distinctly sharp peak in the Soret region with two Q-bands, with the absorbance profile resembling that of when P1d is ligated with maquette in solution. However, the peak positions have all slightly blue shifted for when ensembles are immobilised on the surface compared to in solution (Chapter III), with the Soret peak shifting by ~2 nm and the Q-band peaks shifting up to 5 nm.

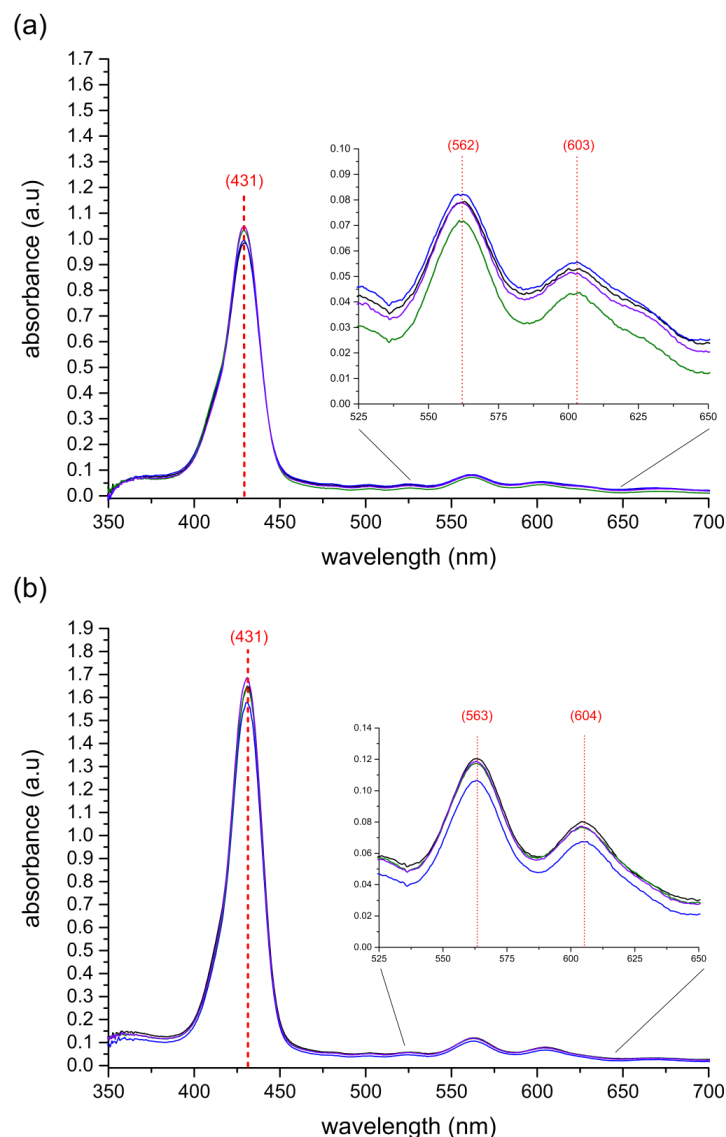


**Figure V-16; Absorbance of TiO<sub>2</sub> treated with maquette-P1d ensembles.** (a) BT-maquette mixed with P1d in a ratio of 1:1.75, drop-casted on 2.5  $\mu\text{m}$  TiO<sub>2</sub> in aqueous buffer. (b) GL-maquette mixed with P1d in a ratio of 1:1.75, drop-casted on 2.5  $\mu\text{m}$  TiO<sub>2</sub> in aqueous buffer.

As analysed for the P1d binding with TiO<sub>2</sub> from aqueous buffer over time (Figure V-15), maquette-P1d ensemble interaction with TiO<sub>2</sub> over time was assessed. As the GL-maquette was observed to interact with TiO<sub>2</sub> more strongly than the BT-maquette, a purified sample via centrifugal purification was used, with a ratio of GL-maquette to P1d being 1:1.95 (as determined previously). To compare directly to the results observed when P1d is free in aqueous buffer (Figure V-15), the GL-P1d ensemble was prepared at a porphyrin concentration of 80  $\mu\text{M}$  (with a resulting maquette concentration of 41  $\mu\text{M}$ ), with the solution drop-casted onto TiO<sub>2</sub>, rinsed in aqueous buffer and dried via N<sub>2</sub> gas stream before measurements. Two TiO<sub>2</sub>

films were used, a 2.5  $\mu\text{m}$  film for analysis of the Soret peak region, and a 12.5  $\mu\text{m}$  film for analysis of the Q-bands. Figure V-17a displays the absorbance of the films treated with GL-P1d ensembles from aqueous buffer, with the inset displaying the Q-band region from 12.5  $\mu\text{m}$   $\text{TiO}_2$ . Thicker films would be expected to limit the movement of maquettes through the nanopores, and as such, take a longer time to reach a ‘saturation’ of immobilised ensembles compared to thinner films. Therefore, the time-based analysis of the Q-band position at 564 nm on the thicker film was analysed for GL-P1d ensemble immobilisation to ascertain any movement limitations. Figure V-17b shows that GL-P1d ensembles bind to  $\text{TiO}_2$  in 24 h, with very little change occurring after saturation of the film. Therefore, immobilisation of GL-P1d ensembles to  $\text{TiO}_2$  can be assumed to reach saturation with treatment times of  $>24$  h.

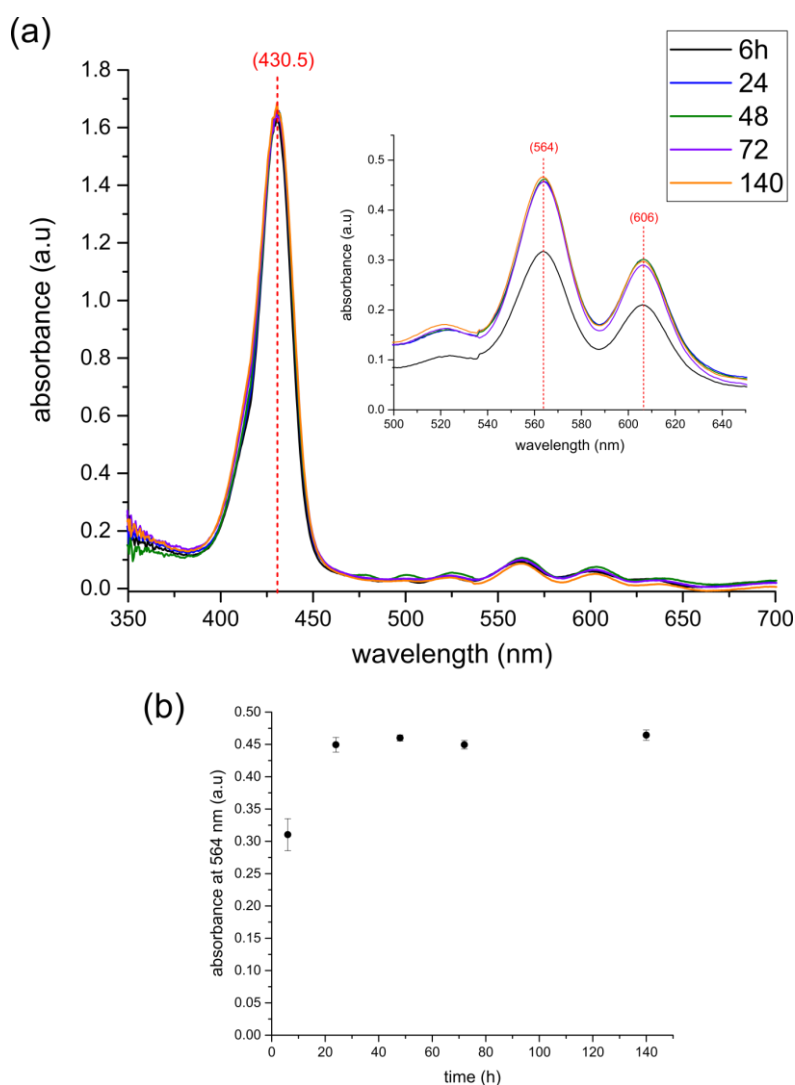


**Figure V-17; Absorbance of  $\text{TiO}_2$  treated with GL-maquette and P1d ensembles from aqueous buffer over time.** (a) 2.5  $\mu\text{m}$   $\text{TiO}_2$  exposed to purified GL-P1d ensembles (1:1.95) in aqueous buffer, with inset showing Q-band region from 12.5  $\mu\text{m}$   $\text{TiO}_2$ . (b) Absorbance changes over time at 564 nm from 12.5  $\mu\text{m}$   $\text{TiO}_2$  exposed to purified GL-P1d ensembles (1:1.95) in aqueous buffer. Averages shown with standard deviations, where  $n=4$ .

With time-based binding of GL-P1d ensembles to  $\text{TiO}_2$  known, the concentration dependence of the maquette in solution for binding to  $\text{TiO}_2$  needed to be analysed. As the maquette showed no distinct peaks within the measurable absorbance range on  $\text{TiO}_2$  films (350–700 nm), a mixture of GL-maquette and P1d in a ratio of 1:1 was used in aqueous buffer and drop-casted onto the surface of  $\text{TiO}_2$ . With the ratio of maquette to porphyrin being 1:1, the porphyrin concentration used when the surface becomes saturated (ie. no significant increase in absorbance at higher concentrations) can be translated to the concentration of maquette needed to saturation of the  $\text{TiO}_2$  film. Furthermore, with the ratio of 1:1 (maquette:porphyrin), all P1d present is expected to be ligated to maquettes. Ensembles were made to various concentrations (at ratios 1:1), and drop-casted on  $\text{TiO}_2$  for 48 h in a sealed petri dish at 4 °C in the dark, with the films rinsed in aqueous buffer and dried via  $\text{N}_2$  gas stream before measurements (Figure V-18). The Soret peak displays a significant increase at 431.5 nm, resulting from the ligated P1d, observed to plateau when concentrations are  $>20 \mu\text{M}$ . Minimal increases in absorbance were observed at concentrations  $\geq 40 \mu\text{M}$ , with small deviations with repeats (Figure V-18 inset). Therefore, for subsequent experiments, a maquette concentration of 40  $\mu\text{M}$  was used to ensure saturation of binding to  $\text{TiO}_2$  surfaces.

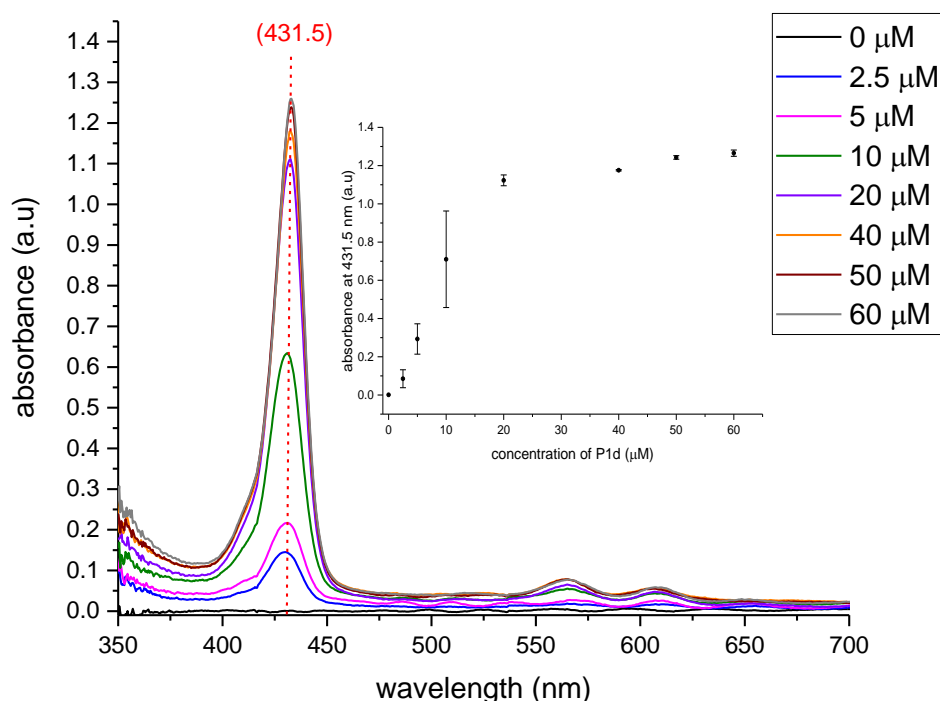


**Figure V-18; Absorbance of  $\text{TiO}_2$  treated with increasing concentrations of GL-maquette and P1d.** 2.5  $\mu\text{m}$   $\text{TiO}_2$  exposed to increasing concentrations of GL-maquette and P1d ensembles from aqueous buffer in a ratio of 1:1, with inset showing the increase in the observed Soret peak at 431.5 nm. Averages shown with standard deviations, where  $n=4$ .

With the ammonium salt porphyrin P3d showing negligible binding to  $\text{TiO}_2$  from aqueous buffer (Figure V-14), all absorbance observed from a treated  $\text{TiO}_2$  surface would invariably result from interactions of maquette-porphyrin ensemble. For comparisons with GL-P1d ensemble binding results, a GL-P3d ensemble was produced in a ratio of 1:1.95. The GL-P3d ensemble solution was drop-casted on  $\text{TiO}_2$  for 3 d, and the absorbance of the rinsed/dried treated film measured (Figure V-19). As shown, a distinct Soret peak at 430.5 nm is observed.  $\text{TiO}_2$  films of 12.5  $\mu\text{m}$  were used for analysis of the Q-bands, with two Q-band peaks observed at 563 and 604 nm (Figure V-19, inset). As was observed with GL-P1d ensemble immobilisation (previous results), these peaks are attributed to the ligated P3d. The peak positions have once again slightly blue shifted by  $\sim 2$  nm when ensembles are immobilised onto  $\text{TiO}_2$  compared to being in aqueous solution (Chapter III).

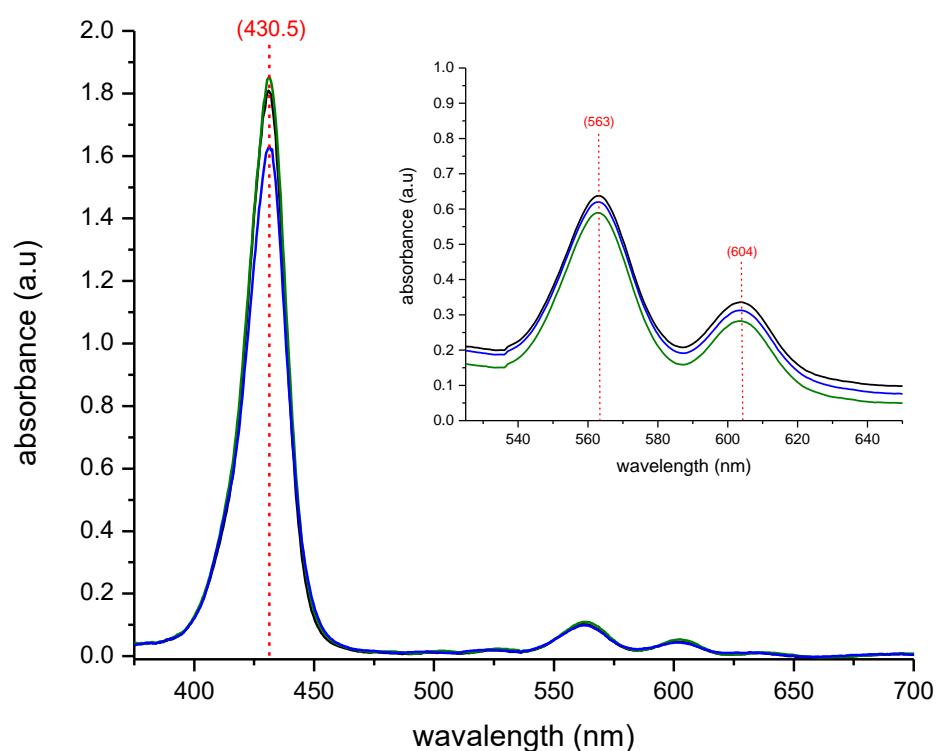


**Figure V-19; Absorbance of  $\text{TiO}_2$  treated with GL-maquette and P3d.** 2.5  $\mu\text{m}$   $\text{TiO}_2$  exposed to 41  $\mu\text{M}$  GL-maquette and 80  $\mu\text{M}$  P3d from aqueous buffer for 3 d, with the inset displaying the Q-band region of 12.5  $\mu\text{m}$   $\text{TiO}_2$  exposed to identical conditions.

## 2.4- TiO<sub>2</sub> modification for covalent attachment of maquette

Modification of TiO<sub>2</sub> was undertaken with self assembling monolayer (SAM) utilizing the strong interactions between phosphonic acid and TiO<sub>2</sub> [29], with subsequent covalent linking between maquette and the SAM. Covalent linking used here is most effective at close to physiological pHs (6.5-7.5) [33], therefore a new buffer was needed. MES buffer was used for all covalent attachment processes, being at pH 6.8.

TiO<sub>2</sub> films were submerged in either 2 mM 3-phosphonopropionic acid in ethanol or 2 mM 2-aminoethylphosphonic acid in milli-Q water for 24 h at RT, for attachment via EDC/NHS reactions (Figure V-4) or for attachment via cysteine linking (Figure V-5), respectively. Following rinsing, covalent attachment via EDC/NHS reaction (to 3-phosphonopropionic acid treated TiO<sub>2</sub>) was undertaken by drop-casting a purified solution of GL-P1d (at a ratio of 1:1.96), or GL-maquette without porphyrin onto the electrode. The electrode was sealed in a petri dish with parafilm, covered in foil and left in the fridge (4°C) for 24 h. Following this, 50 µl of EDC (36 mM) and NHS (17mM) in MES buffer was drop-casted on top of the sample, and left at RT for a further 24 h. Electrodes were then rinsed by dipping into aqueous buffer and drying via N<sub>2</sub> gas stream before further use.

Covalent attachment via 3-(maleimido)propionic acid N-hydroxysuccinimide ester with cysteine residues was undertaken with TiO<sub>2</sub> modified with 2-aminoethylphosphonic acid. 1.0 mM 3-(maleimido)propionic acid N-hydroxysuccinimide ester was dissolved in DMSO and drop-casted (100 µl) onto the modified surface for 3 h at RT. Following this, the surface was rinsed and dried with N<sub>2</sub> gas-stream before use. Either the *cys*GL-maquette by itself (at 40 µM) or the pre-formed ensembles (42 µM *cys*GL-maquette mixed with 80 µM porphyrin) were prepared in MES buffer. Solutions were drop-casted onto the surface and left for 24 h. For comparisons, if no maquette was present (ie. porphyrin interaction with the modified surface), the surface was exposed to MES buffer under the same conditions as if maquette were present. The electrodes were then rinsed in aqueous buffer and dried via N<sub>2</sub> gas-stream before measurements.

### 2.4.1- 3-Phosphonopropionic acid modification for NHS-EDC reaction

As the interactions between GL-maquette and TiO<sub>2</sub> previously observed were predominantly electrostatic, the strength of binding to the surface and maquette arrangement can be controlled through the use of covalent linking. NHS-EDC reactions are well known for



coupling carboxylic groups to primary amines of proteins (or in this case maquettes, Figure V-4). The treatment of oxide surfaces (such as  $\text{TiO}_2$ ) with phosphonic acids (such as 3-phosphonopropionic acid) is well characterised [29, 34, 35], with phosphonic groups self-assembling and binding to  $\text{TiO}_2$ , resulting in a modified surface with carboxylic functional groups. As EDC-NHS reactions (as shown in Figure V-4) are well established in buffered solutions closer to physiological pHs (6.5-7.5), MES buffer was used. The purified GL-P1d (1:1.96) ensembles in MES buffer was drop-casted onto 3-phosphonopropionic acid treated  $\text{TiO}_2$ , followed by addition of EDC-NHS reactants (as stated previously). The resulting treated  $\text{TiO}_2$  was rinsed in aqueous buffer and dried, and the absorbance spectrum measured (Figure V-20). A distinct peak with the Soret region is observed, with a peak position of 432 nm, along with two Q-bands at 564 and 606 nm. These peak positions are near identical to the peak position of P1d ligated to GL-maquette in solution.

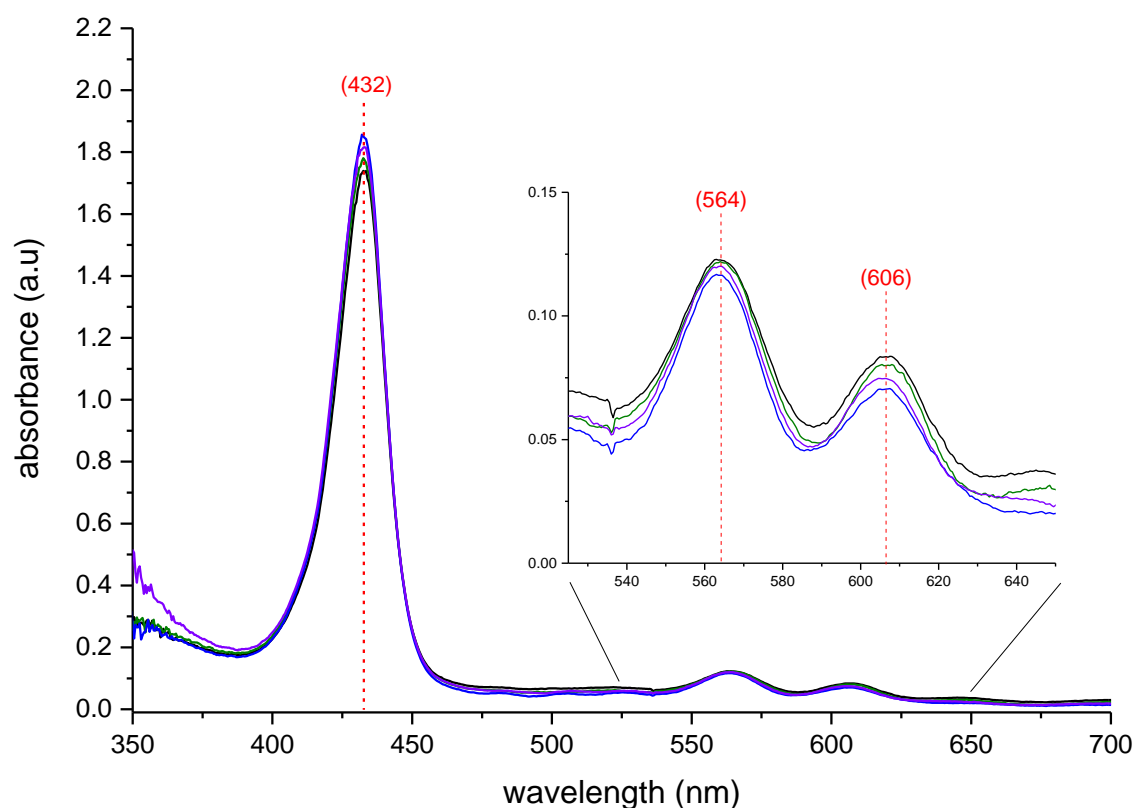


**Figure V-20; Absorbance of modified  $\text{TiO}_2$  covalently attached GL-P1d ensembles via NHS-EDC.**  $2.5 \mu\text{m}$   $\text{TiO}_2$  was modified with 3-phosphonopropionic acid, followed by exposure to purified GL-P1d (1:1.96) ensembles from MES buffer, with subsequent addition of NHS-EDC reactants. Films were rinsed and dried before absorbance measurements.

In contrast to covalently attaching pre-assembled GL-P1d ensembles to TiO<sub>2</sub> (as shown previously), a maquette can be covalently attached to the modified TiO<sub>2</sub>, followed by incorporation of the porphyrin. GL-maquette was covalently attached to the 3-phosphonopropionic acid treated TiO<sub>2</sub> (as was undertaken previously with the pre-formed ensembles), with subsequent rinsing and exposure to the porphyrin (P1d) from a solution. However, to determine if the porphyrin has ligated to the covalently attached maquette as opposed to interacting with the modified surface, 3-phosphonopropionic acid treated TiO<sub>2</sub> was also exposed to P1d. Figure V-21a shows the resulting absorbance of when GL-maquette is covalently attached to modified TiO<sub>2</sub> via NHS-EDC reactions, followed by submerging the films into an aqueous buffer of P1d. As observed, the Soret peak region is centred at 431 nm, with the specific peak position not known due to reaching limitations of measurements. The two observed Q-bands have peak positions at 563 and 605 nm. To compare the potential ligation of P1d to the covalently attached GL-maquette, the experiment was repeated with the single variable that GL-maquette was not in the buffer for attachment (ie. how P1d interacts with the modified surfaces when no maquette is present). As shown in Figure V-21b, two distinct peaks in the Soret peak region are observed, at 406 and 426 nm, along with two distinct Q-bands at 561 and 602 nm. This indicates that P1d can interact with the modified surface of TiO<sub>2</sub> whether or not maquette is covalently attached to the surface, however, produces a double peak when maquette is absent.

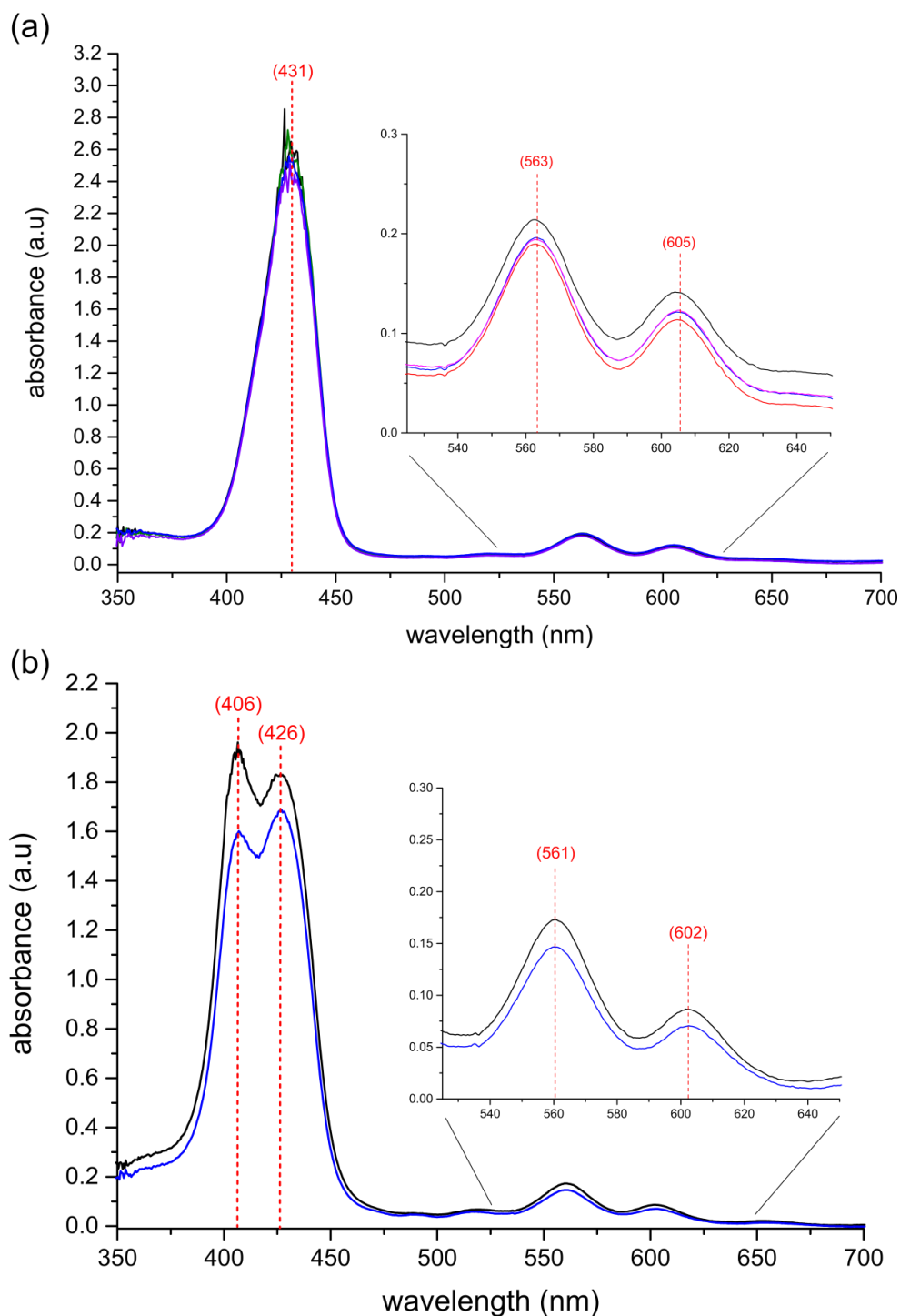


**Figure V-21; Absorbance of modified TiO<sub>2</sub> reacted with NHS-EDC and exposed to P1d.** (a) TiO<sub>2</sub> modified with 3-phosphonopropionic acid reacted with 40 μM GL-maquette in MES buffer via NHS-EDC reaction, followed by submersion into a solution of P1d in aqueous buffer (b) MES buffer on TiO<sub>2</sub> modified with 3-phosphonopropionic acid, with NHS-EDC reactants added, followed by submersion into a solution of P1d in aqueous buffer. Samples are on 2.5 μm TiO<sub>2</sub>, with repeat of samples shown in each figure.

### 2.4.2- 2-Aminoethylphosphonic acid modification for cysteine-maleimide reaction

As was the case for the previous covalent attachment of maquette to TiO<sub>2</sub> via NHS-EDC reactions, sulfhydryl groups on cysteine residues can be exploited to covalently link proteins to amine groups (Figure V-5). Treatment of TiO<sub>2</sub> with 2-aminoethylphosphonic acid via the phosphonic acid group is well characterised [29, 34, 35] (as was the case with 3-phosphonopropionic acid), self-assembling and binding to TiO<sub>2</sub> resulting in a surface with amine functional groups. The resulting amine groups are then functionalised with 3-maleimidopropionic acid *N*-hydroxysuccinimide ester, producing a modified surface, which reacts with sulfhydryl groups (as shown in Figure V-5). Similarly to the EDC-NHS reactions, the sulfhydryl reaction works best at physiological pHs (6.5-7.5), therefore MES buffer was used for a solution at pH 6.8. Furthermore, the *cysGL*-maquette sequence was employed, differing only through the shortening of the loop-region and the addition of a single cysteine residue in a loop section (Figure V-6). Therefore, the single cysteine is the only residue with a sulfhydryl group, and hence a known mode of covalent attachment.

To analyse maquette-porphyrin ensemble binding, purified *cysGL*-P1d ensembles in MES buffer (in a ratio of 1:1.96) were drop-casted onto the 2-aminoethylphosphonic acid/3-maleimidopropionic acid *N*-hydroxysuccinimide ester treated TiO<sub>2</sub> surface for 3 days. The resulting modified TiO<sub>2</sub> was rinsed in aqueous buffer and dried, with the absorbance spectrum obtained (Figure V-22). Absorbance shows a distinct peak within the Soret region at 431 nm, along with two Q-bands at 564 and 605 nm. These peak positions are near identical to the peak position of P1d ligated to *GL*-maquette in solution, and also for when *GL*-P1d ensembles were covalently attached to TiO<sub>2</sub> via NHS-EDC shown previously (Figure V-20).

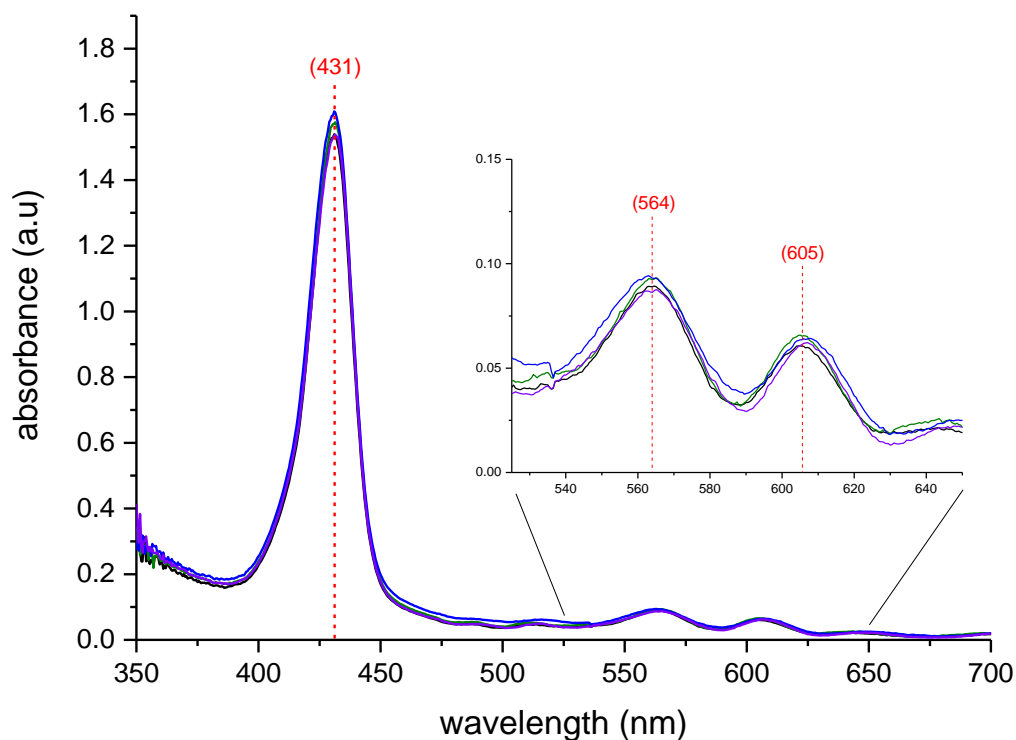


**Figure V-22; Absorbance of modified TiO<sub>2</sub> with covalently attached *cysGL*-P1d ensembles via cysteine-maleimide.** 2.5  $\mu\text{m}$  TiO<sub>2</sub> was modified with 2-aminoethylphosphonic acid, followed by exposure to 3-maleimidopropionic acid *N*-hydroxysuccinimide ester, with subsequent binding of purified *cysGL*-P1d ensembles (1:1.96) from MES buffer. Films were rinsed and dried before absorbance measurements.

In contrast to attaching the *cysGL*-P1d ensembles onto a modified TiO<sub>2</sub> surface, the *cysGL*-maquette can be initially covalently attached, with subsequent addition of the porphyrin. This arrangement links the maquette to the treated TiO<sub>2</sub> surface (with 2-aminoethylphosphonic acid/3-maleimidopropionic acid *N*-hydroxysuccinimide ester, as described previously) via the cysteine residue. Subsequent exposure to porphyrin would result in either porphyrin ligating within the maquette or association with the modified surface. Figure V-23a shows the absorbance of TiO<sub>2</sub> which has *cysGL*-maquette attached to the modified TiO<sub>2</sub> surface via the cysteine residue, with the resulting surface submerged in an aqueous buffer of P1d (shown in blue). As a control, a similar procedure was undertaken, except without using the maquette in the solution during the attachment step (shown in green). It is apparent that P1d has minimal interaction with the modified surface, with a small peak centred at 426 nm. This peak arises from interactions between P1d and the treated TiO<sub>2</sub> surface, potentially with the nitrogen groups on the surface interacting with the zinc of the porphyrin. In stark contrast, when the *cysGL*-maquette is covalently attached to the surface and subsequently exposed to P1d in solution, a

substantial absorbance is observed, having over an 8-fold increase in Soret peak absorbance intensity compared to when no maquette was used. Two distinct Q-bands are observed at 565 and 607 nm when *cys*GL-maquette is present, with a peak in the Soret region reaching the measurable limitations. Therefore, a thinner TiO<sub>2</sub> film was prepared under the same conditions to analyse the Soret peak (Figure V-23b). It is apparent that the Soret peak has a maximum absorbance at 432 nm, and, in conjunction with the Q-bands, is near identical to GL-P1d ensembles in solution.

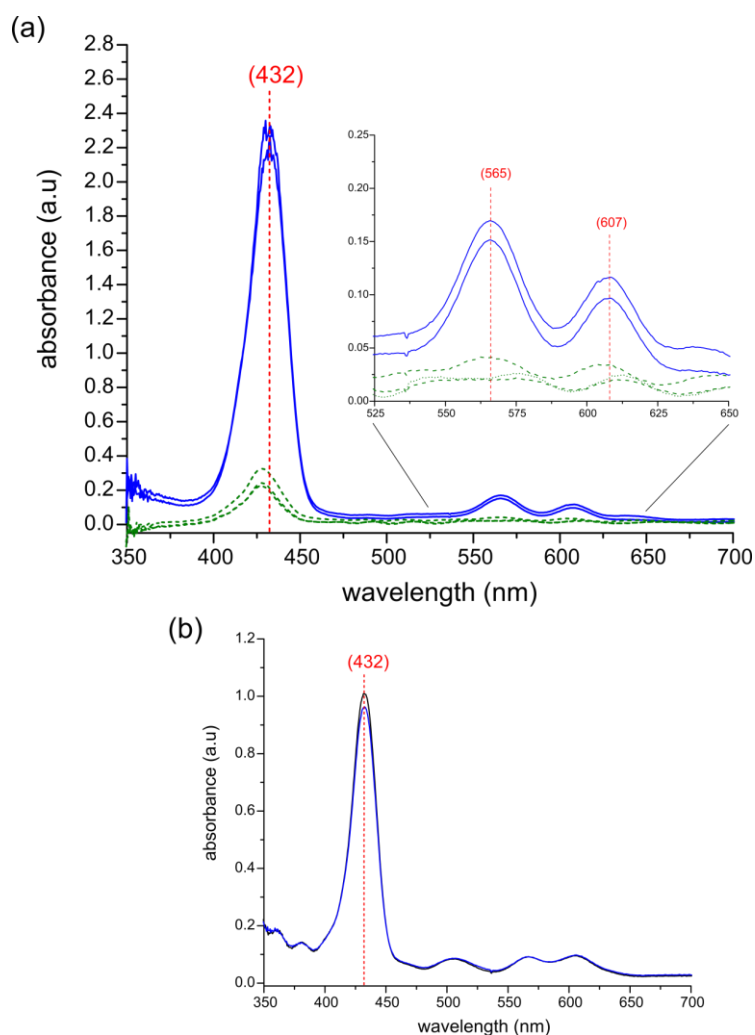


**Figure V-23; Absorbance of treated TiO<sub>2</sub>, reacted with maleimide and exposed to P1d.** (a) Modified 2.5 μm TiO<sub>2</sub> with *cys*GL-maquette attached from MES buffer, followed by submersion into a solution of P1d in aqueous buffer (blue lines). Comparison with modified 2.5 μm TiO<sub>2</sub> exposed to MES buffer, followed by submersion into a solution of P1d in aqueous buffer (green lines). (b) Modified 600 nm TiO<sub>2</sub> with GL-maquette attached from MES buffer, followed by submersion into a solution of P1d in aqueous buffer.

For direct comparison with the previous results using the carboxylic porphyrin (P1d) and 2-aminoethylphosphonic/3-maleimidopropionic acid *N*-hydroxysuccinimide treated TiO<sub>2</sub>, the ammonium salt porphyrin (P3d) was used for interactions with the modified surface. Similarly, as was described previously for P1d, the treated TiO<sub>2</sub> surface either had *cys*GL-

maquette covalently attached prior to exposure to P3d from aqueous buffer, or the surface was exposed to MES buffer prior to exposure to P3d from aqueous buffer. As is shown, when *cysGL*-maquette is covalently attached with subsequent exposure to P3d, a sharp peak in the Soret region at 433 nm is observed, with two Q-bands at 565 and 607 nm (blue lines, Figure V-24). In contrast, when no maquette is present on the surface, the treated  $\text{TiO}_2$  exposed to P3d shows a Soret peak with a maximum at 433 nm, with Q-band peak positions similar to the maquette/P3d positions, however, distinct alterations in peak intensities are apparent between each Q-band (green dotted lines, Figure V-24). Appearance of an absorbance band at  $\sim 500$  nm also became visible when P3d was interacting directly with the modified surface. The Soret peak is shown to increase by approximately 2.5-fold when maquette is present prior to exposure to P3d. This indicates that P3d is able to interact with the modified surface more strongly compared to when maquette is not present. The Soret peak position and intensity indicates that P3d is interacting with the modified surface, likely through a zinc-nitrogen ligation, from P3d central metal to the nitrogen groups present on the treated  $\text{TiO}_2$  surface (Figure V-5).

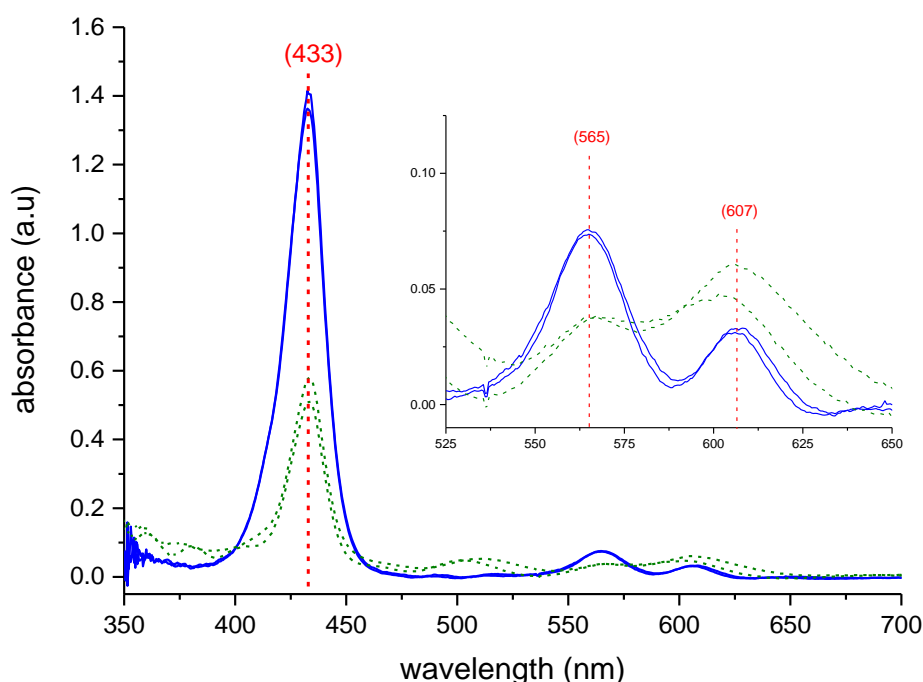


**Figure V-24; Absorbance of modified  $\text{TiO}_2$ , reacted with maleimide and exposed to P3d.** Modified  $2.5 \mu\text{m}$   $\text{TiO}_2$  with *GL*-maquette attached from MES buffer, followed by submersion into a solution of P3d in aqueous buffer (blue lines). Comparison with modified  $2.5 \mu\text{m}$   $\text{TiO}_2$  exposed to MES buffer, followed by submersion into a solution of P3d in aqueous buffer (green lines).

## 2.5- Resonance Raman of treated TiO<sub>2</sub> electrodes

All samples for resonance Raman spectroscopy were prepared in Australia, with measurements and analysis carried out by Jonathan E. Barnsley under supervision of Prof. Keith C. Gordon of the University of Otago, New Zealand (collaborators). As was shown in Chapter III, resonance Raman spectroscopy is used to analyse changes in ‘core size’ marker bands of the porphyrins, known to be sensitive to changes in environment and presence of axial ligands. Changes in absorbance couple with marker band changes provides strong evidence for porphyrin maquette interactions, however, as shown below, the determination of porphyrin marker bands when immobilised onto TiO<sub>2</sub> is more difficult to ascertain compared to solution based porphyrin. Two wavelengths were used to analyse marker bands to increase the possibilities of observing marker bands and observing relative intensities.

As P1d was observed to interact with TiO<sub>2</sub> directly from aqueous buffer as well as binding to TiO<sub>2</sub> when ligated with maquettes producing absorbance differences, resonance Raman spectroscopy was employed to differentiate binding modes. Direct comparisons on transparent 2.5 μm TiO<sub>2</sub> was analysed via resonance Raman, with P1d either sensitized to the surface, P1d bound from aqueous buffer, or P1d-GL ensembles (purified solution in a ratio 1:1.96) exposed to TiO<sub>2</sub> (Figure V-25). For controls, TiO<sub>2</sub> exposed to maquette (with no P1d) was analysed as well as ‘bare’ TiO<sub>2</sub>. As shown in Figure V-25, no peaks are observed for the bare TiO<sub>2</sub> or for TiO<sub>2</sub> with GL-maquette attached to the surface at the high wavenumbers. Therefore, distinct peaks come directly from P1d on the surface. When P1d is bound from THF or aqueous buffer, no difference in the spectra is observed. Furthermore, no significant spectroscopic change of P1d ‘core size’ marker bands is observed for P1d on TiO<sub>2</sub> or when ligated to maquette. However, a small shift in the 1352 cm<sup>-1</sup> is observed, being a marker band showed previous to display distinct changes when P1d is with maquette compared to free in aqueous buffer (Figure III-46). The specific zinc-histidine stretch at lower wavenumbers (150-250 cm<sup>-1</sup>) is not discernible from the background.



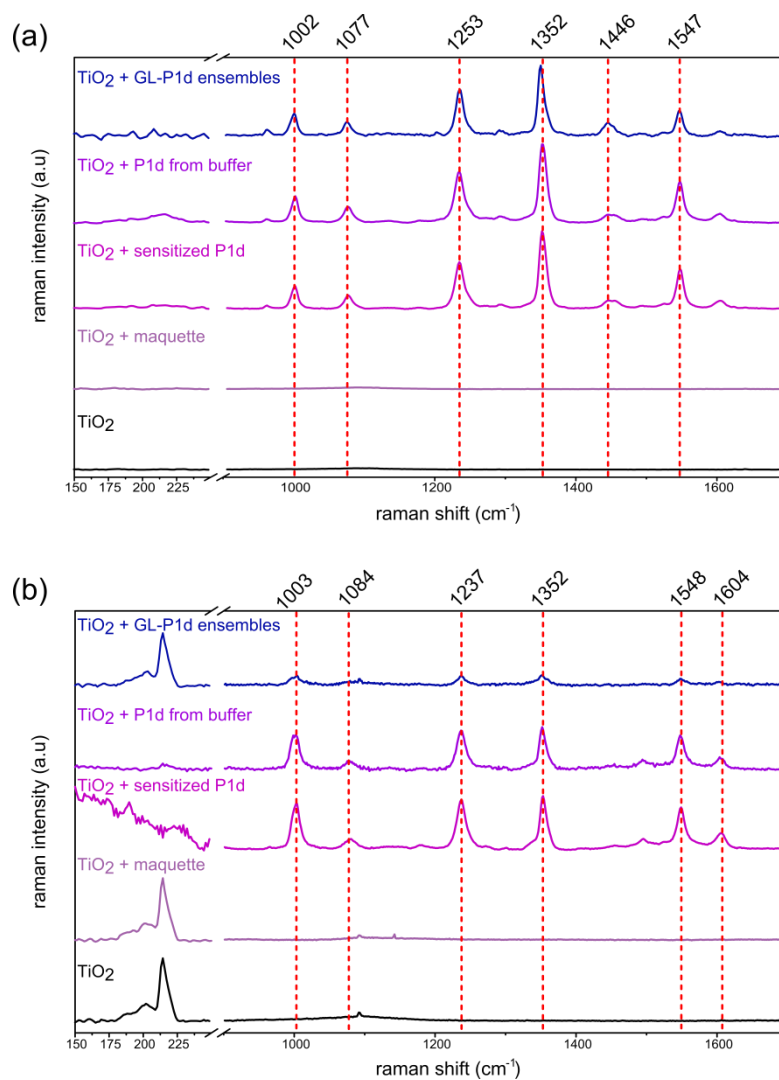


**Figure V-25; Resonance Raman of TiO<sub>2</sub> with GL-maquette and P1d.** 2.5  $\mu\text{m}$  TiO<sub>2</sub> modified with combinations of maquette and P1d. As shown, measured samples are bare TiO<sub>2</sub>, maquette electrostatically attached to TiO<sub>2</sub> from aqueous buffer, TiO<sub>2</sub> sensitized with P1d from THF, P1d bound to TiO<sub>2</sub> from aqueous buffer, and a 1:1.96 GL:P1d ensembles bound to TiO<sub>2</sub> from aqueous buffer. (a) Samples measured at 406 nm. (b) Samples measured at 448 nm.

### 3- Discussion; Immobilization onto TiO<sub>2</sub> Electrodes

Binding of porphyrins and maquette-porphyrin ensembles onto TiO<sub>2</sub> is needed to be determined before potential applications in photo-induced devices. Furthermore, as carboxylates are known to interact with the oxide surface (as described previously), the analysis of results needs to determine if the porphyrin which is ligated within maquettes has; (1) remained in a ligated state when immobilized, and (2) the maquette is binding to the oxide surface as opposed to the functional groups of the porphyrin. Furthermore, covalent attachment of maquettes to a modified TiO<sub>2</sub> surface needs to answer the same two questions (stipulated previously).

#### 3.1- Binding of P1d directly to TiO<sub>2</sub>

Sensitization of P1d directly to TiO<sub>2</sub> is expected to occur through bidentate chelating and/or bidentate bridging binding modes (Figure V-2) [28]. Despite P1d containing three carboxylic functional groups in the para positions, binding occurs via a maximum of two of the groups per molecule (ie. the porphyrin cannot ‘lie flat’ on the surface with all three carboxylic groups binding) [36]. The binding of P1d to TiO<sub>2</sub> from THF produces a broad Soret peak centred at 428 nm with two Q-bands observed at 558 and 600 nm (Figure V-11).

In contrast to binding from organic solvents, porphyrin binding to TiO<sub>2</sub> from aqueous buffer is not well described in the literature. It is known that hydrophilic porphyrins will aggregate on oxide surfaces, such as TiO<sub>2</sub>, from an aqueous solvent, resulting in a peak at ~400 nm [37, 38]. When P1d is bound to TiO<sub>2</sub>, a peak at 405-406 nm is observed, likely due to the aggregation of P1d on the surface (Figure V-13) The second peak at 425 nm likely results from the Soret peak of the monomeric (non-aggregated) P1d interacting with the surface. As observed with P1d binding to TiO<sub>2</sub> over time (Figure V-15), the absorbance peak positions changes significantly over time (for <72 h). This suggests that, as the P1d exists in both aggregated and monomeric states on the surface, it takes >72 h for an equilibrium between states to be reached. The Q-bands observed when P1d is bound to TiO<sub>2</sub> are near identical to those observed when P1d is sensitized to the surface, being at 560 and 600-601 nm.

#### 3.2- Binding of maquette-P1d ensembles

In contrast to the binding of P1d directly to TiO<sub>2</sub>, P1d can be associated with the surface via the ligation of maquette. Proteins are known to bind to oxide surfaces, such as TiO<sub>2</sub>

predominantly via the lysine residues on the protein [7-10]. As such, the maquettes are expected to bind to TiO<sub>2</sub> predominantly through these residues (lysine).

With the BT-maquette containing less lysine residues on the hydrophilic surface of the helices (and an overall more negative surface) compared to the GL-maquette (as shown in Chapter III), the GL-maquette is hypothesised to interact with TiO<sub>2</sub> more strongly. This hypothesis is shown to be true, as is shown in Figure V-16. Either BT-P1d or GL-P1d ensembles (both containing the same ratio and concentrations) were drop-casted onto TiO<sub>2</sub> concurrently, with subsequent rinsing and drying before measurements. Therefore, it can be assumed that any differences in the resulting absorbances come from the differences in maquette-TiO<sub>2</sub> interaction. The maximum absorbance for GL-P1d ensembles on TiO<sub>2</sub> was greater than that for BT-P1d ensembles on TiO<sub>2</sub>, indicating that a higher quantity of GL-P1d ensembles is present on the surface (Figure V-16). This is highly likely due to the fact that the GL-maquette contains more residues that influence stronger binding to the surface, as well as the BT-maquette being more easily removed during the rinsing step as a result of its weaker interaction. Therefore, for all subsequent experiments, GL-maquette was used.

To ensure that there is no non-ligated porphyrin interacting with TiO<sub>2</sub>, and hence contributing to the apparent absorbance, purified samples of maquette-porphyrin were needed to be produced (Section 2.2). Furthermore, as the absorbance is a direct indication of porphyrin present, the centrifugal filtration method was used to purify GL-P1d ensembles (Figure V-10), which results in ~98 % GL-maquettes containing two ligated porphyrins. This resulting purified ensemble solution can hence forth be used for TiO<sub>2</sub> interactions and direct comparisons with non-ligated porphyrin solutions and TiO<sub>2</sub> binding. When the purified GL-P1d ensembles are bound to TiO<sub>2</sub> from aqueous buffer (Figure V-17), a Soret peak is observed at 430.5 nm, with two distinct Q-bands at 564 and 606 nm, being highly similar to the absorbance profile when ensembles are in aqueous buffer. As mentioned previously, this can be compared directly to P1d binding to TiO<sub>2</sub> from aqueous buffer. Two distinct peaks within the Soret region are evident when P1d binds to TiO<sub>2</sub> from aqueous buffer (Figure V-13), at 405 and 425 nm with Q-bands at 560 and 601 nm, discussed previously. Therefore, a distinct shift of 4-6 nm in peak positions is apparent for when P1d is present with GL-maquette before association with TiO<sub>2</sub>. Furthermore, the absorbance spectrum when GL-P1d is bound to TiO<sub>2</sub> displays neither peaks at ~405 nor 425 nm, being apparent when P1d is in a non-ligated state and binding to TiO<sub>2</sub>.

This gives strong evidence that P1d has remained ligated within the maquette, with the maquette associating with the surface.

Further indication that porphyrins remain ligated within maquettes, with maquettes subsequently binding to TiO<sub>2</sub> is evident with TiO<sub>2</sub> modification and covalent binding modes. The lysine residues of the maquette can be covalently linked to TiO<sub>2</sub> surfaces modified with appropriate SAMs such as 3-phosphonopropionic acid (3-PPA) via EDC-NHS reactants (Figure V-4). When purified GL-P1d (1:1.96) ensembles are reacted with 3-PPA treated TiO<sub>2</sub> via EDC-NHS, a Soret peak position at 432 nm is observed, along with two Q-bands at 564 and 606 nm (Figure V-20). These peak positions are near identical to the peak positions of P1d ligated to GL-maquette in solution. However, when P1d is exposed to the modified surface when no maquette is present, two distinct peaks in the Soret peak region are observed, at 406 and 426 nm, along with two Q-bands at 561 and 602 nm (Figure V-21b). This resembles the binding between P1d and 'bare' TiO<sub>2</sub> from aqueous buffer, with the peak at 406 nm arising from P1d aggregating on the surface, as discussed previously. In contrast, GL-maquette can be linked to 3-PPA treated TiO<sub>2</sub> via EDC-NHS with no porphyrin present. Subsequent to covalent binding of maquette to the surface, the treated surface can be exposed to a solution of porphyrin (P1d), with the resulting absorbance shown in Figure V-21a. This treatment process produces an absorbance with a Soret peak centred at 431 nm and two Q-bands at 563 and 605 nm. These absorbance peaks are again near identical to the peaks of P1d ligated to maquette in solution, in conjunction to the resulting absorbance of pre-formed GL-P1d ensemble immobilization on TiO<sub>2</sub> presented previously. Therefore, although P1d can bind to the 3-PPA treated surface, when maquette is present the distinct Soret peak with two Q-band positions indicate that P1d; (1) remains ligated within the maquette with covalent attachment of the ensemble, or (2) can ligate within maquettes that are pre-attached to the surface to form ensembles.

In contrast to the EDC-NHS reactions, the cystein-maleimide reaction allows for a single mode of binding, as the *cys*GL-maquette only has a single sulfhydryl group capable of covalent linking (Figure V-5). Similar to the EDC-NHS binding mode, cystein-maleimide binding of sulfhydryl groups to TiO<sub>2</sub> requires the surface to be modified with an appropriate SAM, such as 2-aminoethylphosphonic acid (2-APA). When purified *cys*GL-P1d (1:1.96) ensembles are covalently attached to the 2-APA modified surface, a Soret peak is observed at 431 nm, along with two Q-bands at 564 and 605 nm (Figure V-22). These peaks are near identical to that for absorbance peaks when GL-P1d ensembles were attached to TiO<sub>2</sub> via EDC-

NHS. However, when no maquette is present during the process, P1d is observed to show minimal signs of interaction with the modified surface (Figure V-23). In stark contrast, if *cysGL*-maquette is attached to the modified surface with subsequent exposure to a solution of P1d, significant absorbance is observed with a Soret peak at 432 nm and two Q-bands at 565 and 607 nm (Figure V-23). These peak positions are identical to that for when P1d is ligated to GL in solution. The resulting Soret peak intensity corresponds closely to the quantity of porphyrin on the surface, with the intensity of the absorbance peak increasing by ~10 fold. Therefore, as P1d interacts with the modified surface weakly, the intense absorbance produced when maquette is present gives strong evidence that P1d is ligating to the covalently linked *cysGL*-maquette to form ensembles on the TiO<sub>2</sub> surface.

As was with resonance Raman spectroscopy from solutions presented in Chapter III, all spectroscopic measurements were undertaken (and resulting spectra analysed) at the University of Otago by Jonathan E. Barnsley under the supervision of Prof. Keith C. Gordon. As was apparent with the ‘core size’ marker bands of the porphyrins significantly altering due to the ligation and hydrophobic partitioning within the maquette as was apparent in Chapter III, it is expected that these altered marker bands would be visible when ensembles were immobilized onto TiO<sub>2</sub>. Resonance Raman results (Figure V-25), however, do not show significant ‘core size’ marker band changes when GL-P1d ensembles are immobilized onto TiO<sub>2</sub> compared to when P1d is bound directly to the surface. However, a small shift in the 1352 cm<sup>-1</sup> band is observed, but not conclusive evidence on its own. The distinctly lacking spectral peaks is likely the culprit for the inconclusive marker band shifts, being due to the difficulty of using relatively low concentrations of porphyrin on the ‘film’ in conjunction with TiO<sub>2</sub> interactions with the incident laser. Furthermore, the obtained spectra from TiO<sub>2</sub> presented here appears desolate compared to the spectra obtained from solution, highlighting the difficulties in determining small changes in ‘core size’ marker bands of the porphyrin when immobilized onto TiO<sub>2</sub>.

### 3.3- Binding of maquette-P3d ensembles

As previously observed for the sensitization of the ammonium salt porphyrin P3d on TiO<sub>2</sub> from both organic solvent (Figure V-12) and aqueous buffer (Figure V-14), interaction with the porphyrin and TiO<sub>2</sub> is weak. Nonetheless, significant absorbance is produced when TiO<sub>2</sub> is exposed to GL-P3d ensembles (Figure V-19), with a distinct Soret peak at 430.5 nm and two Q-band peaks observed at 563 and 604 nm. This represents a ~35 fold increase in porphyrin on the surface when maquette is present. Therefore, this increase must result from

the ligation of the porphyrin to the maquette and remaining as an ensemble once immobilized on the surface. This is further supported by the shifts in the Soret and Q-band positions for when P3d is ligated with maquette and immobilized on the surface, with the peak positions corresponding to the peak positions produced when P3d is ligated to maquette in solution (Chapter III).

In contrast to the ‘bare’ TiO<sub>2</sub>, the modified surfaces used for the cysteine-maleimide reactions interact with P3d in the aqueous buffer (Figure V-24). Therefore, if maquette is covalently attached to the modified surface before exposure to P3d, any absorbance produced could originate from a combination of P3d being bound directly to the modified surface and ligation with the maquette. Despite this, when maquette is pre-attached to the surface and subsequently exposed to a solution of P3d, the resulting absorbance intensity of the Soret peak increases by ~2.8 fold when compared to a surface with no pre-attachment of maquette (Figure V-24). It is notable that the peak positions of the Soret peak are identical whether or not maquette is pre-attached, occurring at 433 nm. This peak position is synonymous with P3d being in a ligated state (as described in Chapter III). Therefore, when maquette is not pre-attached to the surface, P3d is likely ligated to the nitrogen present on the modified surface (see schematic Figure V-5). The intensities of the two P3d Q-bands are observed to become different when maquette is employed compared to when maquette is absent. These intensity variations are due to differences in the electronic state of the porphyrin, with the peak position remaining unchanged [39]. It is likely the relative Q-band intensity changes observed when P3d is interacting with the modified surface is due to the metal becoming partially displaced [40]. The appearance of absorbance peaks at ~500 nm (green lines, Figure V-24) are likely due to the appearance of free-base versions of P3d resulting from the displacement of the zinc through interaction with the modified surface.

### **3.4- Structural integrity of the maquette on TiO<sub>2</sub>**

When the maquette-porphyrin ensembles are immobilised onto the TiO<sub>2</sub> substrate, all of the Soret peaks of the ligated porphyrins within maquettes were in highly similar positions to those of the isolated or dissolved ensembles. This is good evidence that the maquettes retain structural integrity on the TiO<sub>2</sub> surface. The covalent attachment of maquettes to the substrate with subsequent incorporation of porphyrin once again resulting in similar absorbance spectra gives further evidence for the retention of maquette structural integrity.

#### 4- Conclusions; Immobilization onto TiO<sub>2</sub> Electrodes

Purification and isolation of maquette-porphyrin ensembles is needed to be established so that immobilization onto electrodes can be appropriately assessed. It is apparent utilizing a PD-10 column (as presented here) for removing excess porphyrin based on size-exclusion principles results in zinc porphyrin being removed from its ligated state within the maquette. In contrast, using centrifugal principles, zinc porphyrin remains in a ligated state within the maquette, with 'unbound' porphyrin removed. Through this method, GL-P1d ensembles were isolated with a ratio of 1:1.96, indicating that the zinc porphyrin remained in a ligated state with maquettes having both histidine residues ligating to a single zinc. These purified ensembles were used for comparisons with 'free' porphyrin in solution and their interactions with TiO<sub>2</sub>.

Binding modes of carboxylic acid porphyrins to TiO<sub>2</sub> from organic solvents is well characterised [26-28] (Figure V-2), whereby ammonium salt porphyrins are not expected to associate with TiO<sub>2</sub> from organic solvents. Indeed, the carboxylic acid porphyrin (P1d) was shown to interact with TiO<sub>2</sub> strongly, with the ammonium salt porphyrin (P3d) displaying a highly weakened interaction from organic solvents (Figure V-26), displaying no visible colouration of the surface for the later. Furthermore, this trend is identical when an aqueous solvent is used, whereby P1d interacts strongly and P3d interacts weakly with TiO<sub>2</sub> from aqueous buffer with no visible colouration of the surface for the later. However, it is evident that P1d forms aggregates on the surface of TiO<sub>2</sub> when bound from aqueous buffer. In contrast to association of porphyrin directly to TiO<sub>2</sub>, the porphyrin can be ligated within maquettes, with subsequent immobilization onto TiO<sub>2</sub> via maquette interactions (Figure V-26). Both P1d and P3d ligate strongly to the maquette within aqueous solution (from Chapter III), with the resulting maquette-porphyrin ensemble immobilised onto TiO<sub>2</sub> from aqueous buffer. In both instances, strong colouration (after rinsing and drying) of the surface resulted. Strong absorbance peaks resulted with either GL-P1d or P3d ensemble immobilization onto TiO<sub>2</sub> which correspond to the porphyrin being in a ligated state. This gives evidence that the ensemble strongly associates with TiO<sub>2</sub> and that the porphyrin remains in a ligated state within the maquette (Figure V-26). Furthermore, as P3d cannot interact with the TiO<sub>2</sub> directly, all interaction between GL-P3d ensemble and TiO<sub>2</sub> inherently originates from the maquette.

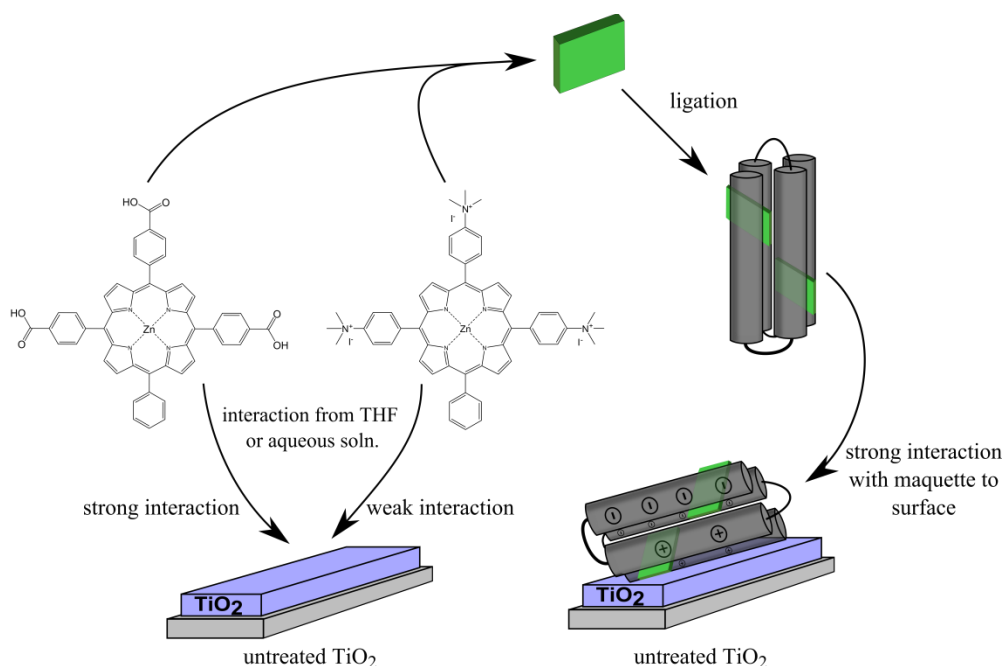


**Figure V-26; Interactions of P1d/P3d or GL-P1d/P3d ensembles with TiO<sub>2</sub>.** P1d interacts and binds strongly to TiO<sub>2</sub> from THF or aqueous buffer. P3d interacts weakly to TiO<sub>2</sub> from THF or aqueous buffer. When either P1d or P3d ligated with GL-maquette, subsequent immobilization onto TiO<sub>2</sub> is a strong interaction, with porphyrin remaining in a ligated state.

Exploration of covalent attachment of maquettes to a treated surface of TiO<sub>2</sub> via EDC-NHS reactions showed that ensembles of GL-P1d can be covalently attached to TiO<sub>2</sub> and that P1d remained in a ligated state. Furthermore, pre-attachment of maquettes to the surface with subsequent exposure to P1d results in porphyrin ligating within the attached maquettes producing strong colouration of the surface. However, the treated TiO<sub>2</sub> with 3-phosphonopropionic acid (needed for EDC-NHS based attachments) interacts strongly with P1d, which once again forms aggregates on the surface producing strong colouration of the surface (Figure V-27).

In contrast to EDC-NHS based attachments, cysteine-maleimide based reactions exploit the single cysteine residue present in the *cysGL*-maquette sequence. Therefore, the maquette would attach to the treated surface via a single point, with the maquette assumed to be able to stand upright, with the loop region (containing the cysteine residue) closest to the surface. Pre-formed ensembles of *cysGL*-P1d or P3d can be attached to TiO<sub>2</sub> through this mechanism which results in strong colouration of the surface, with porphyrin remaining in a ligated state. Furthermore, pre-attachment of maquettes to the surface with subsequent exposure to P1d or P3d results in porphyrin ligating within the attached maquettes producing strong colouration of the surface (Figure V-27). In direct contrast to the 3-phosphonopropionic acid treated TiO<sub>2</sub> used



for EDC-NHS reactions, the 2-aminoethylphosphonic acid treated  $\text{TiO}_2$  for cysteine-maleimide reactions displays weak interaction with both P1d and P3d. The exposure of 2-aminoethylphosphonic acid treated  $\text{TiO}_2$  to P1d or P3d results in a significantly weakened colouration of the surface compared to when maquette is pre-attached (Figure V-27). This unique situation allows for prospects of utilizing pre-attached maquettes to  $\text{TiO}_2$  for post-ligation of porphyrins within the maquette, with the orientation and structure of formed complex known.

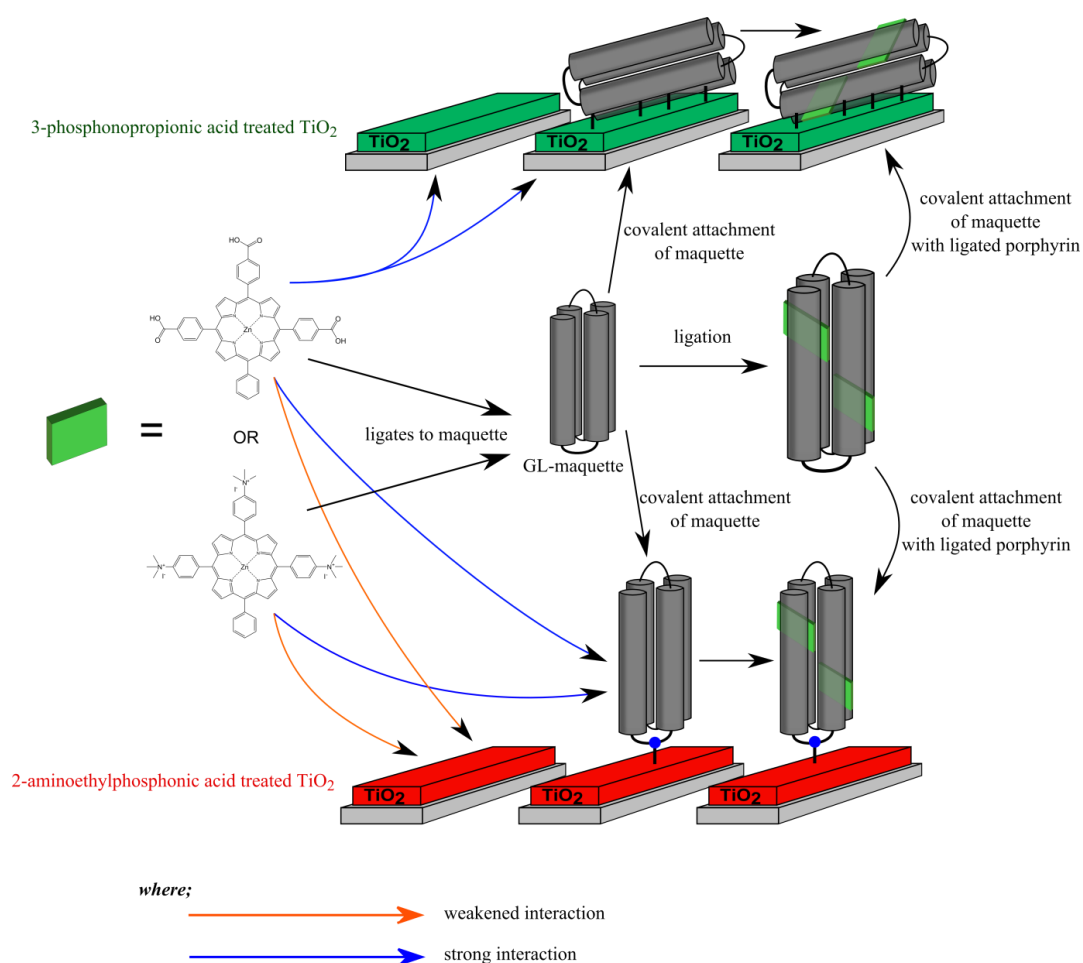


**Figure V-27;  $\text{TiO}_2$  modification for covalent linking of maquette with porphyrin or ensemble binding.** 3-phosphonopropionic acid (3-PPA) is used to modify  $\text{TiO}_2$  for EDC-NHS based linking of maquettes (in green). P1d interacts strongly with this modified surface, however, if maquette is pre-attached to the surface, P1d ligates within the maquette. Pre-formed ensembles can be used to bind to the 3-PPA modified surface, with P1d remaining in a ligated state. 2-aminoethylphosphonic acid (2-APA) is used to modify  $\text{TiO}_2$  for cysteine-maleimide based linking of maquettes (in red). Both P1d and P3d displays a weakened interaction to the 2-APA treated surface, compared to when maquette is pre-attached, with P1d and P3d ligating to the maquette displaying a strong interaction. Pre-formed ensembles can be used to bind to the 2-APA modified surface, with P1d or P3d remaining in a ligated state.

## 5- References; Immobilization onto TiO<sub>2</sub> Electrodes

1. Griffith MJ, Mozer AJ: **Porphyrim based dye sensitized solar cells**: INTECH Open Access Publisher; 2011.
2. O'Regan B, Graetzel M: **A low-cost, high-efficiency solar cell based on dye-sensitized colloidal TiO<sub>2</sub> films**. *Nature* 1991, **353**:737-740.
3. Kennedy JC, Pottier RH: **New trends in photobiology**. *Journal of Photochemistry and Photobiology B: Biology* 1992, **14**(4):275-292.
4. Papkovsky DB, O'Riordan TC: **Emerging Applications of Phosphorescent Metalloporphyrins**. *Journal of Fluorescence* 2005, **15**(4):569-584.
5. Yella A, Lee H-W, Tsao HN, Yi C, Chandiran AK, Nazeeruddin MK, Diao EW-G, Yeh C-Y, Zakeeruddin SM, Grätzel M: **Porphyrim-Sensitized Solar Cells with Cobalt (II/III)-Based Redox Electrolyte Exceed 12 Percent Efficiency**. *Science* 2011, **334**(6056):629-634.
6. Huang H, Song W, Rieffel J, Lovell JF: **Emerging Applications of Porphyrins in Photomedicine**. *Frontiers in Physics* 2015, **3**.
7. Dobson KD, Connor PA, McQuillan AJ: **Monitoring Hydrous Metal Oxide Surface Charge and Adsorption by STIRS**. *Langmuir* 1997, **13**(10):2614-2616.
8. Xia J, Dubin PL, Havel HA: **Electrophoretic light scattering study of counterion condensation of polylysine**. *Macromolecules* 1993, **26**(24):6335-6337.
9. Costa D, Savio L, Pradier CM: **Adsorption of Amino Acids and Peptides on Metal and Oxide Surfaces in Water Environment: A Synthetic and Prospective Review**. *The Journal of Physical Chemistry B* 2016.
10. Roddick-Lanzilotta AD, McQuillan AJ: **An in Situ Infrared Spectroscopic Investigation of Lysine Peptide and Polylysine Adsorption to TiO<sub>2</sub> from Aqueous Solutions**. *Journal of Colloid and Interface Science* 1999, **217**(1):194-202.
11. Jang W-D, Kamruzzaman Selim KM, Lee C-H, Kang I-K: **Bioinspired application of dendrimers: From bio-mimicry to biomedical applications**. *Progress in Polymer Science* 2009, **34**(1):1-23.

12. Svenson S, Tomalia DA: **Dendrimers in biomedical applications—reflections on the field.** *Advanced Drug Delivery Reviews* 2012, **64, Supplement**:102-115.
13. Vieira NCS, Figueiredo A, Faceto AD, de Queiroz AAA, Zucolotto V, Guimarães FEG: **Dendrimers/TiO<sub>2</sub> nanoparticles layer-by-layer films as extended gate FET for pH detection.** *Sensors and Actuators B: Chemical* 2012, **169**:397-400.
14. Kato M, Cardona T, Rutherford AW, Reisner E: **Photoelectrochemical water oxidation with photosystem II integrated in a mesoporous indium-tin oxide electrode.** *J Am Chem Soc* 2012, **134**(20):8332-8335.
15. Kato M, Cardona T, Rutherford AW, Reisner E: **Covalent Immobilization of Oriented Photosystem II on a Nanostructured Electrode for Solar Water Oxidation.** *Journal of the American Chemical Society* 2013, **135**(29):10610-10613.
16. Herrmann M, Boehm H: **Über die chemie der oberfläche des titandioxids. Ii. Saure hydroxylgruppen auf der oberfläche.** *Zeitschrift für anorganische und allgemeine Chemie* 1969, **368**(1-2):73-86.
17. Beranek R: **(Photo) electrochemical methods for the determination of the band edge positions of TiO<sub>2</sub>-based nanomaterials.** *Advances in Physical Chemistry* 2012, **2011**.
18. Bourikas K, Kordulis C, Lycourghiotis A: **Titanium dioxide (anatase and rutile): surface chemistry, liquid–solid interface chemistry, and scientific synthesis of supported catalysts.** *Chemical reviews* 2014, **114**(19):9754-9823.
19. Pujari SP, Scheres L, Marcelis ATM, Zuilhof H: **Covalent Surface Modification of Oxide Surfaces.** *Angewandte Chemie International Edition* 2014, **53**(25):6322-6356.
20. Topoglidis E, Lutz T, Willis RL, Barnett CJ, Cass AE, Durrant JR: **Protein adsorption on nanoporous TiO<sub>2</sub> films: a novel approach to studying photoinduced protein/electrode transfer reactions.** *Faraday discussions* 2000, **116**:35-46.
21. Topoglidis E, Cass AE, Gilardi G, Sadeghi S, Beaumont N, Durrant JR: **Protein adsorption on nanocrystalline TiO<sub>2</sub> films: an immobilization strategy for bioanalytical devices.** *Analytical chemistry* 1998, **70**(23):5111-5113.

22. Topoglidis E, Discher BM, Moser CC, Dutton PL, Durrant JR: **Functionalizing Nanocrystalline Metal Oxide Electrodes With Robust Synthetic Redox Proteins.** *ChemBioChem* 2003, **4**(12):1332-1339.
23. Topoglidis E, Cass AE, O'Regan B, Durrant JR: **Immobilisation and bioelectrochemistry of proteins on nanoporous TiO<sub>2</sub> and ZnO films.** *Journal of Electroanalytical Chemistry* 2001, **517**(1):20-27.
24. Bacarella AL, Grunwald E, Marshall HP, Purlee EL: **The potentiometric measurement of acid dissociation constants and pH in the system methanol-water, pK<sub>a</sub> values for carboxylic acids and anilinium ions.** *The Journal of Organic Chemistry* 1955, **20**(6):747-762.
25. Avdeef A, Comer JEA, Thomson SJ: **pH-Metric log P. 3. Glass electrode calibration in methanol-water, applied to pK<sub>a</sub> determination of water-insoluble substances.** *Analytical Chemistry* 1993, **65**(1):42-49.
26. Zhang L, Cole JM: **Anchoring Groups for Dye-Sensitized Solar Cells.** *ACS Applied Materials & Interfaces* 2015, **7**(6):3427-3455.
27. Brennan BJ, Llansola Portoles MJ, Liddell PA, Moore TA, Moore AL, Gust D: **Comparison of silatrane, phosphonic acid, and carboxylic acid functional groups for attachment of porphyrin sensitizers to TiO<sub>2</sub> in photoelectrochemical cells.** *Physical Chemistry Chemical Physics* 2013, **15**(39):16605-16614.
28. Singh J, Gusain A, Saxena V, Chauhan AK, Veerender P, Koiry SP, Jha P, Jain A, Aswal DK, Gupta SK: **XPS, UV-Vis, FTIR, and EXAFS Studies to Investigate the Binding Mechanism of N719 Dye onto Oxalic Acid Treated TiO<sub>2</sub> and Its Implication on Photovoltaic Properties.** *The Journal of Physical Chemistry C* 2013, **117**(41):21096-21104.
29. Brodard-Severac F, Guerrero G, Maquet J, Florian P, Gervais C, Mutin PH: **High-Field 17O MAS NMR Investigation of Phosphonic Acid Monolayers on Titania.** *Chemistry of Materials* 2008, **20**(16):5191-5196.

30. Weng YJ, Hou RX, Li GC, Wang J, Huang N, Liu HQ: **Immobilization of bovine serum albumin on TiO<sub>2</sub> film via chemisorption of H<sub>3</sub>PO<sub>4</sub> interface and effects on platelets adhesion.** *Applied Surface Science* 2008, **254**(9):2712-2719.
31. Brinkley M: **A brief survey of methods for preparing protein conjugates with dyes, haptens and crosslinking reagents.** *Bioconjugate Chemistry* 1992, **3**(1):2-13.
32. Houseman BT, Gawalt ES, Mrksich M: **Maleimide-Functionalized Self-Assembled Monolayers for the Preparation of Peptide and Carbohydrate Biochips.** *Langmuir* 2003, **19**(5):1522-1531.
33. Mattson G, Conklin E, Desai S, Nielander G, Savage MD, Morgensen S: **A practical approach to crosslinking.** *Molecular Biology Reports* 1993, **17**(3):167-183.
34. Paniagua SA, Hotchkiss PJ, Jones SC, Marder SR, Mudalige A, Marrikar FS, Pemberton JE, Armstrong NR: **Phosphonic acid modification of indium– tin oxide electrodes: Combined xps/ups/contact angle studies†.** *The Journal of Physical Chemistry C* 2008, **112**(21):7809-7817.
35. Hotchkiss PJ, Jones SC, Paniagua SA, Sharma A, Kippelen B, Armstrong NR, Marder SR: **The modification of indium tin oxide with phosphonic acids: mechanism of binding, tuning of surface properties, and potential for use in organic electronic applications.** *Accounts of chemical research* 2011, **45**(3):337-346.
36. Rochford J, Chu D, Hagfeldt A, Galoppini E: **Tetrachelate porphyrin chromophores for metal oxide semiconductor sensitization: effect of the spacer length and anchoring group position.** *Journal of the American Chemical Society* 2007, **129**(15):4655-4665.
37. Schick GA, Schreiman IC, Wagner RW, Lindsey JS, Bocian DF: **Spectroscopic characterization of porphyrin monolayer assemblies.** *Journal of the American Chemical Society* 1989, **111**(4):1344-1350.
38. Azumi R, Matsumoto M, Kawabata Y, Kuroda S, Sugi M, King LG, Crossley MJ: **Orientation change of porphyrin in Langmuir-Blodgett films caused by a trigger molecule.** *The Journal of Physical Chemistry* 1993, **97**(49):12862-12869.

39. Hashimoto T, Choe Y-K, Nakano H, Hirao K: **Theoretical study of the Q and B bands of free-base, magnesium, and zinc porphyrins, and their derivatives.** *The Journal of Physical Chemistry A* 1999, **103**(12):1894-1904.
40. Giovannetti, R. **The Use of Spectrophotometry UV-Vis for the Study of Porphyrins, Macro to Nano Spectroscopy**, Dr Uddin, J. (Ed.), ISBN: 978-953-51-0664-7, InTech, Available from: [<http://www.intechopen.com/books/macro-to-nano-spectroscopy/the-use-of-spectrophotometry-uv-vis-for-the-study-of-porphyrins>]

# **Chapter VI**

## **Electrochemical Analysis**

## 1- Introduction; Electrochemical Analysis

The electrochemical measurement of metallic porphyrins and macrocycles in solvents has been extensively studied in various non-aqueous solvents [1-3]. The electrochemistry of metallic porphyrins containing zinc, copper, and nickel can be stepwise oxidised or reduced by two electrons at the  $\pi$ -ring system to give  $\pi$ -cation radicals and dications or  $\pi$ -anion radicals and dianions for oxidised or reduced porphyrins, respectively [3] (Figure VI-1). The difference between the half-wave potentials of the first oxidation and the first reduction peaks is the difference between the highest occupied molecular orbital (HOMO) and lowest unoccupied molecular orbital (LUMO), the HOMO-LUMO gap (band gap) of the molecule. Much of the reported analysis of half-wave potentials demonstrates that most of the metallic porphyrins exhibit a constant potential difference between the first and second macrocycle-centred oxidations or first and second macrocycle-centred reductions, as well as a similar HOMO-LUMO gap of  $2.25 \pm 0.15$  V [3]. Zinc tetraphenyl-porphyrin (ZnTPP), one of the most well characterised porphyrins, is often used as a 'base' porphyrin, with aromatic substituents added for specific roles. ZnTPP is known to have a band gap of 2.18-2.22 eV in organic solvents such as DMF, using standard supporting electrolytes such as TBAP [4-6].

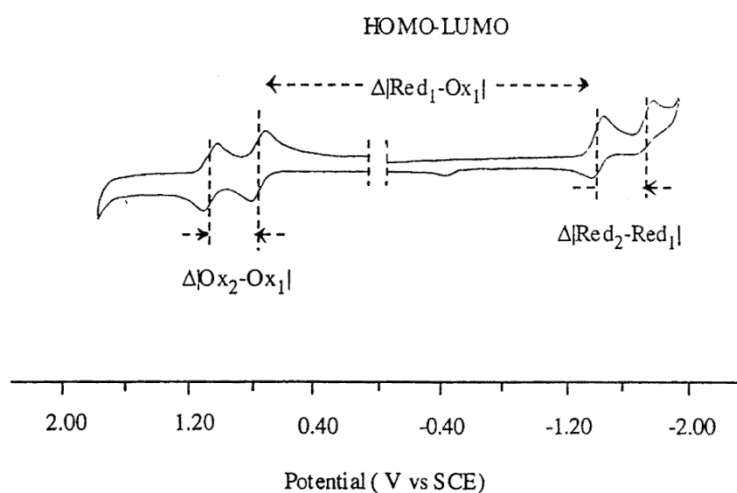


**Figure VI-1; An example of cyclic voltammetry of a metallic porphyrin.** An example of cyclic voltammetry showing the first oxidation and first reduction half-wave potentials, relating to HOMO-LUMO gap of a metal-tetraphenyl porphyrin in acetonitrile (Figure adapted from [3]).

The electrochemical investigation of the zinc-tetraaryl porphyrins studied in Chapter III was undertaken in order to identify changes in the oxidation and reduction levels along with



band-gap changes resulting from the functional groups on the aromatic substituent. The HOMO-LUMO energies are required for potential applications for devices and/or catalytic reactions. The cyclic voltammetry (CV) measurement of metallic porphyrins is a common measurement for oxidation and reduction, used for the analysis of the reversible waves and determination of the half-wave potentials. Another useful electrochemical technique for the analysis of the electroactive materials is the square-wave voltammetry (SWV), a form of linear potential sweep voltammetry that can be applied to extrapolate a half-wave potential peak, using a forward and reverse sweep of step-wise potential to extrapolate current responses. Using this technique, the two reversible peaks observed from CV measurements are portrayed as a single half-wave potential peak.

It has become common practice that electrochemical measurements contain an internal reference, due to relative electrode systems often deviating. It has been well described that the redox couple of ferrocenium/ferrocene ( $\text{Fc}^+/\text{Fc}$ ) be employed as a reference redox system, with the position of waves being directly comparable to the potential of the  $\text{Fc}^+/\text{Fc}$  couple [7, 8]. Therefore, as presented within this chapter, the  $\text{Ag}/\text{Ag}^+$  reference potentials recorded are first referenced to the  $\text{Fc}^+/\text{Fc}$  redox system (by subtracting the half wave potential of  $\text{Fc}^+/\text{Fc}$ ). It is reported that for the conversion between potentials from a ferrocenium/ferrocene ( $\text{Fc}^+/\text{Fc}$ ) reference electrode to a normalised hydrogen electrode (NHE), a value of +0.630 V is added [9]. To convert the electrode potentials from the NHE scale into electronic energies (eV), a value of +4.44 is added [10], with the resulting integer multiplied by -1. Therefore, for all electrochemical measurements, the  $\text{Ag}/\text{Ag}^+$  reference electrode was calibrated against ferrocenium/ferrocene before conversion to potentials against NHE, in accordance with Equation 4. Following this, to differentiate between energies of the various porphyrins, conversion to electronic energies (eV) ensued.

**Equation 4** **electronic energy (eV) = - [( $E_m - E_{\text{Fc}}$  + 0.63) + 4.44]**

Where;  $E_m$  = measured potential;  $E_{\text{Fc}}$  = measured half-wave potential for  $\text{Fc}^+/\text{Fc}$  redox couple.

## 2- Results; Electrochemical Analysis

### 2.1- Porphyrins in solution

The electrochemical analysis of the zinc porphyrins presented here was undertaken in anhydrous organic solvent with TBAP as a supporting electrolyte. The measurements were performed within an argon environment to reduce impacts from atmospheric oxygen. The first reversible oxidation and reduction peaks were prioritised to determine the HOMO and LUMO energy levels, respectively. With the HOMO-LUMO levels of the zinc porphyrins determined, the electronic effects of the substituents can be compared in conjunction with ascertaining the potential application within devices or catalysis.

For determination of the oxidation/reduction peaks produced from the electroactive material, measurements of DMF with TBAP were used as a control. TBAP/DMF produced a peak at  $\sim 0.7$  V (vs NHE) within SWV measurements, being attributed to the presence of oxygen within the solution. Furthermore, a reversible peak with a half-wave potential at  $\sim -0.7$  V (vs NHE) is apparent in many of the measurements of porphyrin in TBAP/DMF. This is also attributed to oxygen being present within the measured solution. To confirm, TBAP/DMF was bubbled with oxygen before electrochemical analysis (data not shown), with the peak positions from the CV and SWV scans aligning with the peak positions from the CV and SWV of porphyrin measurements.

#### 2.1.1- Ferrocene as an internal reference

As stated, the ferrocenium/ferrocene ( $\text{Fc}^+/\text{Fc}$ ) redox couple is commonly used as an internal standard for electrochemical measurements. Therefore, a  $\text{Fc}^+/\text{Fc}$  sweep was performed during electrochemical measurements presented here. A cyclic voltammetry (CV) and square-wave voltammetry (SWV) of the  $\text{Fc}^+/\text{Fc}$  redox couple is shown in Figure VI-2. As shown, the SWV sweep displays a significant peak at the half-wave potential, between the reversible redox peaks of the CV sweep. The half-wave potential (shown here to be 0.09 V [vs  $\text{Ag}/\text{Ag}^+$ ]) is then used for converting subsequent electrochemical measurements to the normalised hydrogen electrode scale (V vs NHE).

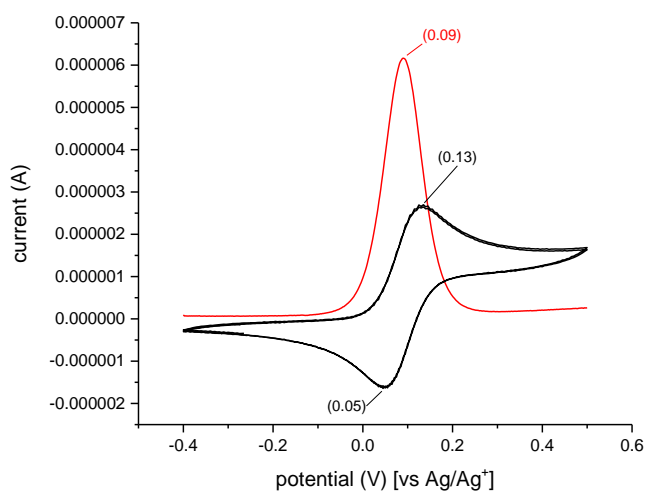


**Figure VI-2; CV and SWV of ferrocene for calibration of electrochemical analysis.** The CV scanned at  $20 \text{ mVs}^{-1}$  (black trace) and SWV scanned at  $20 \text{ mV s}^{-1}$  (red trace) in DMF with 0.1M TBAP as supporting electrolyte.

### 2.1.2- ZnTPP

The electrochemical analysis of zinc tetraphenylporphyrin (ZnTPP) was measured with 0.8 mM ZnTPP dissolved in DMF with 0.1 M TBAP as the supporting electrolyte. Argon was bubbled through the TBAP/DMF solution for 15 min before dissolving the ZnTPP, with the measurements performed in an argon-filled glove box. As shown in Figure VI-3b, the CV of ZnTPP exhibits two distinct reversible oxidation and reduction peaks as expected [4-6]. The half-wave potentials for the oxidation-reduction peaks are easily determined through the use of SWV (Figure VI-3c and d). The half-wave potentials were subsequently used to determine the HOMO-LUMO levels using Equation 4, in conjunction with the band-gap (Table VI-1).

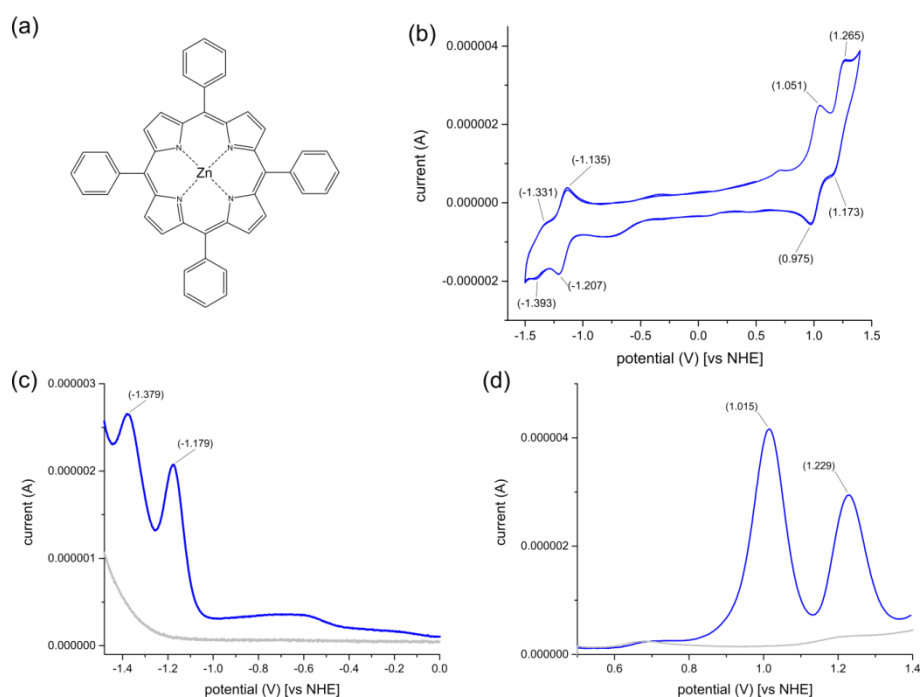


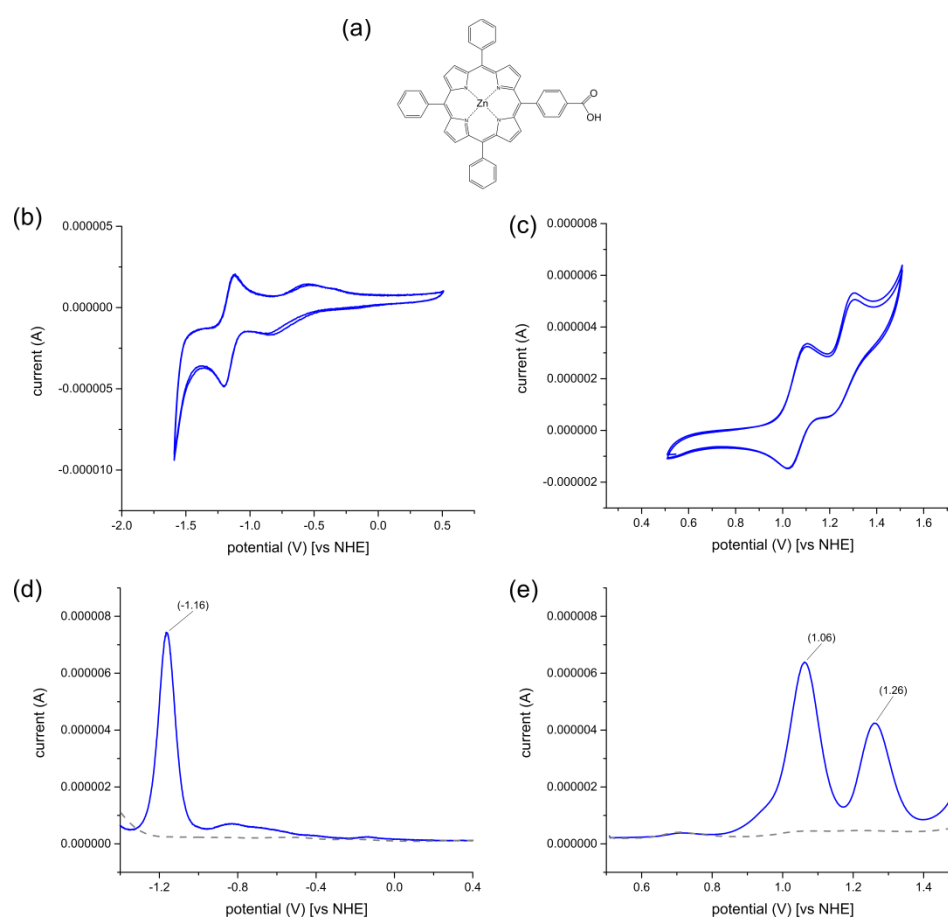
**Figure VI-3; Electrochemical analysis of ZnTPP.** (a) Schematic of ZnTPP. (b) CV of ZnTPP. (c) SWV of ZnTPP (blue trace), with solvent SWV shown (grey trace). (d) SWV of ZnTPP (blue trace), with solvent SWV shown (grey trace). All traces were measured in DMF with 0.1 M TBAP as supporting electrolyte and scanned at a rate of  $20 \text{ mV s}^{-1}$ .

**Table VI-1; Determination of HOMO-LUMO energy levels of ZnTPP.** The half-wave potentials of the first and second oxidation peaks ( $\text{Ox}_1$  and  $\text{Ox}_2$ ) in conjunction with the first reduction and second reduction peaks ( $\text{Red}_1$  and  $\text{Red}_2$ ). HOMO and LUMO levels were subsequently calculated, with the band-gap shown.

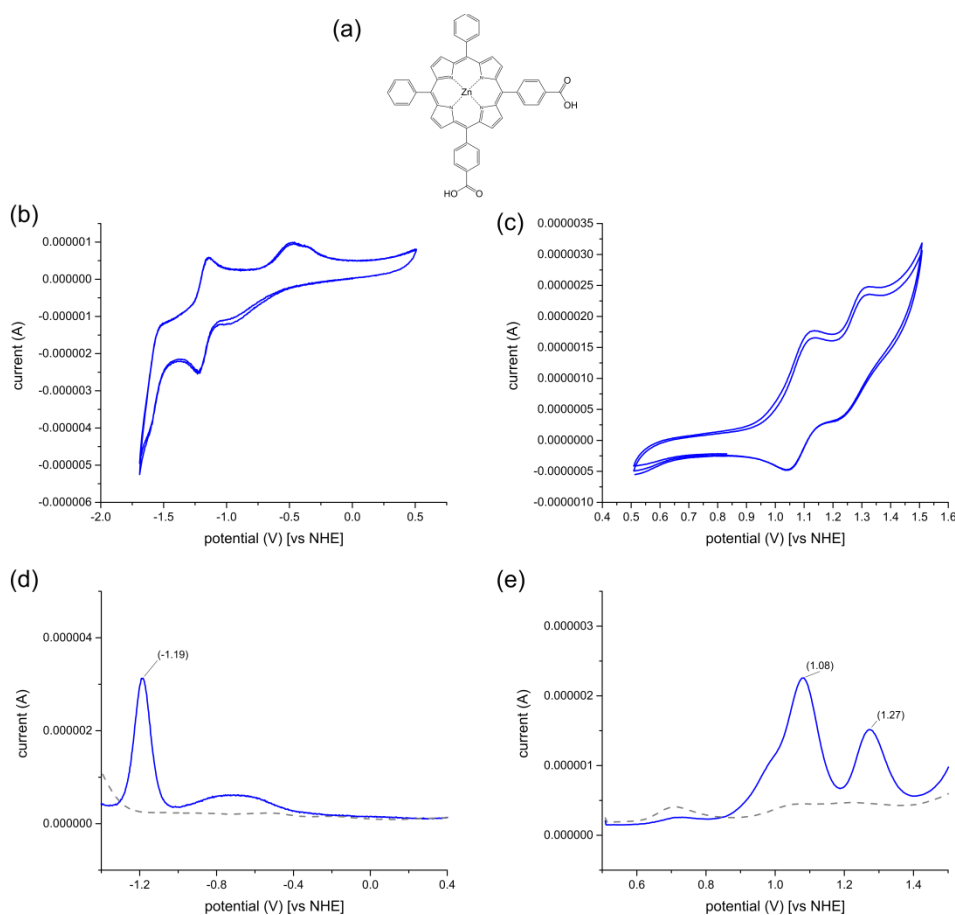
ZnTPP			
<b><math>\text{Ox}_1</math></b> (V vs NHE)	1.02	<b><math>\text{Red}_1</math></b> (V vs NHE)	-1.18
<b><math>\text{Ox}_2</math></b> (V vs NHE)	1.23	<b><math>\text{Red}_2</math></b> (V vs NHE)	-1.38
<b>HOMO</b> (eV)	-5.46	<b>LUMO</b> (eV)	-3.26
	<b>Band-gap</b> (eV)	2.20	

### 2.1.3- Carboxylate substituted tetraphenylporphyrins (P1a-P1e)

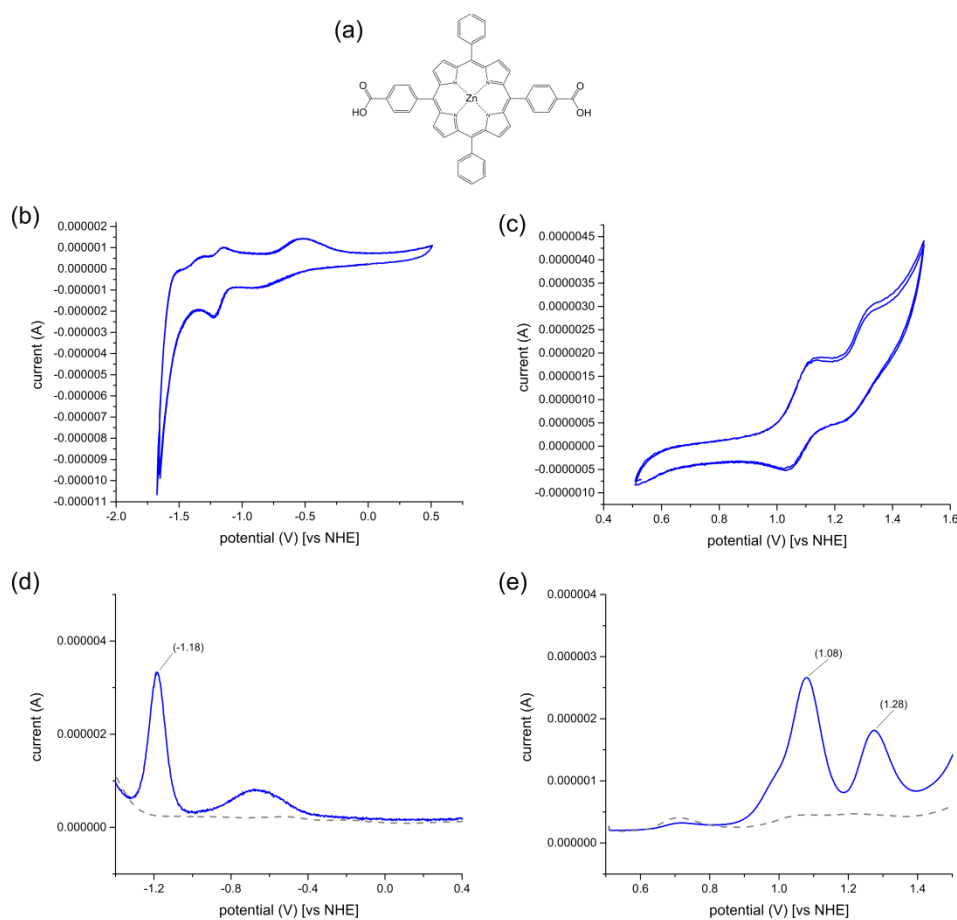
The electrochemical analysis of porphyrins P1a-P1e was undertaken, determining the electronic energy changes through additions of carboxylate groups. The electrochemistry was measured with 0.8 mM porphyrin dissolved in DMF and 0.1 M TBAP as a supporting electrolyte. Argon was bubbled through the TBAP/DMF solution for 15 min before dissolving the porphyrin. The half-wave potentials for the oxidation-reduction peaks were determined through the use of square-wave voltammetry (Figure VI-4 to Figure VI-8). The half-wave potentials were subsequently used to determine the HOMO-LUMO levels (based on Equation 4), in conjunction with the band-gap (Table VI-2).



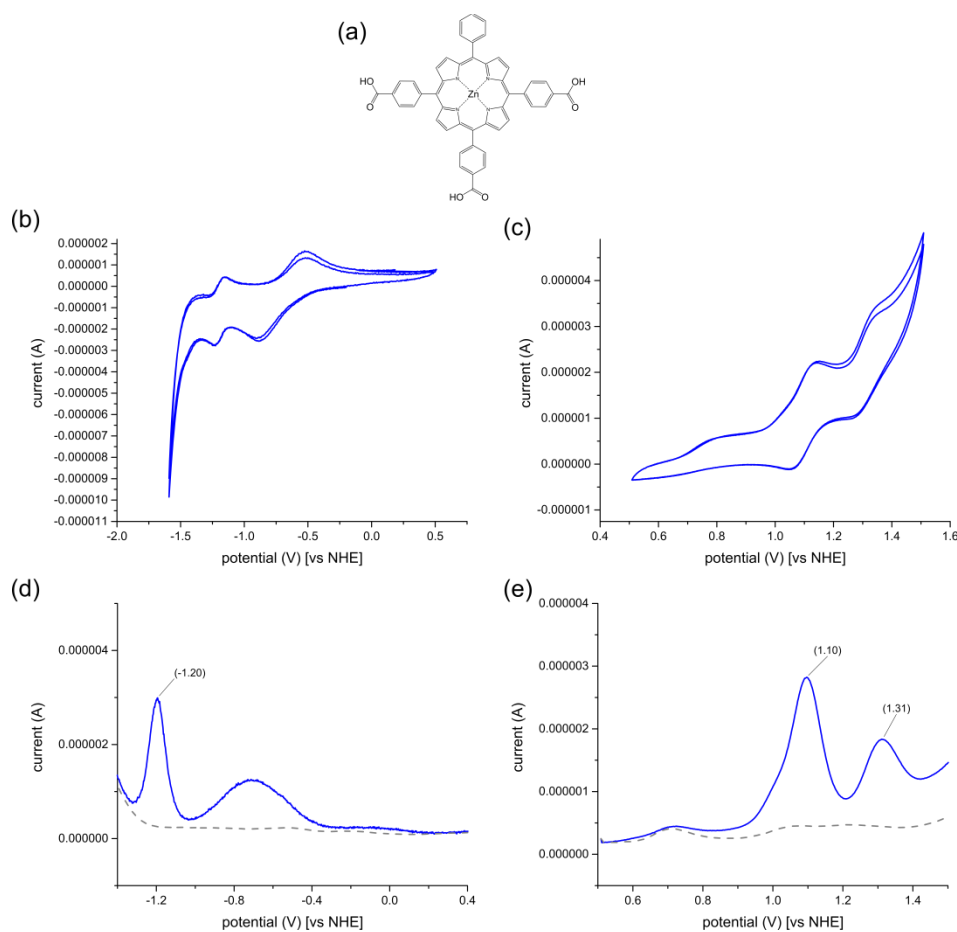
**Figure VI-4; Electrochemical analysis of P1a.** (a) Schematic of P1a. (b) CV of P1a scanned at 50 mV s<sup>-1</sup>. (c) CV of P1a scanned at 50 mV s<sup>-1</sup>. (d) SWV of P1a (blue trace), with solvent SWV shown (grey trace), scanned at 25 mV s<sup>-1</sup>. (e) SWV of P1a (blue trace), with solvent SWV shown (grey trace), scanned at 20 mV s<sup>-1</sup>. All traces were measured in DMF with 0.1 M TBAP as supporting electrolyte.



**Figure VI-5; Electrochemical analysis of P1b.** (a) Schematic of P1b. (b) CV of P1b scanned at 50 mV s<sup>-1</sup>. (c) CV of P1b scanned at 50 mV s<sup>-1</sup>. (d) SWV of P1b (blue trace), with solvent SWV shown (grey trace), scanned at 25 mV s<sup>-1</sup>. (e) SWV of P1b (blue trace), with solvent SWV shown (grey trace), scanned at 20 mV s<sup>-1</sup>. All traces were measured in DMF with 0.1 M TBAP as supporting electrolyte.

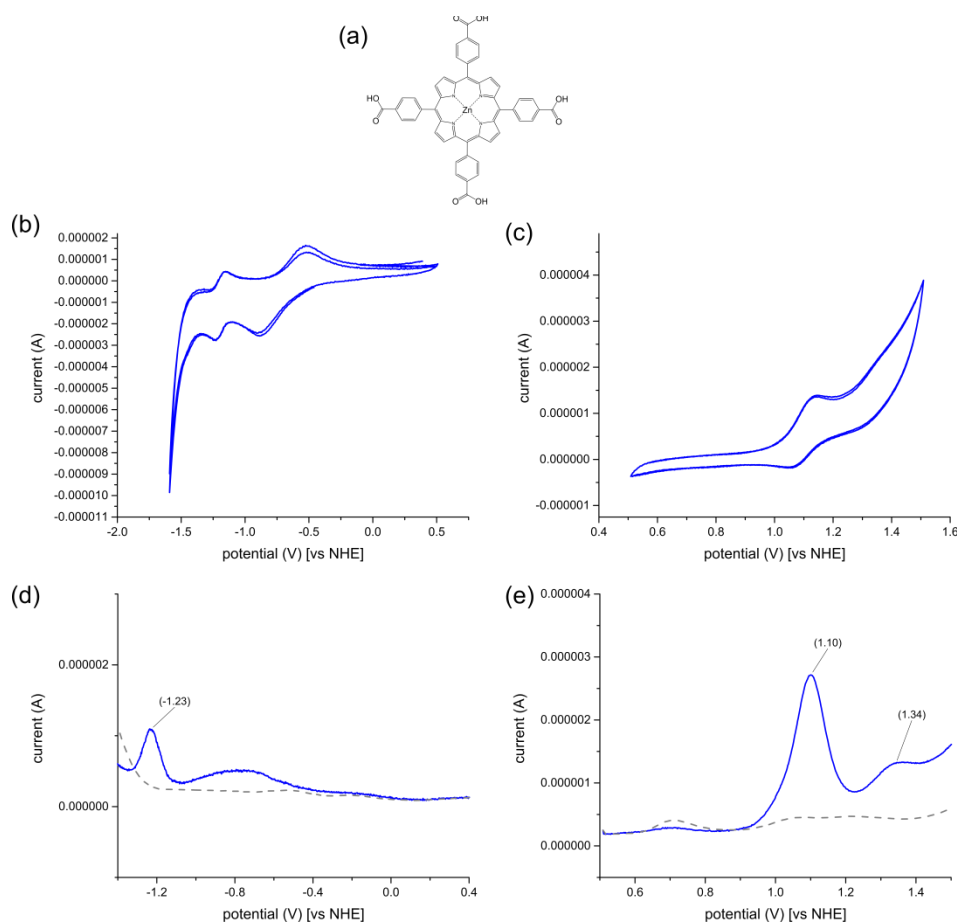


**Figure VI-6; Electrochemical analysis of P1c.** (a) Schematic of P1c. (b) CV of P1c scanned at 50 mV s<sup>-1</sup>. (c) CV of P1c scanned at 50 mV s<sup>-1</sup>. (d) SWV of P1c (blue trace), with solvent SWV shown (grey trace), scanned at 25 mV s<sup>-1</sup>. (e) SWV of P1c (blue trace), with solvent SWV shown (grey trace), scanned at 20 mV s<sup>-1</sup>. All traces were measured in DMF with 0.1 M TBAP as supporting electrolyte.



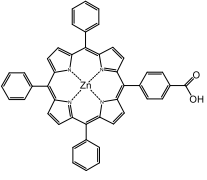
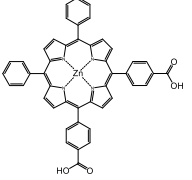
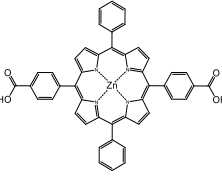
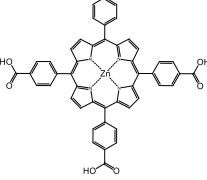
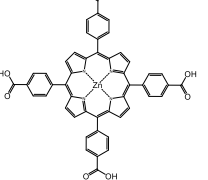
**Figure VI-7; Electrochemical analysis of P1d.** (a) Schematic of P1d. (b) CV of P1d scanned at 50 mV s<sup>-1</sup>. (c) CV of P1d scanned at 50 mV s<sup>-1</sup>. (d) SWV of P1d (blue trace), with solvent SWV shown (grey trace), scanned at 25 mV s<sup>-1</sup>. (e) SWV of P1d (blue trace), with solvent SWV shown (grey trace), scanned at 20 mV s<sup>-1</sup>. All traces were measured in DMF with 0.1 M TBAP as supporting electrolyte.





**Figure VI-8; Electrochemical analysis of P1e.** (a) Schematic of P1e. (b) CV of P1e scanned at 50 mV s<sup>-1</sup>. (c) CV of P1e scanned at 50 mV s<sup>-1</sup>. (d) SWV of P1e (blue trace), with solvent SWV shown (grey trace), scanned at 25 mV s<sup>-1</sup>. (e) SWV of P1e (blue trace), with solvent SWV shown (grey trace), scanned at 20 mV s<sup>-1</sup>. All traces were measured in DMF with 0.1 M TBAP as supporting electrolyte.

**Table VI-2; Determination of HOMO-LUMO energy levels of P1a-P1e.** The half-wave potentials of the first oxidation ( $Ox_1$ ) and reduction ( $Red_1$ ) peaks are shown that were determine the HOMO and LUMO levels, with the subsequent band-gap shown.

	P1a	P1b	P1c	P1d	P1e
					
<b><math>Ox_1</math></b> (V vs NHE)	1.06	1.08	1.08	1.10	1.10
<b><math>Red_1</math></b> (V vs NHE)	-1.16	-1.19	-1.18	-1.20	-1.23
<b>HOMO</b> (eV)	-5.50	-5.52	-5.52	-5.54	-5.54
<b>LUMO</b> (eV)	-3.28	-3.25	-3.26	-3.24	-3.21
<b>Band-gap</b> (eV)	2.22	2.27	2.26	2.30	2.33

#### 2.1.4- Zn butyl-substituted phenylporphyrin carboxylates (P4a-P4d)

The electrochemical analysis of porphyrins P4a-P4d was undertaken, determining the electronic energy changes through replacing butyl groups. The electrochemistry was measured with 0.8 mM porphyrin dissolved DMF and 0.1 M TBAP as a supporting electrolyte. TBAP/DMF was bubbled for 15 min with argon before dissolving porphyrin, with the measurements performed in a argon-filled glove box. As is shown from the measurements (Figure VI-9 to Figure VI-12), the half-wave potentials for the oxidation-reduction peaks were determined through the use of square-wave voltammetry. The half-wave potentials were subsequently used to calculate the HOMO-LUMO levels (Equation 4), in conjunction with the band-gap (Table VI-3).

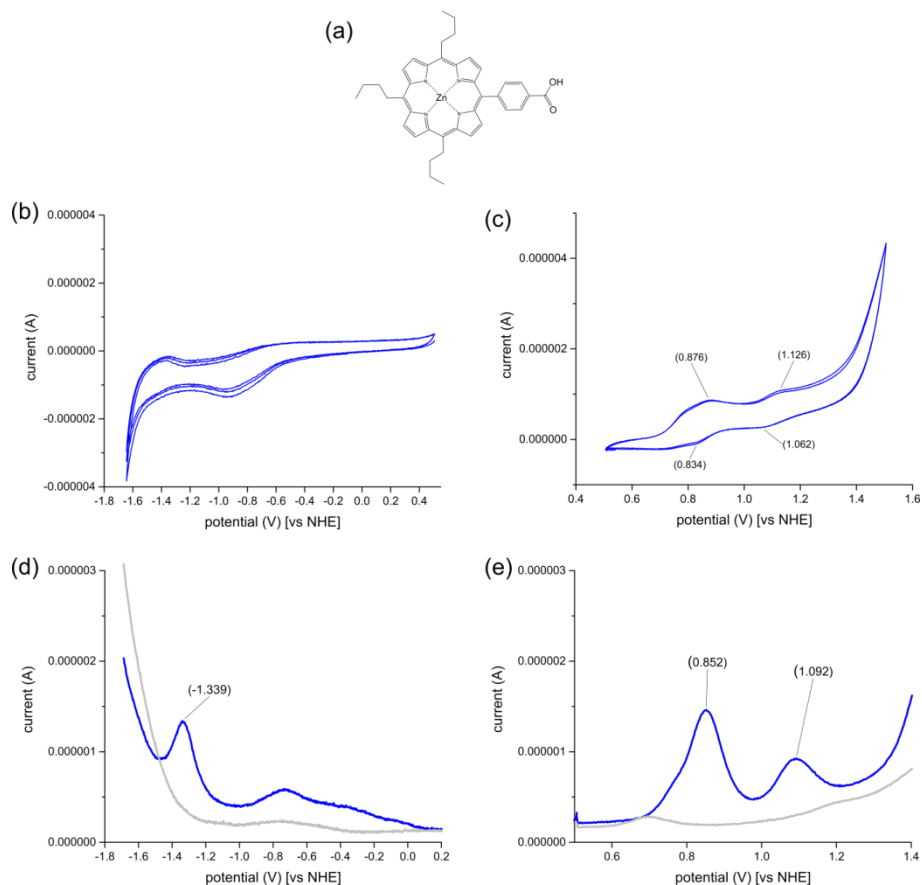


**Figure VI-9; Electrochemical analysis of P4a.** (a) Schematic of P4a. (b) CV of P4a scanned at 50 mV s<sup>-1</sup>. (c) CV of P4a scanned at 50 mV s<sup>-1</sup>. (d) SWV of P4a (blue trace), with solvent SWV shown (grey trace), scanned at 25 mV s<sup>-1</sup>. (e) SWV of P4a (blue trace), with solvent SWV shown (grey trace), scanned at 20 mV s<sup>-1</sup>. All traces were measured in DMF with 0.1 M TBAP as supporting electrolyte.

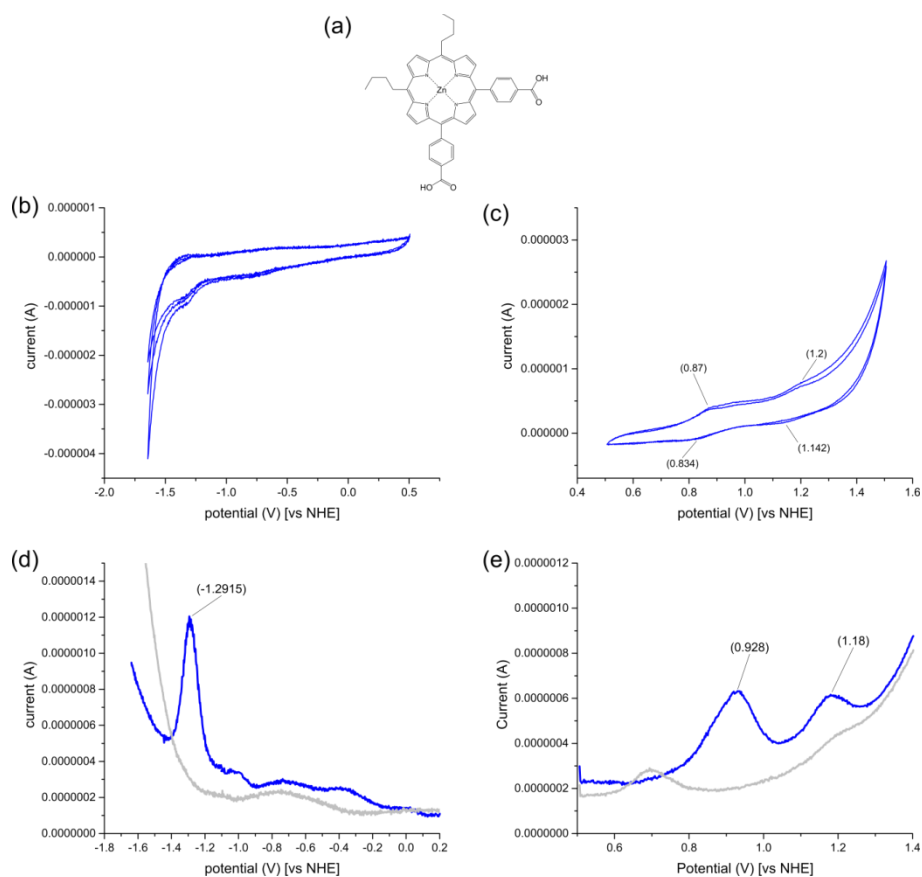


**Figure VI-10; Electrochemical analysis of P4b.** (a) Schematic of P4b. (b) CV of P4b scanned at 50 mV s<sup>-1</sup>. (c) CV of P4b scanned at 50 mV s<sup>-1</sup>. (d) SWV of P4b (blue trace), with solvent SWV shown (grey trace), scanned at 25 mV s<sup>-1</sup>. (e) SWV of P4b (blue trace), with solvent SWV shown (grey trace), scanned at 20 mV s<sup>-1</sup>. All traces were measured in DMF with 0.1 M TBAP as supporting electrolyte.

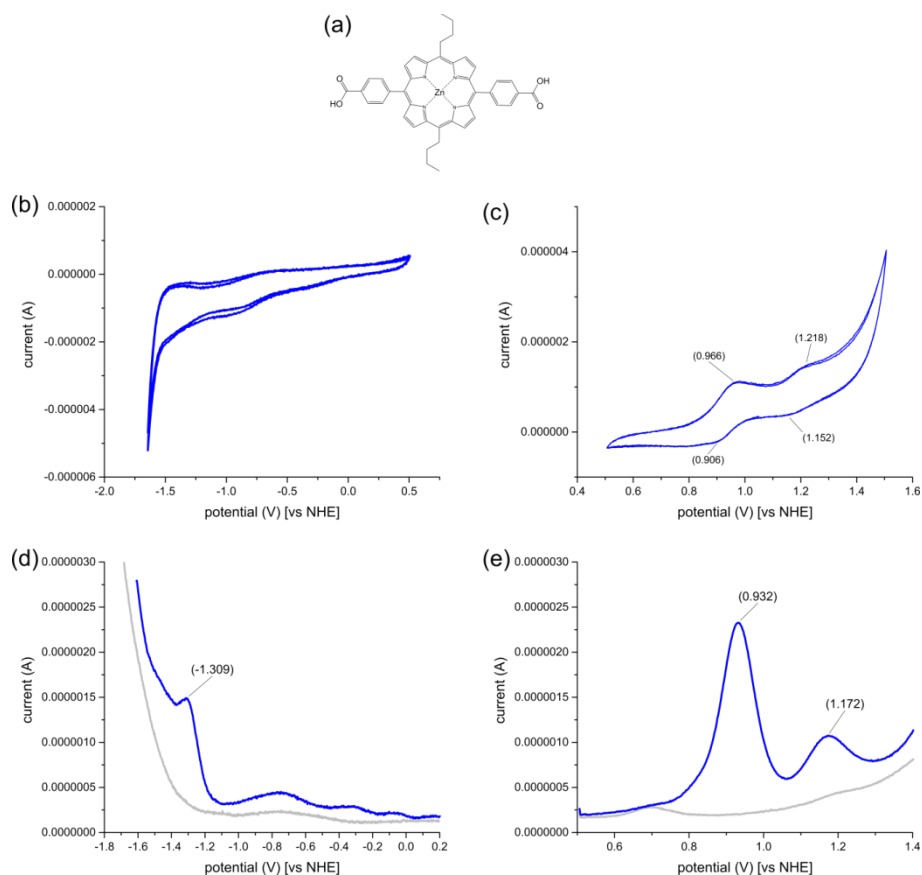


**Figure VI-11; Electrochemical analysis of P4c.** (a) Schematic of P4c. (b) CV of P4c scanned at 50 mV s<sup>-1</sup>. (c) CV of P4c scanned at 50 mV s<sup>-1</sup>. (d) SWV of P4c (blue trace), with solvent SWV shown (grey trace), scanned at 25 mV s<sup>-1</sup>. (e) SWV of P4c (blue trace), with solvent SWV shown (grey trace), scanned at 20 mV s<sup>-1</sup>. All traces were measured in DMF with 0.1 M TBAP as supporting electrolyte.

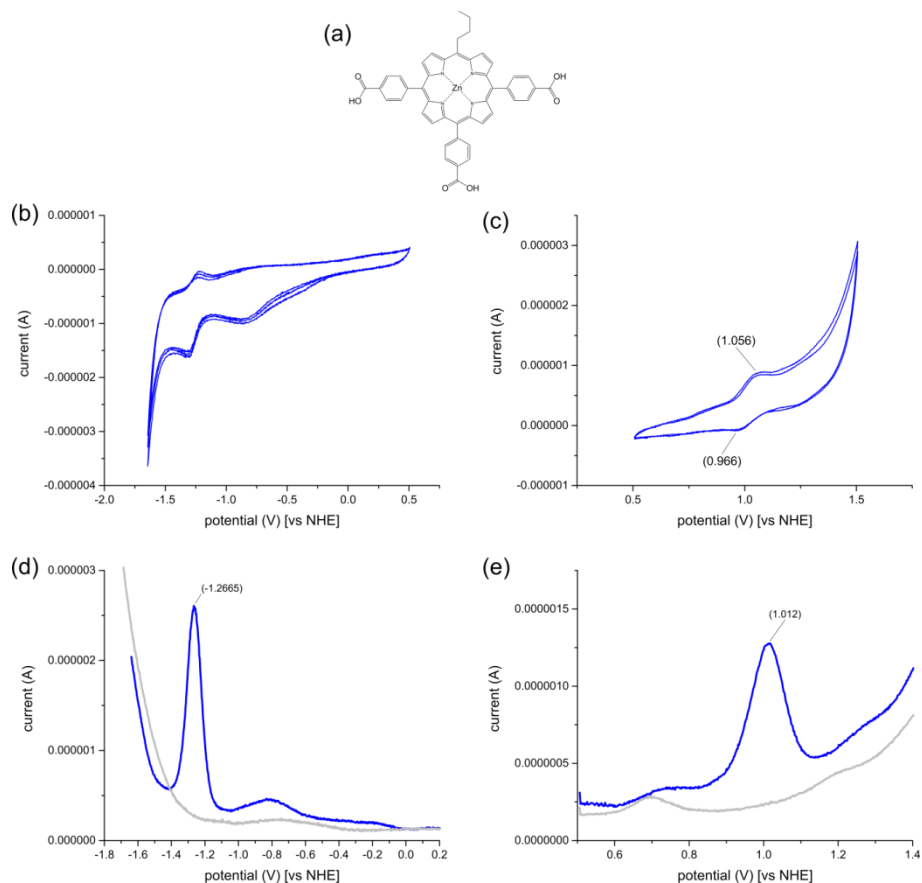


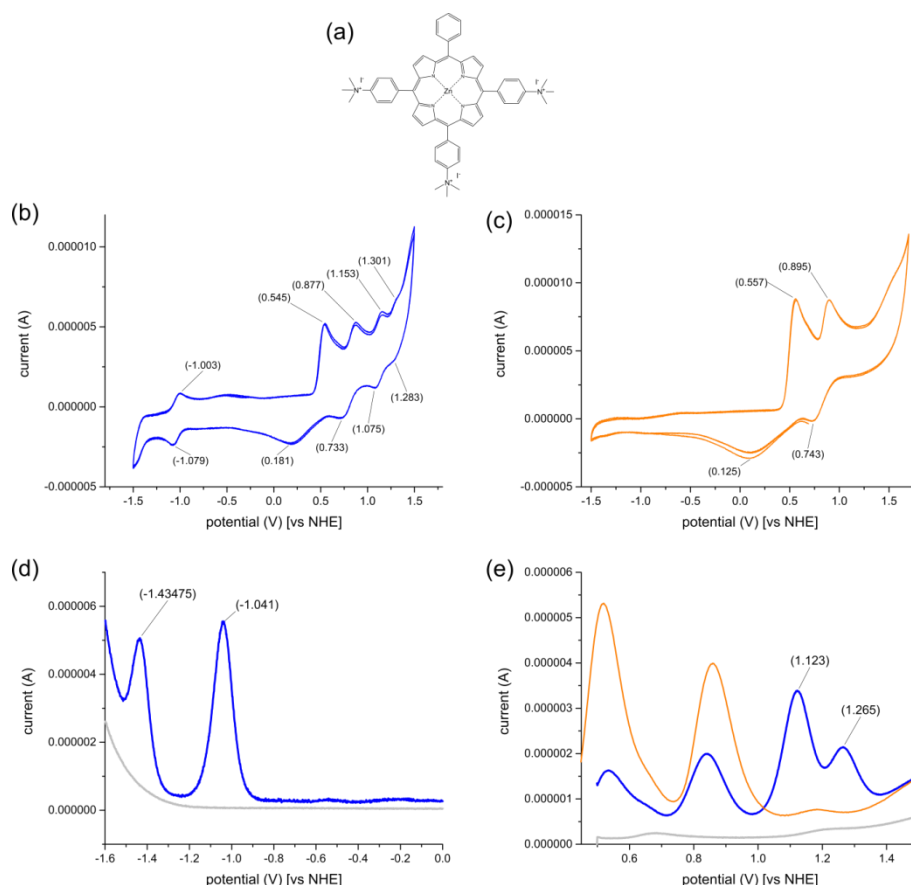
**Figure VI-12; Electrochemical analysis of P4d.** (a) Schematic of P4d. (b) CV of P4d scanned at  $50 \text{ mV s}^{-1}$ . (c) CV of P4d scanned at  $50 \text{ mV s}^{-1}$ . (d) SWV of P4d (blue trace), with solvent SWV shown (grey trace), scanned at  $25 \text{ mV s}^{-1}$ . (e) SWV of P4d (blue trace), with solvent SWV shown (grey trace), scanned at  $20 \text{ mV s}^{-1}$ . All traces were measured in DMF with  $0.1 \text{ M TBAP}$  as supporting electrolyte.

**Table VI-3; Determination of HOMO-LUMO energy levels of P4a-P4d.** The half-wave potentials of the first oxidation ( $\text{Ox}_1$ ) and reduction ( $\text{Red}_1$ ) peaks are shown that were used to determine the HOMO and LUMO levels, with the subsequent band-gap shown.

	P4a	P4b	P4c	P4d
<b><math>\text{Ox}_1</math></b> (V vs NHE)	0.85	0.93	0.93	1.01
<b><math>\text{Red}_1</math></b> (V vs NHE)	-1.34	-1.29	-1.31	-1.27
<b>HOMO</b> (eV)	-5.29	-5.37	-5.37	-5.45
<b>LUMO</b> (eV)	-3.10	-3.15	-3.13	-3.17
<b>Band-gap</b> (eV)	2.19	2.22	2.24	2.28

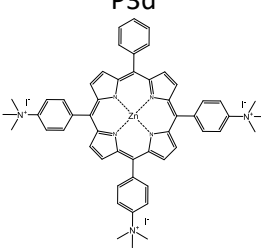
### 2.1.5- Zn-tetraphenyl tri-ammonium salt porphyrin (P3d)

The electrochemical analysis of P3d was undertaken, with 0.8 mM P3d dissolved in DMF with 0.1 M TBAP as a supporting electrolyte. TBAP/DMF was bubbled for 30 min with argon before dissolving P3d, with the measurements performed in an argon-filled glove box. As shown in Figure VI-13, the CV exhibits four distinct reversible oxidation peaks (Figure VI-13b). As there was iodide present as a counter ion for the ammonium group, a measurement of tetrabutylammonium iodide (TBAI) was used to determine the electrochemical responses associated with iodide (Figure VI-13c). The half-wave potentials for the oxidation and reduction peaks were determined through the use of square-wave voltammetry (Figure VI-3d and e). Through the use of TBAI, the oxidation and reduction peaks associated with P3d were determined, with the half-wave potentials subsequently used to calculate the HOMO-LUMO levels (Equation 4), in conjunction with the band-gap (Table VI-4).



**Figure VI-13; Electrochemical analysis of P3d.** (a) Schematic of P3d. (b) CV of P3d scanned at  $50 \text{ mV s}^{-1}$ . (c) CV of 0.1 M TBAI, scanned at  $50 \text{ mV s}^{-1}$ . (d) SWV of P3d scanned at  $20 \text{ mVs}^{-1}$  (blue trace), with solvent SWV shown (grey trace). (e) SWV of P3d (blue trace), with solvent shown (grey trace), and 0.1 M TBAI (orange trace), scanned at  $10 \text{ mV s}^{-1}$ . All traces were measured in DMF with 0.1 M TBAP (or TBAI for orange traces instead of TBAP) as supporting electrolyte.

**Table VI-4; Determination of HOMO-LUMO energy levels of P3d.** The half-wave potentials of the first oxidation ( $Ox_1$ ) and reduction ( $Red_1$ ) peaks are shown that were used to determine the HOMO and LUMO levels, with the subsequent band-gap shown.

			
<b><math>Ox_1</math></b> (V vs NHE)	1.12	<b><math>Red_1</math></b> (V vs NHE)	-1.04
<b><math>Ox_2</math></b>	1.27	<b><math>Red_2</math></b>	-1.43
<b>HOMO</b> (eV)	-5.56	<b>LUMO</b> (eV)	-3.40
	<b>Band-gap</b> (eV)	2.16	

## 2.2- Electrochemistry of porphyrins on $TiO_2$

### 2.2.1- Immobilised P1d on $TiO_2$

The electrochemical analysis of P1d was undertaken when bound on  $2.5 \mu m TiO_2$ . P1d was bound to  $TiO_2$  via sensitization from THF, bound from aqueous buffer, or ligated with maquette and subsequent immobilization onto  $TiO_2$ , with an undyed  $TiO_2$  used as a control (Figure VI-14). The measurements were performed in ACN with 0.1 M TBAP as a supporting electrolyte, and argon bubbled through the ACN/TBAP for 15 min before measurements. As is shown in Figure VI-14, the square-wave potential of the samples display significant peaks compared to the  $TiO_2$  control, which correspond to the half-wave potential of the first oxidation of the porphyrin. As shown, the oxidation peak is 0.91, 0.91, and 0.89 V [vs NHE] for when sensitized, bound from aqueous buffer, or when ligated with maquette, respectively. This indicates that the electronic structure of P1d is highly similar when bound on the surface from THF or aqueous buffer. In contrast, ligation to the maquette results in a small shift in the oxidation potential, likely due to the electronic state being changed via axial ligation of the zinc centre.

The differences in current at the corresponding oxidation peaks for the variably immobilised porphyrin gives further insights into the electron transfer processes. It is likely that



the oxidation peaks arise when the porphyrin is substantially close to the FTO to allow for positive potentials to sufficiently oxidise the dye molecules, whereby  $\text{TiO}_2$  would not allow for effective oxidation of the porphyrin with the applied potentials [11]. Therefore, it becomes apparent that P1d sensitized from THF has the greatest quantity of redox active P1d which is sufficiently close to FTO, with P1d immobilised from aqueous buffer being least accessible to the FTO. In contrast, the maquette-P1d ensembles has an oxidation peak with currents which is approximately half of the peak of P1d sensitized from THF. However, the quantity of P1d when sensitized to the substrate is over 6-fold more than compared to the quantity of P1d when immobilised as maquette-P1d ensembles (results from Chapter VII, Section 2). Consequently, this indicates that the maquette assists in charge transport when close to the FTO substrate.

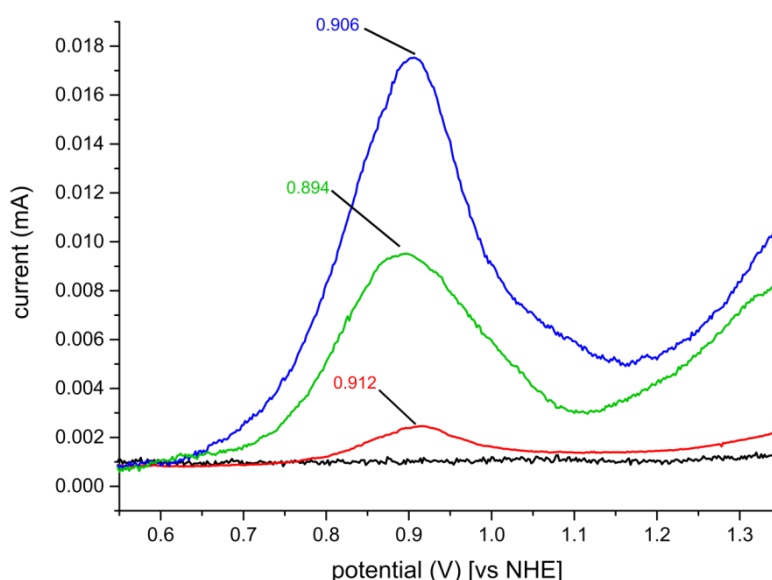


**Figure VI-14; Square-wave voltammetry of P1d on  $\text{TiO}_2$ .** Peaks indicate half wave potential of the first oxidations from the modified surfaces; unmodified  $\text{TiO}_2$  (black line), P1d sensitized from THF (blue line), P1d sensitized from aqueous buffer (red line), and sensitized maquette-P1d ensembles from aqueous buffer (green line).

### 3- Discussion; Electrochemical Analysis

The electrochemical data allows for the determination of the electronic energies associated with the molecule that is useful for determining potential applications of the materials in devices and catalytic reactions.

The electrochemical analysis of the porphyrins provides a way to determine their respective HOMO-LUMO energy levels (Figure VI-16). As shown, the HOMO level for ZnTPP was determined to be -5.46 eV and a LUMO level of -3.26 eV, corresponding to a band-gap of 2.20 eV. This value is in accordance with energy levels reported in the literature [4-6]. Furthermore, P1a has been reported to contain a band-gap of 2.32 eV in THF [12], which deviates by 0.10 eV from the value reported here, likely due to the difference in solvent. As is evident in Figure VI-16, the addition of carboxylic groups to a ZnTPP 'core' induces changes in both the HOMO and LUMO energy levels of the porphyrin. With additions of carboxylic groups, the HOMO energy level of the porphyrin moves to lower energy levels (ie. becomes more negative), with the LUMO energy level moves to higher energy levels (ie. becomes more positive). This has the effect of increasing the band-gap of the porphyrin, with a single carboxylate differing from a tetra carboxylate by 0.11 eV in band-gap energy.

Contrastingly, the substitution of a butyl group with an aromatic carboxylate functional group (as with P4a-P4d) shifts both the HOMO and LUMO levels to lower energy levels. It is evident that substituting a butyl group with an aromatic-carboxylate group shifts the HOMO energy level (by ~8 meV), significantly more shifted than the LUMO energy level (2-5 meV), which results in the band-gap increasing with subsequent substitutions.

The analysis of P3d allows for a direct comparison with P1d, with the difference being trimethylamine groups compared to carboxylic groups, respectively. As is shown, the HOMO energy levels for the two porphyrins (P1d and P3d) differ by only 0.02 eV, which is within experiment deviations. However, the LUMO is shown to be significantly different, with the LUMO of P3d being shifted by 0.16 eV towards lower energies compared to P1d LUMO energy levels. This results in the band gap of P3d being 0.14 eV smaller than the band-gap energy of P1d (as shown in Figure VI-16). This indicates that the trimethyl-ammonium functional groups significantly shift the LUMO level towards lower energy compared to a ZnTPP. It has been reported that the band-gap associated with a zinc tetra-nitrophenylporphyrin is 2.18 eV [13], being comparable to the 2.16 eV reported here for P3d. This gives further evidence that amine

functional group substitution of zinc tetraphenylporphyrin decreases band-gap energies compared to the carboxylic group equivalents. With ammonium groups affecting the porphyrin core via inductive electron withdrawing processes [14], the distinct change in LUMO rather than the HOMO with addition of trimethylammonium substituents suggests that the ammonium groups are making the porphyrin core more accessible for addition of electrons (ie. electrons into the LUMO).

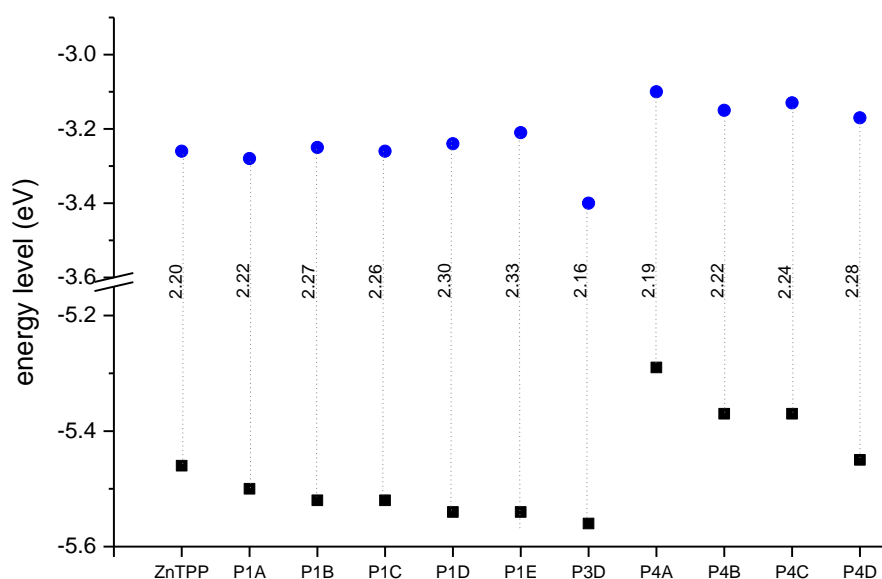


**Figure VI-16; HOMO-LUMO energies of measured porphyrins in solution.** The HOMO (■) and LUMO (●) energy levels calculated from electrochemical measurements, displaying the respective band-gap level.

Electrochemical analysis of P1d on the surface of  $\text{TiO}_2$  shows distinct half-wave potential peaks for the first oxidation of the immobilised porphyrin. This oxidation peak is associated with the HOMO energy level. As is shown, the HOMO levels on  $\text{TiO}_2$  are 0.91, 0.91, and 0.89 V [vs NHE] when P1d is bound from THF, bound from aqueous buffer, or when ligated with maquette and bound from aqueous buffer, respectively. Therefore, it is apparent that the energy levels associated with the HOMO are identical when P1d is bound to the surface either from THF or aqueous buffer, indicating that the electronic states are similar. There is a small shift in the HOMO level when P1d is ligated to the maquette immobilized on  $\text{TiO}_2$ . This

is indicative of a change in the porphyrin electronic state as a result of the axial ligation affecting the electronic state of the core porphyrin electrons. This is in agreement with the shifts observed in solution when P1d is ligated compared to free (non-ligated) in solution. The significant shift in absorbance between non-ligated and ligated states of the porphyrin P1d (Chapter III) is a direct result of the change in electronic state produced from axial ligation with the histidine residues of the maquette.

#### 4- Conclusions; Electrochemical Analysis

Electrochemical analysis allows for determination of the electronic energies associated with redox active compounds, such as porphyrins. The results presented here give evidence that the electronic energy associated with ZnTPP can be significantly altered through substitutions at the *para*-position of the phenyl groups. The subsequent additions of carboxylic-functional groups increase the band-gap of the porphyrin, with shifts in both the HOMO levels (to lower energy states) and LUMO levels (to higher energy states). Conversely, it is apparent that the ammonium salt substituent influences the LUMO levels, shifting towards lower energy which results in a decrease in the band-gap of the porphyrin.

The subsequent removal of butyl groups was shown to significantly shift the HOMO towards lower energy levels, along with the LUMO levels. The replacement of the butyl groups by the phenylcarboxylates were shown to decrease the HOMO energy levels more significantly than the LUMO energy levels, subsequently increasing the band-gap. Therefore, as it has been shown that the addition of carboxylate groups to a tetraphenylporphyrin (P1a-P1e) has a slight impact on the HOMO level of the porphyrin, it can be assumed that the butyl group (rather than phenyl substituents) has a larger impact on the electronic state of the porphyrin core.

## 5- References; Electrochemical Analysis

1. Guillard R, Kadish KM: **Some aspects of organometallic chemistry in metalloporphyrin chemistry: synthesis, chemical reactivity, and electrochemical behavior of porphyrins with metal-carbon bonds.** *Chemical Reviews* 1988, **88**(7):1121-1146.
2. Kadish KM, Caemelbecke EV: **Electrochemistry of Metalloporphyrins in Nonaqueous Media.** In: *Encyclopedia of Electrochemistry.* Wiley-VCH Verlag GmbH & Co. KGaA; 2007.
3. Kadish KM, Van Caemelbecke E: **Electrochemistry of porphyrins and related macrocycles.** *Journal of Solid State Electrochemistry* 2003, **7**(5):254-258.
4. Yasuike M, Yamaoka T, Ohno O, Ichimura K, Morii H, Sakuragi M: **Optical and redox properties of meso-diphenyltetrabenzoporphyrins.** *Inorganica Chimica Acta* 1991, **185**(1):39-47.
5. Lexa D, Reix M: **Studies of redox behaviour of metallic complexes of various tetrapyrrolic rings. 1. Half-wave potentials and nature of complex.** *Journal de Chimie Physique et de PhysicoChimie Biologique* 1974, **71**(4):511-516.
6. Armaroli N, Diederich F, Echegoyen L, Habicher T, Flamigni L, Marconi G, Nierengarten J-F: **A new pyridyl-substituted methanofullerene derivative. Photophysics, electrochemistry and self-assembly with zinc(II) meso-tetraphenylporphyrin (ZnTPP).** *New Journal of Chemistry* 1999, **23**(1):77-83.
7. Gagne RR, Koval CA, Lisensky GC: **Ferrocene as an internal standard for electrochemical measurements.** *Inorganic Chemistry* 1980, **19**(9):2854-2855.
8. Gritzner G, Kůta J: **Recommendations on reporting electrode potentials in nonaqueous solvents.** *Electrochimica Acta* 1984, **29**(6):869-873.
9. Pavlishchuk VV, Addison AW: **Conversion constants for redox potentials measured versus different reference electrodes in acetonitrile solutions at 25°C.** *Inorganica Chimica Acta* 2000, **298**(1):97-102.

10. Trasatti S: **The absolute electrode potential: an explanatory note (Recommendations 1986)**. *Journal of Electroanalytical Chemistry and Interfacial Electrochemistry* 1986, **209**(2):417-428.
11. Li X, Nazeeruddin MK, Thelakkat M, Barnes PRF, Vilar R, Durrant JR: **Spectroelectrochemical studies of hole percolation on functionalised nanocrystalline TiO<sub>2</sub> films: a comparison of two different ruthenium complexes**. *Physical Chemistry Chemical Physics* 2011, **13**(4):1575-1584.
12. Lee C-W, Lu H-P, Lan C-M, Huang Y-L, Liang Y-R, Yen W-N, Liu Y-C, Lin Y-S, Diau EW-G, Yeh C-Y: **Novel Zinc Porphyrin Sensitizers for Dye-Sensitized Solar Cells: Synthesis and Spectral, Electrochemical, and Photovoltaic Properties**. *Chemistry – A European Journal* 2009, **15**(6):1403-1412.
13. Huang C-W, Yuan Chiu K, Cheng S-H: **Novel spectral and electrochemical characteristics of triphenylamine-bound zinc porphyrins and their intramolecular energy and electron transfer**. *Dalton Transactions* 2005(14):2417-2422.
14. Nantz MH, Li L, Zhu J, Aho-Sharon KL, Lim D, Erickson KL: **Inductive electron-withdrawal from ammonium ion headgroups of cationic lipids and the influence on DNA transfection**. *Biochimica et Biophysica Acta (BBA) - Lipids and Lipid Metabolism* 1998, **1394**(2–3):219-223.

# **Chapter VII**

## **Solar Cell Devices**



## 1- Introduction; Solar Cell Devices

Various porphyrins have been shown to ligate within maquettes, with the maquette capable of electrostatic or covalent attachment to surfaces of  $\text{TiO}_2$ . As such, the treated  $\text{TiO}_2$  with porphyrin or maquette-porphyrin ensembles can be used as a photoanode within devices. Within this chapter, devices were developed utilizing the conventional dye sensitized solar cell (DSSC) construct as a ‘proof of principle’ for utilization of maquettes for light harvesting [1, 2]. Furthermore, characterisation techniques are well known for analysis of DSSC based devices, allowing for the various processes associated with light-driven charge separation to be analysed and compared [3]. The use of maquettes and porphyrins within devices draws comparisons to nature, whereby pigments associated with proteins are used as light-harvesters in nature, which have also been implemented in DSSC constructs [4]. However, these invariably produced efficiencies  $<1.5\%$  (except for one which used red turnip extract, reaching efficiencies of  $1.7\%$  [5]). Despite the efficiencies obtained, all pigments resulted in open circuit voltage ( $V_{oc}$ ) measurements of  $>0.6\text{ V}$ , attributed predominantly to electron recombination processes between the electrode and redox mediator. The devices produced here incorporate readily made porphyrins, synonymous with many naturally occurring pigments, with the impacts of incorporating a maquette within the device characterised. Two porphyrins were chosen to be analysed here, P1d and P3d, chosen due to the factors influencing absorbance onto  $\text{TiO}_2$  in conjunction with stabilities in aqueous and non-aqueous solvents (as shown in the previous Chapters).

Predominantly, the characterisation of a DSSC is focused on four values obtained from a current-voltage ( $IV$ ) curve. A typical  $IV$  curve is shown in Figure VII-1, whereby the resulting short circuit current ( $I_{sc}$ ), open circuit voltage ( $V_{oc}$ ), fill factor (FF), and over-all efficiency ( $\eta$ ) of the device can be obtained. With the surface area of the measured device known, the current density ( $J_{sc}$ ) can be determined, allowing calculation of  $\eta$  (Equation 1).  $J_{sc}$  is the highest current obtained under short circuit conditions (no voltage), whereby  $V_{oc}$  is the maximum voltage when there is no current flow and corresponds to the energy difference between Fermi level of  $\text{TiO}_2$  and the energy level of the redox mediator [6].  $J_{sc}$  and  $V_{oc}$  measurements give indications on electron injection and recombination respectively, with the overall efficiency of the cell derived from these two parameters in conjunction with FF. However, as the objective of this work was not to produce a device with maximum efficiency, but rather probe the effectiveness of the

maquette-porphyrin ensemble to undertake electron transport, other characterisation methods were utilised.

### Equation 1

$$\eta (\%) = (J_{sc} V_{oc} FF) / P_{in}$$

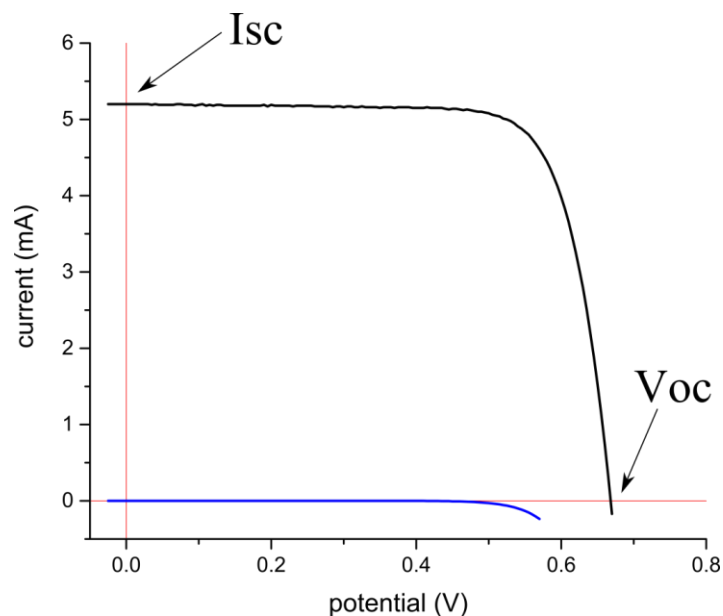


**Figure VII-1;** A typical current-voltage (*IV*) curve from a DSSC. The current from a DSSC at corresponding voltages allows for determination of short circuit current ( $I_{sc}$ ) and open circuit voltage ( $V_{oc}$ ). For comparison, the current response under illumination (black line) is compared to the current response when the device is in the dark (blue line).

Further characterisation of DSSCs can be made through various other techniques such as incident photon to current efficiency (IPCE), and electrochemical impedance spectroscopy (EIS). IPCE allows the wavelengths associated with photocurrent response to be analysed, whereas EIS is used to look specifically at the various interfaces within devices [7]. EIS measurements are represented by two plots, the Nyquist and Bode plots, commonly measured at  $V_{oc}$  (Figure VII-2). When analysed via software using appropriate equivalent circuit conditions for alternating current perturbation, the associated resistance and capacitance at each interface can be determined. DSSCs typically consist of one ohmic resistance ( $R_o$ ) and four arcs ( $\omega_1$ - $\omega_4$ ) attributed to electron transfer at electrochemical interfaces (Figure VII-2a) [7]. An arc present in a Nyquist plot ( $\omega$ ) represents the presence of an electrochemical interface, with the frequency at the top of the observable arc proportional to the resistance ( $R$ ) and capacitance ( $C$ ) at the specific electrochemical interface, which follows the equation  $\omega=(RC)^{-1}$  [7]. The arcs  $\omega_1$ - $\omega_4$  (Figure VII-2a) are ascribed to the electron transfer at the FTO substrate/ $TiO_2$  interface, electron transfer between  $TiO_2$  particles in conjunction with the Pt counter electrode and the electrolyte, ‘back’ transfer of electrons from  $TiO_2$  to  $I_3^-$  in the electrolyte (at the

TiO<sub>2</sub>/dye/electrolyte interface), and diffusion impedance of I<sub>3</sub><sup>-</sup> in the electrolyte, respectively [7]. Within this study, two predominant interfaces (arcs) were observed, and as such, the first arc (referred to herein as  $\omega_{\text{TiO}_2}$ ) was attributed to a combination of both  $\omega_1$ - $\omega_2$ . The second arc (interface) was attributed to  $\omega_3$ , referred to herein as  $\omega_{\text{TiO}_2/\text{D/E}}$ . The lower frequency,  $\omega_4$ , is typically ascribed to the diffusion limitations of the the I/I<sub>3</sub><sup>-</sup> redox electrolyte. In all the devices measured here, no diffusion impedance can be observed due to the closeness (25  $\mu\text{m}$ ) of the electrodes.

Of significance within this study, and indeed affecting DSSC performance most drastically [7], is the resistance associated with  $\omega_3$ , associated with the electron ‘recombination’ from the conduction band (CB) of TiO<sub>2</sub> back to the redox mediator. An electron lifetime in the CB of TiO<sub>2</sub> before recombination with I<sub>3</sub><sup>-</sup> can be determined from the resistance associated with this TiO<sub>2</sub> to I<sub>3</sub><sup>-</sup>. Electron lifetimes ( $\tau$ ) can be calculated from the phase shift versus frequency plots as  $\tau \approx 1/\omega_{\text{min}} = 1/(2\pi f_{\text{min}})$  where  $f_{\text{min}}$  is the frequency at which the phase shift is minimum [8], as shown in Figure VII-2b. Furthermore,  $\tau$  is closely related to the recombination resistance ( $R_{\text{rec}}$ ) and the capacitance ( $C$ ) of  $\omega_{\text{TiO}_2/\text{D/E}}$ , which follows the equation  $\tau = R_{\text{rec}}C$  [7].

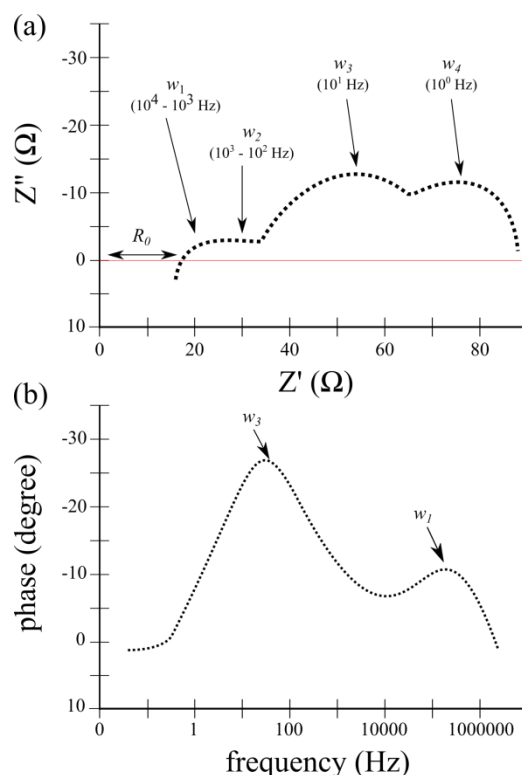


**Figure VII-2; Example of impedance measurements from a TiO<sub>2</sub> based porphyrin DSSC.** (a) Nyquist plot representation showing the series resistance ( $R_0$ ) and the resistances associated with the four potential interfaces ( $\omega_1$ - $\omega_4$ ) of a TiO<sub>2</sub> based DSSC. (b) Bode plot representation displaying the phase shift peaks associated with specific interfaces. Figure adapted from [7].

As the DSSC construct was chosen for the development of devices using porphyrins and maquettes, the driving forces for the electron transfer processes needed to be determined to ensure the effective functioning of the device. Two determining driving forces for DSSCs are the injection of electrons from photoexcited porphyrins into the conduction band of  $\text{TiO}_2$ , and the regeneration of porphyrin cations by the redox mediator. Therefore, the HOMO-LUMO energy levels of the porphyrin must be appropriately aligned with the CB of  $\text{TiO}_2$  and the redox mediator (in this case,  $\text{I}^-/\text{I}_3^-$ ) for the device to function. With the redox potential of  $\text{I}^-/\text{I}_3^-$  known to be  $-4.76$  eV, in conjunction with a driving force for effective regeneration evaluated to be  $0.5$  eV [9, 10], the HOMO energy levels of both P1d and P3d indicate that regeneration with the redox couple will occur readily (Figure VII-3). However, the driving forces attributed to injection of electrons from the photoexcited state of the porphyrin into the CB of  $\text{TiO}_2$  is  $160$  mV different between the two porphyrins present here, as a result of the difference in LUMO energy levels. Furthermore, the CB of  $\text{TiO}_2$  shown ( $-3.94$  eV) [3] is the potential under vacuum when using organic solvents, with the CB known to shift to higher energy levels with increases in pH [11]. Therefore, the driving forces shown here (Figure VII-3) are the maximum driving forces attainable, with the potential shifts in the CB of  $\text{TiO}_2$  likely to reduce driving forces for electron injection when exposed to buffers used within the experiments presented here.

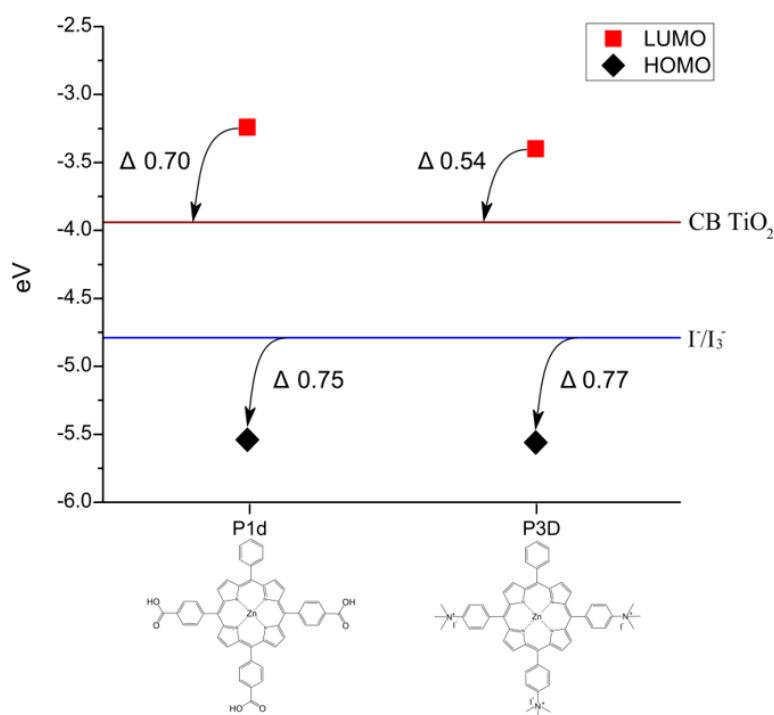


**Figure VII-3; Driving forces associated with DSSCs using P1d or P3d.** The determined HOMO-LUMO energy levels from electrochemical analysis of P1d or P3d allows for calculation of the driving forces for injection into the conduction band of  $\text{TiO}_2$  (CB  $\text{TiO}_2$ ) and regeneration with the redox couple ( $\text{I}^-/\text{I}_3^-$ ).

Utilizing the conventional DSSC construct (as depicted in Chapter I), porphyrins were bound to  $\text{TiO}_2$  on standard 4 x 4 mm electrodes (as described in Chapter II and discussed in Chapter V), with the resulting electrodes fabricated into devices. Two different electrolytes (E1-E2), as shown below, were employed to assess the effects of lithium iodide, since  $\text{Li}^+$  ions interact with the  $\text{TiO}_2$  surface to induce shifts in the conduction band which increases the driving force for electron injection and interacts with the dye [12-15]. The  $\text{Li}^+$  ions were explicitly varied as they are known to also interact with polypeptides [16], therefore likely to interact with the maquette and influence device performance. As is commonly the case, 4-tert-butylpyridine (4-tbp) was used as it leads to a large increase in open circuit potential from its effect on the conduction band of  $\text{TiO}_2$  and increase of electron lifetime [17].

**Electrolyte 1 (E1)**

Prepared in 85:15, vol% acetonitrile/valeronitrile with;

- 0.03 M Iodine ( $\text{I}_2$ ),
- 0.6 M BMII, and
- 0.5 M 4-tbp

**Electrolyte 2 (E2)**

Prepared in 85:15, vol% acetonitrile/valeronitrile with;

- 0.03 M Iodine ( $\text{I}_2$ ),
- 0.6 M BMII,
- 0.1 M LiI, and
- 0.5 M 4-tbp

For all EIS measurements of devices developed and presented here, a 2-time constant model (as shown in Figure VII-4) was used for attaining and analysing resistances and capacitances associated at the observed interfaces [18, 19]. The model was employed for analysis of all measurements to allow for direct comparisons between devices. With all devices prepared in identical manners (apart from binding to  $\text{TiO}_2$ ), electron transfer between  $\text{TiO}_2$  and FTO or at the Pt coated cathode would not be expected to be different between devices [7]. Therefore, differences observed from device performance would arise from differences in electron transfer between  $\text{TiO}_2$  nanoparticles ( $\omega_2$ ). For all EIS results presented here, the series resistance of the device is denoted by  $R_0$ , with the first observed interface being the combination of  $\omega_1$  and  $\omega_2$ , and the second interface  $\omega_3$ , denoted by  $\omega_{\text{TiO}_2}$  and  $\omega_{\text{TiO}_2/\text{D/E}}$  respectively.

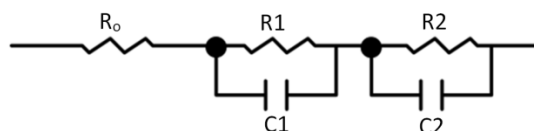


**Figure VII-4; Circuit model used for analysing resistances and capacitances.** A 2-time constant model was used for analysing EIS measurements, attaining associated resistances and capacitances for the associated observed interface.

Within this chapter, two maquette sequences were chosen, the GL-maquette and the *cysGL*-maquette. The sequences and binding strategies to  $\text{TiO}_2$  are discussed in more detail within Chapters III and V. In general, the difference between GL- and *cysGL*-maquette sequences is that the later contains a single cysteine residue in the loop region, which can be used for covalent attachments to a functionalised  $\text{TiO}_2$  surface. In contrast, the GL-maquette immobilises onto  $\text{TiO}_2$  via electrostatic interactions (Chapter V). The maquette sequences contain two histidine residues within the hydrophobic interior, which are independently capable of ligating to the porphyrins P1d and P3d presented here (Chapter III). This chapter looks at not only the utilization of maquettes with porphyrins for light-driven charge separation, but also at the impacts of maquette/porphyrin binding strategies in context of charge separation processes.

## 2- Results; Solar Cell Devices

### 2.1- P1d on non-treated TiO<sub>2</sub>

#### 2.1.1- Devices using sensitized P1d

Conventional sensitization of a TiO<sub>2</sub> surface by P1d itself produced an electrode with a strong absorbance at 420-430 nm (as shown in Chapter V). This electrode was fabricated into a DSSC based device, using either electrolyte E1 or electrolyte E2. The photovoltaic and EIS data for these devices is presented in Figure VII-5 (E1) and Figure VII-6 (E2).

With addition of LiI to the electrolyte (E2, Figure VII-6), the overall efficiency of the device increases by ~40 %, compared to E1 (Figure VII-5). This increase in efficiency is due to the ~45 % increase in  $J_{sc}$  with presence of LiI. In contrast,  $V_{oc}$  decreases with the electrolyte containing LiI by ~8 %. Minimal difference in series resistance ( $R_o$ ) is apparent when E1 or E2 is utilized. Similarly, minimal differences with the resistance and capacitance associated with  $\omega_{TiO_2}$  are apparent for E1 and E2. The most prominent difference observed is the capacitance associated with the TiO<sub>2</sub>/dye/electrolyte interface ( $\omega_{TiO_2/D/E}$ ), increasing by over 6-fold when LiI is employed (E2). The electron lifetime ( $\tau_{\omega_{TiO_2/D/E}}$ ) increases by over 3-fold for devices using E2, with  $\tau_{\omega_{TiO_2/D/E}}$  being closely associated with the resistances of recombination and the chemical capacitance [20]. Therefore, as the resistances for devices employing E1 or E2 vary by ~10 %, the increase in electron lifetime for when Li<sup>+</sup> is present arises from the increase in chemical capacitance (increasing by over 6-fold). This is in agreement with the previous reports, whereby the presence Li<sup>+</sup> reduces the  $V_{oc}$  via a shift in the CB of TiO<sub>2</sub> to lower energy levels, thereby simultaneously increasing the  $J_{sc}$  via an increase in driving force [14, 21].

#### 2.1.2- Devices using P1d bound from aqueous buffer

Immobilization of P1d from aqueous buffer to TiO<sub>2</sub> has been shown in previous Chapters. The resulting electrodes were fabricated into DSSC based devices, with comparisons using either E1 or E2, with the photovoltaic and EIS data shown in Figure VII-7 and Figure VII-8 respectively.

As is shown in Figure VII-8, utilizing E2 within the devices increases overall efficiencies by ~40 % compared to devices utilizing E1 (Figure VII-7). As was shown previously for devices with sensitized P1d to TiO<sub>2</sub>, this increase in efficiency is attributed to the difference in  $J_{sc}$ , increasing by ~45 % when Li<sup>+</sup> is present. As was determined previously, differences in device performance arise from the interface between TiO<sub>2</sub>/dye/electrolyte

( $\omega_{\text{TiO}_2/\text{D/E}}$ ), with minimal differences associated with the series resistance along with the resistance and capacitance associated with  $\omega_{\text{TiO}_2}$  observed. With addition of  $\text{Li}^+$ , it is apparent that the resistance associated with  $\omega_{\text{TiO}_2/\text{D/E}}$  ( $R_{\omega_{\text{TiO}_2/\text{D/E}}}$ ) is halved, whereas the capacitance ( $C_{\omega_{\text{TiO}_2/\text{D/E}}}$ ) increased over 8-fold. The chemical capacitance increase results in an increase of the electron lifetime ( $\tau_{\omega_{\text{TiO}_2/\text{D/E}}}$ ) by over 3-fold when  $\text{Li}^+$  is present.

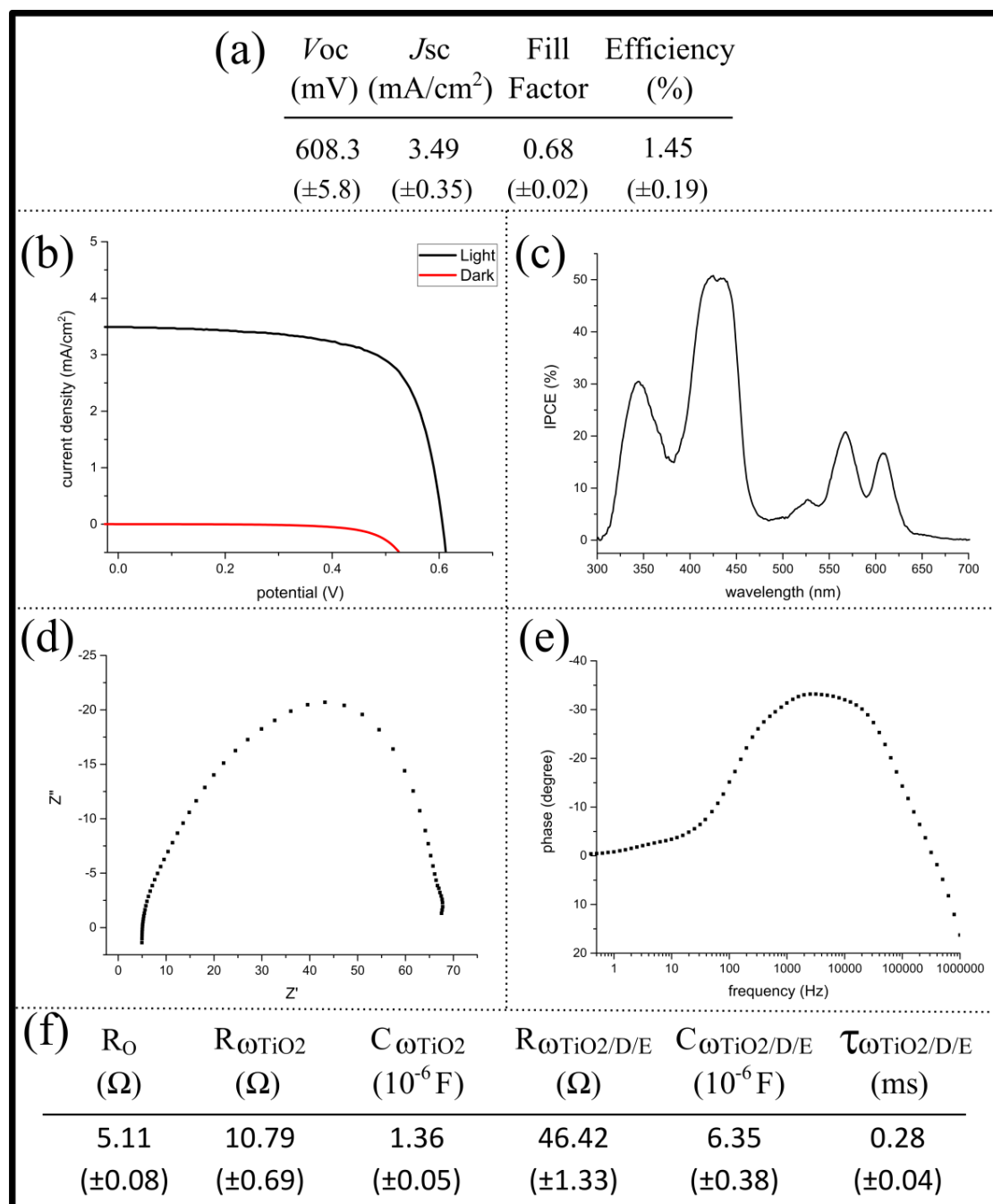


**Figure VII-5; Device measurements utilizing sensitized P1d from THF and E1.** The resulting device measurements of  $2.5 \mu\text{m}$   $\text{TiO}_2$  with sensitized P1d, using electrolyte 1 (E1). (a) Photovoltaic data from illumination under 1 sun. (b) The average  $JV$  curve under illumination (black line) and in the dark (red line). (c) The average IPCE measurement. (d) Nyquist-plot representation of the device. (e) Bode-plot representation of the device. (f) Obtained impedance spectroscopy data from a 2-phase circuit representation of the device. (Averages and standard deviations shown, where number of devices=3).



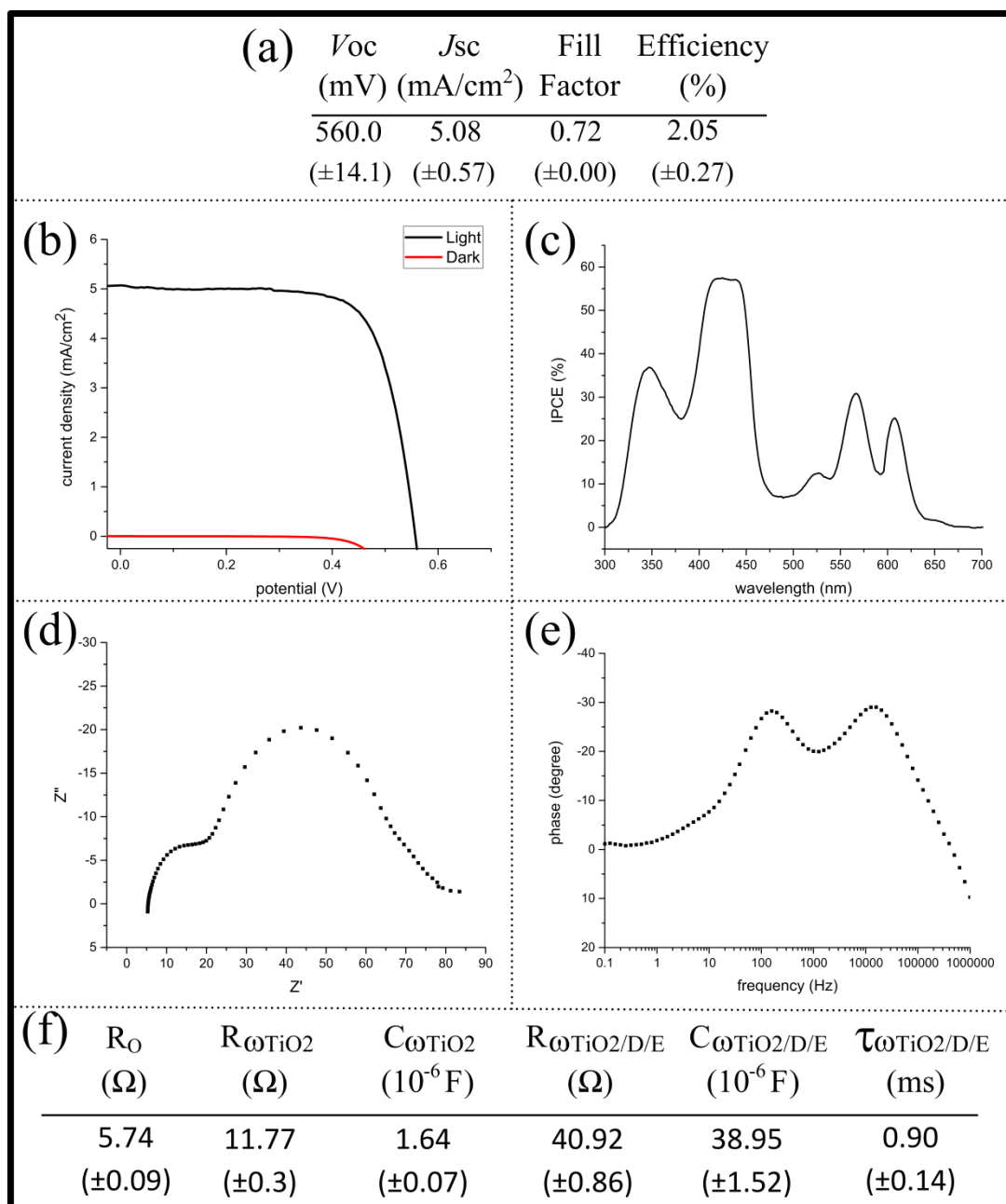


**Figure VII-6; Device measurements utilizing sensitized P1d from THF and E2.** The resulting device measurements of  $2.5 \mu\text{m}$   $\text{TiO}_2$  with sensitized P1d, using electrolyte 2 (E2). (a) Photovoltaic data from illumination under 1 sun. (b) The average  $JV$  curve under illumination (black line) and in the dark (red line). (c) The average IPCE measurement. (d) Nyquist-plot representation of the device. (e) Bode-plot representation of the device. (f) Obtained impedance spectroscopy data from a 2-phase circuit representation of the device. (Averages and standard deviations shown, where number of devices=3).

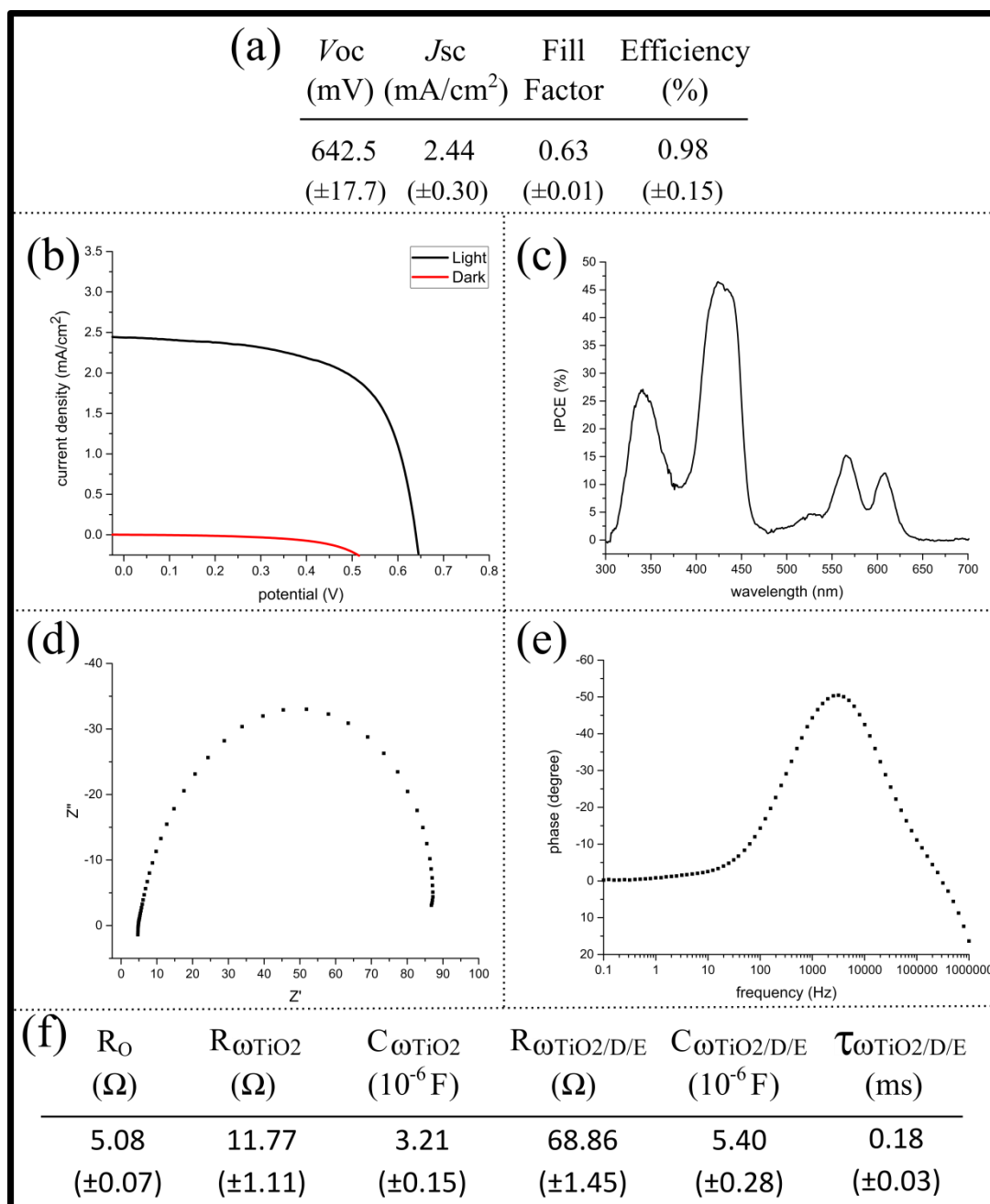


**Figure VII-7; Device measurements utilizing P1d bound from aqueous buffer and E1.** The resulting device measurements of 2.5  $\mu\text{m}$   $\text{TiO}_2$  with P1d bound from aqueous buffer, using electrolyte 1 (E1). (a) Photovoltaic data from illumination under 1 sun. (b) The average  $JV$  curve under illumination (black line) and in the dark (red line). (c) The average IPCE measurement. (d) Nyquist-plot representation of the device. (e) Bode-plot representation of the device. (f) Obtained impedance spectroscopy data from a 2-phase circuit representation of the device. (Averages and standard deviations shown, where number of devices=3).

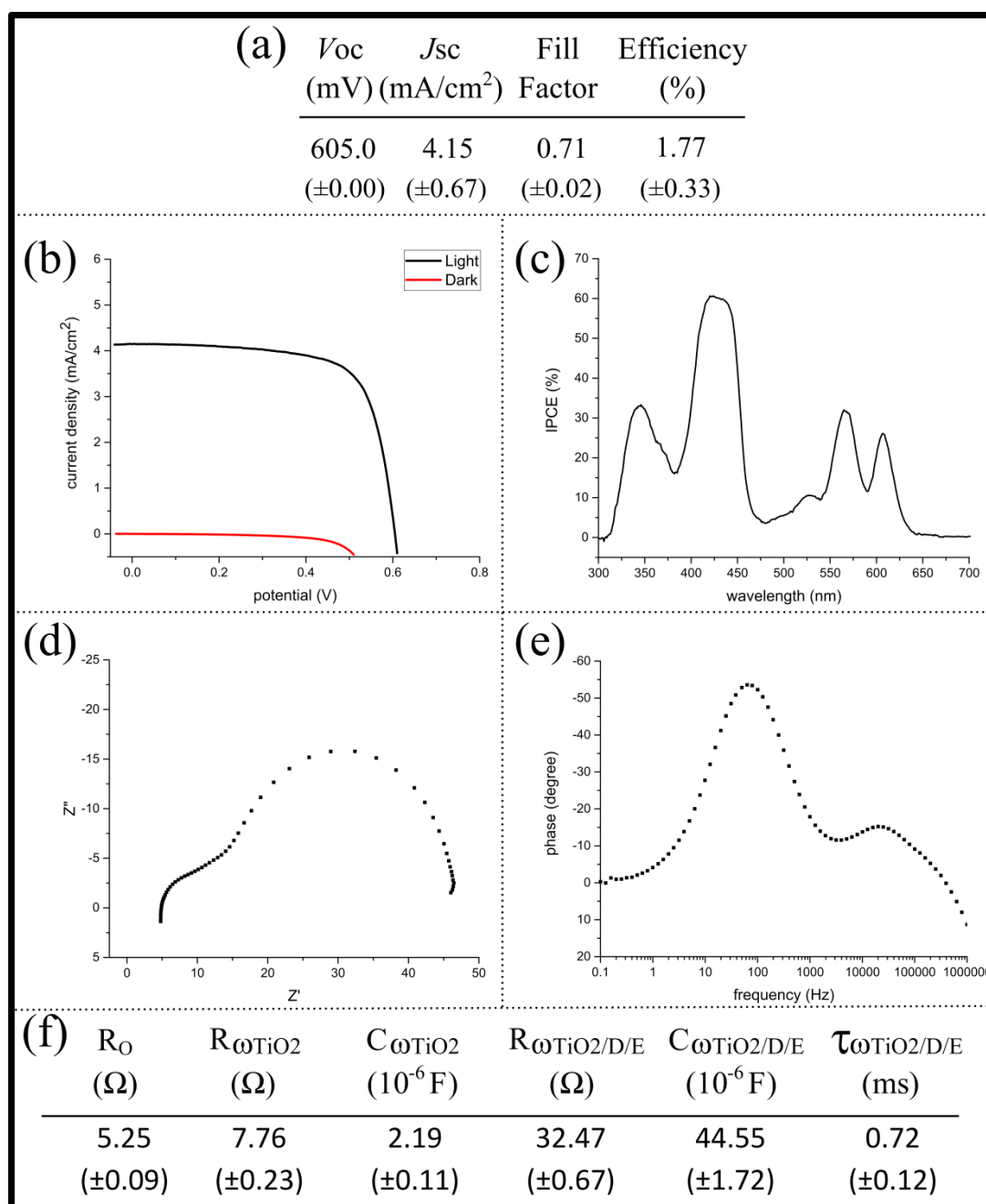


**Figure VII-8; Device measurements utilizing P1d bound from aqueous buffer and E2.** The resulting device measurements of 2.5  $\mu\text{m}$   $\text{TiO}_2$  with P1d bound from aqueous buffer, using electrolyte 2 (E2). (a) Photovoltaic data from illumination under 1 sun. (b) The average  $JV$  curve under illumination (black line) and in the dark (red line). (c) The average IPCE measurement. (d) Nyquist-plot representation of the device. (e) Bode-plot representation of the device. (f) Obtained impedance spectroscopy data from a 2-phase circuit representation of the device. (Averages and standard deviations shown, where number of devices=3).

### 2.1.3- Devices using maquette-P1d ensembles

Assembly, purification, and the binding of maquette-P1d ensembles to  $\text{TiO}_2$  from aqueous buffer have been shown in Chapter V. In short, GL-P1d ensembles were formed in aqueous buffer, which were immobilised onto  $\text{TiO}_2$  electrostatically with subsequent rinsing and drying. Resulting electrodes were fabricated into DSSC based devices using either E1 or E2 for further insight into device performance.

Figure VII-9 displays device data utilizing E1 that are slightly lower in efficiency and  $J_{sc}$  than those utilizing E2 (Figure VII-10). As was shown previously with P1d bound to  $\text{TiO}_2$ , differences in device performance arise from the interface at  $\text{TiO}_2/\text{dye}/\text{electrolyte}$  ( $\omega_{\text{TiO}_2/\text{D}/\text{E}}$ ), with minimal differences observed for  $R_O$  or  $\omega_{\text{TiO}_2}$ . With addition of  $\text{Li}^+$ , the resistance at  $\omega_{\text{TiO}_2/\text{D}/\text{E}}$  ( $R_{\omega_{\text{TiO}_2/\text{D}/\text{E}}}$ ) increases slightly by  $\sim 10\%$ , with the capacitance ( $C_{\omega_{\text{TiO}_2/\text{D}/\text{E}}}$ ) increasing by nearly 2-fold. As was previously observed, this increase in chemical capacitance is attributed to increasing the electron lifetime ( $\tau_{\omega_{\text{TiO}_2/\text{D}/\text{E}}}$ ), increasing by  $\sim 58\%$  in the presence of  $\text{Li}^+$ .

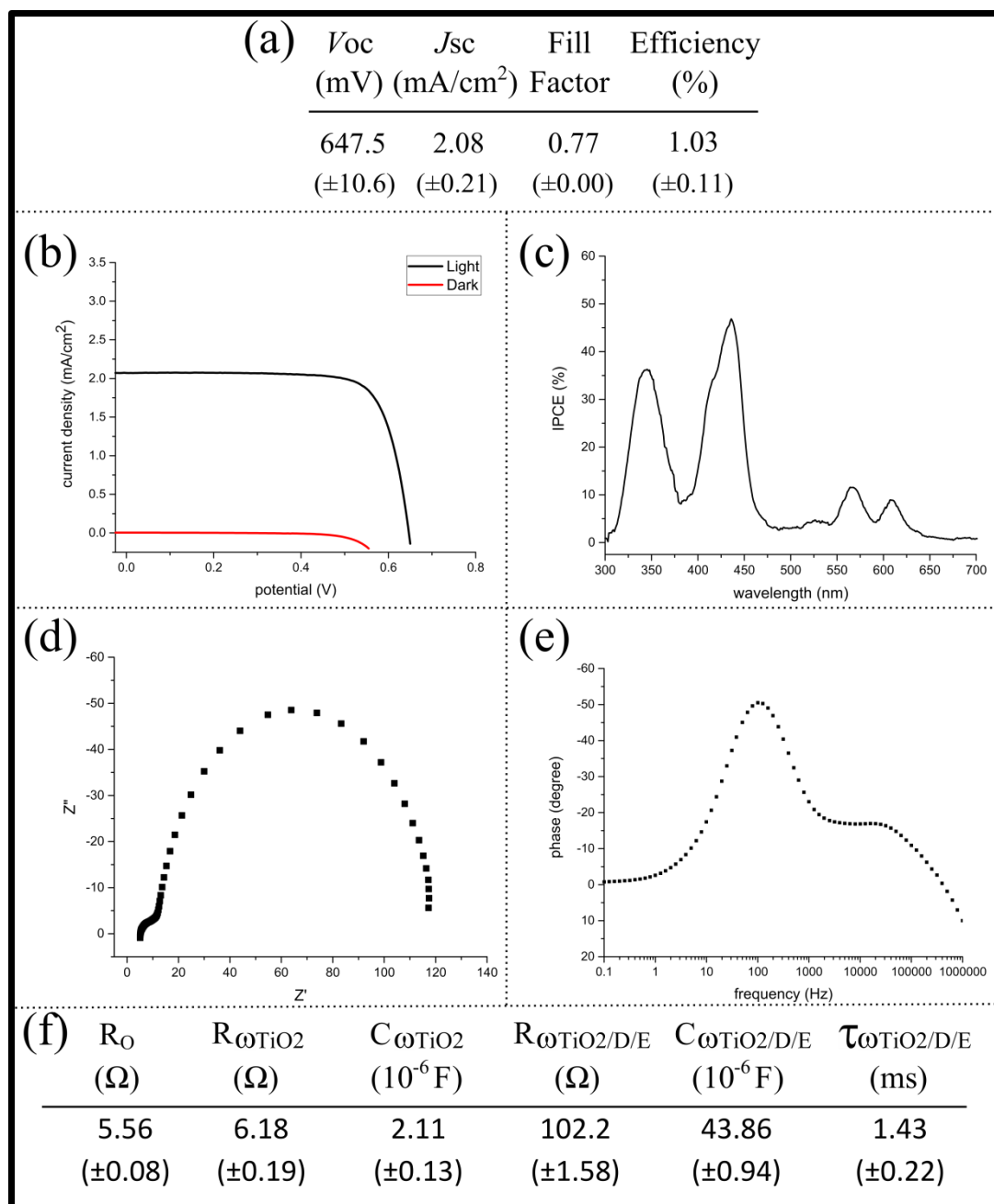


**Figure VII-9; Device measurements utilizing maquette-P1d ensembles electrostatically bound from aqueous buffer and E1.** The resulting device measurements of 2.5  $\mu\text{m}$   $\text{TiO}_2$  with maquette-P1d ensembles, using electrolyte 1 (E1). (a) Photovoltaic data from illumination under 1 sun. (b) The average  $JV$  curve under illumination (black line) and in the dark (red line). (c) The average IPCE measurement. (d) Nyquist-plot representation of the device. (e) Bode-plot representation of the device. (f) Obtained impedance spectroscopy data from a 2-phase circuit representation of the device. (Averages and standard deviations shown, where number of devices=3).

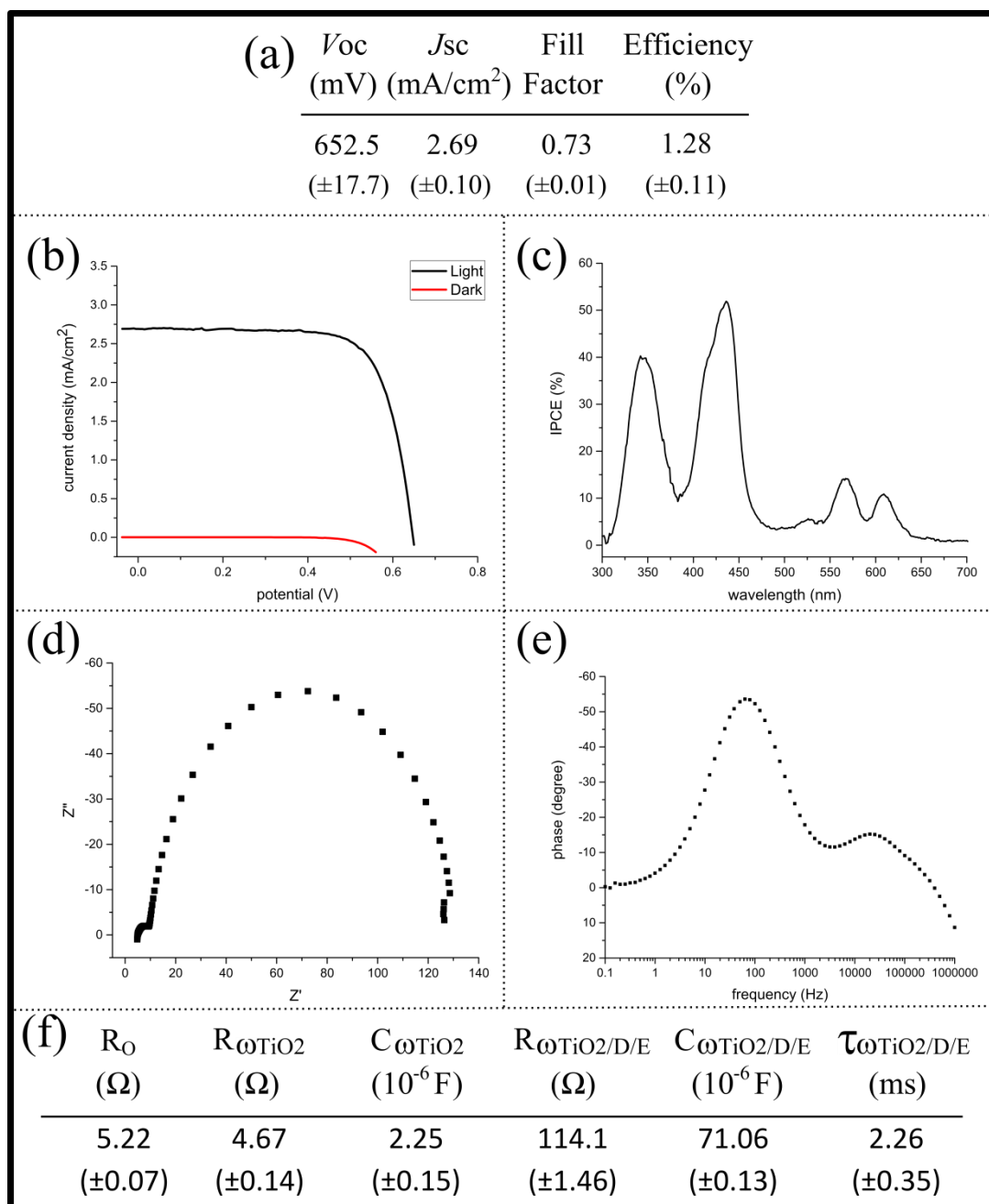


**Figure VII-10; Device measurements utilizing maquette-P1d ensembles electrostatically bound from aqueous buffer and E2.** The resulting device measurements of 2.5  $\mu\text{m}$   $\text{TiO}_2$  with maquette-P1d ensembles, using electrolyte 2 (E2). (a) Photovoltaic data from illumination under 1 sun. (b) The average  $JV$  curve under illumination (black line) and in the dark (red line). (c) The average IPCE measurement. (d) Nyquist-plot representation of the device. (e) Bode-plot representation of the device. (f) Obtained impedance spectroscopy data from a 2-phase circuit representation of the device. (Averages and standard deviations shown, where number of devices=3).

### 2.1.4- Charge retention

During device measurements, it was noted that the ‘dark’ curves for  $JV$  measurements were not at the expected 0 V and 0 A for devices employing maquette-P1d, with the measured  $V_{oc}$  being  $>100$  mV. However, the ‘expected’ values for the dark curve returned after a period of time ( $>10$  min). Therefore, to investigate this phenomenon further, the three modified  $TiO_2$  electrodes, outlined in previous results, were analysed for  $V_{oc}$  ‘survival’ after light exposure with electrolyte E2. As shown in Figure VII-11a, when the light exposure is removed from devices made from P1d sensitized from THF or immobilized from aqueous buffer, the  $V_{oc}$  ‘decays’ to 0 mV within seconds. Conversely, employing maquette-P1d devices, the  $V_{oc}$  ‘decays’ at an extremely slow rate after light exposure is removed, compared to the previous two devices, with the  $V_{oc}$  taking longer than 5 min to return to 0 V. As the  $V_{oc}$  is the difference in potential across the device with no current [22], the results presented here indicate that the charges associated with electron transport under illumination are retained after light exposure when maquette is present (after the light is turned off). To determine if  $Li^+$  is influencing the observed ‘decay’, electrolyte E1 was used (containing no  $Li^+$ ). The results once again show that when P1d is immobilized from aqueous buffer the  $V_{oc}$  ‘decays’ to 0 mV within seconds (Figure VII-11b). When the maquette-P1d ensembles are employed, the  $V_{oc}$  again ‘decays’ slowly, identical to that for when E2 was used. The charge measured here is associated with electrons in the CB of  $TiO_2$ , with this retention of charge giving evidence that the maquette ‘layer’ is inhibiting charge recombination between triiodide and the photoanode.

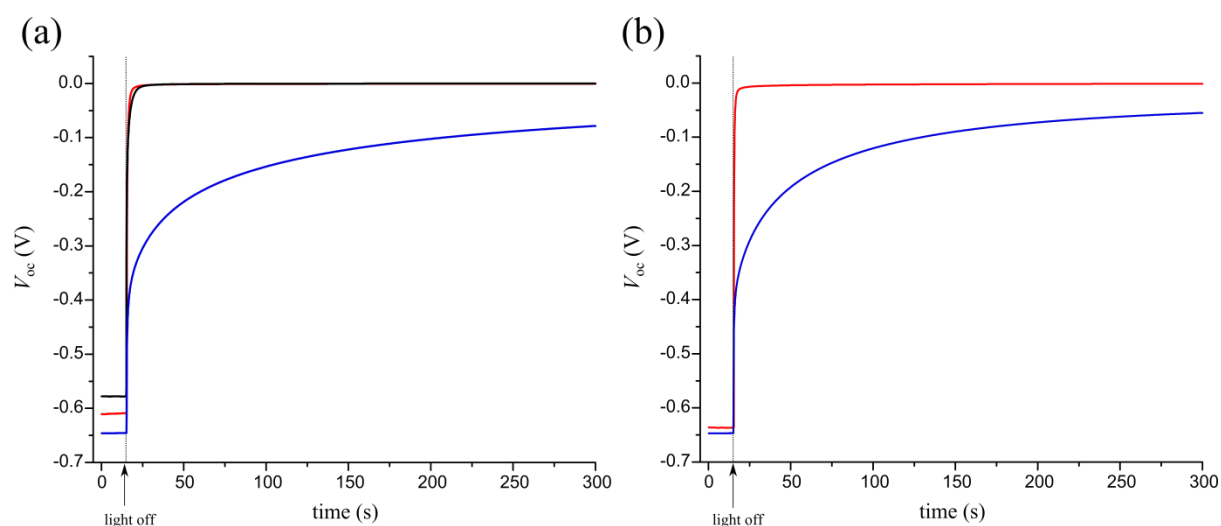


**Figure VII-11; Device open circuit voltage decay using electrolyte E2 (a) or electrolyte E1 (b).** The open circuit voltage ( $V_{oc}$ ) of the devices developed with  $2.5 \mu m$   $TiO_2$  with sensitized P1d from THF (black line), P1d bound from aqueous buffer (red line), or maquette-P1d ensembles (blue line), analysed for  $V_{oc}$  retention (decay) over time after illumination (light is turned off after 15 sec).

### 2.1.5- Quantification of P1d on TiO<sub>2</sub>

In order to compare between devices measured, the quantities of the photoactive P1d is needed. P1d was successfully removed from the surface of TiO<sub>2</sub> using strong base in THF, however, this solution did not completely remove the P1d when it was ligated to the maquette on the surface. Since strong acids readily remove metals from porphyrins, an alternative approach was employed with 2M HCl in THF. As P1d has a significantly altered spectrum in HCl/THF, a standard curve (Figure VII-12) was used to calculate the extinction coefficient and Soret peak position of P1d in HCl/THF. With the standard curve in conjunction with the volume used for desorption of P1d from the surfaces, the concentration of P1d could be determined (Table VII-1). Furthermore, as the surface area and thickness of TiO<sub>2</sub> is known, the quantity of P1d per volume of TiO<sub>2</sub> (cm<sup>2</sup>/μm) could be determined.

As shown, the quantity of P1d is greatest when directly sensitized onto the surface from THF, with the quantity of P1d present on electrodes being the least when ligated with maquettes. This is not surprising given the maquette would occupy a significantly larger surface area than the bound porphyrin. On the other hand, there is much less buffer-bound porphyrin on the surface undoubtedly due to the smaller number of electrostatic binding sites on the TiO<sub>2</sub>. This difference is indeed obvious from the paler colour of the buffer-bound electrodes compared to the THF-sensitized electrodes. Specifically, the ratios for the quantities of P1d present when THF sensitized, buffer-bound, and ligated with maquette is 6.2:2.6:1.0, respectively.



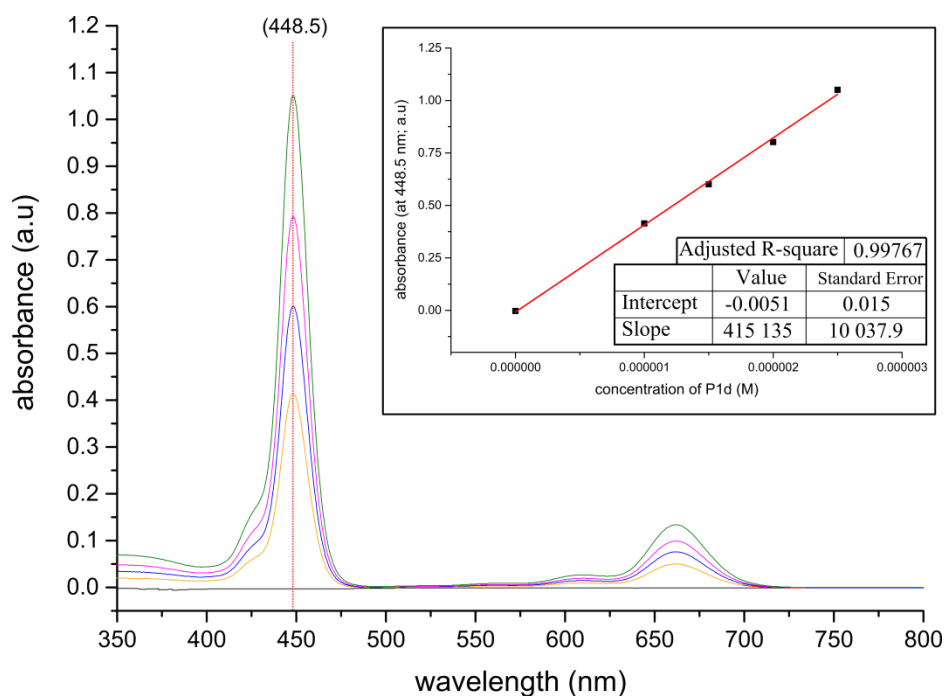


**Figure VII-12; Standard curve determination of P1d in 2 M HCl/THF.** The standard curve of P1d in 2M HCl/THF is used to determine the concentration of P1d in the solvent, with the obtained gradient representing the extinction coefficient at absorbance maximum (448.5 nm), being  $415,135 \text{ M}^{-1} \text{ cm}^{-1}$  ( $\pm 10,038$ ).

**Table VII-1; Quantification of P1d within devices.** Using the known extinction coefficient of P1d in the desorption solution used (2M HCl/THF), a known volume is used to remove P1d from  $\text{TiO}_2$ , with the concentration and subsequent quantity of P1d calculated (Averages and standard deviations shown, where number of repeats=4).

Desorbed sample	Concentration (nmol/L)	Quantity (nmol/cm <sup>2</sup> /μm)
P1d bound from THF	1,799 (±68.9)	13.5 (±0.5)
P1d bound from aqueous buffer	759.2 (±159.3)	5.69 (±1.2)
Maquette-P1d ensembles	292.7 (±13.0)	2.20 (±0.1)

## 2.2- Devices using maquette-P3d ensembles

Previously it was shown that P3d (triammonium salt porphyrin) interacts with  $\text{TiO}_2$  weakly, producing near negligible absorbance (from both THF and aqueous CHES buffer). The resulting electrodes were fabricated into devices, which produced no apparent current (data not shown). In contrast, when P3d was ligated to a maquette with subsequent immobilization onto  $\text{TiO}_2$ , significant absorbance was observed. When P3d was ligated with the GL-maquette and immobilized from CHES buffer (pH=8.5) onto  $\text{TiO}_2$ , the resulting device utilizing electrolyte E2 produced an efficiency of  $0.04 \pm 0.02 \%$  (Figure VII-13a), low due to the small current ( $0.10 \pm 0.03 \text{ mA}$ ). As shown in the IPCE data (Figure VII-13c), there is near undetectable current over the absorbance range of the ligated P3d. There were no significant differences observed for the series resistance ( $R_0$ ), nor the resistance or capacitance associated with  $\omega_{\text{TiO}_2}$  (Figure VII-13f) compared to the devices utilizing P1d. The most prominent difference comes from  $R_{\omega_{\text{TiO}_2/\text{D/E}}}$ , the resistance associated with the  $\text{TiO}_2$  and redox electrolyte interface. This large resistance ( $3,167 \pm 68.1 \Omega$ ) is related to the electron recombination from the CB of  $\text{TiO}_2$  to the triiodide, giving an unusually high electron lifetime ( $\tau_{\omega_{\text{TiO}_2/\text{D/E}}}$ ) value of  $10.34 (\pm 2.41) \text{ ms}$ . However, this phenomenon arises due to two influencing factors, namely, the small current (and therefore restricted electron injection) and the insulating maquette resulting in substantial reduction in the probability of recombination at the observed interface.

As high pHs are known to increase the conduction band edge of  $\text{TiO}_2$  [23-26], the driving force between the LUMO of P3d and the conduction band edge could have been hindering the flow of current. Therefore, maquette-P3d ensembles were immobilized onto  $\text{TiO}_2$  from MES buffer (pH=6.8), having a lower pH compared to the previously used aqueous buffer (pH=8.5). Figure VII-14 shows that this change in pH resulted in the devices having an increased current, with no distinct changes in  $V_{oc}$  or FF. Despite this slight increase in current, it is apparent that the porphyrin still does not inject electrons into the CB of  $\text{TiO}_2$  freely as evident in the IPCE (Figure VII-14c). The resistance associated with the  $\text{TiO}_2$  and electrolyte interface ( $R_{\omega_{\text{TiO}_2/\text{D/E}}}$ , Figure VII-14f), although significantly smaller than  $R_{\omega_{\text{TiO}_2/\text{D/E}}}$  when aqueous CHES buffer was used (Figure VII-13f), is still unusually large  $787.3 (\pm 27.9) \Omega$ . As was evident previously, this phenomenon likely arises due to the hindrance of electron injection into the CB of  $\text{TiO}_2$ , with the maquette layer insulating recombination processes results in substantial reduction in the probability of recombination at the observed interface. This once again results in the observed electron lifetime ( $\tau_{\omega_{\text{TiO}_2/\text{D/E}}}$ ), having the unusually high value of  $11.51 (\pm 1.87) \text{ ms}$ .

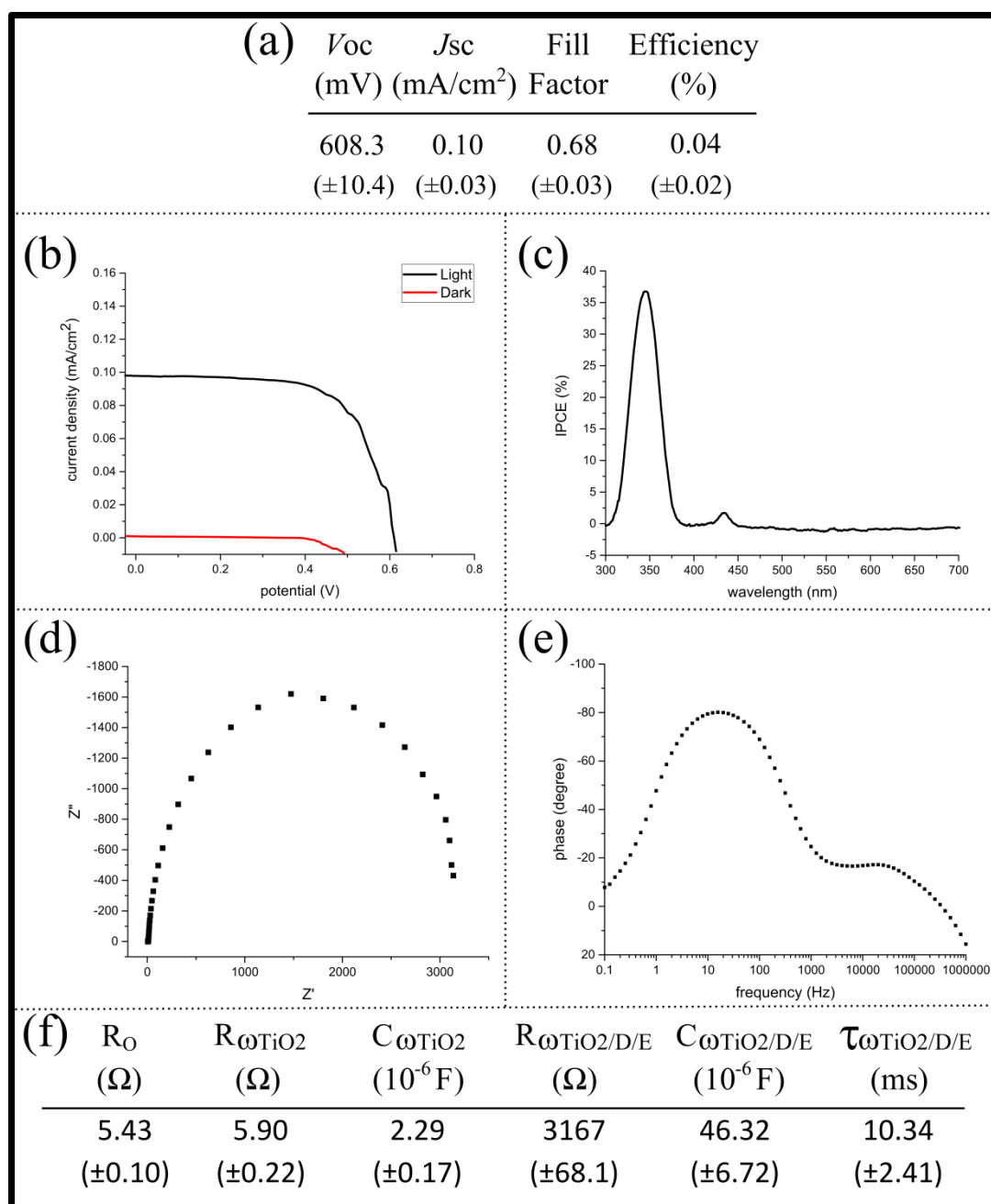


**Figure VII-13; Device measurements utilizing maquette-P3d ensembles from aqueous buffer.** The resulting device measurements of 2.5  $\mu\text{m}$   $\text{TiO}_2$  with maquette-P3d ensembles from aqueous buffer (pH=8.5), using electrolyte 2 (E2). (a) Photovoltaic data from illumination under 1 sun. (b) The average  $JV$  curve under illumination (black line) and in the dark (red line). (c) The average IPCE measurement. (d) Nyquist-plot representation of the device. (e) Bode-plot representation of the device. (f) Obtained impedance spectroscopy data from a 2-phase circuit representation of the device. (Averages and standard deviations shown, where number of devices=3).

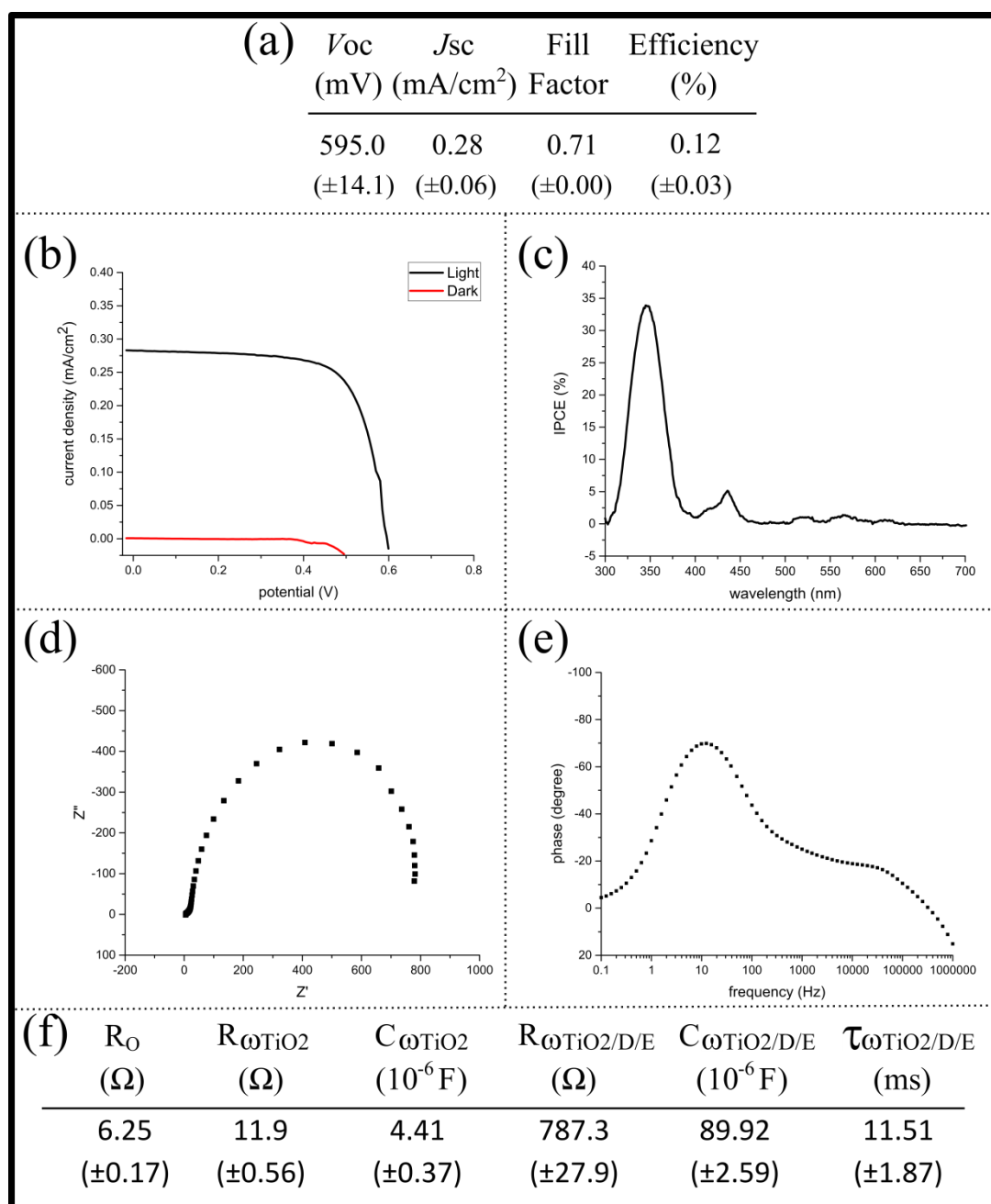


**Figure VII-14; Device measurements utilizing maquette-P3d ensembles from MES buffer.** The resulting device measurements of 2.5  $\mu\text{m}$   $\text{TiO}_2$  with maquette-P3d ensembles from MES buffer (pH=6.8), using electrolyte 2 (E2). (a) Photovoltaic data from illumination under 1 sun. (b) The average  $JV$  curve under illumination (black line) and in the dark (red line). (c) The average IPCE measurement. (d) Nyquist-plot representation of the device. (e) Bode-plot representation of the device. (f) Obtained impedance spectroscopy data from a 2-phase circuit representation of the device. (Averages and standard deviations shown, where number of devices=3).

## 2.3- P1d with functionalised TiO<sub>2</sub>

### 2.3.1- Devices using covalently attached *cysGL-P1d* ensembles

Covalent attachment to a modified TiO<sub>2</sub> surface by linking to the cysteine residue of the maquette has been described previously. As it has been shown that P1d was able to produce good photocurrent responses compared to P3d, P1d was used with *cysGL*-maquette to form ensembles for photovoltaic responses, with the pre-formed ensembles covalently attached to the modified TiO<sub>2</sub>. The method of attachment and absorbance profile of *cysGL-P1d* ensembles covalently attached to TiO<sub>2</sub> is described in Chapter V. The resulting electrodes were developed into devices using E2 as the redox couple.

Initial attempts to obtain satisfactory devices using 2.5 μm TiO<sub>2</sub> films were not successful and led to efficiencies below 0.5 %, typically as a result of low currents. Similarly, 8.5 μm TiO<sub>2</sub> films led to little improvement in photocurrent responses, therefore, the use of much thicker (18 μm) TiO<sub>2</sub> films was explored and gave results comparable to the previous non-covalently bound (electrostatically) ensemble devices. As can be seen in Figure VII-15, the efficiency of the thicker film devices was 1.46 %. The IPCE (Figure VII-15c) clearly shows that the photocurrent response comes from the porphyrin, which is ligated within the maquette. Notably, the electron lifetime at the TiO<sub>2</sub> electrolyte interface ( $\tau_{0\text{TiO}_2/\text{D/E}}$ ) is greater than that for when ensembles are electrostatically immobilised on the surface (5.74 compared to 2.26 ms, see Figure VII-10f), albeit for thinner films (2.5 μm). While functionalisation could create an increased barrier to recombination between the surface of TiO<sub>2</sub> and the electrolyte, the  $V_{\text{oc}}$  of the covalently bound maquette is very similar to that of the electrostatically bound maquette (628.3 ±10.4 vs 652.5 ±17.7 mV, respectively) and consequently, this does not appear to account for the lifetime difference.

As the mode of attachment differs significantly, the photoactive material (the porphyrin, P1d) proximity to TiO<sub>2</sub> is significantly altered. When ensembles are electrostatically immobilized, two positively charged helices (helix numbers II and IV- see Chapter V) of the maquette are likely interacting with the TiO<sub>2</sub> surface, effectively laying flat on its side. In contrast, when ensembles (using *cysGL*-maquette) are covalently attached, the cysteine in the loop region is the only residue capable of covalent attachment, therefore the maquette is likely standing ‘upright’ (refer to Chapter V). Consequently, when the maquette is laying flat, both the ligated porphyrins are close to TiO<sub>2</sub>, in contrast when the maquette is standing upright, proximal and distal ligated porphyrins occur. It is likely that the distal porphyrin is hindered for

efficient electron injection into the CB of TiO<sub>2</sub> due to distance. This is apparent from the  $J_{sc}$  being significantly reduced for when ensembles are covalently attached. It is for this significant reduction in  $J_{sc}$  as to why a thicker film (18  $\mu\text{m}$ ) was needed to be used, compared to the 2.5  $\mu\text{m}$  films used for electrostatic immobilization.

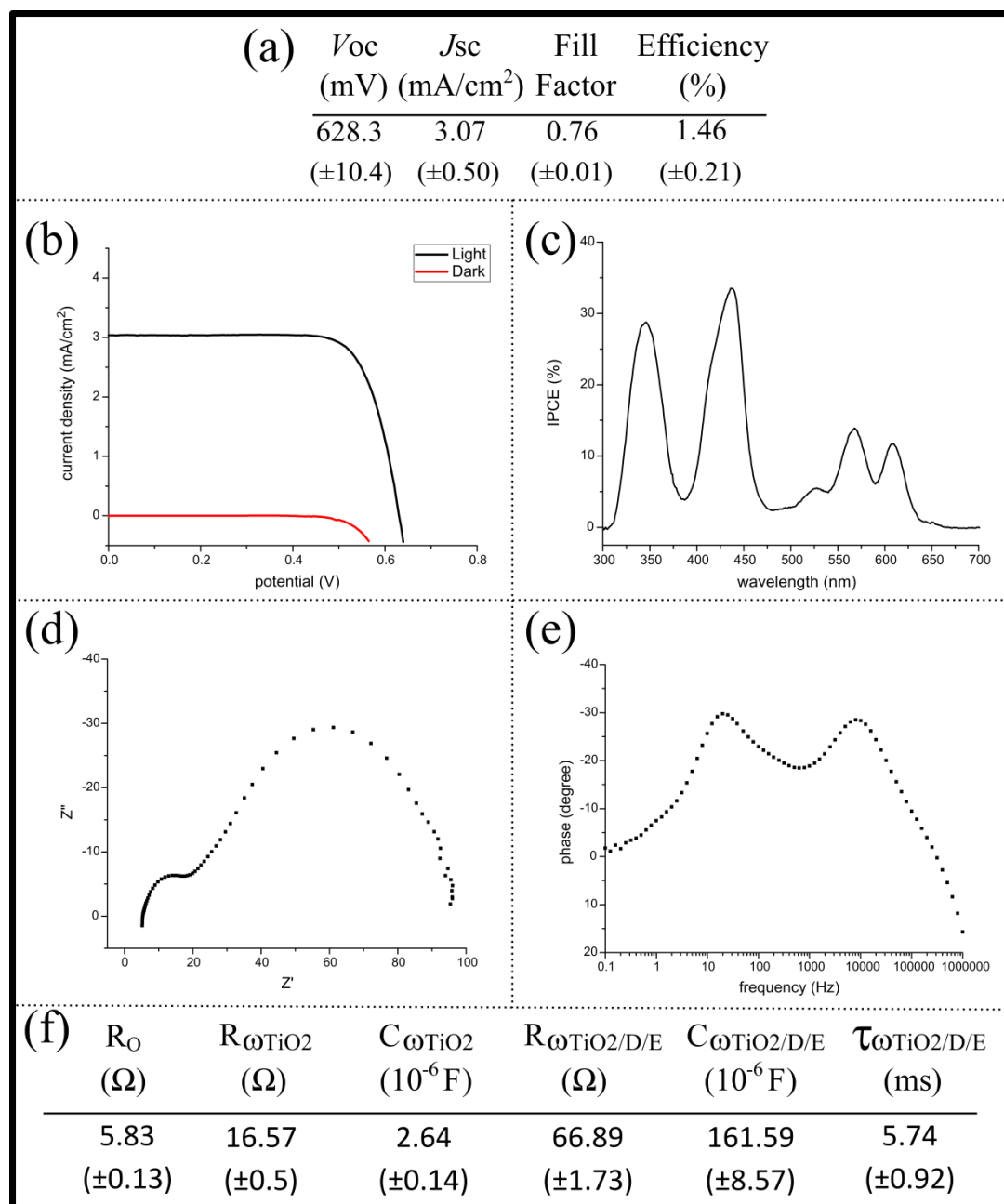


**Figure VII-15; Device measurements utilizing maquette-P1d ensembles covalently linked from MES buffer.** The resulting device measurements of 18  $\mu\text{m}$  TiO<sub>2</sub> with *cys*GL-P1d ensembles covalently attached from MES buffer (pH=6.8), using electrolyte 2 (E2). (a) Photovoltaic data from illumination under 1 sun. (b) The average  $JV$  curve under illumination (black line) and in the dark (red line). (c) The average IPCE measurement. (d) Nyquist-plot representation of the device. (e) Bode-plot representation of the device. (f) Obtained impedance spectroscopy data from a 2-phase circuit representation of the device. (Averages and standard deviations shown, where number of devices=3).

### 2.3.2- Devices using covalently attached maquette with post introduction of P1d

In stark contrast to covalently attaching pre-assembled *cysGL*-P1d ensembles, the maquette can be covalently attached to the modified TiO<sub>2</sub> surface, with introduction of P1d after rinsing. This was accomplished by covalently linking *cysGL*-maquette to the 2-aminoethylphosphonic acid treated TiO<sub>2</sub> via the cysteine residue with the use of 3-(maleimido)propionic acid N-hydroxysuccinimide ester. Following rinsing of excess maquette, the surface was exposed to P1d in aqueous buffer before a final rinse. For direct comparisons, the experimental procedure was repeated but with no maquette present (ie. observing porphyrin interactions with the functionalised surface when *cysGL*-maquette is not attached). The resulting absorbance of the electrodes are displayed and discussed in Chapter V, with the electrodes developed into devices using E2 as the redox couple.

Given this approach, P1d either ligated to the attached maquette, or interacted with the functionalised surface. As was shown previously (Chapter V), there was minimal interaction of P1d with the functionalised surface. As is shown in Figure VII-16, when maquette is covalently attached and porphyrin subsequently added compared to when porphyrin is added with no maquette present, the efficiency is 1.28 compared to 0.01 %. This is derived from both the voltage and current responses increasing dramatically when maquette is present on the surface, with the IPCE demonstrating that the porphyrin is the light absorbing entity, driving photocurrent responses. Minimal differences in the series resistance ( $R_o$ ) and the resistance or capacitance associated with  $\omega_{TiO_2}$  for devices utilizing either approach is apparent (Figure VII-16f). Therefore, the major influencing factor for differences observed in device performance comes from  $\omega_{TiO_2/D/E}$  (being the interface associated with TiO<sub>2</sub>/dye/redox electrolyte). When maquette is present with subsequent P1d addition, the capacitance is significantly larger for  $\omega_{TiO_2/D/E}$  compared to when no maquette is present ( $126.2 \pm 4.86$  compared to  $5.02 \pm 0.22$   $\mu$ F, respectively). However, the resistance at this interface is smaller when maquette was used ( $61.79 \pm 1.59$  compared to  $209.2 \pm 6.84$   $\Omega$ ). In addition,  $\tau_{\omega_{TiO_2/D/E}}$  is observed to be significantly greater when maquette is present (3.66 compared to 0.18 ms, Figure VII-16f). As electron lifetime ( $\tau$ ) is affected by both the resistance and capacitance at the interface [7], the increased capacitance is the influencing factor for the increase in  $\tau$  when maquette is present. Results indicate that the functionalised TiO<sub>2</sub> surface does not inhibit electron recombination processes solely, with the maquette presence influencing recombination processes and hence the electron lifetime most significantly.

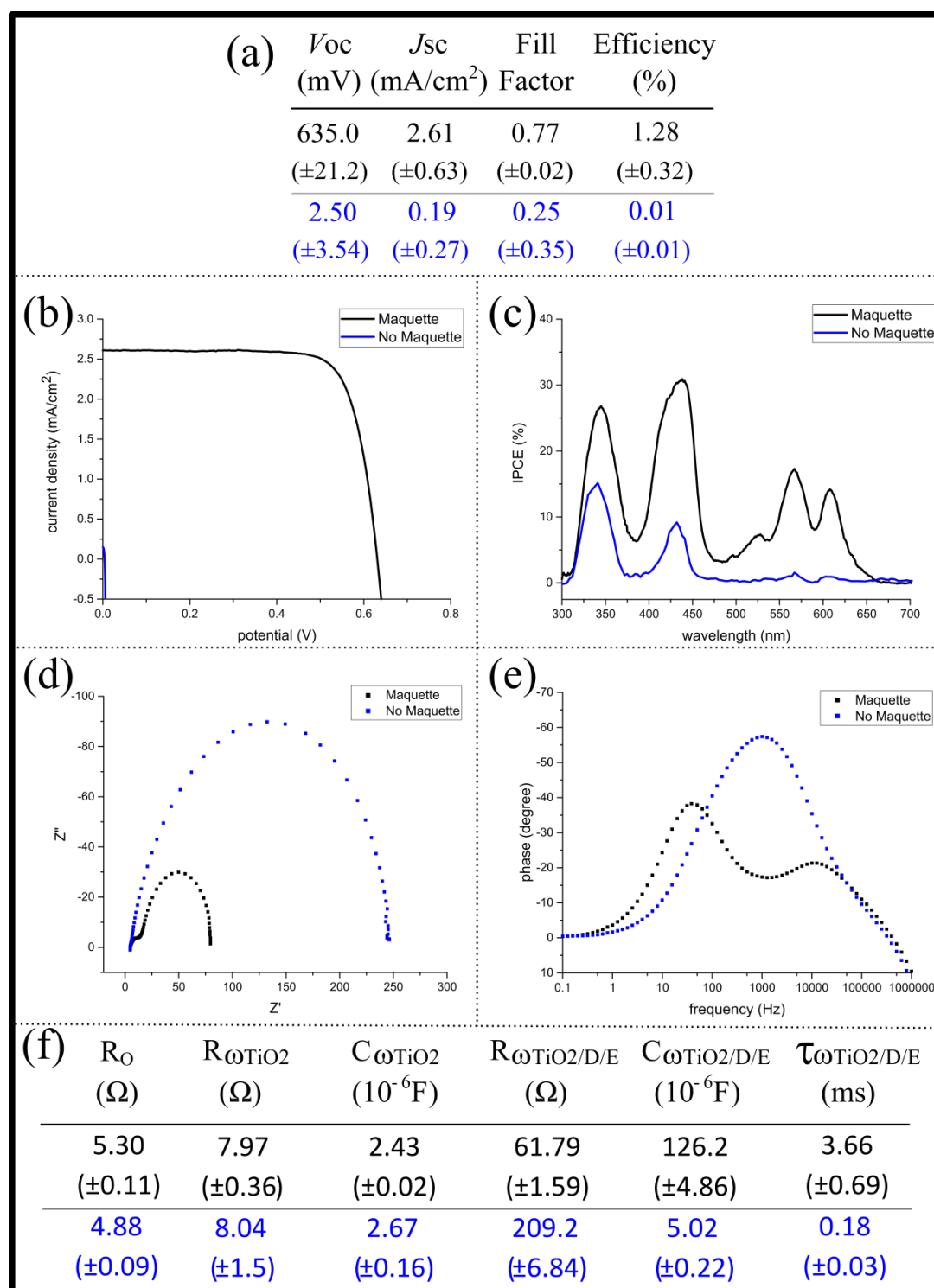


**Figure VII-16; Device measurements utilizing P1d exposed to modified TiO<sub>2</sub> with and without covalently linked cysGL-maquette.** The resulting device measurements of 8.5  $\mu\text{m}$  TiO<sub>2</sub> exposed to P1d when cysGL-maquette was covalently attached (in black) or when maquette was absent (in blue), using electrolyte 2 (E2). (a) Photovoltaic data from illumination under 1 sun. (b) The average  $JV$  curve under illumination (black line) and in the dark (red line). (c) The average IPCE measurement. (d) Nyquist-plot representation of the device. (e) Bode-plot representation of the device. (f) Obtained impedance spectroscopy data from a 2-phase circuit representation of the device. (Averages and standard deviations shown, where number of repeats=2).



#### **2.4- Attempt to determine porphyrin-maquette injection kinetics and overall yield**

Since there appeared to be effective electron injection from the porphyrin-maquette ensemble into  $\text{TiO}_2$ , it would have been able to probe the injection process. This would not only have provided further information about the injection kinetics but also whether both porphyrins in the maquette were contributing to injection. The technique most commonly employed to monitor the injection process in DSSCs is transient absorption spectroscopy with femtosecond pump laser pulses (fs-TAS) [27, 28]. Consequently, a number of attempts were made in association with a member of Associate Professor Mozer's research group to obtain transient absorption data on photoanodes comprising P1d-maquette ensembles on  $\text{TiO}_2$ . However, given the low amount of porphyrin associated with the photoanode and the Soret band shifts as a result of binding to the maquette, only very low transient absorption signals could be inconsistently obtained. The investigation was abandoned after a number of attempts to collect data.

### 3- Discussion; Solar Cell Devices

The development of GL-P1d ensemble devices using a conventional DSSC construct allows for direct comparisons of various critical parameters related to the efficacy of the GL-P1d ensemble as a light harvesting and electron transfer unit. This can be ascertained from the device performance, which has three main outputs;  $V_{oc}$ ,  $J_{sc}$ , and FF. The  $V_{oc}$  relates to the potential of the electrons to do work, with  $J_{sc}$  being the flow of electrons. FF, the ‘squareness’ of the obtained  $JV$  curve gives an idealised maximum-power point, where the voltage and current are balanced. IPCE spectra allows for interpretation of the entities which are photoactive within the device. All devices shown here display a peak at 350 nm within the IPCE spectrum, with this peak corresponding to the  $TiO_2$  absorbance peak for the band gap photoelectron excitation [29, 30].

To compare directly the use of GL-P1d ensembles with P1d bound directly onto the surface of  $TiO_2$  with devices, the photovoltaic data (of interest) from devices utilising electrolyte E1 (no LiI) or E2 (with LiI) are displayed in Table VII-2 below. When P1d is bound directly from either THF or aqueous buffer, it is apparent that the  $V_{oc}$  decreases when E2 is used compared to E1. However, the  $J_{sc}$  significantly increases, with the overall efficiency increasing. This is attributed to the presence of  $Li^+$  in E2, known to reduce the  $V_{oc}$  while simultaneously increasing the  $J_{sc}$  due to  $Li^+$  interactions inducing shifts in the CB of  $TiO_2$  and promoting electron injection [14, 21, 31]. However, devices employing GL-P1d ensembles display a higher  $V_{oc}$  than P1d bound from THF or aqueous buffer (with the exception of P1d bound from aqueous buffer and using E2). Of considerable note is that there is no difference in  $V_{oc}$  for devices using E1 or E2 with GL-P1d ensembles, yet the  $J_{sc}$  is observed to still increase slightly with the presence of  $Li^+$ . The slight increase in  $J_{sc}$  is likely due to the presence of  $Li^+$  promoting electron injection, however, the minimal influence of  $Li^+$  on  $V_{oc}$  for devices utilising GL-P1d ensembles must be due to another phenomenon.

Looking at the EIS data (Table VII-2), two prominent electrochemical interfaces relating to the electron transfer processes were observed in both Nyquist and Bode plot representations of the device. The first interface was attributed to a combination between the substrate/ $TiO_2$  interface ( $\omega_1$ ) and also electron transfer between  $TiO_2$  particles in conjunction with the counter electrode and the electrolyte ( $\omega_2$ ), assigned  $\omega_{TiO_2}$ . The second observable interface was attributed to the  $TiO_2$ /dye/electrolyte interface ( $\omega_{TiO_2/D/E}$ ). The series resistance ( $R_0$ ) for all devices displayed consistent values within deviation, with the small differences in resistance not significantly contributing to device performance. The resistance and capacitance

associated with  $\omega_{\text{TiO}_2}$  are consistent (within standard deviation) for devices utilising P1d bound from THF with either E1 or E2, implying that the main difference in device performance directly comes from  $\omega_{\text{TiO}_2/\text{D/E}}$ . It would be expected that as  $\text{Li}^+$  is known to interact with  $\text{TiO}_2$ , the chemical capacitance ( $C_{\omega_{\text{TiO}_2/\text{D/E}}}$ ) would increase. Indeed, when P1d is bound from THF, the presence of  $\text{Li}^+$  increases the chemical capacitance (with a slight decrease in resistance) at this electrochemical interface. As  $\tau$  is closely related to the recombination resistance ( $R_{\text{rec}}$ ) and the capacitance ( $C$ ) (according to  $\tau=R_{\text{rec}}C$  [7]), this increase in capacitance of  $\omega_{\text{TiO}_2/\text{D/E}}$  results in the observed increase in electron lifetime. This trend for when  $\text{Li}^+$  is present in the electrolyte (E2) compared to E1 is continued for when P1d is bound for aqueous buffer and also for when GL-P1d ensembles are employed within devices. The resistance at  $\omega_{\text{TiO}_2/\text{D/E}}$  is distinctly larger when GL-P1d ensembles are utilised within devices compared to P1d bound directly to  $\text{TiO}_2$  (with both E1 and E2). This resistance ( $R_{\omega_{\text{TiO}_2/\text{D/E}}}$ ) is attributed to the back transfer of electrons with the maquette blocking  $\text{I}_3^-$  access to the surface, thereby resulting in the distinctly large electron lifetimes. However, when  $\text{Li}^+$  is present (using E2), the increase in chemical capacitance results in a further increase in electron lifetime (with slight increase in resistance). Device utilising GL-P1d ensembles show no change in  $V_{\text{oc}}$  when  $\text{Li}^+$  is present in the electrolyte, however, an increase in capacitance is still evident. It is likely that the  $\text{Li}^+$  is interacting with the polypeptide (maquette) [16], rather than the  $\text{TiO}_2$  as would be expected in devices. Of note is that the resistance at  $\omega_{\text{TiO}_2}$  ( $R_{\omega_{\text{TiO}_2}}$ ) is reduced for samples bound from aqueous buffer (AB), whilst displaying an increased capacitance ( $C_{\omega_{\text{TiO}_2}}$ ). It is highly likely that, as the aqueous buffer contained a high concentration of ions, the ions remained on the film post-rinsing and drying, subsequently becoming incorporated within the DSSC. The ions present ( $\text{K}^+$  and  $\text{Cl}^-$ ) would likely induce the slight capacitance affect and decreased electrical resistance observed, whereby devices prepared from THF did not contain the (unintentionally) added ions.

**Table VII-2; Photovoltaic data of devices using non-functionalised TiO<sub>2</sub>.** Devices fabricated using 2.5  $\mu\text{m}$  TiO<sub>2</sub>, with electrolyte 1 or 2 (E1 or E2, respectively). Devices prepared with P1d bound from THF, P1d bound from aqueous buffer (AB), or GL-P1d ensembles bound from aqueous buffer (AB).

Sample	P1d from THF	P1d from THF	P1d from AB	P1d from AB	GL-P1d from AB	GL-P1d from AB
Electrolyte	E1	E2	E1	E2	E1	E2
<b>V<sub>oc</sub></b> <b>(mV)</b>	608.3 ( $\pm 5.8$ )	560 ( $\pm 14.1$ )	642.5 ( $\pm 17.7$ )	605.0 ( $\pm 0.00$ )	647.5 ( $\pm 10.6$ )	652.5 ( $\pm 17.7$ )
<b>J<sub>sc</sub></b> <b>(mA/cm<sup>2</sup>)</b>	3.49 ( $\pm 0.35$ )	5.08 ( $\pm 0.57$ )	2.44 ( $\pm 0.30$ )	4.15 ( $\pm 0.67$ )	2.08 ( $\pm 0.21$ )	2.69 ( $\pm 0.10$ )
<b>Efficiency</b> <b>(%)</b>	1.45 ( $\pm 0.19$ )	2.05 ( $\pm 0.27$ )	0.98 ( $\pm 0.15$ )	1.77 ( $\pm 0.33$ )	1.03 ( $\pm 0.11$ )	1.28 ( $\pm 0.11$ )
<b>R<sub>o</sub></b> <b>(<math>\Omega</math>)</b>	5.11 ( $\pm 0.08$ )	5.74 ( $\pm 0.09$ )	5.08 ( $\pm 0.07$ )	5.25 ( $\pm 0.09$ )	5.56 ( $\pm 0.08$ )	5.22 ( $\pm 0.07$ )
<b>R<sub><math>\omega</math>TiO<sub>2</sub></sub></b> <b>(<math>\Omega</math>)</b>	10.79 ( $\pm 0.69$ )	11.77 ( $\pm 0.30$ )	11.77 ( $\pm 1.11$ )	7.76 ( $\pm 0.23$ )	6.18 ( $\pm 0.19$ )	4.67 ( $\pm 0.14$ )
<b>C<sub><math>\omega</math>TiO<sub>2</sub></sub></b> <b>(<math>\mu\text{F}</math>)</b>	1.36 ( $\pm 0.05$ )	1.64 ( $\pm 0.07$ )	3.21 ( $\pm 0.15$ )	2.19 ( $\pm 0.11$ )	2.11 ( $\pm 0.13$ )	2.25 ( $\pm 0.15$ )
<b>R<sub><math>\omega</math>TiO<sub>2</sub>/D/E</sub></b> <b>(<math>\Omega</math>)</b>	46.42 ( $\pm 1.33$ )	40.92 ( $\pm 0.86$ )	68.86 ( $\pm 1.45$ )	32.47 ( $\pm 0.67$ )	102.2 ( $\pm 1.58$ )	114.1 ( $\pm 1.46$ )
<b>C<sub><math>\omega</math>TiO<sub>2</sub>/D/E</sub></b> <b>(<math>\mu\text{F}</math>)</b>	6.35 ( $\pm 0.38$ )	38.95 ( $\pm 1.52$ )	5.40 ( $\pm 0.28$ )	44.55 ( $\pm 1.72$ )	43.86 ( $\pm 0.94$ )	71.06 ( $\pm 0.13$ )
<b><math>\tau_{\omega</math>TiO<sub>2</sub>/D/E</b> <b>(ms)</b>	0.28 ( $\pm 0.04$ )	0.90 ( $\pm 0.14$ )	0.18 ( $\pm 0.03$ )	0.72 ( $\pm 0.12$ )	1.43 ( $\pm 0.22$ )	2.26 ( $\pm 0.35$ )

Compared to photovoltaic responses of P1d bound directly on TiO<sub>2</sub> from either THF or aqueous buffer, those of maquette ligated P1d show considerable differences. Further insight into this can be gained by considering the quantity of photoactive material, on the titania surface. The binding of P1d from THF results in the highest concentrations of porphyrin on the surface, followed by P1d bound from aqueous buffer, with ligation to maquette resulting in the lowest concentrations. This is likely due to the maquette taking up physical space on the surface, with sensitization being a tightly packed coverage on TiO<sub>2</sub>. The sensitization of P1d to TiO<sub>2</sub> from THF has over 6-times more porphyrin (the photoactive material) on the surface compared to when ligated and immobilized with maquette (GL-P1d ensembles). Despite this, the efficiency is only 1.6 times greater than devices using GL-P1d ensembles (using E2), with the  $J_{sc}$  being 1.9 times greater. Similarly, when P1d is bound from aqueous buffer, the quantity of P1d is over 2.5-times greater than for the GL-P1d ensembles, with efficiencies only 1.4-times greater (and  $J_{sc}$  1.6 times greater) for devices utilising E2. When Li<sup>+</sup> is not present in the electrolyte of the device (using E1), the difference in  $J_{sc}$  and efficiency between when directly bound P1d from either THF or aqueous buffer compared to GL-P1d ensembles is less. Since devices utilising GL-P1d ensembles contain significantly less photoactive material and the  $J_{sc}$  is not correspondingly lower, it can be inferred that the electrons are not being inhibited from

injection from the porphyrin into  $\text{TiO}_2$  when ligated with maquette. It is likely that the higher  $V_{oc}$  in conjunction with the reduced recombination processes (as discussed previously) result in the maquette-porphyrin ensembles injecting electrons more efficiently and effectively into the CB of  $\text{TiO}_2$ .

The slow decay of charge for P1d is ligated with maquette further gives testimony to the effectiveness of maquettes as a ‘blocking’ layer, which effectively reduces recombination processes between the CB of  $\text{TiO}_2$  and  $\text{I}_3^-$ . When illumination is removed from devices using P1d bound directly to  $\text{TiO}_2$  from either THF or aqueous buffer, the  $V_{oc}$  returns to 0 V in milliseconds. However, when P1d is ligated within the maquette and immobilised, the  $V_{oc}$  decays very slowly when illumination is removed, taking >5 min to return to 0 V. When the device is under illumination, electrons flow freely in the CB of  $\text{TiO}_2$  (resulting in the photocurrent/photovoltage response). When the illumination is removed, the ‘built up’ electrons (ie. electrons in the CB of  $\text{TiO}_2$ ) return to a lower energy state by recombining with the redox mediator in the electrolyte. This recombination removes any measurable  $V_{oc}$ , as the  $V_{oc}$  corresponds to the energy difference between Fermi level of  $\text{TiO}_2$  and the energy level of the redox mediator [6]. Therefore, if this recombination of electrons is inhibited, the  $V_{oc}$  remains for a longer period of time after illumination is removed. The device utilising GL-P1d ensembles consequently retain  $V_{oc}$  after illumination due to the reduction in recombination between the CB of  $\text{TiO}_2$  and redox mediator, supporting the results presented previously regarding electron lifetimes.

To further explore the use of maquette-porphyrin ensembles within devices, functionalisation of  $\text{TiO}_2$  was employed to covalently link the maquette. The *cysGL*-maquette contains a cysteine residue in the ‘loop’ region, being the only residue which reacts with the functionalised surface (refer to Chapter V). Three modes of binding treating the functionalised surface were investigated, being a pre-formed *cysGL*-P1d ensemble covalently linked to the surface, *cysGL*-maquettes covalently linked to the surface followed by subsequent ligation of P1d from a solution, or a maquette-free buffer exposure to the surface followed by exposure to P1d (as a direct negative control to the previous mode). The photovoltaic data (of interest) from devices utilising these modifications with E2 are displayed in Table VII-3 below for direct comparison. As has been shown previously (Chapter V), P1d interacts weakly with the functionalised surface producing minimal colouration of the surface. However, if first the *cysGL*-maquette is covalently linked to surface, P1d can ligate within the maquette, displaying

a highly coloured surface. When maquette is not present, the devices produce minimal efficiencies (0.01 %), with FF and  $V_{oc}$  suffering the greatest. This is due to the short electron lifetime (0.18 ms), likely a result of the high levels of recombination, as discussed previously. Comparatively, when the maquette is attached to the surface with P1d subsequently introduced, the efficiency of the device is 1.28 %, with a high  $V_{oc}$  and FF. The electron lifetime is 3.66 ms, indicating low levels of electron recombination between the CB of  $TiO_2$  and the redox mediator.

The differences in photovoltaic data between attachment of pre-formed ensembles and pre-attachment of maquette with post-introduction of P1d can be explained by analysing the mode of attachment. As shown in Table VII-3, the  $V_{oc}$  is identical for the two modes, with the efficiency slightly increased for the pre-formed ensemble due to the slight increase in  $J_{sc}$ , although this is dependent on the film thickness (and consequently the quantity of photoactive material). Devices using pre-formed ensembles had to be fabricated using thicker films (18  $\mu m$ ) so as to produce devices with efficiencies comparable to those of post-introduction of P1d to attached *cysGL*-maquettes. This was surprising, however, since the thicker films should have contained more photoactive material and therefore produced higher currents; it might have been expected that, as the devices using pre-formed ensembles were on >2-fold thicker films, the  $J_{sc}$  should have been close to double that of the other thinner devices. However, this was not observed, with the  $J_{sc}$  being very similar. This could potentially be due to the pre-formed ensembles losing porphyrin from a ligated state while being attached to the surface, whereas post-introduction of porphyrin saturated the histidine binding sites. Furthermore, thicker films invariably contain more trapped states for electrons, which would further reduce the obtained  $J_{sc}$  [3]. The physical size of the maquette (~4 x 5 nm) could also be impacting surface binding, if the ensemble did not readily penetrate into the depths of the thick film. To determine whether this was indeed the case, the quantity of porphyrin (P1d) from each of the films presented here would need to be measured via desorption (as described previously in section 2.1.5). However, due to both material and time constraints, this could not be undertaken and should be part of future work in this area. Nonetheless, it has been demonstrated that controlled binding of maquettes to the  $TiO_2$  surface can be achieved with effective electron injection from a ligated electron donor.

**Table VII-3; Photovoltaic data of devices using functionalised TiO<sub>2</sub>.** Devices fabricated with covalently linking maquettes to TiO<sub>2</sub>, using electrolyte 2 (E2).

Sample	cysGL-P1d Ensemble	cysGL-subsequent P1d	No maquette-subsequent P1d
Film Thickness ( $\mu\text{m}$ )	18	8.5	8.5
Electrolyte	E2	E2	E2
$V_{oc}$ (mV)	628.3 ( $\pm 10.4$ )	635.0 ( $\pm 21.2$ )	2.5 ( $\pm 3.54$ )
$J_{sc}$ ( $\text{mA}/\text{cm}^{-2}$ )	3.07 ( $\pm 0.50$ )	2.61 ( $\pm 0.63$ )	0.19 ( $\pm 0.27$ )
Efficiency (%)	1.46 ( $\pm 0.21$ )	1.28 ( $\pm 0.32$ )	0.01 ( $\pm 0.01$ )
$R_o$ ( $\Omega$ )	5.83 ( $\pm 0.13$ )	5.30 ( $\pm 0.11$ )	4.88 ( $\pm 0.09$ )
$R\omega_{TiO_2}$ ( $\Omega$ )	16.57 ( $\pm 0.50$ )	7.97 ( $\pm 0.36$ )	8.04 ( $\pm 1.50$ )
$C\omega_{TiO_2}$ ( $\mu\text{F}$ )	2.64 ( $\pm 0.14$ )	2.43 ( $\pm 0.02$ )	2.67 ( $\pm 0.16$ )
$R\omega_{TiO_2/D/E}$ ( $\Omega$ )	66.89 ( $\pm 1.73$ )	61.79 ( $\pm 1.59$ )	209.2 ( $\pm 6.84$ )
$C\omega_{TiO_2/D/E}$ ( $\mu\text{F}$ )	161.59 ( $\pm 8.57$ )	126.2 ( $\pm 4.86$ )	5.02 ( $\pm 0.22$ )
$\tau\omega_{TiO_2/D/E}$ (ms)	5.74 ( $\pm 0.92$ )	3.66 ( $\pm 0.69$ )	0.18 ( $\pm 0.03$ )

This work is comparable to many other attempts at utilizing polypeptides or proteins for binding to porphyrins and subsequent immobilization on conductive surfaces. Immobilization of Photosystem II (PSII) on a conductive electrode produced photo-generated currents densities of up to  $22 \mu\text{A cm}^{-2}$  [32, 33]. The maquette-porphyrin complexes presented here are akin to PSII, but reach significantly larger current densities of  $3.07 \text{ mA cm}^{-2}$ . This large increase in photocurrent is attributed to the simplified design of the maquette, allowing for a tightly packed surface coverage compared to the larger natural proteins found in nature. However, if the electrons obtained (current density) were to be used for catalytic reactions, rather than electricity, the predominant focus becomes voltage. Furthermore, the charge separated states for such catalytic reactions need to live long enough so that their oxidising and reducing effects can be utilised [34]. The work presented here demonstrates that the maquette-porphyrin system could be a potential candidate for light-driven catalytic reactions, whereby current is directed with a relatively high  $V_{oc}$  from reduced recombination.

## 4- Conclusions; Solar Cell Devices

Results presented here give evidence for the potential applications of novel proteins in the use of devices for light-driven electron transfer processes. As shown, a hydrophilic porphyrin (P1d) can be immobilized onto  $\text{TiO}_2$  through various means, specifically, sensitized from an organic solvent, immobilized from an aqueous solution, or ligated within a maquette with subsequent maquette immobilization. The presence of the maquette does not inhibit electron injection from the photoexcited state of the ligated porphyrin into the conduction band (CB) of  $\text{TiO}_2$ . This is evident by the relative photocurrent responses from the devices presented here, although being lower for when ligated with maquette, the quantity of porphyrin present can explain the decreased current. Of note however, is the increase in  $V_{oc}$  and fill factor for when maquette is present. This is attributed to the maquette hindering electron recombination from the CB of  $\text{TiO}_2$  back to the redox electrolyte (Figure VII-17). Further evidence for this is the electron lifetime at this interface. When maquette is present, the electron lifetime is  $>1$  ms, reaching 5.74 ms when the maquette is covalently attached. This is compared to when maquette is not present, with the electron lifetimes being  $<1$  ms in all instances, relating to a fast recombination of electrons back to the redox electrolyte.

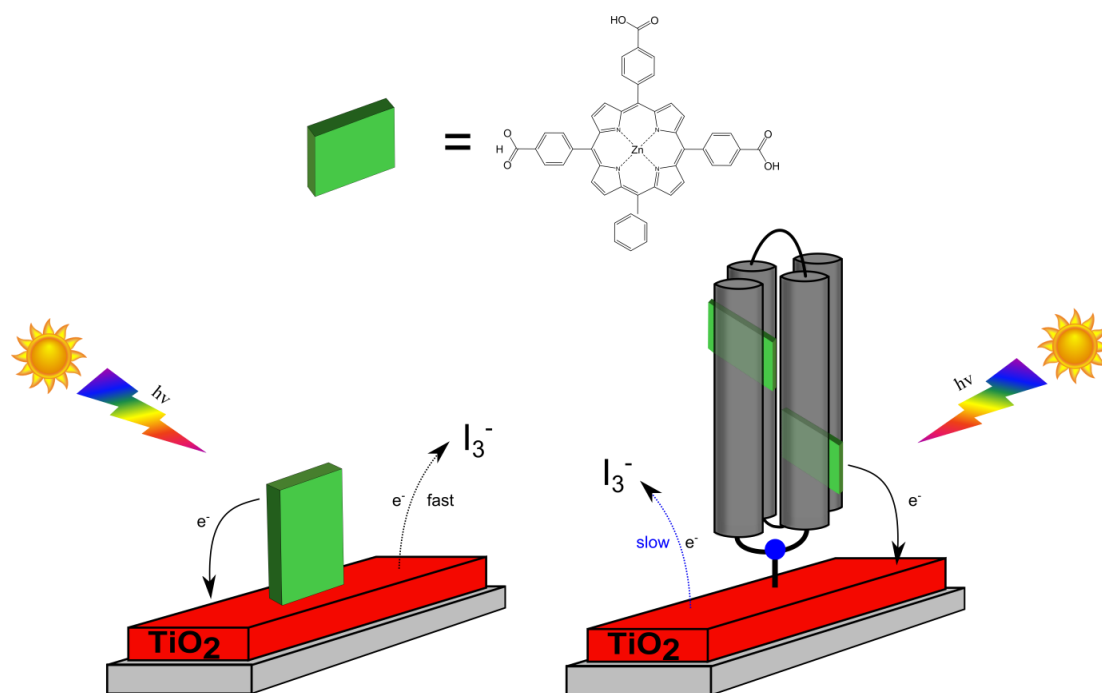


**Figure VII-17; Photoinduced electron transfer processes.** The direct attachment of porphyrin onto  $\text{TiO}_2$  allows for a fast rate of back electron transfer from the conduction band of  $\text{TiO}_2$  to the redox mediator. Ligation of porphyrins into maquettes and subsequent immobilization onto  $\text{TiO}_2$  does not hinder electron injection from the photoexcited state of the porphyrin, rather, inhibiting electron transfer processes back from the conduction band of  $\text{TiO}_2$  back to the redox mediator.



## 5- References; Solar Cell Devices

1. O'Regan B, Gratzel M: **A low-cost, high-efficiency solar cell based on dye-sensitized colloidal TiO<sub>2</sub> films.** *Nature* 1991, **353**(6346):737-740.
2. Hagfeldt A, Grätzel M: **Molecular Photovoltaics.** *Accounts of Chemical Research* 2000, **33**(5):269-277.
3. Hagfeldt A, Boschloo G, Sun L, Kloo L, Pettersson H: **Dye-Sensitized Solar Cells.** *Chemical Reviews* 2010, **110**(11):6595-6663.
4. Narayan MR: **Review: Dye sensitized solar cells based on natural photosensitizers.** *Renewable and Sustainable Energy Reviews* 2012, **16**(1):208-215.
5. Calogero G, Di Marco G, Cazzanti S, Caramori S, Argazzi R, Di Carlo A, Bignozzi CA: **Efficient Dye-Sensitized Solar Cells Using Red Turnip and Purple Wild Sicilian Prickly Pear Fruits.** *International Journal of Molecular Sciences* 2010, **11**(1):254-267.
6. Jena A, Mohanty SP, Kumar P, Naduvath J, Gondane V, Lekha P, Das J, Narula HK, Mallick S, Bhargava P: **Dye Sensitized Solar Cells: A Review.** *Transactions of the Indian Ceramic Society* 2012, **71**(1):1-16.
7. Hoshikawa, T., Yamanda, M., Kikuchi, R., Eguchi, K.: **Impedance analysis of internal resistance affecting the photoelectrochemical performance of dye-sensitized solar cells.** 2005, **152**(2).
8. Kern R, Sastrawan R, Ferber J, Stangl R, Luther J: **Modeling and interpretation of electrical impedance spectra of dye solar cells operated under open-circuit conditions.** *Electrochimica Acta* 2002, **47**(26):4213-4225.
9. Montanari I, Nelson J, Durrant JR: **Iodide Electron Transfer Kinetics in Dye-Sensitized Nanocrystalline TiO<sub>2</sub> Films.** *The Journal of Physical Chemistry B* 2002, **106**(47):12203-12210.
10. Boschloo G, Hagfeldt A: **Characteristics of the iodide/triiodide redox mediator in dye-sensitized solar cells.** *Accounts of chemical research* 2009, **42**(11):1819-1826.
11. Watson DF, Marton A, Stux AM, Meyer GJ: **Insights into Dye-Sensitization of Planar TiO<sub>2</sub>: Evidence for Involvement of a Protonated Surface State.** *The Journal of Physical Chemistry B* 2003, **107**(40):10971-10973.

12. Kelly CA, Farzad F, Thompson DW, Stipkala JM, Meyer GJ: **Cation-Controlled Interfacial Charge Injection in Sensitized Nanocrystalline TiO<sub>2</sub>**. *Langmuir* 1999, **15**(20):7047-7054.
13. Boschloo G, Fitzmaurice D: **Electron accumulation in nanostructured TiO<sub>2</sub> (anatase) electrodes**. *The Journal of Physical Chemistry B* 1999, **103**(37):7860-7868.
14. Yu Q, Wang Y, Yi Z, Zu N, Zhang J, Zhang M, Wang P: **High-Efficiency Dye-Sensitized Solar Cells: The Influence of Lithium Ions on Exciton Dissociation, Charge Recombination, and Surface States**. *ACS Nano* 2010, **4**(10):6032-6038.
15. Furube A, Katoh R, Hara K, Sato T, Murata S, Arakawa H, Tachiya M: **Lithium Ion Effect on Electron Injection from a Photoexcited Coumarin Derivative into a TiO<sub>2</sub> Nanocrystalline Film Investigated by Visible-to-IR Ultrafast Spectroscopy**. *The Journal of Physical Chemistry B* 2005, **109**(34):16406-16414.
16. Balasubramanian D, Shaikh R: **On the interaction of lithium salts with model amides**. *Biopolymers* 1973, **12**(7):1639-1650.
17. Boschloo G, Häggman L, Hagfeldt A: **Quantification of the Effect of 4-tert-Butylpyridine Addition to I-/I<sup>3+</sup>- Redox Electrolytes in Dye-Sensitized Nanostructured TiO<sub>2</sub> Solar Cells**. *The Journal of Physical Chemistry B* 2006, **110**(26):13144-13150.
18. Hsu C-P, Lee K-M, Huang JT-W, Lin C-Y, Lee C-H, Wang L-P, Tsai S-Y, Ho K-C: **EIS analysis on low temperature fabrication of TiO<sub>2</sub> porous films for dye-sensitized solar cells**. *Electrochimica Acta* 2008, **53**(25):7514-7522.
19. Zeng Q, Yu Y, Wu L, Qi B, Zhi J: **Low-temperature fabrication of flexible TiO<sub>2</sub> electrode for dye-sensitized solar cells**. *physica status solidi (a)* 2010, **207**(9):2201-2206.
20. Bisquert J, Fabregat-Santiago F, Mora-Seró I, Garcia-Belmonte G, Giménez S: **Electron Lifetime in Dye-Sensitized Solar Cells: Theory and Interpretation of Measurements**. *The Journal of Physical Chemistry C* 2009, **113**(40):17278-17290.
21. Griffith MJ: **Charge generation and recombination in porphyrin based dye sensitized solar cells**. *PhD Thesis*. University of Wollongong; 2012.

22. Mihailetschi V, Blom P, Hummelen J, Rispens M: **Cathode dependence of the open-circuit voltage of polymer: fullerene bulk heterojunction solar cells.** *Journal of Applied Physics* 2003, **94**(10):6849-6854.
23. Bolts JM, Wrighton MS: **Correlation of photocurrent-voltage curves with flat-band potential for stable photoelectrodes for the photoelectrolysis of water.** *The Journal of Physical Chemistry* 1976, **80**(24):2641-2645.
24. Watanabe T, Fujishima A, Tatsuoki O, Honda K-i: **pH-Dependence of Spectral Sensitization at Semiconductor Electrodes.** *Bulletin of the Chemical Society of Japan* 1976, **49**(1):8-11.
25. Gerischer H: **Neglected problems in the pH dependence of the flatband potential of semiconducting oxides and semiconductors covered with oxide layers.** *Electrochimica Acta* 1989, **34**(8):1005-1009.
26. Yan SG, Hupp JT: **Semiconductor-Based Interfacial Electron-Transfer Reactivity: Decoupling Kinetics from pH-Dependent Band Energetics in a Dye-Sensitized Titanium Dioxide/Aqueous Solution System.** *The Journal of Physical Chemistry* 1996, **100**(17):6867-6870.
27. Haque SA, Palomares E, Cho BM, Green ANM, Hirata N, Klug DR, Durrant JR: **Charge Separation versus Recombination in Dye-Sensitized Nanocrystalline Solar Cells: the Minimization of Kinetic Redundancy.** *Journal of the American Chemical Society* 2005, **127**(10):3456-3462.
28. Griffith MJ, Sunahara K, Wagner P, Wagner K, Wallace GG, Officer DL, Furube A, Katoh R, Mori S, Mozer AJ: **Porphyrins for dye-sensitised solar cells: new insights into efficiency-determining electron transfer steps.** *Chemical Communications* 2012, **48**(35):4145-4162.
29. Senadeera GKR, Kitamura T, Wada Y, Yanagida S: **Photosensitization of nanocrystalline TiO<sub>2</sub> films by a polymer with two carboxylic groups, poly (3-thiophenemalonic acid).** *Solar Energy Materials and Solar Cells* 2005, **88**(3):315-322.
30. Wu J, Yue G, Xiao Y, Lin J, Huang M, Lan Z, Tang Q, Huang Y, Fan L, Yin S *et al*: **An ultraviolet responsive hybrid solar cell based on titania/poly(3-hexylthiophene).** *Scientific Reports* 2013, **3**:1283.

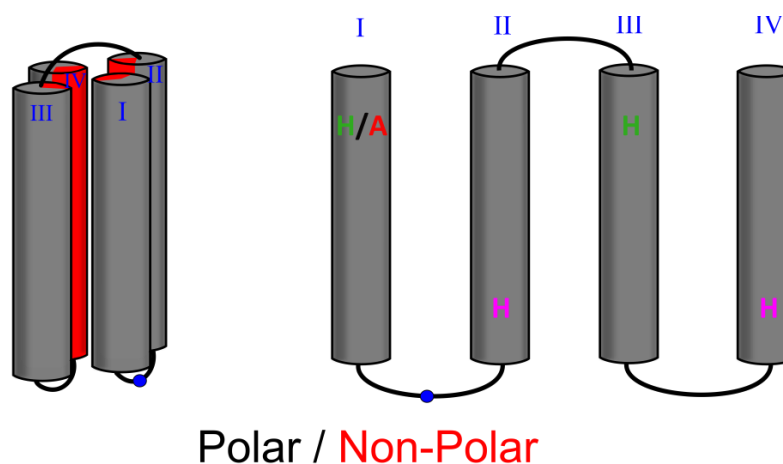
31. Griffith MJ, Sunahara K, Furube A, Mozer AJ, Officer DL, Wagner P, Wallace GG, Mori S: **Cation exchange at semiconducting oxide surfaces: Origin of light-induced performance increases in porphyrin dye-sensitized solar cells.** *The Journal of Physical Chemistry C* 2013, **117**(23):11885-11898.
32. Kato M, Cardona T, Rutherford AW, Reisner E: **Photoelectrochemical water oxidation with photosystem II integrated in a mesoporous indium–tin oxide electrode.** *Journal of the American Chemical Society* 2012, **134**(20):8332-8335.
33. Kato M, Cardona T, Rutherford AW, Reisner E: **Covalent immobilization of oriented photosystem II on a nanostructured electrode for solar water oxidation.** *Journal of the American Chemical Society* 2013, **135**(29):10610-10613.
34. Gust D, Moore TA, Moore AL: **Mimicking photosynthetic solar energy transduction.** *Accounts of Chemical Research* 2001, **34**(1):40-48.

# **Chapter VIII**

## **Gallium Based Porphyrin-Maquette Ensembles**

## 1- Introduction; Gallium Based Porphyrin-Maquette Ensembles

Maquettes can potentially be employed to self-organise cofactors via site-specific axial ligation with histidine. It is known that maquettes need two histidine residues on adjacent helices for a bis-histidine (bis-His) axial ligation to cofactors containing iron [1-3]. Furthermore, the iron porphyrins preferentially ligates via six-coordinate geometry, whereas zinc porphyrins ligate via five-coordinate geometry [4, 5]. Therefore, if a maquette contained two specific sites for potential ligation to cofactors, one being a bis-His site with the other being a single His site, differential binding of cofactors could be achieved based on the preferential coordination [4]. To explore this, maquette sequences were further designed by our collaborators at the University of Pennsylvania, Philadelphia, such as the GL-maquette (Figure VIII-1), containing a cysteine in the loop region for covalent linking to surfaces and either three histidines (3-*his*) or four histidines (4-*his*). The 3-*his* maquette was designed so that the bis-His ligation site was oriented closest to the site of the cysteine residue, with the single histidine residue at the opposite end of the maquette.



Helix Number	Overall Charge	3-His GL-Maquette Sequence	Loop-Region
I	-4	<b>G</b> <b>E</b> <b>I</b> <b>W</b> <b>K</b> <b>Q</b> <b>A</b> <b>E</b> <b>D</b> <b>A</b> <b>L</b> <b>Q</b> <b>K</b> <b>F</b> <b>E</b> <b>E</b> <b>A</b> <b>L</b> <b>N</b> <b>Q</b> <b>F</b> <b>E</b> <b>D</b> <b>L</b> <b>K</b> <b>Q</b> <b>L</b> <b>G</b> <b>G</b> <b>C</b> <b>G</b>	
II	+2	<b>E</b> <b>I</b> <b>K</b> <b>Q</b> <b>R</b> <b>H</b> <b>E</b> <b>D</b> <b>A</b> <b>L</b> <b>R</b> <b>K</b> <b>F</b> <b>E</b> <b>E</b> <b>A</b> <b>L</b> <b>K</b> <b>R</b> <b>F</b> <b>E</b> <b>D</b> <b>K</b> <b>K</b> <b>Q</b> <b>K</b> <b>G</b> <b>G</b> <b>S</b> <b>G</b>	
III	-4	<b>E</b> <b>I</b> <b>W</b> <b>K</b> <b>Q</b> <b>H</b> <b>E</b> <b>D</b> <b>A</b> <b>L</b> <b>Q</b> <b>K</b> <b>F</b> <b>E</b> <b>E</b> <b>A</b> <b>L</b> <b>N</b> <b>Q</b> <b>F</b> <b>E</b> <b>D</b> <b>L</b> <b>K</b> <b>Q</b> <b>L</b> <b>G</b> <b>G</b> <b>S</b> <b>G</b>	
IV	+2	<b>E</b> <b>I</b> <b>K</b> <b>Q</b> <b>R</b> <b>H</b> <b>E</b> <b>D</b> <b>A</b> <b>L</b> <b>R</b> <b>K</b> <b>F</b> <b>E</b> <b>E</b> <b>A</b> <b>L</b> <b>K</b> <b>R</b> <b>F</b> <b>E</b> <b>D</b> <b>K</b> <b>K</b> <b>Q</b> <b>K</b>	
Helix Number	Overall Charge	4-His GL-Maquette Sequence	Loop-Region
I	-4	<b>G</b> <b>E</b> <b>I</b> <b>W</b> <b>K</b> <b>Q</b> <b>H</b> <b>E</b> <b>D</b> <b>A</b> <b>L</b> <b>Q</b> <b>K</b> <b>F</b> <b>E</b> <b>E</b> <b>A</b> <b>L</b> <b>N</b> <b>Q</b> <b>F</b> <b>E</b> <b>D</b> <b>L</b> <b>K</b> <b>Q</b> <b>L</b> <b>G</b> <b>G</b> <b>C</b> <b>G</b>	
II	+2	<b>E</b> <b>I</b> <b>K</b> <b>Q</b> <b>R</b> <b>H</b> <b>E</b> <b>D</b> <b>A</b> <b>L</b> <b>R</b> <b>K</b> <b>F</b> <b>E</b> <b>E</b> <b>A</b> <b>L</b> <b>K</b> <b>R</b> <b>F</b> <b>E</b> <b>D</b> <b>K</b> <b>K</b> <b>Q</b> <b>K</b> <b>G</b> <b>G</b> <b>S</b> <b>G</b>	
III	-4	<b>E</b> <b>I</b> <b>W</b> <b>K</b> <b>Q</b> <b>H</b> <b>E</b> <b>D</b> <b>A</b> <b>L</b> <b>Q</b> <b>K</b> <b>F</b> <b>E</b> <b>E</b> <b>A</b> <b>L</b> <b>N</b> <b>Q</b> <b>F</b> <b>E</b> <b>D</b> <b>L</b> <b>K</b> <b>Q</b> <b>L</b> <b>G</b> <b>G</b> <b>S</b> <b>G</b>	
IV	+2	<b>E</b> <b>I</b> <b>K</b> <b>Q</b> <b>R</b> <b>H</b> <b>E</b> <b>D</b> <b>A</b> <b>L</b> <b>R</b> <b>K</b> <b>F</b> <b>E</b> <b>E</b> <b>A</b> <b>L</b> <b>K</b> <b>R</b> <b>F</b> <b>E</b> <b>D</b> <b>K</b> <b>K</b> <b>Q</b> <b>K</b>	

**Figure VIII-1; Modified GL-maquette sequences for bis-His ligation.** Two new maquette sequences, based on the GL-maquette sequence, designed so that bis-His sites would be available for six-coordinate ligation to cofactors. Histidine residues shown in bold, with cysteine residue highlighted in blue, used for covalent attachment to surfaces.

Iron porphyrins, as well as iron based cofactors, are known to ligate strongly to maquettes containing bis-His binding sites [6, 7]. However, the readily synthesised iron (III) porphyrins are not suitable for use in DSSCs (where  $\text{TiO}_2$  and  $\text{I}^-/\text{I}_3^-$  are employed) as the iron in the porphyrin is typically photoreduced in contrast to the photooxidation of the porphyrin core as in the case of a zinc porphyrin on  $\text{TiO}_2$ . The LUMO energy levels of iron (III) porphyrins (-0.13 V vs NHE in DMSO [8]), or -4.31 eV, being well below that of the conduction band (CB) of  $\text{TiO}_2$  (-0.5 V vs NHE [9], or -3.94 eV), and therefore not able to inject into the CB of  $\text{TiO}_2$ . This has been shown to be the case by Lin et al. [10] who investigated the use of a variety of metal porphyrins in the DSSC; negligible photocurrent was obtained when using an iron (III) porphyrin.

In contrast, gallium, like iron, is a metal with a preference for six-coordinate ligation with histidine; gallium ligates strongly to two histidines with no evidence for single histidine ligation [5]. Furthermore, gallium (III) in porphyrins does not oxidise at a potential lower than the porphyrin core, and the use of a gallium porphyrin dye in a DSSC utilizing  $\text{TiO}_2$  and  $\text{I}^-/\text{I}_3^-$  has been reported [11]. This indicates that a gallium porphyrin could potentially be designed for incorporation into a bis-His site within a maquette and analysed for differential binding as well as photovoltaic performance in a DSSC.

Here, evidence for the differential binding of a gallium porphyrin and a zinc porphyrin into a single maquette sequence is obtained, with the influence on absorbance and photovoltaic performance explored. In principle, if two different cofactors are able to be coordinated within a maquette, the resulting ensemble could absorb across a larger cross section of wavelengths compared to using a single cofactor (assuming the two cofactors used contain different absorbance profiles). The gallium porphyrin presented here (PGa) was designed based on the most promising zinc porphyrin (P1d, explored in previous chapters), with the structure shown in Figure VIII-2. No exploration of gallium cofactors with maquettes has been previously reported.

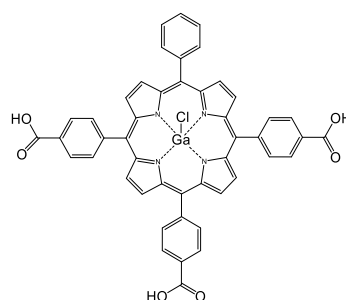


**Figure VIII-2; Gallium porphyrin (PGa) structure.** The gallium porphyrin (PGa) designed for direct comparison with a zinc porphyrin counterpart (P1d).

## 2- Results; Gallium Based Porphyrin-Maquette Ensembles

### 2.1- PGa in solvents and ligation to maquette

The absorbance profile in various solvent of the gallium porphyrin PGa, prepared in our laboratories by Nicholas Roach, was initially explored. In addition, as was done previously with the zinc based porphyrins, the solubility in aqueous buffer was explored, with the ligation with maquettes investigated. The experiments carried out with PGa were identical to those described for P1d in Chapter III, and detailed in the methods (Chapter II). The absorbance spectrum of PGa was determined in DMSO and aqueous CHES buffer, along with the spectra of the PGa with an excess of 4-*his* GL-maquette (Figure VIII-1) and titrations in the aqueous CHES buffer.

The absorbance profile of PGa (Figure VIII-3a) in DMSO (in which it is highly soluble) is very similar to the absorbance profile of P1d, however, the peak positions of the Soret and Q-bands are blue-shifted by 5 nm for PGa compared to P1d (Figure VIII-3b). As with P1d, PGa is soluble and stable in aqueous buffer (Figure VIII-C), with no detectable spectral changes after 30 mins). Similarly, when a 4-*his* GL-maquette is present with PGa, the absorbance spectrum is remarkably stable, with the sharp bands indicative of no aggregation and no observable change in the spectrum over time (Figure VIII-3d). As evident with zinc based porphyrins, a distinct red-shift of 10-11 nm is apparent in the peak positions of PGa when in aqueous buffer compared to when maquette is present (Figure VIII-3e). As outlined for the zinc porphyrins (Chapter III), this distinct red-shift is indicative of ligation between the gallium and the histidine residues within the maquette.



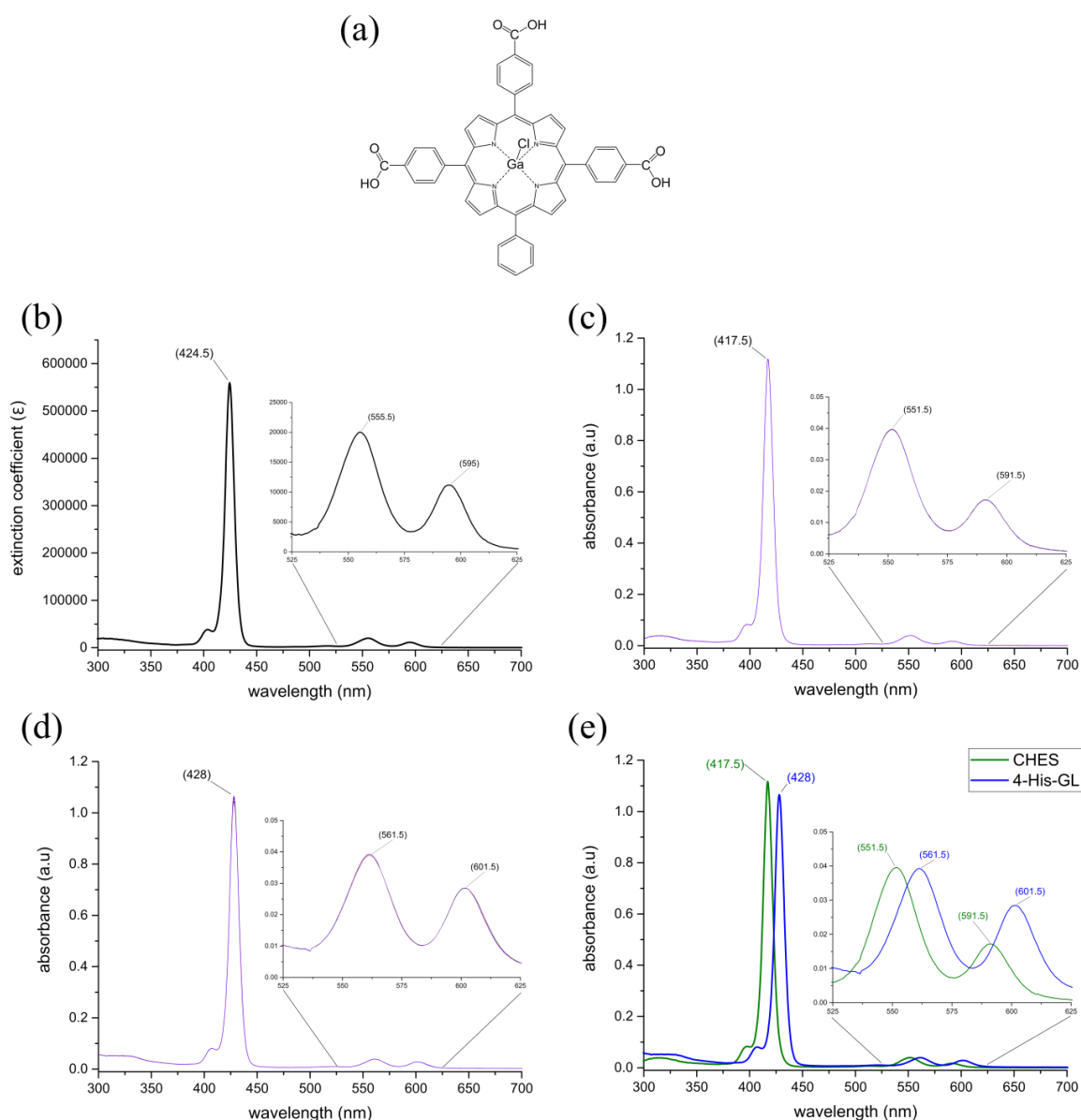


**Figure VIII-3; UV-vis. absorption spectral characterisation of PGa in DMSO, aqueous buffer, and with 4-*his* GL-maquette.** (a) Structure of PGa. (b) PGa in DMSO. (c) PGa in aqueous buffer; measured every 5 min for 30 min. (d) PGa and 4-*his* GL-maquette in aqueous buffer; measured every 5 min for 30 min. (e) Absorption of PGa in aqueous buffer after 30 min (green), and with 4-*his* GL-maquette (blue).

## 2.2- PGa titration with maquette

As presented previously with the zinc based porphyrins (Chapter III), binding of PGa to maquettes can be further analysed through a binding titration. Binding titrations here were performed by adding aliquots of porphyrin from a solution of DMSO to an aqueous buffer containing maquettes, incrementally increasing the concentration of porphyrin present. Aliquots were added at  $0.1 \mu\text{M}$  per aliquot to a  $0.3 \mu\text{M}$  4-*his* GL-maquette solution in aqueous buffer. The maximum peak for the first aliquots corresponded to porphyrin ligation with maquette, with this peak position plotted against the concentration of porphyrin present.

Modelling this fit in accordance with Equation 2 (Chapter II) allowed for analysis of  $K_D$ , stoichiometry, and extinction coefficients.

As shown in Figure VIII-4, the titration of PGa to 4-*his* GL-maquette produces two distinct peaks at 428 and 417 nm. These peak positions correspond to the Soret peak of ligated and free PGa, respectively. Plotting the absorbance rise at 428 nm to the concentration of PGa present produces a curve with a distinct bend (Figure VIII-4 inset). As was discussed previously in Chapter III, the curve represents PGa being in a ligated (bound) state, and a non-ligated (un-bound) state, which occurred when 2 equivalents of PGa were present with 1 equivalent of maquette. Analysis of the fit (Equation 2) gave the extinction coefficient of ligated PGa as  $506,617 (\pm 4,811) \text{ M}^{-1} \text{ cm}^{-1}$  at 428 nm, and a tight binding with the maquette, indicated by a  $K_D$  of  $11 (\pm 1.8) \text{ nM}$ .

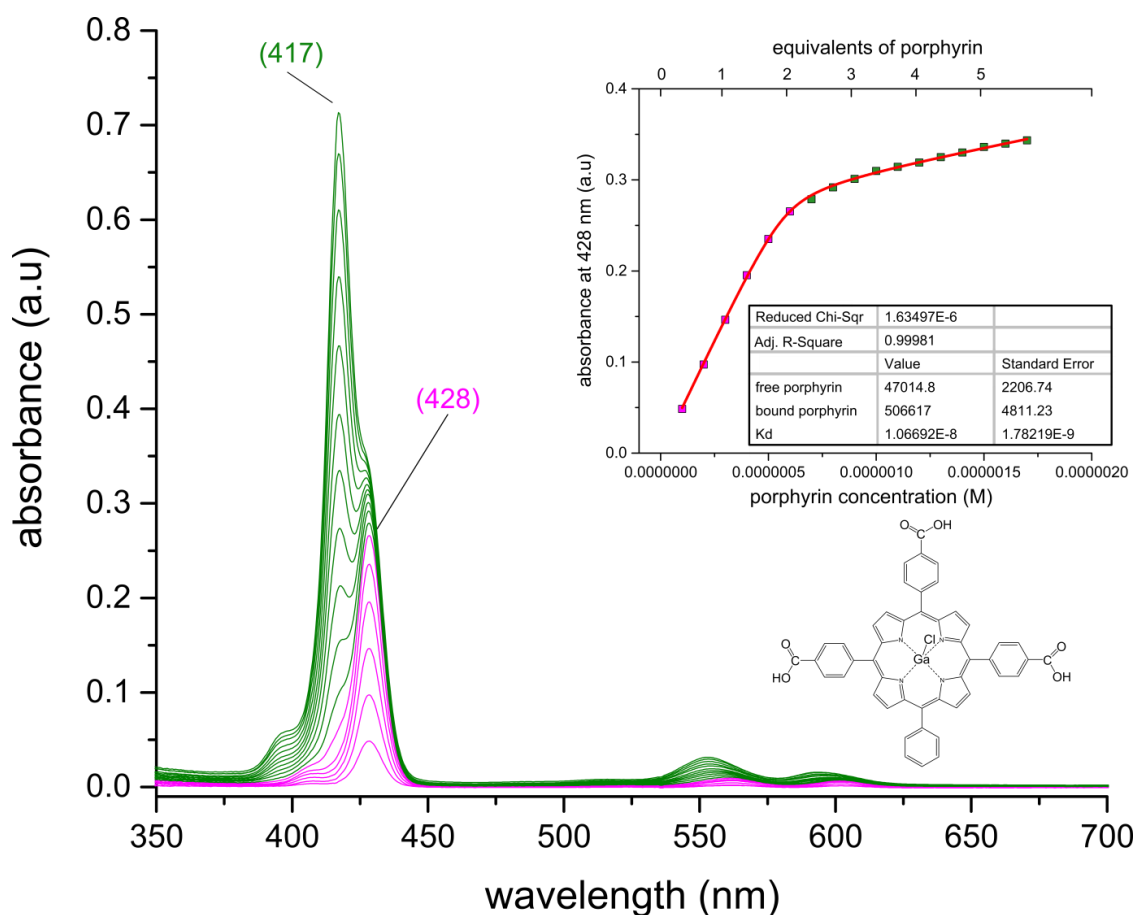


**Figure VIII-4; Titration of PGa with 4-*his* GL-maquette.**  $0.3 \mu\text{M}$  4-*his* GL-maquette with increments of  $0.1 \mu\text{M}$  PGa in aqueous CHES buffer. Inset shows the increase in absorbance of bound PGa at Soret peak maxima against total concentration of PGa, and resulting equivalents of porphyrin compared to maquette.

### 2.3- Electrochemical analysis of PGa

The determination of PGa energy levels was required for applications in devices, with the HOMO and LUMO energy levels determined via electrochemistry in solution. The solvent THF was used instead of DMF, which had been used for all previous solution based electrochemistry (Chapter VI), since PGa was insoluble in DMF. As the conversion of measured potential to electronic energy (eV) relies on the ferrocenium/ferrocene ( $\text{Fc}^+/\text{Fc}$ ) couple, ferrocene was first measured in THF, with the TBAP/THF ‘background’ shown to ensure current responses were indeed from the intended redox species (Figure VIII-5). As shown, the CV (Figure VIII-5a) and SWV (Figure VIII-5b) techniques produced near identical half-wave potentials for  $\text{Fc}^+/\text{Fc}$ , with the value of 0.42 V (vs  $\text{Ag}/\text{Ag}^+$ ) used for subsequent conversions to eV, for PGa. The SWV technique was used to determine the first reduction (Figure VIII-5c) and first oxidation (Figure VIII-5d) half-wave potential peaks (as was done for zinc based porphyrins previously), and these were converted to LUMO and HOMO energy levels, respectively (Figure VIII-5e), using Equation 4 (Chapter VI).

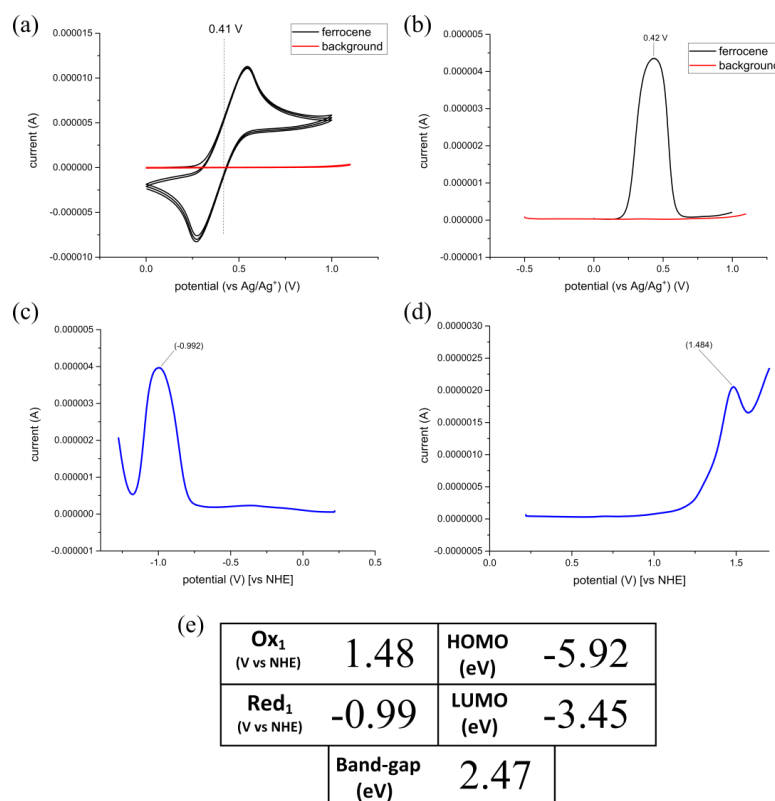


**Figure VIII-5; Electrochemistry of PGa in solution.** (a) CV of ferrocene (black) in THF, with TBAP/THF background (red), scanned at 50 mV s<sup>-1</sup>. (b) SWV of ferrocene (black) in THF, with TBAP/THF background (red). (c) Reduction SWV of 0.8 mM PGa in THF. (d) Oxidation SWV of 0.8 mM PGa in THF. (e) Determination of energy levels based on the first oxidation and first reduction half-wave potential peaks. All traces were measured in THF with 0.1 M TBAP as a supporting electrolyte. SWVs all scanned at 20 mV s<sup>-1</sup>.

The determined energy levels for PGa were compared to the energy levels for the  $I^-/I_3^-$  redox mediator and the CB of  $TiO_2$  (Figure VIII-6). Furthermore, the HOMO-LUMO energy levels can be directly compared to P1d and the impact of replacing the central metal from zinc (P1d) to gallium (PGa) can be assessed. The band-gap for P1d was determined to be 2.30 eV (Chapter VI), with that band-gap of PGa determined to be 2.47 eV. This band-gap is similar to a gallium porphyrin previously reported (2.52 eV [11]). As shown in Figure VIII-6, both the HOMO and LUMO energy levels are shifted to lower levels for PGa, with the HOMO being most affected (resulting in the larger band gap). Furthermore, the driving force for electron injection from the LUMO into the CB of  $TiO_2$  is reduced by 210 mV for PGa. Consequently the use of PGa in a device may be hindered by this reduced driving force.

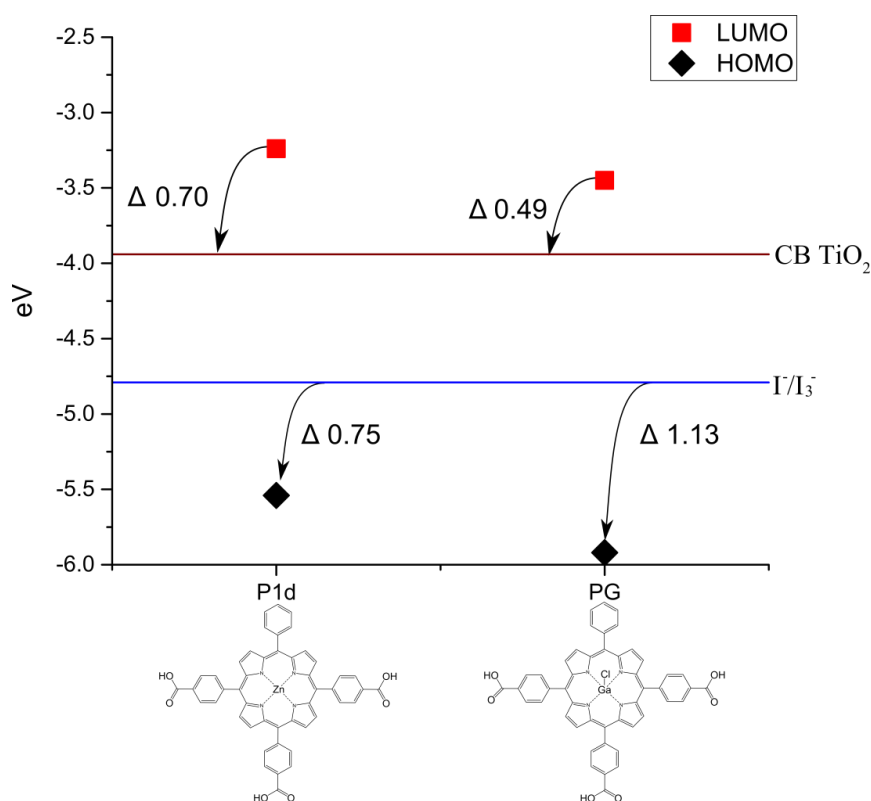


**Figure VIII-6; Driving forces associated with DSSCs using P1d or PGa.** The determined HOMO-LUMO energy levels from electrochemical analysis of P1d or PGa showing the difference in driving forces for injection into the conduction band of  $TiO_2$  (CB  $TiO_2$ ) and regeneration with the redox couple ( $I^-/I_3^-$ ).

#### 2.4- PGa in DSSC based devices

With the HOMO-LUMO energy levels of PGa reasonably well positioned in relation to the CB of  $TiO_2$  and the  $I^-/I_3^-$  redox mediator, the use of PGa within a DSSC construct for photovoltaic analysis was investigated. As was undertaken with P1d, PGa was sensitized directly to  $TiO_2$  from THF (200  $\mu M$ ; see Chapter II, Section 2.4). Sensitization directly to  $TiO_2$

was compared to immobilization of PGa-4-*his* GL-maquette ensembles (100  $\mu\text{M}$  PGa with 51  $\mu\text{M}$  maquette) drop-casted onto  $\text{TiO}_2$  from aqueous CHES buffer (see Chapter II, Section 2.4). As shown in Figure VIII-7a, the two differing modes of sensitization of  $\text{TiO}_2$  produced vastly different absorbances, notably that the absorbance of PGa sensitized to  $\text{TiO}_2$  was distinctly greater than for the PGa-maquette ensembles on the surface. As the absorbance is highly correlated with the quantity of porphyrin present, the quantity of PGa was significantly more when sensitized to  $\text{TiO}_2$  compared to when ligated with maquette and immobilized, although this was not quantitatively determined. This trend is the same as that for P1d (Chapter VII) in which there was 6.2 times more covalently bound porphyrin than in the surface-attached maquette.

Following preparation of analogous PGa and PGa-4-*his* GL-maquette sensitized 8.5  $\mu\text{m}$   $\text{TiO}_2$  photoanodes and fabrication into DSSCs, the photovoltaic responses of the resulting devices were measured (Figure VIII-7b). The data from the *JV* curve (Figure VIII-7f) shows as expected that the current and efficiency is higher for PGa sensitised to the surface. However, the  $V_{\text{oc}}$  and FF for PGa-maquette ensembles are significantly higher. This trend is once again identical to that previously observed for the zinc porphyrin P1d. The IPCE analysis of the resulting devices (Figure VIII-7c) displays two distinct peaks when PGa is sensitized to  $\text{TiO}_2$ . This indicates that there is likely more than one PGa electronic state present, both capable of a photocurrent response. In comparison, one broad peak is predominant when PGa is ligated with a maquette, with the peak position being identical to that for PGa-maquette ensembles in solution.

The devices were further analysed for differences in electrochemical impedance under illumination. As shown in the table in Figure VII-10g, there is a minimal series resistance ( $R_0$ ) difference between the devices. The resistance and capacitance associated with the arc  $\omega_{\text{TiO}_2}$  (allocated to the  $\text{TiO}_2$  grain boundaries and glass substrate interface, Figure VIII-7d) show slight deviation between the two devices, however, the most prominent difference observed is the capacitance associated with the interface between the CB of  $\text{TiO}_2$ , the dye, and the electrolyte ( $\omega_{\text{TiO}_2/\text{D}/\text{E}}$ ), which increased by over 5-fold for when the ensembles were employed. The electron lifetime ( $\tau_{\omega_{\text{TiO}_2/\text{D}/\text{E}}}$ ), being the time for the electron to transfer from the CB of  $\text{TiO}_2$  back to  $\text{I}_3^-$ , is observed to increase by nearly 10-fold when PGa is ligated with maquettes compared to when PGa is sensitized directly to the surface. This is determined via the Bode plot representation of the devices (Figure VIII-7e), with the electron lifetime being closely associated with the

resistances of recombination and the chemical capacitance of  $\omega_{\text{TiO}_2/\text{D}/\text{E}}$  [12], both shown to be significantly increased when ensembles are used.

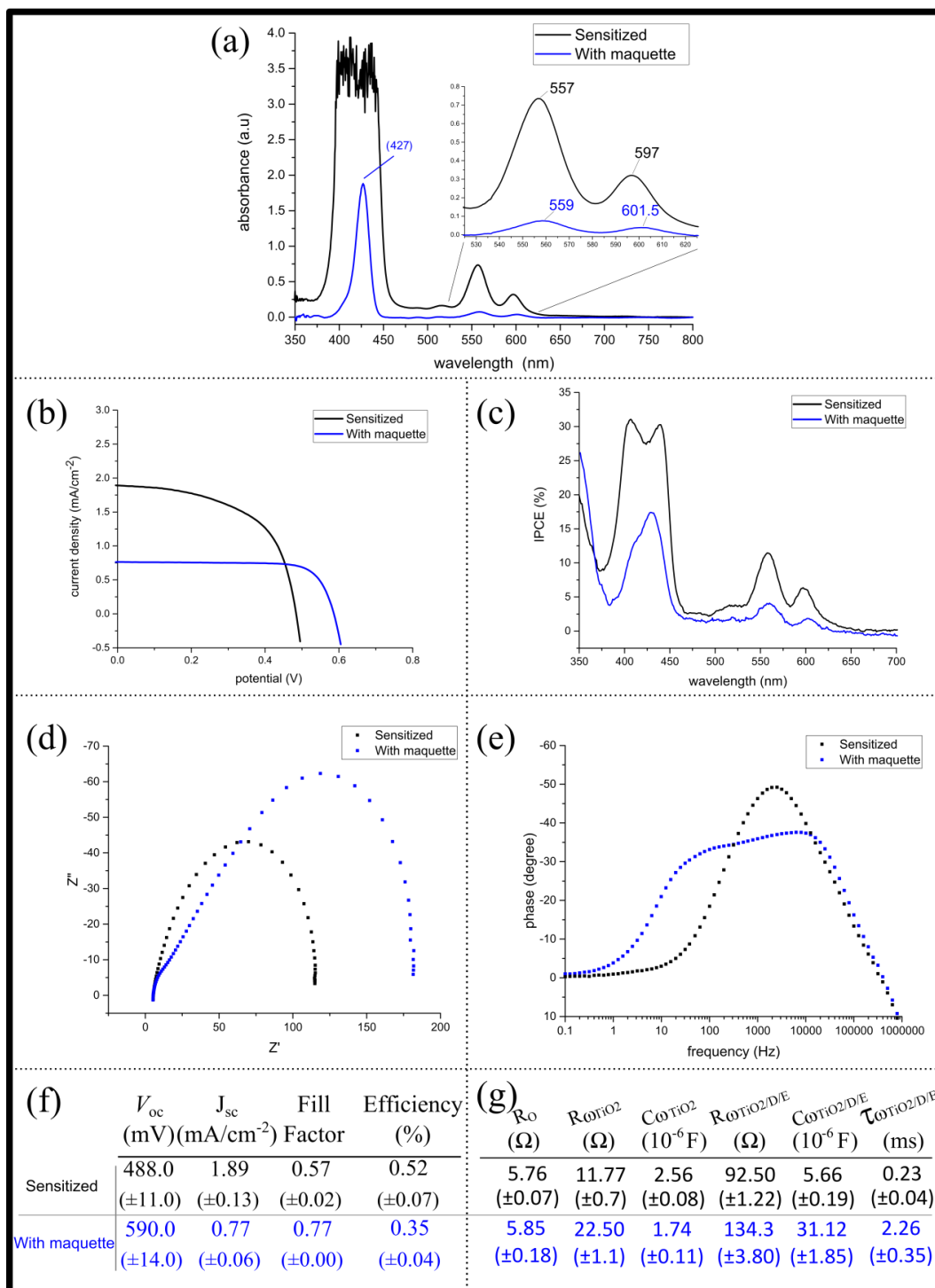


**Figure VIII-7; Device measurements utilizing sensitized PGa or PGa-maquette ensembles with E1.** The resulting device measurements of 8.5  $\mu\text{m}$   $\text{TiO}_2$  with sensitized PGa (in black) or PGa-maquette ensemble (in blue), using electrolyte 1 (E1). (a) Absorbance of either sensitised PGa from THF or PGa-maquette ensembles immobilized from aqueous buffer on 2.5  $\mu\text{m}$   $\text{TiO}_2$ . (b) The average  $JV$  curve under 1-sun illumination. (c) The average IPCE measurements. (d) Nyquist-plot representation of the devices. (e) Bode-plot representation of the devices. (f) The average photovoltaic data. (g) Obtained impedance spectroscopy data from a 2-phase circuit representation (see Figure VII-4) of the device. (Averages shown, where number of devices =3).

## 2.5- PGa and P1d differential binding into maquettes

Differential binding of an iron porphyrin and a zinc porphyrin into a single maquette has been achieved as a result of the different affinities for bis-His ligation (for iron) compared to the single histidinal ligation (for zinc) [4, 5]. Consequently we undertook the differential binding of a gallium porphyrin (PGa) and a zinc porphyrin (P1d) into a maquette is presented. As with the iron-zinc porphyrin differential binding, a *3-his* maquette (GL-maquette in this case) was employed, with the gallium expected to ligate only to the bis-His site and zinc ligating to the single histidine site.

The solution binding of PGa and/or P1d to the *3-his* GL-maquette was undertaken as previously described in Chapter II using the solutions detailed in Figure VIII-8. To achieve the differential binding, *3-his* GL-maquette (Figure VIII-1) was used at a slight excess in concentration (~1.1:1 maquette to porphyrin) compared to either porphyrin. This was done so as to ensure that the availability of histidine binding sites within the maquette was not an influencing factor, whilst still allowing for observation of differential affinities. The absorbance spectra of *3-his* GL-maquette with either P1d (Figure VIII-8 black dotted line) or PGa (Figure VIII-8 blue dotted line) were also obtained to compare directly to *3-his* GL-maquette containing both P1d and PGa. Furthermore, the order of addition of either P1d or PGa to *3-his* GL-maquette was investigated, with P1d mixed with *3-his* GL-maquette before addition of PGa (red line in Figure VIII-8a), or PGa mixed with *3-his* GL-maquette before addition of P1d (red line in Figure VIII-8b).

As shown in Figure VIII-8a, distinct differences were seen when the maquette was in a ~1.1:1 (2:0.9 binding site ratio) with either P1d (blue dotted trace) or PGa (black dotted trace), displaying a ~5 nm shift in the absorbance peaks. Therefore, differential binding of both P1d and PGa into a single maquette would be expected to produce an absorbance profile, which is the combination of the two absorbance profiles with *3-his* GL-maquette. However, differences arose when the order of addition of P1d or PGa to the solution containing *3-his* GL-maquette was varied. Figure VIII-8a (red trace) shows the resulting absorbance when the P1d-maquette was initially obtained followed by PGa incorporation; a broad peak at 431.5 nm was produced with distinct shoulder peak (418 nm) apparent.

The broad peak encompasses the area of both the absorbances of the individually ligated porphyrins (black and red dotted traces) suggesting that both P1d and PGa bind to the maquette. Furthermore, the integral of the broadened peak (red trace, Figure VIII-8a) along with the

apparent shoulder (between 375 and 475 nm) closely matches to the sum of the integrals of P1d-maquette and PGa-maquette (black and blue traces, Figure VIII-8a); 2.80 compared to 2.92, respectively. This indicates that the total amount of porphyrin is similar in both cases (red trace compared to the combination of black and blue traces). Therefore, it appeared that the peak occurring at 431.5 nm arose from the combination of both P1d and PGa in a ligated state bound to maquette; however, some porphyrin was present in a non-ligated state, as evident from the shoulder peak. This shoulder peak aligns to the PGa absorbance that results from unbound porphyrin in the aqueous buffer, as previously shown in Figure VIII-3c. This shoulder peak suggests that not all of the PGa present was able to bind to the bis-His binding site.

In contrast, when PGa was added to the solution containing *3-his* GL-maquette before addition of P1d, a single superimposed absorbance profile was obtained (red trace in Figure VIII-8b), with no absorbance peaks apparent relating to unbound porphyrin. Once again, the integral of the red trace in Figure VIII-8b (between 375 and 475 nm) is closely aligned to the sum of the integrals of P1d-maquette and PGa-maquette (black and blue traces, Figure VIII-8b); 13.0 compared to 13.2, respectively. The quantities present are therefore highly comparable in the two instances (red trace compared to the combination of black and blue traces). With the presence of only a single peak at 431.5 nm, being a combination of the two individual ligated porphyrin spectra, it can be assumed that the *3-his* GL-maquette had incorporated both the porphyrins PGa and P1d within the intended binding sites of the maquette (bis-His and single-His respectively). No shoulder was apparent due to the gallium porphyrin PGa having a preference for bis-His ligation, with subsequent addition of the zinc porphyrin P1d all ligating within the single-His binding site.



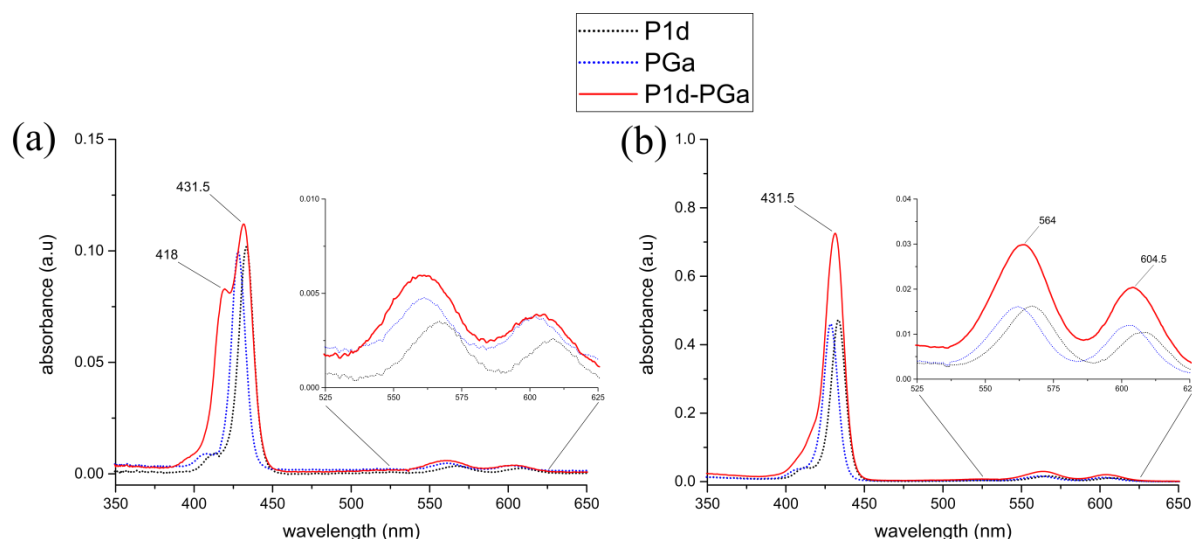


**Figure VIII-8; Differential binding of P1d and PGa into a maquette.** The *3-his* GL-maquette was used to bind both P1d and PGa via single histidinal ligation and bis-His ligation, respectively. (a) 0.2  $\mu\text{M}$  P1d and 0.22  $\mu\text{M}$  *3-his* GL-maquette (black dotted line), 0.2  $\mu\text{M}$  PGa and 0.22  $\mu\text{M}$  *3-his* GL-maquette (blue dotted line), and 0.2  $\mu\text{M}$  P1d mixed with 0.22  $\mu\text{M}$  *3-his* GL-maquette with subsequent addition of 0.2  $\mu\text{M}$  PGa (red line). (b) 1  $\mu\text{M}$  P1d and 1.1  $\mu\text{M}$  *3-his* GL-maquette (black dotted line), 1  $\mu\text{M}$  PGa and 1.1  $\mu\text{M}$  *3-his* GL-maquette (blue dotted line), and 1  $\mu\text{M}$  PGa mixed with 1.1  $\mu\text{M}$  *3-his* GL-maquette with subsequent addition of 1  $\mu\text{M}$  P1d (red line). All solutions were made up in CHES buffer.

The ensembles that were obtained by differential binding of P1d and PGa into the *3-his* GL-maquette (herein referred to as P1d-PGa-maq) were subsequently covalently immobilized from aqueous MES buffer (50  $\mu\text{M}$  PGa and 51  $\mu\text{M}$  *3-his* GL-maquette with subsequent addition of 50  $\mu\text{M}$  P1d) onto 2-aminoethylphosphonic acid (for covalent attachment via 3-(maleimido)propionic acid N-hydroxysuccinimide ester) modified  $\text{TiO}_2$  (2.5  $\mu\text{m}$ ) as described in Section 2.4.3, Chapter II, with the resulting absorbance shown in Figure VIII-9a. As observed for the P1d-maquette on  $\text{TiO}_2$ , there is a slight blue-shift (1.5-2 nm) of all the absorbance bands but there is no indication that the porphyrins have unligated from the maquette and attached to the surface. The two Soret bands of the PGa-maquette and P1d-PGa-maq give a single peak with similar absorbance intensity, analogous to that observed for PGa-maquette on 2.5  $\mu\text{m}$   $\text{TiO}_2$  (Figure VIII-7a).

Subsequently, a photoanode was prepared by covalent attachment of the P1d-PGa-maq (at the same concentrations described above) from aqueous MES buffer onto 3-(maleimido)propionic acid N-hydroxysuccinimide ester modified  $\text{TiO}_2$  (as described in Section 2.4.3, Chapter II) and this was fabricated into a DSSC in an identical manner as previously

reported for the PGa-maquette (see Section 2.4). As for the PGa-maquette, devices were all produced using 8.5  $\mu\text{m}$   $\text{TiO}_2$  with E1 as the redox electrolyte, allowing for direct comparisons of photovoltaic performance. The resulting photovoltaic data is given in Figure VIII-9.

*JV* curve (Figure VIII-9c), with the photovoltaic data (Figure VIII-9b) was compared directly to PGa-maquette devices (Figure VIII-7). It was shown that devices employing P1d-PGa-maq resulted in an increase in all photovoltaic measured performance ( $J_{\text{sc}}$ ,  $V_{\text{oc}}$ , FF, and efficiency) compared to PGa-maquette devices;  $V_{\text{oc}}$  increased by over 6 %,  $J_{\text{sc}}$  by 45 %, and FF by 2 % leading to an overall 60 % increase in DSSC efficiency.

The differences in device performance were further explored using electrochemical impedance spectroscopy (EIS), with analysis of the resulting Nyquist plot (Figure VIII-9e) and Bode plot (Figure VIII-9f) representations giving electrochemical performances from the observable interfaces within the device (Figure VIII-9g). Comparison of EIS performances for devices employing PGa-maquette with P1d-PGa-maq showed no significant difference in the performances of  $R_{\text{O}}$ ,  $R_{\omega\text{TiO}_2}$ , or  $C_{\omega\text{TiO}_2}$ . The predominant difference once again arises from the  $\text{TiO}_2$  and redox electrolyte interface, with the resistance ( $R_{\omega\text{TiO}_2/\text{D/E}}$ ) decreasing slightly whilst the chemical capacitance increased by over 2-fold ( $C_{\omega\text{TiO}_2/\text{D/E}}$ ) when P1d-PGa-maq was used. This increase in chemical capacitance resulted in an increased electron lifetime ( $\tau_{\omega\text{TiO}_2/\text{D/E}}$ ) from 2.26 (for PGa-maquette ensembles) to 3.66 ms using P1d-PGa-maq.

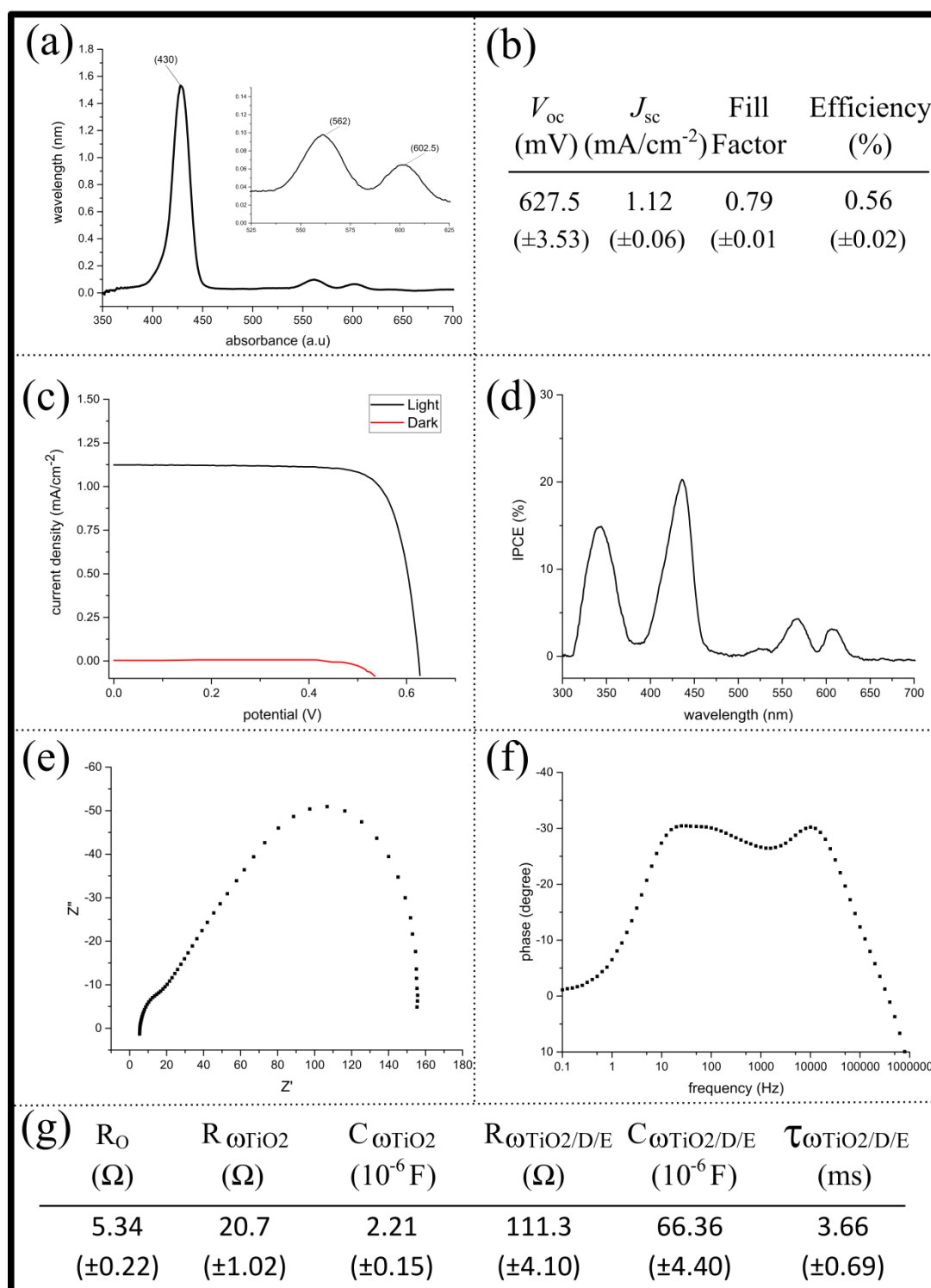


**Figure VIII-9; Device measurements utilizing covalently attached P1d-PGa and 3-his GL-maquette ensembles.** The resulting device measurements were of  $8.5 \mu\text{m}$   $\text{TiO}_2$  with covalently attached P1d-PGa-maq ensembles, using electrolyte 1 (E1). (a) Absorbance of P1d-PGa-maq ensembles covalently attached from aqueous MES buffer on  $2.5 \mu\text{m}$   $\text{TiO}_2$ . (b) The average photovoltaic data. (c) The average  $JV$  curve under illumination (black line) and in the dark (red line). (d) The average IPCE measurement. (e) Nyquist-plot representation of the device. (f) Bode-plot representation of the device. (g) Obtained impedance spectroscopy data from a 2-phase circuit representation of the device (see Figure VII-4). (Averages shown, where  $n=2$ ).

### 3- Discussion; Gallium Based Porphyrin-Maquette Ensembles

The absorbance profile of PGa in DMSO, expected to be completely solubilised, displays a single sharp Soret peak with two Q-bands (Figure VIII-3). This absorbance profile is identical to the absorbance profiles of the zinc porphyrins presented in Chapter III, albeit with peak positions shifted 5-6 nm. The stability of PGa in aqueous solutions was then assessed by comparison to the absorbance profile of PGa in DMSO, with broadening of the Soret peak or appearance of shoulders indicative of aggregation. However, this was not the case, with PGa in the aqueous CHES buffer displaying a highly stable absorbance spectrum with a sharp Soret peak (with no visible changes over 30 min). In a similar manner as for the zinc porphyrin in Chapter III, the binding of PGa to a maquette was assessed by spectral shifts. A 10-11 nm red-shift was apparent in the peak positions of PGa with 4-*his* GL-maquette in aqueous CHES buffer, compared to when maquette was not present. As was determined previously in Chapter III with the zinc porphyrins, this distinct red-shifting was due to the axial ligation and immediate environment of the porphyrin within the maquette [13].

To further explore the binding of PGa into maquettes, the binding titration of PGa to 4-*his* GL-maquette was analysed via a binding titration (Figure VIII-4), used to determine the stoichiometric relationships and binding strengths (dissociation constants) between porphyrin and maquette (as undertaken in Chapter III). The titration of PGa to 4-*his* GL-maquette in aqueous CHES buffer displayed an identical trend to that of the binding titration of P1d to GL-maquette in Chapter III, whereby an absorbance profile with peak positions pertaining to PGa ligating within the maquette was evident for stoichiometries  $\leq 2:1$  (PGa to maquette). When porphyrin concentrations were subsequently increased, an absorbance profile with peak positions resembling the porphyrin (PGa) being unbound in the aqueous CHES buffer became evident. The results indicated that PGa could ligate within both bis-His binding sites present in the 4-*his* GL-maquette. Determination of the dissociation constant indicated that PGa bound strongly into the maquette, indicated by a  $K_D$  of 11 ( $\pm 1.8$ ) nM. In contrast, the zinc porphyrin counterpart (P1d) with GL-maquette (Chapter III) had a dissociation constant ( $K_D$ ) of 25 ( $\pm 3.0$ ) nM, indicating that PGa has twice the affinity for binding into the maquette. This is likely due to PGa requiring a bis-His binding site and therefore the two histidines 'hold' the porphyrin more tightly in a bound state compared to zinc which is only held in a bound state via a single histidine.

The potential use of PGa in a device is reliant on its electrochemical properties, with the determination of the HOMO and LUMO needed to ascertain if PGa can regenerate with the  $I^-/I_3^-$  redox mediator and also inject into the CB of  $TiO_2$ , respectively. The HOMO-LUMO levels were determined to be appropriate for regeneration and injection (Figure VIII-6). The HOMO-LUMO levels for PGa can be compared to the levels determined for P1d (Chapter VI), with P1d having the same structure as PGa except for the metal centre being replaced with zinc. As shown in Figure VIII-6, the substitution of the central metal has a large impact on the electrochemical properties of the porphyrin, with gallium shifting both the HOMO and LUMO energy levels lower. Furthermore, using gallium increased the band-gap by 170 mV compared to zinc. Since these values suggested that injection and regeneration were likely, the implementation of PGa in a DSSC using an  $I^-/I_3^-$  redox mediator and  $TiO_2$  was undertaken. The use of gallium porphyrins in DSSC based devices had not been well reported (with only one published article identified), with the gallium porphyrins producing significantly lower efficiencies than zinc porphyrins [11].

The covalent binding of PGa to  $TiO_2$  from an organic solvent (THF) was compared to immobilization of PGa-maquette ensembles onto  $TiO_2$  for both absorbance and device performance (Figure VIII-7). The quantity of the photoactive material PGa is significantly greater when covalent attached to  $TiO_2$ , compared to when PGa is bound within the maquette and immobilised as expected and seen for P1d. This is evident by the distinct differences in the absorbances, although, a quantitative measurement was not undertaken to determine the exact difference in the amounts of PGa present between the two binding modes. In a similar trend observed with the zinc porphyrin P1d previously reported (see Chapter VII, Table VII-2), when PGa is covalently bound to the surface, the resulting DSSC has a higher  $J_{sc}$  and over-all efficiency compared to DSSCs utilising PGa-maquette ensembles bound to the surface. In contrast, the  $V_{oc}$  increased by over 100 mV with devices using PGa-maquette ensembles compared to PGa covalently bound to the surface. As discussed in the previous chapter for P1d-maquette based DSSCs, this increase in  $V_{oc}$  is attributed to the decrease in the probability of electron recombination between the CB of  $TiO_2$  and the redox mediator. EIS analysis gave further evidence for this, with the electron lifetime (in the CB of  $TiO_2$  before recombination) increasing by ~10-fold when PGa-maquette ensembles are employed. As was evident with the zinc porphyrin (P1d) presented in the previous chapter, this decrease in electron recombination is attributed to the maquette layer on the  $TiO_2$  surface reducing the probability of recombination

whilst facilitating electron injection from the photoexcited state of the bound porphyrin into the CB of TiO<sub>2</sub>.

Differential binding of two cofactors into a single maquette could potentially enhance the efficiency of DSSCs by increasing the light harvesting capabilities through broadening incident spectrum capture. Utilizing a gallium porphyrin that has a preference for bis-His ligation (and no known single-His ligation) in conjunction with a zinc porphyrin would allow for a differential binding into a maquette containing two differing binding sites; such as that in a 3-*his* GL-maquette (Figure VIII-1). However, it was apparent that the procedure of porphyrin introduction into the maquette was important due to the preference for binding. When the zinc porphyrin (P1d) was introduced into the 3-*his* GL-maquette (Figure VIII-8a), subsequent addition of PGa led to only partial binding of PGa, with up to 50 % of the porphyrin being in an unbound state, even though the stoichiometric limit of binding sites was not met. Assuming that P1d did not have a preference for either binding site or that binding at one site did not affect the binding at the second site, therefore the probability that P1d occupied the bis-His binding site was 50 %, with a 50 % chance of occupying the bis-His binding site (at a ratio of 1:1, P1d to 3-*his* GL-maquette). Consequently, four outcomes (each equally probable) were possible when 1 equivalent of porphyrin was reacted with 1 equivalent maquette (which is equal to 2 equivalents of available binding sites). P1d could bind to both available binding sites within a maquette (Figure VIII-10a), which would stop any incorporation of the subsequently added PGa to the maquette. P1d could bind to the single-His binding site and leave the bis-His site available for subsequent incorporation of PGa (Figure VIII-10b). Conversely, if P1d bound to the bis-His site leaving the single-His site available, subsequent PGa would not ligate within the single-His site and so would remain in solution (Figure VIII-10c). Finally, since 25 % of maquettes had both binding sites filled with P1d (Figure VIII-10a), 25 % of maquettes would not incorporate any P1d and subsequent addition of PGa would lead to ligation within the available bis-His site (Figure VIII-10d). Given the four equally likely outcomes (Figure VIII-10a-d), half of the gallium porphyrin is physically blocked from accessing the bis-His binding sites due to P1d occupation, leaving the remaining PGa remaining unbound in solution. Determination of the exact amount of PGa bound and unbound was difficult due to the peak overlaps. However, it can be seen that the peak areas of the two Soret bands are not dramatically different and that the area of the bound PGa (main red band, Figure VIII-8a) is likely no more than the sum of the areas of the individually bound P1d and PGa (black dotted and blue dotted bands, respectively).

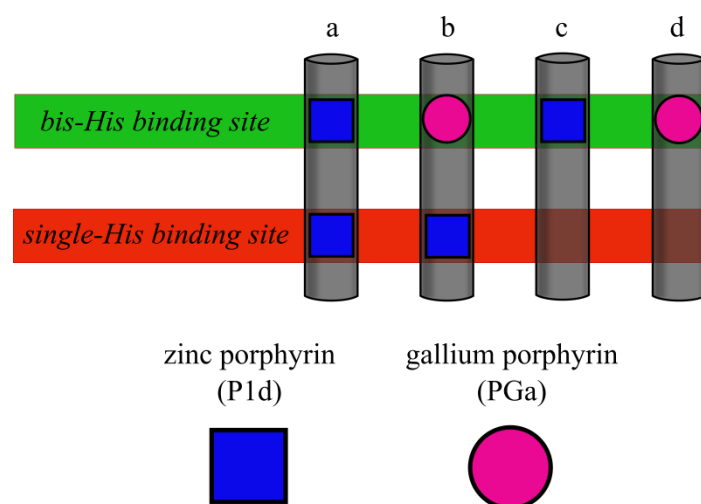


**Figure VIII-10; Binding preferences of P1d and PGa into a maquette.** The 3-*his* GL-maquette contains two different binding sites; a binding site for single-His ligation (red) and bis-His ligation (green). The zinc porphyrin P1d does not have a preference for either binding site, with the probability that P1d binds to the bis-His binding site being 50 %, with a 50 % chance to bind to the bis-His binding site (at a ratio of 1:1, P1d to 3-*his* GL-maquette). With subsequent introduction of the gallium porphyrin PGa (having a preference for bis-His ligation), PGa would bind to the 50 % available bis-His binding sites, with 50 % being unbound in solution (at a ratio of 1:1, PGa to 3-*his* GL-maquette) due to PGa not binding to the single-His binding site.

However, this issue could not occur when the gallium porphyrin was introduced into the maquette first, with subsequent introduction of the zinc porphyrin (Figure VIII-8b). Since the gallium porphyrin had a preference for occupying the bis-His binding site, all these sites were filled leaving the subsequently introduced zinc porphyrin to occupy only the single-His binding site. The relative integral ratio of the mixed P1d-PGa porphyrin Soret band and the individual Soret bands of P1d and PGa was 13.0:13.2 confirming the above result.

With the differential binding of PGa and P1d achieved within 3-*his* GL-maquette, the potential for harnessing a broadened incident spectrum along with light-initiated electron and energy transfer events between the two differing porphyrins could be investigated [4, 14]. Both the HOMO and LUMO energy levels of PGa are below that for P1d (Figure VIII-6), indicating that it is possible to get electron transfer from the photoexcited state of P1d to PGa. With the structure of 3-*his* GL-maquette specifically designed to have the cysteine residue (for covalent attachment to TiO<sub>2</sub>) at the same end as the bis-His binding site (Figure VIII-1), the electron flow would be funnelled, directing electron transfer from the photoexcited state of P1d to PGa, which would then inject electrons into the CB of TiO<sub>2</sub>. Indeed there is an increase in all photovoltaic measured performances ( $J_{sc}$ ,  $V_{oc}$ , FF, and efficiency) in devices using P1d-PGa-maq ensembles (Figure VIII-9) compared to PGa-maquette devices (Table VIII-1). Furthermore, the electron lifetime increased to 3.66 ms, corresponding to a low probability of electron recombination between the CB of TiO<sub>2</sub> and the redox mediator. However, as the

devices using P1d-PGa-maquette ensembles were fabricated using covalent attachment to a 2-aminoethylphosphonic acid modified surface, the increase in electron lifetime may be due to the physically increased distance between the TiO<sub>2</sub> surface and dye/redox mediator as previously discussed for P1d-*cys*GL maquette in Chapter VII. Nonetheless, the increased current (and overall efficiency) displays an enhanced light-harvesting ability of devices utilizing maquettes with differentially bound porphyrin even though the comparison is between different modes of maquette binding. As was clearly shown in Chapter VII, the photovoltaic efficiency of electrostatically bound P1d-maquette devices was superior to the covalently bound maquette devices. Therefore, it might be assumed that, if the type of maquette did not significantly affect the photovoltaic results, the electrostatically bound PGa-maquette device should have been better than the covalently bound one. Nonetheless, P1d is a better dye within DSSC devices compared to PGa. Hence the presence of P1d improved the covalently bound results presented in this section, with the experiments that could have rectified this issue not able to be undertaken due to time constraints.

**Table VIII-1; Comparisons of photovoltaic data of devices using gallium and maquettes.** Photovoltaic data from devices presented in Section 2.

Sample	PGa-4- <i>his</i> GL-maquette Ensembles	P1d-PGa-3- <i>his</i> GL-maquette Ensembles
Mode of attachment	Electrostatic	Covalent
Film Thickness ( $\mu\text{m}$ )	8.5	8.5
Electrolyte	E1	E1
$V_{oc}$ (mV)	590.0 ( $\pm 14.0$ )	627.5 ( $\pm 3.53$ )
$J_{sc}$ (mA/cm <sup>2</sup> )	0.77 ( $\pm 0.06$ )	1.12 ( $\pm 0.06$ )
FF	0.77 ( $\pm 0.00$ )	0.79 ( $\pm 0.01$ )
Efficiency (%)	0.35 ( $\pm 0.04$ )	0.56 ( $\pm 0.02$ )
$\tau_{TiO_2/D/E}$ (ms)	2.26 ( $\pm 0.35$ )	3.66 ( $\pm 0.69$ )

Further experimentation and analysis is needed to determine the true extent of utilizing a maquette with differentially bound porphyrins in a DSSC. A true comparative study should be undertaken, looking specifically at the effects of having a gallium porphyrin differentially bound with a zinc porphyrin. Firstly, the possibility for electron transfer from the photoexcited



zinc porphyrin to the gallium porphyrin should be determined through spectroscopic studies. The impact of differential binding within maquettes for DSSCs could be explored with a comparative study using specially designed maquettes. A series of designed maquettes based on the *3-his* GL-maquette would be ideal, with a maquette which has the bis-His binding site removed (containing only one single-His site) and another maquette with the single-His site removed (containing only one bis-His site). Furthermore, the *4-his* GL-maquette and *cysGL*-maquette (from Chapter VII) would allow for further interpretation. With the series of maquettes available, five different devices (all covalently attached, ie. standing upright on TiO<sub>2</sub>) could be directly compared to one another with the following designs. Devices utilizing the differential binding of gallium and zinc porphyrins in the *3-his* GL-maquette (which was presented here), would be compared directly to devices using the maquette with only the one bis-His binding site with gallium porphyrin bound. This would allow for interpretation of the extent to which the gallium porphyrin contributes to photovoltaic performance. Conversely, devices utilising the maquette with only one single-His binding site with a zinc porphyrin bound (being most distal from TiO<sub>2</sub> when covalently attached) would allow for interpretations of how much a distal zinc porphyrin affects photovoltaic performance directly (ie. how easily it can inject electrons directly into the CB of TiO<sub>2</sub> directly). Devices using the *4-his* GL-maquette as well as devices with *cysGL*-maquette with two bound gallium porphyrin and two bound zinc porphyrin per maquette respectively, would complete the series of devices. If these studies were to be completed, in conjunction with direct evidence for electron transfer between the zinc and gallium porphyrins, a true representation of the extent of differential binding within maquettes for light-harvesting capabilities could be determined.

## 4- Conclusions; Gallium Based Porphyrin-Maquette Ensembles

Work presented here gives evidence that gallium porphyrin can be used for light-harvesting within DSSCs (albeit lower in efficiency than zinc porphyrin counterparts; see Chapter VII). Furthermore, a gallium porphyrin can be successfully incorporated into a maquette through bis-His ligation, with the employment of gallium porphyrin-maquette ensembles increased the  $V_{oc}$ , FF, and electron lifetime compared to devices with the dye directly bound to the surface. However, the quantity of photoactive material was drastically reduced when ensembles were employed, with only a relatively small decrease in  $J_{sc}$ , indicating that the ensembles can effectively inject electrons into the CB of  $TiO_2$ .

It was shown that the differential ligation of two differing metallic porphyrins into a single maquette based on the affinity for either a bis-histidinal or single-histidinal ligation can be achieved. Utilising the preference of a gallium porphyrin for bis-His ligation, the dye can be site directed in a specifically designed maquette, with subsequent incorporation of a single-His ligating porphyrin (in this case, a zinc porphyrin). Furthermore, the resulting ensemble was successfully immobilized onto an electrode and developed into a DSSC. This work presents the possibility of exploring differential binding to increase light-harvesting capabilities of maquettes in DSSCs. If porphyrins are specifically designed to have distinctly different absorbance spectra while allowing for differential binding, the absorbance can potentially be significantly broadened.

The successful differential binding of porphyrins into maquettes, with subsequent employment within DSSCs provides the opportunity to develop devices more closely aligned to natural photosystems within nature. Specifically, the energy of arrays that capture the sunlight is directed towards a central moiety, known as the reaction centre, through a funnelling effect. With differential binding within maquettes and potential for custom designed porphyrins, this process could be employed in future light-harvesting devices.

## 5- References; Gallium Based Porphyrin-Maquette Ensembles

1. Shifman JM, Moser CC, Kalsbeck WA, Bocian DF, Dutton PL: **Functionalized de Novo Designed Proteins: Mechanism of Proton Coupling to Oxidation/Reduction in Heme Protein Maquettes.** *Biochemistry* 1998, **37**(47):16815-16827.
2. Solomon LA, Kodali G, Moser CC, Dutton PL: **Engineering the Assembly of Heme Cofactors in Man-Made Proteins.** *Journal of the American Chemical Society* 2014, **136**(8):3192-3199.
3. Gibney BR, Isogai Y, Rabanal F, Reddy KS, Grosset AM, Moser CC, Dutton PL: **Self-assembly of heme A and heme B in a designed four-helix bundle: implications for a cytochrome c oxidase maquette.** *Biochemistry* 2000, **39**(36):11041-11049.
4. Sharp RE, Diers JR, Bocian DF, Dutton PL: **Differential binding of iron (III) and zinc (II) protoporphyrin IX to synthetic four-helix bundles.** *Journal of the American Chemical Society* 1998, **120**(28):7103-7104.
5. Sander JKM, Bampos N, Clyde-Watson Z, Darling SL, Hawley JC, Kim H-J, Mak CC, Webb SJ: **Axial Coordination Chemistry of Metalloporphyrins.** In: *The Porphyrin Handbook*. Edited by Kadish KM, Van Caemelbecke E, Royal G, vol. 3. San Diego: Academic Press; 2000.
6. Gibney BR, Mulholland SE, Rabanal F, Dutton PL: **Ferredoxin and ferredoxin-heme maquettes.** *Proceedings of the National Academy of Sciences of the United States of America* 1996, **93**(26):15041-15046.
7. Gibney BR, Dutton PL: **Histidine placement in de novo-designed heme proteins.** *PRS* 1999, **8**(09):1888-1898.
8. Constant LA, Davis DG: **Electrochemical characterization of iron porphyrin complexes in aprotic solvents.** *Analytical Chemistry* 1975, **47**(13):2253-2260.
9. Hagfeldt A, Boschloo G, Sun L, Kloo L, Pettersson H: **Dye-Sensitized Solar Cells.** *Chemical Reviews* 2010, **110**(11):6595-6663.
10. Lin C-Y, Lo C-F, Hsieh M-H, Hsu S-J, Lu H-P, Diao EW-G: **Preparation and Photovoltaic Characterization of Free-Base and Metallo Carboxyphenylethynyl**

- Porphyrins for Dye-Sensitized Solar Cells.** *Journal of the Chinese Chemical Society* 2010, **57**(5B):1136-1140.
11. Xiang N, Zhou W, Jiang S, Deng L, Liu Y, Tan Z, Zhao B, Shen P, Tan S: **Synthesis and characterization of trivalent metal porphyrin with NCS ligand for application in dye-sensitized solar cells.** *Solar Energy Materials and Solar Cells* 2011, **95**(4):1174-1181.
  12. Bisquert J, Fabregat-Santiago F, Mora-Seró I, Garcia-Belmonte G, Giménez S: **Electron Lifetime in Dye-Sensitized Solar Cells: Theory and Interpretation of Measurements.** *The Journal of Physical Chemistry C* 2009, **113**(40):17278-17290.
  13. Nappa M, Valentine JS: **The influence of axial ligands on metalloporphyrin visible absorption spectra. Complexes of tetraphenylporphinatozinc.** *Journal of the American Chemical Society* 1978, **100**(16):5075-5080.
  14. Qin L, Kostic NM: **Photoinduced electron transfer from the triplet state of zinc cytochrome c to ferricytochrome b5 is gated by configurational fluctuations of the diprotein complex.** *Biochemistry* 1994, **33**(42):12592-12599.

# **Chapter IX**

## **Future Prospects**

The aim of this thesis research was to develop an artificial photosynthetic reaction centre that could allow effective charge separation with the potential to implement this in a variety of processes such as solar cells and photocatalytic devices. The development of such a system was explored using porphyrins as the light harvesting component of the reaction centre and maquettes, small artificial proteins, as the conduit within which charge separation could be achieved and maintained. While a number of studies had explored the binding of various chromophores into maquettes [1], there had not been a methodical investigation into the type and structure of chromophores that would optimally bind to maquettes.

The study of porphyrin-maquette binding looked specifically at the hydrophobic partitioning of porphyrins within maquettes in order to facilitate axial ligation between the central metal of porphyrins with histidine residues within the maquette. It was found that the maquettes tolerated a diversity of porphyrin amphiphilic structures and some of the resulting porphyrin-maquette ensembles were shown to be capable of photoactivation and charge transfer. However, a more detailed understanding of the forces and parameters influencing coordination of cofactors within maquettes would allow for the development of specialised and tailored cofactors (porphyrins) to be produced, capable of ligation within maquettes to fulfil a specific function, such as driving catalytic reactions. For example, iron porphyrins have been extensively used to catalyse CO<sub>2</sub> reduction and would be expected to form stable porphyrin-maquette complexes as was shown here for the gallium porphyrin-maquettes.

It was demonstrated that the incorporation of porphyrins into maquettes resulted in a light-absorbing ensemble, which could effectively be utilised within a device to produce photovoltaic responses. These types of ensembles are akin to man-made versions of the reaction centre found within natural photosystems, essentially a light-harvesting and charge separating entity. Nonetheless, there is great potential to improve the efficiency and light harvesting capability of the porphyrin through the use of variously functionalised porphyrins or other metals. With porphyrin-maquettes shown to be immobilised onto a TiO<sub>2</sub> surface both electrostatically and covalently, future work should focus on immobilization onto other semiconductor surfaces such as ZnO. This might be particularly significant since ZnO does not tolerate highly acidic dyes of the type normally used for semiconductor sensitisation.

Furthermore, the immobilized porphyrin-maquette ensemble should be investigated for potential use as a 'reaction centre', whereby the electrons obtained are used with a catalyst for some form of photocatalytic reaction. The use of maquettes in such systems is potentially

promising, since we have found in this work that the porphyrin-maquette on the TiO<sub>2</sub> surface reduces electron recombination, with such detrimental processes being a significant issue for catalytic reactions when using dyes on semiconductors [2].

The incorporation of porphyrin dyads into maquettes through hydrophobic partitioning and axial metal ligation was achieved within this study. The advantage of using dyads is that they inherently contain a larger absorbance spectrum cross section, which could harness more of the incident light compared to single monomeric porphyrin entities, translating to higher light-harvesting ability [3]. Further experimentation to implement dyad-maquette ensembles for light-harvesting should be undertaken. Specifically, dyad-maquette ensembles in DSSCs should be analysed with comparisons to dyads without maquette (as was undertaken in this study with monomeric porphyrins). The potential intra- and inter-molecular electron transfer processes occurring with the dyads should also be examined using spectroscopic studies. If these experiments could be achieved, larger porphyrin ‘arrays’ could be investigated for incorporation and use with maquettes for light-harvesting.

Differential binding to site-specific histidines residues within maquettes was shown through the use of different metallic centres of porphyrins (zinc and gallium). Although the use of differentially bound porphyrin into maquettes was successfully utilised for light-harvesting in a DSSC, further experimentation and analysis is needed to ascertain the true extent of using differentially bound porphyrin in light-harvesting devices. Similar to dyads, differentially bound porphyrins have a larger absorbance cross section, which could harness more of the incident light compared to single porphyrin entities. Furthermore, the two different porphyrins could potentially be designed to promote either energy or electron transfer from one entity to the other upon irradiation, therefore directing the harnessed light in a similar manner as in natural photosystems. Further research and analysis of the use of differentially bound porphyrins within maquettes was outlined in Section 3 of Chapter VIII.

With the factors affecting porphyrin and dyad porphyrin incorporation within maquettes better understood, the development of more complex porphyrin arrays could potentially be developed, with hydrophobic functionality driving incorporation and ligation with maquettes (Figure IX-1a). Furthermore, if the metallic centre of the porphyrin arrays were different, differential binding to either bis-his or single-his sites could be exploited, so that ensembles with specific binding sites for the different porphyrin arrays could produce a controlled binding. If the energy levels of these two porphyrin arrays were appropriately aligned (predominantly

the LUMO levels), electron transfer from one array (photoexcited) to the second could ensue (Figure IX-1b). However, the second array should still have a LUMO level, which would effectively inject electrons into the CB of the semiconductor used. With the different energy levels of the porphyrin arrays, the absorbance spectrum would inherently be different too, which would further increase the light-harvesting capability of the possible ensemble due to the broadening of the absorbance spectrum (Figure IX-1c).

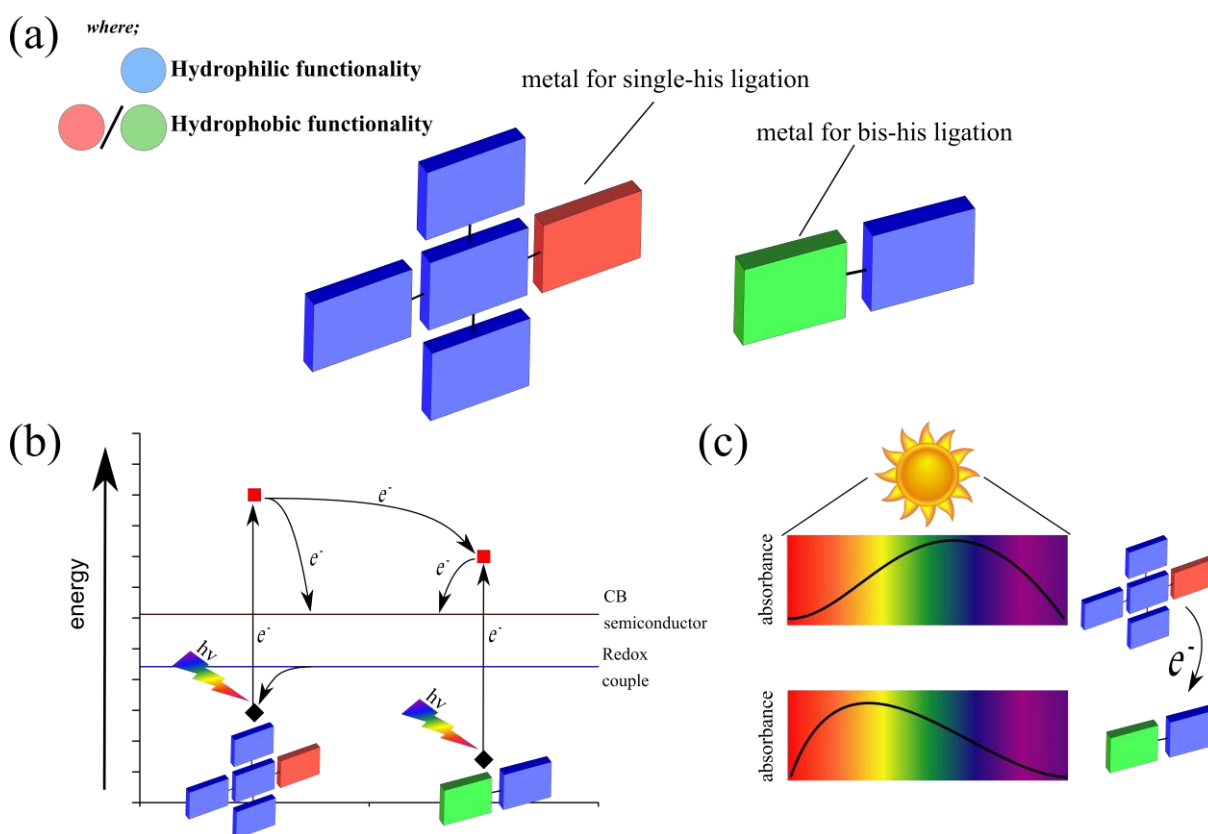


**Figure IX-1; Potential future design of porphyrin arrays for light harvesting and maquette binding.** (a) Porphyrin arrays designed for hydrophilic and hydrophobic functionality for facilitating ligation within maquettes, with metallic centres used for differential ligation to specific sites. (b) Differential binding of arrays could be exploited for electron transfer between array moieties. (c) Differential binding of arrays would increase the spectrum of light available for capture, with the porphyrin arrays containing different absorbance spectra.

The formation of an ensemble containing differentially bound porphyrin arrays could be oriented onto a semiconductor electrode (e.g. via a cysteine residue, as described within this study), thereby orienting the ligated porphyrin arrays (Figure IX-2). With the orientation appropriately positioned on the electrode, electrons could flow from the most distant porphyrin array to the proximal array followed by injection into the electrode, resembling a funnelling



effect (Figure IX-2). If electrons are able to flow effectively in this prospective device, and the energy levels were appropriate, the use of catalysts could be implemented. Ideally, the light-harvesting device would be in an aqueous environment, with a water oxidising catalyst used to donate electrons to the photoexcited distal array, resulting in electrons flowing to a second catalyst for proton reduction (or carbon fixing). This construct could potentially be implemented for new sources of renewable energy, closely aligned to the processes involved within nature.

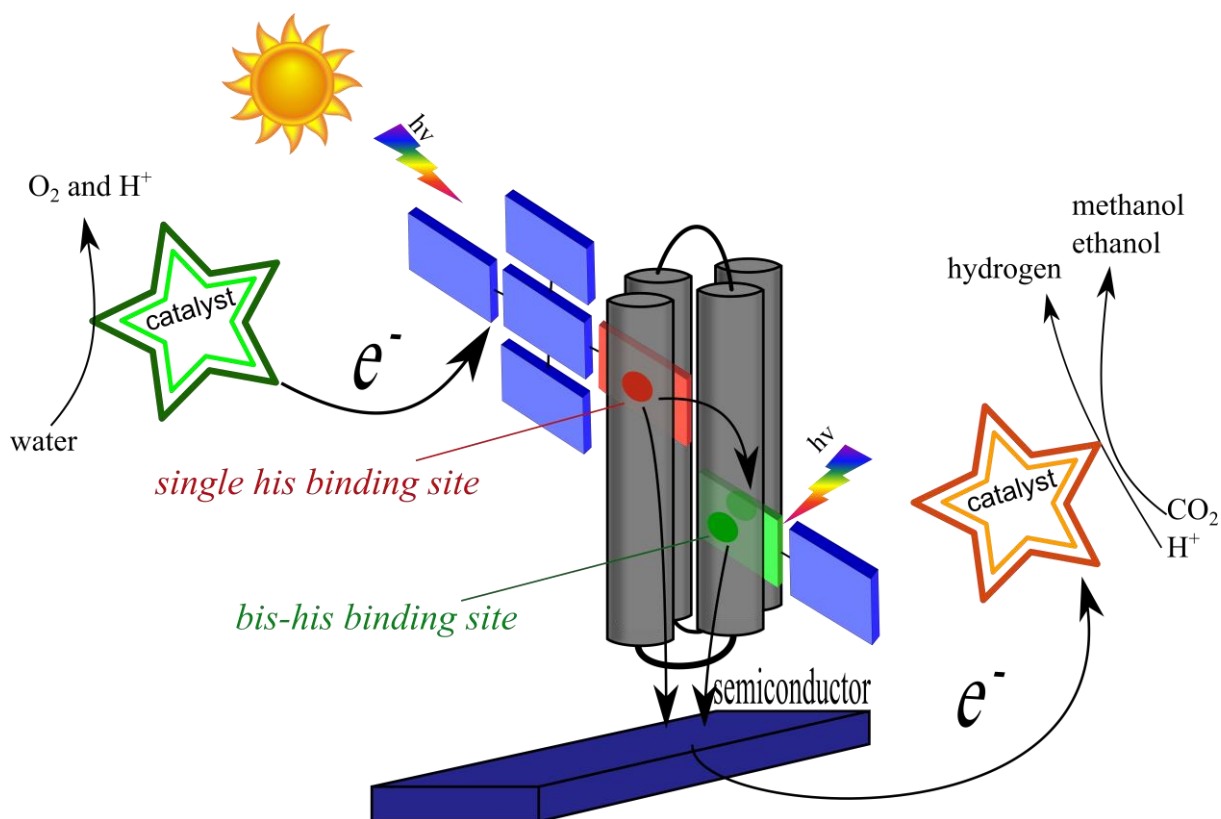


**Figure IX-2; Schematics for potential future application of maquettes with porphyrin arrays for catalytic reactions.** Orientation of maquette onto a semiconductor would result in an electron tunnelling effect, potentially applicable in catalysis.

## References- Future Prospects

1. Farid TA, Kodali G, Solomon LA, Lichtenstein BR, Sheehan MM, Fry BA, Bialas C, Ennist NM, Siedlecki JA, Zhao Z *et al.*: **Elementary tetrahelical protein design for diverse oxidoreductase functions.** *Nature Chemical Biology* 2013, **9**(12):826-833.
2. Gross MA, Reynal A, Durrant JR, Reisner E: **Versatile Photocatalytic Systems for H<sub>2</sub> Generation in Water Based on an Efficient DuBois-Type Nickel Catalyst.** *Journal of the American Chemical Society* 2014, **136**(1):356-366.
3. Mozer AJ, Griffith MJ, Tsekouras G, Wagner P, Wallace GG, Mori S, Sunahara K, Miyashita M, Earles JC, Gordon KC: **Zn–Zn porphyrin dimer-sensitized solar cells: toward 3-D light harvesting.** *Journal of the American Chemical Society* 2009, **131**(43):15621-15623.